Research@ARL

Volume 3, Issue 2, July 2014

Materials Modeling at Multiple Scales

Dr. Jan W. Andzelm, Dr. George A. Gazonas, and Dr. James W. McCauley

Editors-in-Chief

$$\nabla \cdot \sigma + \rho \mathbf{b} = \rho \dot{\mathbf{v}}$$

$$E\Psi(\mathbf{r}) = \left[\frac{-\hbar^2}{2m}\nabla^2 + V(\mathbf{r})\right]\Psi(\mathbf{r})$$

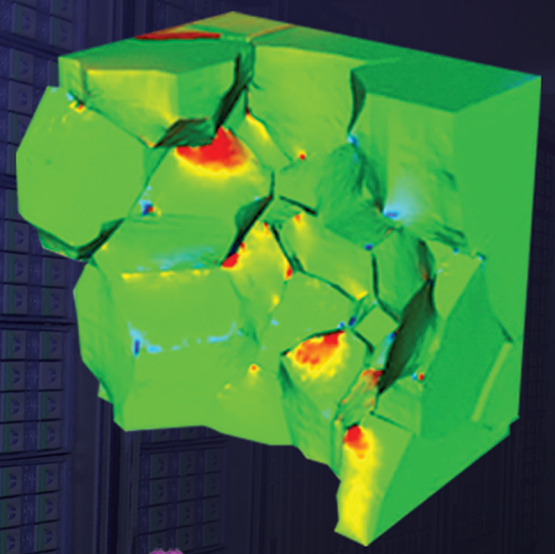

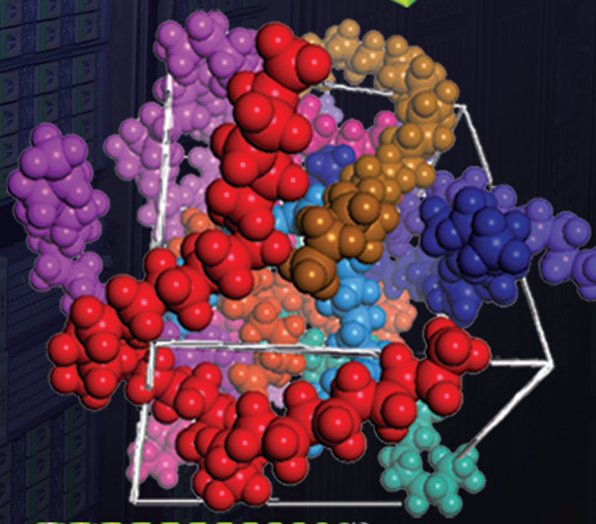

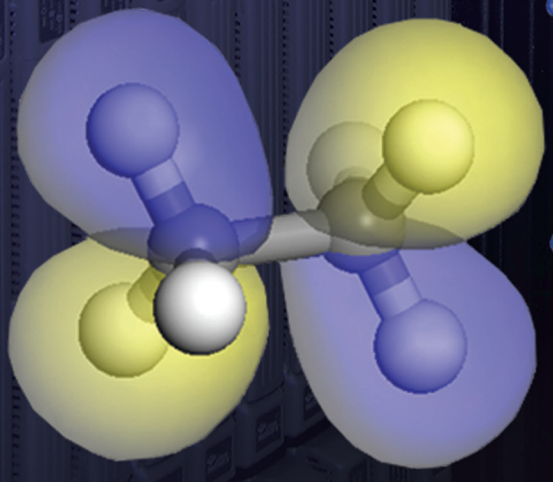

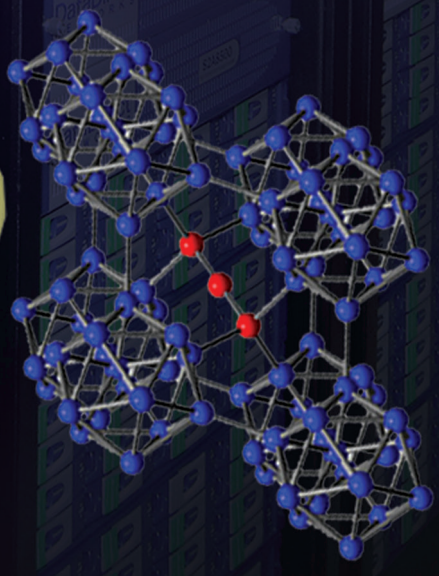

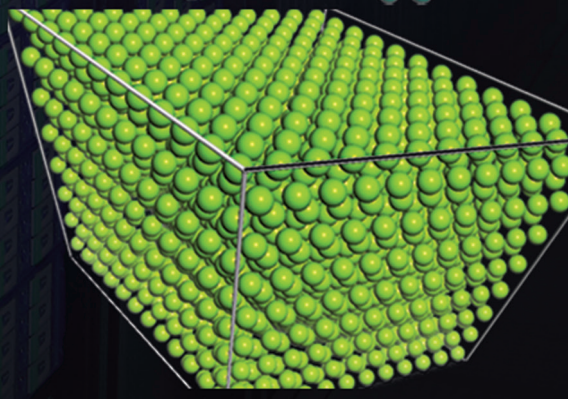

U.S. Army Research Laboratory

Editorial Board

Dr. Jan W. Andzelm
Editor-in-Chief

Dr. George A. Gazonas
Editor-in-Chief

Dr. James W. McCauley
Editor-in-Chief

Advisory Board

Dr. Kwong K. Choi
Dr. Brad E. Forch
Dr. Piotr J. Franaszczuk
Dr. Shashi P. Karna
Dr. Stephen J. Lee
Dr. Joseph N. Mait
Dr. Nasser M. Nasrabadi
Dr. Peter J. Reynolds
Dr. Ananthram Swami
Dr. Bruce J. West

Research@ARL can be accessed electronically at **www.arl.army.mil/ResearchARL**

Research@ARL

Materials Modeling at Multiple Scales • 2014

contents

contents

Introduction to ARL

The Army Research Laboratory of the U.S. Army Research, Development and Engineering Command (RDECOM) is the Army's corporate laboratory. ARL's research continuum focuses on basic and applied research (6.1 and 6.2) and survivability/lethality and human factors analysis (6.6). ARL also applies the extensive research and analysis tools developed in its direct mission program to support ongoing development and acquisition programs in the Army Research, Development and Engineering Centers (RDECs), Program Executive Offices (PEOs)/Program Manager (PM) Offices, and Industry. ARL has consistently provided the enabling technologies in many of the Army's most important weapons systems.

The Soldiers of today and tomorrow depend on us to deliver the scientific discoveries, technological advances, and the analyses that provide Warfighters with the capabilities to execute full-spectrum operations. ARL has Collaborative Technology Alliances in Micro Autonomous Systems Technology, Robotics, Cognition and Neuroergonomics, Network Science, an International Technology Alliance and new Collaborative Research Alliances in Multiscale Multidisciplinary Modeling of Electronic Materials and Materials in Extreme Environments. ARL's diverse assortment of unique facilities and dedicated workforce of government and private sector partners make up the largest source of world class integrated research and analysis in the Army.

ARL Mission

Discover, Innovate, and Transition Science and Technology to Ensure Dominant Strategic Land Power.

Our Vision

The Nation's Premier Laboratory for Land Forces.

ARL's Organization

- Army Research Office (ARO) - Initiates the scientific and far reaching technological discoveries in extramural organizations: educational institutions, nonprofit organizations, and private industry.
- Computational and Information Sciences Directorate - Scientific research and technology focused on information processing, network and communication sciences, information assurance, battlespace environments, and advanced computing that create, exploit, and harvest innovative technologies to enable knowledge superiority for the Warfighter.
- Human Research and Engineering Directorate - Scientific research and technology directed toward optimizing Soldier performance and Soldier-machine interactions to maximize battlefield effectiveness and to ensure that Soldier performance requirements are adequately considered in technology development and system design.
- Sensors and Electron Devices Directorate - Scientific research and technology in electro-optic smart sensors, multifunction radio frequency (RF), autonomous sensing, power and energy, and signature management for reconnaissance, intelligence, surveillance, target acquisition (RISTA), fire control, guidance, fuzing, survivability, mobility, and lethality.
- Survivability/Lethality Analysis Directorate - Integrated survivability and lethality analysis of Army systems and technologies across the full spectrum of battlefield threats and environments as well as analysis tools, techniques, and methodologies.
- Vehicle Technology Directorate - Scientific research and technology addressing propulsion, transmission, aeromechanics, structural engineering, and robotics technologies for both air and ground vehicles.
- Weapons and Materials Research Directorate - Scientific research and technology in the areas of weapons, protection, and materials to enhance the lethality and survivability of the Nation's ground forces.

ARL Workforce in 2014

- 1,835 Civilians - 32 Military
- 1098 Contractors (1051 full-time/47 part-time)
- 1,379 Research Performing Workforce
- 552 (40%) hold PhDs
- 10 STs / 24 ARL Fellows

ARL's Primary Sites

- Aberdeen Proving Ground, MD
- Adelphi Laboratory Center, MD
- White Sands Missile Range, NM
- Raleigh-Durham, NC
- Orlando, FL

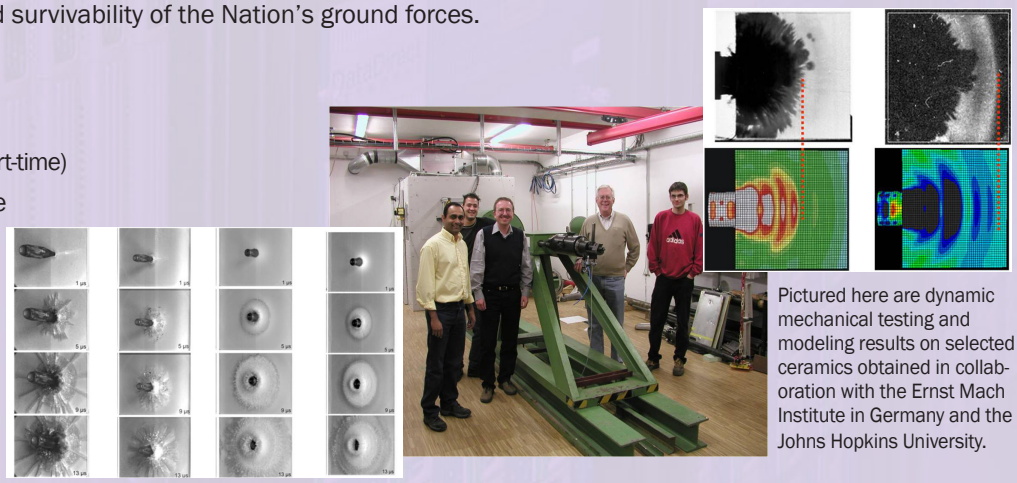

Pictured here are dynamic mechanical testing and modeling results on selected ceramics obtained in collaboration with the Ernst Mach Institute in Germany and the Johns Hopkins University.

Unique ARL laboratory facilities and modeling capabilities provide our scientists and engineers with a world-class research environment. For more information about our facilities, please visit: **https://arlinside.arl.army.mil/inside/labops/PublicAffairs/docs/ARLFacilitiesBook.pdf**

Visit ARL's website at **www.arl.army.mil**

ARL

U.S. ARMY RESEARCH LABORATORY

FOREWORD

Welcome to our most recent edition of the Research@ARL: Materials Modeling at Multiple Scales. Throughout human existence, human beings have used natural (arrow heads) and synthetic (Samurai sword) materials for economic advantage as well as preserving their security.

Materials are ubiquitous in all Army materiel. The Army's critical needs relate to the development of advanced materials for sensors, devices, power and energy, as well as for lightweight vehicle and Soldier protection. The performance and function of every Army system is determined by the underlying properties of the materials and the (structural/electrical) design of the engineering system. In turn, the properties of the materials themselves are a product of the hierarchy of structures found within. From atoms, to molecules, to crystals, to grains, to laminates, etc., the final performance of any system is a "sum of the parts" of the underlying physics down to the smallest level. The potential to gain extraordinary component or system improvements through the effective design and control of the constituent materials remains untapped. Enabling the design of these hierarchical materials structures in concert with the overall design and function of the system will allow for transformational gains in the performance of Army materiel.

The refinement and revolutionary development of new materials can be significantly accelerated with the appropriate use of modeling and simulation at scales that encompass the atomic, single crystal, microstructure, macrostructure and material assembly scales. Success in this activity will make possible a "Materials by Design" process to predict performance and design materials from the atomic to the macroscopic scale for a particular suite of mechanisms and properties that are required for defined performance/applications. Our researchers are at the forefront of this multidisciplinary activity that will dramatically influence the way the U. S. Army operates in the 10, 20 and 30 year time periods.

To achieve these goals, ARL initiated its transformational materials science and engineering program, the "Enterprise for Multiscale Research in Materials," which includes Collaborative Research Alliances in Materials in Extreme Dynamic Environments and Multiscale Modeling of Electronic Materials and also Multiscale Research in Energetic Materials, all supported by in-house development of cross-cutting, multiscale computational science, including advances in physics based algorithms in materials to enhance computational discovery.

The U.S. Army has been a worldwide leader in transformational computer computational processes since funding the development of the ENIAC computer that was used for scientific modeling at the Aberdeen Proving Ground from 1947 until 1955. The ENIAC used fully electronic switches vacuum tubes which resulted in a gigantic 30-ton machine that occupied 1,800 square feet of space. ENIAC was able to perform approximately 400 operations per second, such as multiplications, so we could classify the ENIAC as a 400 floating point operations per second (FLOPS) computer. Currently, ARL researchers have access to petaflop computers, a quadrillion (10^{15}) FLOPS and expect to use a thousand times more powerful exaflop computers within a decade. This ever increasing power of next generation of supercomputers coupled with revolutionary enhancements of computational multiscale methodologies, which are also being developed at ARL, will enable unprecedented transformational change in designing novel materials.

This monograph is a compendium of recent peer-reviewed publications by our scientists and engineers in a variety of archival journals and represents highlights of the best of the ARL efforts in this area. Included are highlights of modeling at a variety of scales in molecular complexes, non-crystalline (amorphous) materials, polymers, ceramics, metals and composites. I hope that you will enjoy perusing the articles contained herein and have some sense of the advances our scientists and engineers are making that will ensure the technological superiority of our warfighter.

Dr. Thomas P. Russell
Director, U.S. Army Research Laboratory

Introduction to ARL Research in Materials Modeling at Multiple Scales
by Dr. Jan W. Andzelm, Dr. George A. Gazonas and Dr. James W. McCauley

1. Introduction and Background

The discovery of novel materials enables advancement in weapon technologies as the history of one of the most important and most beautiful weapons, the sword, shows. Daggers made during the Bronze Age were too brittle. The advent of the Iron Age allowed transformation of the dagger into a powerful cutting weapon, the sword. Adding 0.2-1.2 percent of carbon and improving processing conditions (quenching, tempering) resulted in hard and versatile steel swords.[1] The uniform distribution of carbon throughout the iron gave rise to wootz steel, one of the best materials for swords in antiquity. The improvements in the materials were followed by advancements in sword design to produce lighter and more lethal weapons. The crucial issue for sword design is the center of percussion, the strike point on the blade, where the shock felt by a swordsman is minimized as he strikes a target. The sword design evolved empirically over many centuries until the Renaissance, when giants such as Galileo attempted to understand sword dynamics. At present, using Newtonian dynamics and knowing material properties, we can computationally design the sword and predict the optimal location of the center of percussion.[1] Yet many mysteries of the techniques of medieval swords craftsmen still remain to be rediscovered such as the processing technique that led to the insertion of carbon nanotubes and cementite nanowires in the steel of Damascus blades — one of the most advanced sabres of all time.[2] Clearly, material characteristics at the small atomic level impact material performance at larger, macroscopic scales, and therefore understanding this relation calls for multiscale research.

The U.S. Army Research Laboratory (ARL) recognizes the importance of rational and comprehensive materials development. This recognition is evidenced by establishing the Enterprise for Multiscale Research of Materials, which include the MEDE (Materials in Extreme Dynamic Environments) and MSME (Multiscale Multidisciplinary Modeling of Electronic Materials) programs. These programs focus on the development of revolutionary materials for Soldier protection, in categories such as metals, ceramics, polymers and composites, as well as materials for energy, power and sensor applications. The main stages of a Materials by Design approach, which is the foundation of the program, are modeling and simulations, bridging the scales, multiscale material characteristics and metrics, synthesis and processing and advanced experimental techniques. These stages are pursued within those initiatives. The state of the art in multiscale research in materials, including leading ARL contributions in the MEDE program, is being showcased at the annual MACH conference.[3] Multiscale modeling and simulations have become one of the main stages for advanced material development, and they are recognized as a critical component of the Integrated Computational Materials Engineering (ICME), [4] as well as Material Genome, initiative. In the 20th century, advances in computer hardware, software, and theory enabled multiscale physics-based predictive modeling to become a transformational component of the materials development process.

2. Materials Modeling in Materials Science

The hypothesis that all materials around us are composed of small particles, i.e., atoms, that cannot be divided further, is credited to the Greek philosopher Democritus who lived more than 2400 years ago. However, only with the advent of quantum mechanics (QM) in the 20th century was the true structure of atoms understood. Isaac Newton postulated the existence of forces between atoms. Since atoms have masses, the assembly of atoms can move according to Newton's equations of motion. QM better describes the forces between atoms as a result of interactions between electrons, and the nuclei represented with a wave function as they move according to Schrödinger's equation of motion. Thus, the solution of Newton's and Schrödinger's equations give rise to atomistic and QM modeling of materials, respectively. At the higher scales, beyond atoms, the finite element method (FEM) is typically used to describe continuous media. In this method, the continuum is discretized into various geometries that represent the global structure to be modeled — which is subjected to Newton's laws of motion, the laws of thermodynamics, and possibly even Maxwell's equations.

QM modeling is concerned with studying properties of materials at the angstrom length scale (10^{-10} m) and time events of femtoseconds (10^{-15} s). Quantum chemistry or solid state physics study events such as molecular or

crystal structures, chemical reactions and electronic transitions. At the atomistic modeling level, the length scale events are at nanometer range (10^{-9} m) and the time events probe molecular dynamics (MD) for nanoseconds (10^{-9} s). The sophisticated theories and algorithms implemented for parallel (computer processors operating at the same time on different parts of the overall problem) supercomputers can extend applicability of these techniques for systems much larger and events much slower for several orders of magnitude. Simulations that reach micrometer length (10^{-6} m) and microseconds (10^{-6} s) are typically referred to as mesoscale calculations. The macroscale simulations can extend the temporal and length scales farther to meters and minutes and beyond. The fact that features and processes occurring at angstrom and femtosecond scales impact material behavior at larger space and time scales gave rise to multiscale modeling.[6]

The key challenge for multiscale modeling is scale bridging, for example, passing information about behavior of atoms described at the lower QM scale to the next higher atomic scale. It might be tempting to contemplate simulations only at the most fundamental QM level. However, this is impractical due to the high cost of simulations, because properties of large ensembles of atoms are often unnecessary, and governed by different physical phenomena. For example, the energy of covalent bonds (e.g., C—C bond in the ethane molecule, CH_3—CH_3) is ~85 kcal/mol, while the interaction between two methane molecules (CH_4 — CH_4) is weak and amounts to ~2 kcal/mol, and is comparable with thermal energy at room temperature. Therefore, processes in hard materials (molecules and solids) with many covalent bonds are dominated by their energy landscape, while for soft materials (polymers and proteins) entropy (increasing disorder) dominates the material behavior. Multiscale modeling can be divided roughly into two categories: sequential (or hierarchical) and concurrent. In sequential multiscale modeling, the higher-level model uses homogenized relations from a more detailed, lower-scale model while the concurrent model is two-way coupled and uses input from the lower-scale model to calculate larger-scale properties on-the-fly as the computation proceeds.

The importance of multiscale modeling was finally recognized by a most recent 2013 Nobel Prize in Chemistry awarded to Martin Karplus, Michael Levitt and Arieh Warshel "for the development of multiscale models for complex chemical systems."

Professor Gunnar Karlstrom, on delivering the presentation speech for the 2013 Nobel Prize in Chemistry at the Stockholm Concert Hall, noticed that today's chemistry has merged with other disciplines of physics and biology, and has been advanced and profoundly influenced by ever faster, computers. The 2013 Nobel laureates had made seminal contributions at the intersection of chemistry, physics, biology and computer science.

In the Nobel lectures, laureates presented their work to bridge temporal and length scales between atomistic and mesoscale models of biological systems, such as proteins and enzymes.[7] The Newtonian dynamics with atomic representation of systems was used for short time scales, while other techniques, such as Brownian motion dynamics or Monte Carlo statistical methods, had to be applied to long-time simulations. The details of bond breaking occurring during reactions were studied by using QM methods embedded into an atomistic environment (QM/Molecular Mechanics). Scale bridging for the 2013 Nobel Prize research was accomplished through sequential means. The QM calculations led to approximate interactions between atoms with the so-called force-field that facilitated simulations at the atomistic-scale level. Next, the atoms of a system were divided into groups of atoms (referred to as coarse graining in this work), and the atomistic simulations helped to parameterize interactions for these coarse-grained mesoscale simulations.

The impact of QM modeling on chemistry and physics was also recognized by the 1988 Nobel Prize in Chemistry, which was awarded to Walter Kohn for his development of density-functional theory (DFT) and John Pople for his development of computational methods in quantum chemistry.

The most popular QM methods used at ARL rely on two fundamental quantities describing the motion of electrons in a molecule or solid, the wave function (Ψ) and the electron density (ρ). These quantities can be obtained by solving quantum-mechanical equations, and they are related as the square of the wave function which defines the probability of finding an electron at a particular position in a molecule. The wave function of a system can be ob-

tained by solving Schrödinger equations, which are readily available in numerous solid-state physics and quantum chemistry programs. John Pople, the 1988 Nobel laureate, made seminal contributions to the theory and practical applications in the quantum chemistry field.

Walter Kohn, Pierre Hohenberg, and Lu Jeu Sham in 1964 and 1965 showed that quantum-mechanical equations can be efficiently approximated by containing all of the many-body interactions in an exchange-correlation energy (E_{xc}), which depends on the electron density of the simulated system. Unlike the wave function Ψ, which is a function of the position of all electrons in the system, the electron density ρ is only a function of three positional coordinates. Therefore, the DFT equations can be programmed much more efficiently and applied to more complex solid and molecular systems of practical importance for materials science. Today, most quantum mechanical calculations are performed by using the DFT method. [8,9]

Zienkiewicz[10] attributes the origins of modern computational FEMs to the weighted residual methods of Gauss in 1795, the variational methods of Lord Rayleigh in 1870, and the finite difference methods of Richardson in 1910. Yet the term "finite element method" was coined by Ray Clough in 1960. Legacy FEMs employ macrophenomenological continuum-scale constitutive (stress-strain response) and failure models that exclude smaller spatio-temporal scales needed for the optimal design of new high-performance Army materials. Furthermore, in his monograph on composites, Milton[11] states in his account of the classic heat conduction problem of Tartar that "if one seeks the optimal configuration by using the standard finite elements (FE) numerical approach, the result will be a configuration with a microstructure on the same length scale as the FE, indicating that the FE approach is unreliable." Despite this, material modeling at the global scale is dominated by computational FE solvers (codes) which have been under continuous development since the early 1970s. The codes provide deterministic solutions to boundary value problems governed by the field equations, which include those of kinetics, kinematics, thermodynamics, and material constitution. Regarding material constitution, the codes utilize a number of "hydrodynamic" models for the deviatoric behavior of the material, e.g., Johnson-Cook, Zerilli-Armstrong, Steinberg-Guinan, and Mechanical Threshold Stress, that require definition of a separate set of equations (equations of state) for characterizing the volumetric material behavior, e.g., linear polynomial, Jones-Wilkins-Lee, Gruneisen, etc.

Material failure models in continuum FEMs have been classically treated using continuum damage mechanics (CDM) which employs algorithms that degrade element strength, and are dependent upon effective plastic strain or volumetric strain. In addition, material failure can be coupled to spall (tensile failure) models that are dependent upon user-specified limits on hydrostatic tension or maximum principal stress. However, cohesive zone (CZ) elements and extended finite elements (XFEM) are gradually replacing CDM in large-scale FE codes for modeling fracture and the influence of pre-existing defects on material behavior. Implementation of CZ or XFEM into large-scale FE codes requires considerable code reformulation since the production of new surface area within a finite element mesh poses special programming challenges for codes running on modern parallel architectures. Finally, continuum element erosion (deletion) or conversion to particles can occur in highly deformed regions of the mesh as a result of projectile impact and penetration. The complex many-body contact problem also introduces additional challenges for finite element solution of the already highly nonlinear boundary value problem.

3. Materials Modeling at Multiple Scales at ARL

For more than 20 years researchers at ARL have been studying materials of Army significance with the help of modeling at various scales, from quantum, through atomistic, mesoscale to macroscale using FE techniques. This monograph intends to present representative examples of the most recent achievements of ARL scientists in modeling of the major classes of materials, and the underlying theoretical and computational research performed at ARL.

3.1 Molecular complexes

Molecules are building blocks of many important Army materials. These include molecular crystals used as energetic materials or in thin film flexible electronics, while molecules with nitrogen atoms have applications as propellants in rocket propulsion systems. Performance of electrical storage devices depends on electrochemical

properties of electrolyte molecules. A variety of molecules are used as adhesives, corrosion inhibitors or surface passivation agents. In most calculations on molecules, accurate quantum mechanical methods are used to predict structural, optical and magnetic properties as well as reactivity of molecular systems. At the higher level of multiscale, atomistic simulations often using polarizable or reactive potentials are applied.

Electrical energy storage devices are critical for the success of the Army's mission. Lighter and safer batteries are essential for lightening the warfighter burden. Improvement of battery materials presents a difficult multiphysics and multivariable problem, including designing the electrolytes possessing high ionic conductivity, low viscosity, and good thermal and electrochemical stability and, importantly, being compatible with electrodes. As higher-energy density, high-voltage cathodes are being developed, many standard electrolytes become unstable and undergo oxidative decomposition. Xing and Borodin (2012) — (these references refer to publications in this monograph) — studied oxidation stability and induced decomposition of ethylene carbonate (EC) by determining reaction paths and transition states of various reactions. They used first principles (DFT) and ab initio quantum mechanical techniques, including solvent environment via a polarized continuum model. They concluded that more expensive ab initio calculations support the reaction mechanism predicted from DFT calculations. The key finding was that two EC molecules undergo a concerted oxidation reaction yielding CO_2 and an ethanol radical cation followed by the deprotonation of EC. This deprotonation reaction significantly diminished the oxidation stability of EC. DFT calculations suggested a mechanism for formation of oligo (EC) on the cathode surface that has been observed in recent experiments. Knowledge of electrolyte stability and decomposition is critical for design of novel electrolytes that will be compatible with the high-voltage cathodes.

As most electrolytes are unstable at the graphite and silicon anodes, they decompose and form a solid electrolyte interphase (SEI). The optimal SEI should form a stable electronically insulating, but ionically conducting, layer on the anode surface. Previous experimental work performed at ARL identified dilithium ethylene dicarbonate (Li_2EDC) as one of the major SEI compounds. The conductivity of the lithium ion through Li_2EDC was studied by Borodin et al. (2013) using atomistic MD with the many body polarized APPLE&P® force field.

The accuracy of the force field was improved by adjusting parameters to reproduce the binding energies in lithium carbonate models obtained from extensive ab inito calculations. It was found that ab initio results agree well with the latest DFT potentials. The use of a polarizable force field was confirmed to be of key importance as nonpolarizable force field performed exceptionally poorly for this process. The Li ion transport and conductivity calculated as a function of temperature, and was found it to be in good agreement with experimental data. The novel mechanism of the Li ion motion, such as chainlike or loop-like hopping, was discovered. In addition to improving the understanding of the transport processes in SEI, this work resulted in a much-improved polarizable potential that will be applied to investigate other SEI model compounds to optimize battery interfacial resistance and to minimize battery charging time.

Defect nucleation and propagation in molecular crystals enhance mechanical ductility, which is a beneficial property for material processing but can also degrade the performance of, for example, optical and magnetic devices that contain them. It is therefore important to understand how defects initiate and propagate in such periodic crystalline molecular media. Fortunately, analytical models exist for the nucleation and growth of dislocations, and these can be used to verify atomistic simulations of such processes. The recent article by Munday et al. (2013) examines dislocation nucleation at the tip of a Mode II (shear stress) crack in explosive molecular RDX (cyclotrimethylenetrimitramine) crystals using the LAMMPS MD Simulator. The computational predictions of the generalized stacking fault energy curve induced by the crack are compared with Rice's continuum dislocation nucleation model derived using the J-integral and the Peierls concept relating periodic shear stress and atomic shear displacement on a slip plane in a ductile crystal. The authors find that molecular flexibility plays an important role in predicting the correct energy barrier to dislocation nucleation. This finding impacts research on other molecular crystals of importance to ARL.

To improve the lethality and survivability of its weapons systems, the U.S. Army is interested in developing propellant formulations for guns and rocket motors for tactical missiles with better performance properties than current standards but are less sensitive to ignition produced by various external stimuli. Gun and tactical rocket propel-

lant formulations generally fall into one of three application-defined categories. For gun and minimum-smoke rocket propulsion systems, the formulations' primary ingredients are usually nitrate esters, with nitrocellose and nitroglycerin being common. For high-performance rocket motors, ammonium perchloratep crystals are mixed with polymeric binders that serve as a fuel and provide needed mechanical properties. Lastly, more exotic rocket motor designs that employ pumpable liquid hypergolic bipropellants are being developed and tested. In these cases the fuels are liquid amines or hydrazines, and the oxidizer is red fuming nitric acid. In all cases, the formulations will also include catalysts, stabilizing agents and other additives to meet system requirements. However, propellant type, performance and sensitivity are not the only considerations. Issues ranging from the compatibility of a formulation's ingredients to their risks to human health and the environment must also be addressed. Thus, in the absence of an ability to predict such properties, trial and error approaches must be employed, making the development and qualification of new formulations for emerging technologies a costly and time-consuming undertaking.

To reduce the cost and accelerate the pace with which new propellant formulations can be developed and qualified, ARL has developed models to predict a wide variety of their properties. An Ordnance Environmental Program to prescreen candidate hydrazine-alternative hypergols, demonstrated new efficiencies by the application of this approach to material development. In this monograph, McQuaid et al. (2013) present a paper that provides an overview of the modeling of a critical determinant of a propellant's performance in a propulsion system, namely, the conversion of the propellant (and its stored chemical energy) into sensible heat and a gaseous working fluid. Starting from QM-level descriptions of the molecular potential energy surfaces upon which reactions may take place, reaction networks that can simulate the conversion were developed and employed as submodels in computational fluid dynamics models for system-level performance predictions and design guidance. Future studies will explore the generation and use of such reaction networks for prescreening the compatibility of formulation ingredients.

3.2 Non-crystalline (amorphous) materials

Non-crystalline (amorphous) ceramics or ceramic glasses are used in a variety of vital Army personnel, ground, and air vehicle applications that require transparent armor, which is ubiquitous in tactical vehicular windshields and side windows. For many years it has been known that the properties of glass can be modified and enhanced through compositional modification, chemical strengthening, annealing, and process control of melt cooling. In addition, certain glass formulations have been shown to exhibit enhanced performance against shaped-charge jets.

As such, an interdisciplinary research team was formed at ARL to develop a physics-based multiscale modeling methodology to compositionally design optimum glasses for ballistic and shaped charge jet applications and to predict the performance of glasses that have not yet been synthesized. It was discovered that classical MD potentials cannot predict the shock response of fused silica over the entire ballistic pressure range of interest (0 - 60 GPa), so a new pairwise potential was developed for silica by Izvekov and Rice (2012) that exhibits good transferability to various silica crystalline polymorphs and amorphous silica. It also reproduces the shock Hugoniot curve well at higher pressures. In a typical plate impact experiment a flat plate is propelled at various high velocities (which determine the pressure of impact), and the sample back face deflection is measured. The resulting curve normally exhibits a Hugoniot Elastic Limit at a characteristic pressure, where materials are not responding elastically to the impact pressure; basically, the shock Hugoniot is the locus of thermodynamic states accessible by shock loading from a given thermodynamic initial condition. The new potential has been parameterized to match the total force distribution along quantum mechanical trajectories for the system. The DFT, generalized gradient approximation (GGA) potential was used in this work to calculate the MD trajectory that was subsequently used to develop potentials by applying the multiscale coarse graining (MS-CG) variational approach. The mechanism of silica densification was revealed. Change in oxygen coordination to silicon cations (bonding to Si atoms) was seen as a function of increasing pressure. This paper demonstrates that systematic coarse-graining of DFT structural information can be successfully used to study glasses under high pressure relevant to ballistic events. The model

was also validated using high-pressure diamond anvil cell experiments in glass that were conducted at ARL, and coordinated with external experimental efforts at the Ernst-Mach-Institute, then enhanced with the establishment of a new glass processing facility at ARL/WMRD.

Computational models of the initiation and propagation of discrete defects such as cracks at nanometer scales in glass should seamlessly transition into models of glass comminution relevant to fracture and fragmentation at the global scale. Ceramic glasses do not have a conventional micro- or mesostructure, as it is understood for crystalline ceramics. But these scales must also be accounted for in multiscale modeling of glasses due to the presence of growing defects at these intermediate spatial scales; although this has been done in the past using classical homogenization methods, this approach may not be possible for defects in glass that exhibit time-dependent growth. To remedy this, recent research by Wildman and Gazonas (2012) has focused on the development of a nonlocal formulation of elastodynamics known as peridynamics which shows promise for modeling discontinuities and dynamic fracture in glass. In this work, a perfectly matched layer was implemented into a state-based formulation of peridynamics for simulation of boundary value problems with infinite domains; the new code has been verified with a number of closed-form analytical solutions to boundary value problems arising in elastodynamics and validated by comparison of simulated and observed crack lengths formed in glass indentation experiments. Current research is underway to enhance the computational framework by linking peridynamics to a finite difference time domain code to minimize dispersion effects seen in dynamic simulations of glass fracture; incorporation of the peridynamics code into a concurrent multiscale framework is also planned.

3.3 Polymers and Macromolecules

Polymers are ubiquitous in Army systems and in many civilian applications. Individual Soldier protection devices and shields are often made from light and strong composites composed of high-performance semicrystalline polymer fibers within a polymer cross-linked network matrix. Polymer elastomers are used in armor systems as adhesives and coatings, in a variety of robotic applications, fuel cell membranes or as protective coatings for corrosion or passivation layers in electronic materials. Glassy polymer networks are used in structural polymer composites or in a transparent armor. Polymeric gels have multiple applications, such as materials with mechanical properties of human tissue for ballistic testing or as multifunctional robotic soft materials. ARL develops computational methods and performs simulations addressing critical challenges in modeling of polymers, such as entanglements of extremely long chains, microphase-separated complicated morphologies, dynamics of network and semicrystalline polymers as well as elucidating polymer unique mechanisms of energy dissipation, such as by strain hardening. To successfully treat the extremely large spatial and long temporal time scales of polymer dynamics and micro-phase separation phenomena, mesoscale-level coarse-grained or field theory methods are typically used. Scale bridging is realized by providing interaction parameters between grains (a larger assembly of atoms) that can be obtained from lower-level atomistic or quantum-level simulations.

The behavior of polymers under extreme conditions (high-pressure-strain rates and temperature) is of interest for numerous military applications, such as polymer-bonded explosives or lightweight armor Soldier protective equipment. The material response to such extreme conditions can be determined experimentally through shock experiments; however, these are extremely difficult to characterize. Instead, computations can provide valuable insight at the atomistic level by characterizing non-equilibrium material behavior behind a shock front occurring at extremely short time and length scales. Chantawansri et al. (2012) performed QM and atomistic simulations using MD to predict the shock Hugoniot for several Army-relevant polymers. They have found that a dispersion-corrected DFT method can reproduce experimental Hugoniot curves for the PMMA (Poly [methyl methacrylate]) polymer. The accuracy is less satisfactory for polymers containing rings, such as polycarbonate, because of the complicated phase transition that occurs at long time scales, which cannot be captured through the short time scales accessible to QM simulations. Fracture events were studied at high pressures for the PMMA polymers, where an interconnected network was formed at high pressures and temperatures. This work enables scale bridging by providing constitutive equations for FEM simulations, and it can ultimately lead to optimization of polymer performance at high, ballistic pressures.

Polymer elastomers are being extensively studied at ARL because of their potential for blast-wave mitigation and versatile mechanisms of projectile impact energy dissipation. The architecture, chemistry and composition of elastomers can be tailored to achieve large energy dissipation. In particular, segmented polymers, like poly(urethane urea) (PUU), exhibit a broad range of mechanical response under high-strain-rate deformation. Depending on the distribution, chemical composition and intermolecular interaction of soft and hard segments in PUU, the polymer may undergo a transition from a rubbery into a leathery-like or glassy regime with increasing strain rate, thus enhancing energy dissipation capabilities. Chantawansri et al. (2012) studied the effect of hard and soft segment content and interactions on local morphology and rate-dependent stress-strain behavior in the ballistic regime. They used the Kremer-Grest (KG) and Dissipative Particle Dynamics (DPD) mesocale models to study the equilibrium and dynamic properties of PUU polymers. The DPD method is computationally more efficient and it was used to quickly obtain the morphology for this system as a function of hard and soft segment content and interactions. However, the DPD cannot study mechanical deformations of polymers, so it was replaced with the KG model. Through these calculations, the significance of the hard segment orientation and the intermolecular interactions, particularly at the interface between the hard and soft segments on the stress-strain response, was revealed. Results qualitatively agreed with available experimental data. This research validates the computational model and opens the avenue to study the effect of the microstructure on the segmental dynamics under high-strain-rate deformation.

As mentioned above, the standard DPD method is often used in polymer simulations to determine the morphology of microphase-separated polymer systems due to its advantageous computational performance. However, the soft potentials utilized by the DPD method allow for polymer chains to pass through each other, thus prohibiting the method from capturing the effect of entanglements in the mechanical response. To address this shortcoming, Sirk et al. (2012) has developed a polymer model that prevents such chain crossings and therefore allows the favorable coarse-graining features of DPD to be applied to entangled polymer materials. This new model, which we have termed the modified segmental repulsive potential, includes an additional non-bonded and angle-bending potential that are parameterized to both prevent chain crossings and to preserve the structural and thermodynamic properties of the original DPD method. The method has good computational performance and is broadly used in computing trends in transport and mechanical properties. It was successfully used to study mechanical properties of entangled block copolymers and in design of gel networks with tunable mechanical properties. The method was implemented in the popular program LAMMPS and is already being used by several academic and industrial researchers.

Properties of bio-inspired and biological materials are of increasing importance for ARL research on novel Soldier protection systems or energy-harvesting devices. The biomimetics strategy of seeking inspiration from nature to create hard, tough and lightweight materials is present in numerous mission projects — for example, in bio-derived high-performance fibers, bio-inspired adhesives and transparent nanocrystalline cellulosic composites. Such materials may not only possess superior properties, but will also increase the sustainability and decrease supply chain vulnerability. Utilizing nature's finely tuned light harvesting protein complexes for the conversion of light energy to chemical energy could lead to the development of alternative energy sources. The fabrication of a photocatalytic bio-STET system of Photosystem I and inorganic materials to produce hydrogen gas requires close coupling of experiment and simulation to improve packing and coupling of the protein complex to the electrode surface for enhanced stability and electron transfer. Analysis of the metabolic diversity of clostridium acetobutylicum may impact Army operations in areas as diverse as biofuel formation to firing range remediation. Iterative modeling of peptide-protein interactions for "smart reagent" development yields better understanding of target-ligand interactions and will enable the design of improved efficiency, rugged sensors for biologial and chemical detection. ARL conducts computational analyses in all these areas using QM, MD, an improved in-house docking protocol and systems biology and bioinformatics tools.

In this monograph a recent paper by Adams et al. (2013) is presented outlining the first-ever effort harnessing of E. coli cellular machinery to develop an unconstrained bacterial display peptide library designed for interaction with inorganic materials. Tight coupling between experimental evidence and computational analysis dem-

onstrated the sequence-dependent structure-function relationship leading to improved helicity (axial chirality) and preferred binding group alignment for high-affinity peptide interactions. This work is likely to have significant impact on the design and development of beneficial biofilms, including living paint for common metals subject to corrosion. Future studies will continue to explore the use of this biological approach for advanced material development and improved understanding of hybrid material interactions.

3.4 Ceramics

The ultimate failure of structural ceramics in impact events is a function of the temporal and spatial interaction of the macro-stresses at the macro-, micro- and nano-structural scale. This includes elastic and inelastic (plastic) deformation, damage nucleation and evolution and resulting failure from the macro-scale (top down) or from the nano-scale (bottom up). The majority of research in the past has involved continuum-based modeling and simulations using constitutive stress/strain mechanical relationships at larger scales, where the material is assumed to be a homogeneous mechanically isotropic body. Unfortunately, these methods ignore, for the most part, the anisotropic physics-based spatial/localized nano- and microscale responses at these scales. Current work is now being focused on these very small scales and how to embed these results into the larger-scale models and computer codes.

Boron carbide (BC), due to its extreme hardness, low density, and demonstrated protection performance, has been used as an armor ceramic for many years. The crystal structure is composed of icosahedra with different stoichiometries that depend on the carbon content and processing conditions. Although the structure and formation enthalpy of BC as a function of stoichiometry are rather well known, the deformation and damage mechanisms occurring during mechanical deformations are much less known. But they are critical to predicting the performance of BC as a protective material. Recently, it was discovered that under certain high-strain-rate experiments, BC amorphized into “nano-structural bands” which seem to be an important damage mechanism. Taylor et al. (2012) investigated the effect of stoichiometry on the atomic structure and mechanical properties of various BC crystallites. The authors used a DFT method at the GGA level to optimize unit cells and calculate elastic constants as a function of hydrostatic and uniaxial loads. They also performed MD simulations with the Perdew-Burke-Ernzerhof functional under hydrostatic, uniaxial and shear loading paths. Computed mechanical properties show their significant dependence on the atomic structure and stoichiometry. The mechanism of atomic reorganization within a deformed unit cell was discovered. They found an unexpected behavior of the C_{44} modulus, which undergoes pressure softening, and suggested that this could contribute to the amorphisation of BC under shearing load. The results of this study significantly contributed to the understanding of BC behavior under mechanical loads.

Over the past ten years significant progress has been made in determining the dynamic and quasi-static mechanical properties, deformation and failure mechanisms of aluminum oxynitride (AlON), a transparent polycrystalline cubic spinel structure material used in transparent armor and sensor windows. Characterization of AlON fragments from high-strain-rate Kolsky bar and edge-on impact tests have revealed that dissociated <110> dislocations on {111} planes seemed to be operative and that subsequent fragmentation formed along {111} cleavage planes; use of real-time high-speed photography in these tests has clearly demonstrated the influence of defects on the dynamic mechanical response of AlON.

Recent DFT calculations guided by a genetic algorithm by Batyrev et al. (2014) found that the lowest energy configurations in the AlON ($Al_{23}(AlVac)O_{27}N_5$) system corroborated McCauley’s long-standing constant anion unit cell model for AlON. The model with the lowest energy structure has a random distribution of N atoms not adjacent to the Al vacancy and is in good agreement with experimental X-ray diffraction spectra. DFT-computed cubic elastic constants approached the experimentally measured elastic constants as the number of atoms was increased from 55 (unit cell size) to 440; the cubic elastic constants were predicted to increase monotonically to 40 GPa. Both infrared and Raman spectra were also predicted using density functional perturbation theory and compared with available data supporting the conclusion that some of the Al cations are in tetrahedral sites and the O atoms

are next to the cation vacancy site. Future work is planned that will validate the model with both IR and Raman spectra and possibly applying the MS-CG variational approach (Izvekov and Rice, 2012) to determine shock Hugoniots for AlON.

Another notable paper by Clayton et al. (2012) devoted to explicitly modeling grain boundary (GB) fracture using CZs in AlON and silicon carbide, accurately models shear-induced dilatation and the increasing shear stress with pressure observed in these ceramic materials. The ceramic mesostructure is characterized by a nonlinear anisotropic elastic constitutive model[12] and consists of a 1 mm^3 polycrystal (assuming an average ~200 μm grain size) constructed using a Monte Carlo synthetic grain growth algorithm. The polycrystalline mesostructural models were implemented into the Sierra/Presto suite of codes deformed at increasing pressure and analytically fit to a cap plasticity model useful for larger-scale numerical simulation. Under consideration by the authors is enhancement of the fidelity of the simulations using realistic microstructures obtained through serial sectioning of specimens combined with electron-backscatter diffraction data or using high energy X-ray diffraction microscopy (HEDM) for microstructure reconstruction.

A mere few atoms thick two-dimensional (2D) materials, arranged as periodically repeating units, have the potential to transform Soldier protective systems as well as electronics and sensor devices. This is due to their superior electronic, transport, thermal and mechanical properties. The 2010 Nobel Prize was awarded to the discoverers of graphene, a 2D material that is a planar structural array of single layers of hexagonal rings of carbon atoms, which exhibits extraordinary mechanical, thermal and electrical properties. ARL conducts extensive research in graphene and other 2D materials such as BN, ZnO, and hybrid graphene-polyethylene structures to understand their electronic and mechanical structures and to design superior multifunctional materials with tunable properties. Balu et al. (2012) studied the effects of electric field on the band structures of graphene/boron nitride bilayers by using first-principles quantum mechanical calculations. They found that modulation of the band gap in graphene/BN bilayers is dominated by the graphene electronic structure. This research suggests new applications in semiconductor devices for graphene/BN bilayer materials.

3.5 Metals

Polycrystalline metal alloys play an important role in the ballistic performance of present day and future Army protection/lethality systems. The mechanical, electrical, magnetic, and thermal properties of these alloys heavily depend on the following complex underlying microstructures: nanoscale precipitates and their interfaces, grain orientation and crystallographic texture, various phases or crystal structures (i.e., intermetallics), point defects and solute/impurity atoms, dislocation character and density, and complex GB structures. Understanding and quantifying how these microstructures form and evolve requires modeling techniques that range from the electronic and atomistic scales (QM, MD) all the way up to the macroscale (continuum mechanics), with an associated large span in terms of the time scale as well.

There are, however, a number of challenges for modeling metal systems for protection/lethality applications. For instance, while the microstructure of metal alloys is related to the atomic arrangement of atoms and their kinetics (associated with processing/application), the number of degrees of freedom related to the microstructure complexity may make simulations at the quantum/atomistic scales intractable, necessitating either hierarchical or concurrent scale bridging to higher-scale models. In addition, while mesoscale and continuum-level simulations have the computational efficiency to handle these problems, the parameters in the constitutive relations of these models may be more phenomenological than physically based (i.e., changes in composition or processing that result in different microstructures or properties may require a complete recalibration of these models). Hence, understanding how microstructure complexity affects properties at the atomic scale and influences parameters in higher-scale models is one challenge for multiscale models in general and for metals specifically. The payoff, though, is that the ability to formulate and integrate predictive models over these multiple length and time scales (validated by critical experiments) will enable the Army of the future to computationally tailor alloy composition and processing routes in metals to engineer the next generation of protection and lethality systems.

One example of how microstructural complexity can be explored at the atomic scale is shown in Rhodes et al. (2013). It is well established that impurities segregate to GBs and ultimately influence mechanical properties, such as hardness, toughness and fracture behavior. In their recent work on steels, they studied the segregation process for carbon within multiple substitutional and interstitial GB sites over 125 symmetric tilt GBs in iron. The authors performed molecular simulations using an interatomic potential based on the embedded-atom method formulation, which was fit using and tested against DFT calculations. Thousands of substitutional and interstitial atomic sites for GBs of various tilts were examined. They predicted energetically favorable GB segregation processes and optimal positions of carbon atoms. Statistical analysis was performed to quantify the segregation energy distribution as a function of distance from the GB. This work enabled the authors to build analytical models of the segregation energy distribution for higher-scale simulations. This work was instrumental in developing a methodology capable of ascertaining segregation energies over a wide range of GB structures typical of that observed in polycrystalline materials.

A recently developed phase-field FE model has been used to simulate quasistatic Mode I (tensile stress) and II crack-tip twin nucleation in magnesium, calcite, and sapphire single crystals (Clayton and Knap (2013). The research enhances our fundamental understanding of twinning energetics and whether twinning precedes or is a consequence of fracture (cleavage). The authors plan to extend their phase-field computational model to include transient dynamic effects to enable interpretation of defect kinetics observed in plate impact or indentation experiments.

Concurrent multiscale methods are also under development by ARL Scientists & Engineers. For metals, the method involves development of a parallel dislocation dynamics simulation capability for finite bodies such as in thin metallic films (Leiter et al. [2013]). The concurrent coupling uses distributed shared memory architecture to link a parallel dislocation simulator (ParaDiS) to a parallel FE solver for the solution of problems in small scale plasticity. The authors are studying the dynamic interaction of 4,096 randomly distributed straight-edge dislocations discretized into 280,261 segments within a ~2.5 μm^3 cube of tungsten; the algorithm exhibits nearly ideal scalability to 1,024 processors. Future work is aimed at evaluating the benefits of using either an implicit or explicit integrator for numerical solution of the equations of motion for the dislocation segments and validation of the computational model with experiment.

The constitutive theories of plasticity in metals can be broadly categorized as follows: 1) classical macrophenomenological plasticity theories produce rate-independent flow. These are all infinitesimal plasticity theories that include the definition of a i) yield function, ii) relation between the stress increment tensor and the elastic strain increment tensor, iii) normality conditions, and iv) work-hardening rule for evolution of the yield function under loading. The consistency condition provides the condition needed to produce rate independent behavior; 2) rate-dependent plasticity (viscoplasticity) theories are similar to rate-independent theories in structure but with the consistency condition removed. The plastic flow is normally tied to the direction of (deviatoric) stress and scaled in relation to the distance currently outside the yield surface; 3) crystal plasticity theories are based on considering crystal structure, dislocations, slip planes, slip directions, etc. These can be made exact for large deformations, and are typically in rate form, but can also produce rate-independent equations. The microphenomenological form of the theory provides parameters associated with microstructural events producing, for example, hardening due to dislocation pileup; 4) finite deformation plasticity theories are based on the $F^e F^p$ decomposition and are an extension of the classical phenomenological theory to finite deformations; decompositions such as $F^e F^p F^\theta$ incorporate the laws of thermodynamics and include temperature and heat generation. These are internal variable theories that include all the elements of the classical theory. The defining factor, as in the infinitesimal case, is the inclusion of a consistency condition that produces rate independence.

Within this framework is the recent contribution to classical plasticity of a new continuum plasticity time-integration algorithm which was implemented by Becker (2011) into the arbitrary Lagrange-Eulerian code ALE3D. The algorithm is based on insight obtained by closed-form integration of a quadratic yield function over a single time step and is intended for use with anisotropic and non-quadratic yield functions where numerical integration is often difficult. The new algorithm is numerically robust and successfully predicts localization in an expand-

ing metallic ring and an aluminum plate perforated by a steel projectile. Possible extensions of the algorithm to an implicit FE solver are under consideration, which would enable solution of long-time structural dynamics and material-processing problems.

3.6 Composites

Composite materials have been used successfully since World War II in both personnel and vehicular protection, and the simulation of the anisotropic elastic behavior of homogenized composite materials has been effectively characterized up to fracture failure.[13] However, dynamic fracture in carbon fiber-reinforced composites widely used in the aerospace industry is an extremely challenging physical phenomenon to simulate, particularly in a multiscale computational environment, since fracture process zones exist at the nanometer spatial scale in the relatively brittle carbon fibers, and the sub-millimeter scale in the relatively ductile matrix of polymer-epoxy resin. Modeling progressive failure in composite materials subjected to blast and ballistic impact has been the focus of many researchers over the last several decades.

Love and Batra (2010) studied how particle-matrix debonding influences the formation of material instabilities known as adiabatic shear bands (ASB) in metal matrix particulate composites. Particle-matrix debonding is modeled with CZs, which are dynamically inserted into the FE mesh when tractions in adjoining FE reach a critical value consistent with the Griffith fracture energy. It is shown that in this highly coupled transient thermomechanical problem, the initiation time of the ASBs are strongly influenced by particle-matrix debonding times governed by the CZ failure criterion. Future experimental work is required to find cohesive zone relations that are sensitive to strain, strain rate and temperature histories, and validation of the finding that strong particle-matrix interfaces delays ASB initiation. A review and mathematical analysis of factors that influence ASB formation can be found in the classic text of Wright.[14]

Nilakantan et al. (2012) studied the effects of projectile size and shape on the penetration resistance of a single layer of plain weave Kevlar fabric with statistically variable yarn strengths. An important conclusion of these probabilistic simulations is that projectile shape strongly influences predicted V_{50} (impact velocity at which 50 percent of the projectiles perforate the target) values such that both V_1 and V_{99} velocities should also be considered when designing composite protective barriers.

C.F. Yen (2012) recently developed a rate-dependent multi-parameter lamina model based on CDM which was implemented into the explicit dynamic code LS-DYNA. The model was used to successfully predict the ballistic limit velocity, V_{50}, of a fragment-simulating projectile perforating a composite laminate.

Finally, Wildman and Gazonas (2014) present a fully concurrent multiscale method whereby design loads and boundary conditions are applied and objective functions are measured at the global scale, while optimizing the topology (using computational geometry and genetic programming) of the local cellular composite microstructure described by representative volume elements (RVEs). The multiscale method also has the capability to model local-global fracture transition kinetics by injecting cohesive zone microfractures within the local RVE and transitioning these to global-scale fractures using XFEM. This work represents one of the few open literature publications that optimizes local microstructure using computational geometry, and a forward multiscale FE code MultiMech (see http://multimechrd.com/multimech/) with the additional capability of transitioning defects from the local to the global-scale. The authors intend to extend the algorithms to a 3D framework and simultaneously optimize the global-scale topology with the local-scale microstructure. Despite these advances, challenges remain for material modeling and simulation of composite materials undergoing finite thermoinelastic deformations, and for development of equations-of-state for composites subjected to high pressures induced by shock.

4. Future of multiscale materials modeling

The importance of materials modeling will only increase in the future with the development of new computational techniques and the advent of exascale computers. As documented in this volume, materials modeling at ARL is at the leading edge of multiscale modeling science, yet mostly sequential multiscale modeling and bridging of

few scales is currently the state of the art, while the concurrent modeling concepts begin to emerge. It can be expected that the future will bring more concurrent modeling for a variety of materials that would enable design of materials at the macroscale by using an inverse design methodology.

Concurrent modeling can be achieved through further development of a systematic coarse-graining methodology that retains microstructure heterogeneities and chemistry of the system at higher scales while the reverse process will utilize general backmapping algorithms that can uncover underlying atomistic structure and local heterogeneity from the high-level coarse-grained representation.

The new algorithms will likely improve the validity of the modeling results at every scale by making the representation of the total material system more accurate with better estimates of the uncertainties that have arisen. For example, embedded and adaptive methods may enable more accurate calculations of the material system at the various scales (quantum, atomistic, micro- and meso-scales) subjected to a dynamically adjusted environment. Current, predetermined a priori representation of the multiscale material system for atomistic simulations (force fields) or for FE techniques (constitutive equations) could be calculated on the fly, thus adding accuracy and less uncertainty to the material system simulation.

Concurrent modeling involving lower scales must be accompanied by development of order-N computational methods. These methods have to efficiently utilize the sparsity of the system and improve the performance of iterative methods that solve partial differential equations. For example, accurate ab initio quantum mechanical methods may scale with the number of atoms, N, much more than linearly (e.g., N^4). Therefore, increasing the number of processors in the future exascale computers would not increase much usage of such expensive methods. A new generation of accurate-order N DFT functionals and programming improvements will enable efficient use of parallel architecture and consequently dynamics simulations for hundreds of thousands of atoms.

Future exascale computers may have millions of processors, with relatively slow connectivity between nodes and increasing possibility of node failures. This new architecture may necessitate the emergence of new techniques that currently are not competitive. One such technique could be the Quantum Monte Carlo algorithm that is computationally intensive, but has a reduced need for communication between the nodes. A new computational programming strategy needs to be developed to account for processors with higher failure rates and to exploit incredibly large parallelism. New algorithms must be developed that are resilient to failure of individual processes, asynchronous, and reduce needs for global communication.

Undoubtedly, with increased coupling of different algorithms across spatiotemporal scales, understanding deficiencies and the range of applicability of models, as well as estimation of error on simulations, will become of vital importance. The field of verification, validation, and uncertainty quantification (VVUQ) will become an integral part of concurrent multiscale modeling. The VVUQ procedures will allow determining accuracy of simulations with respect to uncertainty of input and will provide guidance on how to perform simulations across the scales with predetermined levels of accuracy in the solutions.

In the future, we can expect an increasing integration of multiphysics with multiscale modeling, allowing for realistic simulations under various external fields and extreme conditions. Bulk calculations will be replaced with realistic simulations including local heterogeneities, such as stochastically distributed defects, grain and interface boundaries or microphase-separated morphologies that can dynamically evolve upon influence of external fields. Transport and reactions across the scales and interfaces including fracture and toughness studies will become commonplace.

Finally, emerging computer architectures such as quantum and DNA computers, novel programming environments and languages capable of data-intensive and fault-tolerant algorithms will provide an opportunity for revolutionary progress in multiscale modeling of materials. Appropriate incorporation of VVUQ procedures will allow for the discovery and designing of new classes of materials from the atomic scale, and the prediction of the properties and performance of these materials in many extreme environments. Important applications for the

Army include some of the following: energy storage, chemical-biological sensing, IR sensing, aviation materials, ultralight structural materials, protection materials, and lethality materials, among others.

Seventy years ago with the installation of ENIAC, ARL's predecessor, the Ballistic Research Laboratory (BRL), was at the forefront of computational science, including materials science applications. Today, ARL's commitment to the development of multiscale theoretical and computational methodologies is as strong as ever, and is documented in the ARL Computational and Materials Sciences Campaign plans.[15]

References

[1] M. Denny, "Swordplay: an exercise in rotational dynamics", European Journal of Physics, 27 (2006) 943-950.
[2] M. Reibold, P. Paufler, A. A. Levin, W. Kochmann, N. Pätzke and D. C. Meyer, "Materials: Carbon nanotubes in an ancient Damascus sabre", Nature 444 (2006) 286
[3] http://machconference.org/
[4] http://www.tms.org/meetings/2015/icme2015/home.aspx
[5] 50 Years of Army Computing From ENIAC to MSRC: A Record of a Symposium and Celebration November 13 and 14, 1996 Aberdeen Proving Ground, ARL-SR-93, September 2000.
[6] J. Fish, "Multiscale Methods: Bridging the Scales in Science and Engineering", Oxford University Press, 2009, Print ISBN-13: 9780199233854
E. Tadmor and R. Miller, "Modeling Materials: Continuum, Atomistic and Multiscale Techniques", Cambridge University Press, 2011
[7] http://www.nobelprize.org/nobel_prizes/chemistry/laureates/2013/
[8] http://www.nobelprize.org/nobel_prizes/chemistry/laureates/1998/
[9] http://www.chemistryviews.org/details/ezine/5039611/DFT_2013_Virtual_Issiously ue.html
[10]Zienkiewicz, O.C., "The Finite Element Method," McGraw Hill Book Co., UK; 1977.
[11]Milton, G.W., "The Theory of Composites," Cambridge Monographs on Applied and Computational Mathematics, Cambridge University Press, Cambridge, UK, 2002, 719 pp.
[12]Clayton J.D., "Nonlinear Mechanics of Crystals." Dordrecht: Springer; 2011.
[13]Ashton, J.E., Halpin, J.C., and Petit, P.H., "Primer on Composite Materials: Analysis," Technomic Publishing Company, Stamford, CT, 1969, 124 pp.
[14] Wright, T. "The Physics and Mathematics of Adiabatic Shear Bands," Cambridge: Cambridge University Press; 2002.
[15] Army Research Laboratory Technical Strategy 2015-2035, https://arlinside.arl.army.mil/inside/pages/home/boxes/publications/tech_strategy/ARL_Technical_Strategy_FINAL.pdf

Oxidation Induced Decomposition of Ethylene Carbonate from DFT Calculations – Importance of Explicitly Treating Surrounding Solvent

Lidan Xing and Oleg Borodin

Physical Chemistry Chemical Physics (2012)

Cite this: DOI: 10.1039/c2cp41103b

www.rsc.org/pccp

PAPER

Oxidation induced decomposition of ethylene carbonate from DFT calculations – importance of explicitly treating surrounding solvent†

Lidan Xing[ab] and Oleg Borodin*[c]

Received 5th April 2012, Accepted 20th July 2012
DOI: 10.1039/c2cp41103b

The oxidation induced reactions of the common lithium battery electrolyte solvent ethylene carbonate (EC) have been investigated for EC_2 using density functional theory and for selected reaction paths using Møller–Plesset perturbation theory (MP4). The importance of explicitly treating at least one solvent molecule interacting with EC during oxidation (removal of an electron) on the EC oxidation potential and decomposition reactions was shown by comparing oxidation of EC and EC_2. Accuracy of DFT results was evaluated by comparing with MP4 and G4 values for oxidation of EC. The polarized continuum model (PCM) was used to implicitly include the rest of the surrounding solvent. The oxidation potentials of EC_2 and EC_4 were found to be significantly lower than the intrinsic oxidation potential of an isolated EC and also lower than the oxidation potential of EC–BF_4^-. The exothermic proton abstraction from the ethylene group of EC by the carbonyl group of another EC was responsible for the decreased oxidative stability of EC_2 and EC_4 compared to EC. The most exothermic path with the smallest barrier for EC_2 oxidation yielded CO_2 and an ethanol radical cation. The reaction paths with the higher barrier yielded oligo(ethylene carbonate) suggesting a pathway for the experimentally observed poly(ethylene carbonate) formation of EC-based electrolytes at cathode surfaces.

1. Introduction

Understanding the oxidation induced reaction of electrolytes is essential in order to improve the performance of lithium ion batteries, especially with the interest of developing electrolytes compatible with high-voltage cathode materials that will improve battery energy density.[1,2] At high voltage cathodes electrolytes containing solvents such as propylene carbonate (PC) and ethylene carbonate (EC) become electrochemically unstable resulting in the solvent oxidation and decomposition.[1–7] Gaseous products generated during the oxidation reaction were identified, specifically, CO_2 has been shown to be the main gas component of the PC, EC and diethyl carbonate (DEC) oxidation,[8–10] but not from dimethyl carbonate (DMC).[4] Besides gaseous products, formation of polycarbonates[2,3] and compounds with carboxylic groups[11] has been proposed as a result of oxidation reaction of EC on a cathode. The growth of this polycarbonate layer on the cathode surface leads to performance degradation of the battery upon aging and cycling.[12,13]

Density functional theory (DFT) calculations have been used to predict oxidative stability of solvents,[8,14–21] redox-shuttles,[22–24] anions[25–28] and solvent decomposition pathways.[8,29,30] Most of the DFT studies of oxidation stability of electrolyte components focused on understanding oxidation stability of an isolated molecule and relating it to the bulk electrolyte oxidation potential. Recent work,[30–32] however, demonstrated that the oxidation process in electrolytes is far more complex. For example, oxidation of the carbonate and the sulfone complex with anions such as PF_6^-, BF_4^- and ClO_4^- resulted in the anion nucleophilic attack on the solvent occurring upon oxidation (electron removal) and leading to deprotonation of carbonates and sulfones.[31,32] The oxidative decomposition reactions of PC were significantly influenced by the presence of PF_6^- and ClO_4^- in DFT study.[32] MD simulations provided evidence of the PF_6^- anion being present at the surface of charged positive electrodes,[33] simulations of the $LiFePO_4$ cathode–electrolyte interface revealed a pronounced solvent ordering at the cathode surface.

In this work we explore an intriguing possibility that the carbonyl group of EC might initiate the nucleophilic attack on the ethylene group of another EC during oxidation of the EC_2 complex. Moreover, we examine to what extent such nucleophilic attack influences the EC oxidative stability and oxidation induced decomposition reactions. We consider this work as an initial step towards understanding complicated oxidation electrochemistry of carbonate electrolytes on non-active

[a] *Department of Materials Science and Engineering, University of Utah, Salk Lake City, Utah 84112, USA*
[b] *School of Chemistry and Environment, South China Normal University, Guangzhou 510006, China*
[c] *Electrochemistry Branch, Army Research Laboratory, 2800 Powder Mill Rd., Adelphi, MD 20783, USA. E-mail: oleg.a.borodin.civ@mail.mil*

† Electronic supplementary information (ESI) available: Additional graphs, chemical structures. See DOI: 10.1039/c2cp41103b

electrodes, while oxidation induced reactions on active electrodes[30] are quite complex and depend on a myriad of additional factors such as activity of the cathode surface, its structure and crystal orientation.[34]

2. Oxidation stability

We begin by exploring the initial step of EC_2 oxidation, calculating the EC_2 oxidation potential and comparing it to the oxidation potential of an isolated EC and an EC–BF_4^- complex as shown in Fig. 1. The most stable EC_2 configuration with the binding energy of $\sim$50 kJ mol^{-1} from our previous work[35] was used as a starting point for DFT calculations.

DFT calculations at the B3LYP/6-311++G(d) level were primarily used in this study to investigate the oxidation-induced reactions. The energies for a few selected reactions were also calculated at the MP4/6-311++G(d) level using B3LYP/6-311++G(d) geometries and compared to B3LYP/6-311++G(d) results to assess reliability of DFT results as deficiency of many DFT functionals for predicting the EC–Li^+ binding energy[36] and H-transfer in radicals[37] might yield inaccurate results for the EC–anion and EC_2 complexes of interest in this work.

The initial oxidation step for EC_2 was also investigated at M05-2X/cc-pvTz, MP2/cc-pvTz, MP4/6-311++G(d)//B3LYP/6-311++G(d) and G4MP2[38] levels to further establish reliability of DFT predictions. The Gaussian 09 package was used.[39] Vibration frequency and intrinsic reaction coordinate (IRC) analyses were employed to confirm all the transition states of the reaction pathways at the same level. An effect implicit solvent with dielectric properties of water (dielectric constant = 78.4) was included *via* a polarized continuum model (PCM). Dielectric constant of the order of 78.4 is close to that of EC (ε = 89.78) based electrolytes at room temperature.[1] Oxidation potential (E_{ox}) was converted from the absolute oxidation potential of Li^+/Li by subtracting 1.4 V from the former, as shown in eqn (1).

$$E_{ox}\,(Li^+/Li) = [G(M^+) - G(M)]/F - 1.4\ V, \quad (1)$$

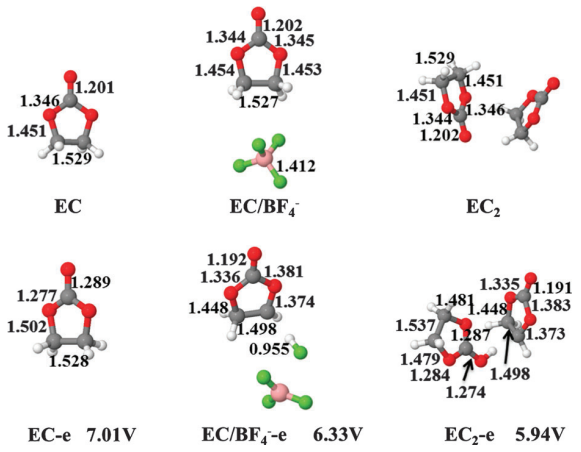

Fig. 1 Optimized structures and selected bond lengths (Å) of EC, EC–BF_4^-, and EC_2 before and after oxidation from B3LYP/6-311++G(d) optimization. The calculated oxidation potential *vs.* Li^+/Li is listed below each complex.

where $G(M)$ and $G(M^+)$ is the free energy of the solvated complex M and its solvated oxidized form M^+ at 298.15 K, respectively, and F is the Faraday constant.

Geometry optimization of the oxidized EC–BF_4^- complex revealed the BF_4^- nucleophilic attack on EC leading to HF formation resulting in the reduced oxidation potential of the EC–BF_4^- complex compared to the isolated EC oxidation potential as shown in Fig. 1. Furthermore, initial oxidation of EC–BF_4^-, EC_2–BF_4^-, EC_3–BF_4^- complexes studied at the M05-2X/cc-pvTz level with PCM (acetone) confirmed that H-abstraction from EC by BF_4^- also occurs in these EC_n–BF_4^- clusters as shown in ESI.† Location of the solvent separated anion near the EC ethylene group as shown in Fig. 1 is consistent with MD simulation results.[36,40]

Remarkably, in the oxidized EC_2 complex the carbonyl group of EC that is hydrogen-bonded to the ethylene group on another EC also initiates a nucleophilic attack on EC resulting in a spontaneous proton abstraction and lower oxidation potential of EC_2 compared not only to the isolated EC oxidation potential but also oxidation potential of EC–BF_4^-. We confirmed that similar H-abstraction occurred during energy optimization performed at MP2/cc-pvTz, M05-2X/cc-pvTz, LC-ωPBE/6-31+G** and G4MP2 levels using PCM (acetone) indicating that the correlated methods such as MP2 and other density functionals support the B3LYP results. Analysis of the electrostatic potential fit to the grid around $EC_2 - e$ was performed using the ChelpG method with results shown in ESI.† This analysis revealed that in the oxidized complex EC(+H) is a cation, while the radical EC(−H) is essentially neutral. Furthermore, the H-transfer from one EC to its neighboring EC upon oxidation occurred in the larger oxidized EC_4 complex as a result of geometry optimization at the LC-ωPBE/6-31+G** level with PCM (EC) indicating that H-abstraction upon oxidation is not limited to EC_2 clusters.

The oxidation potential for EC_2 of 5.94 V from B3LYP/6-311++G(d) calculations agreed well with the G4MP2 value of 5.8 V, the M05-2X/cc-pvTz value of 5.9 V, and the oxidation energy of 6.0 from MP4/6-311++G(d)//B3LYP/6-311++G(d) calculations. The energy was used instead of free energy for the latter calculations as vibrational analysis at MP4/6-311++G(d) is too expensive. The calculated oxidation potential values agree well with the experimental values of 6 V for EC–$LiPF_6$ (1 M) on Pt,[41] and a value of 6.2 V for EC with 0.65 M [Et_4N][BF_4] reported by Ue *et al.*[42]

3. Decomposition reactions

We proceed with exploration of the oxidation induced decomposition of $EC_2 - e$ and comparing results to the decomposition reactions of an isolated EC.[8] The transition state (TS) energies and products of the $EC_2 - e$ decomposition were calculated. They corresponded to the energies needed to break each of eight C–O bonds along paths 1–8 shown in Fig. 2.

Geometries of all TS states are given in ESI.† The reaction path activity follows the order path 2 > path 1 > path 7 > path 3 > path 4 > path 5 > path 6 > path 8 based upon transition states calculated at the B3LYP/6-311++G(d) level. The reaction paths 1–4 yielded identical oxidation products: CO_2, EC and an ethanol radical cation with the lowest TS2 of

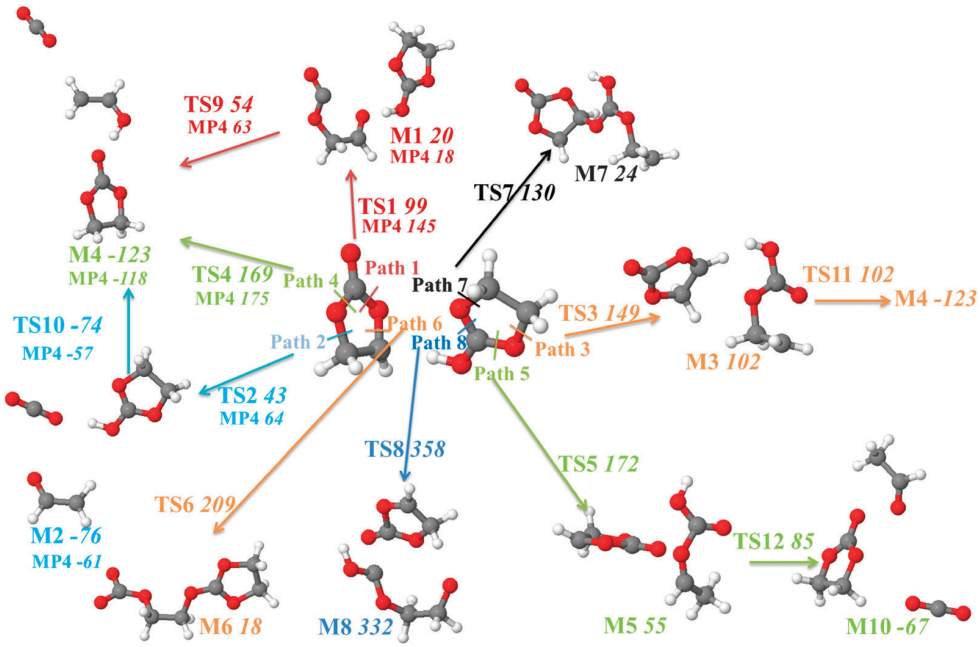

Fig. 2 The energies (kJ mol^{-1}) of transition states and products in EC_2 – e decomposition paths from B3LYP/6-311++G(d) calculations. Selected MP4/6-311++G(d) energies are also shown and denoted as MP4.

43 kJ mol^{-1} from B3LYP/6-311++G(d) and 64 kJ mol^{-1} from MP4/6-311++G(d) calculations for path 2. The second lowest barrier TS1 is 99 kJ mol^{-1} from B3LYP/6-311++G(d) calculations and 145 kJ mol^{-1} from MP4/6-311++G(d) calculations. The lowest TS for breaking the C(ethylene)–O bond as opposed to the C(carbonyl)–O bond upon oxidation found in our calculations is in accord with the conclusions of the electron-spin-resonance study by Matsuta *et al.*[6] but does not support possible EC oxidation patterns suggested earlier by Moshkovich *et al.*,[3] who suggested the C(carbonyl)–O bond cleavage as the first step of EC oxidation decomposition. Interestingly, Moshkovich *et al.*[3] suggested numerous H-abstraction reactions to occur during EC oxidative decomposition.

The reaction path 5 that results in generation of CO_2, EC and aldehyde (M10) is less exothermic than the reactions along paths 1–4 and is also expected to be significantly hindered by the large barrier TS5 of 172 kJ mol^{-1}. Path 7 has the third lowest TS of 130 kJ mol^{-1} and yields a dimer product that can be potentially recombined with the reaction product M6 to form an oligomer of ethylene carbonate. While both reaction products M6 and M7 are slightly endothermic from DFT calculations, they might proceed at high temperature or larger overpotential. Alternatively, large molecular weight products M6 and M7 might get stabilized by their interactions with the cathode surfaces that are not considered in this work. Finally, path 8 is highly improbable as it is very endothermic and has the highest barrier TS8 of 358 kJ mol^{-1}.

Comparison of the barriers from MP4/6-311++G(d) energy calculations with the B3LYP/6-311++G(d) barriers is also shown in Fig. 2. It indicates that MP4 barriers are systematically higher than B3LYP barriers but, importantly, the order of the barrier energies is largely the same for MP4 and B3LYP results, with the exception of TS9 and TS2. The MP4 energies for these barriers (TS9 and TS2) are essentially the same, while in B3LYP/6-311++G(d) calculations TS9 has 11 kJ mol^{-1} higher barrier than TS2. The reaction product energies from MP4 calculations were slightly higher than B3LYP energies with the largest difference of 15 kJ mol^{-1} between MP4 and B3LYP energies observed for the M2 product. We conclude that selected MP4 calculations support the reaction mechanism extracted from B3LYP calculations.

Oxidation reactions of EC_2 are compared to the isolated EC oxidation decomposition reactions shown in Fig. 3. The EC oxidation induced decomposition reaction energies were

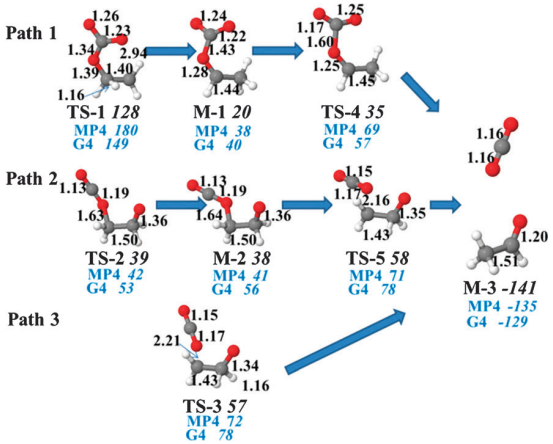

Fig. 3 Optimized structures, bond lengths (in Å) and reaction energies (in kJ mol^{-1}) of the oxidation decomposition paths of EC – e in implicit solvent from B3LYP/6-311++G(d). MP4/6-311++G(d) and G4 energies are also shown and denoted as MP4 and G4, respectively.

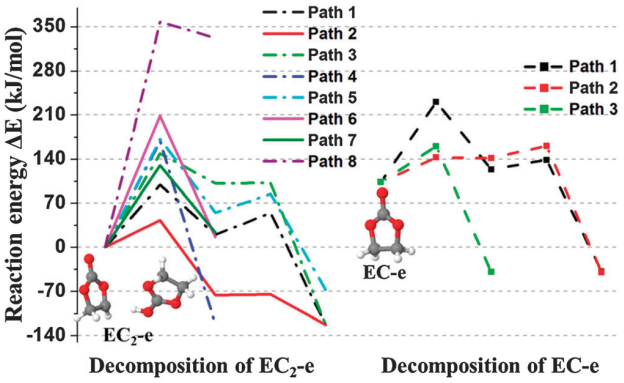

Fig. 4 Reaction energy profile of oxidation decomposition of EC_2 – e and EC – e in implicit solvent, from B3LYP/6-311++G(d) calculations.

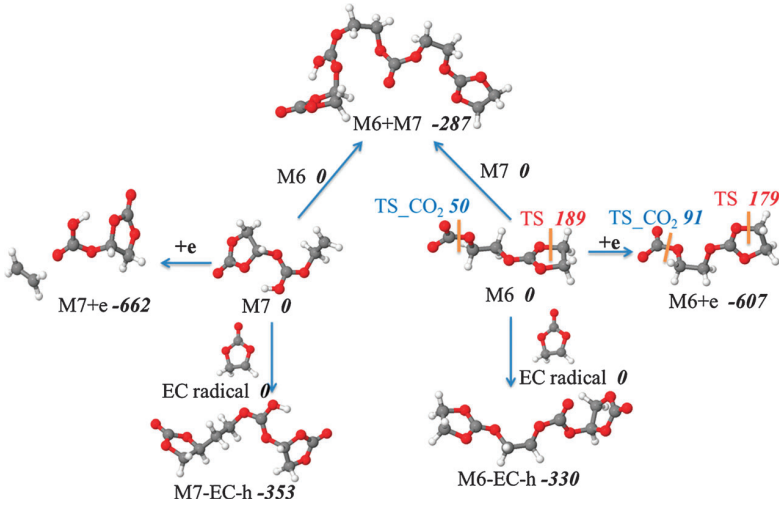

Fig. 5 Possible termination reaction paths and energy of M6 and M7 in implicit solvent from B3LYP/6-311++G(d). Energies are shown in kJ mol^{-1}.

calculated at B3LYP/6-311++G(d), MP4/6-311++G(d)//B3LYP/6-311++G(d) and using the composite G4 theory[43] that builds on the G3SX method that was successfully used for radicals.[37] The EC – e decomposition reactions shown in Fig. 3 yield CO_2 and an aldehyde radical as the main reaction products in contrast to the formation of the ethanol radical cation as the most active reaction of the EC_2 – e decomposition. Paths 2 and 3 are the most probable decomposition reaction paths, yielding similar activation energies for TS-5 (58 kJ mol^{-1} from B3LYP, 78 kJ mol^{-1} from G4) and TS-3 (57 kJ mol^{-1} from B3LYP and 78 kJ mol^{-1} from G4). Path 1 has a significantly higher barrier than paths 2 and 3 by ~70 kJ mol^{-1}. Comparison of B3LYP, MP4 and G4 results indicates that B3LYP systematically underestimates reaction barriers compared to MP4 and G4 but predicts the energy of the final product M-3 in good agreement with MP4 and G4 results. The MP4 energy agrees well (<6 kJ mol^{-1}) with the more accurate G4 estimate for M-1, M-3, TS-3, TS-5, while larger deviations up to 14 kJ mol^{-1} were observed for M-2, TS-2 and TS-4. Overall we conclude that while B3LYP/6-311++G(d) systematically underestimates the transition state barriers compared to G4 and MP4 results, it predicted the correct order of the EC oxidation induced decomposition reactions and the accurate value of the energy of the final product M-3.

Comparison of the barriers for the most active reaction paths for EC – e and EC_2 – e indicated that the barriers TS-5 and TS-3 for EC – e reactions are slightly higher by 14 kJ mol^{-1} at the B3LYP level and 7 kJ mol^{-1} for the MP4 level than the lowest barrier TS-2 for EC_2 – e when measured relative to the energy of the oxidized closed EC – e and EC_2 – e complexes. However, when one corrects for the large difference of 1.06 eV = 103 kJ mol^{-1} in the oxidation potentials between EC and EC_2, the barrier of the isolated EC oxidative decomposition becomes significantly higher. Fig. 4 compares oxidation induced reactions of EC_2 and isolated EC. The initial energy of the isolated EC was offset by the difference in the oxidation potentials between EC and EC_2 that corresponds to neutral EC_2 and EC used as a baseline instead of the oxidized counterparts. In addition to lower barriers for EC_2 compared to EC, this figure also shows that EC_2 oxidation yields more stable products than EC oxidation.

Possible reactions of the EC_2 – e products M6 and M7 were investigated because they could explain poly(ethylene carbonate) formation observed on cathodes as a result of EC-based electrolyte oxidation, especially at high temperature cycling.[2,35]

Specifically, M6 + M7 termination reactions between radicals result in the highly exothermic reaction shown in Fig. 5, forming an oligo(ethylene carbonate) product. Recombination of M6 and M7 with EC radicals is even more exothermic with ethylene carbonate groups present in both products. Alternatively, M6 and M7 radicals might cross to the anode side and undergo reduction reactions. One electron reduction is the most energetically favourable for both M6 and M7 as shown in Fig. 5. C_2H_4 is generated from the reduction of M7, this reaction would complement C_2H_2 evolution from EC reduction and it is consistent with reports of C_2H_4 generation upon battery charging with EC-based electrolytes.[9] The ring opening barrier and CO_2 detachment were investigated for M6 and neutral M6 + e, as also shown in Fig. 5. The TS for CO_2 detachment was 50.2 and 91.2 kJ mol^{-1} for M6 and M6 + e, respectively, suggesting that CO_2 would generate from this terminal carbonyl group, even at room temperature, while TS for ring opening had much higher values of 179–190 kJ mol^{-1}. This is another pathway for formation of CO_2 and alkyl carbonates at the anode.

4. Conclusions

It has been demonstrated that it is important to consider at least two EC molecules to accurately predict oxidation potential and reaction products of EC oxidation induced decomposition. The carbonyl group of the neighbouring EC initiates a nucleophilic attack on the EC ethylene group upon electron removal (oxidation) resulting in a spontaneous proton abstraction from the ethylene group and lowering of the oxidation potential of EC_2 compared to the isolated EC similar to the mechanism suggested by Jang and Oh.[44] The oxidation potential calculated with PCM was found to follow the order EC_2 (or EC_4) < EC_n–BF_4^- < EC (isolated), where n = 1,2,3. The investigated decomposition reaction paths of EC_2 yielded CO_2 and an ethanol radical cation, which were found to be the most probable oxidation products at room temperature. The isolated EC oxidation yielded aldehyde and CO_2. DFT calculations suggest that at high temperature or cathode potential, the high activation energy reaction paths will be activated that will yield oligo(ethylene carbonate), which was observed experimentally.[2] Our calculations also suggest a path for formation of the lithium alkyl carbonate products on the anode part of SEI by reduction of the intermediate oxidation products such as M6.

Acknowledgements

This work was supported *via* an Interagency Agreement between the U.S. Department of Energy and the U.S. Army Research Laboratory under DE-IA01-11EE003413 for the Office of Vehicle Technologies Programs including Batteries for Advanced Transportation Technologies (BATT) and ABR Programs. This research used resources of the National Energy Research Scientific Computing Center, which is supported by the Office of Science of the U.S. Department of Energy under Contract No. DE-AC02-05CH11231, the Natural Science Foundation of Guangdong Province, China (Grant No. 1035106310 1000001). Helpful discussions with Arthur von Wald Cresce, T. Richard Jow, Kang Xu, Shengshui Zhang and Kevin Leung are highly appreciated. Support from the University of Utah Center for High Performance Computing, DoD's High Performance Computing Modernization Program (HPCMP) is greatly acknowledged.

References

1 K. Xu, *Chem. Rev.*, 2004, **104**, 4303–4417.
2 L. Yang, B. Ravdel and B. L. Lucht, *Electrochem. Solid-State Lett.*, 2010, **13**, A95–A97.
3 M. Moshkovich, M. Cojocaru, H. E. Gottlieb and D. Aurbach, *J. Electroanal. Chem.*, 2001, **497**, 84–96.
4 F. Joho and P. Novak, *Electrochim. Acta*, 2000, **45**, 3589–3599.
5 J. Ufheil, A. Wursig, O. D. Schneider and P. Novak, *Electrochem. Commun.*, 2005, **7**, 1380–1384.
6 S. Matsuta, Y. Kato, T. Ota, H. Kurokawa, S. Yoshimura and S. Fujitani, *J. Electrochem. Soc.*, 2001, **148**, A7–A10.
7 K. Edstrom, T. Gustafsson and J. O. Thomas, *Electrochim. Acta*, 2004, **50**, 397–403.
8 L. D. Xing, W. S. Li, C. Y. Wang, F. L. Gu, M. Q. Xu, C. L. Tan and J. Yi, *J. Phys. Chem. B*, 2009, **113**, 16596–16602.
9 M. Onuki, S. Kinoshita, Y. Sakata, M. Yanagidate, Y. Otake, M. Ue and M. Deguchi, *J. Electrochem. Soc.*, 2008, **155**, A794–A797.
10 M. Arakawa and J.-i. Yamaki, *J. Power Sources*, 1995, **54**, 250–254.
11 T. Matsushita, K. Dokko and K. Kanamura, *J. Power Sources*, 2005, **146**, 360–364.
12 N. Dupre, J. F. Martin, J. Oliveri, P. Soudan, D. Guyomard, A. Yamada and R. Kanno, *J. Electrochem. Soc.*, 2009, **156**, C180–C185.
13 D. Aurbach, M. D. Levi, E. Levi, H. Teller, B. Markovsky, G. Salitra, U. Heider and L. Heider, *J. Electrochem. Soc.*, 1998, **145**, 3024–3034.
14 X. R. Zhang, J. K. Pugh and P. N. Ross, *J. Electrochem. Soc.*, 2001, **148**, E183–E188.
15 M. Ue, A. Murakami and S. Nakamura, *J. Electrochem. Soc.*, 2002, **149**, A1572–A1577.
16 Y. Fu, L. Liu, H. Z. Yu, Y. M. Wang and Q. X. Guo, *J. Am. Chem. Soc.*, 2005, **127**, 7227–7234.
17 P. Johansson, *J. Phys. Chem. A*, 2007, **111**, 1378–1379.
18 R. S. Assary, L. A. Curtiss, P. C. Redfern, Z. C. Zhang and K. Amine, *J. Phys. Chem. C*, 2011, **115**, 12216–12223.
19 S. P. Ong and G. Ceder, *Electrochim. Acta*, 2010, **55**, 3804–3811.
20 N. Shao, X.-G. Sun, S. Dai and D.-e. Jiang, *J. Phys. Chem. B*, 2012, **116**, 3235–3238.
21 N. Shao, X. G. Sun, S. Dai and D. E. Jianel, *J. Phys. Chem. B*, 2011, **115**, 12120–12125.
22 R. L. Wang, L. M. Moshurchak, W. M. Lamanna, M. Bulinski and J. R. Dahn, *J. Electrochem. Soc.*, 2008, **155**, A66–A73.
23 Y. K. Han, J. Jung, S. Yu and H. Lee, *J. Power Sources*, 2009, **187**, 581–585.
24 T. Li, L. Xing, W. Li, B. Peng, M. Xu, F. Gu and S. Hu, *J. Phys. Chem. A*, 2011, **115**, 4988–4994.
25 P. Johansson, *J. Phys. Chem. A*, 2006, **110**, 12077–12080.
26 P. Johansson and P. Jacobsson, *J. Power Sources*, 2006, **153**, 336–344.
27 M. Armand and P. Johansson, *J. Power Sources*, 2008, **178**, 821–825.
28 J. Scheers, P. Johansson and P. Jacobsson, *J. Electrochem. Soc.*, 2008, **155**, A628–A634.
29 L. D. Xing, C. Y. Wang, W. S. Li, M. Q. Xu, X. L. Meng and S. F. Zhao, *J. Phys. Chem. B*, 2009, **113**, 5181–5187.
30 K. Leung, *J. Phys. Chem. C*, 2012, **116**, 9852–9861.
31 O. Borodin and T. R. Jow, *ECS Trans.*, 2011, **33**, 77–84.
32 L. Xing, O. Borodin, G. D. Smith and W. Li, *J. Phys. Chem. A*, 2011, **115**, 13896–13905.
33 J. Vatamanu, O. Borodin and G. D. Smith, *J. Phys. Chem. C*, 2012, **116**, 1114–1121.
34 T. Matsushita, K. Dokko and K. Kanamura, *J. Electrochem. Soc.*, 2005, **152**, A2229–A2237.

35 O. Borodin and G. D. Smith, *J. Phys. Chem. B*, 2006, **110**, 6279–6292.
36 O. Borodin and G. D. Smith, *J. Phys. Chem. B*, 2009, **113**, 1763–1776.
37 K. T. Kuwata, T. S. Dibble, E. Sliz and E. B. Petersen, *J. Phys. Chem. A*, 2007, **111**, 5032–5042.
38 L. A. Curtiss, P. C. Redfern and K. Raghavachari, *J. Chem. Phys.*, 2007, **127**, 124105.
39 M. J. Frisch, G. W. Trucks, H. B. Schlegel, G. E. Scuseria and M. A. Robb, 2009.
40 O. Borodin and G. D. Smith, *J. Phys. Chem. B*, 2006, **110**, 4971–4977.
41 K. Abe, T. Hattori, K. Kawabe, Y. Ushigoe and H. Yoshitake, *J. Electrochem. Soc.*, 2007, **154**, A810–A815.
42 M. Ue, M. Takeda, M. Takehara and S. Mori, *J. Electrochem. Soc.*, 1997, **144**, 2684–2688.
43 L. A. Curtiss, P. C. Redfern and K. Raghavachari, *Wiley Interdiscip. Rev.: Comput. Mol. Sci.*, 2011, **1**, 810–825.
44 D. H. Jang and S. M. Oh, *J. Electrochem. Soc.*, 1997, **144**, 3342–3348.

Molecular Dynamics Simulations and Experimental Study of Lithium Ion Transport in Dilithium Ethylene Dicarbonate

Oleg Borodin, Guorong V. Zhuang, Philip N. Ross, and Kang Xu

Journal of Physical Chemistry: Condensed Matter, 117 (2013)

THE JOURNAL OF PHYSICAL CHEMISTRY C

Article

pubs.acs.org/JPCC

Molecular Dynamics Simulations and Experimental Study of Lithium Ion Transport in Dilithium Ethylene Dicarbonate

Oleg Borodin,*[,†] Guorong V. Zhuang,[‡] Philip N. Ross,[‡] and Kang Xu[†]

[†]U.S. Army Research Laboratory, Electrochemistry Branch, Sensors & Electron Devices Directorate, 2800 Powder Mill Road, Adelphi, Maryland 20783, United States

[‡]Lawrence Berkeley National Laboratory, Berkeley, California 94720, United States

Supporting Information

ABSTRACT: Understanding the properties of the solid electrolyte interphase (SEI) of lithium batteries is important for minimizing interfacial resistance and improving battery safety and cycling. Ion transport has been investigated in the dilithium ethylene dicarbonate (Li_2EDC) component of the SEI by impedance spectroscopy and molecular dynamics (MD) simulations employing a revised many-body polarizable APPLE&P force field. The developed force field accurately described the binding energies in $LiCH_3CO_3$, its dimer, and Li_2EDC calculated at the G4MP2 and MP2 levels. M05-2X and LC-ωPBE functionals predicted too high binding energy in lithium alkyl carbonates compared to the G4MP2 results, while the MP2 and M06-L predictions agreed well with the G4MP2 data. The conductivity of Li_2EDC at room temperature was found to be 10^{-9} S/cm from impedance measurements and extrapolation of MD simulation results. A near Arrhenius temperature dependence of Li_2EDC's conductivity was found in the MD simulations with an activation energy ranging from 64 to 84 kJ/mol. At room temperature, the lithium transport was subdiffusive on time scales shorter than $\sim 10^{-2}$ s in MD simulations corresponding to the onset of the plateau of resistivity vs frequency occurring at frequencies lower than 10^2 Hz. The influence of Li_2EDC ordering on the ion transport was investigated by contrasting supercooled amorphous melts and ordered material. At 393 K Li^+ transport was heterogeneous, showing chainlike and looplike Li^+ correlated displacements. The non-Gaussianity of Li^+ transport was examined. The influence of polarization on the structure of the lithium coordination shell and ion transport has been investigated in the molten phase of Li_2EDC and contrasted with the previous results obtained for room-temperature ionic liquids (RTILs). Nonpolarizable Li_2EDC exhibited orders of magnitude slower dynamics below 600 K and a higher activation energy for the Li^+ diffusion coefficient. Initial simulations of Li_2EDC dissolved in an EC:DMC(3:7)/$LiPF_6$ liquid electrolyte were performed at 450 K and showed a strong aggregation of Li_2EDC consistent with its phase separation from the electrolyte. The plasticizing effects of carbonate electrolyte on Li_2EDC dynamics were examined.

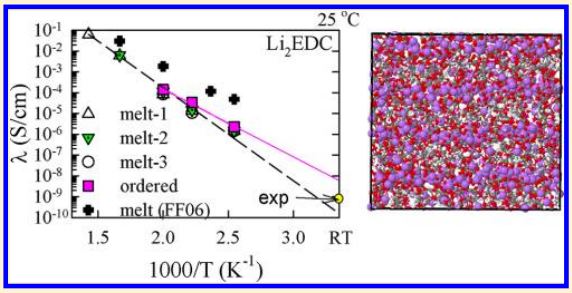

I. INTRODUCTION

During the first cycle of lithium battery operation, common carbonate-based electrolytes undergo reduction on lithium battery anodes such as graphite, lithium, or silicon (Si) anodes, leading to formation of the solid electrolyte interphase (SEI) from the reduction compounds after their precipitation on the anode surface. The ability of electrolytes in lithium ion batteries to form a stable electronically insulating but ionically conducting SEI on the anode surface is paramount for achieving practical cycle life, high power density, and improved safety.[1−3] It is generally accepted that electrolytes containing ethylene carbonate (EC) solvent form a cohesive SEI that usually contains dilithium ethylene dicarbonate Li_2EDC $(CH_2OCO_2^-/Li^+)_2$, while reducing linear carbonates leads to the formation of lithium alkyl carbonates, as reported from Fourier transform infrared spectroscopy,[4,5] gas chromatography,[6] and nuclear magnetic resonance (NMR)[7] studies. LiF and Li_2CO_3 were also frequently detected in the SEI, especially if traces of water were present.[1,4,5,8] Li_2EDC was reported to be moisture sensitive.[9] Its melting point could not be determined because it showed an onset of decomposition at around 120 °C, while most of the weight loss occurs at temperature higher than 200 °C before melting was observed.[9]

Battery impedance is typically the sum of the bulk electrolyte resistance (R_{bulk}), resistance of the SEI (R_{SEI}), and a charge transfer resistance (R_{ct}) that is associated with the Li^+ desolvation from the electrolyte or SEI and intercalation into the electrode and electrode resistance.[10] The electrolyte resistance is usually associated with the high frequency of the impedance spectrum; R_{ct} is associated with the lowest frequency of the impedance spectrum; while R_{SEI} is attributed to the intermediate frequency processes. Analysis of the temperature dependence of the impedance spectra indicated the following order to the activation energies associated with these

Received: January 2, 2013
Revised: March 15, 2013
Published: March 21, 2013

resistance contributions—$\Delta E(R_{ct}) > \Delta E(R_{SEI}) > \Delta E(R_{bulk})$—with the charge transfer resistance dominating at low temperatures and limiting cell power capabilities.[11] Interfacial resistance at the anode side with the thick SEI and a cathode with a much thinner passivation layer were also reported to have different activation energies.[10,12] For example, the interfacial impedance at the graphite anode was found[10,12] to have an activation energy of ΔE = 64 kJ/mol, which is noticeably higher than the activation energy for the $LiNi_{0.80}Co_{0.15}Al_{0.05}O_2$ cathode side (ΔE = 50 kJ/mol). These results suggest that the charge-transfer process and diffusion through the SEI formed on the anode might influence low-temperature battery power density to a larger extent than the cathode passivation layer. The activation energy for the interfacial impedance was also dependent on the electrolyte composition, which also influences SEI composition, structure, and activation energy for the Li^+ desolvation part to the interfacial impedance.[7,13−17]

While ion transport in bulk liquid and ionic liquid electrolytes doped with lithium salts has gotten significant attention from molecular dynamics (MD) simulations,[18−26] ab initio simulations,[27,28] and quantum chemistry,[21,23,29−36] studies of the ion transport in SEI compounds are rare. Wang et al.[37] have studied interactions of the lithium alkyl dicarbonate (Li_2EDC) clusters in the gas phase and identified bridging of carbonate groups through intermolecular O···Li···O interactions. Tasaki[38,39] studied interactions of the supercooled Li_2EDC with graphite, focusing on the difference between Li_2EDC and dilithium 1,2-propylene glycol dicarbonate cohesive binding energy to graphite; however, short simulation times did not allow the complete relaxation of Li_2EDC at low simulated temperatures. Tasaki et al.[39] also investigated the solubility of lithium carbonates and alkyl carbonate SEI components in electrolytes in MD and experimentally and the Li^+ diffusion in them at room temperature.[39] Iddir et al.[40] used density functional theory (DFT) to investigate the Li_2CO_3 modulus and the migration barriers for Li^+ diffusion between the planes defined by Li_2CO_3 with units along the open channels [010] having small migration barriers of 0.28 eV, while a higher migration barrier of 0.60 eV was found for the diffusion across the planes. Shi et al.[41] discussed the knock-off mechanism of Li^+ diffusion in crystalline Li_2CO_3 found in DFT calculations at a reported range of activation energies for Li^+ diffusion from 0.67 to 1.07 eV.

In our previous study,[42] we reported transport in lithium methyl carbonate and Li_2EDC in a molten supercooled state. The Li^+ diffusion coefficient from our simulations[42] was found to be in stark contrast with a dramatically faster ion transport in Li_2EDC predicted by Tasaki et al.[39] at room temperature. Specifically, the Li^+ diffusion in Li_2EDC of 8×10^{-12} m^2/s predicted by Tasaki et al.[39] is approximately four and a half orders of magnitude higher than $D(Li^+) = 2 \times 10^{-17}$ m^2/s reported by Borodin et al.[42] This discrepancy suggests a need for experimental measurements to validate our previous Li^+ transport predictions and establish the Li^+ diffusion and conductivity of Li_2EDC. Such experimental measurements are reported in this manuscript together with the development of the revised force field for Li_2EDC and MD simulations. We also found that when the previous force field[42] for Li_2EDC was combined with the APPLE&P force field in simulations of Li_2EDC dissolved in EC:DMC/$LiPF_6$ the simulated system crashed due to a close approach involving the ethereal oxygen of Li_2EDC indicating a need to revise the previous Li_2EDC force field to enable investigation of the Li_2EDC|electrolyte interface and mixtures of SEI compounds in electrolytes.

In this manuscript, the conductivity of the Li_2EDC SEI component[1,43] is investigated by impedance spectroscopy at room temperature as reported in Section II. Development of the revised polarizable force field for MD simulations of lithium alkyl carbonates is reported in Section III. MD simulation methodology is given in Section IV, while bulk properties of Li_2EDC are given as a function of temperature and compared with impedance spectroscopy data in Section V. Two states of Li_2EDC were simulated: a molten (or disordered) state and a crystal-like ordered Li_2EDC. Comparison between these simulations will allow examination of the influence of ordering on conductivity of Li_2EDC. The influence of polarization on the structural and transport properties of Li_2EDC is reported in Section VI and compared with the results for room-temperature ionic liquids (RTILs). Finally, initial results for Li_2EDC aggregation in EC:DMC/$LiPF_6$ electrolytes are reported in Section VII.

II. EXPERIMENTAL SECTION

The impedance characteristics of SEI-related pure Li compounds, specifically Li oxalate and Li_2EDC, were measured using stainless steel blocking electrodes in a Swageloc-type cell in a glovebox. The LEC and Li_2EDC were synthesized at the U.S. Army Research Laboratory (ARL) as described previously.[9] The samples were thin (0.02−0.1 mm) disks made from compacted (1 tonne) crystals/powders. Qualitatively, the characteristics of all three compounds were very similar and characteristic of that for pure Li ion conductors. As an example, the Nyquist plot for Li oxalate in Figure 1 consists of a single semicircle with a characteristic spur

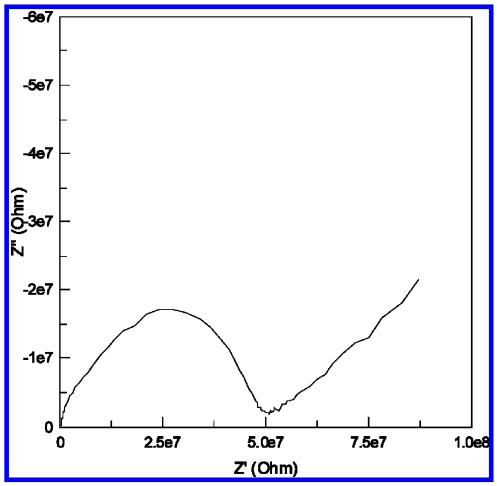

Figure 1. Nyquist plot of complex impedance of Li oxalate at ambient temperature.

at low frequency, which points to blocking of Li ions at the stainless steel electrodes. The compound with the highest conductivity was Li_2EDC. The Bode plot for resistivity and phase angle are shown for LEDC in Figure 2. The Bode plots for lithium oxalate and LEC were the same as for LEDC, differing only in the magnitude of the conductivity.

The dispersion of conductivity with frequency in the high-frequency range (e.g., above 100 Hz) is indicative of dielectric relaxation as described by the Cole−Cole relaxation model. The low-frequency dispersion is characteristic of compounds

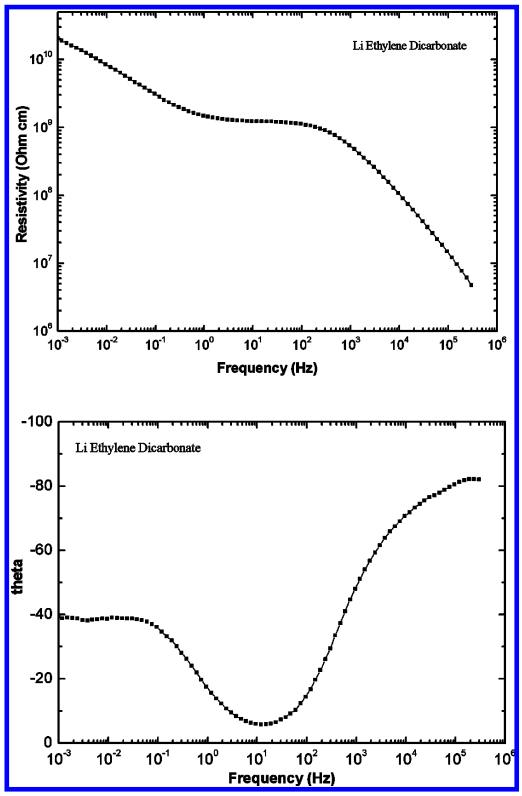

Figure 2. Bode plots of the resistivity and phase angle (proportional to the dielectric constant) for Li ethylene dicarbonate (Li_2EDC) at ambient temperature.

that become oriented in the electric field of the electrode and accumulate ions at the electrode interface, i.e., the behavior of a blocking electrode with a solid electrolyte. The impedance behavior of Li_2EDC and related compounds is qualitatively similar to that of Li ion conducting glasses like $Li_2O-V_2O_5-P_2O_5$.[44] The electrical response of Li_2EDC is therefore very similar to that of a solid electrolyte, as befits a compound that functions as a "solid electrolyte interface" between a metallic electrode and a liquid electrolyte. However, the absolute value of the conductivity in Li_2EDC is a few orders of magnitude lower than in Li ion conducting solid electrolytes. Nonetheless, if the SEI layer thickness is of the order of magnitude suggested by many studies, e.g., 10−100 nm, the conductivities are high enough to transport Li ions at a high rate (1 mA/cm^2) with only a small potential drop (10−100 mV) at ambient temperature. The temperature dependence of the conductivity was measured for Li_2EDC between −20 and 30 °C, yielding an apparent activation energy of 0.5 ± 0.1 eV.

III. QUANTUM CHEMISTRY CALCULATIONS AND FORCE FIELD DEVELOPMENT

Quantum chemistry calculations were performed for the purpose of APPLE&P[45] force field parametrization for lithium alkyl carbonates. We began by investigating the dependence of the binding energy between a Li^+ cation and a methyl carbonate anion ($MeCO_3^-$) on the level of theory at two geometries shown in Figure 3. The binding energy was calculated relative

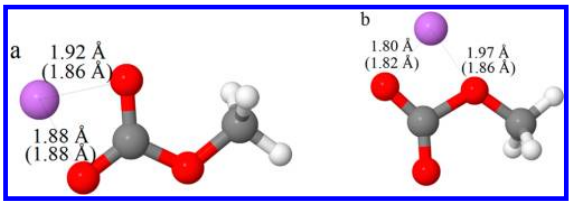

Figure 3. $Li^+/MeCO_3^-$ optimized geometries (a,b) from MP2/aug-cc-pvTz and MM using the APPLE&P force field. Selected distances from MM optimization and MP2/aug-cc-pvTz (in parentheses) are shown.

Table 1. Binding Energy of $Li^+/MeCO_3^-$ from QC Calculations and MM Using a Developed Force Field (FF)

level of theory	Geom.-a	Geom.-b	
$Li^+/MeCO_3^-$	(Li···O_2C−)	(Li···O−)	
G4MP2	−163.0	−157.4	
MP2/aug-cc-pvTz	−164.2	−158.4	
MP2(fc)/aug-cc-pvTz //MP2/cc-pvTz	−164.2	−158.4	
MP2(fc)/aug-cc-pvDz	−162.8	−157.4	
MP2(fc)/cc-pvTz	−171.6	−165.9	
M05-2X/aug-cc-pvTz	−169.7	−162.7	
M05-2X/aug-cc-pvDz	−168.5	−161.5	
M05-2X/cc-pvTz	−173.8	−165.9	
M06-L/aug-cc-pvTz	−164.3	−159.0	
M06-L/aug-cc-pvDz	−163.6	−158.1	
FF,f1e36	−162.4	−154.5	
$(Li^+/MeCO_3^-)_2$	Geom.-a	Geom.-b	Geom.-c
G4MP2	−372.3		
MP2/aug-cc-pvTz	−374.5		
MP2/aug-cc-pvDz[a]	−373.5	−372.3	−368.8
M05-2X/aug-cc-pvDz	−385.0	−384.8	
B3LYP/aug-cc-pvDz	−382.7		
M06-L/aug-cc-pvTz	−374.2	−374.3	
M06-L/aug-cc-pvDz	−372.3	−372.9	−368.5
FF,f1e36	−374.4	−373.6	−365.8

to the isolated Li^+ and $MeCO_3^-$. The results of this investigation are given in Table 1. Stronger binding is observed for geometry (a) where Li^+ has a bidentate binding to carbonate oxygens. The $Li^+/MeCO_3^-$ binding energy from the G4MP2 calculations was very similar to the MP2/aug-cc-pvTz and MP2/aug-cc-pvDz results, while calculations performed at MP2/cc-pvTz yielded a significantly higher binding energy, indicating that omission of diffuse functions in the $MeCO_3^-$ anion leads to inaccurate binding energies. The M05-2X density functional was found to predict too strong binding between Li^+ and $MeCO_3^-$ in accord with previous studies of the Li^+ binding to carbonates[24,25] and acetonitrile (AN).[46] However, in the Li^+/AN_n complexes, little difference was observed for the binding energy calculated employing the cc-pvTz and aug-cc-pvTz basis sets in contrast to the significant difference observed here for Li_2MeCO_3. Total binding energy was also calculated for $(Li^+/MeCO_3^-)_2$ as shown in Figure 4. A comparison of $(Li^+/MeCO_3^-)_2$ binding energies is given in Table 1. It indicates that binding energies from the MP2/aug-cc-pvTz and MP2/aug-cc-pvDz level calculations agree well with the G4MP2 energies, while M05-2X and B3LYP DFT methods significantly overestimate the Li^+ binding energy and are not reliable for force field parametrization. The M06-L density functional, on the

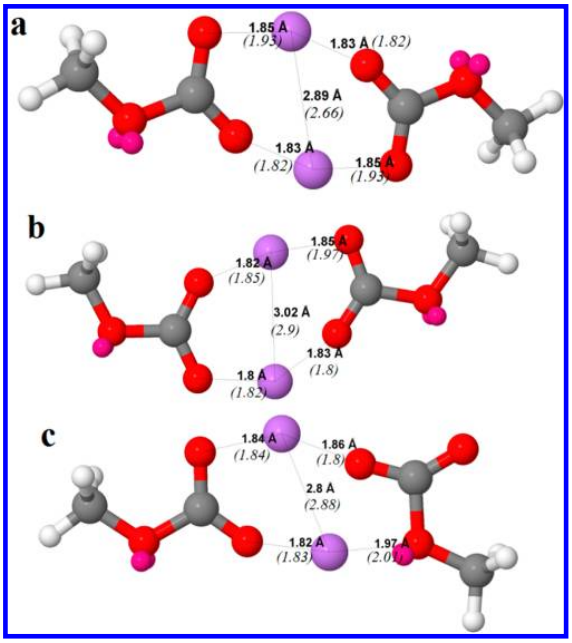

Figure 4. $(Li^+/MeCO_3^-)_2$-optimized geometries (a–c) from MM using the APPLE&P force field. Selected distances from MM and MP2/aug-cc-pvDz optimization are shown, with the MP2/aug-cc-pvDz results given in parentheses. The distances from MP2/aug-cc-pvTz optimization differed from the MP2/aug-cc-pvDz distances by less than 0.02 Å for complex (a) and are not shown.

other hand, has much better agreement with the G4MP2 and MP2 results than the M05-2X and B3LYP functionals. Recently, Bryantsev[47] also reported good accuracy in predicting Li^+–solvent binding energies using the M06-L functional.

Next, the force field parameters were fit for $LiMeCO_3$ and Li_2EDC using a many-body polarizable APPLE&P force field[45] functional form that was previously applied for ionic liquids[45,48,49] and liquid electrolytes.[25] Here we briefly outline the main features of the force field. The nonbonded energy $U^{NB}(\mathbf{r})$ consists of the sum of the two-body repulsion and dispersion energy terms $U^{RD}(\mathbf{r})$, the energy due to interactions of fixed charges $U^{coul}(\mathbf{r})$, and the polarization energy $U^{pol}(\mathbf{r})$ arising from the interaction between the induced dipoles with fixed charges and other induced dipoles

$$U^{NB}(\mathbf{r}) = U^{RD}(\mathbf{r}) + U^{coul}(\mathbf{r}) + U^{pol}(\mathbf{r})$$
$$= \sum_{i>j}\left(A_{\alpha\beta}\exp(-B_{\alpha\beta}r_{ij}) - C_{\alpha\beta}r_{ij}^{-6} + D\left(\frac{12}{B_{\alpha\beta}r_{ij}}\right)^{12}\right)$$
$$+ \sum_{i>j}\left(\frac{q_iq_j}{4\pi\varepsilon_0 r_{ij}}\right) - 0.5\sum_i \vec{\mu}_i\vec{E}_i^{\,0} \quad (1)$$

where $\vec{\mu}_i = \alpha_i\vec{E}_i^{tot}$ is an induced dipole at a force center i; α_i is the isotropic atomic polarizability; $\vec{E}_i^{tot}$ is the total electrostatic field at the atomic site i due to permanent charges q_j and induced dipoles $\vec{\mu}_j$; ε_0 is the dielectric permittivity of vacuum; $\vec{E}_i^0$ is the electric field due to fixed charges only; $A_{\alpha\beta}$ and $B_{\alpha\beta}$ are the repulsion parameters; and $C_{\alpha\beta}$ is the dispersion parameter for interaction between atoms i and j with atom types α and β. The term $D(12/B_{\alpha\beta}r_{ij})^{12}$, with $D = 5 \times 10^{-5}$ kcal/mol for all pair interactions, is essentially zero at typical nonbonded atomic separations but becomes the dominant term at $r_{ij} < 1$ Å, ensuring that exp-6 potential is repulsive at distances much smaller than the size of an atom. Intramolecular nonbonded interactions are included for atoms separated by three or more covalent bonds. We used Thole screening[50] ($a_T = 0.2$) that smears the induced dipoles to prevent the so-called "polarization catastrophe" from occurring. The interaction between an induced dipole and a partial charge separated by three bonds was scaled by 0.8. Finally, for heteroatom interactions, the modified Waldman–Hagler combining rules[50] were used. The exp-6 force of the repulsion–dispersion parameters was used to represent nonbonded interactions, while atomic charges centered on atoms and off-atom positions in conjunction with the atom-centered isotropic dipole polarizability represented Coulomb and polarization interactions.

The repulsion–dispersion parameters for all interactions including Li^+–X (X = O,C,H) were taken from previous works.[25,45] Bond increments from an oligoether force field[45] were used for the O–CH_2 and O–CH_3 groups, while other bond increments were fit to the electrostatic potential of $MeCO_3^-$, EDC^{2-}, and $LiEDC^-$ calculated at MP2/aug-cc-pvTz. The polarization of C and H in the –CH_2– and –CH_3 groups from the oligoether force field was used, while the polarizability of the other atoms was fit to the molecular polarizability calculated at the MP2/cc-pvTz level and multiple paths probing interactions with the test charge of +0.5e, as shown in Figure 5.

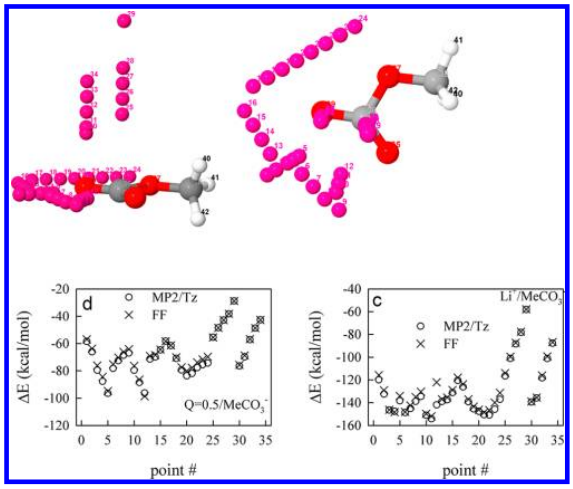

Figure 5. Binding energy of $MeCO_3^-$ with Li^+ and a test charge of Q = +0.5e from the MP2/aug-cc-pvTz calculations and FF along the path shown in (a,b).

Developed force field parameters are given in the Supporting Information.

The developed force field predicted Li^+ binding energy in $Li^+/MeCO_3^-$ only 0.6 kcal/mol higher than the G4MP2 level for the most stable geometry (a) and 3 kcal/mol lower binding energy for the less stable geometry (b), as shown in Table 1. The $Li^+\cdots O$ distances in the $Li^+/MeCO_3^-$ complexes from MM using a developed force field were in good agreement with the MP2/aug-cc-pvTz results, as shown in Figure 3. Away from the most stable Li^+ position, the force field also predicted a Li^+ binding energy in good agreement with the MP2/aug-cc-pvTz

results, as shown in Figure 5 for the $Li^+/MeCO_3^-$ cluster. The total binding energy of the $LiMeCO_3$ dimer was accurately predicted by the developed force field for the geometries shown in Figure 4a,b, as seen in Table 1. The accuracy of predicting the binding energy by the force field is similar to the accuracy of quantum chemistry calculations for these geometries. For the higher-energy, and therefore less important, cluster geometry shown in Figure 4c, the developed force field predicted a binding energy that was ~3 kcal/mol lower than the QC estimates. The previous force field,[42] however, predicted a binding energy of $Li^+/MeCO_3^-$ equal to −170.7 kcal/mol for the most stable cluster, which is 8.3 kcal/mol higher than the revised force field developed in this work. The total binding energy for a $(Li^+/MeCO_3^-)_2$ cluster of −374.4 kcal/mol from the developed force field is also significantly lower than the binding energy of this cluster from the previous force field (−382.2 kcal/mol), indicating a significant difference between previous[42] and recent versions. The ability of the force field to accurately predict binding energy in $Li^+/MeCO_3^-$ clusters indicates that the cation−anion binding is essentially ionic, as expected. This view is also consistent with the negligible occupancy of the valence 2S Li orbital compared to the 1S core orbital observed in the $(Li^+/MeCO_3^-)_2$ cluster. The ability of the developed force field to predict the conformational energies of Li_2EDC is shown in the Supporting Information. The $g^-g^+g^-$ Li_2EDC conformer was found to be more stable than the ttt conformer by 31 kcal/mol in MM calculations using a developed force field and by 28.5 kcal/mol from the MP2/aug-cc-pvTz//MP2/cc-pvTz calculations.

IV. SIMULATION METHODOLOGY

A MD simulation package *Lucretius* that includes many-body polarization was used for all the MD simulations. The Ewald method was used for calculating charge−charge and charge-induced dipole interactions with $k = 8^3$ vectors used. The Thole screening parameter of 0.2, as described in the force field section, was used. The interaction between an induced dipole and a partial charge separated by three bonds was scaled by 0.8, providing an improved description of the electrostatic potential around the molecules. Multiple time step integration was used with an inner time step of 0.5 fs (bonded interactions), a central time step of 1.5 fs for all nonbonded interactions within a truncation of 7.0 Å, and an outer time step of 3.0 fs for all nonbonded interactions between 7.0 Å and the nonbonded truncation distance of 12 Å, as well as for the reciprocal part of Ewald. A Nose−Hoover thermostat and a barostat were used to control the temperature and pressure with the associated frequencies of 10^{-2} and 0.1×10^{-4} fs.

The initial configuration of Li_2EDC was generated by replicating a Li_2EDC complex in a ttt EDC^{2-} conformation along the *x*, *y*, and *z* directions to generate an orthorhombic box in which EDC molecules in each layer were bridged by two Li^+. Thus, the simulation box contained 512 Li^+ and 256 EDC^{2-}. A 20 ns run was performed at 393 K using *NPT* conditions, where *P* is the stress tensor. At that point, simulations at 450 and 500 K were initiated using an orthorhombic box, and the 393 K runs were continued. Simulation run lengths are given in Table 2. Well-ordered layers of Li^+ were observed in these simulations, as shown in Figure 6. The layered structure of Li_2EDC is consistent with XRD data.[9] We refer to these simulations as simulations of the ordered (or crystal-like) Li_2EDC. The crystal was orthorhombic in agreement with experiments,[9] but no crystal structure was available from experiments to compare with the simulation results.[9] The simulation box shape was constrained to be orthorhombic. The average shear stress was ~300 atm at 450 and 393 K, indicating that simulated crystalline Li_2EDC is expected to be slightly nonorthorhombic.

Table 2. Density of Simulated Li_2EDC Melts and Crystals and Simulation Run Lengths

	Li_2EDC melt (v1)			
temp (K)	700	600	500	450
length of equilibration (ns)	14	35	40	160
length of the production run (ns)	15	57.6	144	140
MD, density (kg/m^3)	1517	1567	1612	1610
	Li_2EDC melt (v2)			
temp (K)	600	500	450	393
length of equilibration (ns)	18	50	150	95
length of the production run (ns)	21	142.4	180	127
MD, density (kg/m^3)	1568	1610	1622	1631
	Li_2EDC melt (v3)			
temp (K)	500	450	393	
length of equilibration (ns)	30	150	170	
length of the production run (ns)	56	300	300	
MD, density (kg/m^3)	1613	1621	1636	
	Li_2EDC melt			
(polarization set to zero)				
temp (K)	700	600		
length of equilibration (ns)	12	25		
length of the production run (ns)	25	60		
MD, density (kg/m^3)	1544	1591		
	Li_2EDC ordered			
temp (K)	500	450	393	
length of equilibration (ns)	80	160	150	
length of the production run (ns)	280	341	420	
MD, density (kg/m^3)	1626	1634	1645	

To investigate the influence of Li^+ order−disorder on ion diffusion, a molten (disordered) Li_2EDC configuration was generated from the ordered sample by melting (disordering) Li_2EDC at 900 K during a 4 ns *NPT* run following a 20 ns equilibration at 600 K to obtain a starting configuration for 700, 600, and 500 K runs. At 600 K, the residence time of Li with the carbonyl group is 1.3 ns, thus more than 15 exchanges occurred between the Li^+ and carbonyl group, indicating that the system underwent a significant relaxation toward equilibrium. The length of the equilibration and production runs is given in Table 2, while details of the protocol used to create and equilibrate the three molten Li_2EDC systems are summarized in the Supporting Information. MD simulations of the molten Li_2EDC were also performed with the polarization turned off, denoted as the two-body (TB) nonbonded potential, to examine the influence of polarization on the Li_2EDC structure and ion transport. The initial configuration at 700 K for these simulations was taken from the final configuration of the simulation run, employing a many-body polarizable APPLE&P force field at the same temperature.

MD simulations of Li_2EDC in EC:DMC(3:7)/$LiPF_6$, solvent/salt = 10, were performed to obtain initial information on the time scale of the Li_2EDC percolating network formation in electrolyte. The simulation cell contained 192 EC, 448 DMC, 64 $LiPF_6$, and 128 Li_2EDC molecules. These simulations were performed at 450 K. Higher temperature was chosen to observe aggregation on a time scale of 30 ns. The Li_2EDC in EC:DMC(3:7)/$LiPF_6$ was pre-equilibrated at 500 K with the increased repulsion

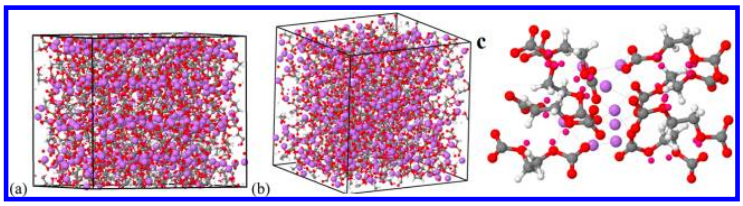

Figure 6. Snapshot from the MD simulations of Li_2EDC of the ordered and amorphous (molten phase) states at 450 K (Li^+ are highlighted as pink balls). A representative cluster from bulk Li_2EDC (ordered) with distances less than 2.4 Å connected by dashed lines is also shown (c).

interaction between the carbonate groups of EDC^{2-} to reduce aggregation.

V. SIMULATION RESULTS FOR BULK LI_2EDC

Structural Properties of Li_2EDC. We begin analysis of the Li_2EDC structure by examining radial distribution functions (RDFs) for ordered and molten Li_2EDC, as shown in Figure 7.

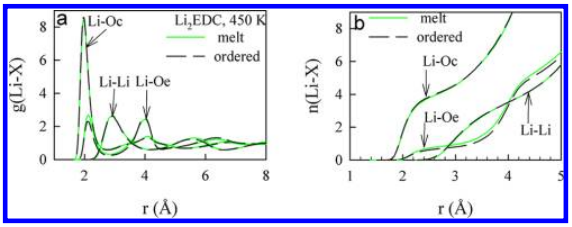

Figure 7. Radial distribution function (a) and coordination number (b) for Li_2EDC in the molten and ordered states at 450 K. O_c (carbonyl oxygen), O_e (ether oxygen). Arrows indicate the size of the first coordination shell: 2.4 Å for Li−O and 4.3 Å for Li−Li.

The Li−O_c first peak is around 2 Å, where O_c denotes oxygen from O*═C. The Li−O_e (ethereal oxygen) is shifted to slightly larger distances of 2.1 Å compared to the Li−O_c peak. The Li−Li first peak is located around 3 Å. We observe a strong preference for Li^+ to coordinate carbonate oxygen atoms as opposed to ether oxygen atoms, with coordination numbers of 3.6 carbonyl oxygen and 0.65 ether oxygen atoms within 2.4 Å of a Li^+ cation. These coordination numbers are similar to previous Li_2EDC simulations.[42] The choice of a 2.4 Å cutoff for the Li−O coordination shell is dictated by the distance where the Li−O RDFs decay to 1 after the first peak, and thus oxygens closer than 2.4 Å are considered to be strongly coordinating to a Li^+. The extended Li^+ coordination shell of 4.3 Å, defined by the minimum after the first peak of the Li−Li RDF, indicated that the Li^+ cation is surrounded by four other Li^+ in this extended coordination shell. In a molten state, we observed a slightly enhanced probability for a Li^+ to coordinate the ether oxygen compared to the ordered state because close packing of the EDC^{2-} anions in the ordered state is expected to impede access of Li^+ to ether groups of EDC^{2-}. The following picture emerges: a network of Li^+ bridges together layers or aggregates of EDC^{2-} anions where each Li^+ coordinates ∼4 oxygens of EDC^{2-} that come predominantly from the different EDC^{2-} chains. The Li cations are spaced at ∼3 Å from each other with the preference for each Li^+ to be surrounded by four other Li^+.

Transport Properties. Ion transport in Li_2EDC was examined by calculating ion self-diffusion coefficients for ordered and molten material, ionic conductivity, and Li^+ residence times near anions. The self-diffusion coefficient D_i for species i was calculated using the Einstein relation at temperatures when a diffusive regime has been reached in *NVT* simulations

$$D_i = \lim_{t\to\infty} \frac{\langle \mathrm{MSD}(t)\rangle}{2nt} \tag{2}$$

where MSD(t) is mean-square displacement of a molecule (of type i) center-of-mass during time t, and ⟨ ⟩ denotes an ensemble average. n is the dimensionality of the space: n = 3 for 3-D diffusion in molten samples, n = 2 for the Li^+ diffusion within Li^+ layers in the ordered sample (x−y plane), and n = 1 for Li^+ diffusion perpendicular to Li^+ layers (z-direction). At the lowest simulated temperatures when a diffusive regime has not been reached, we followed our previous work[51] and calculated the diffusion coefficient by superimposing MSD(t) plots at different temperatures for displacements greater than 1 $Å^2$ using the temperature-dependent time shift factor, $a(T)$, as shown in Figure 8a. The MSD(t) values below 1 $Å^2$ do not superimpose due to a smaller Li^+ vibrational amplitude at denser cages observed at lower temperatures that reflect a decrease of the Debye−Waller factor with decreasing temperature. Assuming that the same temperature-dependent shift factor that applies in the subdiffusive regime also applies in the diffusive regime, the temperature-dependent Li^+ self-diffusion coefficients were determined using eq 3.

$$D(T) = D(500\ \mathrm{K})/a(T) \tag{3}$$

where D(500 K) is the ion self-diffusion coefficient at 500 K that was obtained using eq 1 and $a(T)$ is the temperature-dependent time-shift factor obtained by superimposing Li^+ MSD(t).

Changes of the ion mobility were carefully monitored as MD simulations progressed to ensure that equilibrium ion diffusion coefficients were reached during simulations. Figure 8b illustrates changes of the apparent ion diffusion coefficient obtained from the consequent blocks of the trajectory. The apparent self-diffusion coefficient was extracted from the fit to MSD(t) for time greater than 15 ns for each 40−80 ns block of the trajectory. Figure 8b indicates that the Li^+ self-diffusion coefficient decreases by a factor of 2 over the first 200 ns at 450 K, indicating that this part of the trajectory should be excluded from analysis. During the first 200 ns the Li^+ cation moves ∼10 $Å^2$, which is the size of the carbonate group; thus, at least one Li^+ jump should occur on average to reach equilibrium transport properties. Obtaining the equilibrium Li^+ diffusion coefficient for temperatures 500 K and above required a short equilibration time of less than 30 ns. On the other hand, at lower temperature of 393 K, the extracted Li^+ self-diffusion coefficients likely suffer from an additional uncertainty due to incomplete equilibration.

Diffusion coefficients for Li_2EDC in the molten and ordered states are shown in Figure 9. For the ordered sample, the Li^+ diffusion coefficient within the Li^+ layers, denoted as $D(x,y)$, was found to be a factor of 2−3 faster than the average diffusion in the molten state and at least factor of 4−7 faster than the Li^+

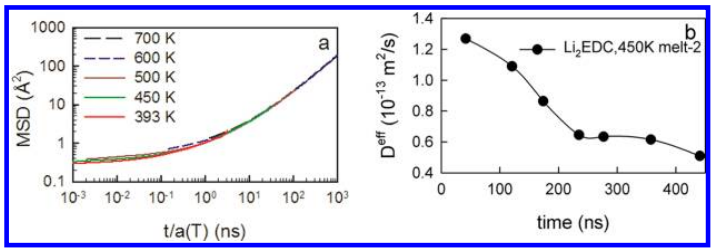

Figure 8. Li^+ mean-squared displacements (a) of Li_2EDC melt-1 for 700, 600, and 500 K; melt-2 at 450 K; and melt-3 at 393 K and the effective diffusion coefficient for melt-2 at 450 K (b).

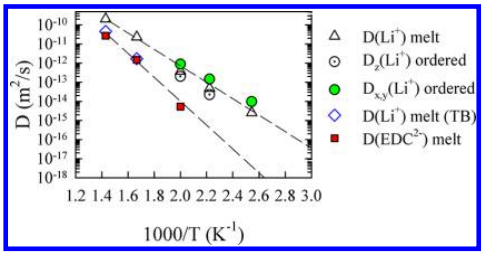

Figure 9. Diffusion coefficients from MD simulations using a polarizable APPLE&P force field and from simulations with the polarization turned off (a two-body (TB) force field).

diffusion coefficient in the direction perpendicular to the Li^+ layers at 450 K. As temperature decreases, the Li^+ diffusion coefficient between Li^+ layers in the ordered sample decreases faster than the diffusion coefficient along the layers, indicating that at low temperature the Li^+ diffusion across the layers will be negligibly small compared to the diffusion within the Li^+ layers. The Li^+ diffusion in Li_2EDC of 8×10^{-12} m^2/s predicted from Tasaki et al.[39] at room temperature is significantly higher than the diffusion coefficient $\sim 10^{-16}$ m^2/s extrapolated to 333 K as shown in Figure 9. It is likely that the reason behind the too high diffusion coefficient reported by Tasaki at et.[39] at room temperature is that he fit the diffusion coefficient to MSD(t) in the subdiffusive regime. Application of the time−temperature superposition with the activation energies from Figure 9 to MSD shown in Figure 8 gives an estimate of the subdiffusive regime extending to 10^{-2} s at room temperature as discussed below. Figure 9 also shows the anion diffusion coefficient, which is significantly slower than the Li^+ diffusion coefficient and has a high higher activation energy. We estimate that the anion charge transport will have the following contributions to conductivity: 53% at 700 K, 25−32% at 600 K, 7−9% at 500 K, and negligible contribution at temperatures below 393 K. Thus, below 393 K, Li_2EDC essentially acts as a single ion conductor.

The isotropic ionic conductivity from MD simulations is given by the Einstein relation

$$\lambda = \lim_{t\to\infty} \lambda^{app}(t) = \lim_{t\to\infty} \frac{e^2}{6tVk_BT} \int_{i,j}^{N} z_i z_j \langle([\mathbf{R}_i(t) - \mathbf{R}_i(0)])([\mathbf{R}_j(t) - \mathbf{R}_j(0)])\rangle \quad (4)$$

where e is the electron charge; V is the volume of the simulation box; k_B is Boltzmann's constant; T is the temperature; t is time; z_i and z_j are the charges over ions i and j in electrons; $\mathbf{R}_i(t)$ is the displacement of the ion i during time t; the summation is performed over all ions; $\langle\ \rangle$ denotes the ensemble average; and N is the number of cations plus anions in the simulation cell. For the anisotropic system, eq 4 will yield an average over all directions. Here $\lambda^{app}(t)$ is the apparent time-dependent conductivity whose long-time limit corresponds to the equilibrium DC conductivity. Conductivity can be decomposed into an "ideal" conductivity that would be realized if ion motion was uncorrelated, denoted $\lambda_{uncorr}(t)$, and the degree to which ion motion is in fact uncorrelated, or α_d. The degree of uncorrelated ion motion is given as the ratio of the collective (total) charge transport (λ) to the charge transport due to self-diffusion only (λ_{uncorr})

$$\lambda_{uncorr}^{app} = \lim_{t\to\infty} \lambda_{uncorr}^{app}(t) = \lim_{t\to\infty} \frac{e^2}{6tVk_BT} \int_i^n z_i^2 \langle[\mathbf{R}_i(t) - \mathbf{R}_i(0)]^2\rangle = \frac{e^2}{Vk_BT}(n_+D_+^{app} + 4n\_D_-^{app}) \quad (5)$$

$$\alpha_d = \frac{\lambda}{\lambda_{uncorr}} = \lim_{t\to\infty} \alpha_d(t) = \lim_{t\to\infty} \frac{\lambda^{app}(t)}{\lambda^{app}{}_{uncorr}(t)} \quad (6)$$

Here n_i is the number of atoms of type i = (Li^+ or EDC^{2-}); above that one uses N instead of n, where $n = n_+ + n_-$. We found that α_d is above 0.95, indicating that the anion and Li^+ motion is essentially uncorrelated, and the conductivity can be calculated using eq 5 at 600 K and below. The conductivity of molten and ordered Li_2EDC is shown in Figure 10.

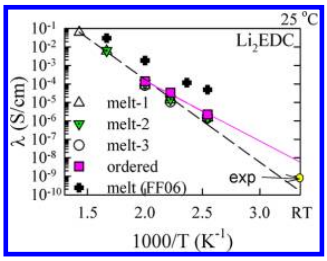

Figure 10. Conductivity from MD simulations using a polarizable APPLE&P force field for melts and ordered Li_2EDC materials. Results from the MD simulations using a previous force field FF06 are also shown for comparison (crosses). ΔE(melt) = 84 kJ/mol, ΔE(ordered) = 64 kJ/mol.

Molten Li_2EDC shows a slightly lower conductivity than ordered Li_2EDC, which is in agreement with the behavior of the Li^+ self-diffusion coefficients. The Arrhenius fit to conductivity for molten Li_2EDC yields the activation energy of 84 kJ/mol, while an Arrhenius fit to only ordered Li_2EDC yields a lower activation energy of 64 kJ/mol. However, ordered Li_2EDC was simulated only at three temperatures, and

the conductivity at 393 K was extracted from the subdiffusive behavior as discussed above and, therefore, bears the largest error bar. Extrapolation of the conductivity from these two Arrhenius fits to room temperature yields a conductivity of 2×10^{-10}–10^{-8} S/cm, which is in good agreement with the experimentally measured value of 10^{-9} S/cm. MD simulations using a previous Li_2EDC force field[42] predict a conductivity significantly higher than the MD simulations, employing a revised force field and experimental data.

It is interesting to compare the activation energy for conductivity from simulations with the published values for the interfacial impedance extracted from impedance fits at a number of temperatures. Fits to impedance data at the graphite anode[10,12] yielded an activation energy of ΔE = 64 kJ/mol, which is noticeably higher than the activation energy for the $LiNi_{0.80}Co_{0.15}Al_{0.05}O_2$ cathode side (ΔE = 50 kJ/mol). The Li_2EDC activation energy of 64–84 kJ/mol extracted from MD simulations is similar to the experimentally determined activation energy for the anode side,[10,12] as Li_2EDC is expected to be present in the anode SEI. Interestingly, the activation energy attributed to the Li^+ desolvation from EC:DMC/$LiPF_6$ electrolytes also had a similar activation energy, ~60–70 kJ/mol.[7] Recent DFT studies of the Li^+ transport in crystalline SEI model compounds such as Li_2CO_3 also reported an activation energy for Li^+ diffusion in the range of 70 kJ/mol at low voltage with the activation energy for the proposed knock-off mechanism in Li_2CO_3 in the range of 64–103 kJ/mol.[41] Thus, we suggest that both amorphous and crystalline Li^+ carbonates and alkyl dicarbonates have a similar activation energy of around 60–80 kJ/mol, which is in a reasonable agreement with the estimate of 50 ± 10 kJ/mol from the limited experimental data on Li_2EDC impedance. These data indicate that the portion of the impedance spectra with the activation energy around 20 kJ/mol that was assigned[7] to the Li^+ transport in SEI cannot be attributed to transport in Li_2EDC or Li_2CO_3. It is important to note that the proposed mechanism for Li_2CO_3 conduction by Shi et al.[41] was dependent on the charged defects and, therefore, is voltage dependent. In our simulations no external electric field but a Li^+ hop creates a vacancy in the cage surrounded by negatively charged anions.

Next, we use time–temperature superposition assumption to estimate the time scale for the Li^+ subdiffusive motion. From Figure 10, we expect ion transport at room temperature to be ~10^5 times slower than at 500 K. Thus, the time it takes for a Li^+ to reach diffusive behavior at 500 K should be multiplied by 10^5 to obtain an estimate of the time scale of subdiffusive behavior at room temperature. Therefore, it takes 10^{-2} s to reach the Li^+ diffusive behavior at room temperature using the definition that Li^+ motion is considered to be subdiffusive if it diffuses less than 10 Å^2. Interestingly, impedance spectroscopy data shown in Figure 2 also indicate that the plateau for the Li^+ resistance is observed at frequencies below 100 Hz. This allows us to clearly associate resistance at frequencies higher than 100 Hz with the subdiffusive behavior expected at times less than 10^{-2} s observed in MD simulations.

Residence Time Analysis. To further understand details of the Li^+ diffusion mechanism in the molten and ordered states, the Li–Li and Li–O residence times were calculated as integrals of the residence time autocorrelation function (ACF) $P(t - t_0)$. It gives the probability that the complex existing at time t_0 will still exist at time t. It is formally defined as

$$P_{Li^+-X}(t) = \frac{\langle H_{ij}(t)H_{ij}(0)\rangle}{\langle H_{ij}(0)H_{ij}(0)\rangle} \quad (7)$$

where $H_{ij}(t)$ is 1 if a Li^+–X complex is formed and zero otherwise and $\langle\ \rangle$ denotes average over all time origins and pairs of Li^+–X complexes, where X is O(carbonyl) or Li^+. The Li···O(carbonyl) complex is considered formed if the Li–O distance is less than 2.4 Å, while the Li^+···Li^+ complex is formed if the distance between Li^+ cations is less than 4.3 Å, which is consistent with the analysis of RDFs presented earlier. Figure 11

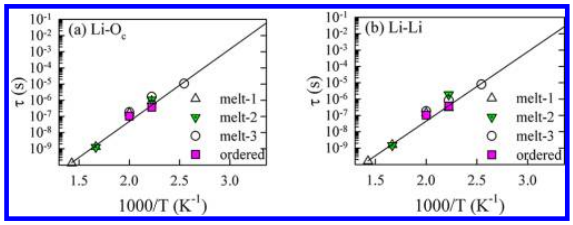

Figure 11. Residence time (τ) extracted from MD simulations of Li_2EDC.

shows temperature dependence of the Li–O and Li–Li residence times for both molten and ordered Li_2EDC. Interestingly, the Li–Oc and Li–Li residence times are slightly lower for the ordered state than for molten Li_2EDC, indicating a slightly faster exchange in the ordered state. The residence times exhibit an Arrhenius temperature dependence reminiscent of strong glasses with activation energies of 84 kJ/mol for Li–Oc and 81 kJ/mol for Li–Li residence times, respectively. The activation energy for the residence time is similar to the activation energy extracted for diffusion coefficients, thus the product of residence time and diffusion coefficient shows only minor variations as shown in the Supporting Information. Figure 11 also indicates that the extrapolated residence time at room temperature is around 10^{-2} s, which is consistent with the Li^+ cation motion being subdiffusive, at times shorter than 10^{-2} s as discussed earlier. It is instructive to compare the Li–O residence times in Li_2EDC with the Li–solvent and Li–anion residence times found in common electrolytes such as EC:DMC/$LiPF_6$.[25] The Li–EC and Li–DMC residence times were found to be in the range of 0.2–0.7 ns, while the Li–PF_6 residence time was in the range 1.6–3 ns at room temperature.[25] Thus, the characteristic Li^+ hopping time is approximately 7 orders of magnitude slower in Li_2EDC than in liquid electrolytes.

Non-Gaussianity of Lithium Motion. The distribution of relaxation processes occurring with different rates is often related to the non-Gaussian effects in ionic liquids[52,53] and supercooled model liquids.[54] A connection between $\alpha_2(t)$ and the degree of heterogeneity is often observed and discussed. A high non-Gaussianity parameter is also associated with the deviation from the diffusive behavior. The non-Gaussian parameter $\alpha_2(t)$ is given by

$$\alpha_2(t) = \frac{3\langle R(t)^2\rangle}{5\langle R(t)^2\rangle^2} \quad (8)$$

where $R(t)$ is the displacement of Li^+ over time t and $\langle\ \rangle$ denotes average over all time origins and Li^+. The non-Gaussian parameter was calculated for Li_2EDC and is shown in Figure 12(a) as a function of mean-squared displacement R^2. In all cases, $\alpha_2(t)$ exhibits a maximum at displacements from 1 to 3 Å^2,

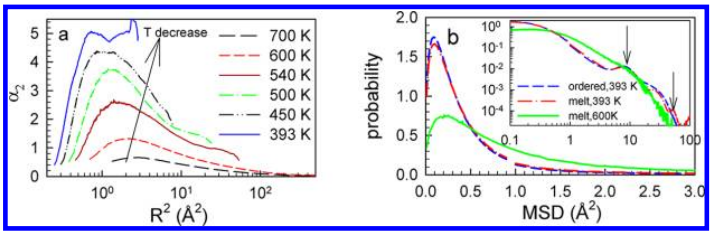

Figure 12. Non-Gaussian parameter for molten Li_2EDC (a) and probability density for distribution of Li^+ squared displacements for time, at which $\langle MSD(t_0)\rangle$ = 2 Å^2 (b).

indicating that Li^+ motion is the most non-Gaussian and heterogeneous on this length scale, which is related to the Li^+ escape from a cage. The maximum of α_2 shifts to smaller distances with decreasing temperature as the material density increases and the cage surrounding Li^+ becomes tighter. The absolute value of the α_2 peak dramatically increases with decreasing temperature, which is associated with the Li^+ motion becoming more heterogeneous and non-Gaussian as the temperature decreases. A comparison of α_2 for Li_2EDC with observations in ionic liquids indicates that $\alpha_2(t)$ in Li_2EDC is significantly higher than values reported for RTILs. For example, α_2 was found to be 0.25−0.35 for $[C_3mim][Ntf_2]$ RTIL at room temperature and decreased by a factor of 2.5 upon a temperature increase from 298 to 460 K,[52,53] suggesting that Li^+ motion in Li_2EDC is significantly more heterogeneous than observed in RTILs and that heterogeneity increases more significantly in Li_2EDC than in RTILs with decreasing temperature. The α_2 behavior is consistent with the picture of Li^+ hops occurring quite randomly and uniformly at high temperature, but at low temperature Li^+ hops become heterogeneous, leading to the formation of slow and fast domains or/and increasingly longer waiting times between hops, which lead to a longer homogenization time and space scale.

The distribution of Li^+ displacements provides a more detailed picture of the Li^+ motion. It was calculated for time t_0, at which $\langle MSD(t_0)\rangle$ = 2 Å^2, which is in the region of the maximum of non-Gaussianity α_2. For the molten Li_2EDC, t_0 = 180 ns at 393 K, while t_0 = 48 ps at 600 K. Figure 12b shows that the distribution of Li^+ displacements is much wider at 393 K than at 600 K with an increased population of the slow and fast moving Li^+ at 393 K. This is consistent with Li^+ dynamics being increasingly heterogeneous with decreasing temperature. At 393 K, two additional peaks were observed in the distribution of Li^+ displacements as indicated by arrows in the inset to Figure 12b. These peaks are attributed to the Li^+ hops to the next cage and the cage beyond it. To provide further insight into Li^+ transport mechanism and spatial distribution of fast moving Li^+, the displacement of the top 10% of the fastest moving Li^+ over 50 ns was visualized in Figure 13. Two colors show the initial and final position of Li^+ during 50 ns simulation segments. Arrows were drawn to demonstrate displacements of each Li^+. Two types of Li^+ motion were evident: (a) a chainlike motion in which the final position of one Li^+ is close to the initial position of the other Li^+ and (b) a looplike motion when two or more Li^+ exchanged their positions.

VI. INFLUENCE OF MANY-BODY POLARIZATION OF LI_2EDC MELT STRUCTURE AND TRANSPORT

Many-body polarization was found to be important for accurate description of ion transport in RTILs, where the removal of

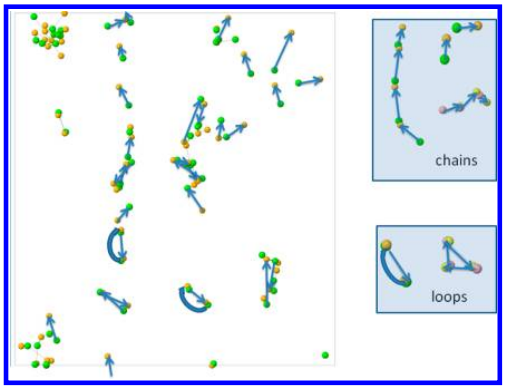

Figure 13. Displacements of the Li^+ over 50 ns for ordered Li_2EDC at 393 K.

polarization or representation of the many-body polarizable forces using two-body forces resulted in slower ion dynamics and a higher activation energy for ion transport.[45,55−59] The influence of the many-body polarization was investigated in Li_2EDC molten salts here and compared to previous observations for RTILs. Polarization significantly influences the $Li^+/MeCO_3^-$ binding energy as removal of polarization reduces the $Li^+/MeCO_3^-$ binding energy from −162.4 to −148.8 kcal/mol. In MD simulations with polarization turned off, the structure of the Li^+ coordination shell changed little, as shown in Figure 14,

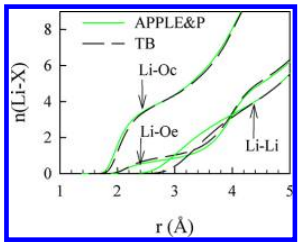

Figure 14. Coordination number for Li_2EDC melts at 700 K from the polarizable force field (APPLE&P) and two-body (TB) equivalent with polarization turned off.

indicating that polarization has little influence on the Li^+ coordination shell, which is consistent with the relatively minor influence of polarization observed in RTILs.[45,55−59] This is likely due to the cancellation of the polarization contribution in the most stable configurations of the melt and crystal.

Unlike the minor influence of polarization on structural properties, turning off polarization resulted in a significant slowing down of ion transport, as shown in Figure 9. The Li^+ diffusion

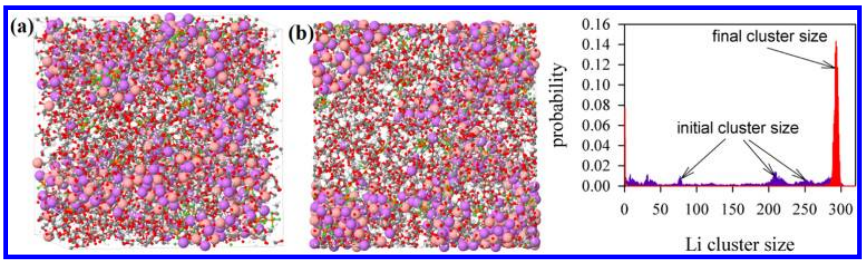

Figure 15. Snapshots of EC:DMC(3:7)/$LiPF_6$/Li_2EDC at the beginning of the run (a) and the end of the run (b) and Li cluster distribution. In (a) and (b), the large purple is Li^+, and the large pink is C of the OCO_2 group from EDC.

coefficient decreased by 4.5 and 13.6 times at 700 and 600 K, respectively, upon turning off polarization. The observed slowing down is significantly larger than the slowing down observed in RTILs, which is typically a factor of 1.5−3 in the temperature range of 298−393 K. A more pronounced effect on the dynamics of Li_2EDC is consistent with the observation that slower RTILs with a higher heat of vaporization[60] show a more pronounced effect of polarization on ion transport.[55] We also observed an increased of the activation energy for the diffusion coefficient with turning off polarization, which is in accord with observations for RTILs.[55] These results demonstrate the complicated relationship between the many-body polarizable contribution to the binding energy and ion transport, specifically, how reduction of the $Li^+/MeCO_3^-$ binding energy might counterintuitively lead to a dramatic slowing down in ion transport.

VII. INITIAL SIMULATIONS OF LI_2EDC IN EC:DMC(3:7)/$LIPF_6$

Initial simulations of Li_2EDC in EC:DMC(3:7)/$LiPF_6$ were performed to confirm that the revised version of the Li_2EDC will allow stable simulations of Li_2EDC doped in EC:DMC(3:7)/$LiPF_6$ and do not crash, as was observed when the previous version[42] of the Li_2EDC force field was combined with the APPLE&P force field for EC:DMC(3:7)/$LiPF_6$.[25] We also wish to investigate the initial stages of Li_2EDC aggregation and/or phase separation in a carbonate electrolyte. Li_2EDC was dispersed in EC:DMC(3:7)/$LiPF_6$ in the beginning of MD simulations by applying additional repulsive forces between anions. The Li_2EDC cluster size distribution before and after the 30 ns simulation at 450 K is shown in Figure 15. At the beginning of this MD run, a broad distribution of cluster sizes was observed, while at the end of the 30 ns simulation most clusters formed a percolating network as reflected by the strong peak of probability distribution for cluster sizes around 300 Li^+ for the simulation box that contained the 320 Li^+ total. Localization of the Li_2EDC percolating network at the end of simulations indicated phase separation, which is consistent with the low solubility of Li_2EDC in carbonate electrolytes.[39]

We also observed that the Li-Oc(EDC) residence time was ∼9 ns during the last 18 ns of the simulations, which is 2 orders of magnitude lower than the residence time in the melt, indicating a significantly faster Li^+ exchange between anionic groups in the EC:DMC(3:7)/$LiPF_6$/Li_2EDC solution compared to the Li_2EDC melt due to electrolyte plasticizing effects. Electrolyte plasticizing is dramatic despite the fact that a Li^+ cation is surrounded on average by 2.8 Oc from EDC^{2-} with only a small fraction of 0.4 Oc from DMC and 0.17 Oc from the EC liquid solvent (plasticizer). The Li-Oc(EC) and Li-Oc(DMC) residence times were ∼0.1 ns, about 2 orders of magnitude lower than the Li-Oc(EDC) residence time, which is consistent with previous observations for EC:DMC(3:7)/$LiPF_6$ electrolytes.[25]

VIII. CONCLUSIONS

The revised quantum chemistry-based force field was derived for Li_2EDC and $LiMeCO_3$ and is consistent with the APPLE&P force field for electrolytes, ionic liquids, and polymers. Ordered and disordered Li_2EDC was studied in MD simulations as a function of temperature. The extrapolation of Li_2EDC conductivity to room temperature yielded values in the range 2×10^{-10}−10^{-8} S/cm, which are in good agreement with the experimentally measured value of 10^{-9} S/cm. In contrast to this excellent agreement between MD results and experiments, the previous force field[42] predicted ion transport that was significantly faster than the revised force field. MD simulations predicted an activation energy for Li^+ diffusion and conductivity in the range from 64 to 84 kJ/mol, which is similar to the activation energy for interfacial impedance at the graphite anode of 64 kJ/mol found experimentally[10,12] and the activation energy associated with the ion desolvation step[7] of ∼60−70 kJ/mol. MD simulations also suggest that a 20 kJ/mol activation energy attributed during analysis of the impedance data to ion transport in SEI[7] is inconsistent with the activation energy for ion transport in Li_2EDC observed in this work. A comparison of ion transport in ordered and disordered Li_2EDC indicated little influence of ordering on it with Li^+ diffusion being only slightly faster at high temperatures in the ordered material. At room temperature, the Li^+ transport is expected to be subdiffusive on time scales shorter than $\sim 10^{-2}$ s from analysis of the MD data, which is in good agreement with the frequency-dependent impedance spectroscopy data that showed a plateau of resistivity vs frequency occurring at frequencies lower than 10^2 Hz. Li^+ motion was also significantly more non-Gaussian and heterogeneous in Li_2EDC compared to RTILs with the motion of the fast moving Li^+ being spatially correlated, exhibiting chainlike and looplike hopping by Li^+.

The influence of polarization on the Li_2EDC structure and transport was investigated. Turning off polarization resulted in a significant slowing down of ion transport and an increase in the activation energy for ion transport to a much greater extent than was previously observed for RTILs. Finally, initial simulations of Li_2EDC dissolved in EC:DMC(3:7)/$LiPF_6$ indicated a strong aggregation of Li_2EDC that lead to the formation of the percolating cluster localized in one part of the simulation cell, which is consistent with a Li_2EDC phase separating from the EC:DMC(3:7)/$LiPF_6$. The Li^+ cation exchange between anionic EDC^{2-} groups was multiple orders of magnitude faster in

EC:DMC(3:7)/$LiPF_6$/Li_2EDC than in the Li_2EDC melt due to the effect of solvent plasticizing Li^+ transport in Li_2EDC.

■ ASSOCIATED CONTENT

Supporting Information

Force field parameters, dihedral scans for Li_2EDC from MP2/cc-pvTz, and molecular mechanics using developed force field (FF) parameters, details of MD simulations, and analysis. This material is available free of charge via the Internet at http://pubs.acs.org.

■ AUTHOR INFORMATION

Corresponding Author

*E-mail: oleg.a.borodin.civ@mail.mil. Phone: (301) 394-0066.

Notes

The authors declare no competing financial interest.

■ ACKNOWLEDGMENTS

This work was supported via an Interagency Agreement between the U.S. Department of Energy and the U.S. Army Research Laboratory (ARL) under DE-IA01-11EE003413 for the Office of Vehicle Technologies Programs within Batteries for Advanced Transportation Technologies (BATT) and ABR Program. Computational resources from DoD's High Performance Computing Modernization Program's (HPCMP) program are acknowledged. Insightful discussions with T. Richard Jow (ARL) are highly appreciated.

■ REFERENCES

(1) Xu, K. Nonaqueous Liquid Electrolytes for Lithium-Based Rechargeable Batteries. *Chem. Rev.* **2004**, *104*, 4303−4418.

(2) Aurbach, D.; Markovsky, B.; Levi, M. D.; Levi, E.; Schechter, A.; Moshkovich, M.; Cohen, Y. New Insights into the Interactions between Electrode Materials and Electrolyte Solutions for Advanced Nonaqueous Batteries. *J. Power Sources* **1999**, *81*, 95−111.

(3) Aurbach, D. Review of Selected Electrode−Solution Interactions Which Determine the Performance of Li and Li Ion Batteries. *J. Power Sources* **2000**, *89*, 206−218.

(4) Aurbach, D.; Einely, Y.; Zaban, A. The Surface-Chemistry of Lithium Electrodes in Alkyl Carbonate Solutions. *J. Electrochem. Soc.* **1994**, *141*, L1−L3.

(5) Aurbach, D.; Zaban, A.; Schechter, A.; Eineli, Y.; Zinigrad, E.; Markovsky, B. The Study of Electrolyte Solutions Based on Ethylene and Diethyl Carbonates for Rechargeable Li Batteries. *J. Electrochem. Soc.* **1995**, *142*, 2873−2882.

(6) Sasaki, T.; Abe, T.; Iriyama, Y.; Inaba, M.; Ogumi, Z. Formation Mechanism of Alkyl Dicarbonates in Li-Ion Cells. *J. Power Sources* **2005**, *150*, 208−215.

(7) Xu, K.; Lam, Y. F.; Zhang, S. S.; Jow, T. R.; Curtis, T. B. Solvation Sheath of Li^+ in Nonaqueous Electrolytes and Its Implication of Graphite/Electrolyte Interface Chemistry. *J. Phys. Chem. C* **2007**, *111*, 7411−7421.

(8) Nie, M. Y.; Chalasani, D.; Abraham, D. P.; Chen, Y. J.; Bose, A.; Lucht, B. L. Lithium Ion Battery Graphite Solid Electrolyte Interphase Revealed by Microscopy and Spectroscopy. *J. Phys. Chem. C* **2013**, *117*, 1257−1267.

(9) Xu, K.; Zhuang, G. V.; Allen, J. L.; Lee, U.; Zhang, S. S.; Ross, P. N.; Jow, T. R. Syntheses and Characterization of Lithium Alkyl Mono- and Dicarbonates as Components of Surface Films in Li-Ion Batteries. *J. Phys. Chem. B* **2006**, *110*, 7708−7719.

(10) Jow, T. R.; Marx, M. B.; Allen, J. L. Distinguishing Li^+ Charge Transfer Kinetics at NCA/Electrolyte and Graphite/Electrolyte Interfaces, and NCA/Electrolyte and LFP/Electrolyte Interfaces in Li-Ion Cells. *J. Electrochem. Soc.* **2012**, *159*, A604−A612.

(11) Zhang, S. S.; Xu, K.; Jow, T. R. Charge and Discharge Characteristics of a Commercial Licoo2-Based 18650 Li-Ion Battery. *J. Power Sources* **2006**, *160*, 1403−1409.

(12) Jow, T. R.; Allen, J.; Marx, M.; Nechev, K.; Deveney, B.; Rickman, S. (Invited) Electrolytes, SEI and Charge Discharge Kinetics in Li-Ion Batteries. *ECS Trans.* **2010**, *25*, 3−12.

(13) Xu, K. Erratum: "Charge-Transfer" Process at Graphite/Electrolyte Interface and the Solvation Sheath Structure of Li+ In Nonaqueous Electrolytes (vol 154, pg A162, 2007). *J. Electrochem. Soc.* **2007**, *154*, S9−S9.

(14) Xu, K. "Charge-Transfer" Process at Graphite/Electrolyte Interface and the Solvation Sheath Structure of Li+ In Nonaqueous Electrolytes. *J. Electrochem. Soc.* **2007**, *154*, A162−A167.

(15) Abe, T.; Sagane, F.; Ohtsuka, M.; Iriyama, Y.; Ogumi, Z. Lithium-Ion Transfer at the Interface between Lithium-Ion Conductive Ceramic Electrolyte and Liquid Electrolyte - a Key to Enhancing the Rate Capability of Lithium-Ion Batteries. *J. Electrochem. Soc.* **2005**, *152*, A2151−A2154.

(16) Yamada, Y.; Iriyama, Y.; Abe, T.; Ogumi, Z. Kinetics of Lithium Ion Transfer at the Interface between Graphite and Liquid Electrolytes: Effects of Solvent and Surface Film. *Langmuir* **2009**, *25*, 12766−12770.

(17) Ogumi, Z. Interfacial Reactions of Lithium-Ion Batteries. *Electrochemistry* **2010**, *78*, 319−324.

(18) Borodin, O.; Smith, G. D. Molecular Dynamics Simulation Study Of LiI-Doped Diglyme and Poly(Ethylene Oxide) Solutions. *J. Phys. Chem. B* **2000**, *104*, 8017−8022.

(19) Borodin, O.; Smith, G. D. LiTFSI Structure and Transport in Ethylene Carbonate from Molecular Dynamics Simulations. *J. Phys. Chem. B* **2006**, *110*, 4971−4977.

(20) Takeuchi, M.; Kameda, Y.; Umebayashi, Y.; Ogawa, S.; Sonoda, T.; Ishiguro, S. I.; Fujita, M.; Sano, M. Ion−Ion Interactions of $LiPF_6$ and $LiBF_4$ in Propylene Carbonate Solutions. *J. Mol. Liq.* **2009**, *148*, 99−108.

(21) Masia, M.; Rey, R. Computational Study of λ-Butyrolactone and Li^+/λ-Butyrolactone in Gas and Liquid Phases. *J. Phys. Chem. B* **2004**, *108*, 17992−18002.

(22) Silva, L. B.; Freitas, L. C. G. Structural and Thermodynamic Properties of Liquid Ethylene Carbonate and Propylene Carbonate by Monte Carlo Simulations. *J. Mol. Struct.-Theochem* **2007**, *806*, 23−34.

(23) Wang, Y. X.; Balbuena, P. B. Combined Ab Initio Quantum Mechanics and Classical Molecular Dynamics Studies of Polyphosphazene Polymer Electrolytes: Competitive Solvation of Li^+ and $LiCF_3SO_3$. *J. Phys. Chem. B* **2004**, *108*, 15694−15702.

(24) von Wald Cresce, A.; Borodin, O.; Xu, K. Correlating Li^+ Solvation Sheath Structure with Interphasial Chemistry on Graphite. *J. Phys. Chem. C* **2012**, *116*, 26111−26117.

(25) Borodin, O.; Smith, G. D. Quantum Chemistry and Molecular Dynamics Simulation Study of Dimethyl Carbonate: Ethylene Carbonate Electrolytes Doped with $LiPF_6$. *J. Phys. Chem. B* **2009**, *113*, 1763−1776.

(26) Seo, D. M.; Borodin, O.; Han, S.-D.; Boyle, P. D.; Henderson, W. A. Electrolyte Solvation and Ionic Association II. Acetonitrile−Lithium Salt Mixtures: Highly Dissociated Salts. *J. Electrochem. Soc.* **2012**, *159*, A1489−A1500.

(27) Ganesh, P.; Jiang, D.-e.; Kent, P. R. C. Accurate Static and Dynamic Properties of Liquid Electrolytes for Li-Ion Batteries from ab initio Molecular Dynamics. *J. Phys. Chem. B* **2011**, *115*, 3085−3090.

(28) Yu, J.; Balbuena, P. B.; Budzien, J.; Leung, K. Hybrid DFT Functional-Based Static and Molecular Dynamics Studies of Excess Electron in Liquid Ethylene Carbonate. *J. Electrochem. Soc.* **2011**, *158*, A400−A410.

(29) Masia, M.; Probst, M.; Rey, R. Ethylene carbonate-Li^+: A Theoretical Study of Structural and Vibrational Properties in Gas and Liquid Phases. *J. Phys. Chem. B* **2004**, *108*, 2016−2027.

(30) Wang, Y. X.; Balbuena, P. B. Theoretical Studies on Cosolvation of Li Ion and Solvent Reductive Decomposition in Binary Mixtures of Aliphatic Carbonates. *Int. J. Quantum Chem.* **2005**, *102*, 724−733.

(31) Sutjianto, A.; Curtiss, L. A. Li+-Diglyme Complexes: Barriers To Lithium Cation Migration. *J. Phys. Chem. A* **1998**, *102*, 968−974.
(32) Johansson, P.; Jacobsson, P. Rational Design of Electrolyte Components by Ab Initio Calculations. *J. Power Sources* **2006**, *153*, 336−344.
(33) Scheers, J.; Kalita, M.; Johansson, P.; Zukowska, G. Z.; Wieczorek, W.; Jacobsson, P. Anion−Additive Interactions Studied by Ab Initio Calculations and Raman Spectroscopy. *J. Electrochem. Soc.* **2009**, *156*, A305−A308.
(34) Jonsson, E.; Armand, M.; Johansson, P. Novel Pseudo-Delocalized Anions for Lithium Battery Electrolytes. *Phys. Chem. Chem. Phys.* **2012**, *14*, 6021−6025.
(35) Scheers, J.; Johansson, P. Comment on "Transport and Electrochemical Properties and Spectral Features of Non-Aqueous Electrolytes Containing LiFSI in Linear Carbonate Solvents" [J. Electrochem. Soc., 158, A74 (2011)]. *J. Electrochem. Soc.* **2012**, *159*, S1−S2.
(36) Wang, Y. X.; Balbuena, P. B. Associations of Alkyl Carbonates: Intermolecular C−H···O Interactions. *J. Phys. Chem. A* **2001**, *105*, 9972−9982.
(37) Wang, Y. X.; Balbuena, P. B. Associations Of Lithium Alkyl Dicarbonates Through O···Li···O Interactions. *J. Phys. Chem. A* **2002**, *106*, 9582−9594.
(38) Tasaki, K. Solvent Decompositions and Physical Properties of Decomposition Compounds in Li-Ion Battery Electrolytes Studied by DFT Calculations and Molecular Dynamics Simulations. *J. Phys. Chem. B* **2005**, *109*, 2920−2933.
(39) Tasaki, K.; Goldberg, A.; Lian, J. J.; Walker, M.; Timmons, A.; Harris, S. J. Solubility of Lithium Salts Formed on the Lithium-Ion Battery Negative Electrode Surface in Organic Solvents. *J. Electrochem. Soc.* **2009**, *156*, A1019−A1027.
(40) Iddir, H.; Curtiss, L. A. Li Ion Diffusion Mechanisms in Bulk Monoclinic Li_2CO_3 Crystals from Density Functional Studies. *J. Phys. Chem. C* **2010**, *114*, 20903−20906.
(41) Shi, S. Q.; Lu, P.; Liu, Z. Y.; Qi, Y.; Hector, L. G.; Li, H.; Harris, S. J. Direct Calculation of Li-Ion Transport in the Solid Electrolyte Interphase. *J. Am. Chem. Soc.* **2012**, *134*, 15476−15487.
(42) Borodin, O.; Smith, G. D.; Fan, P. Molecular Dynamics Simulations of Lithium Alkyl Carbonates. *J. Phys. Chem. B* **2006**, *110*, 22773−22779.
(43) Zhuang, G. V.; Xu, K.; Yang, H.; Jow, T. R.; Ross, P. N. Lithium Ethylene Dicarbonate Identified as the Primary Product of Chemical and Electrochemical Reduction of EC in 1.2 M $LiPF_6$/EC:EMC Electrolyte. *J. Phys. Chem. B* **2005**, *109*, 17567−17573.
(44) Jozwiak, P.; Garbarczyk, J. E. Mixed Electronic−Ionic Conductivity in the Glasses of the Li_2O−V_2O_5−P_2O_5 System. *Solid State Ionics* **2005**, *176*, 2163−2166.
(45) Borodin, O. Polarizable Force Field Development and Molecular Dynamics Simulations of Ionic Liquids. *J. Phys. Chem. B* **2009**, *113*, 11463−11478.
(46) Seo, D. M.; Borodin, O.; Han, S.-D.; Ly, Q.; Boyle, P. D.; Henderson, W. A. Electrolyte Solvation and Ionic Association. I. Acetonitrile−Lithium Salt Mixtures: Intermediate and Highly Associated Salts. *J. Electrochem. Soc.* **2012**, *159*, A553−A565.
(47) Bryantsev, V. Calculation Of Solvation Free Energies of Li^+ and O_2^- Ions and Neutral Lithium−Oxygen Compounds in Acetonitrile Using Mixed Cluster/Continuum Models. *Theor. Chim. Acta* **2012**, *131*, 1−11.
(48) Borodin, O.; Smith, G. D.; Kim, H. Viscosity of a Room Temperature Ionic Liquid: Predictions from Nonequilibrium and Equilibrium Molecular Dynamics Simulations. *J. Phys. Chem. B* **2009**, *113*, 4771−4774.
(49) Borodin, O.; Gorecki, W.; Smith, G. D.; Armand, M. Molecular Dynamics Simulation and Pulsed-Field Gradient NMR Studies of Bis(fluorosulfonyl)imide (FSI) and Bis[(trifluoromethyl)sulfonyl]-imide (TFSI)-Based Ionic Liquids. *J. Phys. Chem. B* **2010**, *114*, 6786−6798.
(50) Borodin, O.; Smith, G. D. Development of Many-Body Polarizable Force Fields for Li-Battery Components: 1. Ether, Alkane, and Carbonate-Based Solvents. *J. Phys. Chem. B* **2006**, *110*, 6279−6292.
(51) Borodin, O.; Smith, G. D. Mechanism of Ion Transport in Amorphous Poly(Ethylene Oxide)/LiTFSI from Molecular Dynamics Simulations. *Macromolecules* **2006**, *39*, 1620−1629.
(52) Koddermann, T.; Ludwig, R.; Paschek, D. On the Validity of Stokes−Einstein and Stokes−Einstein−Debye Relations in Ionic Liquids and Ionic-Liquid Mixtures. *ChemPhysChem* **2008**, *9*, 1851−1858.
(53) Liu, H. J.; Maginn, E. A Molecular Dynamics Investigation of the Structural and Dynamic Properties of the Ionic Liquid 1-*n*-Butyl-3-methylimidazolium Bis(trifluoromethanesulfonyl)imide. *J. Chem. Phys.* **2011**, 135.
(54) Shell, M. S.; Debenedetti, P. G.; Stillinger, F. H. Dynamic Heterogeneity and Non-Gaussian Behaviour in a Model Supercooled Liquid. *J. Phys.: Condens. Matter* **2005**, *17*, S4035−S4046.
(55) Bedrov, D.; Borodin, O.; Li, Z.; Smith, G. D. Influence of Polarization on Structural, Thermodynamic, and Dynamic Properties of Ionic Liquids Obtained from Molecular Dynamics Simulations. *J. Phys. Chem. B* **2010**, *114*, 4984−4997.
(56) Salanne, M.; Rotenberg, B.; Jahn, S.; Vuilleumier, R.; Simon, C.; Madden, P. A. Including Many-Body Effects in Models for Ionic Liquids. *Theor. Chem. Acc.* **2012**, 131.
(57) Salanne, M.; Madden, P. A. Polarization Effects in Ionic Solids and Melts. *Mol. Phys.* **2011**, *109*, 2299−2315.
(58) Chaban, V. V.; Voroshylova, I. V.; Kalugin, O. N., The Phenomenological Account for Electronic Polarization in Ionic Liquid. In *Non-Aqueous Electrolytes for Lithium Batteries*; Lucht, B., Henderson, W. A., Jow, T. R., Ue, M., Eds.; Electrochemical Soc Inc: Pennington, 2011; Vol. 33, pp 43−55.
(59) Chaban, V. Polarizability versus Mobility: Atomistic Force Field for Ionic Liquids. *Phys. Chem. Chem. Phys.* **2011**, *13*, 16055−16062.
(60) Borodin, O. Relation between Heat of Vaporization, Ion Transport, Molar Volume, And Cation and Anion Binding Energy for Ionic Liquids. *J. Phys. Chem. B* **2009**, *113*, 12353−12357.

Role of Molecule Flexibility on the Nucleation of Dislocations in Molecular Crystals

Lynn B. Munday, Robert L. Mitchell, Jaroslaw Knap, and Peter W. Chung

Applied Physics Letters, 103 (2013)

APPLIED PHYSICS LETTERS **103**, 151911 (2013)

Role of molecule flexibility on the nucleation of dislocations in molecular crystals

Lynn B. Munday,[1,a)] Robert L. Mitchell,[2] Jaroslaw Knap,[1] and Peter W. Chung[1,b)]
[1]*Computational and Information Sciences Directorate, U.S. Army Research Laboratory, Aberdeen Proving Ground, Maryland 21005, USA*
[2]*Department of Mechanical Engineering, University of California Irvine, Irvine, California 92717, USA*

(Received 12 August 2013; accepted 25 September 2013; published online 11 October 2013)

We show that a molecule's flexibility described by changes to its conformation and orientation during deformation is vital for the proper representation of dislocation nucleation in molecular crystals. This is shown for the molecular crystal hexahydro-1,3,5-trinitro-s-triazine (RDX) by comparing direct atomistic simulations to two alternate forms of a continuum dislocation nucleation model for a crack tip loaded in pure shear. The atomistic simulations show the emission of partial dislocations. These are compared to continuum dislocation nucleation models based on generalized stacking fault (GSF) energy surfaces where the molecules are allowed to be either rigid or flexible. The rigid molecules are unable to represent the partial dislocations whereas the flexible molecules agree with the direct atomistic model to within 17% of the stress intensity factor for emission of the first partial dislocation and to within 1% for the second partial. This agreement first indicates that the molecule flexibility serves a critical role in the ductile behavior of the molecular crystal and, second, the continuum dislocation nucleation model represents the correct atomistic behavior, showing two partial dislocations connected by a stacking fault, when parameterized with GSF energy surfaces that account for the molecule flexibility. © *2013 AIP Publishing LLC*. [http://dx.doi.org/10.1063/1.4824711]

Molecular crystals are used in a broad range of technologies as energetic materials (including the α polymorph of RDX, the exemplar of the present article), active ingredients in pharmaceuticals and organic semiconductors in thin film flexible electronics. However, such applications are often restricted by their tendency to undergo brittle fracture. Plastic deformation, as opposed to brittle fracture, is generally a desired mechanical property in their manufacturing and handling. For example, plastic deformation of pharmaceutical crystals during compaction into tablets greatly enhances their mechanical strength.[1] In some instances, plastic deformation is regarded as responsible for reducing sensitivity of energetic materials to accidental initiation.[2]

Plastic deformation occurs through the collective motion of dislocations in crystalline solids. The theory of dislocations is particularly well developed for simpler metallic crystals such as copper (cf. Hirth and Lothe[3] and reference therein), but remains also applicable to molecular crystals, albeit with modifications.[4–7] As in the case of metallic crystals, the structure of molecular crystals contains a repeating lattice cell but with several molecules occupying each unit cell (8 molecules in the case of αRDX, Figure 1(b)). Molecular crystals commonly exhibit layered structures with 2D networks of strongly bonded molecules.[8] The interactions between layers are considerably weaker and particularly susceptible to brittle fracture.[4,8] So, it is surprising that dislocation activity on those planes has been observed in nanoindentation experiments of αRDX,[9] saccharin,[10] and succinic acid.[11] Moreover, our previous work[12,13] has shown the molecule's flexibility as described by changes to its conformation and orientation during deformation to dramatically alter the atomistically derived generalized stacking fault (GSF) surfaces of αRDX. The flexible molecule GSF surfaces suggested stable partial dislocation structures that were energetically favorable when compared to crack opening. Thus, these observations could be better understood in the context of crystal plasticity if it can be shown that (a) molecule flexibility plays an active role in the ductile response and (b) the flexible molecule GSF surface correctly predicts the dislocation structure of partial dislocations nucleated from a crack tip.

In this Letter, we isolate the role of molecule flexibility on dislocation nucleation in the molecular crystal αRDX. This is demonstrated by contrasting atomistic simulations of dislocation nucleation from a crack tip to a continuum model parameterized with data for either rigid or flexible molecules. The present focus is on the case of nucleation under pure mode II loading where the crack plane and slip plane coincide (cf. Figure 1(c)). Under these conditions, the continuum dislocation nucleation model due to Rice[14] adopts a very simple analytical form amenable to direct comparison with results of atomistic simulations.

Rice's dislocation nucleation model is based on solving the elastic boundary value problem for a traction free crack tip. In this analysis, the boundary condition on the slip-plane ahead of the crack tip is provided by an interplanar potential relating the shear stress to atomic displacement. The interplanar potential is represented by means of a GSF energy surface, a planar potential energy function describing slip of one crystal half with respect to the other.[15] A dislocation is nucleated when the energy at the crack tip due to an applied load becomes larger than the energy barrier to slip corresponding to the first maximum on the GSF surface, γ_{us}. Rice's dislocation nucleation model using atomistically

[a)]Electronic mail: lynn.munday@us.army.mil
[b)]Current address: Department of Mechanical Engineering, University of Maryland, College Park, Maryland 20742, USA

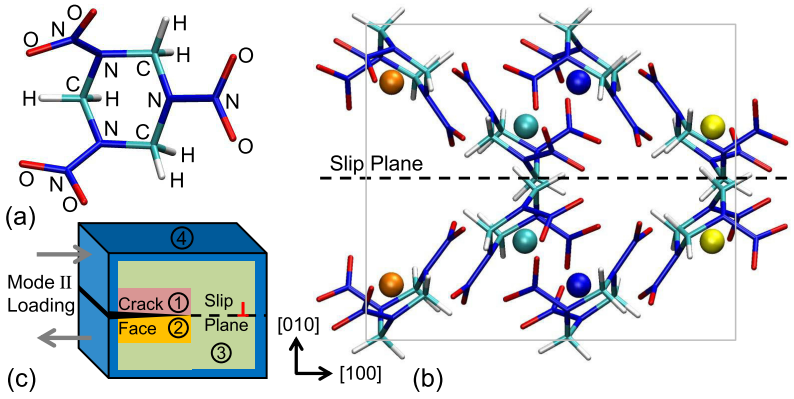

FIG. 1. (a) Labeled RDX molecule ($C_3H_6N_6O_6$). (b) Eight molecules of the αRDX unit cell with lattice dimensions indicated by the gray box. The dashed line represents the slip plane studied in this work. The molecule centers of mass are also shown with colors matching those used in Figure 3(a). (c) Simulation cell showing the mode II loading (gray arrows) of the crack tip. The simulation cell is broken up into colored regions where regions 1 (red) and 2 (orange) do not interact creating the traction free crack face, region 3 (green) is the perfect crystal where the dislocation (shown by red "⊥") will be emitted onto the slip plane (shown by the dashed line) and the atoms in region 4 (blue) are held fixed during the relaxation simulation.

derived GSF surfaces has been shown to be in general agreement with atomistic simulations for several metallic crystals under pure mode II and mixed mode loading.[16,17] The GSF energy surface can also capture the effects of molecule flexibility as was shown in our previous work for the molecular crystal αRDX.[12,13] By using the flexible molecule parameterization of the GSF surface, no modifications need to be made to Rice's continuum-based model for it to accurately capture dislocation nucleation in molecular crystals.

We consider dislocation nucleation from a semi-infinite crack (Figure 1(c)) with a (010) crack face in the bulk crystal of αRDX. Under plane strain conditions in the [001] direction, mode II shear loading will cause this crack to emit an edge dislocation in the (010)[100] slip system. The atomic configuration of the (010) slip plane is shown in Figure 1(b). A cross section of the GSF energy surface along the (010)[100] slip system obtained from our previous results[13] is shown in Figure 2 for the rigid and flexible molecule approximations. The GSF surfaces were determined in our previous work[13] by first rigidly shifting the crystal halves relative to one another and allowing them to separate, producing the rigid GSF energy data shown by the blue curve in Figure 2. Next, the molecules at the interface of the rigid configurations were allowed to relax through conformation and orientation changes, producing the flexible GSF energy

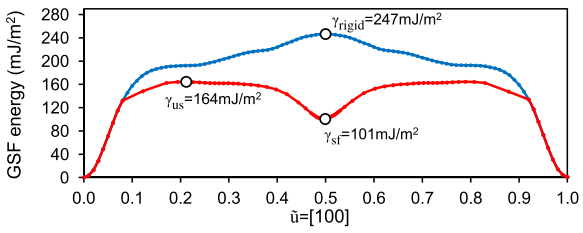

FIG. 2. αRDX GSF energy curve obtained from our previous work (Refs. 12 and 13) for the (010)[100] slip system for fully flexible molecules (red) and rigid molecules (blue). The unstable stacking fault energies, γ_{us} and γ_{rigid}, and stable stacking fault energy, γ_{sf}, are shown by the large hollow circles. The filled dots are computed values.

data shown by the red curve in Figure 2. The rigid GSF energy surface produces a single maximum unstable stacking energy labeled γ_{rigid}. Alternatively, the presence of molecule flexibility alters the flexible GSF surface by lowering the unstable stacking energy, γ_{us}, and creating a local energy minimum, γ_{sf}. The presence of the local energy minimum, γ_{sf}, indicates the likely dissociation of a full dislocation into two partial dislocations separated by a stacking fault. The stacking fault region has an excess energy over the perfect crystal equal to γ_{sf}.

The anisotropic version of Rice's model[18] using orthotropic elastic constants for αRDX[19] and applied to the flexible αRDX GSF data predicts nucleation of the first partial dislocation when the available energy at the crack tip due to an externally applied load (K_{II}) becomes larger than the energy barrier to slip given by $\gamma_{us} = 164\,\mathrm{mJ/m^2}$ in Figure 2. Using this value, the mode II stress intensity factor for emission of the first partial dislocation is $K_{II}^{flex} = 0.058\,\mathrm{MPa\,m^{1/2}}$. The first partial dislocation shields the crack tip from the applied $K_{II}^{flex} = 0.058\,\mathrm{MPa\,m^{1/2}}$ and the stress intensity factor at the crack tip for nucleation of the second partial is reduced to zero. After the first partial has been emitted, the material at the crack tip is in the stacking fault configuration. This configuration lowers the dislocation nucleation energy barrier for the second partial to $\gamma_{us} - \gamma_{sf}$, requiring an additional $K_{II}^{flex} = 0.036\,\mathrm{MPa\,m^{1/2}}$. Once both partials have nucleated, which corresponds to a total intensity factor of $K_{II}^{flex} = 0.094\,\mathrm{MPam^{1/2}}$, the material at the crack tip is again that of the perfect crystal. The separation distance between the two partials in the bulk crystal from anisotropic elasticity[3] may be estimated to be $r_a^{flex} = 73$ Å. In contrast, under a rigid molecule assumption, $\gamma_{rigid} = 247\,\mathrm{mJ/m^2}$ and a single dislocation nucleates at $K_{II}^{rigid} = 0.072\,\mathrm{MPa\,m^{1/2}}$.

Rice's dislocation nucleation model can now be contrasted with direct atomistic simulations. We employ the LAMMPS Molecular Dynamics Simulator[20] where the atomic interactions are modeled using the Smith and Bharadwaj (SB) potential.[21] Atomistic studies have shown the SB potential to accurately describe RDX material properties,[19] its polymorphism,[19] and

dislocations.[6,7,22] The SB potential was developed by parameterizing a DREIDING[23] style potential to quantum chemistry calculations of octahydro-1,3,5,7-tetranitro-1,3,5,7-tetrazocine (HMX),[21] a nitroamine similar in structure to RDX.

The atomistic model of αRDX, shown in Figure 1(c), is composed of 60 unit cells (790 Å) in the [100] direction and 36 unit cells (416 Å) in the [010] direction. The [001] direction is modeled with 3 unit cells (32 Å) and periodic boundary conditions. Plane strain conditions are applied through periodic boundary conditions and by holding the unit cell dimension fixed in [001]. A 30 unit cell crack plane is represented by disallowing dispersion/repulsion and electrostatic pairwise interactions between atoms directly above and below the crack plane within a 12 Å range (regions 1 and 2 in Figure 1(c)). Unfortunately, the long range portion of the Ewald sum used to compute electrostatic interactions cannot be removed and leads to 7% error when comparing the energy of the crack face to that of a free surface. This error was minimized by choosing a large cut-off radius (12 Å) for the real space portion of the Ewald sum. All molecules in the simulation cell are then incrementally displaced according to the plane strain anisotropic elastic crack tip displacement field for a prescribed K_{II}^{sim} value.[24] At each K_{II}^{sim} load step, the molecules in the 3 unit cell thick border (region 4) are held fixed while the remaining atoms in the system (regions 1–3) are allowed to relax by means of molecular dynamics with viscous damping. For subsequent K_{II}^{sim} load increments, all molecules are again rigidly displaced from their previous configuration and relaxed. This process is repeated until two partial dislocations are emitted from the crack tip.

The relative positions of the centers of mass (COM) of the molecules are used to identify the dislocations. The partial dislocation and stacking fault causes the first planes of molecules above and below the slip plane to be in disregistry. We define the disregistry given by the relative positions of the COMs in the [100] direction normalized by the [100] lattice vector of 13.18 Å as $\tilde{u}$. Figure 3(a) depicts the COMs in the deformed configuration after the first partial has been emitted for an applied $K_{II}^{sim} = 0.07\,\mathrm{MPa\,m^{1/2}}$. For the perfect crystal lattice, $\tilde{u} \approx 0$ across the slip plane, as is the case for $x > 80$ Å in Figure 3. In Figure 3(a), the dislocation appears as a localized disregistry in the lattice across the slip plane near $x \approx 60$ Å marked by the dashed vertical line. This lattice disregistry translates to an increase in $\tilde{u}$ as observed for the region 55 Å $< x <$ 75 Å marked by the solid vertical lines. The half width of the dislocation core marked by the solid vertical lines is defined, somewhat arbitrarily, as the region where $0.125 < \tilde{u} < 0.375$ [Ref. 25] giving a half width of 20 Å for the first partial dislocation core or $\sim 1.5b$, where b is the magnitude of the full Burgers vector. This is a relatively smaller core than the $\sim 2.2b$ width calculated from an atomistically determined GSF energy curve for partial edge dislocations in Aluminum.[25] There is a plateau in $\tilde{u} \approx 0.5$ between the dislocation core and crack tip indicating a stacking fault or antiphase boundary.

It is also helpful to use a quantity to represent the local dislocation core density which we define by $\rho(x) = \mathrm{d}\tilde{u}/\mathrm{d}x$ and determined by direct numerical differentiation of $\tilde{u}$. It is shown as the red line in Figure 3(b). The position of the dislocation is given by the local maximum of ρ, which coincides with $\tilde{u} \approx 0.25$ marked by the dashed vertical line.

The structure on the slip plane, as represented by $\tilde{u}$ and ρ, is shown in Figure 4 for several values of K_{II}^{sim} above and below the critical value for partial emission. At $K_{II}^{sim} = 0.065\,\mathrm{MPa\,m^{1/2}}$, $\tilde{u} > 0.125$ near the crack tip indicating the incipient formation of a partial dislocation. The partial dislocation becomes trapped due to localized conformation and orientation changes in the molecules at the crack tip. The flexible GSF energy curve shown in Figure 2 does not resolve these shear induced changes, and therefore, this feature cannot be captured by our parameterization of Rice's model. However, as previously shown in Figure 3, the first partial dislocation becomes fully formed and is emitted at $K_{II}^{sim} = 0.07\,\mathrm{MPa\,m^{1/2}}$. The comparison of K_{II}^{sim} with the previously given continuum result $K_{II}^{flex} = 0.058\,\mathrm{MPa\,m^{1/2}}$ for the emission of the first partial dislocation indicate a

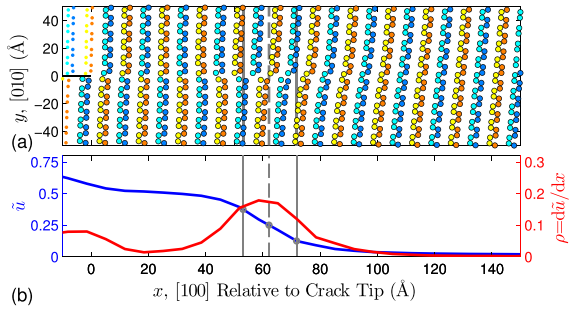

FIG. 3. (a) Molecule COM positions near the crack tip for an applied K_{II}^{sim} load factor of 0.07 MPa m$^{1/2}$. The crack tip is indicated by the black line ending at $(x,y) = (0,0)$. COMs are colored according to the COMs shown in Figure 1(b). COMs without a black outline near the left edge are initially part of the crack face in the unloaded crystal, regions 1 and 2 in Figure 1(c). (b) Plot of COM displacement discontinuity across the slip plane. The blue line and axis belong to $\tilde{u}$, the [100] displacement discontinuity. The red line and axis belong to $\rho(x) = \mathrm{d}\tilde{u}/\mathrm{d}x$, the dislocation core density. The half width of the dislocation core is the region contained within the solid vertical lines in (a) and (b) and the dashed line indicates the dislocation center.

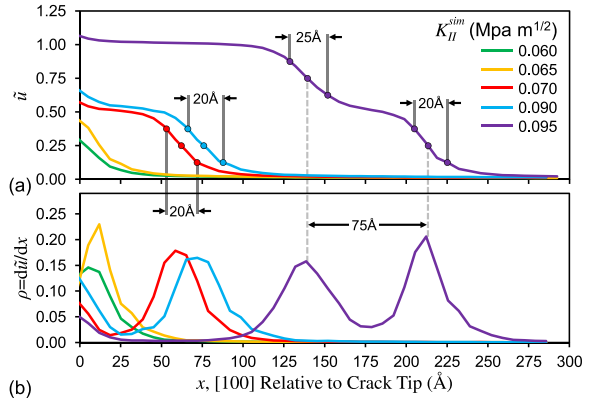

FIG. 4. Dislocation core structure as a function of K_{II}^{sim}. (a) [100] displacement discontinuity $\tilde{u}$ across the (010) slip plane. Partial dislocation half widths have been indicated by filled in data points and their dimensions labeled. (b) $\rho = \mathrm{d}\tilde{u}/\mathrm{d}x$, dislocation core density. The separation distance between the two emitted partials at $K_{II}^{sim} = 0.095\,\mathrm{MPam^{1/2}}$ is labeled and shown as the distance between the two peaks of $\rho(x)$. Line color indicates increasing mode II load factor as shown by the legend in (a).

maximum disparity of 17%. This disparity appears in line with earlier predictions for FCC crystals.[16]

After the first partial dislocation is nucleated, the crystal across the slip plane at the crack tip contains a stacking fault. Continued loading of this configuration from $K_{II}^{sim} = 0.070$ to 0.090 MPa $m^{1/2}$ causes the first partial dislocation to continue moving away from the crack[26] tip extending the stacking fault region by ~10 Å. Then, at $K_{II}^{sim} = 0.095$ MPa $m^{1/2}$, the second partial dislocation is nucleated and the pair moves away from the crack tip. This value of K_{II}^{sim} is within 1% error of K_{II}^{flex} from Rice's model. The separation between the two partials given as the distance between the two peaks of ρ is $r_a^{sim} = 75$Å, nearly identical to the value determined from the anisotropic elastic solution.

The purple line in Figure 4(a) for $K_{II}^{sim} = 0.095$ MPa $m^{1/2}$ depicts three distinct plateaus in $\tilde{u} = 0$, 0.5, and 1. The first plateau is the defect-free lattice. The next plateau at $\tilde{u} = 0.5$ represents the stacking fault between the leading and trailing partials. The plateau at $\tilde{u} = 1$ indicates the lattice across the slip plane has been displaced by one full Burgers vector, recreating the original lattice at the crack tip. The core half width for the leading partial $(0.125 < \tilde{u} < 0.375)$ is ~20 Å and for the trailing partial $(0.625 < \tilde{u} < 0.875)$ is ~25 Å. The relative half widths of the core are consistent with the lattice restoring forces determined from the gradient of the GSF energy curve.[25] The lattice restoring force on the trailing partial is smaller leading to a wider core.

The implications of these findings may reach beyond RDX. This inference comes from the similarities in layered crystal structures of pharmaceutical molecular crystals such as acetaminophen and caffeine[8] as well as organic semiconductor crystals.[27] The present results specifically point to two observations. First, despite the weak interactions between layers, which would otherwise favor strain accommodation through crack opening, the effect of the molecule's flexibility appears to play a critical role in the ductile response. Due to the long-range, intermolecular nature of the dispersion and electrostatic interactions, it is tempting to assume the molecules can be represented as rigid assemblies of particles whose internal interactions do not contribute substantially to the lattice material properties. However, such an assumption would lead to no stable stacking fault and the nucleation of only full dislocations. This improper representation of steric interactions will also yield a relatively higher dislocation nucleation threshold and an unnaturally greater tendency for the material to appear brittle. The effect of molecule flexibility on ductility will also likely carry over to the more general case of mixed mode loading where tensile loads have been shown to ease dislocation nucleation allowing for blunting of the crack tip.[17,26]

Second, although the mechanisms involved in plastic deformation of molecular crystals are found to be far more complicated than in metals, through a proper calculation of the GSF energy curve, it is remarkable that Rice's dislocation nucleation model is still valid for materials in which molecule flexibility and long-ranged dispersion and electrostatic interactions are present. The test of the rigid molecule assumption confirms that the absence of molecule flexibility results in complete disagreement with direct fully atomistic simulations of dislocation nucleation whereas the consideration of full flexibility in the molecules is in good agreement. The GSF energy curve was also used to accurately predict the separation distance between the partial dislocations and qualitatively match the fully atomistic dislocation structure. Thus, GSF energy surfaces that account for the flexibility of molecules in crystals may also be suited for direct use in other mesoscopic or macroscopic models such as the phase field approaches to dislocations[5] or the direct calculation of individual dislocation properties via the Peierls-Nabarro model.[6,7,25]

In conclusion, we compared direct atomistic simulations with alternate parameterizations of a dislocation nucleation model to identify the critical role of molecular flexibility on the ductile response of molecular crystals. The molecule's flexibility as described by changes to its conformation and orientation were found to be essential to correctly represent the energy barrier to dislocation nucleation and the resulting partial dislocation structure.

Support of the DoD High Performance Computing Modernization Office through the Multiscale Reactive Modeling of Insensitive Munitions Software Applications Institute is gratefully acknowledged. Computing resources were provided by the DoD Supercomputing Resource Center located at the US Army Research Laboratory.

[1]C. C. Sun, J. Adhes. Sci. Technol. **25**, 483 (2011).
[2]J. J. Dick and J. P. Ritchie, J. Appl. Phys. **76**, 2726 (1994).
[3]J. P. Hirth and J. Lothe, *Theory of Dislocations* (Wiley, New York, 1982).
[4]R. J. Roberts, R. C. Rowe, and P. York, J. Mater. Sci. **29**, 2289 (1994).
[5]L. Lei and M. Koslowski, Philos. Mag. **91**, 865 (2011).
[6]N. Mathew, C. Picu, and P. W. Chung, J. Phys. Chem. A **117**, 5326 (2013).
[7]N. Mathew and R. C. Picu, Chem. Phys. Lett. **582**, 78–81 (2013).
[8]C. C. Sun and Y. H. Kiang, J. Pharm. Sci. **97**, 3456 (2008).
[9]K. J. Ramos, D. E. Hooks, and D. F. Bahr, Philos. Mag. **89**, 2381 (2009).
[10]M. Kiran, S. Varughese, C. M. Reddy, U. Ramamurty, and G. R. Desiraju, Cryst. Growth Des. **10**, 4650 (2010).
[11]Y. Jing, Y. Zhang, J. Blendell, M. Koslowski, and M. T. Carvajal, Cryst. Growth Des. **11**, 5260 (2011).
[12]L. B. Munday, Ph.D. dissertation (University of Maryland, College Park, 2011), see http://hdl.handle.net/1903/12254.
[13]L. B. Munday, S. D. Solares, and P. W. Chung, Philos. Mag. **92**, 3036 (2012).
[14]J. R. Rice, J. Mech. Phys. Solids **40**, 239 (1992).
[15]V. Vitek, Philos. Mag. **18**, 773 (1968).
[16]J. Knap and K. Sieradzki, Phys. Rev. Lett. **82**, 1700 (1999).
[17]S. J. Zhou, A. E. Carlsson, and R. Thomson, Phys. Rev. B **47**, 7710 (1993).
[18]Y. Sun and G. E. Beltz, J. Mech. Phys. Solids **42**, 1905 (1994).
[19]L. B. Munday, P. W. Chung, B. M. Rice, and S. D. Solares, J. Phys. Chem. B **115**, 4378 (2011).
[20]S. Plimpton, J. Comput. Phys. **117**, 1 (1995).
[21]G. D. Smith and R. K. Bharadwaj, J. Phys. Chem. B **103**, 3570 (1999).
[22]M. J. Cawkwell, K. J. Ramos, D. E. Hooks, and T. D. Sewell, J. Appl. Phys. **107**, 063512 (2010).
[23]S. L. Mayo, B. D. Olafson, and W. A. Goddard, J. Phys. Chem. **94**, 8897 (1990).
[24]H. Liebowitz and G. C. Sih, *Mathematical Theories of Brittle Fracture* (Academic Press, Inc., New York, 1968), Vol. 2.
[25]G. Lu, N. Kioussis, V. V. Bulatov, and E. Kaxiras, Phys. Rev. B **62**, 3099 (2000).
[26]Y. Sun, G. E. Beltz, and J. R. Rice, Mater. Sci. Eng., A **170**, 67 (1993).
[27]R. Li, W. Hu, Y. Liu, and D. Zhu, Acc. Chem. Res. **43**, 529 (2010).

Computationally Based Development of Chemical Kinetics Mechanisms for Modeling the Combustion Chamber Dynamics of Rocket Propulsion Systems

Michael J. McQuaid, Chiung-Chu Chen, Anthony J. Kotlar, William R. Anderson, and Michael J. Nusca

International Journal of Energetic Materials and Chemical Propulsion, 12 (2013)

International Journal of Energetic Materials and Chemical Propulsion, 12 (1): 27–40 (2013)

COMPUTATIONALLY BASED DEVELOPMENT OF CHEMICAL KINETICS MECHANISMS FOR MODELING THE COMBUSTION CHAMBER DYNAMICS OF ROCKET PROPULSION SYSTEMS

Michael J. McQuaid, Chiung-Chu Chen, Anthony J. Kotlar, William R. Anderson, & Michael J. Nusca*

U.S. Army Research Laboratory, Aberdeen Proving Ground, Maryland, USA

*Address all correspondence to Michael J. McQuaid
E-mail: michael.j.mcquaid.civ@mail.mil

The U.S. Army Research Laboratory is developing finite-rate, gas-phase chemical kinetics mechanisms for use in modeling the combustion chamber dynamics of novel rocket propulsion systems. For propellant systems whose combustion chemistry has not been previously investigated at a fundamental level, postulated reaction paths are simulated with quantum chemistry methods, and predictions for individual paths are converted to kinetic rate expressions using transition state theory. Rate expressions for individual reactions are then assembled to yield detailed mechanisms whose reasonableness for specific applications are evaluated by employing them to model relevant measured data. Detailed mechanisms then serve as the basis for deriving reaction sets that can be employed as submodels in computational fluid dynamics codes. This approach has been successfully employed to develop submodels for a number of hypergolic (liquid) bipropellant combinations and a (liquid–solid) hybrid system. It is also being employed to develop submodels for (solid) minimum-smoke propellant formulations. This paper discusses the application, efficacy, and benefits of the approach through the presentation of some representative examples.

KEY WORDS: *computational chemistry, hypergolic bipropellants, ethyl nitrate*

1. INTRODUCTION

The U.S. Army is developing a number of novel rocket motor concepts with the potential to increase the performance and/or reduce the vulnerability of tactical missiles. To accelerate these efforts, the U.S. Army Research Laboratory (ARL) is developing and applying computational fluid dynamics (CFD) models to obtain insight into these concepts' performance as a function of various design parameters. The development of system-specific, finite-rate, gas-phase chemical kinetics mechanisms is a significant part of these efforts. Built on a foundation laid by prior ARL efforts to model the ignition and

combustion of gun propellants (Anderson et al., 2011), the Army's support for mechanism development has been based on the demonstrated ability of such mechanisms to improve the predictive power of the CFD models. Timeliness and practicality are also important considerations. Specifically, the mechanisms need to be developed in time for CFD simulations to be run concurrent with the motor development programs they hope to benefit, and the number of reactions and species constituting a mechanism needs to be small enough for the CFD simulations to be computationally tractable. These objectives have been met by exploiting computationally based methods to develop rate expressions for elementary reaction steps for the decomposition of propellant ingredients for which little or no relevant kinetic data exist, creating a detailed mechanism by combining the rate expressions for these steps with a set of rate expressions for small molecule reactions that have been developed and employed to model other propellant systems, then producing a reduced mechanism from the detailed one.[1] This paper reviews the methods ARL has developed and/or employed for this purpose, referencing results that have been obtained for some of the propulsion systems that have been modeled.

2. EXAMPLES AND DISCUSSION

2.1 Monomethylhydrazine–Red Fuming Nitric Acid

In the early 2000's, ARL began to construct a CFD model that could be employed to advance a U.S. Army Aviation and Missile Research, Development and Engineering Center effort to develop a hypergolic propulsion system concept referred to as the impinging stream vortex engine (ISVE) (Wilson and Connaughton, 1967; Michaels and Wilson, 1995; Nusca and Michaels, 2004). The bipropellant combination being employed for the effort at that time was monomethylhydrazine-(inhibited) red fuming nitric acid (MMH–RFNA). The foundation for the CFD model was a methodology developed at ARL for simulating unsteady, multi-component, chemically reacting flows, and a representation for MMH–RFNA's reaction chemistry was needed for the application. Since an existing chemical kinetics mechanism for MMH–RFNA could not be identified, a one-step reaction mechanism was constructed and employed as a starting point. The mechanism assumed that MMH–RFNA (with additives including silica) reacted to produce 18 product species [O_2, N_2, CO_2, CO, H_2, H, H_2O, H_2O_2, HO_2, HNO, NO, NO_2, O, OH, SiO, SiO_2(s), SiO_2(g), and $SiO_2(l)$]. The reaction's rate was

[1]In this paper, detailed mechanisms (as opposed to reduced mechanisms) are sets of rate expressions for elementary reactions that are assembled with the objective of representing all paths for a chemical system of interest that have a non-negligible potential to impact the performance of a rocket motor. To achieve that objective, and because at the outset it is known that such sets are going to be reduced (making the presence of unimportant reactions to a large extent irrelevant), large families of reactions from mechanisms developed for related systems are included without prescreening. Rate expressions for all reactions considered in the course of the research conducted to complete a representation for a specific system are also included.

an adjustable parameter (Nusca and Michaels, 2004), and the relative concentrations of the species produced by the reaction were specified on the basis of calculations performed with the NASA-Lewis equilibrium thermodynamics code (McBride and Gordon, 1996).

It was observed that when run with the one-step reaction mechanism the CFD model's results were strongly dependent on the reaction rate chosen. For example, if the rate was chosen to be infinitely fast (i.e., equilibrium product concentrations were produced at each time step), the CFD model would predict steady-state operating pressures that were higher than those measured in ISVE test stand firings. Also, if it was assumed that no reaction occurred, the steady-state operating pressure would be under-predicted (as would be expected). With judicious selection of the reaction rate, steady-state pressures measured in test stand firings could be reproduced; however, large pressure transients observed during the ignition phase were not reproduced. It was also observed that a rate that would well-reproduce the steady-state pressure measured for one design (or a set of operating conditions) would not necessarily well-reproduce the steady-state pressure measured for another design. Therefore, the development of a more realistic chemical kinetics submodel was considered necessary.

Based on prior experience, the approach taken to develop a more realistic MMH–RFNA chemical kinetics submodel was to develop a detailed finite-rate chemical kinetics mechanism for the system and derive a submodel from it. Reactions involving MMH and the components of RFNA having been fairly well studied, a detailed mechanism could be built for the combination based primarily on data in the open literature. However, because its (initial) formulation included 489 reactions and 72 species, it was too large to be practical as a CFD submodel. (When its development was discontinued, the mechanism involved 513 reactions and 81 species [Anderson et al., 2010].) More specifically, the complete inclusion of this mechanism as a submodel would have required that 71 partial differential equations (PDEs) be added to the five (Navier–Stokes) PDEs required to model mass, momentum, and energy transport. (The total number of additional PDEs required to include a chemical kinetics mechanism in a CFD model equals the mechanism's total number of species minus 1.) Given the millions of grid points needed to discretize the internal volumes of an ISVE's components (including the injectors, combustion chamber, and nozzle) and the millions of time steps needed to provide adequate temporal resolution of transients occurring during a ballistic cycle, even with the considerable computing resources available to ARL through the Department of Defense (DoD) Shared Resource Center, the time that would have been needed to perform simulations with that number of PDEs was untenable. Therefore, a means had to be implemented for reducing the number to one that was tenable yet retained the ability to well-represent MMH–RFNA reaction chemistry under conditions of interest.

Although a number of mechanism reduction methods have been proposed and demonstrated, ARL chose to develop a new method, which is referred to as the trial mechanism

method (TMM). The TMM is described in detail elsewhere (Kotlar, 2010). Briefly, subsets of elementary reactions of a detailed mechanism are produced by ordering (usually randomly, but deterministically if desired) a detailed mechanism's reactions, sequentially eliminating individual reactions from it on a trial basis, running a constant-volume or constant-pressure homogenous reactor simulation for each trial elimination, and permanently eliminating any reaction whose deletion does not change beyond specified tolerances selected results of the simulation produced with the detailed mechanism. Results of the homogeneous reactor simulations that are compared are the magnitudes of maxima for volumetric and mass-specific heat release, the times at which those maxima occur, and the final (adiabatic) temperature. Following the same reaction step order (minus reactions that have been eliminated), this trial process is repeated for a given set of tolerances if at least one reaction is permanently eliminated in the course of a complete pass. When no more reactions can be eliminated without exceeding the given set of tolerances, the tolerances can be relaxed and the process repeated. With mechanisms having less than 70 reactions and 50 species being the target, the TMM generated many such mechanisms that were able to produce homogenous reactor simulations similar to those produced with the full mechanism. Figure 1 shows a representative result. More importantly, CFD simulations with these mechanisms as submodels proved to reproduce ISVE test stand data without any adjustable kinetic parameters (Nusca and Michaels, 2005) (see Fig. 2).

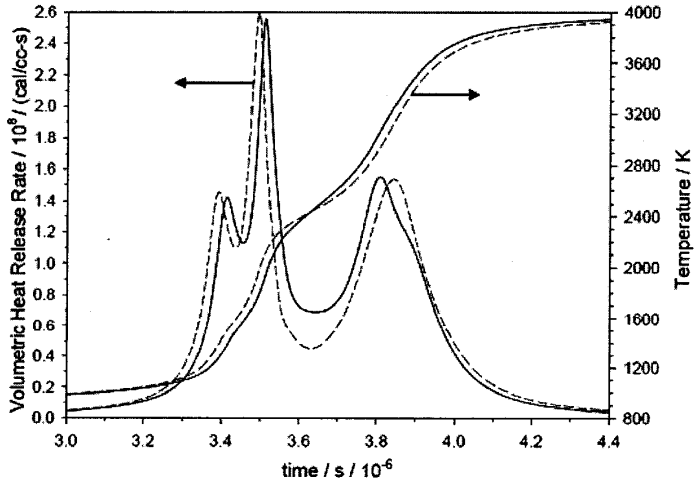

FIG. 1: Homogenous reactor simulations based on full (513 reaction, 81 species) and reduced (36 reaction, 31 species) MMH–RFNA mechanisms (Nusca et al., 2008) (the dashed lines correspond to results obtained with the reduced mechanism).

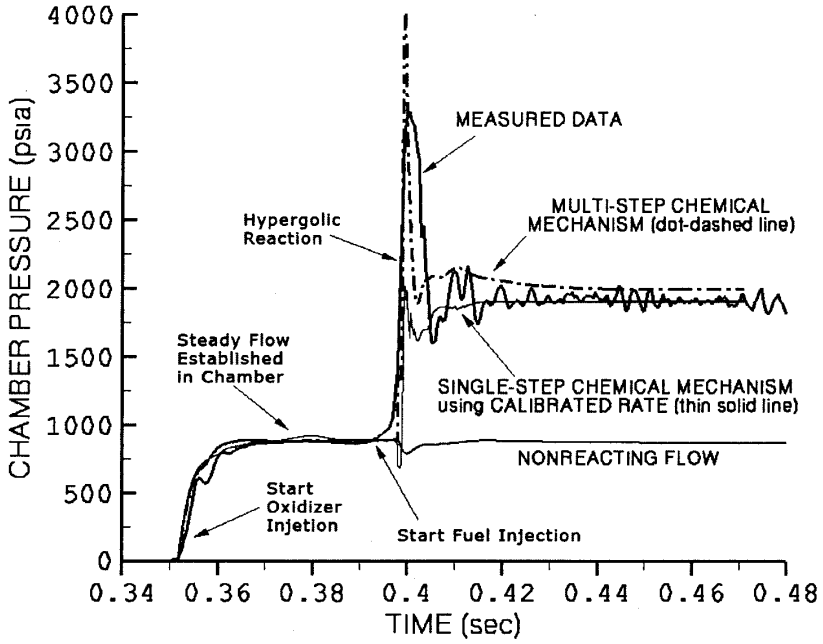

FIG. 2: Measured and CFD-simulated combustion chamber pressure histories for an ISVE test firing (Nusca and Michaels, 2005).

2.2 Tetramethylethylenediamine–2-Azido-N,N-Dimethylethanamine–Red Fuming Nitric Acid

Although the performance of MMH–RFNA in the ISVE was exceptional, the carcinogenic potential of MMH prompted the Army to develop alternative hypergols, with a blend of tetramethylethylenediamine (TMEDA) and 2-azido-*N,N*-dimethylethanamine (DMAZ), which is referred to as TEDMAZ, emerging as the leading candidate (Stevenson et al., 2011). However, the development of a TEDMAZ–RFNA mechanism presented a huge challenge. Unlike MMH–RFNA, very little had been reported on the combustion of amines (in general), let alone TMEDA–RFNA or DMAZ–RFNA. Therefore, the detailed mechanisms for them had to be built essentially from scratch. In addition, as shown in Fig. 3, TMEDA and DMAZ are much larger molecules than MMH, and thus there are many more potential pathways for their decomposition.

To produce detailed TMEDA–RFNA and DMAZ–RFNA mechanisms in a timely and cost-effective manner, quantum chemistry (QC) models were employed to simulate postulated reaction pathways, and rate expressions for individual reactions were derived

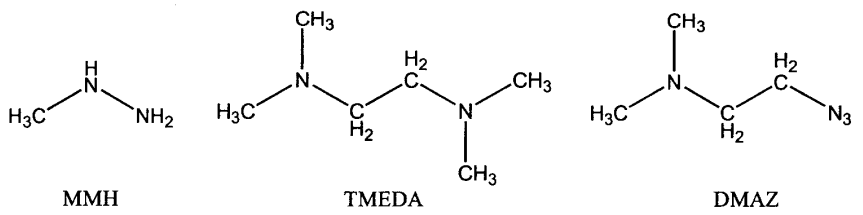

FIG. 3: Hypergolic fuels.

from the results (Chen and McQuaid, 2007, 2011). Experience gained from the development of the MMH–RFNA mechanism informed the effort. Specifically, it led us to assume (exothermic) complexation and addition reactions provide the energy needed to promulgate H-atom abstraction reactions involving the (parent) fuel and its dehydrogenated daughters. It was further expected that radical products of these reactions would decompose via β-scission reactions, and that products of these reactions would be oxidized, completing the combustion process.

Molecular structures and vibrational frequencies for stationary points of paths to the decomposition of TMEDA and DMAZ were obtained via density functional theory–based models. Refined thermochemical characterizations of the points/structures were then obtained with composite QC methods such as G3, G3MP2, and CBS-Q. Coupled cluster calculations with relatively large basis sets were also performed for (small) molecules for which they were practical. Figure 4 provides an example of the type of results that were obtained; a potential energy diagram for DMAZ reacting with NO_2 is shown (Chen and McQuaid, 2011). Entropies and heat capacities for stationary points of all such paths were calculated from methods of macro-canonical statistical mechanics using vibrational frequencies, moments of inertia, and hindered internal rotation data obtained from the QC models (and literature sources when available). Rate expressions for elementary steps were then derived from the data on the basis of canonical transition state theory or variational transition state theory.

Detailed mechanisms for TMEDA–RFNA and DMAZ–RFNA were developed by combining such computationally based results with the set of reactions that was assembled for MMH–RFNA. However, measured data that could be employed to validate these mechanisms were fairly limited. In the case of DMAZ–RFNA, the rate of DMAZ's decomposition in an *n*-dodecane bath at 34 atm had been measured as a function of temperature (Striebich and Lawrence, 2003), and simulations based on the DMAZ pyrolysis subset of the DMAZ–RFNA mechanism reasonably reproduced the measurements (Chen and McQuaid, 2012) (see Table 1). Simulations based on the DMAZ–RFNA mechanism also produced time-to-ignition values that are consistent with the approximately 6-ms ignition delays observed in drop-into-drop experiments (Thompson, 2000) (see Fig. 5).

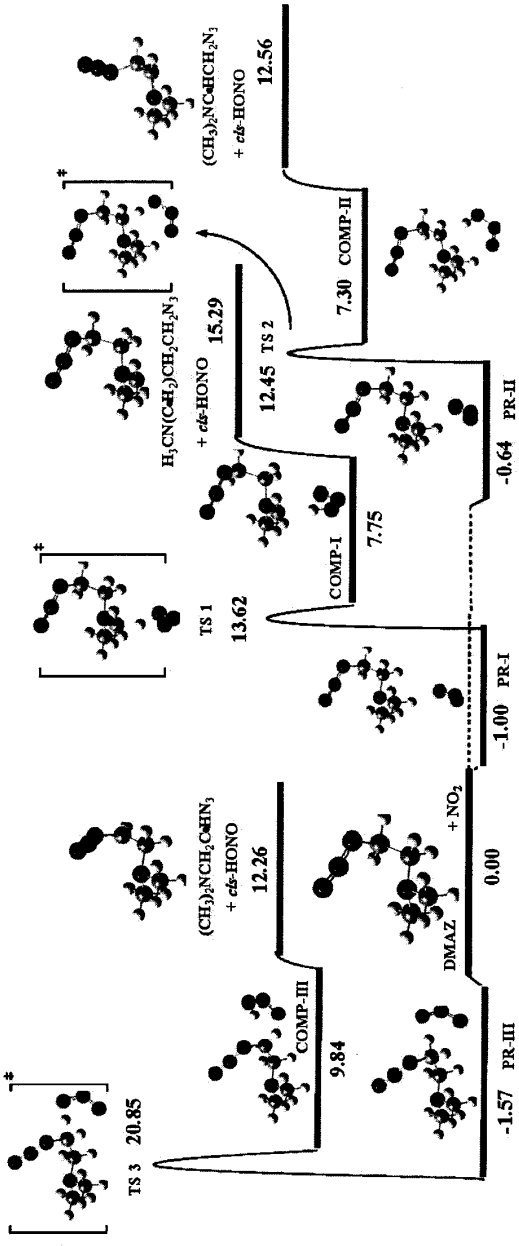

FIG. 4: Potential energy diagram for H-atom abstraction from DMAZ by NO_2: G3MP2/MPWB1K/6-31 + G(d,p) results (Chen and McQuaid, 2011).

TABLE 1: Flow reactor exit concentrations of *n*-dodecane-solvated DMAZ as a function of residence time and temperature: measured and simulated results (Chen and McQuaid, 2012)

Temperature (°C)	Residence time (s)	Exit concentration (%)		
		Measured[1]	Simulated	
			QC Model 1	QC Model 2
100	4.75	100	100	100
200	4.27	100	100	100
300	3.71	70	83	59
400	2.89	0	0	0
500	1.67	0	0	0

[1] Measured values were read from a graph published by Striebich and Lawrence (2003), and therefore are approximate.

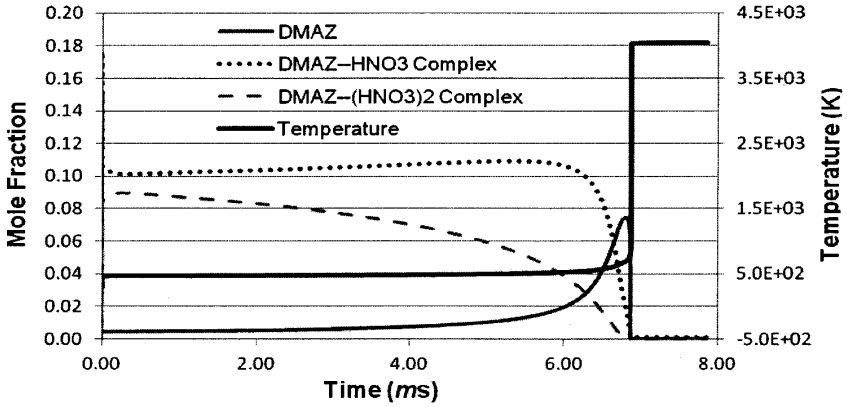

FIG. 5: Homogenous reactor simulation of DMAZ–RFNA reaction dynamics (Chen and McQuaid, 2011).

The TMEDA–RFNA and DMAZ–RFNA mechanisms were subsequently combined to produce a detailed TEDMAZ–RFNA mechanism (Nusca et al., 2008). It consists of 1950 reactions and 460 species. Being much larger than mechanisms that had previously been reduced, it posed a much bigger challenge for the TMM, and led to the incorporation of several upgrades, which included the implementation of a more robust and efficient differential-algebraic equation solver (Brown et al., 1994) for the homogeneous reactor model and the porting of the code to a multi-processing environment.

Reduced mechanisms with less than 100 reactions and 100 species were achieved, and CFD simulations employing such mechanisms well-reproduced data measured in TEDMAZ–RFNA-fueled ISVE test stand firings (Nusca et al., 2009) (see Fig. 6).

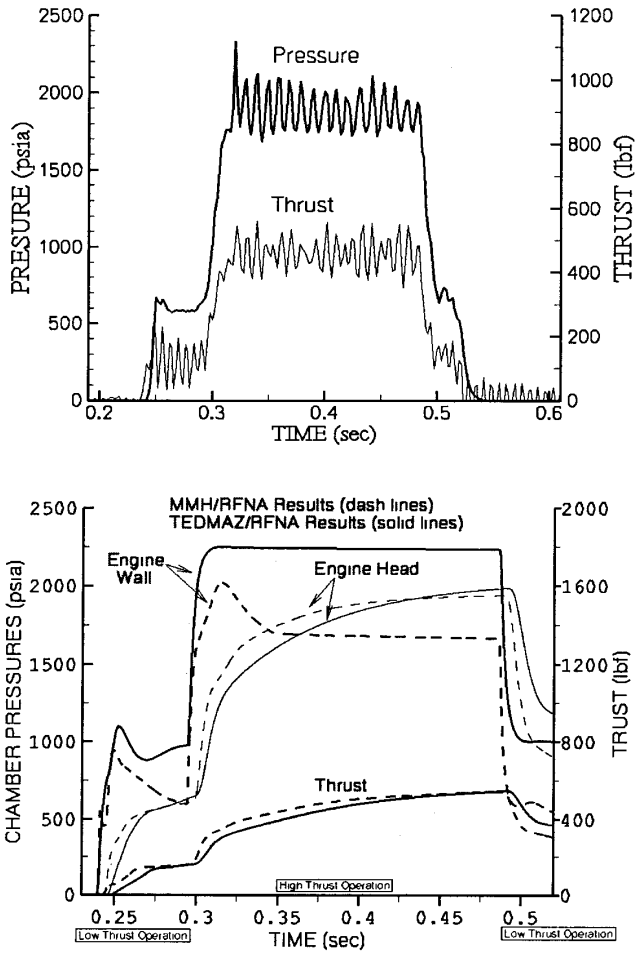

FIG. 6: Measured engine head pressure and thrust for a TEDMAZ–RFNA-fueled ISVE test firing (top), and CFD results that compare the performance of MMH–RFNA-fueled versus TEDMAZ–RFNA-fueled ISVE firings when the same throttle schedule is employed (bottom) (Nusca et al., 2009).

2.3 Ethyl Nitrate

As a step toward the development of a capability for modeling the combustion of (solid) minimum-smoke rocket propellants, a detailed chemical kinetics mechanism for modeling the combustion of methyl and/or ethyl nitrate was developed. Minimum-smoke propellants are formulated with relatively large organic nitrate esters such as nitrocellulose and nitroglycerin, and the development of chemical kinetics mechanisms for them is being pursued. However, desiring to develop and test other aspects of the CFD model while these mechanisms are being completed, we sought alternatives for which mechanisms could be quickly developed and tested. Being the simplest organic nitrate esters, and their burning rates having been measured (Steinberger et al., 1955), methyl and ethyl nitrate met those criteria.

The detailed mechanism for methyl and ethyl nitrate was constructed by combining computationally derived rate expressions for postulated decomposition reactions with a set of rate expressions for reactions involving small molecules developed for other propellants. For validation, the mechanism and a reduced version of it were (separately) employed with a one-dimensional model (Miller and Anderson, 2004) to simulate the burning of (liquid) ethyl nitrate as a function of pressure. As shown in Fig. 7, simulations based on the full and reduced mechanisms produce similar results, predicting burn rates that are approximately three times lower than measured values. Given some of the assumptions underlying the simulations, the agreement is considered reasonable. At the same time, an investigation into the source of the discrepancy is being pursued in the hope of reconciling differences and incorporating improvements.

In addition to testing the detailed and reduced ethyl nitrate mechanisms' abilities to reproduce measured data, the reduced mechanism was used with a CFD model to simulate the burning of a 0.5-cm-diameter by 1.0-cm-long strand of the material with and without an embedded silver (Ag) wire. Embedding propellant strands with wires is known to increase their burning rate; however, detailed knowledge of the mechanisms underlying the increase remains to be established. Figure 8 shows computed temperature contours for three cases. They include a strand with no wire [Fig. 8(a)], a strand with a 0.1-mm-diameter Ag wire embedded along the centerline [Fig. 8(b)], and a strand with a 0.4-mm-diameter Ag wire embedded along the centerline [Fig. 8(c)]. The domain of the calculation extended 1.25 cm above the strand surface. Plotted in gray scale and corresponding to a time when burning is fully developed, Figs. 8(a)–8(c) show the simulations' predictions for each strand's surface topology and the location and structure of the flame. The conically shaped burning surfaces predicted for the strands with an embedded wire are consistent with photographs of burning, wire-embedded, nitrate ester formulations (Kubota et al., 1982). Further simulations are planned to elucidate the interplay between various design parameters and the shape of the surface in the hope of generating insights that can be employed to guide grain design.

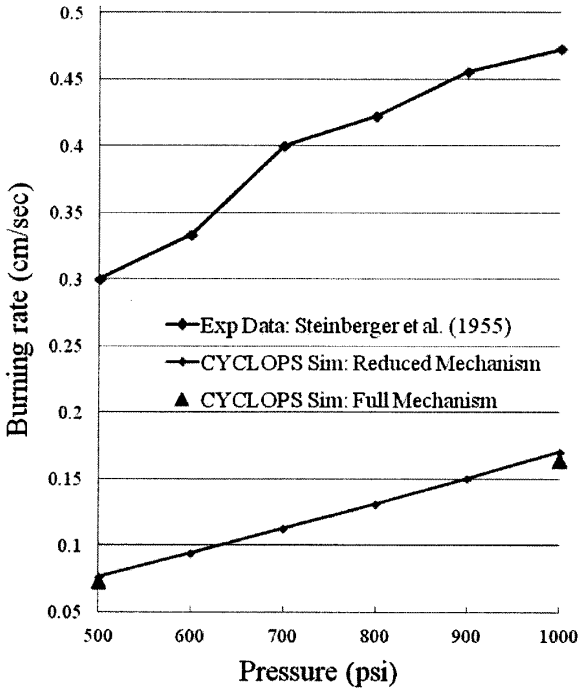

FIG. 7: Burning rate of (liquid) ethyl nitrate as a function of pressure: measured and simulated results.

3. SUMMARY

ARL has developed gas-phase chemical kinetics mechanisms for use in modeling the combustion chamber dynamics of novel rocket propulsion systems. To develop mechanisms for propellant systems whose ignition and combustion chemistry is not well known, postulated reaction paths are simulated with QC methods, and results for individual paths are converted to kinetic rate expressions using transition state theory. Rate expressions for elementary reactions are then assembled to yield detailed mechanisms whose reasonableness for modeling a given application is established by employing it to model relevant measured data (to the extent that they exist). Subsets of rate expressions in detailed mechanisms that can serve as submodels in CFD models are then produced with an ARL-developed methodology called the trial mechanism method. This approach to the construction of chemical kinetics submodels has been successfully employed for a number of hypergolic bipropellant systems and a hybrid propellant system. It is also

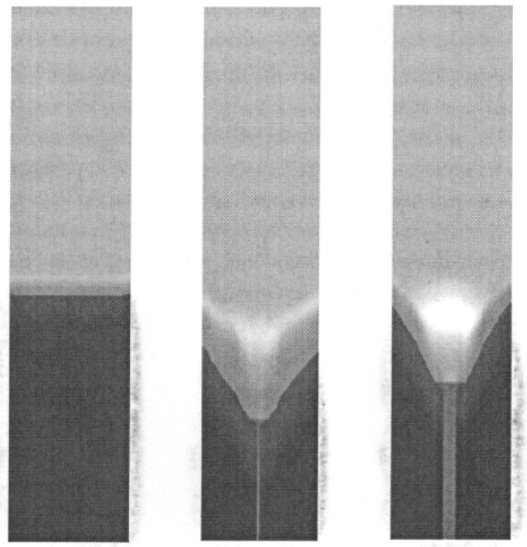

FIG. 8: CFD simulated temperature contours for burning ethyl nitrate strands with and without an embedded wire (cold → hot: black → white): (a) strand with no wire; (b) strand with embedded 0.1-mm-diameter Ag wire; (c) strand with embedded 0.4-mm-diameter Ag wire.

being applied to develop submodels for simulating the reaction kinetics of minimum-smoke propellant formulations.

REFERENCES

Anderson, W. R., McQuaid, M. J., Nusca, M. J., and Kotlar, A. J., A detailed finite-rate chemical kinetics mechanism for monomethylhydrazine-red fuming nitric acid systems, *ARL-TR-5088*, U.S. Army Research Laboratory, Aberdeen Proving Ground, MD, 2010.

Anderson, W. R., Meagher, N. E., and Vanderhoff, J. A., Dark zones of solid propellant flames: Critical assessment and quantitative modeling of experimental datasets with analysis of chemical pathways and sensitivities, *ARL-TR-5424*, U.S. Army Research Laboratory, Aberdeen Proving Ground, MD, 2011.

Brown, P. N., Hindmarsh, A. C., and Petzold, L. R., Using Krylov methods in the solution of large-scale differential algebraic systems, *SIAM J. Sci. Comput.*, vol. **15**, pp. 1467–1488, 1994.

Chen, C.-C. and McQuaid, M. J., Tetramethylethylenediamine-red fuming nitric acid (TMEDA-

RFNA) reaction kinetics, *Proc. of 34th Propellant & Explosives Development and Characterization Subcommittee Meeting*, CPIA Publication JSC-CD-47, 2007.

Chen, C.-C. and McQuaid, M. J., Thermochemical and kinetics modeling of 2-azido-N,N-dimethylethanamine-red fuming nitric acid (DMAZ-RFNA) systems, *Proc. of 6th Liquid Propulsion Subcommittee Meeting*, CPIA Publication JSC-CD-67, 2011.

Chen, C.-C. and McQuaid, M. J., Mechanisms and kinetics for the thermal decomposition of 2-azido-N,N-dimethylethanamine (DMAZ), *J. Phys. Chem. A*, vol. **116**, pp. 3561–3576, 2012.

Kotlar, A. J., A general approach for the reduction of chemical reaction mechanisms. I: Methodology and application to MMH–RFNA, *Proc. of 5th JANNAF Liquid Propellant Subcommittee Meeting*, CPIA Publication JSC-CD-62, 2010.

Kubota, N., Ichida, M., and Fujisawa, T., Combustion processes of propellants with embedded wires, *AIAA J.*, vol. **20**, pp. 116–121, 1982.

McBride, B. J. and Gordon, S., Computer program for calculation of complex chemical equilibrium compositions and applications. II. Users' manual and program description, *NASA RP 1311*, Lewis Research Center, Cleveland, OH, 1996.

Michaels, R. S. and Wilson, B. F., The low L/D vortex engine for gel propulsion, *Proc. of JANNAF Gel Propulsion Technology Symposium*, CPIA Publication 627, pp. 9–16, 1995.

Miller, M. S. and Anderson, W. R., Burning-rate predictor for multi-ingredient propellants: Nitrate-ester propellants, *J. Propul. Power*, vol. **20**, pp. 440–454, 2004.

Nusca, M. J., Chen, C.-C., and McQuaid, M. J., Combustion chamber fluid dynamics and hypergolic gel propellant chemistry simulations for selectable thrust rocket engines, *Proc. of DoD High Performance Computing Modernization Office Users Group Conference*, Seattle, WA, 2008.

Nusca, M. J., Mathis, N. P., and Michaels, R. S., Computational study comparing potential bipropellant compositions for Army's impinging stream vortex engine, *Proc. of 43rd JANNAF Combustion Subcommittee Meeting*, CPIAC Publication JSC CD-60, 2009.

Nusca, M. J. and Michaels, R. S., Development of a computational model for the Army's impinging stream vortex engine, *Proc. of 1st JANNAF Liquid Propellant Subcommittee Meeting*, CPIA Publication JSC CD-33, 2004.

Nusca, M. J. and Michaels, R. S., Computational modeling of hypergolic ignition in the army's impinging stream vortex engine, *Proc. of 40th JANNAF Combustion Subcommittee Meeting*, CPIA Publication JSC-CD-39, 2005.

Steinberger, R., Orlick, C. A., and Schaaf, V. P., Burning rates of deuterated nitrate esters, *J. Am. Chem. Soc.*, vol. **77**, pp. 474–475, 1955.

Stevenson, W. H., Felton, L. D., and Slocum-Wang, Z., Hypergolic liquid or gel fuel mixtures, U.S. Patent 2011/0272071, 2011.

Striebich, R. C. and Lawrence, J., Thermal decomposition of high-energy density materials at high pressure and temperature, *J. Anal. Appl. Pyrolysis*, vol. **70**, pp. 339–352, 2003.

Thompson, D. M., Tertiary amine azides in hypergolic liquid or gel fuels propellant systems, U.S. Patent 6,013,143, 2000.

Mechanism of Densification in Silica Glass Under Pressure as Revealed by a Bottom-Up Pairwise Effective Interaction Model

Sergiy Izvekov and Betsy M. Rice

The Journal of Chemical Physics, 136 (2012)

THE JOURNAL OF CHEMICAL PHYSICS **136**, 134508 (2012)

Mechanism of densification in silica glass under pressure as revealed by a bottom-up pairwise effective interaction model

Sergei Izvekov and Betsy M. Rice
U.S. Army Research Laboratory, Aberdeen Proving Ground, Maryland 21005, USA

(Received 13 December 2011; accepted 6 March 2012; published online 6 April 2012)

A new short-range pairwise numerical potential for silica is presented. The potential is derived from a single *ab initio* molecular dynamics (AIMD) simulation of molten silica using the force-matching method with the forces being represented numerically by piecewise functions (splines). The AIMD simulation is performed using the Born-Oppenheimer method with the generalized gradient approximation (BLYP) for the XC energy functional. The new effective potential includes a soft-repulsive shoulder to describe the interactions of oxygen ions at short separations. The new potential, despite being short-ranged and derived from single-phase data, exhibits a good transferability to silica crystalline polymorphs and amorphous silica. The importance of the O–O soft-repulsive shoulder interaction on glass densification under cold and shock compressions is assessed from MD simulations of silica glass under room and shock Hugoniot conditions, respectively. Results from these simulations indicate that the appearance of oxygen complexes (primarily pairs) interacting through soft-repulsive shoulder potential occurs at 8–10 GPa, and under cold compression conditions becomes notable at 40 GPa, essentially coinciding with the transition to a Si sixfold coordination state. An analysis of changes in system structure in compressed and shocked states reveals that the O ions interacting through the soft-repulsive shoulder potential in denser states of silica glass may create a mechanical multi-stability under elevated pressures and thus to contribute to the observed anomalous densification. [http://dx.doi.org/10.1063/1.3696865]

I. INTRODUCTION

A fundamental understanding of the atomic-level details of the structural order and phase transformations in silica glasses at high pressure and temperature is an important issue in modern condensed-matter physics. One of the most puzzling anomalous properties of silica glass is its irreversible densification under pressures above 10–20 GPa (at room temperature).[1–9] In the widely accepted picture, pressure-induced structural changes in SiO_2 glass are attributed to competing transformations of the intermediate- and near-range topology of the glass bond network. Under lower pressures (e.g., 10–20 GPa), structural changes in SiO_2 glass are thought to be mostly rebonding-driven topological reconstructions[10] at the intermediate range (second and third coordination shells) rather than a change in a Si–O coordination number (near-range order). Under higher pressures, the experimental and simulation studies univocally suggest the gradual modification of near-range order: the transition in the Si–O coordination number from fourfold (tetrahedral SiO_4) to sixfold (octahedral SiO_6) begins at about 10–20 GPa,[4–8,11] with the sixfold coordinated structure predominantly observed above 40 GPa (Refs. 6 and 7) (although some controversy still exists on the exact picture of coordination number transition based on results from different experimental techniques). The anomalous increase in density between 10 and 40 GPa cannot be explained by estimated density-dependent elastic properties.[6,7] This suggests that SiO_2 glass does not behave as a single amorphous polymorph, but its short-ranged and intermediate structure undergoes irreversible changes in this pressure range. These changes lead to what could be a low-density amorphous (lda) to high-density amorphous (hda) first-order phase transition.[12] On the other hand, above ∼40 GPa the estimated bulk modulus follows well the pressure dependence of the density, indicating that SiO_2 glass behaves as a single amorphous polymorph[6,7] with no obvious structural phase transition. The anomalous densification is an important factor controlling the response of silica to shock loading and largely determines the anomalous shape of the $\rho(P)$ Hugoniot curve above 16 GPa. A comparison of the ambient temperature and the Hugoniot $\rho(P)$ curves may reveal the effect of temperature on the lda-hda transition as the Hugoniot states correspond to significantly higher system temperatures.

Analogous to the densification of amorphous ice,[12,13] it has been suggested that the pressure-induced lda-hda mechanical instability arises from the disappearance of the transition barrier on the potential energy landscape separating the inherent metastable structural states. This picture has gained some support from the phenomenological modeling of instabilities in glass based on a double-well potential.[14] However, despite numerous experimental and theoretical studies, the precise nature of the potential energy landscape of SiO_2 glass (denoted g-SiO_2 hereafter) that controls the pressure initiated lda-hda transition is not known. The picture in which the appearance of the hda state(s) in the potential energy surface (PES) of g-SiO_2 is explained by purely topological and rebonding arguments precludes consideration of the role of changes in interatomic interactions due to pressure effects on the electronic structure. In fact, the changes in interatomic interactions within certain structural units of g-SiO_2 may be

the source of structure instability leading to a collapse of the network into the hda state. Indeed, a similar range of pressures at which the transition of the network to fivefold and then to sixfold coordination state begins and the lda-hda transition occurs suggests that the appearance of closely packed structures of oxygen atoms might be a possible microscopic pathway facilitating the network topology reorganization at the intermediate range, eventually leading to the development of mechanical instabilities.

The attempts to relate the appearance of sixfold coordination defects to bond network instabilities have been made in the past. However, the proposed models still consider the sixfold coordination defect as a special topological complex, the presence of which merely triggers the network reorganization. These models do not invoke explicitly the effect of pressure on the microscopic interactions. For instance, within the original model by Stolper and Ahrens,[15] the coordination defects are spontaneously formed under pressure through a special displacement mechanism. Meanwhile, because of the high polarizability of oxygen ions and their ionicity, the appearance of closely packed oxygen sublattice units could be indicative of changes in the oxygen-oxygen effective interaction; this is supported by Raman scattering measurements.[2,8] Such changes in the effective interaction may play a dominant role in the appearance of additional metastable states in the PES of g-SiO_2, as will be discussed below. Moreover, the lda-hda barrier might be due solely to the pressure-dependent effective interactions irrespective of reorganization in the bonding topology across the barrier.

The importance of pressure-related changes in the microscopic interactions on the formation of dense polymorphs of g-SiO_2 can be conclusively studied only using *ab initio* electronic structure methods or molecular simulation methods with accurate empirical potentials. The *ab initio* electronic structure calculation approaches are best suited for such studies as these methods treat all interactions from first principles. Although the *ab initio* methods have provided important insight into properties of g-SiO_2,[16,17] they are limited in addressing whether the modification of microscopic interactions under pressure is a cause of topological changes or merely a result of the latter, in particular, due to the limitations of system sizes that can be simulated in this method and the complexity in analyzing a multi-dimensional PES in condensed phases. Thus, empirical interatomic potentials that can accurately map out the PES of g-SiO_2 under different conditions are probably the only tractable way to address this issue. A construction of such potentials for SiO_2 is a challenge, as evidenced by the great variety of the empirical models that have been proposed.[17–25]

Within empirical potential modeling, different types of the interatomic interactions are usually represented by separate terms having preselected functional forms with adjustable parameters; these terms are optimized to reproduce a selected set of target macroscopic properties within *top-down* parameterization schemes or to project the microscopic level interactions within *bottom-up* parameterization approaches. The analytical pair potentials, especially those of the simplest central form, are attractive options due to computational efficiency, and have been used to model silica from the 1980 until the present. Although it was originally believed that many-body terms, such as bond-angle three-body and bond-order terms, or terms describing interactions due to charge redistribution, are necessary to reproduce the directionality of the covalent bonding in silica evidenced by the presence of SiO_4 units, bottom-up fixed-charge pairwise potentials of analytical form by Tsuneyuki *et al.*[26] and by van Beest *et al.*[19] (TTAM and BKS models, respectively) proved that pair potentials could effectively capture many-body features of interactions in both crystalline and amorphous silica. These models adequately described the ambient and low pressure structures of several silica polymorphs. Still it is imperative to mention that the use of predetermined *ad hoc* analytical forms to construct pairwise models may significantly limit the ability to represent many-body features of silica PES. Meanwhile, the importance of different types of interactions for silica has been heavily debated. A significant deviation of the elastic constants of quartz and other silica crystalline polymorphs from Cauchy relations[27] has been cited as indirect experimental evidence of the importance of many-body interactions in ordered phases. The existing pairwise models have also predicted a lda-hda transition at lower pressures than observed experimentally;[24] this discrepancy suggests the importance of many-body interactions in amorphous silica. This is further supported by the substantial improvement in simulated structural, vibrational, and elastic properties as well as better transferability across thermodynamic states achieved using pairwise models augmented with bond-angle[20,25] and electronic polarizability[22,25,28] terms. Since then, empirical potentials for silica have evolved mostly through design and inclusion of new elaborate terms tailored to represent different types of many-body contributions into PESs of condensed-phase silica. An exhaustive overview of such developments would exceed the scope of this work and we limit ourselves to referring the most representative works pertinent to our study. The BKS form has been extended to account for bond stretching and augmented with polarization term to account dynamically for a modification of oxygen ionicity due to polarization effects.[22] The valence bonding has been explicitly modeled using Keating-type models[29] and models based on Stillinger-Weber or Tersoff concepts.[20,30] More recently, the charge redistribution phenomena beyond polarization effects have been addressed using bond-order ReaxFF and COMB force fields.[25,31] However, similar to *ab initio* representations, these models do not offer insight into the effect of interaction modification on the densification phenomenon as the many-body interactions are explicitly represented by complex terms. Thus, an analysis of changes in silica PES under pressure remains an essentially multi-dimensional problem.

The first main objective of the present paper is the development of a simple bottom-up effective pairwise interaction model for g-SiO_2 that is not constrained to a particular analytical form, and, therefore, may adequately and clearly address the role of pressure effects on the microscopic interactions and their role in the polymorphism of g-SiO_2. Specifically, we present a numerical pairwise central and nonpolarizable silica potential. The potential is parameterized solely using information on microscopic forces obtained from the *ab initio* MD (AIMD) simulation of a silica melt at high

temperature. High temperature conditions facilitate sampling of configurations which are pertinent to denser states of g-SiO_2. The bottom-up methodology used to project the *ab initio* ionic forces onto effective pairwise interactions is the multi-scale coarse-graining (MS-CG) approach,[32–37] which couples the functional-free representation of interactions with a thermodynamically consistent force-matching parameterization scheme. As shown in the past, superior pairwise models for condensed-matter systems in which many-body interactions are important can be developed with the MS-CG method.[32,35,37–39] To our knowledge it is the first time a numerical potential for silica is presented. The resulting oxygen-oxygen potential exhibits a distinct repulsive shoulder at short separations suggesting a softer repulsion between oxygen atoms under extreme conditions than that expected when assuming the conventional monotonic descriptions of repulsive interactions such as in BKS-type potentials. This might be a reason that BKS and similar models perform unsatisfactorily under high pressures.[40] Despite being fitted to the highly disordered liquid state, the force-matching (FM) model demonstrates adequate performance for many crystalline polymorphs of silica. The other major objective of the paper is to examine the role of the soft-repulsive shoulder interaction for oxygen pairs on the densification of glass under ambient and shock compression conditions.

The rest of this paper is organized as follows: in Sec. II we present details of the FM potential development; in Sec. III we discuss the obtained potentials; and in Sec. IV we evaluate the performance of the new models. Finally, in Sec. V we discuss the application of the new models to study silica glass under various compression conditions and summarize the results in Sec. VI.

II. POTENTIAL DEVELOPMENT WITH THE MS-CG METHOD

The MS-CG method is a variational approach for particle-based coarse-graining which yields the best (in a least-squares sense) pairwise decomposition $\sum_{i<j} u(r_{ij}, \Omega)$ of the effective PES $U^{eff}(\mathbf{r}^N)$ of a system of N particles with translational coordinates $\mathbf{r}^N = (\mathbf{r}_i, i = 1, N)$ and intraparticle set of coordinates $\boldsymbol{\rho}$ if the latter are integrated out (or coarse-grained). Here, for simplicity, we assume that particles are of same kind. The terms $u(r_{ij}, \Omega)$ are functions of interparticle distance r_{ij} and a set of adjustable parameters Ω used in the least-squares minimization scheme. The development of empirical atomistic potentials from *ab initio* models amounts to the coarse-graining of the electronic degrees of freedom ($\boldsymbol{\rho}$) and, thus, represents a special case of particle-based coarse-graining. The description of the MS-CG methodology with emphasis on the parameterization of potentials from AIMD is given in Ref. 37. Within the MS-CG framework the pairwise force terms, $f(r_{ij}, \Omega)$, which determine the $u(r_{ij}, \Omega)$ potentials as

$$u(r, \Omega) = \int_r^{r_{cut}} f(r', \Omega) dr', \tag{1}$$

are obtained first through a predetermined FM parameterization scheme. The $f(r, \Omega)$ force is represented by a piecewise cubic spline function defined on a mesh $\{r_k\}$ that extends to a cutoff distance $r_{k_{max}} = r_{cut}$. With such a choice, the $f(r, \Omega)$ depends linearly on the spline parameters f_k, f''_k, which are values of the $f(r, \Omega)$ and its second derivative at the kth node r_k of the mesh. Therefore, the $\Omega = (\{f_k\}, \{f''_k\})$ parameter set is chosen as the parameters to fit. The linear system of FM equations, which is equivalent to a least-squares minimization problem, is solved by a block averaging scheme.[32,37] The piecewise form of $f(r, \Omega)$ combined with an adequate sampling of system phase space may result in a proper description of interatomic interactions particularly at short distances, thus, improving performance in modeling dense polymorphs of silica.

In the present work, the SiO_2 potential has been derived from a single phase AIMD simulation of molten silica at $T = 5000$ K under constant *NVT* conditions. The AIMD simulation was carried out using the Born-Oppenheimer MD scheme within the standard implementation of the plane-wave-basis density functional theory (DFT) with a generalized gradient approximation (GGA) to the exchange-correlation (XC) energy using the BLYP functional[41] and pseudopotentials of the Troullier-Martins form[42] within the Kleinman-Bylander approximation.[43] In particular, the oxygen pseudopotential was generated using a cutoff radius of 1.05 a.u. for $l = 0, 1$, where the $l = 1$ channel is local. The system was represented by 64 SiO_2 in a cubic box at a density of 2280.3 kg/m^3. The Kohn-Sham orbitals were expanded in the plane waves up to a cutoff of 100 Ry. The starting configuration was generated from a 500 ps of *NVT* MD simulation using the empirical potential by Pedone *et al.*[23] and then re-equilibrated in an AIMD simulation for 5 ps. The *ab initio* dynamics was integrated for 30 ps with a timestep of 10 a.u. (0.24 fs) under constant *NVT* conditions using the CPMD code version 3.13.[44] Temperature control was imposed through coupling to a chain of four Nosé-Hoover thermostats. The configurations and corresponding forces were recorded at every 20 a.u. in the simulation, producing a total of ~62 000 configurations for use in the FM. The implementation of the FM scheme is the same as in Refs. 32, 34, 35, and 37 with the only difference being that an explicit fit of partial charges was not performed [cf. Eqs. (11) and (12) in Ref. 37]. The short-ranged FM force was represented by a spline over a mesh with a grid of 0.1 a.u.; a cutoff $r_{cut} = 13.3$ a.u. (0.7038 nm) was applied. The overdetermined system of FM equations was solved using a block averaging scheme with a block size of 10 (however, the solution was insensitive to variations in a block size). An analytical representation of the FM force obtained through a least-squares fit of the tabulated spline data by powers of $1/r$ as

$$f_{\alpha\beta}(r) = \sum_{n=2}^{n_{max}} A^n_{\alpha\beta}/r^n \tag{2}$$

is summarized in Table I. The force profiles and respective potentials [Eq. (1)] are displayed in Fig. 1. In the simulations reported below we used the original numerical representation of the FM models, which may produce results slightly different from those of the polynomial fit due to limited accuracy of the latter.

TABLE I. Coefficients $A^n_{\alpha\beta}$ of the least-squares fit for the BLYP FM SiO_2 force field $f_{\alpha\beta}(r)$ using the expansion in Eq. (2) with $n_{max} = 16$. Atomic units are used. At small separations $r < r_{core}$, the $f_{\alpha\beta}(r)$ is extrapolated as $f_{\alpha\beta}(r) = f(r^{\alpha\beta}_{core})$. The following core radii are used: $r^{\mathrm{SiSi}}_{core} = 3.5$ a.u., $r^{\mathrm{SiO}}_{core} = 2.3$ a.u., and $r^{\mathrm{OO}}_{core} = 2.4$ a.u. The cutoff of 0.7038 nm must be applied to this expansion. The original numerical forces and potentials are provided in the supplementary material.[66]

n	A^n_{SiSi}	A^n_{SiO}	A^n_{OO}
2	$8.38569797246 \times 10^{3}$	$-6.93672060032 \times 10^{2}$	$-1.53413111467 \times 10^{3}$
3	$-6.71569564738 \times 10^{5}$	$4.75552324617 \times 10^{4}$	$1.08746957292 \times 10^{5}$
4	$2.39814415405 \times 10^{7}$	$-1.45146806739 \times 10^{6}$	$-3.42727907962 \times 10^{6}$
5	$-5.04157703840 \times 10^{8}$	$2.60941072636 \times 10^{7}$	$6.35540171618 \times 10^{7}$
6	$6.93493814038 \times 10^{9}$	$-3.07784865663 \times 10^{8}$	$-7.73139251048 \times 10^{8}$
7	$-6.55520712182 \times 10^{10}$	$2.50876846644 \times 10^{9}$	$6.50715662006 \times 10^{9}$
8	$4.34393610920 \times 10^{11}$	$-1.44825707078 \times 10^{10}$	$-3.88749344879 \times 10^{10}$
9	$-2.01460775895 \times 10^{12}$	$5.95616803341 \times 10^{10}$	$1.65947848433 \times 10^{11}$
10	$6.36630631246 \times 10^{12}$	$-1.72258877705 \times 10^{11}$	$-4.99937327889 \times 10^{11}$
11	$-1.27452424588 \times 10^{13}$	$3.35528112036 \times 10^{11}$	$1.01930872147 \times 10^{12}$
12	$1.29603005238 \times 10^{13}$	$-3.89065597083 \times 10^{11}$	$-1.25049468617 \times 10^{12}$
13	$7.12201564397 \times 10^{11}$	$1.38817387532 \times 10^{11}$	$5.14911154410 \times 10^{11}$
14	$-1.16317019524 \times 10^{13}$	$2.73228278176 \times 10^{11}$	$8.57529170524 \times 10^{11}$
15	$-2.29569192322 \times 10^{12}$	$-3.95712647692 \times 10^{11}$	$-1.35814993601 \times 10^{12}$
16	$1.28627766169 \times 10^{13}$	$1.67143495856 \times 10^{11}$	$6.06638707829 \times 10^{11}$

The importance of many-body effects and, therefore, the quality of pairwise FM models is reflected in how well the reference distribution of the total forces is reproduced by the FM model and can be measured by the relative force deviation ΔF as defined in Refs. 37 and 45. The ΔF represents a fraction of root-mean-squared difference between the *ab initio* (reference) and FM total ionic forces relative to the root-mean-squared *ab initio* forces within the instant *ab initio* ionic configuration and it can defined for all ions (ΔF_{tot}) or for ions of one kind ($\Delta F_{\mathrm{O,\,Si}}$) in the configuration. Figure 2(a) shows the time dependence of ΔF along the AIMD trajectory with the respective running time averages $\langle \Delta F \rangle_t$ [$\langle \Delta F \rangle_{t_{max}} = \langle \Delta F \rangle$]. The density probability distributions $P(\Delta F)$ are displayed in Fig. 2(b). The values of $\langle \Delta F \rangle$ and standard deviation $\delta\langle \Delta F \rangle = [\int (\Delta F - \langle \Delta F \rangle)^2 P(\Delta F) d\Delta F]^{1/2}$ were: 0.304, 0.047 for oxygen; 0.367, 0.055 for silicon; and 0.336, 0.051 for the cumulative distribution, respectively. Interestingly, the $\langle \Delta F_{\mathrm{O}} \rangle$, $\delta\langle \Delta F_{\mathrm{O}} \rangle$ are close to similar quantities of 0.333, 0.048 for AIMD (BLYP) simulations of liquid water at $T = 300$ K reported in Ref. 37 despite a drastic difference in chemical composition and thermodynamic conditions. As discussed in the literature[37,45] the magnitude of departure of the instantaneous atomistic forces from the effective FM value is not a conclusive measure of the quality of the effective interaction model. The accuracy of the FM model largely depends on the nature of the force deviations and, in particular, whether or not they average to zero on short-time scales.[45]

III. FORCE-MATCHING MODELS

The force and potential profiles (Fig. 1) clearly show a soft-repulsive shoulder of the effective O–O interaction at separations $r < 0.195$ nm indicating a weakening of the Coulomb repulsion between oxygen atoms due to a number of possible factors (e.g., polarizability, charge transfer causing change in ionicity of oxygens, chemical bond formation, etc.), that are effectively captured by the FM method. The O–O force reaches a local minimum at $r = 0.159$ nm, corresponding to a repulsive potential energy of 416 kJ/mol. In order to access this repulsive shoulder, an oxygen pair must overcome an energy barrier of 307 kJ/mol ($r = 0.195$ nm). Under high temperature conditions of the reference AIMD simulation, the kinetic energy of the oxygen atoms is sufficient to access the O–O repulsive shoulder. As we will discuss, in g-SO_2 modeled with the FM potential under ambient conditions the O–O repulsive shoulder is not accessed, and a stronger repulsion keeps the oxygen atoms separated by distances well beyond 0.2 nm. However, under elevated pressures the changes in the g-SO_2 local environment may effectively reduce energy requirements for accessing the O–O repulsive shoulder, which, in turn, might introduce rich complexity in the phase behavior of this system, such as a transition to five- and then six-coordinated states of Si as well as modification of the shape of the equation of state (EOS). Past studies of highly idealized model systems have demonstrated that the extension of model interactions with the soft shoulder repulsion significantly affects the phase behavior of the system and leads to the appearance of new phases.[46,47] Systems of particles interacting through such pair potentials can possess a rich variety of phase transitions and thermodynamic anomalies, including liquid-liquid and liquid-glass phase transitions, and isostructural transitions in the solid region.[47] It is conceivable that for compressed g-SiO_2, islands of oxygen atoms interacting through the soft-repulsive shoulder could contribute to the observed anomalous densification.

Softening of the O–O FM repulsion occurs at distances at which the overlap of electronic orbitals is significant and several mechanisms may contribute to this phenomenon. The bonding in silica is a mix of ionic and covalent bonds, and exhibits continual rebonding when in the liquid phase (used to derive the FM models), although a high level of local chemical order is still maintained. The continual presence of broken bonds may lead to a high probability of formation of valence alternation pairs (VAPs),[48] which may effectively contribute

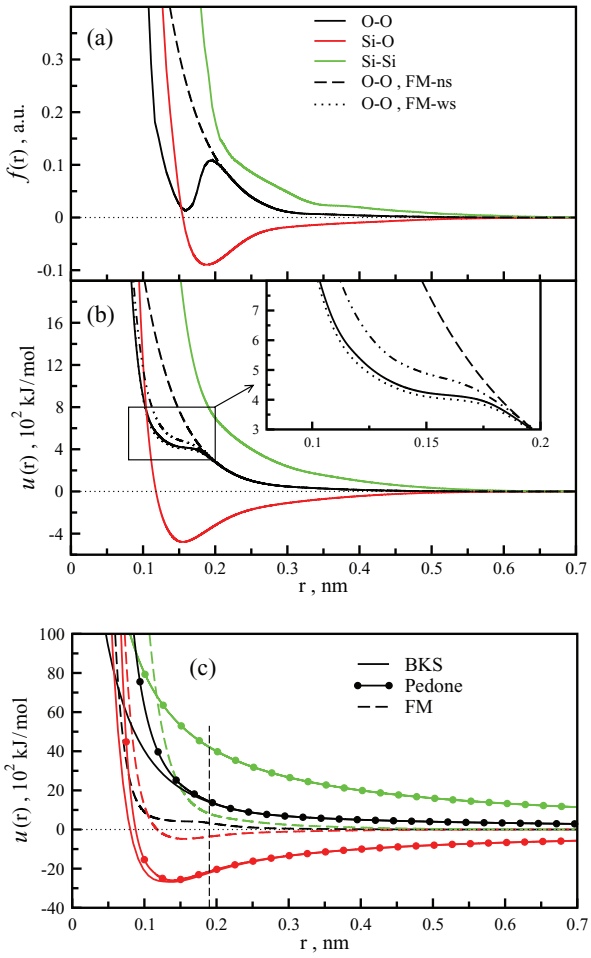

FIG. 1. Effective atom-atom forces [panel (a)] and corresponding potentials [panel (b)] in liquid SiO_2 generated through the FM method as functions of interatomic separation: O–O (black), Si–O (red), and Si–Si (green). The dashed line corresponds to the model without the repulsive shoulder (FM-ns model). In panel (b) the dotted (FM-ws model) and dotted-dotted-dashed lines indicate the variation of the O–O repulsion in FM with block averaging along reference trajectories as discussed in the text. In panel (c) a comparison of the BKS (solid), Pedone (solid/circles), and FM (dashed) potentials is given. Due to the aphysical behavior of the BKS exp-6 at small interatomic separations, we modified the function to generate the BKS curve shown in this figure as follows: For $r < r_{infl}$, where r_{infl} is the position of the inflection point [$u''(r_{infl}) = 0$] on the repulsive wall of the original BKS exp-6 potential, the curve is described by an exponential function whose energy and energy first derivative are the same as the original BKS exp-6 function at r_{infl}. The vertical dashed line marks the location of the repulsive shoulder in the O–O FM potential.

to the ionicity of the oxygen atoms leading to softening of the O–O FM repulsion. However, such a potential is not expected to be well transferable to g-SiO_2 as the probability of VAP defects in amorphous silica is low. On the other hand, the FM potentials are realizations of a pairwise approximation to the many-body PES in the liquid state. Therefore, the FM potentials effectively incorporate higher order effects in the interaction. Consequently, the softer O–O repulsion may represent a cumulative average effect of changes in the local environment of oxygen pairs that are not affected by broken bonds. If such a mechanism significantly contributes to the

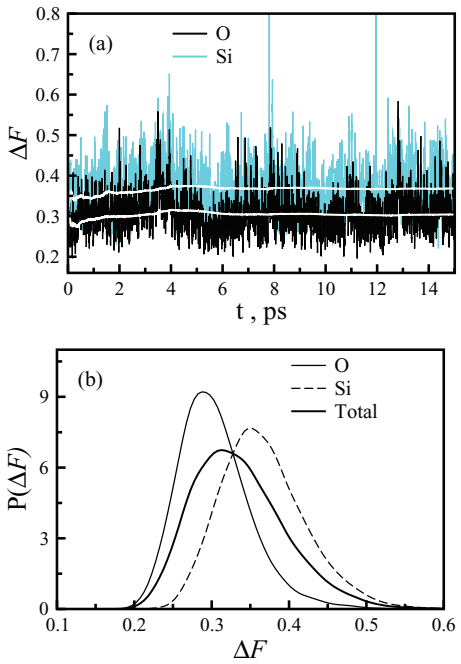

FIG. 2. Panel (a): Errors ΔF vs. time. Instant values of ΔF are shown for oxygen ions (black) and silicon ions (cyan). White lines show corresponding running time averages $\langle \Delta F \rangle_t$. Panel (b): Distributions of errors $P(\Delta F)$ for oxygen (solid/thin), silicon (dashed), and total (solid/thick).

shape of the O–O FM potential, then the FM model may be transferable to crystalline or amorphous states of silica under high pressures for which a largely preserved local bond order is characteristic.

The FM potential does not include explicitly Coulomb charges, however, it still effectively accounts for the entire spectrum of electrostatic interactions within the reference *ab initio* system. Similar to water,[49] the effective electrostatics is expected to decay rapidly in the liquid (and possibly amorphous) SiO_2 states. This conjecture is supported by the negligible FM forces at distances larger of 0.7 nm [Fig. 1(a)], leading to use only the short-ranged version of the FM model, although the FM algorithm allows explicit fitting of the effective Coulomb charges.[32,37] Crystalline polymorphs may pose difficulties for the short-ranged FM model due to the importance of Coulomb interactions in ionic crystals. Furthermore, it is worth noting that empirical top-down potentials for g-SiO_2 are often poorly transferable to crystalline states and vice versa.[17,18] The pairwise FM model was parameterized to a system which is characterized by a much higher level of disorder than that of the amorphous silica so that transferability to glassy systems could be in question. The potential might be even less transferable to silica crystalline states. However, in Sec. IV we demonstrate that the FM model performs remarkably well for an array of silica polymorphs. Since this bottom-up potential was derived solely from a liquid state ensemble, an adequate performance for crystalline states gives confidence that the FM model may still capture the essential physics for the less ordered g-SiO_2 systems.

As seen from Fig. 1(c) the FM O–O potential is significantly softer as compared to the BKS potential. The BKS

potential uses an exp-6 function for short-ranged interactions. The same conclusion holds for the potential by Pedone *et. al*.[23] (referred to as the Pedone model), which is very similar to the BKS model but more repulsive at short separations. In contrast to the BKS model, which is bottom-up, the Pedone potential was parameterized in a top-down fashion by fitting the sum of the Morse-12 and Coulomb terms to structural and elastic properties of g-SiO_2 at ambient conditions.

As one of the major purposes of our study is to assess the effects of the softer repulsive shoulder of the O–O potential on glass densification under cold and shock compression conditions, we compare these results with those using the FM potential without the repulsive shoulder. The latter potential, referred to as the FM-ns (no-shoulder) model, was obtained by simply removing the part of the original O-O FM force profile $f_{OO}(r)$ at $r < r_{shld} = 0.195$ nm, and smoothly replacing it with a profile of the $f_{OO}(r_{shld})\exp(a(r_{shld} - r))$ form with the parameter a determined from a least-squares fit of the $f_{OO}(r)$ within the interval $r_{shld} < r < r_{shld} + 1.0$ a.u. The FM-ns model is shown in Figs. 1(a) and 1(b) by the dashed line. We also introduce a FM potential with a "weak shoulder," referred to as the FM-ws potential [dotted line in Fig. 1(b)], to demonstrate the existing uncertainty within the repulsive shoulder potential due to the limited statistics of the AIMD simulation. Relatively poor sampling of short O–O separations within the limited length of the AIMD trajectories causes the repulsive shoulder region of the O–O potential to fluctuate significantly with the number of configurations used in the FM. The magnitude of the changes is outlined in Fig. 1(b) by the strongest and softest O-O shoulder repulsions observed during the FM block averaging procedure. The FM-ws model was obtained by using an initial shorter portion of the AIMD trajectories and corresponds to the *softest* shoulder repulsion as observed in the force-matching. Finally, the FM and FM-ns (and in some cases the FM-ws) models are compared with the Pedone model.

The reported simulations were performed using the DL_POLY 2.20 simulation package.[50] Some properties of the glass were calculated using ISAACS computer program.[51] The files with the silica FM, FM-ns, and FM-ws potentials are provided in the supplementary material;[66] these are in a tabulated form in the format of the DL_POLY 2.20 simulation package.

IV. TRANSFERABILITY OF THE FM MODEL TO SILICA POLYMORPHS

The structural and elastic properties of several silica crystalline polymorphs and glass by the FM model are compared to DFT-GGA calculations and experimental values in Table II. The FM properties were calculated at 4.5 K from MD simulations under isostress-isothermal (*NsT*) conditions

TABLE II. Structural parameters, *a, b, c, β* (length in nm and angle in deg), density ρ (kg/m^3), cohesive energy per SiO_2 E^c (eV), elastic constants C_{ij} (GPa), and bulk modulus B (GPa), for silica polymorphs.

	FM	DFT-GGA[a]	Expt.[b]
α-quartz:			
a, c	0.4968,0.5465	0.5027,0.5509	0.4916,0.5405
ρ, E^c, B	2553,−14.65,36.3	2483,−23.83,31.3	2646,−19.23,34-37
C_{11}, C_{12}, C_{13}	86.2,28.7,9.6	87.1,−7.8,6.3	85.9,7.2,10.9
C_{14}, C_{33}, C_{44}	−16.5,80.6,9.6	−17.0,87.1,49.1	−17.7,89.6,57.8
coesite(*C2/c*):			
a, b, c	0.7093,1.2592,0.7311	0.7242,1.2467,0.7233	0.7136,1.2369,0.7174
β	120.01	120.17	120.34
ρ, E^c, B	2828,−14.61,95.6	2828,−23.73,91.2	2915,...,96.0
α-cristobalite:			
a, c	0.5062,0.6939	0.5119,0.7168	0.4972,0.6922
ρ, E^c, B	2244,−14.46,10.6	2125,−23.86,9.4	2333,...,11.5
β-cristobalite(*Fd3m*):			
a	0.7483	0.7417	0.7131[c]
ρ, E^c, B	1830,−14.43,116.6	1956,−23.84,119.5	2201,...,...
β-tridymite($P6_3/mmc$):			
a, c	0.5360,0.8769	0.5248,0.8568	0.5052,0.8270
ρ, E^c, B	1826,−14.42,126.4	1952,−23.84,130.5	2198,...,...
stishovite:			
a, c	0.4208,0.2716	0.4239,0.2701	0.4179,0.2666
ρ, E^c, B	4149,−14.23, 371	4113,−23.19,261	4282,...,313
glass (FM-l, FM-h):			
ρ, E^c, B	2294,−14.28,23.2	2330,−23.65, 33[d]	2219–2231,...,38
ρ, E^c, B	2562,−14.36,29.5		

[a]Reference 16.
[b]References 63 and 64.
[c]Reference 64 (the $I\bar{4}2d$ setting).
[d]Reference 54.

using an anisotropic barostat in which the cell geometry is allowed to vary.[52] For quartz, the elastic matrix was obtained using the direct finite stress-strain method. The bulk moduli were calculated from a fit to $P-V$ data using the Murnaghan equation.[53]

We have used samples of amorphous silica of different densities. The first structure denoted as (FM-l) has a lower density, and was obtained following a protocol similar to that described in Ref. 23. A system of 1536 SiO_2 molecules at an initial density of 2100 kg/m^3 was cooled down from 5000 to 500 K at a constant rate by decreasing the temperature in 500 K increments; the trajectory integration was performed under constant *NVT* conditions using the Evans thermostat for $T > 1500$ K. At temperatures less than 1500 K, the trajectory integration was performed under constant *NsT* conditions with the rectangular cell shape being maintained. The total cooling time was 1.8 ns with a nominal cooling rate of 2.5×10^{12} K/s. The final (298 K) density of the sample was 2294.4 kg/m^3. This quenching algorithm uses schedules similar to those recommended in the literature to produce samples free of configurational defects.[23,54] The second structure (FM-h) was obtained using the following protocol: (1) the same system as in the previous case was equilibrated at 5000 K in the *NVT* ensemble using the Nosé-Hoover thermostat with a small (0.2 ps) relaxation time; (2) the target temperature was reset to 1000 K and the thermostat relaxation time was increased to 800 ps; (3) the simulation continued for 1.4 ns until the system temperature cooled to 1500 K. While the latter protocol has the same cooling rate as for the (FM-l) structure, the system abruptly exhibited solid-like behavior (i.e., discontinuous change in the diffusion coefficient) at about 1460 K. The density of the (FM-h) sample at 298 K was 2561.7 kg/m^3. Simulations were also performed using the Pedone potential to generate a sample of glass [referred to as the (P-l) structure]; the sample was prepared using the same protocol used to generate the (FM-l) structure. The ambient density of this sample was 2292.5 kg/m^3. Further simulations for this sample using the FM model resulted in an increase in density to 2331.8 kg/m^3. Figure 3 provides structural information of the three glass samples, including ring statistics [King's shortest path criterion[55]], $P(N^{ring})$, all-particle radial distribution function (RDF), $g(r)$, and running integration number, $N^{coor}_{Si-O}(r)$. Despite significant differences in density, the ring statistics and RDFs are nearly identical for the (FM-l) and (FM-h) samples. The $N^{coor}_{Si-O}(r)$ for the two samples exhibit differences at intermediate ($r > 0.3$ nm, second and third shells) distances.

Crystal lattice potentials using pairwise and central interactions result in additional symmetry relations for the elastic constants (the Cauchy relations) beyond those imposed by the crystal symmetry. For example, for a trigonal case, to which α-quartz belongs, there are six independent elastic constants C_{11}, C_{12}, C_{13}, C_{14}, C_{33}, and C_{44}, [C_{66} is given by $(C_{11} - C_{12})/2$]. The Cauchy relations are: $C_{12} = C_{66}$ and $C_{13} = C_{44}$. For α-quartz, the experimental Cauchy pressures $C_{12} - C_{66}$ and $C_{13} - C_{44}$ are nonzero, indicating deviation from a pairwise description of the crystal lattice interactions. A comparison of experimental values with a model having angle-bending (i.e., three-body) terms suggests that one-half of $C_{12} - C_{66}$ and one-third of $C_{13} - C_{44}$ Cauchy differences originate from angle-bending forces.[56] As seen from Table II for α-quartz, despite deviations from experiment caused by a zero Cauchy pressure, the bulk modulus is in good agreement with the experiment as well as with the DFT-GGA calculations. It is possible this reflects the fact that the contributions to bulk elasticity from angle-bending forces are relatively unimportant for α-quartz.

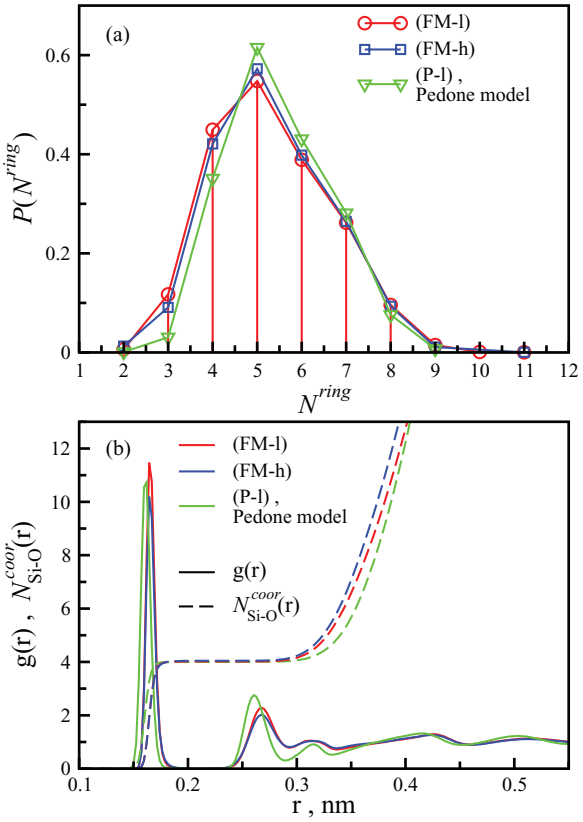

FIG. 3. King's ring size distribution [panel (a)] and all-particle RDF, $g(r)$, (solid) with corresponding running integration number, $N^{coor}_{Si-O}(r)$, (dashed) [panel (b)] for the (FM-l) (red), (FM-h) (blue) structures using the FM model and for the (P-l) structure using the Pedone model (green).

The absence of many-body terms in the FM models is manifested in the behavior of α-cristobalite and β-tridymite structures in *NsT* simulations in which angles between cell vectors are allowed to vary. In these simulations, these structures are unstable; however, if the cell vector angles are kept fixed (allowing only cell edges to vary independently), the structures become stable, and satisfactorily reproduce the lattice geometries and bulk moduli. For amorphous silica systems, regardless of density, the FM potential routinely yields a bulk modulus that is lower than the experimental value (38 GPa). The lack of bond-angle interactions is the most probable reason for the observed discrepancy. On the other hand, the Pedone model, which is also pairwise, predicts a bulk modulus of 37 for the (P-l) structure. The better prediction of bulk elasticity of glass given by the Pedone model is a result of the top-down parameterization scheme in which elastic properties were included in the training set. This

results in a more rigid potential at the ambient state [see Fig. 1(c)], which emulates a rigid glass network due to bond directionality. As discussed below, the introduction of rigidity into the potential in this manner improves its performance at low pressures but the performance deteriorates at higher pressure, a common problem of top-down models.

The cohesive energies for all polymorphs are consistently lower than those calculated using DFT-GGA. The major source of the differences is the absence of long-ranged Coulomb interaction in the FM models. Such an underestimation of cohesive energy might result in predictions of melting points for these systems that are too low. However, despite a lower value of cohesive energy, the FM potential adequately describes silica melting properties. Determination of melting for quartz is complicated by the fact that quartz undergoes phase transitions to β-tridymite and then to β-cristobalite with increasing temperature, with experiment reporting melting of the cristobalite at 1983 $\pm$ 10 K. It was also observed experimentally that the silica melt crystallizes directly into β-tridymite at 1943 $\pm$ 10 K at high cooling rates. We simulated the melting of bulk crystalline β-tridymite and β-cristobalite using the FM potential within the *NsT* ensemble. For β-tridymite the cell shape was fixed to prevent structural transformation (also as mentioned β-tridymite is stable only within the fixed cell shape ensemble). The translational melting temperature T determined using the rate of diffusion as a criterion was 2010 K for tridymite and 2050 K for cristobalite. The observed values are higher than the experimental counterparts, however, it is commonly known that in MD simulations, the bulk crystal structures should be superheated, sometime significantly, to initiate melting. On the other hand, in simulations using the FM potential to generate a glass sample using the second protocol, diffusion becomes abruptly solid-like at about 1460 K, close to the experimental value of 1450 K for the glass transition temperature for vitreous silica.[57]

V. GLASS UNDER PRESSURE

The simulations have been carried out at pressures 1, 2, 3, 5, 8.118, 10, 15.861, 20, 27, 35, 40, 45, 51, 59, 65, and 74 GPa for the (FM-l) and (FM-h) samples using the FM, FM-ns, FM-ws models and for the (P-l) sample using the Pedone model. The systems were simulated in the *NPT* ensemble at each pressure point at 298 K and the corresponding Hugoniot (Hg) temperature, $T_{\rm Hg}$. The latter condition corresponds to the material subjected to shock compression. The shock compression drives the material to a point on the Rankine-Hugoniot curve, $H_g(T_{\rm Hg}, V) = 0 = E - E_0 - (P + P_0)(V_0 - V)/2$, which is the locus of all final states characterized by the specific volume, internal energy, and pressure ($V = 1/\rho$, E, P) that can be accessed from an initial thermodynamic state ($V_0 = 1/\rho_0$, E_0, P_0) by shock loading. The Rankine-Hugoniot states were calculated using the adaptive Erpenbeck[58](AE-EOS) procedure as proposed by Brennan *et al.*[59] in which a succession of *NPT* simulations converges to the Hugoniot state for a given pressure. Each simulation consisted of a 400 ps equilibration period followed by a 200 ps production run. From each pressure point, a number of structural and thermodynamic properties were collected. In particular, the X-ray RDF was calculated in accordance with $g_{\rm X}(r) = \sum_{\alpha,\beta} c_\alpha b_\alpha c_\beta b_\beta g_{\alpha\beta}(r)/(\sum_\alpha c_\alpha b_\alpha)^2$, where $g_{\alpha\beta}(r)$ are particle partial RDFs and c_α and b_α are concentrations and scattering lengths for particles of type α, respectively. For this study, we used $b_{\rm Si,\,O} = 4, 8$.

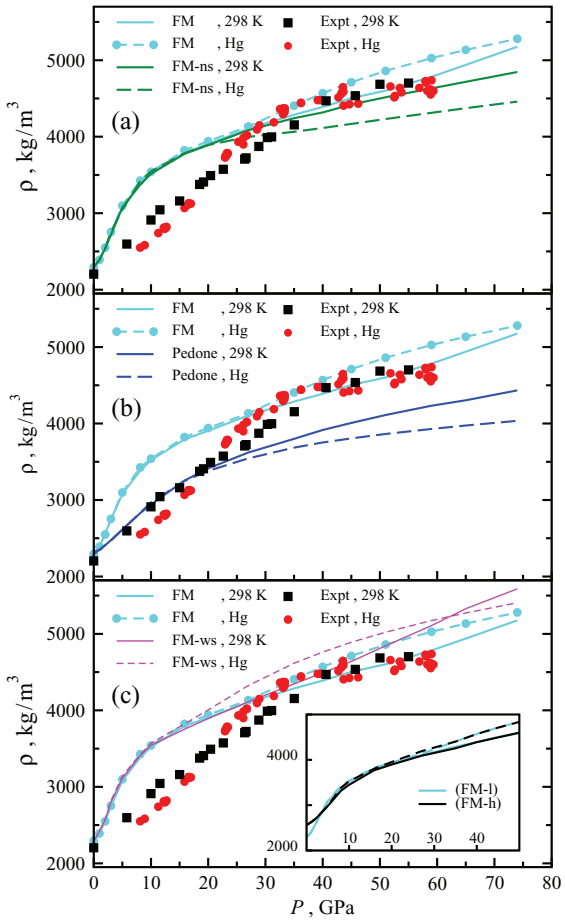

FIG. 4. Density vs. pressure at $T = 298$ K (solid lines) and along the Hugoniot locus (dashed lines) from simulations of (FM-l) structure using the FM (cyan), FM-ns (green) [panel (a)], Pedone (blue) [panel (b)], and FM-ws (magenta) [panel (c)] models. Simulations were carried out at the same pressure points (given in the text) as marked by filled circles on the cyan line. Experimental EOS obtained by cold compression (black squares) and by shock compression (red circles) is from Refs. 6 and 65, respectively. Inset to panel (c) compares the 298 K (solid) and Hugoniot (dashed) EOS from simulations of the (FM-l) (cyan) and (FM-h) (black) structures using the FM model.

Comparisons of density as a function of P from cold and shock compressions using different models, $\rho_{\rm cold}(P)$, $\rho_{\rm Hg}(P)$, respectively, to experimental values are provided in Figs. 4(a)–4(c). The Hg temperature curves, $T_{\rm Hg}(P)$, for several $\rho_{\rm Hg}(P)$ are given in Fig. 5. For the FM and FM-ns models [Fig. 4(a)], two stages of compression under both cold and shock compression can be clearly identified on a basis of the slope of the $\rho(P)$. In the low pressure region ($P < 8-10$ GPa), the glass is compressed with P at a faster rate than experiment and the system simulated using the Pedone model [Fig. 4(b)]. This behavior is consistent with the lower value of the bulk modulus for amorphous silica

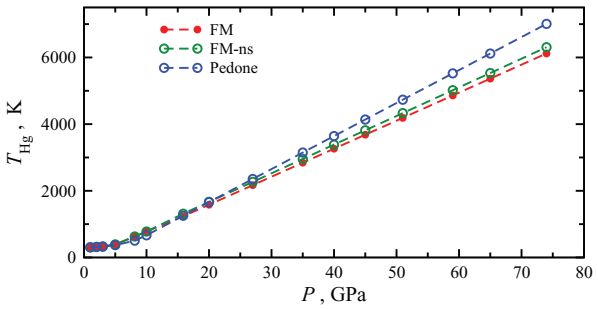

FIG. 5. Temperature along the Hugoniot locus, $T_{Hg}(P)$, simulated using the FM (red), FM-ns (green), and Pedone (blue) models at the same pressure points as in Fig. 4.

predicted by the FM models (see Table II). At pressures of about 8−10 GPa, both the $\rho_{cold}(P)$ and $\rho_{Hg}(P)$ curves show a significant decrease in the compressibility of the system. Also at these pressures for all models the $\rho_{cold}(P)$ and $\rho_{Hg}(P)$ start differing from one another. At $P < 20$ GPa, the FM $\rho_{cold,\,Hg}(P)$ are excessively compressed compared to the experimental values. Meanwhile, the Pedone model shows a relatively good agreement with experiment up to 20 GPa. The shape of the FM $\rho(P)$ at low pressures as well as the deviations from experiment and the Pedone model results are most likely due to the absence of potential terms describing effective interactions due to directionality of covalent bonding, which are at least three-body (e.g., angle-bending terms). As discussed above for the glass, the Pedone model effectively accounts for such interactions at conditions close to ambient due to the explicit fit of the model to the glass ambient elasticity. However, this same feature is probably the source of the failure of the top-down model in describing glass densification at higher pressures.

Importantly, at $P < 8-10$ GPa, the densification by the FM model occurs predominantly due to structure deformation and topological reorganization rather than a weakening of the O–O repulsion due to the soft-repulsive shoulder of the FM potential. This is evident in Fig. 6, for cold and shock compressions, in the appearance of O–O pairs in the $g_X(r)$ as a first major peak positioned within $r < 0.153$ nm, which, as will be shown later, originates from the $g_{OO}(r)$, and progressively grows with the pressure. For shock compression, the peak is well defined for loads up to 40 GPa and then smears out due to high T_{Hg} [see Figs. 6(b) and 5]. The FM $g_X(r)$ is in reasonable agreement with the X-ray data by Sato and Funamori.[7] The observed disagreement with the experiment at elevated pressures can be explained by the aforementioned deficiency of the FM model regarding angle-bending terms. The double-hump structure of the second peak in the FM $g_X(r)$ (centered at about 0.3 nm), which is due to O–O and Si–Si nearest-neighbors, is resolved in the experimental $g_X(r)$ only at pressures >20 GPa. At $P > 10$ GPa, the front slope of the first peak in the experimental $g_X(r)$ (presumably due to the Si–O nearest pairs) extends to 0.125 nm, leaving open the possibility it also encompasses the high-pressure O–O peak predicted by the FM model [$r < 0.153$ nm, Fig. 6(a)].

The pressure dependence of the average O–O coordination number N^{coor}_{O-O} corresponding to the first peak in

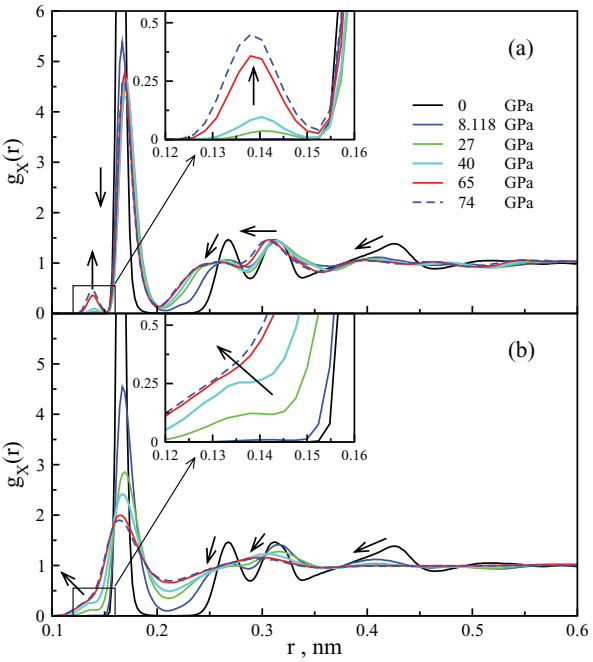

FIG. 6. Pressure dependence of $g_X(r)$ at $T = 298$ K [panel (a)] and along the Hugoniot locus [panel (b)] for the (FM-l) structure using the FM model. The inset is a magnification of the region of the first peak. Arrows show the direction of changes in peak positions with pressure.

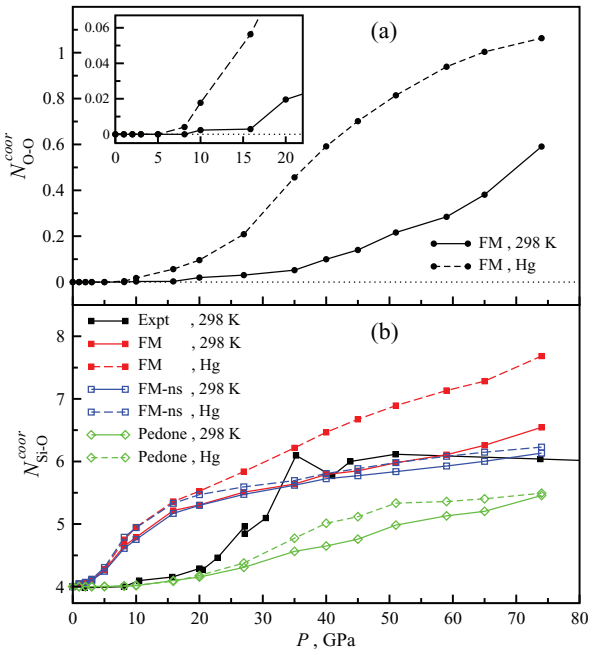

FIG. 7. Panel (a): $T = 298$ K (solid) and shocked (dashed) O–O coordination number within the shell $r < 0.153$ nm, $N^{coor}_{O-O}(P)$, for the (FM-l) structure using the FM model. The inset is an enlargement of the low pressure region. Panel (b): $T = 298$ K (solid) and shocked (dashed) Si–O coordination number, $N^{coor}_{Si-O}(P)$, from FM (red, filled squares), FM-ns (blue, empty squares), and Pedone (green, empty diamonds) models. Experimental cold compression data obtained by X-ray adsorption measurements (black, filled squares) are from Refs. 7 and 9.

the $g_{OO}(r)$ [or equally $g_X(r)$] is displayed in Fig. 7(a). The coordination number is defined as $N^{coor}_{\alpha-\beta} = 4\pi N_\beta \int_0^{r[g_{min}]} g_{\alpha\beta}(r) r^2 dr$, where $r[g_{min}]$ is a position of the first minimum in $g_{\alpha\beta}(r)$ and N_β is total number of particles of type β in the system. Below 8–10 GPa, O–O pairs do not exist under either cold or shock compression, affirming that the structural changes at these pressures are not affected by the O–O repulsive shoulder. There is a marked increase in the number of O–O pairs within the 15–20 GPa pressure range. Notably, in this pressure range, the slopes of the FM $\rho(P)$ curves decrease relatively to those at lower pressures, and the differences in the $\rho_{cold}(P)$ and $\rho_{Hg}(P)$ become larger with pressure.

Furthermore, the appearance of oxygen pairs correlates with the creation of fivefold and sixfold coordination defects, the probability of which is quantified by the N^{coor}_{Si-O} [Fig. 7(b)]. The shape of the FM $N^{coor}_{Si-O}(P)$ curve resembles that of the corresponding $\rho(P)$ in Fig. 4(a). At $P > 40$ GPa, the cold FM $N^{coor}_{Si-O}(P)$ indicates a transition to sixfold coordination [$N^{coor}_{Si-O}(40\ GPa) = 5.8$ and slowly increases to 6 within 40–50 GPa interval] that is in good agreement with the recent experimental data by Sato and Funamori[7] and Benmore *et al.*[9] At lower pressures ($P < 10-20$ GPa), the FM $N^{coor}_{Si-O}(P)$ overestimates the experimental value as well as the value from the Pedone model. The origin of this disagreement is the same as that for the $\rho(P)$ data in Fig. 4(a), namely, the absence of angle-bending forces in the FM model. However, Fig. 7(b) shows that at $P = 10$ GPa, the FM $N^{coor}_{Si-O}(P)$ is fairly close to 5 (e.g., 4.8 and 4.95 for the ambient and Hg EOS, respectively) and remains below 5.5 up to ~30 GPa. This behavior is consistent with the suggestions made in the literature that the presence of five-fold coordinated states is responsible for the minimum glass yield strength experimentally observed at about 10 GPa.[3] Also, the Pedone model severely underestimates $N^{coor}_{Si-O}(P)$ at the high pressures ($P > 20$ GPa), similar to the underestimation of $\rho(P)$ at the same pressures and for the same reasons. On the other hand, as seen from comparison of $\rho(P)$ by the FM and FM-ws models shown in Fig. 4(c), quantitatively, the high pressure behavior of the FM model is fairly sensitive to the quality of force-matching of the repulsive shoulder.

An examination of the pressure-induced changes in the $g_X(r)$ (Fig. 6) and in the bond-angle probability distributions for the O–Si–O and Si–O–Si angles (Fig. 8) for the FM model reveals that both intermediate-range pairwise and three-body structures exhibit dramatic changes at $P < 8.0$ GPa, while at higher pressures the changes are relatively mild. This observation supports our early conclusion that densification in the low pressure region is driven mostly by shape and topology changes of the network glass as opposite to $P > 10$ GPa, at which densification is mostly due to the O–O interactions through the repulsive shoulder portion of the FM potential. It is important to note that the Pedone model qualitatively follows overall evolution of the FM bond-angle probability distributions [Figs. 8(b) and 8(d)], but the changes are shifted to higher pressures. For example, the $P(\angle O - Si - O)$ at 8.118 GPa for the Pedone model is very close to that of the FM model at 0 GPa, whereas the curve for 40 GPa resem-

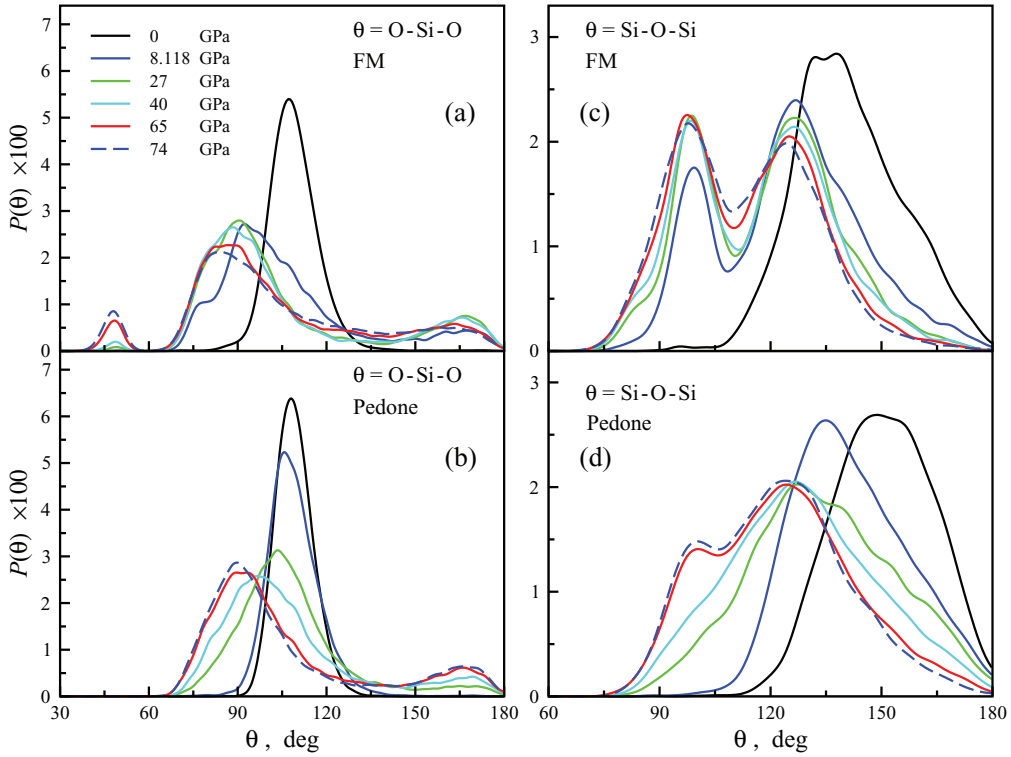

FIG. 8. Comparison of the probability density distributions of O–Si–O angles at $T = 298$ K and different pressures by the FM model for the (FM-l) structure [panel (a)] and the Pedone model for structure (P-l) [panel (b)]. The panels (c) and (d) show similar comparison for Si–O–Si angle distributions.

bles that of the FM model at 27 GPa. The $P(\angle \mathrm{Si}-\mathrm{O}-\mathrm{Si})$ from the Pedone model adopts the characteristic double-hump profile only at 65 GPa, while this feature is already well pronounced at 8.118 GPa for the FM model. These observations lend further support to our earlier discussion that the pairwise interactions of the Pedone model are excessively rigid emulating the presence of angle-bending forces. These observations highlight the drawbacks of the top-down parameterization approaches, which may significantly limit the model transferability across different thermodynamic conditions due to disproportionate incorporation of many-body effects into the model interactions in an attempt to match the target macroscopic properties that rely on such effects. Although the transferability issues also apply to bottom-up models too, condensed-phase PESs used to fit bottom-up models are typically less sensitive to changes in thermodynamic state as compared to microscopic properties. Accordingly, such models may perform more evenly across different thermodynamic conditions compared to top-down models.

At $P = 0$ GPa the average values of $\angle \mathrm{Si}-\mathrm{O}-\mathrm{Si}$ and $\angle \mathrm{O}-\mathrm{Si}-\mathrm{O}$ angles (standard deviation shown in parentheses) are, respectively, 141.1°(14.2°), 109.0°(8.1°) for the FM model and 150.3°(12.3°),109.2°(6.3°) for the Pedone model. For samples prepared using the BKS potential that were approximately twice as small as that of the FM sample, the DFT-GGA calculations[54] yield $\angle \mathrm{Si}-\mathrm{O}-\mathrm{Si} = 147.8°(14.3°)$ and $\angle \mathrm{O}-\mathrm{Si}-\mathrm{O} = 109.3°(7.3°)$. However, with an increase of sample size the average DFT-GGA angles tend to decrease while the distribution becomes broader.[54] The $\angle \mathrm{O}-\mathrm{Si}-\mathrm{O}$ Pedone distribution is more narrow, reflecting highly directional bonds that make up the silicon tetrahedra. Meanwhile, the FM model results and, in particular, the directionality of the $\mathrm{Si}-\mathrm{O}$ bonds, are in fairly good agreement with the *ab initio* calculations, taking into consideration the aforementioned system size dependence. At $P > 8-10$ GPa, the $P(\angle \mathrm{O}-\mathrm{Si}-\mathrm{O})$ distribution from the FM model shows a pressure-induced peak centered at 48°–49°. The peak is a manifestation of the paired oxygen atoms interacting through the soft-repulsive shoulder, and has the same origin as the first peak in the $g_{\mathrm{X}}(r)$ [or equally $g_{\mathrm{OO}}(r)$] (see Figs. 6(a) and 9).

The aforementioned results correspond to the (FM-l) structure, however, identical trends are observed for the (FM-h) structure. As evident in the inset in Fig. 4(c), the only difference between the $\rho(P)$ for (FM-l) and (FM-h) structures is observed in the $P < 8-10$ GPa region. Within this pressure range, the repulsive shoulder of the O–O FM potential is not accessed, and pressure-induced structural changes between the (FM-l) and (FM-h) samples are similar to those observed under low pressure. One possible mechanism for compression in the low pressure region ($P < 8-10$ GPa) is the increased number of Si–O–Si plane-normal reversals[17,60] that are not accompanied by rebonding. In such a scenario, the ring statistics remain unchanged. The statistics of Si–O–Si plane-normal reversals for the (FM-l) and (FM-h) samples are likely a source of the pressure-dependent differences in density, as the ring statistics are only slightly different between the two structures [see Fig. 3(a)]. Thus, it is possible that the compression of the FM samples could occur through such a mechanism at $P < 8$ GPa.

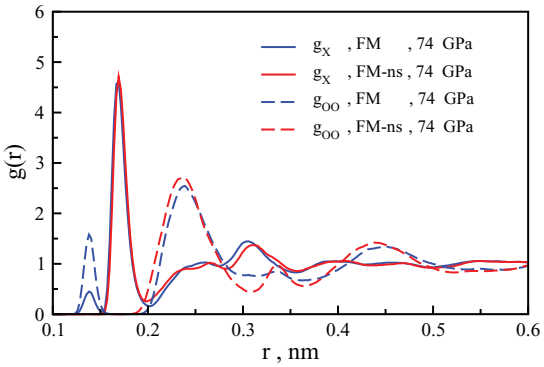

FIG. 9. $g_{\mathrm{X}}(r)$ (solid) and $g_{\mathrm{OO}}(r)$ (dashed) from $T = 298$ K simulations at $P = 74$ GPa for the (FM-l) structure using FM (blue) and FM-ns (red) models.

Comparison of the $g_{\mathrm{X}}(r)$ and $g_{\mathrm{OO}}(r)$ for samples simulated with the FM and FM-ns models at 298 K, 74 GPa (Fig. 9) reveals the effect of the soft-repulsive shoulder in the O–O FM potential on the intermediate-range order. For instance, the FM-ns $g_{\mathrm{OO}}(r)$ has more structure beyond a first coordination shell than the FM model, thus, reflecting a higher ordering of the oxygen sublattice exhibited in the structure in the second and third shells of the $g_{\mathrm{X}}(r)$ (i.e., intermediate range) as compared to the RDFs by the FM model. As seen, the lack of proper treatment of short-ranged O–O interactions in dense states excessively stabilizes the intermediate-range order; this, in turn, may affect the degree and reversibility of densification. A similar comparison holds for other $P > 20$ GPa.

Comparison of cold and Hg $\rho(P)$ curves from the FM model to those simulated with the FM-ns and Pedone models (Fig. 4) shows a remarkable feature: the shocked FM system at $P > 15$ GPa is more compressed than the same system subjected to cold compression, while both FM-ns and Pedone models show an opposite trend, i.e., the shocked system is less compressed. The trend demonstrated by the FM model is consistent with that of the experimental results, namely, the experimental $\rho_{\mathrm{Hg}}(P)$ is more compressed versus $\rho_{\mathrm{cold}}(P)$ in the pressure range of $20-40$ GPa. Because the temperatures of the shocked system are higher than those corresponding to cold compression (see Fig. 5), such a behavior suggests the existence of multiple states separated by activation barriers in the glass PES by the FM model that are not predicted by the FM-ns and Pedone models. The gradual appearance of the well-defined peak in the $g_{\mathrm{X}}(r)$ at 0.15 nm [Figs. 6(a) and 9] in the compressed FM system due to paired oxygens is indicative of the metastable states in the PES. The origin of such minima could be elucidated by comparing cold and Hg near-range order within the oxygens subsystem from the FM model with that of the models without O–O soft-core repulsion (FM-ns and Pedone models). In particular, the cold and Hg $N^{coor}_{\mathrm{O-O}}(P)$, $N^{coor}_{\mathrm{Si-O}}(P)$ curves differ only for the FM model [see Fig. 7] pointing to a higher probability of formation of oxygen complexes interacting through the repulsive shoulder under higher temperature conditions of shocked system. On the other hand, the observed correlation in the value of pressure at which $\rho_{\mathrm{cold}}(P)$ and $\rho_{\mathrm{Hg}}(P)$ start deviating and

paired oxygens appear [see Figs. 4(a) and 7(a)] suggests that the higher compressibility of the FM system under shock is likely caused by the oxygen complexation due to the soft-core repulsion. Therefore, the presence of multiple states in the glass PES could be associated with the presence of the soft-repulsive O–O FM shoulder.

Conclusively, we can speculate that for the FM model the strong repulsion between oxygens (of 416 kJ/mol), which precedes the weaker shoulder repulsion [see Fig. 1(b)], may contribute to a buildup of the barrier in the PES between the metastable (lda and hda) states at low pressures (below 8–10 GPa at room temperatures). The barrier gradually diminishes within the studied 10–75 GPa pressure interval, thus contributing to anomalous densification. This is particularly evident from the gradual appearance of the first O–O peak in the FM $g_X(r)$ under compression, which indicates that the corresponding (hda) minima in the FM PES become more accessible by the glass configurations. Under cold compression, the hda local minimum continues to exist in all studied range of compression above 8 GPa up to 74 GPa. Such scenario has been widely discussed in the literature. In particular, it was speculated that after disappearance of the barrier the system becomes mechanically unstable leading to spinodal decomposition,[12,13] in which the lda energy minimum vanishes. Furthermore, the pressure-induced amorphous-amorphous phase transition has been established in model mono-component systems with interactions described by a repulsive-step potential that are linked to particle penetration to the region of short interparticle separations in which the interaction is due to the soft-repulsive shoulder of the potential.[47] This scenario is fully analogous to the formation of closed packed oxygen structures in g-SiO_2 due to the repulsive shoulder accessed under high pressures.

On the other hand, the presence of a first-order liquid-liquid phase transition has been reported for the BKS model of g-SiO_2 (Ref. 61) at temperature T_c higher than the glass transition temperature T_g. The BKS O–O interaction does not have a repulsive shoulder [Fig. 1(c)] and the mechanism of the phase transition was rather related to the tetrahedral liquid structure and believed to be of the same origin as in supercooled water. It was then proposed that the polymorphs in real g-SiO_2 are sub-T_g manifestations of a liquid-liquid instability as for real g-SiO_2 $T_c < T_g$. It is possible that a similar mechanism could be invoked for the FM model and will be the subject of our future studies.

Decompression simulation experiments for the (FM-l) structure are summarized in Fig. 10. In these simulations, the samples are compressed to the various pressures along the abscissa through cold and shock compression (open circles and squares, respectively). The samples are then decompressed by resetting the imposed pressures in the *NPT* simulations to zero, and integrating the equations of motion until the results have converged. For all $P \geq 10$ GPa, the residual densification of the decompressed samples are similar and about 25% larger than the ambient value. For both cold and shock compressed structures, decompression with the FM-ns model results in 2%–5% less dense systems compared to those produced with the FM model. The shock-compressed structures

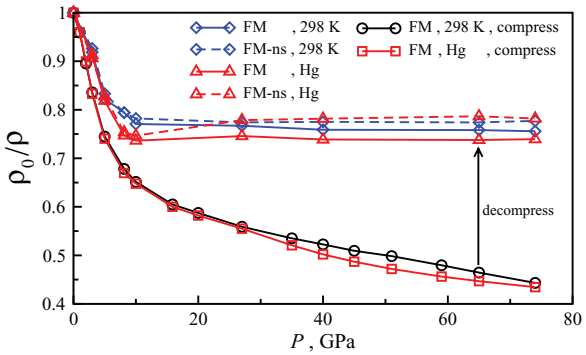

FIG. 10. Compression ρ_0/ρ, where ρ_0 is ambient density vs. pressure curves for the (FM-l) structure decompressed using FM (solid) and FM-ns (dashed) models, which was previously compressed with the FM model under cold (diamonds, blue) and shock (red, triangles) conditions. Densities in samples compressed under cold (solid black, empty circles) and shock (solid red, empty squares) conditions are shown for a comparison.

exhibit a slightly higher (about 3%–4%) magnitude of permanent densification versus the ones subjected to cold compression. Figure 11 shows the $g_X(r)$ for decompressed structures resulting from compression at various pressures, and are compared with the $g_X(r)$ of structures at 0 and 74 GPa. As seen from Fig. 11(a), upon decompression, the intermediate-range pairwise structure reverts to that seen in the samples compressed at $P = 8-10$ GPa. Meanwhile, the $g_X(r)$ at 0 and 8.118 GPa differ substantially (see also Fig. 6). Importantly, in all decompressed structures using the FM models, the $N^{coor}_{Si-O}(P)$ is fairly close to 5. The presence of fivefold coordinated states has been observed in silica glasses and crystals quenched from high pressure.[62]

Interestingly, the decompression simulations show that irreversible densification events occur at $P < 8-10$ GPa, a pressure regime in which oxygen ion complexation due to the O–O soft-repulsive shoulder potential is virtually absent, and is entirely due to a change in intermediate-range order as clearly seen from Fig. 11(a). In this pressure region, the residual density upon decompression is determined solely by a restructuring of the network topology. This observation is evidenced by the experiment,[6] which also suggests that the g-SiO_2 behaves as a single amorphous polymorph as these pressures. Furthermore, experimentally the irreversible densification continues at further pressure increases up to 45 GPa, but the interpretation of X-ray data[6,7] indicates that irreversible changes in short-range order start contributing to this process at $P > 25$ GPa. The simulations with the FM model reveals a significant increase of oxygen pairs at distances smaller than the position of major peak in the $g_{OO}(r)$ at these pressures that occurs due to penetration of the oxygens into the region of the soft shoulder interaction. Although in the FM simulations upon decompression the glass nearly completely reverses to a decompressed state at 8–10 GPa, in real silica near-range structural changes as induced by oxygen complexation could be stabilized due to many-body interaction effects. Such many-body effects may not be fully captured by the FM model but strongly affect the behavior of the material at high

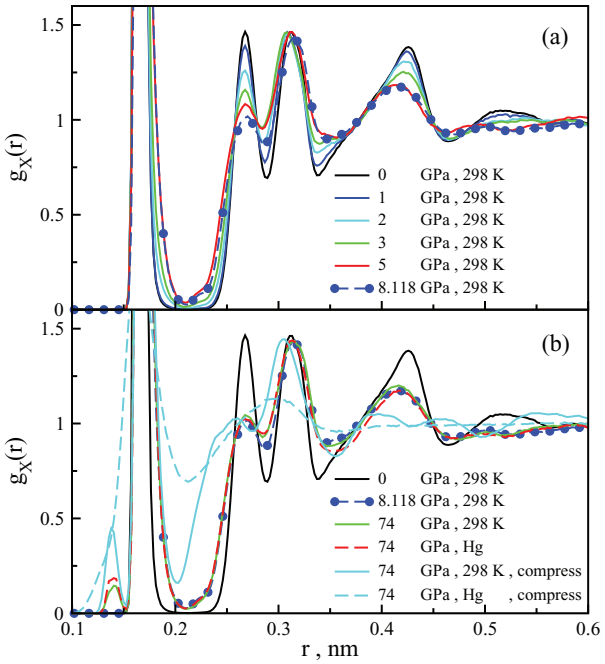

FIG. 11. $g_X(r)$ for the decompressed (FM-l) sample from selected simulations using the FM model from Fig. 10. Panel (a): For samples compressed at pressures 1, 2, 3, 5, and 8.118 GPa under cold conditions. Panel (b): For samples compressed at pressure 74 GPa under cold (solid green) and shock (dashed red) conditions. The cyan lines show the original $g_X(r)$ in the sample compressed at 74 GPa under cold (solid cyan) and shock (dashed cyan) conditions. In both panels the ambient structure is shown by the black solid line.

pressures. This conjecture gains some support from observed remnants of oxygen complexation in samples decompressed at 75 GPa [see Fig. 11(b)].

Conclusively, at higher pressures (20–40 GPa), the modification of interactions within the O–O sublattice could be a major channel for anomalous densification. Also, inclusion of more elaborate terms with the explicit semiempirical treatment of electronic structure to describe more realistically the modification of interactions within oxygen sublattice may lead to further improvements when developing the FM model.[38]

VI. CONCLUSIONS

We have created a new numerical potential for silica from *ab initio* microscopic interaction data obtained from a high temperature liquid phase at a single thermodynamic point. The new potential is of a pairwise central form with cutoff of about 7 Å and has been parameterized to match the total force distribution along *ab initio* trajectories for the system. Within this parameterization, there is no reliance on macroscopic data; thus, this effort demonstrates systematic coarse-graining of *ab initio* electronic structural information. We have demonstrated that despite being matched to a highly disordered silica melt and not including long-ranged electrostatic interactions, the new potential exhibits good transferability to silica crystalline and amorphous polymorphs. The observed deficiencies in the potential are likely related to the absence of angle-bending terms needed to treat the directionality of covalent bonding. The numerical potential between oxygen ions has a soft-repulsive shoulder at short-separations. This sort of interaction is not present in the existing silica models, which are largely based on predetermined analytical forms. The origin of the soft-repulsive shoulder is an averaged effect reflecting changes in the electronic structure of oxygen ion complexes in various bonding environments encountered in the reference high temperature melt simulations of silica; these are effectively captured by our force-matching approach. The soft-repulsive shoulder feature of the O–O interaction potential affects the glass structure under pressures above 10 GPa in a fashion different from models that do not have this feature. We demonstrate that this feature leads to additional complexity, and in particular the existence of a new metastable high density state in the potential energy surface of the silica glass that is not present in the other models we examined. Additionally, in contrast to existing pairwise potentials lacking this soft-repulsive shoulder, the new potential is able to predict a higher compression under shock load above 10–20 GPa as compared to cold compression in agreement with experiment, therefore, capturing an activation character of transition to high density state due to oxygen complexation. Thus, we have presented evidence that properties of interactions within oxygen sublattice of silica glass is very important to describe glass polymorphism.

ACKNOWLEDGMENTS

The authors wish to thank Dr. George Gazonas, Dr. Iskander Batyrev, and Dr. Scott Weingarten for helpful comments. This research was supported by the DoD High Performance Computing Modernization Program Software Application Institute for Multi-scale Reactive Modeling of Insensitive Munitions and the ARL Director under the Director's Strategic Initiative program "Multi-scale Modeling of Non-Crystalline Ceramics (Glass)." Computing support was provided by the DoD Supercomputer Resource Center located at the Army Research Laboratory.

[1]P. W. Bridgman and I. Simon, J. Appl. Phys. **24**(4), 405 (1953); E. B. Christiansen, S. S. Kistler, and W. B. Gogarty, J. Am. Ceram. Soc. **45**(4), 172 (1962); P. McMillan, B. Piriou, and R. Couty, J. Chem. Phys. **81**(10), 4234 (1984); M. Grimsditch, Phys. Rev. B **34**(6), 4372 (1986); A. Polian and M. Grimsditch, *ibid.* **41**(9), 6086 (1990); S. Susman, K. J. Volin, D. L. Price, M. Grimsditch, J. P. Rino, R. K. Kalia, P. Vashishta, G. Gwanmesia, Y. Wang, and R. C. Liebermann, *ibid.* **43**(1), 1194 (1991); C.-S. Zha, R. J. Hemley, H.-K. Mao, T. S. Duffy, and C. Meade, *ibid.* **50**(18), 13105 (1994); O. B. Tsiok, V. V. Brazhkin, A. G. Lyapin, and L. G. Khvostantsev, Phys. Rev. Lett. **80**(5), 999 (1998); S. N. Tkachev, M. H. Manghnani, and Q. Williams, *ibid.* **95**(5), 057402 (2005); B. Champagnon, C. Martinet, C. Coussa, and T. Deschamps, J. Non-Cryst. Solids **353**(44-46), 4208 (2007); D. Vandembroucq, T. Deschamps, C. Coussa, A. Perriot, E. Barthel, B. Champagnon, and C. Martinet, J. Phys.: Condens. Matter **20**(48), 485221 (2008); T. Rouxel, H. Ji, T. Hammouda, and A. Moreac, Phys. Rev. Lett. **100**(22), 225501 (2008); H. Fukui, M. Kanzaki, N. Hiraoka, and Y. Q. Cai, Phys. Rev. B **78**(1), 012203 (2008); T. Rouxel, H. Ji, J. P. Guin, F. Augereau, and B. Ruffle, J. Appl. Phys. **107**(9), 094903 (2010); B. Hehlen, J. Phys.: Condens. Matter **22**(2), 025401 (2010).
[2]M. Grimsditch, Phys. Rev. Lett. **52**(26), 2379 (1984).
[3]C. Meade and R. Jeanloz, Science **241**(4869), 1072 (1988).
[4]C. Meade, R. J. Hemley, and H. K. Mao, Phys. Rev. Lett. **69**(9), 1387 (1992).

[5]Y. Inamura, Y. Katayama, W. Utsumi, and K.-I. Funakoshi, Phys. Rev. Lett. **93**(1), 015501 (2004).
[6]T. Sato and N. Funamori, Phys. Rev. Lett. **101**(25), 255502 (2008).
[7]T. Sato and N. Funamori, Phys. Rev. B **82**(18), 184102 (2010).
[8]M. Murakami and J. D. Bass, Phys. Rev. Lett. **104**(2), 025504 (2010).
[9]C. J. Benmore, E. Soignard, S. A. Amin, M. Guthrie, S. D. Shastri, P. L. Lee, and J. L. Yarger, Phys. Rev. B **81**(5), 054105 (2010).
[10]K. Trachenko and M. T. Dove, Phys. Rev. B **67**(21), 212203 (2003).
[11]R. J. Hemley, H. K. Mao, P. M. Bell, and B. O. Mysen, Phys. Rev. Lett. **57**(6), 747 (1986); Q. Williams and R. Jeanloz, Science **239**(4842), 902 (1988).
[12]D. J. Lacks, Phys. Rev. Lett. **84**(20), 4629 (2000).
[13]D. J. Lacks, Phys. Rev. Lett. **80**(24), 5385 (1998); G. D. Mukherjee, S. N. Vaidya, and V. Sugandhi, *ibid.* **87**(19), 195501 (2001).
[14]V. G. Karpov and M. Grimsditch, Phys. Rev. B **48**(10), 6941 (1993); N. S. O. Ekunwe and D. J. Lacks, *ibid.* **66**(21), 212101 (2002).
[15]E. M. Stolper and T. J. Ahrens, Geophys. Res. Lett. **14**(12), 1231, doi:10.1029/GL014i012p01231 (1987).
[16]T. Demuth, Y. Jeanvoine, J. Hafner, and J. G. Angyan, J. Phys.: Condens. Matter **11**(19), 3833 (1999).
[17]L. Huang and J. Kieffer, Phys. Rev. B **69**(22), 224203 (2004).
[18]B. P. Feuston and S. H. Garofalini, J. Chem. Phys. **89**(9), 5818 (1988).
[19]B. W. H. van Beest, G. J. Kramer, and R. A. van Santen, Phys. Rev. Lett. **64**(16), 1955 (1990).
[20]P. Vashishta, R. K. Kalia, J. P. Rino, and I. Ebbsjo, Phys. Rev. B **41**(17), 12197 (1990).
[21]G. J. Kramer, N. P. Farragher, B. W. H. van Beest, and R. A. van Santen, Phys. Rev. B **43**(6), 5068 (1991).
[22]P. Tangney and S. Scandolo, J. Chem. Phys. **117**(19), 8898 (2002); J. R. Kermode, S. Cereda, P. Tangney, and A. D. Vita, *ibid.* **133**(9), 094102 (2010).
[23]A. Pedone, G. Malavasi, M. C. Menziani, A. N. Cormack, and U. Segre, J. Phys. Chem. B **110**(24), 11780 (2006).
[24]A. Takada and A. N. Cormack, Phys. Chem. Glasses **49**(3), 127 (2008).
[25]T.-R. Shan, B. D. Devine, J. M. Hawkins, A. Asthagiri, S. R. Phillpot, and S. B. Sinnott, Phys. Rev. B **82**(23), 235302 (2010).
[26]S. Tsuneyuki, M. Tsukada, H. Aoki, and Y. Matsui, Phys. Rev. Lett. **61**(7), 869 (1988).
[27]L. Elcoro and J. Etxebarria, Eur. J. Phys. **32**(1), 25 (2011).
[28]M. J. Sanders, M. Leslie, and C. R. A. Catlow, J. Chem. Soc.-Chem. Commun. **1984**(19), 1271.
[29]Y. Tu, J. Tersoff, G. Grinstein, and D. Vanderbilt, Phys. Rev. Lett. **81**(22), 4899 (1998).
[30]S. R. Billeter, A. Curioni, D. Fischer, and W. Andreoni, Phys. Rev. B **73**(15), 155329 (2006).
[31]J. Yu, S. B. Sinnott, and S. R. Phillpot, Phys. Rev. B **75**(8), 085311 (2007).
[32]S. Izvekov, M. Parrinello, C. J. Burnham, and G. A. Voth, J. Chem. Phys. **120**(23), 10896 (2004).
[33]S. Izvekov and G. A. Voth, J. Phys. Chem. B **109**(7), 2469 (2005).
[34]S. Izvekov and G. A. Voth, J. Chem. Phys. **123**(13), 134105 (2005).
[35]S. Izvekov and G. A. Voth, J. Phys. Chem. B **109**(14), 6573 (2005).
[36]W. G. Noid, G. S. Ayton, S. Izvekov, and G. A. Voth, in *Coarse-Graining of Condensed Phase and Biomolecular Systems*, edited by G. A. Voth (Taylor and Francis, Boca Raton, 2008), pp. 21; L. Larini, L. Y. Lu, and G. A. Voth, J. Chem. Phys. **132**(16), 164107 (2010); W. G. Noid, J. W. Chu, G. S. Ayton, V. Krishna, S. Izvekov, G. A. Voth, A. Das, and H. C. Andersen, *ibid.* **128**(24), 244114 (2008); W. G. Noid, P. Liu, Y. Wang, J. W. Chu, G. S. Ayton, S. Izvekov, H. C. Andersen, and G. A. Voth, *ibid.* **128**(24), 244115 (2008); A. Das and H. C. Andersen, *ibid.* **131**(3), 034102 (2009); V. Krishna, W. G. Noid, and G. A. Voth, *ibid.* **131**(2), 024103 (2009); S. Izvekov, P. W. Chung, and B. M. Rice, *ibid.* **133**(6), 064109 (2010).
[37]S. Izvekov and J. M. J. Swanson, J. Chem. Phys. **134**(19), 194109 (2011).
[38]S. Iuchi, S. Izvekov, and G. A. Voth, J. Chem. Phys. **126**(12), 124505 (2007).
[39]C. Knight, C. M. Maupin, S. Izvekov, and G. A. Voth, J. Chem. Theory Comput. **6**(10), 3223 (2010).
[40]M. R. Farrow and M. I. J. Probert, J. Chem. Phys. **135**(4), 044508 (2011).
[41]A. D. Becke, Phys. Rev. A **38**(6), 3098 (1988); C. Lee, W. Yang, and R. G. Parr, Phys. Rev. B **37**(2), 785 (1988).
[42]N. Troullier and J. L. Martins, Phys. Rev. B **43**(3), 1993 (1991).
[43]L. Kleinman and D. M. Bylander, Phys. Rev. Lett. **48**(20), 1425 (1982).
[44]J. Hutter, P. Ballone, M. Bernasconi, P. Focher, E. Fois, S. G. D. Marx, M. Parrinello, and M. Tuckerman, CPMD, version 3.13, Copyright IBM Corp 1990–2001, Copyright MPI fur Festkorperforschung Stuttgart 1997–2001, 2007; D. Marx and J. Hutter, *Ab Initio Molecular Dynamics: Basic Theory and Advanced Methods* (Cambridge University Press, Cambridge, England, 2009).
[45]P. Tangney, J. Chem. Phys. **124**(4), 044111 (2006).
[46]G. Stell and P. C. Hemmer, J. Chem. Phys. **56**(9), 4274 (1972).
[47]Y. D. Fomin, N. V. Gribova, V. N. Ryzhov, S. M. Stishov, and D. Frenkel, J. Chem. Phys. **129**(6), 064512 (2008).
[48]L. Martin-Samos, Y. Limoge, and G. Roma, Phys. Rev. B **76**(10), 104203 (2007).
[49]S. Izvekov, J. M. J. Swanson, and G. A. Voth, J. Phys. Chem. B **112**(15), 4711 (2008).
[50]W. Smith and T. R. Forester, J. Mol. Graphics **14**(3), 136 (1996); W. Smith, C. W. Yong, and P. M. Rodger, Mol. Simulat. **28**(5), 385 (2002).
[51]S. Le Roux and V. Petkov, J. Appl. Crystallogr. **43**(1), 181 (2010).
[52]S. Melchionna, G. Ciccotti, and B. L. Holian, Mol. Phys. **78**(3), 533 (1993).
[53]F. D. Murnaghan, Proc. Natl. Acad. Sci. U.S.A. **30**(9), 244 (1944).
[54]R. M. Van Ginhoven, H. Jónsson, and L. R. Corrales, Phys. Rev. B **71**(2), 024208 (2005).
[55]D. S. Franzblau, Phys. Rev. B **44**(10), 4925 (1991).
[56]M. E. Striefler and G. R. Barsch, Phys. Rev. B **12**(10), 4553 (1975).
[57]R. Brückner, J. Non-Cryst. Solids **5**(2), 123 (1970).
[58]J. J. Erpenbeck, Phys. Rev. A **46**(10), 6406 (1992).
[59]J. K. Brennan and B. M. Rice, Mol. Phys. **101**(22), 3309 (2003).
[60]Y. Liang, C. R. Miranda, and S. Scandolo, Phys. Rev. Lett. **99**(21), 215504 (2007).
[61]I. Saika-Voivod, F. Sciortino, and P. H. Poole, Phys. Rev. E **63**(1), 011202 (2000).
[62]J. F. Stebbins, Nature (London) **351**(6328), 638 (1991).
[63]L. Levien, C. T. Prewitt, and D. J. Weidner, Am. Mineral. **65**(9–10), 920 (1980); E. Gregoryanz, R. J. Hemley, H.-K. Mao, and P. Gillet, Phys. Rev. Lett. **84**(14), 3117 (2000); L. Levien and C. T. Prewitt, Am. Mineral. **66**(3–4), 324 (1981); R. T. Downs and D. C. Palmer, *ibid.* **79**(1–2), 9 (1994); K. Kihara, Z. Kristallogr. **148**(3–4), 237 (1978); M. Sugiyama, S. Endo, and K. Koto, Mineral. J. **13**(7), 455 (1987); G. Ennas, M. P. Medda, A. Musinu, G. Piccaluga, and G. Pinna, J. Non-Cryst. Solids **150**(1–3), 65 (1992).
[64]A. F. Wright and A. J. Leadbetter, Philos. Mag. **31**(6), 1391 (1975).
[65]*LASL Shock Hugoniot Data* (University of California, Berkeley, 1980).
[66]See the supplementary material at http://dx.doi.org/10.1063/1.3696865 for the files with the silica FM, FM-ns, and FM-ws potentials.

A Perfectly Matched Layer For Peridynamics In Two Dimensions

Raymond A. Wildman and George A. Gazonas

Journal of Mechanics of Materials and Structures, Volume 7, No. 8-9 (2012)

JOURNAL OF MECHANICS OF MATERIALS AND STRUCTURES
Vol. 7, No. 8-9, 2012
dx.doi.org/10.2140/jomms.2012.7.765

msp

A PERFECTLY MATCHED LAYER FOR PERIDYNAMICS IN TWO DIMENSIONS

RAYMOND A. WILDMAN AND GEORGE A. GAZONAS

A perfectly matched layer (PML) absorbing boundary is formulated for and numerically applied to peridynamics in two dimensions. Peridynamics is a nonlocal method, derived to be insensitive to discontinuities, more easily simulating fracture. A PML is an absorbing boundary layer, which decays impinging waves exponentially without introducing reflections at the boundary between the computational region and the absorbing layer. Here, we use state-based peridynamics as PMLs are essentially anisotropic absorbing materials, therefore requiring arbitrary material parameters. State-based peridynamics is also more convenient for auxiliary field formulations, facilitating the implementation of the PML. Results show the efficacy of the approach.

1. Introduction

Originally introduced in [Silling 2000], peridynamics is a nonlocal formulation of elastodynamics, which can more easily incorporate discontinuities such as cracks and damage. Derivatives of field variables in the classical continuum model are replaced by integrals over a small neighborhood of microelastic kernels that replace standard constitutive relations. In its discretized form, an elastic solid is treated as a collection of particles or nodes, each connected to its neighbors by breakable bonds. Bond breakage can be defined to occur when a bond is stretched past some predetermined limit. After a bond is broken, any supported force transfers to the remaining bonds, increasing their supported load, and encouraging more breakage. Eventually, this process autonomously leads to cracking and failure. The end result is a method capable of predicting crack growth in brittle elastic materials [Gerstle et al. 2005; Silling and Askari 2005; Emmrich and Weckner 2006; Demmie and Silling 2007; Kilic et al. 2009; Ha and Bobaru 2010].

Over the last decade, peridynamics has been extended past its original formulation. First, the numerical method originally outlined in [Silling and Askari 2005] has been extended to include adaptive refinement [Bobaru et al. 2009], replaced with different quadrature rules [Emmrich and Weckner 2007], and implemented in a parallel, molecular dynamics code [Parks et al. 2008]. In addition, it has been extended to different material types including viscoplastic [Foster et al. 2010], micropolar [Gerstle et al. 2011], and nanofiber networks [Bobaru 2007]. It has also been applied to different fields such as heat conduction [Bobaru and Duangpanya 2010] and electromigration [Gerstle et al. 2008]. Aside from practical applications, the mathematics behind the approach have been studied: Weckner et al. [2009] derived a Green's function for the peridynamic equation and Weckner and Abeyaratne [2005] discussed dispersion relations for various kernels. Most importantly for this work, state-based peridynamics was introduced,

allowing for more flexible constitutive relations [Silling et al. 2007]. As will become clear later, state-based peridynamics allows for an auxiliary field formulation, which is necessary for the implementation of a perfectly matched layer (PML).

While most peridynamics work has focused on simulating problems with free or fixed boundary conditions, there are applications in which the simulation of an infinite medium may be useful, such as wave or crack propagation in a half-space. Absorbing boundary conditions are a way of simulating an infinite medium by absorbing any impinging waves at the computational boundaries so they do not reflect back into the simulation. A PML is such an absorbing boundary, and was originally introduced for electromagnetic simulations [Berenger 1994; Chew and Weedon 1994]. PMLs differ from traditional absorbing boundary conditions in that they are an absorbing layer, placed between the computational region of interest and the truncation of the grid or mesh. They can also be thought of as an anisotropic absorbing material, which is why the flexibility of a state-based peridynamics is necessary.

PMLs have two important qualities: First, waves in a PML decay exponentially, and second, in their analytic form, no waves reflect at the interface of a PML and the computational region. These properties make them ideal for simulating wave propagation in infinite, unbounded regions. Since their introduction, PMLs have been extended to many different types of media [Uno et al. 1997; Teixeira and Chew 1998; Dong et al. 2004], different numerical methods [Pissoort and Olyslager 2003; Pissoort et al. 2005; Alles and van Dongen 2009], and different fields [Chew and Liu 1996; Liu and Tao 1997; Festa and Nielsen 2003].

This paper implements a peridynamic formulation of elastodynamics in two dimensions and terminates the boundary with a PML. As is discussed, the use of a PML is facilitated with an auxiliary field formulation, derived from state-based peridynamics, and the peridynamic equation is broken into five coupled equations. A PML was applied to one-dimensional peridynamics in [Wildman and Gazonas 2011], which used the results of [Du et al. 2012] to formulate an auxiliary field equation. This approach required a matrix representation of the auxiliary field, which may be memory prohibitive in higher dimensions.

The remainder of the paper is organized as follows: Section 2 discusses the formulation of peridynamics, PMLs, and their numerical implementation; Section 3 gives some results; and Section 4 summarizes the report and details future work.

2. Formulation

In this section, a PML is formulated for state-based two-dimensional peridynamics. First, in Section 2A, a linear elastic, state-based peridynamics formulation will be reviewed. Next, Section 2B reviews the formulation of a PML. Section 2C then applies the PML to state-based peridynamics, and finally Section 2D discusses a discretization of the formulation using the standard node-based peridynamics method.

2A. ***Two-dimensional, state-based peridynamics.*** The continuum equation of motion in an elastic solid can be stated as

$$\rho \frac{\partial^2}{\partial t^2} \boldsymbol{u} = \nabla \cdot \bar{\boldsymbol{\sigma}} + \boldsymbol{b}, \tag{2-1}$$

where (in two dimensions) $\rho(\boldsymbol{x})$ [kg/m^2] is the density, $\boldsymbol{u}(\boldsymbol{x}, t)$ [m] is the displacement, $\bar{\boldsymbol{\sigma}}(\boldsymbol{x}, t)$ [N/m] is the stress tensor, and $\boldsymbol{b}(\boldsymbol{x})$ [N/m^2] is a body force [Malvern 1969]. (Throughout, boldface type denotes a vector and a boldface variable with an overbar denotes a tensor.) Equation (2-1) is a local formulation

because the divergence of the stress (and gradient of the displacement implied in its definition) represents a local operation on a variable. In other words, the action of $\nabla \cdot \bar{\boldsymbol{\sigma}}$ only depends on $\bar{\boldsymbol{\sigma}}$ at a single spatial point. In problems involving discontinuities, such as cracks, the divergence at such discontinuities is not well defined, leading to numerical implementation problems. Peridynamics proposes replacing $\nabla \cdot \bar{\boldsymbol{\sigma}}$ with a nonlocal operation that nonetheless also represents a force

$$\rho \frac{\partial^2}{\partial t^2} \boldsymbol{u} = \int_{\mathcal{H}_{\boldsymbol{x}}} \boldsymbol{f}(\boldsymbol{u}' - \boldsymbol{u}, \boldsymbol{x}' - \boldsymbol{x}) \, dV_{\boldsymbol{x}'} + \boldsymbol{b}, \tag{2-2}$$

where $\boldsymbol{f}(\boldsymbol{x}' - \boldsymbol{x}, \boldsymbol{u}' - \boldsymbol{u})$ [N/m^4] represents a micromodulus force function (or kernel) that defines a force between two points and $\mathcal{H}_{\boldsymbol{x}}$ represents a horizon or maximum distance over which two points can influence each other [Silling 2000]. The micromodulus function becomes the constitutive response in the formulation, replacing Hooke's law in the continuum case. In its original form, the micromodulus function was developed as a simple elastic response following

$$\boldsymbol{f}(\boldsymbol{\eta}, \boldsymbol{\xi}) = c \frac{\boldsymbol{\xi} + \boldsymbol{\eta}}{|\boldsymbol{\xi} + \boldsymbol{\eta}|} \frac{|\boldsymbol{\xi} + \boldsymbol{\eta}| - |\boldsymbol{\eta}|}{|\boldsymbol{\eta}|} H(\delta - |\boldsymbol{\xi}|), \tag{2-3}$$

where c is some constant, $H(\cdot)$ is the Heaviside step function, and δ is the radius of the horizon region, which defines $\mathcal{H}_{\boldsymbol{x}}$ [Silling 2000]. Note that in contrast to [Silling 2000], for simplicity there is no history-dependent failure term in (2-3). Equation (2-3) is isotropic, though not strictly linear in terms of $\boldsymbol{u}$. Linearizing (2-3) gives

$$\boldsymbol{f}(\boldsymbol{\eta}, \boldsymbol{\xi}) = \bar{\boldsymbol{C}}(\boldsymbol{\xi})\boldsymbol{\eta}, \quad \bar{\boldsymbol{C}}(\boldsymbol{\xi}) = C(\boldsymbol{\xi}) \frac{\boldsymbol{\xi} \otimes \boldsymbol{\xi}}{|\boldsymbol{\xi}|^3}, \quad C(|\boldsymbol{\xi}|) = cH(\delta - |\boldsymbol{\xi}|), \tag{2-4}$$

where $\otimes$ denotes an outer product [Silling 2000]. The function $C(|\boldsymbol{\xi}|)$ is the kernel function, typically taken to be a Heaviside function. Here, we will also use a Gaussian kernel function, which tends to give smoother results with less apparent ringing in the solution. A Gaussian kernel is defined as

$$C_{\text{Gauss}}(|\boldsymbol{\xi}|) = ce^{-(|\boldsymbol{\xi}|/\delta)^2}. \tag{2-5}$$

For the Gaussian kernel, the horizon δ does not delineate a strict bond family as the Heaviside function, but describes the decay of the kernel. To determine the bond family, $\mathcal{H}_{\boldsymbol{x}}$, a small, arbitrary value can be chosen as a cutoff for the kernel. Note that the cutoff has a large impact on the efficiency of the method: too small a cutoff and a large number of bonds must be included in each calculation. Throughout, we set the cutoff to 10^{-6}.

A PML application requires an auxiliary field formulation, as it is essentially an anisotropic absorbing material, if a nonphysical one. Consequently, a state-based peridynamic formulation [Silling et al. 2007] is necessary to implement the required constitutive relations in the absorber. State-based peridynamics uses a family of bonds to determine a given force rather than a single bond independently. This more general approach allows for inelastic behavior and more general elastic behavior, and is governed by

$$\rho \frac{\partial^2}{\partial t^2} \boldsymbol{u} = \int_{\mathcal{H}_{\boldsymbol{x}}} (\bar{\boldsymbol{T}}[\boldsymbol{x}, t]\langle \boldsymbol{x}' - \boldsymbol{x} \rangle - \bar{\boldsymbol{T}}[\boldsymbol{x}', t]\langle \boldsymbol{x} - \boldsymbol{x}' \rangle) \, dV_{\boldsymbol{x}'} + \boldsymbol{b}, \tag{2-6}$$

where $\bar{\boldsymbol{T}}[\boldsymbol{x}, t]\langle \boldsymbol{x}' - \boldsymbol{x} \rangle$ is a peridynamic vector state, with the parameters in the square brackets indicating variables that act as arguments to any functions referenced in the vector state and the variables in the

angle brackets acting as arguments to the vector state itself. In the state-based formulation of [Foster et al. 2010], the deformation gradient, given by

$$\bar{\boldsymbol{F}} = \bar{\boldsymbol{I}} + \boldsymbol{u}\nabla, \tag{2-7}$$

can be approximated as a vector state as

$$\bar{\boldsymbol{F}}[\boldsymbol{x}, t] = \left[\int_{\mathcal{H}_{\boldsymbol{x}}} C(|\boldsymbol{\xi}|)(\boldsymbol{Y}[\boldsymbol{x}, t]\langle\boldsymbol{\xi}\rangle \otimes \boldsymbol{\xi})\, dV_{\boldsymbol{x}'}\right]\bar{\boldsymbol{K}}^{-1}, \tag{2-8}$$

where $\boldsymbol{\xi} = \boldsymbol{x}' - \boldsymbol{x}$, $\bar{\boldsymbol{K}}$ is a shape tensor given by

$$\bar{\boldsymbol{K}}[\boldsymbol{x}, t] = \int_{\mathcal{H}_{\boldsymbol{x}}} C(|\boldsymbol{\xi}|)(\boldsymbol{\xi} \otimes \boldsymbol{\xi})\, dV_{\boldsymbol{x}'}, \tag{2-9}$$

and $\boldsymbol{Y}$ is a deformation vector state given by

$$\boldsymbol{Y}[\boldsymbol{x}, t]\langle\boldsymbol{\xi}\rangle = \boldsymbol{\eta} + \boldsymbol{\xi}, \tag{2-10}$$

with $\boldsymbol{\eta} = \boldsymbol{u}[\boldsymbol{x}', t] - \boldsymbol{u}[\boldsymbol{x}, t]$ [Foster et al. 2010].

The deformation gradient can now be substituted into Hooke's law and strain-displacement relations, giving a stress term $\bar{\boldsymbol{\sigma}}$ in terms of $\boldsymbol{u}$ in plane strain

$$\rho\frac{\partial^2}{\partial t^2}\boldsymbol{u} = \nabla \cdot \bar{\boldsymbol{\sigma}} = \nabla \cdot (\bar{\boldsymbol{c}} : \bar{\boldsymbol{\epsilon}}), \tag{2-11}$$

where

$$\bar{\boldsymbol{\epsilon}}[\boldsymbol{x}, t] = \tfrac{1}{2}(\nabla\boldsymbol{u} + \boldsymbol{u}\nabla) = \tfrac{1}{2}(\bar{\boldsymbol{F}}[\boldsymbol{x}, t] + \bar{\boldsymbol{F}}[\boldsymbol{x}, t]^{\boldsymbol{T}} - 2\bar{\boldsymbol{I}}), \tag{2-12}$$

$$\bar{\boldsymbol{c}} = \frac{E}{(1+\nu)(1-2\nu)}\begin{bmatrix} 1-\nu & \nu & 0 \\ \nu & 1-\nu & 0 \\ 0 & 0 & 1-2\nu \end{bmatrix} = \begin{bmatrix} \lambda+2\mu & \lambda & 0 \\ \lambda & \lambda+2\mu & 0 \\ 0 & 0 & 2\mu \end{bmatrix}, \tag{2-13}$$

E is the Young's modulus, ν is the Poisson's ratio, and λ and μ are the Lamé parameters. Ultimately, the peridynamic vector state $\boldsymbol{T}$ for plane strain elasticity is given by

$$\bar{\boldsymbol{T}}[\boldsymbol{x}, t]\langle\boldsymbol{\xi}\rangle = C(|\boldsymbol{\xi}|)\bar{\boldsymbol{\sigma}}[\boldsymbol{x}, t]\bar{\boldsymbol{K}}^{-1}\boldsymbol{\xi}. \tag{2-14}$$

2B. ***Perfectly matched layer.*** The first step in formulating a PML is to construct an analytic continuation to the complex plane

$$\hat{x} = x + ig(x), \tag{2-15}$$

where $g(x)$ is a given function describing the deformation [Johnson 2010]. This mapping has the effect of transforming traveling waves of the form e^{ikx}, where $k = \omega/c$ is the wave number, into evanescent waves of the form $e^{ikx}e^{-kg(x)}$, thus attenuating such waves in the PML region.

Substituting $\hat{x}$ into the above equations would yield a viable method, though one that requires complex coordinates. A simpler solution is to change variables back to the real part x, which requires a relation

for the differential quantities, given as

$$\partial\hat{x} = \left[1 + i\frac{d}{dx}g\right]\partial x; \tag{2-16}$$

partial differential quantities are used, as this is used as a substitution for the above equations involving functions of both x and t [Johnson 2010]. A convenient choice for $g(x)$ is

$$\frac{d}{dx}g(x) = \frac{\phi(x)}{\omega}, \tag{2-17}$$

because the $1/\omega$ factor creates a frequency-independent attenuation rate in dispersionless materials [Johnson 2010]. (Peridynamic formulations are not dispersionless, as discussed in [Weckner and Abeyaratne 2005], though this standard choice is used for simplicity.) Finally, the substitution that must be made for any spatial derivative can be written

$$\frac{\partial}{\partial x} \to \frac{1}{1 + i\phi(x)/\omega}\frac{\partial}{\partial x}. \tag{2-18}$$

Before applying a PML directly to the peridynamic equation, (2-1) will be treated so that the PML application to peridynamics will be clear. It is convenient to convert (2-1) to the Laplace domain, assuming e^{-st} time dependence, giving

$$\rho s^2\tilde{\boldsymbol{u}} = \nabla\cdot\bar{\tilde{\boldsymbol{\sigma}}}, \tag{2-19}$$

where the Laplace transform of a variable is indicated by $\mathcal{L}\{f\} = \tilde{f}$. Next, we express the wave equation as two coupled first-order partial differential equations, the first in $\tilde{\boldsymbol{u}}$ and the second in $s\bar{\tilde{\boldsymbol{\psi}}} = \bar{\tilde{\boldsymbol{\sigma}}}$:

$$\rho s\tilde{\boldsymbol{u}} = \nabla\cdot\bar{\tilde{\boldsymbol{\psi}}}, \quad s\bar{\tilde{\boldsymbol{\psi}}} = \bar{\boldsymbol{c}} : \bar{\tilde{\boldsymbol{\epsilon}}}. \tag{2-20}$$

Expanding (2-20) into components gives five coupled equations:

$$\begin{gathered}\rho s\tilde{u}_x = \frac{\partial}{\partial x}\tilde{\psi}_x + \frac{\partial}{\partial y}\tilde{\psi}_\tau, \quad \rho s\tilde{u}_y = \frac{\partial}{\partial x}\tilde{\psi}_\tau + \frac{\partial}{\partial y}\tilde{\psi}_y, \\ s\tilde{\psi}_x = (\lambda+2\mu)\frac{\partial}{\partial x}\tilde{u}_x + \lambda\frac{\partial}{\partial y}\tilde{u}_y, \quad s\tilde{\psi}_y = \lambda\frac{\partial}{\partial x}\tilde{u}_x + (\lambda+2\mu)\frac{\partial}{\partial y}\tilde{u}_y, \quad s\tilde{\psi}_\tau = \mu\left(\frac{\partial}{\partial y}\tilde{u}_x + \frac{\partial}{\partial x}\tilde{u}_y\right).\end{gathered} \tag{2-21}$$

Here, we will make the substitution given in (2-18) for all spatial derivatives, written as

$$\frac{\partial}{\partial x} \to \frac{s}{s+\phi(x)}\frac{\partial}{\partial x} \tag{2-22}$$

in the Laplace domain, and later define ϕ_x and ϕ_y in the desired absorbing boundary locations. Using $(2\text{-}21)_1$ as an example, we get

$$\begin{aligned}\rho s\tilde{u}_x &= \frac{s}{s+\phi_x}\frac{\partial}{\partial x}\tilde{\psi}_x + \frac{s}{s+\phi_y}\frac{\partial}{\partial y}\tilde{\psi}_\tau \\ &\implies \rho(s+\phi_x)(s+\phi_y)\tilde{u}_x = (s+\phi_y)\frac{\partial}{\partial x}\tilde{\psi}_x + (s+\phi_x)\frac{\partial}{\partial y}\tilde{\psi}_\tau.\end{aligned} \tag{2-23}$$

The remaining components of (2-21) can be expanded in a similar way.

Wherever $\phi > 0$, $\boldsymbol{u}$ and $\bar{\boldsymbol{\sigma}}$ will exponentially decay. Before discretization, any change in ϕ will not result in any reflections, so the region of interest would have $\phi = 0$, and the PML region could have a

discontinuity in applying ϕ. In practice, however, numerical reflections can result from discontinuous material parameters after discretization, so it is better to use a smooth transition for ϕ. Here, we divide the PML region into two parts, one in which ϕ is a constant value, and the other in which ϕ ramps up to that constant value following a Gaussian distribution. An example is shown in Figure 1, with the constant region set to 0.1 m and the Gaussian region 0.2 m. The variance of the distribution is set so that the minimum value in the Gaussian region is 10^{-6}.

2C. ***Auxiliary field formulation and PML application.*** Peridynamics is not typically stated in terms of Cartesian components as in (2-24), but we can expand the state-based formulation into components and match terms to (2-24). Following this approach yields a viable method for performing PML substitutions.

First, the state-based peridynamic equations (2-6)–(2-14) can be written explicitly as

$$
\begin{aligned}
\rho s\tilde{u}_x[\boldsymbol{x},s] &= \int_{\mathcal{H}_{\boldsymbol{x}}} C(|\boldsymbol{\xi}|)\big[(\tilde{\psi}_x[\boldsymbol{x},s]k_{xx}^{\mathrm{inv}}+\tilde{\psi}_\tau[\boldsymbol{x},s]k_{yx}^{\mathrm{inv}})\xi_x+(\tilde{\psi}_x[\boldsymbol{x}',s]k_{xx}'^{\mathrm{inv}}+\tilde{\psi}_\tau[\boldsymbol{x}',s]k_{yx}'^{\mathrm{inv}})\xi_x\big]dV_{\boldsymbol{x}'}\\
&\quad+\int_{\mathcal{H}_{\boldsymbol{x}}} C(|\boldsymbol{\xi}|)\big[(\tilde{\psi}_x[\boldsymbol{x},s]k_{xy}^{\mathrm{inv}}+\tilde{\psi}_\tau[\boldsymbol{x},s]k_{yy}^{\mathrm{inv}})\xi_y+(\tilde{\psi}_x[\boldsymbol{x}',s]k_{xy}'^{\mathrm{inv}}+\tilde{\psi}_\tau[\boldsymbol{x}',s]k_{yy}'^{\mathrm{inv}})\xi_y\big]dV_{\boldsymbol{x}'},\\
\rho s\tilde{u}_y[\boldsymbol{x},s] &= \int_{\mathcal{H}_{\boldsymbol{x}}} C(|\boldsymbol{\xi}|)\big[(\tilde{\psi}_\tau[\boldsymbol{x},s]k_{xx}^{\mathrm{inv}}+\tilde{\psi}_y[\boldsymbol{x},s]k_{yx}^{\mathrm{inv}})\xi_x+(\tilde{\psi}_\tau[\boldsymbol{x}',s]k_{xx}'^{\mathrm{inv}}+\tilde{\psi}_y[\boldsymbol{x}',s]k_{yx}'^{\mathrm{inv}})\xi_x\big]dV_{\boldsymbol{x}'}\\
&\quad+\int_{\mathcal{H}_{\boldsymbol{x}}} C(|\boldsymbol{\xi}|)\big[(\tilde{\psi}_\tau[\boldsymbol{x},s]k_{xy}^{\mathrm{inv}}+\tilde{\psi}_y[\boldsymbol{x},s]k_{yy}^{\mathrm{inv}})\xi_y+(\tilde{\psi}_\tau[\boldsymbol{x}',s]k_{xy}'^{\mathrm{inv}}+\tilde{\psi}_y[\boldsymbol{x}',s]k_{yy}'^{\mathrm{inv}})\xi_y\big]dV_{\boldsymbol{x}'},\\
s\tilde{\psi}_x[\boldsymbol{x},s] &= (\lambda+2\mu)\left[\int_{\mathcal{H}_{\boldsymbol{x}}} C(|\boldsymbol{\xi}|)(\tilde{Y}_x[\boldsymbol{x},s]\xi_x k_{xx}^{\mathrm{inv}}+\tilde{Y}_x[\boldsymbol{x},s]\xi_y k_{yx}^{\mathrm{inv}})\,dV_{\boldsymbol{x}'}-1\right]\\
&\quad+\lambda\left[\int_{\mathcal{H}_{\boldsymbol{x}}} C(|\boldsymbol{\xi}|)(\tilde{Y}_y[\boldsymbol{x},s]\xi_x k_{xy}^{\mathrm{inv}}+\tilde{Y}_y[\boldsymbol{x},s]\xi_y k_{yy}^{\mathrm{inv}})\,dV_{\boldsymbol{x}'}-1\right],\\
s\tilde{\psi}_y[\boldsymbol{x},s] &= \lambda\left[\int_{\mathcal{H}_{\boldsymbol{x}}} C(|\boldsymbol{\xi}|)(\tilde{Y}_x[\boldsymbol{x},s]\xi_x k_{xx}^{\mathrm{inv}}+\tilde{Y}_x[\boldsymbol{x},s]\xi_y k_{yx}^{\mathrm{inv}})\,dV_{\boldsymbol{x}'}-1\right]\\
&\quad+(\lambda+2\mu)\left[\int_{\mathcal{H}_{\boldsymbol{x}}} C(|\boldsymbol{\xi}|)(\tilde{Y}_y[\boldsymbol{x},s]\xi_x k_{xy}^{\mathrm{inv}}+\tilde{Y}_y[\boldsymbol{x},s]\xi_y k_{yy}^{\mathrm{inv}})\,dV_{\boldsymbol{x}'}-1\right],\\
s\tilde{\psi}_\tau[\boldsymbol{x},s] &= \mu\int_{\mathcal{H}_{\boldsymbol{x}}} C(|\boldsymbol{\xi}|)\big(\tilde{Y}_x[\boldsymbol{x},s]\xi_x k_{xy}^{\mathrm{inv}}+\tilde{Y}_x[\boldsymbol{x},s]\xi_y k_{yy}^{\mathrm{inv}}\big)\,dV_{\boldsymbol{x}'}\\
&\quad+\mu\int_{\mathcal{H}_{\boldsymbol{x}}} C(|\boldsymbol{\xi}|)\big(\tilde{Y}_y[\boldsymbol{x},s]\xi_x k_{xx}^{\mathrm{inv}}+\tilde{Y}_y[\boldsymbol{x},s]\xi_y k_{yx}^{\mathrm{inv}}\big)\,dV_{\boldsymbol{x}'},
\end{aligned}
\tag{2-24}
$$

where

$$
\overline{\boldsymbol{K}}^{-1}=\begin{bmatrix} k_{xx}^{\mathrm{inv}} & k_{xy}^{\mathrm{inv}}\\ k_{yx}^{\mathrm{inv}} & k_{yy}^{\mathrm{inv}}\end{bmatrix}. \tag{2-25}
$$

Though no derivatives appear in (2-24), the correspondence of each term to those in (2-21) is apparent — with partial derivatives following the component of $\boldsymbol{\xi}$ — and the PML substitutions can be made. For

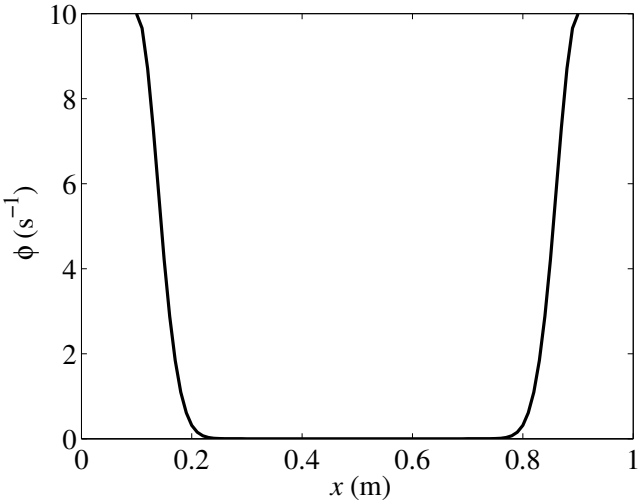

Figure 1. An example of a PML across one dimension using a Gaussian ramp.

example, the first equation in (2-24) can be rewritten as

$$\begin{aligned}\rho(s+\phi_x)(s+\phi_y)\tilde{u}_x = {} & (s+\phi_y)\int_{\mathscr{H}_{\boldsymbol{x}}} C(|\boldsymbol{\xi}|)\big(\tilde{\psi}_x[\boldsymbol{x},s]k_{xx}^{\text{inv}}+\tilde{\psi}_{xy}[\boldsymbol{x},s]k_{yx}^{\text{inv}}\big)\xi_x\,dV_{\boldsymbol{x}'}\\ & +(s+\phi_y)\int_{\mathscr{H}_{\boldsymbol{x}}} C(|\boldsymbol{\xi}|)\big(\tilde{\psi}_x[\boldsymbol{x}',s]k_{xx}'^{\text{inv}}+\tilde{\psi}_{xy}[\boldsymbol{x}',s]k_{yx}'^{\text{inv}}\big)\xi_x\,dV_{\boldsymbol{x}'}\\ & +(s+\phi_x)\int_{\mathscr{H}_{\boldsymbol{x}}} C(|\boldsymbol{\xi}|)\big(\tilde{\psi}_x[\boldsymbol{x},s]k_{xy}^{\text{inv}}+\tilde{\psi}_{\tau}[\boldsymbol{x},s]k_{yy}^{\text{inv}}\big)\xi_y\,dV_{\boldsymbol{x}'}\\ & +(s+\phi_x)\int_{\mathscr{H}_{\boldsymbol{x}}} C(|\boldsymbol{\xi}|)\big(\tilde{\psi}_x[\boldsymbol{x}',s]k_{xy}'^{\text{inv}}+\tilde{\psi}_{\tau}[\boldsymbol{x}',s]k_{yy}'^{\text{inv}}\big)\xi_y\,dV_{\boldsymbol{x}'},\end{aligned}\tag{2-26}$$

with the remaining equations following similarly.

2D. ***Discretization.*** For the temporal discretization, forward Euler will be used to simplify the presentation and implementation. Higher-order temporal discretizations can be used, though they lead to more terms in what follows. The Laplace domain was used throughout to facilitate the temporal discretization of the final equations. Because differentiation in the Laplace domain is represented by s, approximations to s can be directly substituted in terms of the z-transform. This technique is used in the design of digital filters, where it is known as "filter design by approximation of derivatives" or "the bilinear transformation" [Proakis and Manolakis 1996], and in integral equation methods where it is known as "convolution quadrature" [Lubich 1988a; 1988b], or "finite difference delay modeling" [Wang et al. 2008]. A forward Euler approximation can be stated as the substitution

$$s \to \frac{z-1}{\Delta t},\tag{2-27}$$

where z is the z-transform[1] variable representing a unit advance and Δt is the time step size. Substitution

[1]The z-transform is defined here as $X(z) = Z\{x[n]\} = \sum_{n=0}^{\infty} x[n]z^{-n}$ for causal signals.

into (2-26) gives

$$\begin{aligned}\rho(z-1+\Delta t\phi_x)(z-1+\Delta t\phi_y)U_x = (z-1+\Delta t\phi_y)\int_{\mathcal{H}_{\boldsymbol{x}}} C(|\boldsymbol{\xi}|)\big(\Psi_x[\boldsymbol{x},z]k_{xx}^{\text{inv}}+\Psi_\tau[\boldsymbol{x},z]k_{yx}^{\text{inv}}\big)\xi_x\,dV_{\boldsymbol{x}'}\\ +(z-1+\Delta t\phi_y)\int_{\mathcal{H}_{\boldsymbol{x}}} C(|\boldsymbol{\xi}|)\big(\Psi_x[\boldsymbol{x}',z]k_{xx}'^{\text{inv}}+\Psi_\tau[\boldsymbol{x}',z]k_{yx}'^{\text{inv}}\big)\xi_x\,dV_{\boldsymbol{x}'}\\ +(z-1+\Delta t\phi_x)\int_{\mathcal{H}_{\boldsymbol{x}}} C(|\boldsymbol{\xi}|)\big(\Psi_x[\boldsymbol{x},z]k_{xy}^{\text{inv}}+\Psi_\tau[\boldsymbol{x},z]k_{yy}^{\text{inv}}\big)\xi_y\,dV_{\boldsymbol{x}'}\\ +(z-1+\Delta t\phi_x)\int_{\mathcal{H}_{\boldsymbol{x}}} C(|\boldsymbol{\xi}|)\big(\Psi_x[\boldsymbol{x}',z]k_{xy}'^{\text{inv}}+\Psi_\tau[\boldsymbol{x}',z]k_{yy}'^{\text{inv}}\big)\xi_y\,dV_{\boldsymbol{x}'},\end{aligned} \tag{2-28}$$

where capital letters indicate the z-transform of a variable. Expanding the quadratic term on the left-hand side gives

$$\begin{aligned}(z-1+\Delta t\phi_x)(z-1+\Delta t\phi_y) &= \Delta t^2\phi_x\phi_y+\Delta t\phi_x z-\Delta t\phi_x+\Delta t\phi_y z+z^2-z-\Delta t\phi_y-z+1\\ &= z^2+(\Delta t\phi_x+\Delta t\phi_y-2)z+\Delta t^2\phi_x\phi_y-\Delta t\phi_x-\Delta t\phi_y+1.\end{aligned} \tag{2-29}$$

Multiplying by z^{-2} and rearranging gives an update equation in terms of z, which can be converted to a time-stepping method via the inverse z-transform[2] (assuming vanishing initial conditions and an appropriate region of convergence) as

$$\begin{aligned}u_x[\boldsymbol{x},l] = -(\gamma_x+\gamma_y)u_x[\boldsymbol{x},l-1]-\gamma_x\gamma_y u_x[\boldsymbol{x},l-2]\\ +\frac{\Delta t}{\rho}\int_{\mathcal{H}_{\boldsymbol{x}}} C(|\boldsymbol{\xi}|)\big(\psi_x[\boldsymbol{x},l-1]k_{xx}^{\text{inv}}+\psi_\tau[\boldsymbol{x},l-1]k_{yx}^{\text{inv}}\big)\xi_x\,dV_{\boldsymbol{x}'}\\ +\frac{\Delta t}{\rho}\int_{\mathcal{H}_{\boldsymbol{x}}} C(|\boldsymbol{\xi}|)\big(\psi_x[\boldsymbol{x}',l-1]k_{xx}'^{\text{inv}}+\psi_\tau[\boldsymbol{x}',l-1]k_{yx}'^{\text{inv}}\big)\xi_x\,dV_{\boldsymbol{x}'}\\ +\frac{\Delta t}{\rho}\gamma_y\int_{\mathcal{H}_{\boldsymbol{x}}} C(|\boldsymbol{\xi}|)\big(\psi_x[\boldsymbol{x},l-2]k_{xx}^{\text{inv}}+\psi_\tau[\boldsymbol{x},l-2]k_{yx}^{\text{inv}}\big)\xi_x\,dV_{\boldsymbol{x}'}\\ +\frac{\Delta t}{\rho}\gamma_y\int_{\mathcal{H}_{\boldsymbol{x}}} C(|\boldsymbol{\xi}|)\big(\psi_x[\boldsymbol{x}',l-2]k_{xx}'^{\text{inv}}+\psi_\tau[\boldsymbol{x}',l-2]k_{yx}'^{\text{inv}}\big)\xi_x\,dV_{\boldsymbol{x}'}\\ +\frac{\Delta t}{\rho}\int_{\mathcal{H}_{\boldsymbol{x}}} C(|\boldsymbol{\xi}|)\big(\psi_x[\boldsymbol{x},l-1]k_{xy}^{\text{inv}}+\psi_\tau[\boldsymbol{x},l-1]k_{yy}^{\text{inv}}\big)\xi_y\,dV_{\boldsymbol{x}'}\\ +\frac{\Delta t}{\rho}\int_{\mathcal{H}_{\boldsymbol{x}}} C(|\boldsymbol{\xi}|)\big(\psi_x[\boldsymbol{x}',l-1]k_{xy}'^{\text{inv}}+\psi_\tau[\boldsymbol{x}',l-1]k_{yy}'^{\text{inv}}\big)\xi_y\,dV_{\boldsymbol{x}'}\\ +\frac{\Delta t}{\rho}\gamma_x\int_{\mathcal{H}_{\boldsymbol{x}}} C(|\boldsymbol{\xi}|)\big(\psi_x[\boldsymbol{x},l-2]k_{xy}^{\text{inv}}+\psi_\tau[\boldsymbol{x},l-2]k_{yy}^{\text{inv}}\big)\xi_y\,dV_{\boldsymbol{x}'}\\ +\frac{\Delta t}{\rho}\gamma_x\int_{\mathcal{H}_{\boldsymbol{x}}} C(|\boldsymbol{\xi}|)\big(\psi_x[\boldsymbol{x}',l-2]k_{xy}'^{\text{inv}}+\psi_\tau[\boldsymbol{x}',l-2]k_{yy}'^{\text{inv}}\big)\xi_y\,dV_{\boldsymbol{x}'},\end{aligned} \tag{2-30}$$

[2]The only necessary property is the delay: $x[n-k]\leftrightarrow z^{-k}X(z)$

where l is the time step number, $\gamma_x = \Delta t \phi_x - 1$, and $\gamma_y = \Delta t \phi_y - 1$. A stress component update equation becomes, for example,

$$\begin{aligned}
\psi_x[\boldsymbol{x}, l] = &-(\gamma_x + \gamma_y)\psi_x[\boldsymbol{x}, l-1] - \gamma_x\gamma_y\psi_x[\boldsymbol{x}, l-2] \\
&+ \Delta t(\lambda + 2\mu)\left[\int_{\mathcal{H}_{\boldsymbol{x}}} C(|\boldsymbol{\xi}|)(Y_x[\boldsymbol{x}, l-1]\xi_x k_{xx}^{\text{inv}} + Y_x[\boldsymbol{x}, l-1]\xi_y k_{yx}^{\text{inv}})\, dV_{\boldsymbol{x}'} - 1\right] \\
&+ \Delta t\gamma_y(\lambda + 2\mu)\left[\int_{\mathcal{H}_{\boldsymbol{x}}} C(|\boldsymbol{\xi}|)(Y_x[\boldsymbol{x}, l-2]\xi_x k_{xx}^{\text{inv}} + Y_x[\boldsymbol{x}, l-2]\xi_y k_{yx}^{\text{inv}})\, dV_{\boldsymbol{x}'} - 1\right] \\
&+ \Delta t\lambda\left[\int_{\mathcal{H}_{\boldsymbol{x}}} C(|\boldsymbol{\xi}|)(Y_y[\boldsymbol{x}, l-1]\xi_x k_{xy}^{\text{inv}} + Y_y[\boldsymbol{x}, l-1]\xi_y k_{yy}^{\text{inv}})\, dV_{\boldsymbol{x}'} - 1\right] \\
&+ \Delta t\lambda\gamma_x\left[\int_{\mathcal{H}_{\boldsymbol{x}}} C(|\boldsymbol{\xi}|)(Y_y[\boldsymbol{x}, l-2]\xi_x k_{xy}^{\text{inv}} + Y_y[\boldsymbol{x}, l-2]\xi_y k_{yy}^{\text{inv}})\, dV_{\boldsymbol{x}'} - 1\right]. \quad (2\text{-}31)
\end{aligned}$$

Finally, (2-30) can be discretized spatially using a simple one-point integration and point match testing, giving, for the x-component of displacement,

$$\begin{aligned}
u_x[\boldsymbol{x}_i, l] = &-(\gamma_x + \gamma_y)u_x[\boldsymbol{x}_i, l-1] - \gamma_x\gamma_y u_x[\boldsymbol{x}_i, l-2] \\
&+ \frac{\Delta t}{\rho}\sum_{j=1}^{N_i} C(|\boldsymbol{\xi}_{ij}|)(\psi_x[\boldsymbol{x}_i, l-1]k_{i,xx}^{\text{inv}} + \psi_\tau[\boldsymbol{x}_i, l-1]k_{i,yx}^{\text{inv}})\xi_x V_j \\
&+ \frac{\Delta t}{\rho}\sum_{j=1}^{N_i} C(|\boldsymbol{\xi}_{ij}|)(\psi_x[\boldsymbol{x}_j, l-1]k_{j,xx}^{\text{inv}} + \psi_\tau[\boldsymbol{x}_j, l-1]k_{j,yx}^{\text{inv}})\xi_x V_j \\
&+ \frac{\Delta t}{\rho}\gamma_y\sum_{j=1}^{N_i} C(|\boldsymbol{\xi}_{ij}|)(\psi_x[\boldsymbol{x}_i, l-2]k_{i,xx}^{\text{inv}} + \psi_\tau[\boldsymbol{x}_i, l-2]k_{i,yx}^{\text{inv}})\xi_x V_j \\
&+ \frac{\Delta t}{\rho}\gamma_y\sum_{j=1}^{N_i} C(|\boldsymbol{\xi}_{ij}|)(\psi_x[\boldsymbol{x}_j, l-2]k_{j,xx}^{\text{inv}} + \psi_\tau[\boldsymbol{x}_j, l-2]k_{j,yx}^{\text{inv}})\xi_x V_j \\
&+ \frac{\Delta t}{\rho}\sum_{j=1}^{N_i} C(|\boldsymbol{\xi}_{ij}|)(\psi_x[\boldsymbol{x}_i, l-1]k_{i,xy}^{\text{inv}} + \psi_\tau[\boldsymbol{x}_i, l-1]k_{i,yy}^{\text{inv}})\xi_y V_j \\
&+ \frac{\Delta t}{\rho}\sum_{j=1}^{N_i} C(|\boldsymbol{\xi}_{ij}|)(\psi_x[\boldsymbol{x}_j, l-1]k_{j,xy}^{\text{inv}} + \psi_\tau[\boldsymbol{x}_j, l-1]k_{j,yy}^{\text{inv}})\xi_y V_j \\
&+ \frac{\Delta t}{\rho}\gamma_x\sum_{j=1}^{N_i} C(|\boldsymbol{\xi}_{ij}|)(\psi_x[\boldsymbol{x}_i, l-2]k_{i,xy}^{\text{inv}} + \psi_\tau[\boldsymbol{x}_i, l-2]k_{i,yy}^{\text{inv}})\xi_y V_j \\
&+ \frac{\Delta t}{\rho}\gamma_x\sum_{j=1}^{N_i} C(|\boldsymbol{\xi}_{ij}|)(\psi_x[\boldsymbol{x}_j, l-2]k_{j,xy}^{\text{inv}} + \psi_\tau[\boldsymbol{x}_j, l-2]k_{j,yy}^{\text{inv}})\xi_y V_j, \quad (2\text{-}32)
\end{aligned}$$

where V_j is the volume of node j, N_i is the number of nodes in the neighborhood of node i, and $\boldsymbol{\xi}_{ij} = \boldsymbol{x}_j - \boldsymbol{x}_i$.

3. Results

The PML was tested on two types of problems, first a wave propagation problem, to demonstrate the effectiveness of the PML, and second a crack propagation problem.

3A. ***Wave propagation.*** The PML was first tested on a wave propagation problem with PML boundary layers and a Gaussian distribution as an initial condition. Specifically, the x-directed displacement was set to

$$u_x(\boldsymbol{x}, t = 0) = e^{-200|\boldsymbol{x}-\boldsymbol{p}_{\text{mid}}|^2}, \tag{3-1}$$

where $\boldsymbol{p}_{\text{mid}}$ is the midpoint of the region, which in this example was defined as $0 \le x,\ y \le 1$ and discretized with $\Delta x = \Delta y = 0.01$ m. The Young's modulus for the region was set to 1 Pa, the Poisson's ratio was $\frac{1}{4}$, and the density was $1\,\text{kg/m}^3$. The PML region was defined as the 0.3 m border around the $1\text{ m} \times 1\text{ m}$ region and used a Gaussian ramp with a width of 0.2 m, finally reaching a maximum of $50\,\text{s}^{-1}$ for the remaining 0.1 m. For the Gaussian kernel, a horizon size of $\delta = 1.1\Delta x$ was used, and for the Heaviside kernel, a horizon of $\delta = 3.1\Delta x$ was used. The kernel constant c in (2-4) and (2-5) is set to 1 throughout.

The simulation was run with both the Heaviside and Gaussian kernels, with the total strain energy shown in Figure 2. The Gaussian kernel (the dotted line) shows the largest drop in energy, reaching a minimum of 5.6×10^{-7}, and the Heaviside kernel (the dashed line) decreases to $1. \times 10^{-4}$. A bounded simulation is shown for reference (the solid line), which used a fixed displacement boundary condition and the Gaussian kernel. Figure 3 shows a waterfall plot of the x-directed displacement along the $y = 0.5$ line for the Gaussian kernel with the PML function ϕ_x shown in gray on the far end of the plot (corresponding to $t = 1$ s). Figure 4 shows the absolute value of the x-directed displacement at the edge of the PML region, in simulations terminated by a PML and with a fixed boundary condition. The wave

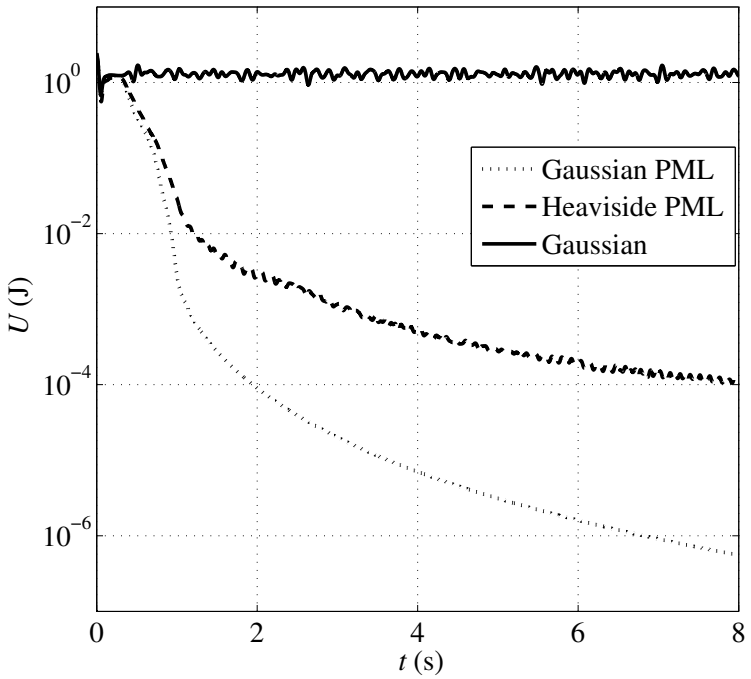

Figure 2. Total strain energy in a simulation terminated by a PML.

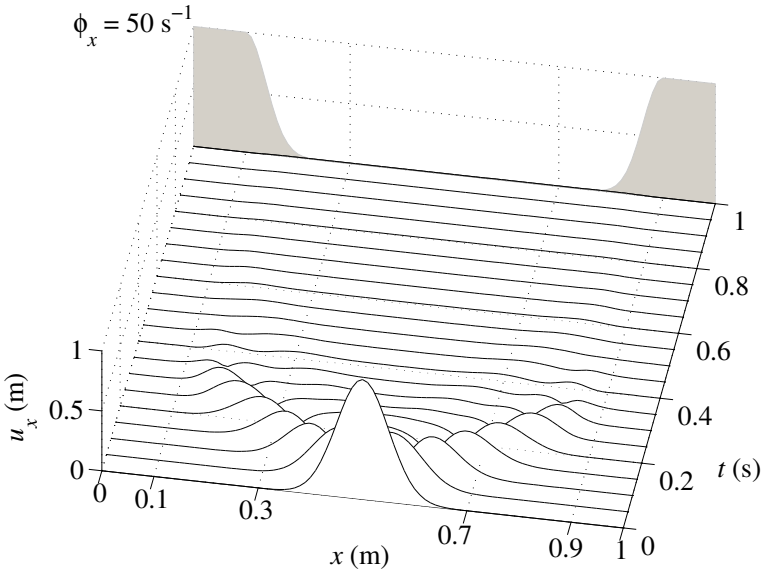

Figure 3. The x-directed displacement at $y = 0.5\,\mathrm{m}$, terminated by a PML.

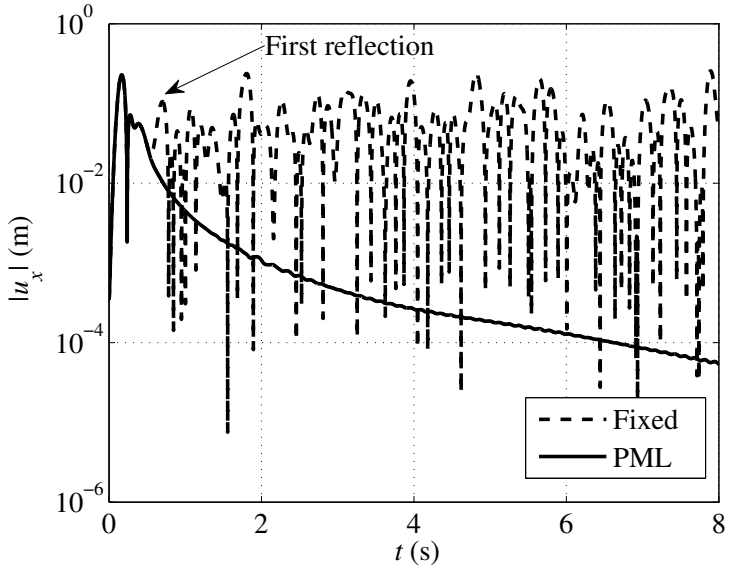

Figure 4. The x-directed displacement at $x = 0.3$, $y = 0.5\,\mathrm{m}$. The solid line shows results terminated by a PML, and the dashed line used a fixed boundary condition.

is absorbed at the boundary with minimal reflections: as can be seen, the plots align for a time, and where they deviate (indicating a reflection from the hard boundary), the PML simulation remains in decay.

For verification, the method was compared with an exact analytical solution. Consider a cylindrically symmetric wave propagating in an infinite elastic medium with the same constitutive parameters as the above example, and with an initial condition given by

$$u_0(r) = b\left(\frac{r}{a}\right)\left[1 + \left(\frac{r}{a}\right)^2\right]^{-3/2}, \tag{3-2}$$

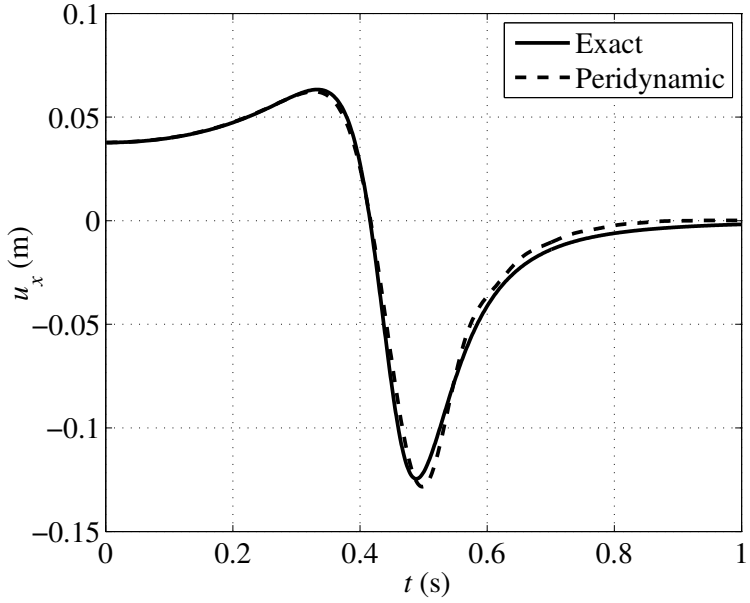

Figure 5. The x-directed displacement at $x = 0.5$, $y = 0$ m. The solid line shows the exact solution and the dashed line results terminated by a PML.

where here we take $b = 1$ and $a = 0.1$. The exact solution is given by [Eringen and Suhubi 1975]

$$u(r,t) = \frac{br}{\sqrt{2}aR^6}\sqrt{R^2+\alpha}(2\alpha - R^2), \quad \alpha = 1 + \frac{r^2 - c^2t^2}{a^2}, \quad R^2 = \sqrt{\alpha^2 + \frac{4c^2t^2}{a^2}}, \tag{3-3}$$

where c is the longitudinal wave speed. This problem was simulated in a two-dimensional region, 2 m $\times$ 2 m and $\Delta x = \Delta y = 0.01$ m, terminated by a PML with the same dimensions and magnitude as the above problem. The Gaussian kernel was used with a horizon size of $\delta = 0.75\Delta x$, with an actual cutoff of 0.028 m. The results are shown in Figure 5, with the exact solution shown as the solid line and the peridynamic solution shown as the dashed line. The peridynamic solution shows good agreement with the exact solution and minimal reflections from the PML boundary.

3B. ***Crack propagation.*** Crack propagation in a half-space can be useful for modeling physical phenomena such as indentation experiments. As an example, we model such a problem as a body force applied to a finite region with small precracks in a region terminated on three sides with PMLs. One addition to the algorithm for this problem was a drag term, used to reduce noise. For crack problems with a sudden force application, noise and oscillations can cause hot spots and undesirable cracking. To remedy this, a drag term can be added to smooth oscillations, by adjusting the nodal velocity as

$$\boldsymbol{v}^*[\boldsymbol{x}_i, l] = (1 - D)\boldsymbol{v}[\boldsymbol{x}_i, l] + \frac{D}{N_b}\sum_{j=1}^{N_b}\boldsymbol{v}[\boldsymbol{x}_j, l], \tag{3-4}$$

where D is the drag coefficient and N_b is the remaining number of bonds in the family of node n [Becker and Lucas 2011].

An absorbing boundary ensures that no reflections from the boundaries interfere with the crack propagation, possibly causing it to deviate. Figure 6 gives a schematic of the problem: the extent of the

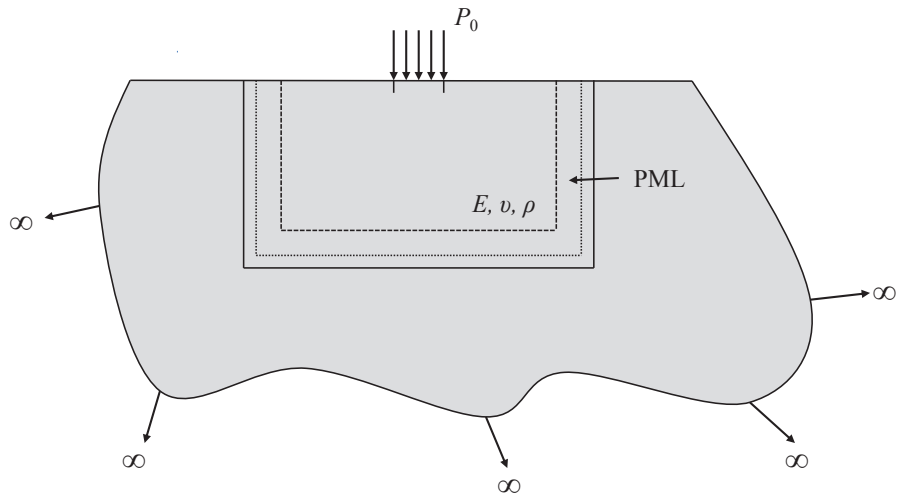

Figure 6. Schematic diagram of the problem for crack propagation in a half-space.

computation region is designated by the solid line, the PML ramp begins at the dashed line, and the PML plateaus at the dotted line. The computational region was 70 mm wide and 35.25 mm high, the PML region began at 15 mm from each edge (except the top) and peaked at 5 mm to a value of $5 \times 10^6\ \mathrm{s}^{-1}$. The node spacing was 0.496 mm and the time step size was 1 ns. For material values, the density was $2235\ \mathrm{kg/m}^3$, the Young's modulus was 65 GPa, the Poisson's ratio was 0.2, and the fracture criteria used a fracture energy of $204\ \mathrm{J/m}^2$. The failure criteria used in this simulation was bond-based, that is, a bond failed if it was stretched past a given limit, determined by the fracture energy [Ha and Bobaru 2010]. The maximum relative bond stretch was then 2.971×10^{-3}. The load was applied across a 10 mm region, centered at the top surface, with precracks on each edge with a length of two nodes or 0.993 mm. The simulation was run for a total of 10 μs, and the cracks were measured manually from the edge of the precracks to the extent of the damaged area.

Figure 7 shows a result which had an applied load of 250 N, yielding a 2.11 mm crack. Figure 8 shows a close-up of the damaged area from Figure 7. As can be seen, the crack extends three nodes down and

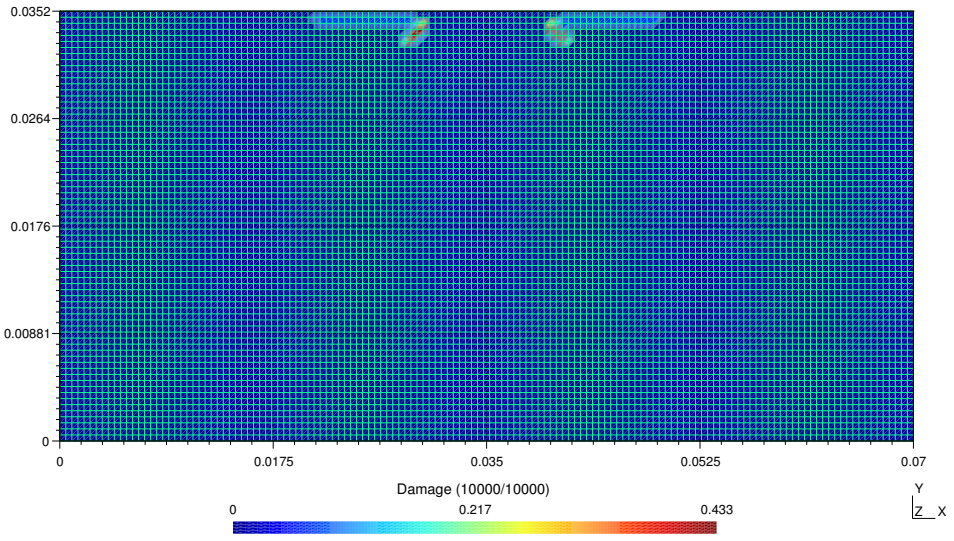

Figure 7. Damage map resulting from a 250 N applied load after 10 μs.

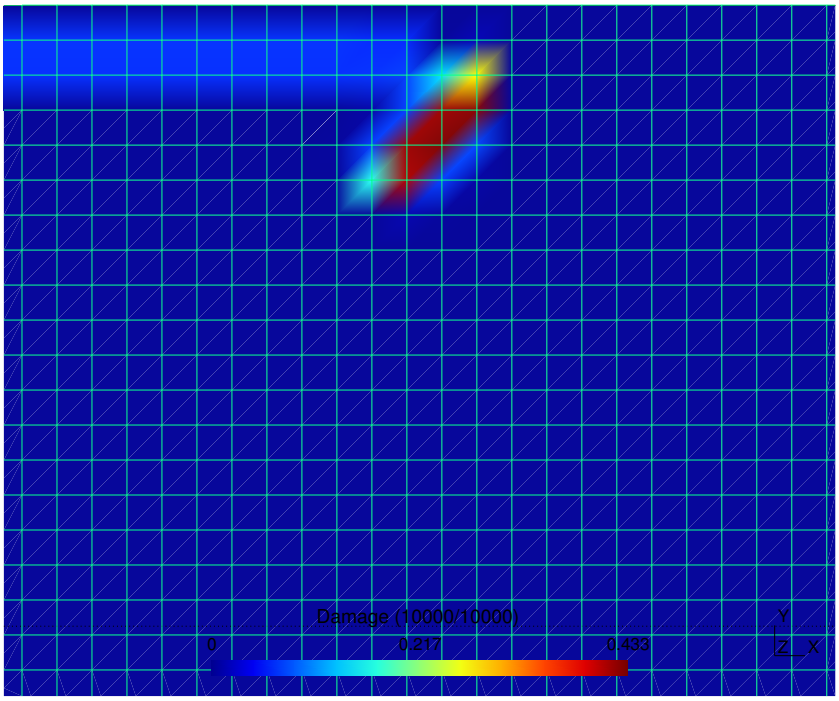

Figure 8. Close-up of damage map from Figure 7.

three nodes across. Finally, the applied load was varied between 140 N and 500 N, with the distance between the crack tips (the crack separation) versus the applied load shown as the dots in Figure 9. A curve, shown as the solid line in Figure 9, was fit using the form

$$d = Ap^s + B, \tag{3-5}$$

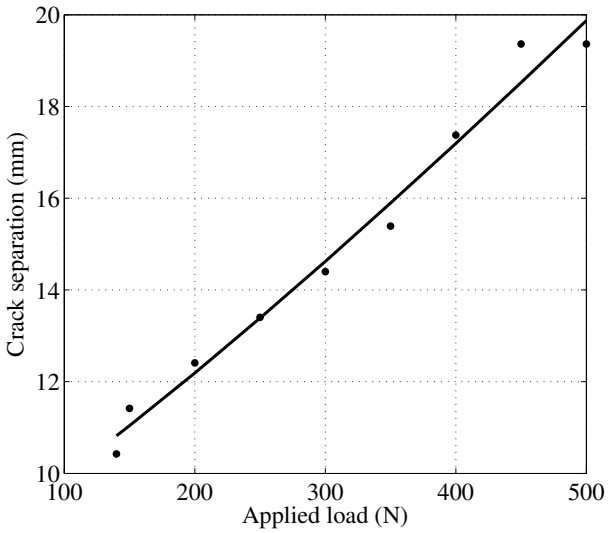

Figure 9. Crack separation versus applied force for indentation into an elastic half-space. Dots represent data points from the peridynamic simulation and the solid line is a curve fit.

where d is the crack tip separation distance, p is the applied load, and $A = 8.49 \times 10^{-3}\,\mathrm{mm/N}^s$, $s = 1.16$ and $B = 8.15\,\mathrm{mm}$ were determined using least squares. The norm of the residual for the curve fit was 1.65×10^{-6}.

4. Conclusions

A perfectly matched layer (PML) was applied to peridynamics in two dimensions, allowing for the simulation of infinite regions. State-based peridynamics was used as more flexible constitutive relations are necessary to implement a perfectly matched layer, essentially an artificial anisotropic absorbing material. Standard discretization techniques were used: one-point integration and point-matching for the spatial discretization and forward Euler for the temporal discretization. Results show that the PML absorbs incoming waves and results in minimal reflections at the boundary between the absorbing layer and the computational region. A Gaussian function was used as a ramp to avoid these numerical reflections. Finally, a crack propagation problem was simulated in a half-space, modeling indentation problems. A three-dimensional implementation of the method would be straightforward, following an identical procedure for the peridynamics and PML formulation.

References

[Alles and van Dongen 2009] E. J. Alles and K. W. A. van Dongen, "Frequency domain perfectly matched layers for acoustic scattering integral equation problems", pp. 1610–1613 in *2009 IEEE International Ultrasonics Symposium* (Rome, 2009), edited by M. P. Yuhas, IEEE, Piscataway, NJ, 2009.

[Becker and Lucas 2011] R. Becker and R. J. Lucas, "An assessment of peridynamics for pre and post failure deformation", Technical report ARL-TR-5811, U.S. Army Research Laboratory, Aberdeen, MD, November 2011, Available at http://www.dtic.mil/cgi-bin/GetTRDoc?AD=ADA553977.

[Berenger 1994] J.-P. Berenger, "A perfectly matched layer for the absorption of electromagnetic waves", *J. Comput. Phys.* **114**:2 (1994), 185–200.

[Bobaru 2007] F. Bobaru, "Influence of van der Waals forces on increasing the strength and toughness in dynamic fracture of nanofibre networks: a peridynamic approach", *Model. Simul. Mater. Sci. Eng.* **15**:5 (2007), 397–417.

[Bobaru and Duangpanya 2010] F. Bobaru and M. Duangpanya, "The peridynamic formulation for transient heat conduction", *Int. J. Heat Mass Transf.* **53**:19-20 (2010), 4047–4059.

[Bobaru et al. 2009] F. Bobaru, M. Yang, L. F. Alves, S. A. Silling, E. Askari, and J. Xu, "Convergence, adaptive refinement, and scaling in 1D peridynamics", *Int. J. Numer. Methods Eng.* **77**:6 (2009), 852–877.

[Chew and Liu 1996] W. C. Chew and Q. H. Liu, "Perfectly matched layers for elastodynamics: a new absorbing boundary condition", *J. Comput. Acoust.* **4**:4 (1996), 341–359.

[Chew and Weedon 1994] W. C. Chew and W. H. Weedon, "A 3D perfectly matched medium from modified Maxwell's equations with stretched coordinates", *Microw. Opt. Tech. Lett.* **7**:13 (1994), 599–604.

[Demmie and Silling 2007] P. N. Demmie and S. A. Silling, "An approach to modeling extreme loading of structures using peridynamics", *J. Mech. Mater. Struct.* **2**:10 (2007), 1921–1945.

[Dong et al. 2004] X. T. Dong, X. S. Rao, Y. B. Gan, B. Guo, and W. Y. Yin, "Perfectly matched layer-absorbing boundary condition for left-handed materials", *IEEE Microw. Wirel. Compon. Lett.* **14**:6 (2004), 301–303.

[Du et al. 2012] Q. Du, M. D. Gunzburger, R. B. Lehoucq, and K. Zhou, "A nonlocal vector calculus, nonlocal volume-constrained problems, and nonlocal balance laws", *Math. Models Methods Appl. Sci.* (2012). Accepted for publication. Preprint SAND2010-8353J available from Sandia National Laboratories, 2010.

[Emmrich and Weckner 2006] E. Emmrich and O. Weckner, "The peridynamic model in non-local elasticity theory", *Proc. Appl. Math. Mech.* **6**:1 (2006), 155–156.

[Emmrich and Weckner 2007] E. Emmrich and O. Weckner, "The peridynamic equation and its spatial discretisation", *Math. Model. Anal.* **12**:1 (2007), 17–27.

[Eringen and Suhubi 1975] A. C. Eringen and E. S. Suhubi, *Elastodynamics*, Academic Press, New York, 1975.

[Festa and Nielsen 2003] G. Festa and S. Nielsen, "PML absorbing boundaries", *Bull. Seismol. Soc. Am.* **93**:2 (2003), 891–903.

[Foster et al. 2010] J. T. Foster, S. A. Silling, and W. W. Chen, "Viscoplasticity using peridynamics", *Int. J. Numer. Methods Eng.* **81**:10 (2010), 1242–1258.

[Gerstle et al. 2005] W. Gerstle, N. Sau, and S. A. Silling, "Peridynamic modeling of plain and reinforced concrete structures", pp. 54–88 in *18th International Conference on Structural Mechanics in Reactor Technology* (Beijing, 2005), edited by Y. Zhou, Atomic Energy Press, Beijing, 2005.

[Gerstle et al. 2008] W. Gerstle, S. A. Silling, D. Read, V. Tewary, and R. Lehoucq, "Peridynamic simulation of electromigration", *Comput. Mater. Continua* **8**:2 (2008), 75–92.

[Gerstle et al. 2011] W. Gerstle, N. Sau, and E. Aguilera, "Micropolar peridynamic constitutive model for concrete", pp. 1–8 in *19th International Conference on Structural Mechanics in Reactor Technology* (Toronto, ON, 2007), edited by V. C. Matzen, Elsevier, Amsterdam, 2011.

[Ha and Bobaru 2010] Y. D. Ha and F. Bobaru, "Studies of dynamic crack propagation and crack branching with peridynamics", *Int. J. Fract.* **162**:1-2 (2010), 229–244.

[Johnson 2010] S. G. Johnson, "Notes on perfectly matched layers", 2010, Available at http://math.mit.edu/~stevenj/18.369/pml.pdf.

[Kilic et al. 2009] B. Kilic, A. Agwai, and E. Madenci, "Peridynamic theory for progressive damage prediction in center-cracked composite laminates", *Compos. Struct.* **90**:2 (2009), 141–151.

[Liu and Tao 1997] Q.-H. Liu and J.-P. Tao, "The perfectly matched layer for acoustic waves in absorptive media", *J. Acoust. Soc. Am.* **102**:4 (1997), 2072–2082.

[Lubich 1988a] C. Lubich, "Convolution quadrature and discretized operational calculus, I", *Numer. Math.* **52**:2 (1988), 129–145.

[Lubich 1988b] C. Lubich, "Convolution quadrature and discretized operational calculus, II", *Numer. Math.* **52**:4 (1988), 413–425.

[Malvern 1969] L. E. Malvern, *Introduction to the mechanics of a continuous medium*, Prentice-Hall, Englewood Cliffs, NJ, 1969.

[Parks et al. 2008] M. L. Parks, P. Seleson, S. J. Plimpton, R. B. Lehoucq, and S. A. Silling, "Peridynamics with LAMMPS: a user guide", Technical report SAND2008-0135, Sandia National Laboratories, Albuquerque, NM, July 2008. Superseded by SAND2010-5549, version 0.2 Beta, August 2010.

[Pissoort and Olyslager 2003] D. Pissoort and F. Olyslager, "Termination of periodic waveguides by PMLs in time-harmonic integral equation-like techniques", *IEEE Antenn. Wirel. Propag. Lett.* **2**:20 (2003), 281–284.

[Pissoort et al. 2005] D. Pissoort, D. Vande Ginste, and F. Olyslager, "Including PML-based absorbing boundary conditions in the MLFMA", *IEEE Antenn. Wirel. Propag. Lett.* **4**:1 (2005), 312–315.

[Proakis and Manolakis 1996] J. G. Proakis and D. G. Manolakis, *Digital signal processing: principles, algorithms, and applications*, Prentice-Hall, Upper Saddle River, NJ, 1996.

[Silling 2000] S. A. Silling, "Reformulation of elasticity theory for discontinuities and long-range forces", *J. Mech. Phys. Solids* **48**:1 (2000), 175–209.

[Silling and Askari 2005] S. A. Silling and E. Askari, "A meshfree method based on the peridynamic model of solid mechanics", *Comput. Struct.* **83**:17-18 (2005), 1526–1535.

[Silling et al. 2007] S. A. Silling, M. Epton, O. Weckner, J. Xu, and E. Askari, "Peridynamic states and constitutive modeling", *J. Elasticity* **88**:2 (2007), 151–184.

[Teixeira and Chew 1998] F. L. Teixeira and W. C. Chew, "A general approach to extend Berenger's absorbing boundary condition to anisotropic and dispersive media", *IEEE Trans. Antenn. Propag.* **46**:9 (1998), 1386–1387.

[Uno et al. 1997] T. Uno, Y. He, and S. Adachi, "Perfectly matched layer absorbing boundary condition for dispersive medium", *IEEE Microw. Guided Wave Lett.* **7**:9 (1997), 264–266.

[Wang et al. 2008] X. Wang, R. A. Wildman, D. S. Weile, and P. Monk, "A finite difference delay modeling approach to the discretization of the time domain integral equations of electromagnetics", *IEEE Trans. Antenn. Propag.* **56**:8, part 1 (2008), 2442–2452.

[Weckner and Abeyaratne 2005] O. Weckner and R. Abeyaratne, "The effect of long-range forces on the dynamics of a bar", *J. Mech. Phys. Solids* **53**:3 (2005), 705–728.

[Weckner et al. 2009] O. Weckner, G. Brunk, M. A. Epton, S. A. Silling, and E. Askari, "Green's functions in non-local three-dimensional linear elasticity", *Proc. R. Soc. Lond. A* **465**:2111 (2009), 3463–3487.

[Wildman and Gazonas 2011] R. A. Wildman and G. A. Gazonas, "A perfectly matched layer for peridynamics in one dimension", Technical report ARL-TR-5626, U.S. Army Research Laboratory, Aberdeen, MD, 2011.

Received 2 Apr 2012. Revised 17 Jul 2012. Accepted 18 Jul 2012.

RAYMOND A. WILDMAN: raymond.a.wildman.civ@mail.mil
Weapons and Materials Research Directorate, U.S. Army Research Laboratory, Attn: RDRL-WMM-B, Aberdeen Proving Ground, MD 21005, United States

GEORGE A. GAZONAS: george.a.gazonas.civ@mail.mil
Weapons and Materials Research Directorate, U.S. Army Research Laboratory, ATTN: RDRL-WMM-B, Aberdeen Proving Ground, MD 21005, United States

Shock Hugoniot Calculations of Polymers using Quantum Mechanics and Molecular Dynamics

Tanya L. Chantawansri, Timothy W. Sirk, Edward F. C. Byrd, Jan W. Andzelm, and Betsy M. Rice

The Journal of Chemical Physics, 137 (2012)

THE JOURNAL OF CHEMICAL PHYSICS **137**, 204901 (2012)

Shock Hugoniot calculations of polymers using quantum mechanics and molecular dynamics

Tanya L. Chantawansri, Timothy W. Sirk, Edward F. C. Byrd, Jan W. Andzelm, and Betsy M. Rice
U.S. Army Research Laboratory, Aberdeen Proving Ground, Maryland 21005, USA

(Received 13 August 2012; accepted 22 October 2012; published online 26 November 2012)

Using quantum mechanics (QM) and classical force-field based molecular dynamics (FF), we have calculated the principle shock Hugoniot curves for numerous amorphous polymers including poly[methyl methacrylate] (PMMA), poly[styrene], polycarbonate, as well as both the amorphous and crystalline forms of poly[ethylene]. In the FF calculations, we considered a non-reactive force field (i.e., polymer consistent FF). The QM calculations were performed with density functional theory (DFT) using dispersion corrected atom centered pseudopotentials. Overall, results obtained by DFT show much better agreement with available experimental data than classical force fields. In particular, DFT calculated Hugoniot curves for PMMA up to 74 GPa are in very good agreement with experimental data, where a preliminary study of chain fracture and association was also performed. Structure analysis calculations of the radius of gyration and carbon-carbon radial distribution function were also carried out to elucidate contraction of the polymer chains with increasing pressure. [http://dx.doi.org/10.1063/1.4767394]

I. INTRODUCTION

The behavior of polymers under extreme conditions (high pressure and temperature) is of interest for both civilian and military applications, such as polymer-bonded explosives, coatings, adhesives, light-weight armor for both military and civilian police forces, civilian protective equipment such as sports equipment, and automobile structural materials. In order to improve the performance of these materials, insight into the behavior of these materials under high pressure is necessary. Although the material properties and response at extreme conditions can be determined through shock experiments, results are not easily obtained with available instrumentation because of difficulties in traversing a large range of pressures (up to hundreds of gigapascals [GPa]) and temperatures (thousands of Kelvin). In addition, non-adiabatic, non-equilibrium behavior behind a shock front occurs at extremely short time- and length scales (nanoscale), thus posing problems in characterizing the material using current experimental capabilities. To further understand shocked systems, simulation methods such as quantum mechanics (QM) and force field (FF) based molecular dynamics (MD) can be used to provide insight into atomic-level phenomena that is not amenable to experimentation, specifically by calculation of the shock Hugoniot of the material. The shock Hugoniot is the locus of thermodynamic states accessible by shock loading from a given thermodynamic initial condition.

FF and QM (using density functional theory (DFT)) calculations of shock Hugoniot curves for polymers in the literature have highlighted the potential of simulation methods as a valid way to predict material behavior under extreme conditions. Mattsson and co-workers[1,2] calculated curves for two polymeric systems polyethylene (PE) and poly(4-methyl-1-pentene) using both FF and DFT for pressures up to 350 and 200 GPa, respectively. For their FF simulations, they considered both reactive (ReaxFF,[3] AIREBO[4]) and non-reactive (OPLS,[5] exp-6[6,7]) force fields, while they used the Armiento-Mattsson (AM05)[8] functional for their DFT simulations. Comparing the FF calculations, they found that both polymers were well described by the exp-6 force field and ReaxFF, where the former was accurate for weak shocks and the latter for a larger range of shock. For very strong shocks up to 80 GPa, only the DFT simulations were able to capture the correct behavior. Wang *et al.*[9] performed PW91 DFT simulations using the projector augmented wave pseudopotential for polystyrene (PS) for pressures between 22 and 790 GPa; where they observed qualitatively good agreement with experimental data. Grujicic *et al.*[10] used the condensed-phase optimized molecular potentials for atomic simulation studies (COMPASS)[11] force field in nonequilibrium MD to study the generation and propagation of shock waves, where shock Hugoniot relations were determined for polyurea in reasonable agreement with experiment. Hooper and co-workers[12] calculated the Hugoniot curves for the following polymer binders: poly(dimethylsiloxane), 1,4-poly(butadiene), and Estane® using FF simulations utilizing a quantum-chemistry-based potential, where they observed good agreement at relatively high pressures. Even so, these studies are limited to only a few polymers with most relying on classical force fields. We intend to expand investigations using both a DFT approach and a polymer derived force field in order to further elucidate the high pressure behavior of polymeric materials.

QM calculations can be performed using DFT where the electronic structure of a many-body system is determined through an electronic density instead of a wave function. Although conventional DFT has been largely successful in modeling strongly interacting systems, it is unable

to fully capture van der Waals (vdW) interactions due to an inadequate description of dispersion.[13,14] Various methods exist to remedy this deficiency, including semiempirical C_6/R^6 corrections,[15–19] non-local vdW corrected functional,[20,21] highly parameterized DFT functional,[22] the symmetry-adapted perturbation theory parameterized dispersionless DFT method[23,24] and the dispersion corrected atom centered pseudopotentials (DCACPs), in which adjustments are made to the pseudopotential to correct for dispersion.[25,26] In our study, we use DCACPs[26] which have been shown to be applicable to a diverse range of systems and allows for the treatment of larger periodic systems than those obtainable by more rigorous wave function calculations.[27–31] The atomic pseudopotentials consist of both a local and a high-order angular momentum dependent nonlocal term that act on different length scales, where the nonlocal term is parameterized using highly accurate wave function based methods.

Although force-field based methods allow for much larger systems sizes than QM methods, the accuracy of the results are highly dependent on the potential functions acting between atoms. Thus, it is important to determine the quality and applicability of the force field. Therefore, in order to properly depict the material properties of materials subjected to the extreme temperatures and pressures corresponding to shock conditions, force fields must also be accurate for both the shocked and unshocked states. This will be one of the main goals of this paper, i.e., to determine the pressures for which the empirical force fields adequately represent the systems of interest. In addition, during shock experiments bonds between atoms in the material may break, and the formation of new reaction products can occur. This behavior will require the use of a reactive potential whose parameterization is currently an area of interest.[3,32] Since we only considered low to moderate pressures and compressions, we did not consider a reactive force field in this paper, which are 50-100 times more expensive than non-reactive force fields.[33] However, preliminary results using a reactive force field can be found in Ref. 34.

Due to limitations associated with both DFT and FF, there are distinct advantages and disadvantages that must be assessed in respect to the Hugoniot calculations. To assess the validity of both simulation methods for polymers, we have simulated the shock compression of four different polymers using DFT and FF: poly[methyl methacrylate] (PMMA), PE, PS, and polycarbonate (PC). Both amorphous and crystalline PE were considered. DFT simulations were performed with the CP2K[35] program using the BLYP DFT-GGA potential with DCACPs. In our FF simulations, we used the large-scale atomic/molecular massively parallel simulator (LAMMPS)[36] program with the non-reactive polymer consistent force field (PCFF) with COMPASS[11] charges.

II. COMPUTATIONAL METHODS

A. Hugoniot calculation using the Erpenbeck approach

Hugoniot state calculations can be performed through several types of simulations, including one method that directly calculates material properties behind the shock discontinuity in a shock wave simulation.[37] Another method introduced by Erpenbeck[38,39] involves generating an equation of state for the subsequent evaluation of Hugoniot conservation relations. An equilibrium uniaxial Hugoniostat method can also be employed that uses equations of motion which restrain the system during the simulation such that the time averaged properties correspond to those on the Hugoniot curve.[40] Finally, a technique based on the Navier-Stokes equations for compressible flow, the multiscale shock-wave molecular dynamics (MSST) technique, follows a Lagrangian point through the shock wave to calculate shock properties.[41]

We evaluated the Hugoniot points through the procedure developed by Erpenbeck,[38] which involves performing several constant particle, volume, and temperature (*NVT*) simulations at multiple temperatures for several compressed structures. The Hugoniot curve consists of the set of (*PVT*) points for which the Hugoniot expression

$$H_g = E - E_o + 1/2(P + P_o)(V - V_o) \quad (1)$$

is zero. This Hugoniot equation is derived from mass, momentum, and energy balance equations in addition to the definition of enthalpy, where details of the derivation can be found in Fickett *et al.*[42] In this equation, E is the specific internal energy (sum of the kinetic and potential energies), P is the pressure, and $V = 1/\rho$ is the specific volume (ρ is the density). The subscript "o" refers to the quantity in the initial unshocked reference state under ambient conditions. The Hugoniot points were calculated through several simulations, where a series of *NVT* simulations were performed over a range of temperatures at a fixed specific volume after the system is annealed and relaxed. To obtain systems at different specific volumes, the polymer was compressed isotropically from ambient to an elevated pressure and allowed to relax under constant temperature and pressure (*NPT*) at 298 K. Using the relaxed structure obtained at the desired pressure, we performed a series of *NVT* simulations. This was performed in two different ways. In our DFT calculations, various *NVT* simulations were performed in parallel at different temperatures, while in the FF calculations the temperature was incrementally increased after a prescribed simulation time (i.e., temperature scan). After the *NVT* simulation, the Hugoniot function (Eq. (1)) was evaluated at each temperature; this produces a series of equation-of-state points as a function of temperature for each specific volume. A linear interpolation of these points was used to determine the Hugoniot temperature, the point at which the function is zero. Similarly, a linear interpolation of the corresponding pressures as a function of temperature was used to determine the Hugoniot pressure, the pressure corresponding to the Hugoniot temperature. In these calculations, only the two points which bracket the Hugoniot temperature and pressure were used to calculate the linear fit.

Experimentalists often report shock Hugoniot data in terms of the shock velocity (U_{st}) and particle or mass velocity (U_{pt}). To obtain these values from the P and V data points, the following equations can be used:

$$U_{st} = \sqrt{\frac{V_o(P - P_o)}{1 - V/V_o}}$$

and

$$U_{pt} = \sqrt{V_o(P - P_o)(1 - V/V_o)}. \quad (3)$$

The experimental data can be converted into P-V data by rearranging Eqs. (2) and (3)

$$V = \frac{V_o(U_{st} - U_{pt})}{U_{st}} \quad (4)$$

and

$$P = P_o + \frac{U_{st}U_{pt}}{V_o}. \quad (5)$$

B. Sensitivity of the Hugoniot calculation

The effect of varying simulation time, system size, and chain size on the Hugoniot curve was extensively tested using the FF method for a model system of PMMA and are published in Refs. 34 and 43. In summary, we determined no significant difference in the Hugoniot curves obtained for a system with approximately 5000 or 50 000 atoms, where the smaller system was composed of shorter (45 vs. 100 repeat units) and fewer (8 vs. 34) chains.

The Hugoniot curve was also found to be relatively insensitive to the simulation time for the reference state, where values of the reference state after 10 ns or 100 ps of *NPT* simulation do not noticeably change the shape of the curve. In addition, we also determined if it was necessary to further relax the reference state and the points around the Hugoniot states that are used to interpolate the Hugoniot temperature and pressure. Changes in the Hugoniot curves calculations were explored by performing an additional 10 ns of *NVT* simulations; these showed that additional simulation time does not lead to statistically significant differences in the Hugoniot curves.

Similar results with respect to system size and simulation time were also verified for other amorphous polymers. In addition, calculations were found to be relatively insensitive to the number of repeat units in the chain. Although the concept of chain connectivity was found to be important since we observed a clear difference in the curve when PMMA was modeled as a liquid (1 monomer), only a minimal number of monomers are needed to represent the polymer chain. For instance, we observed that a chain of 4 monomers was able to reproduce the Hugoniot curves calculated using chains of 45 and 100 monomers. Even so, this system composed of 4 monomer chains does not exhibit Gaussian behavior, which can be checked by calculating $\langle R\rangle^2/\langle R_g\rangle^2$, where R and R_g are the polymer's end-to-end distance and radius of gyration, respectively, and the brackets indicate an average over all chains in the simulation box.[44] A value of 6 indicates Gaussian behavior. The reference state for the 4-monomer chain system had a $\langle R\rangle^2/\langle R_g\rangle^2 \sim 7.5$, while the larger 100-monomer chain reference system exhibited a value of $\langle R\rangle^2/\langle R_g\rangle^2 \sim 6.2$. This finding allows us to use oligomeric chains, which do not exhibit the Gaussian behavior of an ideal chain, to approximate polymer chains for calculations of the shock Hugoniot. This observation is especially important for our DFT simulations, where smaller systems are necessary due to the additional computational cost of the method. It is also important to note that the amorphous cell method[45] used to produce the initial configurations did produce chains configurations that were near Gaussian, where the larger 100-monomer system exhibited $\langle R\rangle^2/\langle R_g\rangle^2 \sim 6.3$, while the smaller 4-monomer system had a $\langle R\rangle^2/\langle R_g\rangle^2 \sim 6.9$. A description of the amorphous cell method is given in Sec. II C.

TABLE I. Polymer density as a function of the kinetic energy cutoff for BLYP DFT-GGA with DCACPs. Experimental values from PMMA, PS, PC taken from Ref. 48. Experimental values of PE taken from Ref. 49.

Kinetic energy cutoff (Ry)	Density (g/cm^3)				
	PMMA	PS	PC	Amorphous PE	Crystalline PE
300	1.076	1.021	1.094	0.819	1.062
600	1.078	1.021	1.087	0.82	1.062
900	1.066	1.024	1.089	0.818	1.061
Experimental	1.18	1.05	1.20	0.853	1.004

C. Simulation details: Density functional theory

QM simulations using DFT were performed using CP2K.[35] The BLYP DFT-GGA[46,47] potential was used together with the DCACPs.[26] The DFT calculations were performed at the Γ point of the Brillouin zone with Gaussian double-ζ valence basis sets in addition to an auxiliary plane wave basis set with kinetic energy cutoff of 300 Ry. This cutoff was deemed sufficient since increasing the value to 600 and 900 Ry was found to change the density of the polymers of interest by at most 1.4% as seen in Table I. The CP2K default convergence criteria were used for calculations of energies and gradients (i.e., 1E-10).

The three-dimensional periodic simulation cells of the polymers were initially built using the Materials Studio program through the amorphous cell module.[50] This program uses a well established Monte Carlo technique to build an amorphous structure of the polymer followed by the energy minimization of the bulk structure. The polymeric chains are built by using rotational isomeric state theory, which takes into account non-bonded interactions and neighboring chains during construction.[45] Guided by our previous sensitivity analysis with PMMA, every polymer chain was built to contain at least 4 monomer units. The simulation cell for crystalline PE was acquired by producing a supercell of the unit cell obtained through the Materials Studio structural database. This process produces infinite chains of PE. The smallest simulation cell contains a minimum of about 500 atoms, which appears to be the smallest cell possible to allow for about 50% volume reduction and approximate, periodic calculations at the Γ point of the Brillouin zone. Information on each simulation cells are listed in Table II.

Extensive tests were performed using a PS model where the effect of different basis sets, kinetic energy cutoff criteria, optimization, and DFT MD parameters were tested to optimize density. In addition to the BLYP DFT-GGA potential, the PBE[51,52] DFT was also tested together with the DCACP pseudopotential. The basis set was also extended to include polarization functions on hydrogen atoms. We also tested

TABLE II. Information for each simulation cell for DFT simulations.

Polymer	# of atoms in simulation cells	# of chains	# of repeat units per chain
PMMA	496	8	4
PC	1200	6	6
PS	528	8	4
Crystalline PE	1008	24	7
Amorphous PE	500	10	8

the TZVP basis set and a kinetic energy cutoff as large as 1200 Ry. Additionally, simulations were performed using a time step of 0.1 fs and the effect of varying the time constants of the barostat and thermostat were also studied. Using our initial selection of parameters, basis sets, and plane wave cutoff, the calculated density of PS is 1.02 g/cm^3 which is in reasonable agreement with the experimental value of 1.05 g/cm^3. Varying the basis set and other parameters changed the value of the density by at most 1%, indicating a reasonable choice of parameters. It is also worthwhile to mention that the BLYP potential without DCACPs resulted in much smaller density of 0.83 g/cm^3, thus illustrating the critical need for the accurate treatment of van der Waals forces.

The amorphous cells were initially annealed and relaxed using the COMPASS force field under the Discover module of Materials Studio. The simulation cell was then subjected to two to three cycles of minimizations and annealing under constant pressure and temperature conditions where the temperature was increased from 298 K to 600 K. The lowest energy structure was then used in the DFT calculations. The amorphous simulation cells were again annealed in CP2K using a simplified protocol consisting of one optimization and NPT_I procedure (constant temperature and pressure simulation using an isotropic cell). The system was then relaxed for 4 ps under constant volume and temperature conditions to produce the reference values for the Hugoniot calculations. Thermostat and barostat were used with time constants of 50 and 200 fs, respectively, with a time step of 0.5 fs.

Following the Erpenbeck procedure, each optimized polymer unit cell was subjected to an elevated and isotropic pressure. Snapshots of these simulations were taken at various V/V_o values and subsequently used in *NVT* simulations to predict the Hugoniot points as defined in Eq. (1), where values of the E, V, and P at the reference state and at a given T where obtained by averaging the last 0.2 ps. Multiple *NVT* simulations for up to 2 ps were performed at various temperatures that bracket the Hugoniot point. The Hugoniot pressure and temperature were then interpolated from points that bracket the Hugoniot point as mentioned in Sec. I. In the case of very high pressures and temperatures which may lead to bond breaking, the DFT procedure was verified by performing calculations using the unrestricted DFT option of CP2K. The MD step of simulations was also lowered to 0.15 fs, however, those changes do not affect the Hugoniot curves.

D. Simulation details: Force field based

FF simulations were performed using the classical molecular dynamics code LAMMPS.[36] We have interfaced the amorphous polymer builder with LAMMPS using the commercial visualization package materials processes and simulations (MAPS).[53] MAPS was used to create an periodic cell of PMMA, PC, and PS and assign the PCFF force field, where the COMPASS charges were obtained using Materials Studio.[50] As before, the simulation cell for crystalline PE and the amorphous polymers were obtained through the supercell method and the Monte Carlo technique, respectively.

To describe the interactions between atoms, we use PCFF with COMPASS charges. PCFF is a class 2 force field where the nonbonded interactions are composed of a 9-6 Lennard-Jones potential (van der Waals) and a Coulombic pairwise (electrostatic) interaction. Several of the parameters in PCFF are derived through a least-squares fit[54] of *ab initio* data, where many of the nonbonded parameters were taken from the CFF91 force field. These nonbonded parameters were calculated through fitting to molecular crystal data at the ambient state based on energy minimization calculations. Although an improved PCFF force field has been developed for condensed phase applications called COMPASS,[11,55–58] several of the force field parameters are proprietary and are not readily available for use in LAMMPS. COMPASS is an extension based on PCFF derived through both *ab initio* and empirical methods, where the number of molecular classes covered were extended and the nonbonded parameters were re-parameterized. Since a limited number of the COMPASS parameters are published, we utilized its precursor PCFF where the improved atomic partial charges were taken from COMPASS.

In COMPASS, partial charges were derived by least-squares fitting to *ab initio* quantum mechanical data calculated from a training set of model compounds at the Hartree-Fock level with the 6-31G* basis set (HF/6-31G*). These calculations were further scaled using generic factors to correct systematic errors in the HF/6-31G* calculations.[11] To determine if the COMPASS partial charges used in our FF simulations adequately represent our polymers of interest, they are compared to charges calculated using density functional theory with the M06 functional and 6-31G* basis set (M06/6-31G*)[22,59] as implemented in GAUSSIAN 09,[60] where the charges were produced to fit the electrostatic potential at points selected according to the CHarges from Electronic Potentials using a Grid based method (CHelpG) scheme.[60,61] Although this is a simple method to compare charges, we observe good agreement between the COMPASS charges and the calculated partial charges. In addition, we calculated the density of an amorphous cell composed of PS trimers using PCFF with PCFF, COMPASS, and QM charges, where we observe a difference of at most 2%. Since only a minimal difference in the particle charges and density was observed, COMPASS charges were used for our FF calculations.

We used a cutoff of 12 Å for the nonbonded 9-6 Lennard-Jones potential and Coulombic pairwise interactions. The particle-particle particle-mesh method was used to correct for long-range electrostatic interactions with a precision of

TABLE III. Components of polymer simulation cell for FF simulations.

Polymer	# of atoms in simulation cells	# of chains	# of repeat units per chain
PMMA	5416	8	45
PC	4970	10	15
PS	6420	10	40
Crystalline PE	4680	60	13
Amorphous PE	5016	33	25

1.0E-6.[62] Temperature and pressure were controlled using the Nose-Hoover thermostat with a 100 fs coupling constant and an isotropic Nose-Hoover barostat with a 1000 fs coupling constant, respectively. A time step of 1.0 fs was used for all simulations.

Due to the sensitivity study discussed above and in Ref. 43, we only considered systems containing approximately 5000 atoms for our FF calculations. This system size was sufficient to ensure that the shortest perpendicular distance between two faces of the simulation cell was at least twice the maximum cutoff considered, 12 Å. The components of the polymer simulation cell are described in Table III.

All simulations were initially relaxed using energy minimization and annealed through five cycles of heating and to 600 K and cooling to 298 K at a rate of 0.67 ps/K and 0.1656 ps/K, respectively, which were sufficient to converge the potential energy. In addition, values for the reference state (T = 298 K, P = 101 kPa) were obtained from an average of the entire 100 ps *NVT* simulation, which was performed after the minimization and annealing procedure described above and 100 ps of *NPT* simulation. After calculating the reference state, compressed simulation cells were obtained by performing 100 ps *NPT* simulations at elevated pressures. We considered pressures ranging from 2 to 30 GPa in increments of 2 GPa, producing 15 compressed configurations. For each compressed system, a temperature ramp was performed in the *NVT* ensemble at a rate of 0.005 μs/K until the Hugoniot point is bracketed. A slower temperature ramp of 0.015 μs/K was also considered, but the results were not noticeably different.

III. RESULTS

A. Density of the reference state

The calculated DFT densities for the PMMA, PS, PC, amorphous PE, and crystalline PE reference states can be found in Table I and vary 8.8%, 2.8%, 8.8%, 4%, and 5.8%, respectively, from experimental values. The box lengths for the PMMA, PS, PC, and amorphous PE reference states are approximately 17 Å, 18 Å, 24 Å, and 17 Å, respectively. The calculated lattice parameters for the 3 × 4 × 7 crystalline PE supercell are 21.14, 19.14, and 18.23 Å for a, b, and c, respectively, which vary by at most 4.6% from experimental values. The orthorhombic nature of the crystal structure is maintained. In the FF simulations, values of the ambient density were 1.08 g/cm^3, 0.95 g/cm^3, 1.14 g/cm^3, 0.74 g/cm^3, and 0.97 g/cm^3, for PMMA, PS, PC, amorphous PE, and crystalline PE, respectively. The densities for PMMA, PS, PC, amorphous PE, and crystalline PE vary 8.5%, 9.5%, 5%, 13.2%, and 3.4% from experimental values, respectively. The box length for the cubic simulation cell of PMMA, PS, PC, and amorphous PE are 38.25 Å, 41.79 Å, 38.18 Å, and 37.27 Å, respectively. The lattice parameters for the 5 × 6 × 13 supercell of crystalline PE were 37, 29.92, and 33.39 Å for a, b, and c, respectively, where the orthorhombic shape of the crystal structure was maintained. The lattice parameters varied by less than 2% from experimental values. Although the values of density can vary by as much as 8.8% or 13.2% in DFT and FF simulations, the compressive behavior of the material may still be captured.

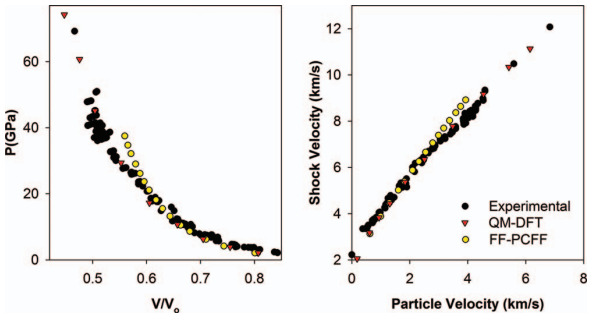

FIG. 1. Hugoniot curves for atactic-PMMA. Experimental data were obtained from Refs. 63 and 64.

B. Comparision of computational and experimental Hugionot curves

DFT and FF simulations were performed to predict the Hugoniot curve for the four polymers, where results are presented in Figures 1–7. For polyethylene we considered the amorphous, crystalline, and a mixture of the two forms. The Hugoniot results are presented in two different representations, as pressure versus the ratio of the volume to the reference volume (V/V_o), and as the shock velocity versus the particle velocity. The predicted values of Hugoniot pressure and the specific volume were expressed as shock and particle velocities using Eqs. (2) and (3).

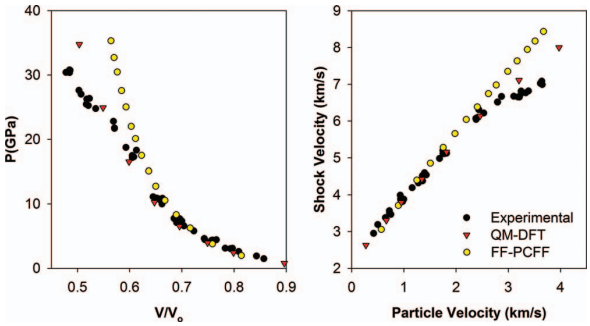

FIG. 2. Hugoniot curves for PC. Experimental data were obtained from Ref. 63.

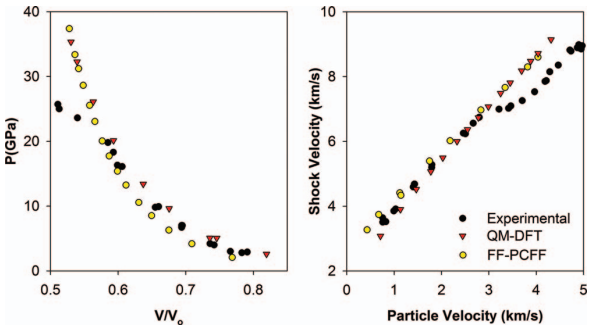

FIG. 3. Hugoniot curve for PS. Experimental data were obtained from Ref. 65.

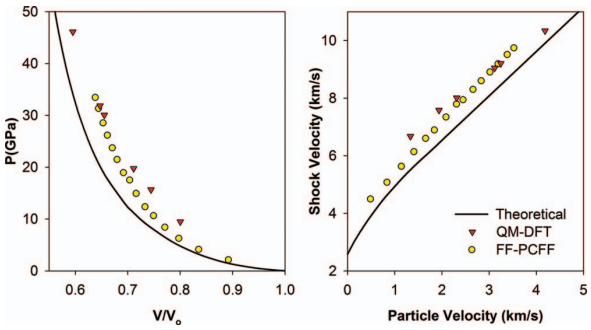

FIG. 4. Hugoniot curve for crystalline PE. Theoretical curves were obtained from Refs. 65, 69, and 72.

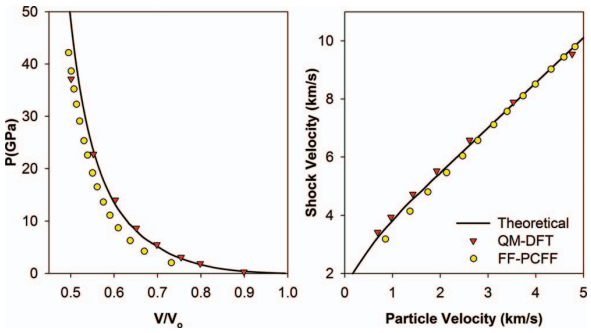

FIG. 5. Hugoniot curve for amorphous PE. Theoretical curve were obtained from Refs. 65, 69, and 72.

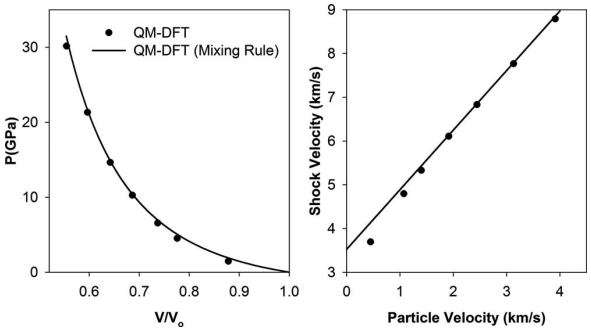

FIG. 6. Hugoniot curve for 29% crystalline PE obtained using DFT and through a simple mixing rule of the DFT calculated Hugoniot curves for the pure amorphous and crystalline system.

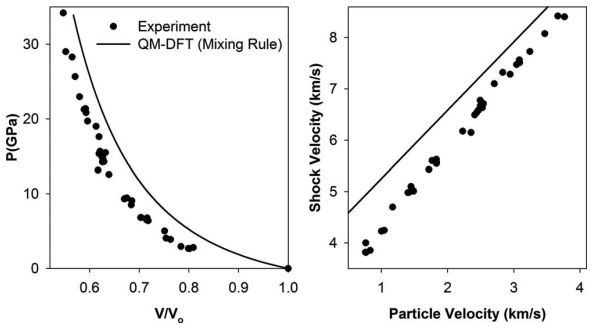

FIG. 7. Comparison of the experimental Hugoniot[63] curve for 46% crystalline polyethylene with the curve calculated using the mixing rule and the DFT Hugoniot curves for the pure amorphous and crystalline system.

1. PMMA, PC, and PS

The simulated Hugoniot curves for PMMA are shown in Figure 1, where we observe close agreement with experimental data, which was taken from the LASL shock handbook[63] and Isbell *et al.*[64] The FF method was able to capture the correct mechanical response for shocks up to approximately 25 GPa, though deviations are observed at higher shock. PCFF appears to be too stiff and underestimates the compression data at high pressures for PMMA, where this deviation can at least in part be contributed to the parameterization of the PCFF force field which was performed under ambient conditions. On the other hand, DFT predicts the correct shock values for our entire pressure range, up to approximately 74 GPa. Bond breaking and formation occur at the higher end of the pressure range and will be discussed in detail in Sec. III C.

Hugoniot curves for PC and PS are shown in Figs. 2 and 3, respectively, where we again observe better agreement between our DFT computational results (vs. FF results) with available experimental data. For PC, we also observe similar agreement to that of PMMA with our FF results, but deviations from the experimental curve occur at lower pressures than with DFT. Our calculations also indicate that the Lennard-Jones 9-6 potential in the PCFF force field is too soft for PS, where it overestimates the compression behavior even at low pressures. Unlike with PMMA, our DFT simulations show deviations from the experimental curve at approximately 25 and 20 GPa for PC and PS, respectively, where the experimental data exhibit associated volume changes indicative of phase transitions. Wang *et al.*[9] also used DFT to calculate the Hugoniot curve for PS, but they only considered pressures above the phase transition in their calculations. The nature of this transition has been associated with a major reordering on the atomic level, where the high pressure compresses the system such that breaking and reformation of covalent bonds can occur. The most prevailing reorganization would occur in polymers with open ring structures made up of covalently bonded carbons,[65] which are present in both PC and PS. This ordering was also observed and well studied computationally for liquids such as benzene.[66–68] This reordering could not be captured using our FF and DFT method for different reasons. PCFF is a non-reactive force

field, which does not capture the breaking and formation of covalent bonds. For the DFT simulations, the time scales that we considered were not long enough to allow any significant reorganization.

It should be noted that a higher pressure range was considered for DFT for PMMA than for PC, PS, and PE due to the excellent agreement of the simulated results with experimental data up to the maximum pressure in those systems (i.e., approximately 40 GPa). The larger range was used to assess the applicability of the method to larger levels of compression. This agreement can, in part, be due to the lack of a significant phase transition, which is observed in PS and PC.

2. PE: Amorphous and crystalline

Since the majority of experimental Hugoniot data for PE is for systems that contain both crystalline and amorphous regions, there is a lack of data to compare our simulation results which are purely amorphous or crystalline. Instead we will compare our simulated Hugoniot curves with theoretical curves derived by Pastine[65,69] for the pure crystalline and pure amorphous forms of polyethylene. In these calculations, Pastine assumed that the forces along the polymer backbone are approximately an order of magnitude larger than the forces between adjacent chains. Thus, the initial compressibility of the polymer can be specified using only the interchain forces and geometric rearrangements. In addition, the dominant repulsive force was assumed to be between nonbonded nearest-neighbor hydrogen atoms, while the dominant attractive forces are of the London dispersion type. With these approximations, Pastine calculated theoretical pressure-volume and particle velocity-shock velocity relations, where the pressure was computed using a Buckingham potential for the crystalline, and a slightly modified form of the Buckingham potential for the amorphous form. The theoretical curves are shown in Figs. 4 and 5 for crystalline and amorphous PE, respectively, along with our DFT and FF calculations, and are considered as upper and lower bounds for experimental results of mixed PE systems.[65] Agreement between the theoretical and DFT calculations for amorphous PE is excellent, where our simulated data points overlay the theoretical curve. For crystalline PE, we observe deviations in behavior from the Pastine results for both the FF and DFT simulations. This can be due in part from the isotropic compression that was used for our Hugoniot calculations in which the x, y, and z directions of the simulation box contract together during the simulation, contrary to Pastine's assumptions that compression along the fiber axis is small relative to the compression along the other two axes. Although this discrepancy does not appear to be significant for non-crystalline PE which lacks the long range order of the crystalline state, the high order of the crystalline PE where the fibers orient along one axis may require a semi-isotropic or anisotropic barostat.

Mattsson *et al.*[2] also considered the crystalline form of PE, though the initial structure of the polyethylene crystal was taken as the tetragonal phase which has not been found experimentally. They observed that for shocks above 50 GPa, that the DFT-AM05 predictions agreed with experimental data, while results obtained using classical potentials such as ReaxFF, OPLS, exp-6, and AIREBO, were quantitatively more accurate near ambient conditions. A notable difference between the study of Mattson *et al.* and ours is the reference data used to access the quality of the simulated Hugoniot curve. The experimental reference data used to access the quality of the DFT and FF methods in the study of Mattson *et al.* crystalline PE were for semi-crystalline PE. Since there are data only for mixtures, i.e., semi-crystalline PE, we used a theoretical benchmark.[65,69]

DFT was also used to calculate the curve for a mixture of crystalline and amorphous PE to better represent an experimental system. In this simulation, a layered structure was built, where amorphous PE was placed perpendicular to the PE fibers in the crystalline region. We also compared the shock Hugoniot calculated using the mixed amorphous/crystalline system with the DFT Hugoniot curves for the individual phases using a simple mixing rule which places weights based on crystallinity on the particle velocity-mass velocity linear Hugoniot curve for the pure amorphous and crystalline systems. For this calculation, the fraction of the sample that is crystalline (C) in the layered structure was calculated based on density using the following formula:[70]

$$\mathrm{C} = \frac{\rho_c(\rho - \rho_{am})}{\rho(\rho_c - \rho_{am})}, \tag{6}$$

where ρ, ρ_c, and ρ_{am} are the density of the mixed amorphous/crystalline, crystalline, and amorphous PE, respectively. To calculate the crystallinity for our DFT system, we used the density calculated through our DFT simulations for the reference state for consistency. The calculated values for ρ, ρ_c, and ρ_{am} are 0.876, 1.066, and 0.818 g/cm^3, respectively, which gives us C = 0.29. The shock velocity-particle velocity Hugoniot data for the DFT pure systems are fitted to obtain the individual crystalline and amorphous Hugoniot equations. This produced the expressions $U_{st} = 1.24\ U_{pt} + 5.18$ and $U_{st} = 1.41\ U_{pt} + 2.85$ for the crystalline and amorphous systems, respectively. The Hugoniot curve for the mixture can then be approximated through the simple mixing rule

$$U_{st} = \mathrm{C}(1.24\,U_{pt} + 5.18) + (1 - \mathrm{C})(1.41\,U_{pt} + 2.85). \tag{7}$$

The curve can also be converted to the pressure and V/V_o reference frame using Eqs. (4) and (5), where the density was approximated by rearranging Eq. (6) to solve for ρ. A comparison of the Hugnoiot curve for the mixed system calculated through direct DFT simulations and through the curve generated using the simple mixing rule is shown in Fig. 6. With this approximation, we observe very good agreement between both curves. Even so, the layered model for semi-crystalline PE is rudimentary, where the polymer chains are either solely amorphous or crystalline. This differs from reality where a single polymer chain can contain both regions and arrange with other chains to form crystalline and amorphous domains.

The simple mixing model described in Eq. (7) was also used to calculate the Hugoniot curve at the same crystallinity as available experimental data.[63] The crystallinity of the experimental system was estimated using Eq. (6), but

where experimental values[49] of $\rho_c = 1.004$ g/cm^3, and $\rho_{am} = 0.853$ g/cm^3 were used instead of those calculated using DFT. The reference density of the experimental sample[63] (ρ) is 0.916 g/cm^3, which equates to C = 0.46. A comparison of the experimental data and the curve derived using the mixing rule is shown in Figure 7, where we observe a clear deviation between the two curves. The shock velocity derived using the mixing rule is higher for a given particle velocity than its experimental counterpart. This could be in part due to the overestimation of the shock velocity for the purely crystalline PE in the DFT simulations as seen in Figure 4. Some DFT calculated values for the purely crystalline and amorphous samples also exhibit an inconsistent error in that some quantities may be overestimated in one, and underestimated in the other. For instance, the density at ambient conditions is overestimated for crystalline and underestimated for amorphous PE, which may affect the overall reference state. In addition, we use a simple mixing rule which assumes that both phases are independent, which is not the case. Instead of using this approximation, simulations should be performed on a more realistic model of semi-crystalline PE.[71] The effect of this model on the Hugoniot curve will be discussed in a future publication.

C. Chain dissociation/association

Although the time scales considered in the MD-DFT simulations (2 ps) were too short for significant reorganization within the simulation cell, it was found to be ample time to initialize bond dissociation and formation. In addition to offering insight into the composition of the simulation box after a shock wave, which will affect the physical properties of the material, the onset of the chain dissociation/association is an important measure of the appropriateness of a nonreactive force field such as PCFF, which was used in our FF calculations.

To study the effect of compression on chain dissociation/association we considered PMMA for which we observed the greatest agreement with experimental data and for which we have considered the highest value of pressure, corresponding to the shock velocities of approximately 11 km/s. In this study, we will consider the number of atoms in each segment in the simulation cell at a point that brackets the Hugoniot. When a segment has a total number of atoms greater than a single PMMA chain we associate this with bond formation while bond dissociation occurs when the total number is less than a single chain. A segment is defined as a cluster of atoms covalently bonded together, where a bond between two atoms were determined by a distance cutoff. In this study, we used a cutoff that allows for deviations between 0.6 and 1.15 of the ideal bond length, where the ideal bond length is calculated as the sum of the covalent radii of the two atoms involved in the bonding. This monitoring was performed in Materials Studio[27] for a total of 5 snapshots (from the final 1 ps) in the simulation corresponding to the lower bracket of the Hugoniot point, though similar results were observed for the upper bracket. Although distance cutoffs would affect the number of associations/dissociations, its effect was found to be rather insensitive.[2]

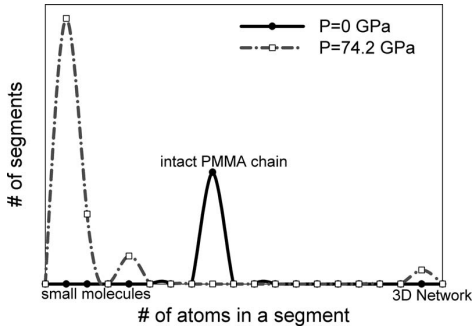

FIG. 8. Qualitative description of the bond dissociation and formation for PMMA using DFT. Lines between data points are provided to guide the eye.

A representative plot, taken from a single snapshot, of the number of segments as function of the number of atoms is shown in Figure 8 for P = 0 GPa and 74.2 GPa. At near ambient pressures (i.e., 0 GPa), we observe only 8 segments corresponding to the initial 8 PMMA chains (62 atoms each) which remain completely intact (i.e., no dissociation and formation). At approximately 75 GPa, we observe the formation of a 3D network-like structure within an environment comprised of small molecules as seen in Figure 9. Although the actual composition of the 3D network in the 75 GPa simulation cell differs depending on the specific snapshot, the features of this structure are maintained in each of the snapshots. A more comprehensive study of bond dissociation and formation will be considered in a future publication.

D. Structural properties

The radial distribution function (RDF, $g_{\alpha\beta}(r)$) measures the probability of an atom at the origin of type α having an atom of type β within a spherical shell of infinitesimal thickness dr at the distance r. The RDF can be used to characterize the structure of a material such as the short or long range order of the system. We have calculated the carbon-carbon RDF ($g_{cc}(r)$) for both our DFT and FF simulations for various V/V_o at approximately the Hugoniot pressure and temperature for our four polymers. For brevity, we will only discuss the DFT results since both methods yield similar results.

The $g_{cc}(r)$ for our small DFT systems are shown in Figure 10 for PMMA, PS, PC, and PE. For PE, we considered both the crystalline and amorphous forms. When analyzing

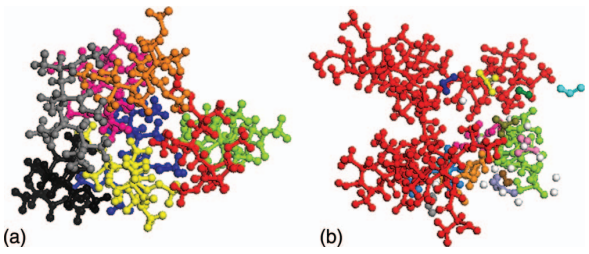

FIG. 9. Representative structures observed using DFT at (a) P = 0 GPa and (b) P = 74.2 GPa. Each connected chain is represented by a different color for convenience to the reader. Free hydrogens are shown in white.

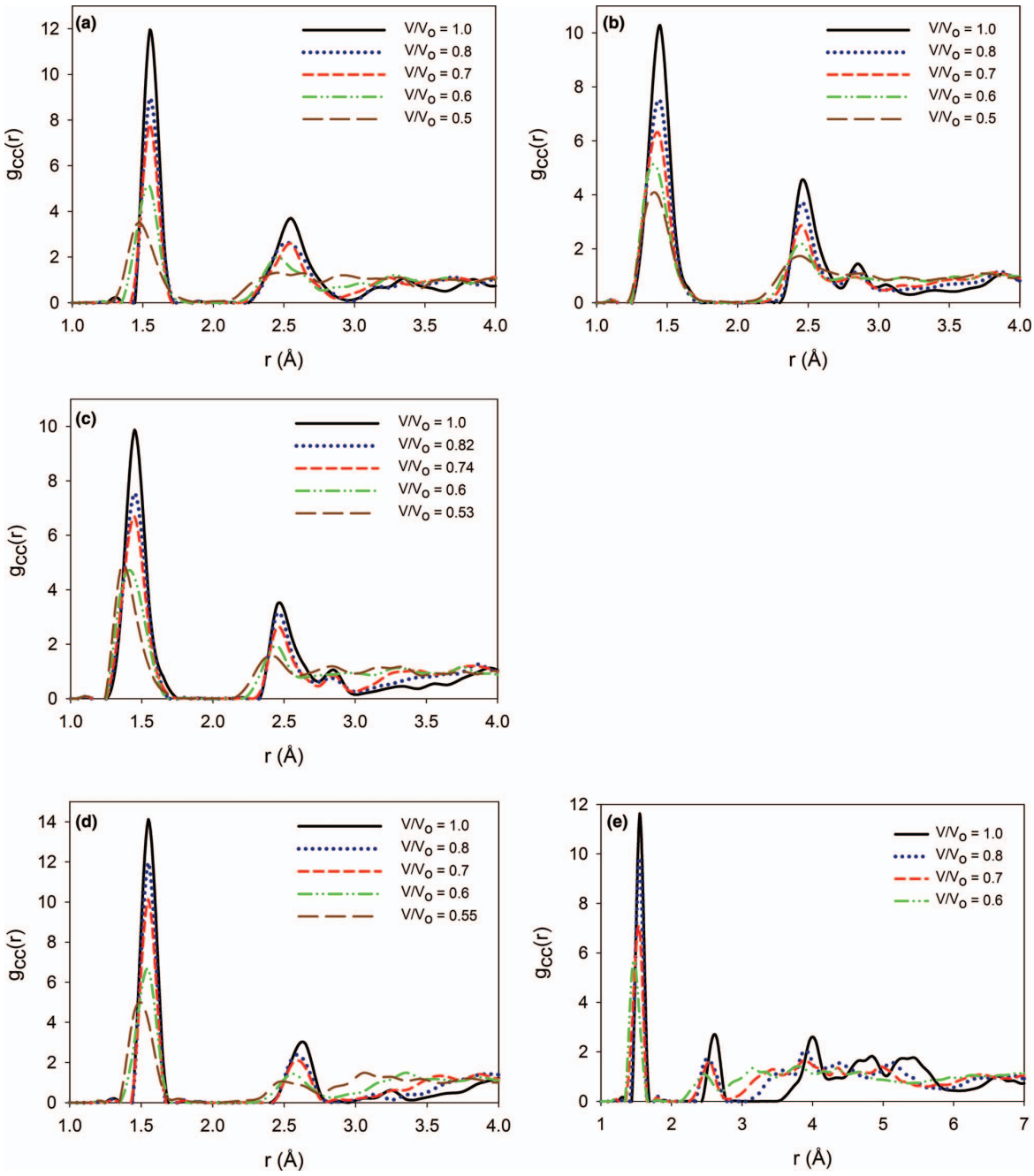

FIG. 10. Carbon-carbon radial distribution function for (a) PMMA, (b) PC, (c) PS, (d) PE amorphous, (e) PE crystalline at various values of V/V_o calculated using DFT.

the radial distribution function, it is important to note that the Hugoniot temperature and pressure increases as the system is compressed. Thus, as the system is compressed, we observe that the $g_{cc}(r)$ for all of the systems exhibit both a broadening and flattening of peaks due to an increase in temperature which leads to amplified thermal motion. We observe a shift in the position of the peaks to lower r as the simulation cell is compressed due to a decrease in the distance between carbon atoms. Unlike the RDF of the amorphous polymer systems, the RDF of crystalline PE indicates correlation for distances of r beyond the range of 4 Å shown in Figure 7 indicating long range order.

The size of a polymer, regardless of architecture, can be characterized using the radius of gyration (R_g). The square of this quantity is calculated by taking the average square distance between monomers in a given conformation and the polymer's center of mass. To calculate R_g, an additional 200 ps of *NVT* simulation were performed after the

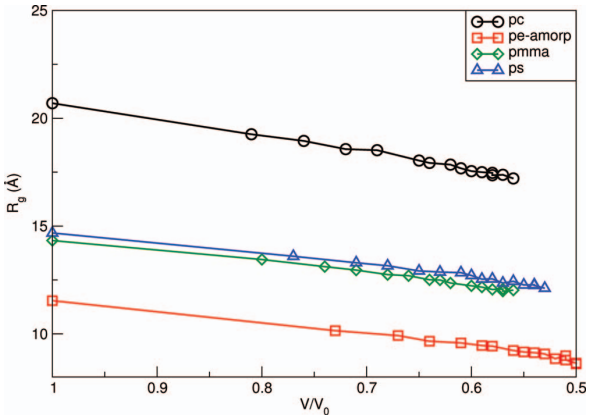

FIG. 11. Average radius of gyration obtained from FF simulations at approximately the Hugoniot temperature and pressures for various V/V_o.

temperature scan at the Hugoniot temperature. Snapshots of the trajectory were taken every 1 ps, where the average R_g was calculated from the last 1000 snapshots. The average radius of gyration for our amorphous polymers calculated in our FF simulations is shown in Fig. 11, where we omit crystalline PE since we considered semi-infinite chains in our simulations. This calculation was only performed for our FF simulations, since the chains in the DFT simulation only consist of between 4 and 8 monomers. In Fig. 9, a slow decrease in the average R_g is observed as the system transverses the Hugoniot curve to larger compression. This is due to the compression of the chains as the box is compacted.

IV. CONCLUSIONS

Classical FF and DFT were used to calculate the principle shock Hugoniot curves for poly[methyl methacrylate], poly[ethylene], poly[styrene], and polycarbonate, where both crystalline and amorphous forms of poly[ethylene] were studied. In the FF calculations, we considered the non-reactive polymer-consistent force field, where calculations were performed in LAMMPS. Density functional theory at the GGA–BLYP level using dispersion corrected atom centered pseudopotentials as implemented in CP2K was used for our quantum simulations. Overall, the Hugoniot curves obtained using DFT agree with available experimental data at higher pressures than classical force fields. Even so, phase transitions such as those observed in our ring containing polymers are difficult to capture through DFT due to the long time scales associated with significant reorganization. For PMMA, for which the greatest agreement between experimental and DFT derived data is observed (i.e., pressures up to 74.2 GPa), further structural analysis at P = 74.2 GPa was performed to quantify the formation and dissociation of bonds. Further research is needed to extend the applicability of the DFT methods to higher pressures and may involve the use of other simulation methods and techniques to account for fracture and phase rearrangement of polymer chains. In addition, we will also consider the effect of classical reactive force fields[34] in conjunction with the MSST,[41] which is a highly efficient computational method for studying systems under dynamical shock conditions.

ACKNOWLEDGMENTS

This work was funded by the U.S. Army Research Laboratory Enterprise for Multi-scale Research of Materials. Calculations were performed using the DOD Supercomputing Resource Center located at the Air Force Laboratory. Calculations were performed on DOD High Performance Computing site at the AFRL through the Challenge Project C5M. Dr. T. W. Sirk was supported by an appointment to the Postgraduate Research Participation Program at the U.S. Army Research Laboratory administered by the Oak Ridge Institute for Science and Education through an interagency agreement between the U.S. Department of Energy (DOE) and the U.S. Army Research Laboratory. We would like to thank Dr. C. K. Knox for help with LAMMPS scripts and Dr. Y. R. Sliozberg for useful discussion.

[1] K. Cochrane, M. Desjarlais, and T. Mattsson, AIP Conf. Proc. **1426**, 1271 (2012).
[2] T. R. Mattsson, J. M. D. Lane, K. R. Cochrane, M. P. Desjarlais, A. P. Thompson, F. Pierce, and G. S. Grest, Phys. Rev. B **81**, 054103 (2010).
[3] K. Chenoweth, A. van Duin, and W. Goddard III, J. Phys. Chem. A **112**, 1040 (2008).
[4] S. J. Stuart, A. B. Tutein, and J. A. Harrison, J. Chem. Phys. **112**, 6472 (2000).
[5] W. L. Jorgensen, D. S. Maxwell, and J. Tirado-Rives, J. Am. Chem. Soc. **118**, 11225 (1996).
[6] O. Borodin and G. Smith, J. Phys. Chem. B **110**, 6279 (2006).
[7] O. Borodin, G. Smith, and D. Bedrov, J. Phys. Chem. A **106**, 9912 (2002).
[8] R. Armiento and A. E. Mattsson, Phys. Rev. B **72**, 085108 (2005).
[9] C. Wang, X.-T. He, and P. Zhang, Phys. Plasmas **18**, 082707 (2011).
[10] M. Grujicic, B. Pandurangan, W. Bell, B. A. Cheeseman, C.-F. Yen, and C. L. Randow, Mater. Sci. Eng. A **528**, 3799 (2011).
[11] H. Sun, J. Phys. Chem. B **102**, 7338 (1998).
[12] J. Hooper, D. Bedrov, G. Smith, B. Hanson, O. Borodin, D. Dattelbaum, and E. Kober, J. Chem. Phys. **130**, 144904 (2009).
[13] S. Kristyan and P. Pulay, Chem. Phys. Lett. **229**, 175 (1994).
[14] I. G. Kaplan, *Intermolecular Interactions* (Wiley, Chichester, 2006).
[15] M. Elstner, P. Hobza, T. Frauenheim, S. Suhai, and E. Kaxiras, J. Chem. Phys. **114**, 5149 (2001).
[16] S. Grimme, J. Comput. Chem. **25**, 1463 (2004).
[17] P. Jurečka, J. Černý, P. Hobza, and D. R. Salahub, J. Comput. Chem. **28**, 555 (2006).
[18] S. Grimme, J. Antony, S. Ehrlich, and H. Krieg, J. Chem. Phys. **132**, 154104 (2010).
[19] Q. Wu and W. Yang, J. Chem. Phys. **116**, 515 (2002).
[20] Y. Andersson, D. DLangreth, and B. Lundqvist, Phys. Rev. Lett. **76**, 102 (1996).
[21] T. Sato, T. Tsuneda, and K. Hirao, Mol. Phys. **103**, 1151 (2005).
[22] Y. Zhao and D. G. Truhlar, Acc. Chem. Res. **41**, 157 (2008).
[23] K. Pernal, R. Podeszwa, K. Patkowski, and K. Szalewicz, Phys. Rev. Lett. **103**, 263201 (2009).
[24] R. Podeszwa and K. Szalewicz, J. Chem. Phys. **136**, 161102 (2012).
[25] G. A. DiLabio, Chem. Phys. Lett. **455**, 348 (2008).
[26] O. A. von Lilienfeld, I. Tavernelli, U. Rothlisberger, and D. Sebastiani, Phys. Rev. Lett. **93**, 153004 (2004).
[27] E. Tapavicza, I.-C. Lin, O. A. von Lilienfeld, I. Tavernelli, M. D. Coutinho-Neto, and U. Rothlisberger, J. Chem. Theory Comput. **3**, 1673 (2007).
[28] I.-C. Lin and U. Rothlisberger, Phys. Chem. Chem. Phys. **10**, 2730 (2008).
[29] O. A. von Lilienfeld, I. Tavernelli, U. Rothlisberger, and D. Sebastiani, Phys. Rev. B **71**, 195119 (2005).
[30] I.-C. Lin, O. A. von Lilienfeld, M. D. Coutinho-Neto, I. Tavernelli, and U. Rothlisberger, J. Phys. Chem. B **111**, 14346 (2007).
[31] R. Balu, E. F. C. Byrd, and B. Rice, J. Phys. Chem. B **115**, 803 (2011).
[32] A. van Duin, S. Dasgupa, F. Lorant, and W. Goddard III, J. Phys. Chem. A **105**, 9396 (2001).

[33]M. Muehler, J. Mech. Mater. Struct. **2**, 1019 (2007).
[34]J. Andzelm, T. Chantawansri, T. Sirk, E. Byrd, and B. Rice, in *Proceedings of the 15th International Conference on Deformation, Yield, and Fracture of Polymers, Book of Abstracts* (Materials Technology Group, Roldoc Abbey, 2012), p. 165.
[35]CP2K Developers Group, CP2K Code 2000-2006.
[36]LAMMPS Molecular Dynamics Simulator, see http://lammps.sandia.gov.
[37]D. Swanson, M. Mintmire, D. Robertson, and C. White, Chem. Phys. Rep. **18**, 1871 (2000).
[38]J. Erpenbeck, Phys. Rev. A **46**, 6406 (1992).
[39]B. Rice, W. Mattson, J. Grosh, and S. Trevino, Phys. Rev. E **53**, 611 (1996).
[40]J. Maillet, M. Mareschal, L. Soulard, R. Ravelo, P. Lomdahl, T. Germann, and B. Holian, Phys. Rev. E **63**, 016121 (2000).
[41]E. Reed, L. Fried, and J. Joannopoulos, Phys. Rev. Lett. **90**, 235503 (2003).
[42]W. Fickett, *Introduction to Detonation* (University of California Press, Berkeley, CA, 1985).
[43]T. L. Chantawansri, E. F. C. Byrd, B. M. Rice, and J. W. Andzelm, *ARL-TR-5819: Molecular Dynamics Simulations of Hugoniot Relations for Poly[Methyl Methacrylate]* (Army Research Laboratory, Aberdeen Proving Ground, MD, 2011).
[44]M. Rubinstein and R. Colby, *Polymer Physics* (Oxford University Press, New York, 2003).
[45]D. Theodorou and U. Suter, Macromolecules **18**, 1467 (1985).
[46]A. D. Becke, Phys. Rev. A **38**, 3098 (1988).
[47]C. Lee, W. Yang, and R. G. Parr, Phys. Rev. B **37**, 785 (1988).
[48]J. Mark, *Physical Properties of Polymers Handbook*, 2nd ed. (Springer, New York, 2007).
[49]J. Runt, "Crystallinity determination," in *Encylopedia of Polymer Science and Engineering* (Wiley, New York, 1989).
[50]Accelrys, Inc. Materials Studio 5.0, San Diego, CA, 2010.
[51]J. P. Perdew, K. Burke, and M. Ernzerhof, Phys. Rev. Lett. **77**, 3865 (1996).
[52]Y. Zhang and W. Yang, Phys. Rev. Lett. **80**, 890 (1998).
[53]MAPS interface, see http://www.scienomics.com.
[54]J. R. Maple, U. Dinur, and A. T. Hagler, Proc. Natl. Acad. Sci. U.S.A. **85**, 5350 (1988).
[55]H. Sun, P. Ren, and J. Fried, Comput. Theor. Polym. Sci. **8**, 229 (1998).
[56]S. W. Bunte and H. Sun, J. Phys. Chem. B **104**, 2477 (2000).
[57]J. Yang, Y. Ren, A.-M. Tian, and H. Sun, J. Phys. Chem. B **104**, 4951 (2000).
[58]M. J. McQuaid, H. Sun, and D. Rigby, J. Comput. Chem. **25**, 61 (2003).
[59]Y. Zhao and D. G. Truhlar, Theor. Chem. Acc. **120**, 215 (2008).
[60]M. J. Frisch, G. W. Trucks, H. B. Schlegel *et al.*, GAUSSIAN 09, Revision A.1., Gaussian Inc., Wallingford, CT, 2009.
[61]C. M. Breneman and K. B. Wiberg, J. Comput. Chem. **11**, 361 (1990).
[62]R. W. Hockney and J. W. Eastwood, *Computer Simulation Using Particles* (Taylor & Francis, New York, 1989).
[63]S. P. March, *LASL Shock Hugoniot Handbook* (University of California Press, Berkeley, CA, 1980).
[64]W. Isbell, F. Shipman, and A. Jones, *Hugoniot Equation of State Measurements for Eleven Materials to Five Megabars* (General Motors Technical Center, Warren, MI, 1968).
[65]W. J. Carter and S. P. Marsh, *Hugoniot Equation of State of Polymers* (Los Alamos National Laboratory, Los Alamos, NM, 1995).
[66]J. Maillet and N. Pineau, J. Chem. Phys. **128**, 224502 (2008).
[67]C. Wang and P. Zhang, J. Appl. Phys. **107**, 083502 (2010).
[68]S. R. Bickham, J. Kress, and L. A. Collins, J. Chem. Phys. **112**, 9695 (2000).
[69]D. J. Pastine, *Colloque Internationale du C.N.R.S. sur Les Propriétés Physiques des Solides Sous Pression* (CNRS, Paris, 1970), p. 49.
[70]C. Vasile and M. Pascu, *Practical Guide to Polyethylene* (Rapra Technology Limited, Shrewsbury, 2005).
[71]S. Lee and G. C. Rutledge, Macromolecules **44**, 3096 (2011).
[72]The theoretical curve shown in Figs. 4 and 5 used data extracted from digitizing the published curve in Ref. 65. Once extracted, the curve was fitted and interpolated to higher pressures/shock velocities.

Coarse-Grained Modeling of Model Poly(urethane urea)s: Microstructure and Interface Aspects

Tanya L. Chantawansri, Yelena R. Sliozberg, Jan W. Andzelm, and Alex J. Hsieh

Polymer, 53 (2012)

Contents lists available at SciVerse ScienceDirect

Polymer

journal homepage: www.elsevier.com/locate/polymer

Coarse-grained modeling of model poly(urethane urea)s: Microstructure and interface aspects

Tanya L. Chantawansri*, Yelena R. Sliozberg, Jan W. Andzelm, Alex J. Hsieh

U.S. Army Research Laboratory, 4600 Deer Creek Loop, Aberdeen Proving Ground, MD 21005, USA

ARTICLE INFO

Article history:
Received 5 June 2012
Received in revised form
18 July 2012
Accepted 21 July 2012
Available online 31 July 2012

Keywords:
Poly(urethane urea)
Morphology
Mechanical properties

ABSTRACT

Poly(urethane urea) elastomers are versatile and can be tailored to exhibit a broad range of mechanical response under high strain rate deformation. In this work, we utilize coarse-grained molecular dynamics simulations to elucidate the molecular mechanisms, particularly the effects of hard segment content, intermolecular interaction, and rigidity of the interface between the hard and soft segments on local morphology and rate-dependent stress-strain behavior in the ballistic regime. Simulation results qualitatively agree with available experimental data, where analysis of hard segment orientation during tensile and compression deformation and dynamic strain rate sensitivity was also performed. Further study of the intermolecular interaction on the stress-strain behavior reveals that it has a strong effect on strain hardening, particularly for a rigid interface, once the hard segment content reaches the percolation threshold. Simulation results also show that interface intermolecular interaction could become more dominant over interface rigidity in the initial stress-strain response, particularly below percolation.

Published by Elsevier Ltd.

1. Introduction

High performance elastomers have received enormous attention for a broad variety of applications including blast mitigation and impact-resistant coatings for metallic substrates, structure adhesives, foams for composite structures, and films for structural retrofit [1–4]. In particular, segmented poly(urethane urea) (PUU), like polyurethanes and polyureas, exhibit versatile physical and mechanical properties. This class of materials can be tailored to transition from the rubbery-like into the leathery-like regime or even into the glassy regime with increasing strain rate, where stress levels may be greatly enhanced and large energy dissipation mechanisms can be realized [2]. Other potential mechanisms including shock impedance mismatch, shock-wave dispersion and strain delocalization have also been proposed for the improvement in the blast-wave mitigation and projectile impact energy absorption [5].

The cohesive strength of the bidentate hydrogen bonding interaction in urea is much stronger than the monodentate interaction in urethane, thus favoring mechanical stiffening in polyureas and PUUs over polyurethanes. Extensive hydrogen bonding can occur in PUU, where various types of hydrogen bonds can be formed between the two proton donors (urethane N–H and urea N–H groups) and the three proton acceptors (urethane C=O, urea C=O, and C–O–C groups). The type of hydrogen bonds can be classified as either monodentate or bidentate, where binding occurs at one or two sites, respectively, and where, in PUU, the latter is associated with hydrogen bonding between the urea segments. The association of the hard segments is facilitated by their ability to form a hydrogen bonded network, which serve as physical cross-link sites due to the inter-chain joining that reinforce the soft matrix [6–10].

PUUs also exhibit more versatility than the commercially available polyureas, and have also attained renewal interests and shown potential for property optimization for various applications including, but not limited to, chem/bio protection, adhesives in composite laminates, and matrix for fiber reinforced composites. The challenges for the rational design of hierarchical elastomeric materials to achieve a simultaneous improvement in dynamic mechanical strengthening and chemical hardening critical for the next generation protective materials applications reside on the realization of the key physical events that occur on various temporal and spatial scales.

There have been several studies on the in-situ microstructure of polyurethane and PUU elastomers upon mechanical deformation using synchrotron radiation with in-situ small-angle X-ray scattering (SAXS), wide-angle X-ray diffraction and time-resolved Fourier transform infrared spectroscopy [11–13]. It has been noted that disruption of the domain morphology and reorganization of hard segments could be induced in response to stress at slow or moderate strain rates, and as a result the SAXS scattering pattern

* Corresponding author. Tel.: +1 410 306 2777; fax: +1 410 306 0676.
E-mail address: tanya.chantawansri.civ@mail.mil (T.L. Chantawansri).

was found distinctly anisotropic [11–13]. However, recent work by Pathak et al. indicated that at higher strain rates this behavior was not apparent in polyurea, as the morphology response of the hard segments was too slow and an isotropic scattering pattern was observed in SAXS [13].

Bogoslow et al. [2] demonstrated that impact testing of polybutadiene-based polyurea, backed by steel plates showed a transition to the glassy state causing a brittle failure mode and increasing the energy dissipation in comparison to the bulk polybutadiene rubber, which remained rubbery during impact. This discrepancy in dynamic strain rate hardening characteristics was attributed to a difference in segmental dynamics, determined through dielectric spectroscopic measurements, which is almost three orders of magnitude faster in the polybutadiene rubber than those for polybutadiene-based polyurea [2]. Hence the polybutadiene rubber chains were able to accommodate the impact and respond in a rubbery mode since the frequency of segmental relaxation required to transition them to a glassy state under ambient conditions of temperature and pressure was more than three orders of magnitude greater than the strain rate of impact ($\sim 10^5\ s^{-1}$). On the other hand, similar impact caused a transition to a glassy state in the polybutadiene-based polyurea due to its much slower local segmental dynamics, subsequently resulting in greater energy dissipation through large-scale fragmentation but a brittle mode of failure [2]. Roland and co-workers in their recent study on a series of polyurea with varying stoichiometry further quantified the segmental dynamics and its pressure dependence [14]. The variations in polyurea stoichiometry corresponding to a difference of less than 3 wt.% in hard segment content resulted in large differences in modulus, tensile strength and failure strain. However, the segmental relaxation times measured by dielectric spectroscopy and the calorimetric glass transition temperature (T_g) by differential scanning calorimetry at ambient pressure were not affected by stoichiometry. They also noted similar ballistic performance in the polyurea coated steel plates against the impact of a 0.50-caliber fragment simulating projectile, which was attributed to the equivalent segmental dynamics that governed the high strain rate mechanical response of the select polyureas. Nevertheless extensive intermolecular hydrogen bonding of polyurea was regarded as an important attribute for high mechanical toughness, and it has also been suggested that better performance for polyureas requires more substantial changes in the structure and morphology than an approach based simply on stoichiometry variations. Roland and co-workers also pointed out that to best utilize the advanced elastomers for blast and impact protection the calorimetric T_g should be relatively high but lower than the service temperature [2] (with the optimal calorimetric T_g value depending on the deformation strain rate of interest) [5].

Results from recent studies of select model 4,4′-dicyclohexylmethane diisocyanate (HMDI)–poly(tetramethylene oxide) (PTMO) based transparent PUU materials further demonstrated the key role of a tunable microstructure in varying T_g as well as in enabling the design of high performance elastomers with desired dynamic mechanical strengthening and chemical hardening capabilities. Altering the molecular weight of the soft segment (SS) PTMO from 2000 (2K) to 1000 (1K) g/mol, these PUU 1K materials exhibited a $\sim 17\ ^\circ C$ shift of the SS T_g toward higher temperature and a broadening of the SS relaxation based on dynamic mechanical analysis (DMA) data. The latter was attributed to relaxation associated with the amorphous phase which consists of predominantly random fibrillars as a result of phase mixing between hard and soft segments, presumably facilitated by intermolecular hydrogen bonding, which gave rise to a prominent second peak relaxation closer to room temperature [15–17]. As a result, the PUU 1K materials, in the vicinity of room temperature, exhibited a greater modulus change with temperature and a greater rate sensitivity. The fibrillar-like microstructure clearly identified via atomic force microscopy (AFM) [18] is in contrast to the self-assembly of lamellar hard segments into other microstructure features including rod-like hard domains as well as supramolecular spherulite-like hard domains [19]. Additionally, a drastic improvement in permeation resistance against chloroethyl ethyl sulfide, including significantly longer breakthrough time and slower steady-state flux, was observed in the PUU 1K materials than in the corresponding PUU 2K materials of similar hard segment contents [16,17]. This property enhancement was also attributed to the presence of a fibrillar-like microstructure dominant amorphous phase.

There have been a number of ballistic evaluation and continuum modeling studies of polyureas in composite structures [5]; however, very little work has focused specifically on the investigation of molecular influence on high strain rate deformation. In this work, we exploit a coarse-grained (CG) particle-based model that is solely based on polymer physics and not atomistic detail to determine microstructure characteristics as well as the corresponding mechanical properties of select model PUUs. Through CG simulations, our goal is to elucidate the molecular mechanisms, particularly the effects of hard segment content, the role of intermolecular hydrogen bonding as well as the rigidity and interaction at the interphase on local morphology and stress-strain behavior of PUUs in the ballistic regime. Results will also be compared to our experimental PUU data when available.

2. Model PUU

Select model PUU materials were synthesized with varying molar ratio of poly(tetramethylene oxide) (PTMO – PolyTHF, BASF Corporation), 4,4′-dicyclohexylmethane diisocyanate(HMDI – Desmodur W, Bayer MaterialScience) and diethyltoluenediamine (DETA – Ethacure® 100-LC, Albemarle Corporation, Baton Rouge, Louisiana), where the molecular weight (MW) of PTMO was fixed at 2000 g/mol. The repeat unit is shown in Fig. 1a. These PUUs were prepared using a two-step, pre-polymer synthesis method, and details of the materials synthesis can be found elsewhere [15]. Typically, PTMO, the soft segment, was first reacted with HMDI to form a pre-polymer with a urethane linkage, and was also end-capped with diisocyanate groups. The pre-polymer was then reacted with the chain extender, DETA, to complete polymerization. The reaction of HMDI with the DETA diamine resulted in hard segments with urea linkages, which could self-assemble to form domains and thus leading to microphase separation.

In this work, we consider three model systems of PUU, where the molecular weight of the PTMO is fixed at 2000 g/mol and the molar ratio of diisocyanate (HMDI): diamine (DETA) chain extender: PTMO is varied to increase the hard segment content. Specifically, we consider ratios of 2:1:1, 3:2:1, and 4:3:1, which we label system 1, 2, and 3, respectively. This nomenclature corresponds to the molar ratio of [HMDI-DETA]:[HMDI-PTMO], or more concisely, the molar ratio of DETA:PTMO in the PUU chain. In addition, the nomenclature is also consistent with the parameter n is the repeat unit shown in Fig. 1a. The index m in Fig. 1a is fixed to 28 for all three systems. These three systems are specifically studied to elucidate available experimental data published [15–17].

The motivation for using HMDI includes its ultra-violet (UV) radiation stability characteristic desired for long-term outdoor durability performance [20], and additionally to explore potential energy dissipation as a result of the deformation of the boat- and chair-conformations associated with the cyclohexane rings in HMDI [21]. To study the effect of the rigidity of diisocyanate, we considered two definitions of the hard segment:

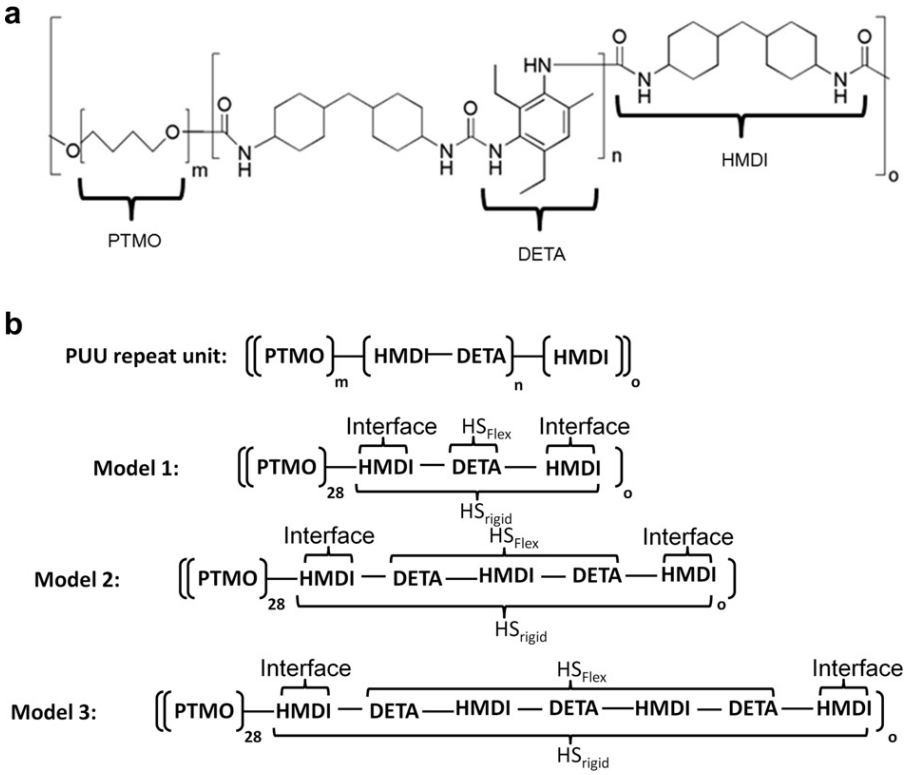

Fig. 1. a) Repeat unit for PUU. b) Schematic of the two definitions of the hard segment (HS_{Rigid} and HS_{Flex}) for our three model PUU systems.

$$\%HS_{\text{Rigid}} = \frac{100((R-1)M_{da} + (R)M_{di})}{(M_g + (R)M_{di} + (R-1)M_{da})} \quad (1)$$

$$\%HS_{\text{Flex}} = \frac{100((R-1)M_{da} + (R-2)M_{di})}{(M_g + (R)M_{di} + (R-1)M_{da})} \quad (2)$$

where R is the molar ratio of the diisocyanate to PTMO, and M_{di}, M_{da} and M_g are the number average molecular weights of the HMDI, DETA and PTMO, respectively. The difference between HS_{Rigid} and HS_{Flex} is that the diisocyanate group at the interface between PTMO and the diamine is considered as part of the hard segment in the former, but not in the latter. Thus in HS_{Flex} the interface is considered to be flexible. For the remainder of the manuscript, references to the interface would refer to the diisocyanate group between PTMO and diamine (see Fig. 1). This is shown schematically in Fig. 1b for our three model systems, where Table 1 lists numerical values of the molar ratio and wt.% of hard segment defined through Eqs. (1) and (2) for each system. It is also important to note that HS_{Rigid} corresponds to the hard segment content, HS, as defined in reference [15], which is an experimental study of PUU for our three model systems.

To simulate our model PUU systems, we use a particle-based mesoscale simulation method, where atoms are grouped into larger entities called particles. The total number of coarse-grained particles in the simulation cell (N_{tot}), in a single repeat unit (N_{rep}), and in a single chain (N_c), along with the box size of the cubic periodic simulation cell (L_x, L_y, L_z) are given in Table 2. In calculating the number of these coarse-grained particles, which are of constant volume, we have assumed that the experimental density of each component of PUU is approximately 1 g/cm^3. In each PUU repeat unit, 32 beads in N_{rep} represents PTMO of molecular weight 2000 g/mol. Four beads were used to represent each diisocyantate group at the interface between PTMO and the diamine resulting in a total of 8 beads per repeat unit for the interface. These beads will be modeled as either being rigid or flexible depending on if the hard segment is defined as HS_{Rigid} or HS_{Flex}, respectively. If the hard segment is defined by the former, the beads used to represent the interface are considered to be part of the hard segment. The remainder of the beads in the repeat unit was used to represent the remainder of the hard segment in HS_{Rigid} or the hard segment in HS_{Flex}.

To model the effect of interaction and rigidity of the interface on the mechanical response of our model PUU systems, we will consider a total of four computational models. The rigidity of the interface produces two different models, where the effective hard segment is defined either by HS_{Rigid} or HS_{Flex}. These two models will be identified simply by the tag, Rigid or Flex, respectively (See Fig. 2). We will also consider a weak interaction and a strong interaction models to study the effect of the hydrogen bonding interaction strength on morphology and mechanical properties. To model the weak interaction, the self and binary interactions between the hard segment and interface are kept the same, while in the strong interaction model they are differentiated such that the magnitude of the attractive interaction follows the following trend: hard segment-hard segment > hard segment−interface > interface−interface. Combining both keywords will describe our computational model; for instance

Table 1
Composition including the molar ratio, wt.% of hard segment, HS_{Rigid} and HS_{Flex}, defined in Eqs. (1) and (2), respectively for select model PUUs.

Model PUU	Molar ratio of HMDI:DETA:PTMO	$\%HS_{Rigid}$	$\%HS_{Flex}$
1	2:1:1	26	6
2	3:2:1	36	19
3	4:3:1	44	29

Table 2
Number of coarse-grained particles in the simulation cell (N_{tot}), in a single repeat unit (N_{rep}), and in a single chain (N_c), and the dimensions of the periodic simulation cell (L_x, L_y, L_z).

Model PUU	N_{tot}	N_{rep}	N_c	L_x, L_y, L_z (a)
1	260064	43	344	67.38
2	260050	50	350	67.38
3	259920	57	342	67.37

Flex-weak would represent a model where the hard segment is defined by HS_{Flex} (interface is flexible) and the hard segments interact through the weak interaction model. A summary of the four models considered and the parameters with corresponding strength is given in Table 3.

The Rigid-strong model most closely resembles the experimental PUU system, where the interaction model mimics the monodentate hydrogen bonding that can occur between the urethane groups at the interface and the bidentate bonding that can occur between the urea–urea and urea-urethane groups. The magnitude of the attractive interaction reflects the stronger bond energy associated with bidentate urea–urea hydrogen bond (corresponding to the interaction strength III) compared to the monodentate urethane–urethane bonding (interaction strength I), where Yilgor et al. found that the bond energies are 21.8 kJ/mol and 18.4 kJ/mol, respectively, using quantum mechanics [22]. Our quantum calculations also support this finding [23]. Experimental data of morphology and mechanical properties will be compared to the Rigid-strong model when available.

In addition to the Rigid-strong model, we also considered the effect of changing the magnitude of the attractive interactions strength and the rigidity at the interface. This was done to study the effect of these polymeric relevant parameters on the morphology and mechanical properties. For instance, by comparing the Rigid-weak and Rigid-strong models we can elucidate the effect of monodentate hydrogen bonding versus bidentate bonding at the interface. Thus, these models, as well as the other two models, (Flex-strong, Flex-weak) will be used to explore design space where the effects of flexibility at the interface and the hydrogen bonding interaction are investigated.

3. Computational model & method

To obtain the local morphology and stress-strain behavior of our model systems under mechanical deformation including compression and tension, we utilized the following scheme:

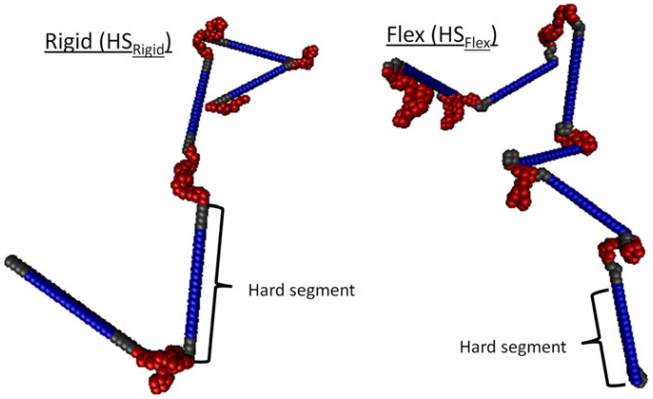

Fig. 2. Representative CG chains of PUU for the Flex and Rigid models. Beads that represent the soft segment, hard segment, and interface are shown in red, blue, and gray, respectively. For the Rigid models, the hard segment as defined by HS_{Rigid} includes the interface. (For interpretation of the references to color in this figure legend, the reader is referred to the web version of this article.)

Table 3
A summary of parameters with corresponding strength for the four models considered (HS and I denote hard segments and interface, respectively. The numerals I, II, and III are used to represent the relative magnitude of the attractive interaction strength between the particles, where the magnitude increases from I to III.

	Interface	Relative magnitude of attractive interaction strength		
		HS–HS	HS–I	I–I
Rigid-strong	Rigid	III	II	I
Rigid-weak	Rigid	I	I	I
Flex-strong	Flexible	III	II	I
Flex-weak	Flexible	I	I	I

1. Generation of initial configurations
2. Dissipative Particle Dynamics (DPD) to equilibrate the system
3. Fast push-off method to remove overlap
4. Equilibration through Kremer-Grest (K-G) model
5. Temperature quench using K-G model
6. Constant pressure simulation using K-G model
7. Deformation simulations using K-G model

This equilibration protocol [24] utilizes a soft potential which is standard in DPD [25] simulations to facilitate the quick equilibration of the system before transition to the K-G [26] model. Equilibration through DPD and K-G were monitored to ensure that the run time was sufficient for convergence of pressure within 1%. For each model PUU system, three different initial conformations were generated, and then subjected to the same equilibration and deformation scheme.

In this section, we will describe the procedure and parameters used in each step. In the simulation, the model PUU systems are represented with a coarse-grained bead-spring model, where the rigidity in polymer chains, which is observed in the hard segment, is enforced using a harmonic angular potential $U_a(r) = K(\theta-\theta_0)^2$. The parameter θ is the angle between triplets of connected beads, where parameters values of $K = 150U_0$ and $\theta_0 = \pi$ were used. We also considered the effect of using larger values of K (200 and $300U_0$), which resulted in only marginal changes in our results. All quantities are expressed in terms of the inter-monomer binding energy U_0, monomer diameter a, particle mass m, and characteristic time $\tau_{LJ} = \sqrt{ma^2/U_0}$. All simulations were executed using LAMMPS [27,28] which is a molecular dynamics program from Sandia National Laboratories.

3.1. Generation and initial equilibration of model PUU systems

Initial configurations of our model PUU systems were first generated as a non-reversal-random-walk. Short simulations using a soft-repulsion potential, that is commonly used in DPD and allows for chain crossing, $U_{DPD}(r) = \frac{a_{DPD}}{2} r_c \left(1 - \frac{r}{r_c}\right)^2$ were then used to speed-up the polymer dynamics involved in phase separation, followed by a push-off procedure that was used to introduce excluded volume before transition to the KG model. This procedure, which includes polymer building, equilibration, and push-off, is called the DPD-push-off algorithm which we will describe briefly. A detailed description of the method can be found elsewhere [24].

Since the brute force equilibration of entangled polymers is nontrivial, even for a case of coarse-grained chains because of the slow diffusive dynamics [29], equilibration was done by temporarily turning off the excluded volume interactions thus allowing the chains to pass through each other. This speed-up comes from the removal of the hard core from the interaction potential, which leads to a caging effect where an atom undergoes many collisions

before it is actually transported. Thus before utilizing the K-G model, DPD [25] was first used to quickly equilibrate the phase-separating system. In a DPD simulation of polymers, particles interact with each other via a pairwise, two-body, short ranged force, **F**, that is written as the sum of a conservative force, $\mathbf{F}^C$, dissipative force, $\mathbf{F}^D$, and random force, $\mathbf{F}^R$, as follows:

$$\mathbf{F}_i = \sum_{j\neq i}\mathbf{F}_{ij}^C + \sum_{j\neq i}\mathbf{F}_{ij}^D + \sum_{j\neq i}\mathbf{F}_{ij}^R \tag{3}$$

The conservative force, $\mathbf{F}^C$, accounts for the pairwise interaction between dissipative particles and also includes a contribution from bonded particles. The remaining two forces, $\mathbf{F}^D$ and $\mathbf{F}^R$, provide the thermostat in the DPD method, where the dissipative force slows down the particles by decreasing kinetic energy, which is balanced by the random force due to thermal fluctuations. A detailed description of DPD method and thermostat can be found elsewhere [30,31].

The repulsive parameter a_{ij} is used to parameterize the repulsion between unlike particle such as those that represent PTMO with those that represent the hard segments and interface, while a_{ii} is the repulsive parameter for like-particles. The repulsive parameters for unlike-particles a_{ij} is related to the Flory-Huggins parameter [25]. Initially, the DPD simulation was performed with $\Delta a = a_{ij} - a_{ii} = 0$ kBT, to remove artificial strain in the system after the building process for $75\tau_{DPD}$ with a time step of $0.0075\tau_{DPD}$. After this, Δa between the beads that represent PTMO and the beads that represent the hard segment or interfaces was increased to $100k_BT$ for the weak interaction model, and to $100k_BT$ between PTMO and hard segment, $50k_BT$ between PTMO and the interface, and $10k_BT$ between the hard segment and interface for the strong interaction model. The simulation was then performed for $15{,}000\tau_{DPD}$ with a time step of $0.0075\tau_{DPD}$ to obtain phase separation. A $r_c = 1.0a$ was used for both DPD runs, where r_c represents the cutoff distance.

After this initial equilibration, a standard "push-off" procedure was performed to remove overlap and to introduce excluded volume. This fast push-off from the DPD soft potential to the full Lennard-Jones potential has been shown to not significantly modify the structural properties of the polymer. In this procedure, Δa was maintained at the values specified above in the second DPD simulation, but the values of a_{ij} and a_{ii} are gradually increased to remove overlap that occurs between the beads due to the use of the DPD method before transition into the K-G model.

3.2. Kremer-Grest model

After equilibration using the DPD-push-off algorithm, the pair interaction between topologically non-connected particles was switched from DPD to the Kremer-Grest [26] standard truncated Lennard-Jones. The standard truncated Lennard-Jones pair potential is given by:

$$U_{LJ}(r) = 4U_0^*\left[\left(\frac{a}{r}\right)^{12} - \left(\frac{a}{r}\right)^{6} - \left(\frac{a}{r_c}\right)^{12} + \left(\frac{a}{r_c}\right)^{6}\right], \tag{4}$$

where U_0^* is the depth of the potential well and a is the distance where the inter-particle force is zero. A $r_c = 2^{1/6}a$ was chosen for interactions involving the coarse-grained beads of PTMO, which yields the so-called Weeks-Chandler-Andersen excluded volume potential, U_{WCA}. In order to drive phase separation, we require an attractive interaction energy between pairs of particles that constitute the hard segment and interface, where for attractive interactions we choose $r_c = 2.5a$. This attraction was chosen to model the association of the hard segments and interfaces which is driven, in part, by their ability to hydrogen bond. For the weak interaction model, U_0^* values of $1.0U_0$ were used between all non-connected pairs of beads, regardless of type. In the strong interaction model, U_0^* values of $1.0U_0$ was used in interactions involving PTMO beads, $1.5U_0$ for interactions between the interface and the hard segment, $1.0U_0$ for interaction between interface beads, and $2.0U_0$ for interaction between hard segment beads.

Topologically bound monomers interact according to the standard FENE/Lennard-Jones bonded potential, $U_{FENE/LJ}$, where $U_{FENE/LJ}(r) = U_{FENE}(r) + U_{WCA}(r)$ and U_{FENE} is a finite extensible non-linear elastic potential defined as

$$U_{FENE}(r) = -\frac{a_{FENE}}{2}R_0^2\ln\left[1 - \left(\frac{r}{R_0}\right)^2\right] \tag{5}$$

Standard parameter values of $R_0 = 1.5a$ and $a_{FENE} = 30U_0/a^2$ were used.

Using the Kremer-Grest model while maintaining the DPD thermostat, we equilibrated the system for $75{,}000\tau_{LJ}$ (time step $0.0075\tau_{LJ}$) with $T = \text{const} = 1.0\,U_0/k_B$. After equilibration, we performed a temperature quench to $T = 0.3\,U_0/k_B$ with a cooling rate of $\dot{T} = 7\cdot10^{-5}\,U_0/k_B\tau_{LJ}$, followed by an constant pressure and temperature (NPT) simulation for $1\times10^4\tau_{LJ}$ (time step $0.01\tau_{LJ}$), where both were performed with a Langevin thermostat [32]. The temperature was quenched to $T = 0.3\,U_0/k_B$ to mimic experimental conditions where the operating temperature is above T_g for the rubbery PTMO block and below T_g for the hard segment. Based purely on the potentials used in our model, the PTMO coarse-grained particles, which are described by a repulsive potential, have a T_g that is below $0.2\,U_0/k_B$ [33], while the remaining particles that are described by an attractive potential (interface and hard segment) have a T_g above$0.4\,U_0/k_B$ [34]. Introducing rigidity into the interface and hard segment will further increase this value of T_g [35].

3.3. Deformation

After the NPT simulation, uni-axial-stress tensile or compression deformations were imposed on the simulation cell in the z direction. A constant true strain rate of $\dot{e} = 10^{-6}$, 10^{-5}, $10^{-4}\tau_{LJ}^{-1}$ was applied to the simulation box for the tensile deformations, which expands the simulation box in the positive and negative directions. Negative values of the true strain rates were also used to simulate compression. During the simulation the box dimension, L_z changes with time as $L_z(t) = L_0\exp(\dot{e}\Delta t)$ where L_0 is the initial box size in the z dimension.

Stress-strain calculations were performed under the assumption of constant pressure. Thus extension/compression in z is accompanied by lateral compression/extension (in x and y), such that pressure in x and y are constant. The deformation simulation is performed with the Langevin thermostat with a damping time $1.0\tau_{LJ}$ to maintain temperature and the Nose-Hoover barostat with damping time $100\tau_{LJ}$ to maintain constant pressure along the transverse directions. Simulation runs have been done for continuous uniform strain (every time step) using a time step $\Delta t = 0.0075\tau_{LJ}$. At every time step Δt, the positions of the particles are rescaled by the factor $x/L\dot{L}\Delta t$, where x_i is the component of the position vector in the direction of deformation, and $\dot{L}$ is the deformation velocity. The elongational stress, σ in the system is then calculated from the normal pressure differences:

$$-\sigma = P_{zz} - \frac{1}{2}(P_{xx} + P_{yy}). \tag{6}$$

4. Analysis

Below we briefly review the analysis methods that we employed to analyze our computational results.

4.1. Radial distribution function

The microstructure of our model PUU systems can be studied computationally through the radial distribution function (RDF) which measures both intra- and inter-chain correlation, and has been used to characterize micelle ordering in numerous computational studies [36–39]. The RDF between particles that represent the hard segment will be used to discern qualities of the average structure, where short range peaks are due to correlations within the clusters formed by the rods. The long range peak corresponds to the average distance between clusters of rods, where the area under the peak can gives us an indication of the ordering. The Fourier transform of the RDF are directly related to scatter intensities that can be obtained experimentally through techniques such as neutron scattering and SAXS.

4.2. Calculation of the rod orientation

The morphology details as identified by AFM for select model PUUs appear to be complex. To characterize the orientation of the rods in our model PUU systems, we can calculate the orientation angle of the hard segments relative to the x, y, and z axis. This orientation is characterized by the polar (θ) and azimuthal (ϕ) angles defined in Eqs. (7) and (8), respectively.

$$\theta = \cos^{-1}\left(\frac{(z_2 - z_1)}{r}\right) \tag{7}$$

$$\phi = \tan^{-1}\left(\frac{(y_2 - y_1)}{(x_2 - x_1)}\right) \tag{8}$$

In these equations, (x_1, y_1, z_1) and (x_2, y_2, z_2) denote the coordinates at either end of the hard segment as seen in Fig. 3a, where r is defined as the radial distance of the rod defined as $r = \sqrt{(x_2 - x_1)^2 + (y_2 - y_1)^2 + (z_2 - z_1)^2}$.

Since the ends associated with (x_1, y_1, z_1) and (x_2, y_2, z_2) can be interchanged, the vector describing the hard segment is unique only within a half space. In this study, the half space is defined by $0 \leq \phi \leq \pi$ and $0 \leq \theta \leq \pi$.

4.3. Order parameter

To characterize the order of rods relative to the positive z-axis, we define an order parameter $S = \langle 2\cos^2\theta - 1\rangle$, where θ is the angle between the long axis of a particle and the positive z-axis, and the brackets denote an average overall observations. The order parameter ranges from -1 and $+1$, where large absolute values represent higher order (See Fig. 3b). The sign of S indicates the orientation of the rod, where positive or negatives value indicates that the rod aligns parallel or perpendicular to the z-axis, respectively.

5. Results

CG simulations of local morphology can account for various possible scenarios with respect to the self-assembly of hard segments such as isolated hard segments domains within the continuous soft segments matrix, or interconnected disordered hard segments. Through the procedure described in the computational model & methods section, we are able to study the local morphology and stress-strain behavior of segmented PUUs composed of alternating hard and soft segments. Computational results presented in this section were obtained by averaging three replicas unless otherwise indicated. Data for the stress-strain curves was sampled every $0.75\tau_{LJ}$, where each data point in the stress-strain curves is a box average of 10,000 points. In the following, we highlight the key material characteristics derived from modeling for comparison with experimental observations, to enable a better understanding of the role of molecular influence on both tunable microstructure and dynamic mechanical strengthening.

5.1. Local morphology: after equilibration scheme

The morphology observed in the select model PUUs is complex and can affect the mechanical deformation, which can range from rubbery to leathery-like response under quasi-static loading conditions. The evolution of tunable microstructure can depend not only on the hard segment content, but also greatly on the molecular moieties including the rigidity of the interface and intermolecular interaction. Using our CG model, we can study the effect of these parameters on the local morphology for our PUU model systems. Although finite size effects and time constrains would prevent us from obtaining a well-equilibrated morphology, the model is able to capture important morphological features. That being said, for the time scales we are able to access, the properties of interest did not noticeably change with further simulation time.

A snapshot of the morphology for Rigid-strong and Flex-strong are shown in Figs. 4 and 5, respectively. For the Rigid models, clusters composed of aligned hard segments are observed for system 1, while increasing the hard segment content as in systems 2 and 3 disrupts this ordering. In the Rigid models, the clusters

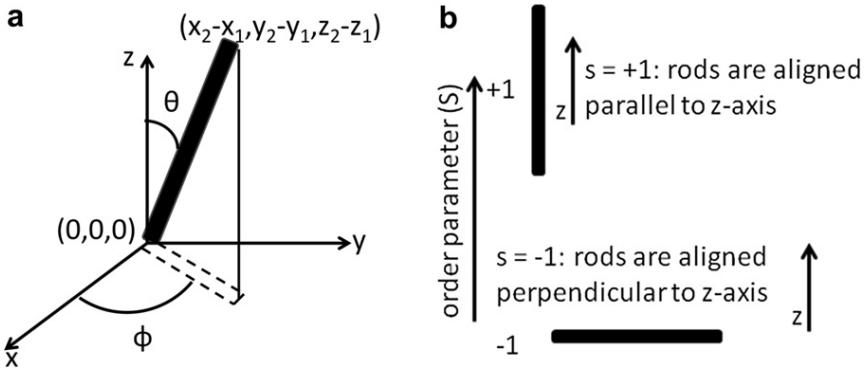

Fig. 3. a) Definition of the azimuthal (ϕ) and polar angle (θ). b) Definition of the order parameter.

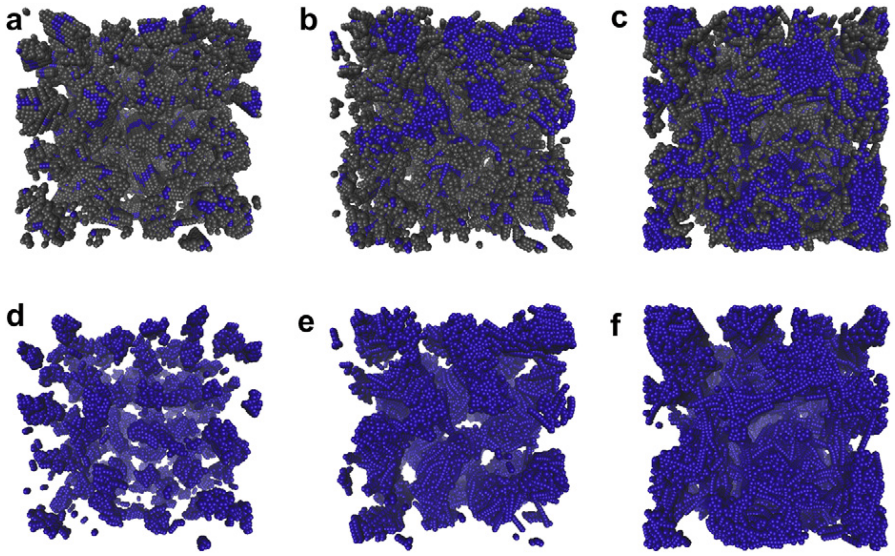

Fig. 4. Representative morphology for Rigid-strong after equilibration procedure for model (a,d) 1, (b,e) 2, and (c,f) 3. (top row) Only the hard segments defined by Eq. (1) are shown. (bottom row) Only the hard segments not including the interface are shown for clarity. Beads that represent the interface are shown in gray while the remaining hard segment is shown in blue. Simulation box sizes are listed in Table 2. (For interpretation of the references to color in this figure legend, the reader is referred to the web version of this article.)

observed in system 1 are formed of groupings of hard segments (which include the interface) which tend to align in the same direction as seen in Fig. 6.

These clusters are not necessarily isolated, but can be connected to other clusters through bridges composed of the hard segments. At higher hard segment content we observe less alignment of the hard segments and greater percolation, i.e. long range connectivity, of disordered hard segments through the simulation cell. Similar morphology was also observed in the Rigid-weak model. For the Flex-strong computational model, we observe the predominance of hard segments in the form of elongated micellar structures as shown in Figs. 5a and 7b for system 1, in comparison to mostly isolated clusters seen for Rigid-strong as highlighted in Fig. 7a. As the hard segment content increases, significantly greater clustering of the rods is observed for the Flex-strong model for systems 2 and 3 (Fig. 5), partly as a result of the tangible association of flexible interface beads onto the hard segments in addition to the increasing propensity for percolation. However, as seen in Fig. 8, this clustering is less ordered than in the Rigid-strong model for system 1, where increasing percolation with increasing hard segment in part accounts for this disordering. In the Flex models, the interface, due to its flexibility, also has a tendency to coil around the hard segment (see Fig. 9), which hinders the organization of the hard segments.

This coiling of interface is more prevalent in the weak interaction model than in the strong interaction model, which is due to the intermolecular interaction. In the former, the attraction between the beads that represent the hard segment and the interface are the same as the hard segment-hard segment and interface−interface self interactions, while in the strong interaction model, the attractions between the beads that represent the rods is stronger than the other interaction. Because of this stronger interaction between the rods in the Flex-strong model, the interface has a lower tendency to coil around the rods resulting in more of the interface beads residing at the boundary between the domains composed mostly of the soft segments and the hard segments. An indication of this is illustrated in Table 4, which lists the number of beads representing the rigid segments that are at the cutoff distance of $2^{1/6}a$ away from beads that represent the soft segment. This shows that the number of hard segments beads that are in contact with the soft segment is less for Flex-strong than for Flex-weak for all of our model PUU systems.

Additional information on morphology can be extracted by considering the RDF between the particles that represent the hard segments. The RDF data for our four computational models are

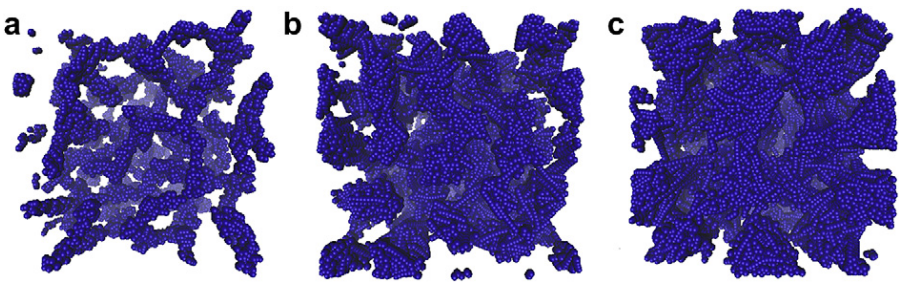

Fig. 5. Representative morphology for Flex-strong after equilibration procedure for model (a) 1, (b) 2, and (c) 3. Only the hard segments (blue) defined by Eq. (2) are shown for clarity. Simulation box sizes are listed in Table 2. (For interpretation of the references to color in this figure legend, the reader is referred to the web version of this article.)

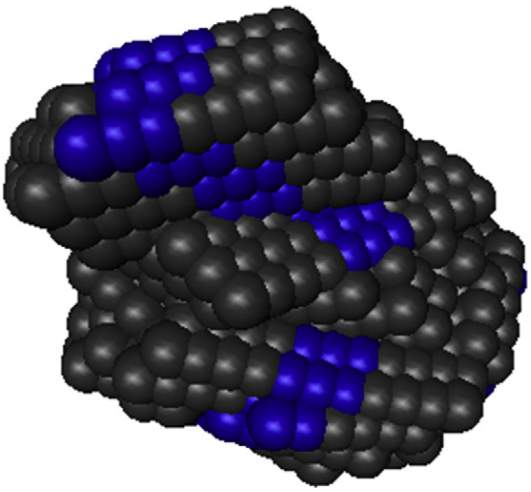

Fig. 6. Representative cluster formed by the hard segments (which include interface) observed in model 1 for the Rigid models.

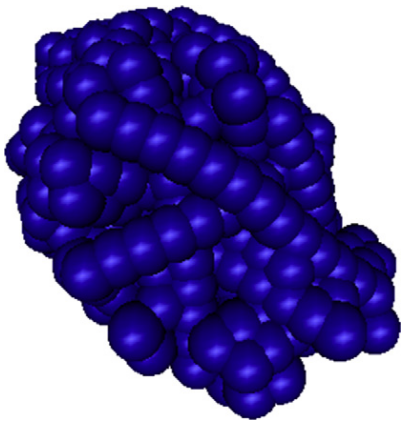

Fig. 8. Representative cluster formed by the hard segments observed in system 3 for the Flex models..

shown in Fig. 10 for our three model PUUs. Instead of focusing on the short range peaks, which are due to intra-cluster order, these RDF data highlight the subsequent peaks that are primarily associated with inter-cluster correlations. The RDFs in Fig. 10 were obtained by averaging the RDFs obtained from the three replicas, which were evaluated from the final conformation in the constant pressure simulation prior to deformation. The RDF indicates significant long range cluster ordering of the rods for systems 1 and 2 for all four computational models, though little cluster ordering for system 3 is observed for the Rigid models. Within the Flex model, greater ordering of the rods into clusters for system 3 is observed for Flex-strong compared to Flex-weak, presumably due to difference in intermolecular interactions, which in the former model reduces the tendency of the interface to coil around the hard segments. The calculated values of average separation for these clusters obtained based on the position of the secondary peak are also given in Table 5.

Due to the poor ordering for system 3 in the Rigid model, the location of the secondary peak is less well-defined so the values for the average separation were not calculated. The magnitude of the short range peak in the RDF, ordered from largest to smallest is system 1 (Rigid ~ 13, Flex ~ 37), system 2 (Rigid ~ 6, Flex ~ 9), and system 3(Rigid ~ 4, Flex ~ 6) for both the Rigid and Flex models indicating that the clusters formed from the hard segment are more ordered and compact in system 1, and become less compact as the hard segment content is increased to system 3. In the case of Flex models the smaller hard segment content results in a slightly higher percolation threshold, where cluster like morphologies are easier to distinguish for systems 2 and 3 compared to the corresponding Rigid models. This is also manifested in the short range peaks which are larger in the Flex models.

The isolated hard domains in Rigid-strong for system 1 from simulation (Figs. 5a and 7a) clearly resemble the microphase-separated morphology observed through atomic force microscopy (AFM) phase images [18] (Fig. 11), where a mixture of fine grains with particle size in the range of 30, 60, and 120 nm were observed. These spherical fine grains are composed of the hard segments, and reside in a matrix composed of the soft segments PTMO. In addition, both AFM images [40] and SAXS results [15] do suggest greater phase mixing between the soft and hard segments for systems 2 and 3, which agree with the disordering observed in the morphology obtained using the Rigid models. This indicates that our model is capable of capturing important features in the morphology. This is vital since the phase behavior of the hard and soft segments are known to be responsible for the mechanical behavior of this class of material [41,42].

5.2. Uni-axial tension and compression

In this study, we use the microstructure derived from our coarse-grained model to calculate the stress-strain behavior at

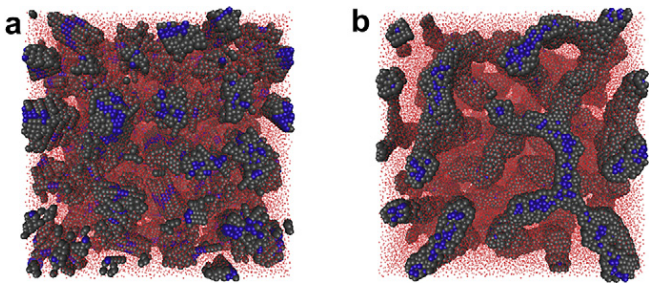

Fig. 7. Representative morphology for model 1 for a) Rigid-strong b) Flex-strong after equilibration procedure. Interface beads shown in gray and hard segment as defined by HS_{Flex} are shown in blue. PTMO segments are shown as red points. Note: For Rigid-strong, the interface beads are part of the hard segment as defined by HS_{Rigid} in Eq. (1). (For interpretation of the references to color in this figure legend, the reader is referred to the web version of this article.)

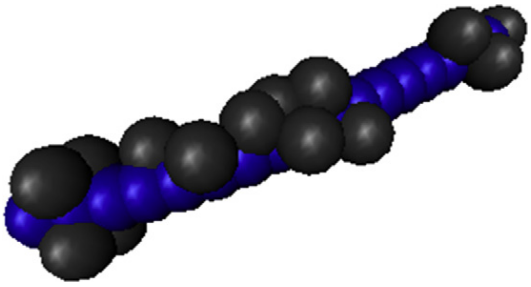

Fig. 9. Representative image of the interface wrapping around the hard segment in the Flex models.

Table 4
Number of beads representing the rigid segments that are $2^{1/6}a$ away from beads that represent the soft segments.

	1	2	3
Flex-weak	1009 ± 20	10440 ± 145	16496 ± 93
Flex-strong	434 ± 5	6825 ± 64	10637 ± 405

Table 5
The calculated values of average distance between clusters from four models.

	Average distance between clusters (a)		
	1	2	3
Rigid-strong	15.63 ± 0.16	21.85 ± 0.16	–
Rigid-weak	15.65 ± 0.32	22.83 ± 0.29	–
Flex-strong	16.79 ± 0.42	17.49 ± 0.22	22.59 ± 0.40
Flex-weak	17.11 ± 0.36	16.77 ± 0.16	20.15 ± 0.34

strain rates of $\dot{e} = \pm 10^{-6}, \pm 10^{-5}, \pm 10^{-4}\ \tau_{LJ}^{-1}$, where the positive and negative values correspond to uni-axial tension and compression, respectively.

In this section, we will first compare our stress-strain results with experimental data. In addition, we will characterize the orientation of the rods during the simulation. The effects of rigidity at the interface and intermolecular interaction on the deformation behavior will also be investigated through our model systems.

5.2.1. Comparison with experimental system

The composition dependence of the stress-strain behavior for PUUs under uni-axial tension and compression is displayed in Fig. 12 for $\dot{e} = \pm 10^{-6}\ \tau_{LJ}^{-1}$, which is the slowest rate that we consider, for the Rigid-strong model which most closely models our PUU experimental system. Computational results for Rigid-strong agree qualitatively well with published experimental results shown in Fig. 13 [15], which was obtained under uni-axial compression, where the unit of computational unit of stress, a^3/U_0, roughly corresponds to 50 MPa [43,44]. The experimental data were obtained through the split Hopkinson bar impact measurements typically at strain rates on the order of $10^4\ s^{-1}$, while our lowest computational strain rates of $\dot{e} = \pm 10^{-6}\ \tau_{LJ}^{-1}$ roughly correspond to strain rates of order $10^5\ s^{-1}$. This conversion was calculated from our simulation time scale $\tau_{LJ} \sim 3$ ps, which was derived for a hydrocarbon polymer chain [45,46]. It is difficult to compare results at the same strain rate due to restrictions in our computational simulations which become more computationally expensive with decreasing strain rates.

By comparing Figs. 12 and 13, we observe the same trend in the stress-strain behavior under high strain rate uni-axial compression between the simulated and experimental systems. For instance, the modulus increases with increasing hard segment content (from system 1–3). Even so, one noted difference is that the simulated modulus for system 1 and 2 are much lower than those observed in experiments. This difference occurs since our simulations cannot reach the large time and length scales accessible though experiments, which leads to differences in morphology (i.e. size of agglomerate, extent of ordering), that subsequently affects the modulus. No experimental data exists for comparison of tensile stress-strain behavior under high strain rates.

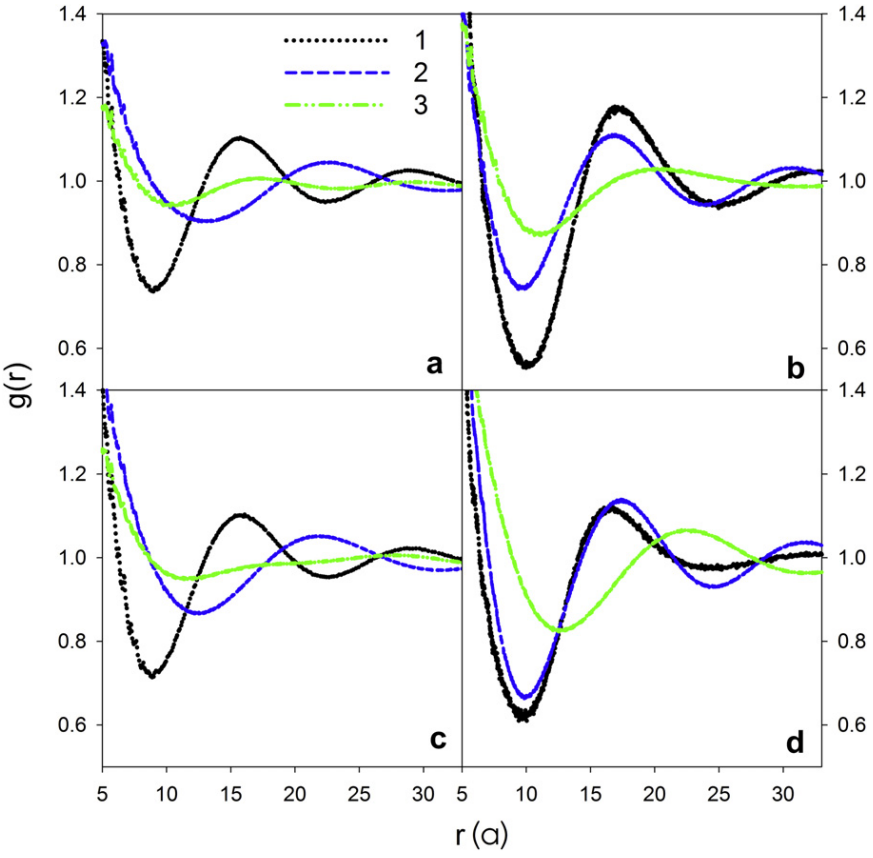

Fig. 10. Radial distribution functions (zoomed to long range peaks) for a) Rigid-weak, b) Flex-weak, c) Rigid-strong d) Flex-strong.

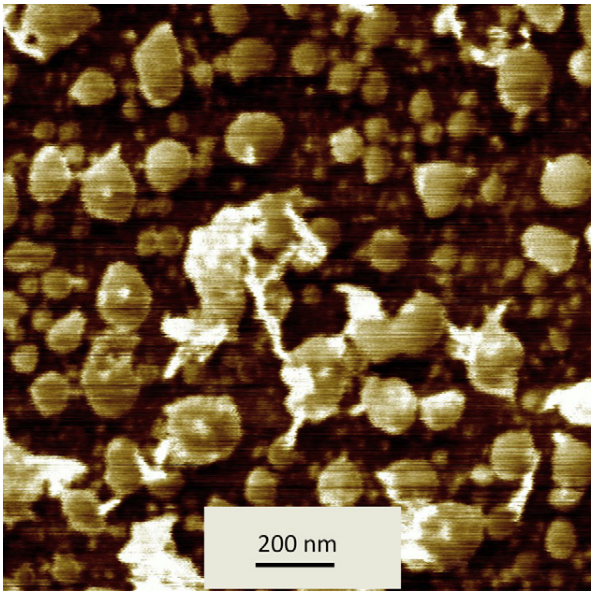

Fig. 11. Experimental AFM for Model 1.

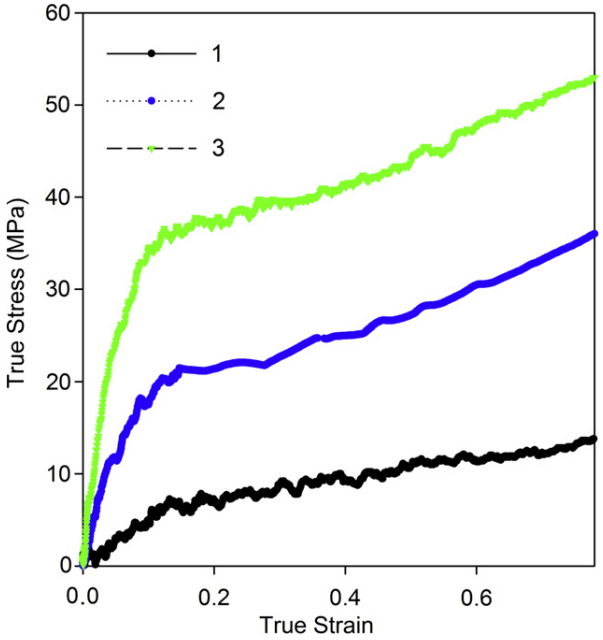

Fig. 13. Experimental stress-strain curve under uni-axial compression for PUUs at strain rate of 4500 s^{-1} (color online) Experimental data from Ref. [15] reproduced with permission from Polymer Elsevier.

To qualify the orientation of the hard segment during the simulation, we first calculated the azimuthal and polar angle as defined in Section 4.2 before deformation and at various strains for our lowest strain rate of $\dot{e} = \pm 10^{-6}\ \tau_{LJ}^{-1}$. During the simulation, we do not observe a statistically significant change in the azimuthal angle which measures the angle in the x–y plane from the x axis, though we do observe variation in the polar angle which measures that angle from the positive z-axis (see Fig. 3a). This is due to the uni-directional nature of the deformation which was performed along the z direction. In general, we observe that the hard segments begin to orient parallel in the z direction during tension, while in compression they orient perpendicular to the z-axis. In the Rigid-strong model, this reorganization is more significant in system 3. Among these PUUs, increasing hard segment content gives rise to increased rod interaction and percolation which facilitates more efficient chain orientation in system 3, and as a result greater strain hardening in the stress-strain data. This same trend is also observed for Rigid-weak model, though in the Flex model there is no clear distinction when accounting for the amounts of reorganization between PUUs, suggesting that the rod size and the rigidity of interface are factors that can affect the rods reorientation during deformation.

To compactly characterize the rods organization, an order parameter, S, was defined which quantifies the deviation in the orientation of the hard segment away from the z-axis. The definition of this order parameter can be found in Section 4.3. Variation in S as a function of strain for the Rigid-strong computational model is highlighted in Fig. 14 for the three model PUU systems at a strain rate of $\dot{e} = \pm 10^{-6}\ \tau_{LJ}^{-1}$. From this plot we can study the behavior of the rod orientation as a function of strain. In the Rigid models the behavior is non-linear, where we observe a sharp increase in orientation for system 1 and system 2, whereas an almost linear change is noted for system 3 presumably due to the dominance of rods interaction and percolation. This is consistent with the trend observed in the RDF data (Fig. 10). In addition, this behavior in the order parameter does not statistically change when the strain rate is increased to $\dot{e} = \pm 10^{-5}, \pm 10^{-4}\ \tau_{LJ}^{-1}$, presumably due to the high

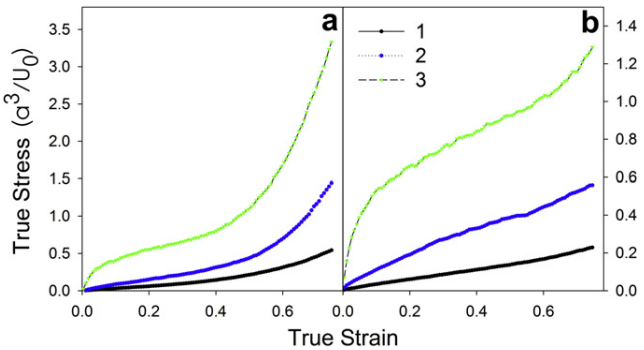

Fig. 12. Stress-strain curve under a) tension and b) compression calculated from Rigid-strong at strain rate $10^{-6}\tau_{LJ}^{-1}$.

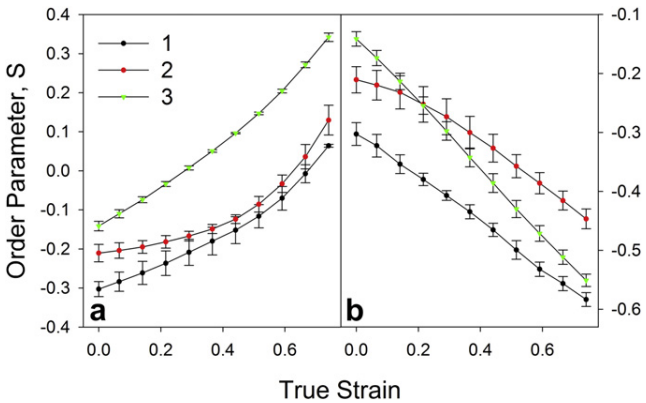

Fig. 14. Order parameter for a) tension and b) compression for the Rigid-strong model at strain rate of $10^{-6}\tau_{LJ}^{-1}$.

strain rates used in simulation, which is consistent to the observation by Pathak et al. [13].

The flow stress, which is typically used to denote the stress at a particular strain beyond the yield point, increases with increasing HS_{Rigid} content in PUUs, regardless of the loading conditions either under tension or compression, as seen in Fig. 15 for a strain of 0.3, though greater strain hardening is evident when PUUs are under tension than under compression (Fig. 12). At the higher strain rates of $\dot{e} = \pm 10^{-5}, \pm 10^{-4}\ \tau_{LJ}^{-1}$, we observe similar stress-strain curves as at $\dot{e} = \pm 10^{-6}\ \tau_{LJ}^{-1}$ (Fig. 12) though the magnitude of stress increases with strain rate, indicative of viscoelastic characteristic. Furthermore, greater dynamic strain rate sensitivity is noted for systems 2 and 3 in comparison to system 1, as shown in Fig. 15 for PUUs.

These observations are consistent with experimental stress-strain data extrapolated to strain rates comparable to those used in simulation. These results clearly indicate that greater phase mixing of the hard and soft segments as a result of disordering with increasing hard segment content gives rise to dynamic strain hardening in our PUU model systems. This phase mixing can also induce changes in segmental dynamics, which has been linked to greater shock mitigation in polyurea [47], is currently under study.

5.2.2. Taking into account of rigidity and interaction at the interface

The optimal calorimetric T_g value with respect to the attendant dynamic deformation strain rate as mentioned above is key to substantial energy absorption and dissipation. We also observed in DMA [15] that increasing the hard segment content gave rise to multiple relaxation peaks in addition to the relaxation associated with the PTMO-rich region, suggesting greater phase mixing between soft and hard segments in systems 2 and 3, which is validated by the disordering from the Rigid models seen in Fig. 4b and c. Here we examine the intermolecular interaction and the flexibility associated with the interface and highlight their influence on the stress-strain behavior.

By varying the intermolecular interaction, we can observe variation in the stress-strain behavior. This is illustrated in Fig. 16, where the stress-strain curves under tension at $\dot{e} = 10^{-6}\ \tau_{LJ}^{-1}$ are plotted for the Rigid-weak and Rigid-strong for all three PUU model systems. Under tension, greater strain hardening is evident in Rigid-strong as a result of the stronger intermolecular interaction which loosely resembles bidentate hydrogen bonding, while the weak interaction model resembles monodentate hydrogen bonding. Additionally, the extent of strain hardening becomes more

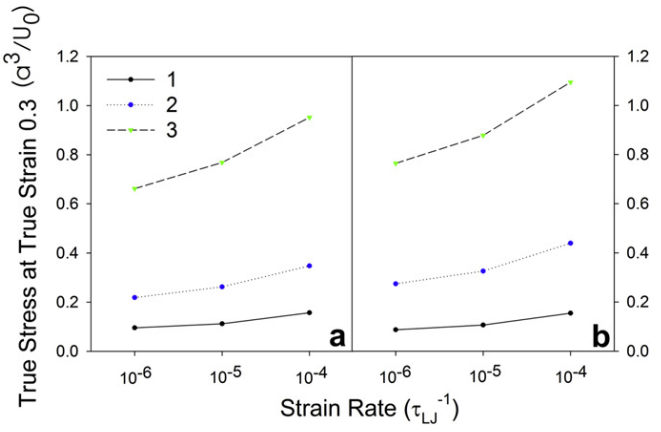

Fig. 15. Flow stress obtained at a true strain of 0.3 for Rigid-strong model under a) tension and b) compression.

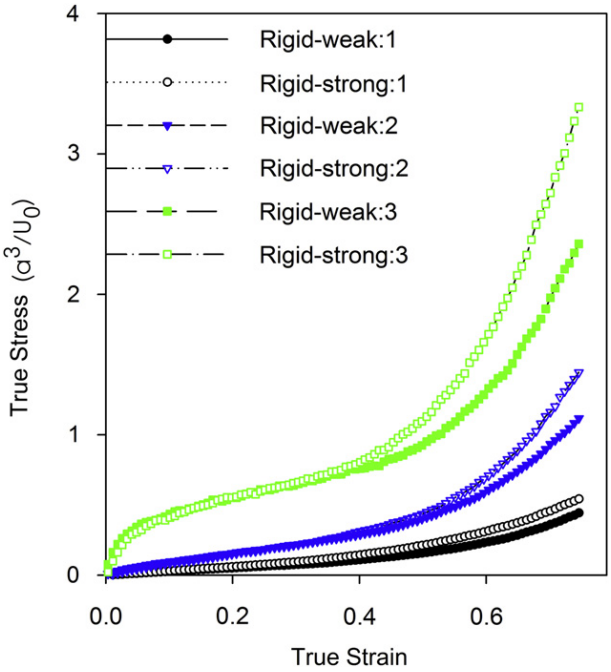

Fig. 16. Comparison of stress-strain behavior for the Rigid-weak and Rigid-strong for all three PUUs under tension at $\dot{e} = 10^{-6}\tau_{LJ}^{-1}$.

significant in Rigid-strong vs. Rigid-weak once it is near the percolation threshold, where a change from dispersed microphase-separated domains at lower hard segment content (system 1) to interconnected disordered hard segments occurs as hard segment content increases.

5.2.3. Consideration of the phase-mixed regions

From the simulation results above, we can see that the Flex model more closely resembles a flexible interphase, which could represent a phase-mixed region in contrast to the rigid interface in microphase-separated domains simulated in the Rigid model. To further examine the effect of this phase-mixed region, we compare the Flex-strong and Rigid-strong models.

During the initial stress-strain response ($< \sim 0.15$–0.2 strain), which is well below the incipient point of strain hardening, both Flex-strong and Rigid-strong exhibit similar mechanical deformation, regardless of tension or compression, despite a much lower hard segment content in Flex-strong. In the Flex model as shown in Fig. 9, a flexible interface tends to coil around the hard segment, suggesting a propensity to facilitating phase mixing. These phase-mixed domains are shown to give rise to similar mechanical response as the more microphase-separated domains observed in the Rigid-strong model, predominantly for system 1 as shown in Fig. 17. This indicates that intermolecular hydrogen bonds, which were modeled by an attractive potential, dominates over the stiffness or the size of the hard segment. This intermolecular interaction may also facilitate the formation of elongated hard segments for Flex-strong as seen in Fig. 7b as compared to mostly isolated hard segment clusters for Rigid-strong. Once reaching or above the percolation threshold Rigid-strong, as expected, becomes more dominated in the stress-strain behavior under both tensile and compression. These observations imply that increasing intermolecular interaction via molecular mechanisms can be the key to local morphology and robust mechanical strengthening, particularly well below the percolation threshold. Thus it is an important

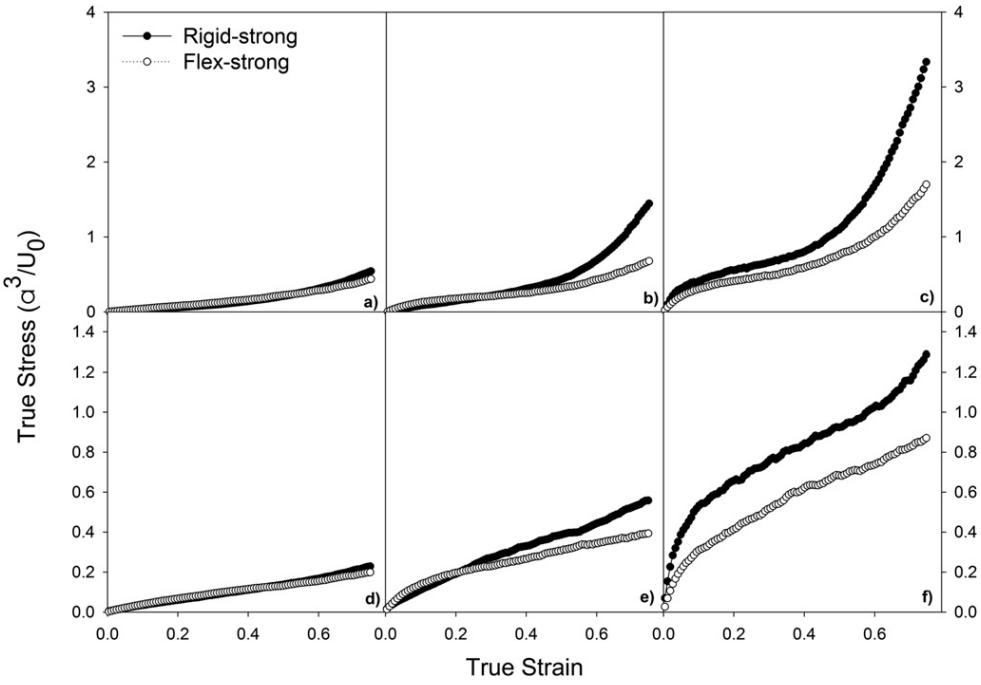

Fig. 17. Stress-strain curves at $\dot{e} = \pm 10^{-6}\tau_{LJ}^{-1}$ for the Rigid-strong and Flex-strong models under tension (top row) and compression (bottom row) for model (a,d) 1, (b,e) 2, and (c,f) 3.

parameter for use in the design of high performance elastomeric materials.

6. Conclusion

Through coarse-grained modeling, we have identified material characteristics including the rigidity of the interface, the intermolecular interaction, and the hard segment content as well as their influences on the morphology and mechanical deformation behavior in three model PUU systems. Our results indicate that the hard segment content and interface rigidity both play a large role on the morphology, where lower hard segment contents correspond to more ordered microstructures, while higher hard segment content gives rise to increasingly disordered microstructures that exhibit long range connectivity of the hard segment. The flexibility of the interface was also shown to affect the overall morphology including promoting the formation of elongated micellar structures at low hard segment content along with a slightly higher percolation threshold. Additionally the propensity of the interface to coil around the hard segment favors disordering that could lead to phase mixing. Simulation results based on the Rigid-strong model qualitatively agree with available experimental data in terms of both morphology and the trend in the stress-strain behavior with respect to the PUU composition. The effect of intermolecular interaction was found significant once the hard segment content reaches the percolation threshold particularly for a rigid interface, where a stronger attraction leads to greater strain hardening upon tensile loading. On the other hand, simulation results also revealed that for a flexible interface, the intermolecular interactions could even dominate over interface rigidity in the initial stress-strain response, particularly when below percolation. Analysis of the hard segment orientation during both tensile and compression deformation was also performed and results indicate that it was dominated by percolation. Furthermore, greater dynamic strain rate sensitivity was evidenced with increasing hard segment content, corroborated well with the extrapolation of available experimental data, which as expected is partly of viscoelastic characteristic, and additionally a result of disordering leading to phase mixing. We are currently exploiting coarse-grained modeling to further study the influence of tunable microstructure on local segmental dynamics during high strain rate deformation for our PUU model systems which as reported can have a profound effect on ballistic impact protection and blast mitigation. In addition, the effects of varying the size of the PTMO segment would also be studied and results will be reported in a future publication. Furthermore, in the current manuscript the values of the potential well depth in the standard truncated Lennard-Jones pair potential were qualitatively chosen to approximate monodentate and bidentate hydrogen bonding. To quantify these values, Quantum mechanics may be used in the future.

These simulation results clearly demonstrate the coarse-grained modeling capability and additionally highlight the versatility of a three-component PUU system over commercially available two-part elastomers, wherein tunable microstructure and interface strength can be optimized. Both, along with the glass transition temperature, are necessary for the development of a phase diagram which is pertinent for use in the design of next generation high performance elastomers.

Acknowledgments

The authors would like to thank Professor R. Riggleman (PENN) for useful discussion. Funding has been provided by the Director's Research Initiative program at the Army Research Laboratory. YRS was supported in part by an appointment to the Postgraduate Research Participation Program at the U.S. Army Research Laboratory administered by the Oak Ridge Institute of Science and Education through an interagency agreement between the U.S. Department of Energy and ARL. The DoD HPC Modernization Office supported this project by supplying supercomputer time under the Computing Challenge Project C5M. This computer time was made available at the DoD Major Shared Resources Centers at the AFRL DSRC.

References

[1] Porter JR, Dinan RJ, Hammons MI, Knox KJ. AMPTIAC Quart 2002;6(4):47–52.
[2] Bogoslovov RB, Roland CM, Gamache RM. Appl Phys Lett 2007;90: 221910–221911-221913.
[3] Tekalur SA, Shukla A, Shivakumar K. Compos Struct 2008;84(3):271–81.
[4] Bahei-El-Din YA, Dvorak GJ, Fredricksen OJ. Int J Solid Struct 2006;43(25–26): 7644–58.
[5] Grujicic M, Pandurangan B, He T, Cheeseman BA, Yen C-F, Randow CL. Mater Sci Eng A 2010;527:7741–51.
[6] Grujicic M, Pandurangan B, King AE, Runt J, Tarter J, Dillon G. J Mater Sci 2011; 46:1767–79.
[7] Miller CE, Edelman PG, Ratner BD, Eichinger BE. Appl Spectrosc 1990;44(4): 581–6.
[8] Lee HS, Wang YK, Hsu SL. Macromolecules 1987;20(2089).
[9] Zhao G-S, Zhang G-B, Liu Q. Spectro Spect Anal (China) 1987;6:14.
[10] Luo N, Wang D-N, Ying S-K. Polymer 1996;37(16):3577–83.
[11] Yeh F, Hsiao BS, Sauer BB, Michel S, Siesler HW. Macromolecules 2003;36: 1940–54.
[12] Rinaldi RG, Boyce MC, Weigand SJ, Londono DJ, Guise MW. J Polym Sci Part B Polym Phys 2011;49:1660–71.
[13] Pathak J, Twigg J, Nugent K, Ho D, Lin E, Mott P, et al. Macromolecules 2008; 41(20):7543–8.
[14] Fragiadakis D, Gamache RM, Bogoslovov RB, Roland CM. Polymer 2010;51: 178–84.
[15] Sarva SS, Hsieh AJ. Polymer 2009;50(13):3007–15.
[16] Rinaldi RG, Hsieh AJ, Boyce MC. J Polym Sci Part B: Polym Phys 2011;49(2): 123–35.
[17] Hsieh AJ, Yu JH, Rinaldi RG, Krogman KC, Hammond PT, Boyce MC, et al. Poly(urethane urea)s with tunable microstructures – from robust mechanical strengthening to chemical hardening. 27th army science conference; 2010. Orlando, FL.
[18] Hsieh AJ, Strawhecker KE. Microstructure analysis of transparent poly(-urethane urea) elastomers via AFM. In: PMSE preprints of the American chemical society, vol. 105. Denver, CO: American Chemical Society; 2011. p. 162–3.
[19] Chantawansri T, Hsieh AJ. Hierarchical elastomers with tunable microstructures-molecular modeling from robust mechanical strengthening to multifunctionalities (first-year report). In: Laboratory AR, editor. ARL-MR-0800. Aberdeen Proving Ground; 2012.
[20] Holden G, Legge N, Quirk R, Schroeder H. Thermoplastic elastomers. 2nd ed. Munich: Hanser Publishers; 1996.
[21] Clayden J, Greeves N, Warren S, Wothers P. Organic chemistry. 1st ed. New York: Oxford University Press; 2001.
[22] Yilgör E, Burgaz E, Yurtsever E, Yilgör I. Polymer 2000;41:849–57.
[23] Quantum mechanics calculation using density functional theory M05 was performed using the software package Gaussian. Results indicate that the hydrogen bonding between the urea segments are stronger (bond energy = 14.2 kcal/mol) than the hydrogen bonding between the urethane linkages (bond energy = 10.3 kcal/mol).
[24] Sliozberg YR, Andzelm JW. Chem Phys Lett 2011;523(27):139–43.
[25] Groot RD, Warren PB. J Chem Phys 1997;107(11):4423–35.
[26] Kremer K, Grest GS. J Chem Phys 1990;92(8):5057–87.
[27] http://lammps.sandia.gov.
[28] Plimpton SJ. J Comput Phys 1995;117:1–19.
[29] Rubinstein M, Colby RH. Polymer physics. New York: Oxford University Press; 2003.
[30] Hoogerbrugge PJ, Koelman JMVA. Europhys Lett 1992;19(3):155–60.
[31] Español P, Warren PB. Europhys Lett 1995;30(4):191–6.
[32] Schnider T, Stoll E. Phys Rev B 1978;17:1302–22.
[33] Yamamoto R, Onuki A. J Chem Phys 2002;117(5):2359–67.
[34] Bennemann C, Paul W, Binder K, Dunweg B. Phys Rev E 1998;57(1):843–51.
[35] Bulacu M, van der Giessen E. Phys Rev E 2007;76:011807.
[36] Arman B, Reddy AS, Arya G. Macromolecules 2012 [Article ASAP].
[37] Sliozberg YR, Strawhecker KE, Andzelm JW, Lenhart JL. Soft Matter 2011;7: 7539–51.
[38] Wijmans CM, Eiser E, Frenkel D. J Chem Phys 2004;120:5839–48.
[39] Guo L, Luijten E. J Poly Phys B 2004;43:959–69.
[40] Hsieh AJ. unpublished, 2011.
[41] Yi J, Boyce MC, Lee GF, Balizer E. Polymer 2006;47:319–29.
[42] Aneja A, Wilkes GL. Polymer 2003;44(23):7221–8.
[43] Robbins MO, Hoy RS. J Poly Phys B 2009;47(14):1406–11.
[44] Rottler J, Barsky S, Robbins MO. Phys Rev Lett 2002;89(14):148304.
[45] Hoy RS, Robbins MO. J Chem Phys 2009;131:244901.
[46] Rottler J, Robbins MO. Phys Rev E 2003;68:011507.
[47] Grujicic M, Pandurangan B. J Mater Sci 2012;47:3876–89.

An Enhanced Entangled Polymer Model for Dissipative Particle Dynamics

Timothy W. Sirk, Yelena R. Sliozberg, John K. Brennan, Martin Lisal
and Jan W. Andzelm

The Journal of Chemical Physics 136, (2012)

THE JOURNAL OF CHEMICAL PHYSICS **136**, 134903 (2012)

An enhanced entangled polymer model for dissipative particle dynamics

Timothy W. Sirk,[1] Yelena R. Slizoberg,[1] John K. Brennan,[2,a)] Martin Lisal,[3,4] and Jan W. Andzelm[1,b)]
[1]*Macromolecular Science and Technology Branch, Army Research Laboratory, Aberdeen, Maryland, USA*
[2]*Energetic Materials Science Branch, Army Research Laboratory, Aberdeen, Maryland, USA*
[3]*E. Hála Laboratory of Thermodynamics, Institute of Chemical Process Fundamentals of the ASCR, v. v. i., Czech Republic*
[4]*Department of Physics, Faculty of Science, J. E. Purkinje University, Czech Republic*

(Received 21 November 2011; accepted 12 March 2012; published online 5 April 2012)

We develop an alternative polymer model to capture entanglements within the dissipative particle dynamics (DPD) framework by using simplified bond-bond repulsive interactions to prevent bond crossings. We show that structural and thermodynamic properties can be improved by applying a segmental repulsive potential (SRP) that is a function of the distance between the midpoints of the segments, rather than the minimum distance between segments. The alternative approach, termed the modified segmental repulsive potential (mSRP), is shown to produce chain structures and thermodynamic properties that are similar to the softly repulsive, flexible chains of standard DPD. Parameters for the mSRP are determined from topological, structural, and thermodynamic considerations. The effectiveness of the mSRP in capturing entanglements is demonstrated by calculating the diffusion and mechanical properties of an entangled polymer melt. © *2012 American Institute of Physics*. [http://dx.doi.org/10.1063/1.3698476]

I. INTRODUCTION

Mechanical properties of polymers with molecular weights ranging from 20 000 to 200 000 are dominated by topological constraints or entanglements. Atomistic or high-resolution coarse-grain models are often computationally impractical because of the slow reptation dynamics exhibited by high molecular weight chains. The presence of fast collision and vibrational timescales are problematic for long, entangled chains where theory predicts that center-of-mass diffusivity D scales with monomer number N as $D \sim N^{-2.0}$ or slower for flexible chains.[1,2] In atomistic models, hard core interaction potentials are used to maintain excluded volume, which consequently requires timesteps on the order of one femtosecond. The conventional coarse-grain models, such as those built using structure matching with Boltzmann inversion or force matching, Kremer-Grest,[3] and the standard bead-spring model used in dissipative particle dynamics (DPD),[4] recognize that an atomistically detailed description is often not required because modeling the overall structure of the polymer chain is sufficient for capturing dynamics and mechanical properties.

In the DPD model, the loss of atomic degrees of freedom causes beads to follow trajectories with fewer collisions,[5] and allows a larger timestep to be used in the equations of motion. The DPD soft-repulsive potential represents a large number of monomers as a single coarse-grained particle, and allows structural and dynamic relaxation to occur with less computational effort than a fully atomistic simulation. The decrease in relaxation time may be quantified by the ratio of viscosity to diffusion coefficient, the Schmidt number S_c. For example, a reduction in S_c of three orders of magnitude is noted for lipids modeled with DPD relative to molecular dynamics.[6]

However, the use of coarse-grain models with soft-repulsive potentials allows unphysical crossing of the polymer chains (topology violations), making the simulation of dynamical and mechanical properties inaccurate for entangled chains. Use of the standard DPD soft potential results in long chains effectively behaving as if they are short, unentangled chains that follow the Rouse model of diffusivity where $D \sim N^{-1.0}$.[7] Preserving the chain's topological structure is particularly critical in modeling rheological properties, since entanglements resist relative motion between chains during strain. For bead-spring models using soft potentials, several possible techniques to address chain crossing have become available, such as uncrossability constraints,[8] segmental repulsive potential,[9–12] modified DPD parameters,[13] and adaptive timestepping.[14] Of these, the segmental repulsive potential (SRP) is especially interesting because of its computational efficiency and ease of implementation. In this work, we will introduce a modified SRP (mSRP) that maintains these attributes, but yields chain structures and thermodynamic properties similar to the near-ideal structures and thermodynamic properties of softly repulsive DPD chains.

This paper is organized as the following: we first review the standard DPD polymer model for bead-spring chains, then provide a description of our modified segmental repulsive potential. Next, we develop parameters for the modified potential and characterize the resulting chain structure. A diffusion study is then performed to evaluate the Rouse and reptation behavior for a range of chain lengths. Finally, we demonstrate the basic mechanical characteristics of the new chain model.

a)Electronic mail: john.k.brennan.civ@mail.mil.
b)Electronic mail: jan.w.andzelm.civ@mail.mil.

II. DPD POLYMER MODELS

In the usual model for DPD polymers, the force acting between beads i and j is computed as the sum of a non-bonded conservative force $\mathbf{F}^C$, a dissipative force $\mathbf{F}^D$, a random force $\mathbf{F}^R$, and a bond force $\mathbf{F}^B$.

$$\mathbf{F}_{ij} = \mathbf{F}^C_{ij} + \mathbf{F}^D_{ij} + \mathbf{F}^R_{ij} + \mathbf{F}^B_{ij}. \tag{1}$$

The non-bonded conservative force can be given by

$$\mathbf{F}^C_{ij} = a_{ij}\left(1 - \frac{r_{ij}}{r_c}\right)\hat{\mathbf{r}}_{ij}, \tag{2}$$

where a_{ij}, r_{ij}, $\hat{\mathbf{r}}_{ij}$, and r_c are the force constant, bead separation, bead separation unit vector and force cutoff, respectively. The dissipative force is often taken as

$$\mathbf{F}^D_{ij} = -\gamma\left(1 - \frac{r_{ij}}{r_c}\right)^2(\hat{\mathbf{r}}_{ij}\cdot\mathbf{v}_{ij})\hat{\mathbf{r}}_{ij}, \tag{3}$$

where γ is a dissipative scaling factor and $\mathbf{v}_{ij}$ is the relative velocity. A corresponding random force[4] is taken as

$$\mathbf{F}^R_{ij} = \frac{\sigma\theta_{ij}}{\sqrt{\delta t}}\left(1 - \frac{r_{ij}}{r_c}\right)\hat{\mathbf{r}}_{ij}, \tag{4}$$

where σ, θ_{ij}, and δt are the noise level, random number, and timestep, respectively. Additionally, polymers are often modeled within the DPD framework using a Fraenkel spring[15] between bonded beads i and j,

$$\mathbf{F}^B_{ij} = -K_B(r_{ij} - R_0)\hat{\mathbf{r}}_{ij}, \tag{5}$$

where K_B and R_0 are the bond force constant and equilibrium bond length, respectively. Espanõl and Warren[16] have shown that the DPD method will sample the canonical ensemble if the random and dissipative forces are related by

$$\gamma = \frac{\sigma^2}{2k_B T_{set}}, \tag{6}$$

where T_{set} is the temperature and k_B is the Boltzmann constant. The instantaneous temperature is computed from the kinetic energy KE and number of beads N_b as $KE = \frac{3}{2}N_b kT$.

III. SEGMENTAL REPULSIVE POTENTIAL

The segmental repulsive potential (SRP) removes unphysical chain crossings by applying a pairwise force between non-neighboring bonds if the bond-bond distance is within a specified cutoff. The SRP was first introduced by Kumar and Larson[9] as a method of repelling springs in Brownian dynamics using a bead-spring model. The Lennard-Jones potential function originally used by Kumar and Larson was steeply repulsive and required small timesteps, which is undesirable in simulations of coarse-grain models. Pan and Manke[11] later implemented a SRP with the same functional form as the DPD conservative potential,

$$\mathbf{F}^{SRP}_{kl} = b\left(1 - \frac{d_{kl}}{d_c}\right)\hat{\mathbf{d}}_{kl}, \tag{7}$$

where $\mathbf{F}^{SRP}_{kl}$ is a force acting between bonds k and l separated by distance d_{kl}; b and d_c are the force constant and bond-bond cutoff distance, respectively.

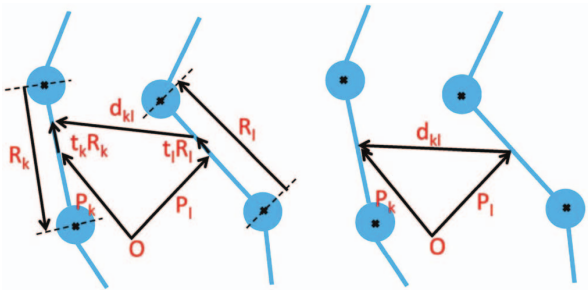

FIG. 1. The minimum and midpoint distance between two bonds. (Left) The minimum distance vector d_{kl} is found by adding midpoint vectors (P_k, P_l) with two vectors of unknown length (t_kR_k,t_lR_l), then minimizing the magnitude of d_{kl}. The position of the vector head and tail along the bond (t_k, t_l) is used along with the minimum distance to apply weighted forces to each bead. (Right) The midpoint-to-midpoint distance of two bonds is found by subtracting P_k and P_l.

The distance between two bonds can be calculated in at least two ways. The current SRP methods define the bond-bond separation as the minimum distance between two bonds.[9–11,14,17] The minimum distance vector $\mathbf{d}_{kl}$ is often evaluated[9–11,17,18] as a vector sum of each bond's midpoint vector ($\mathbf{P}_k$, $\mathbf{P}_l$) and a fragment of each bond's vector ($t_k\mathbf{R}_k$, $t_l\mathbf{R}_l$), where t_k and t_l are the distances from the center of a bond, normalized by the bond length. The vector sum, $\mathbf{d}_{kl} = \mathbf{P}_k + t_k\mathbf{R}_k - \mathbf{P}_l - t_l\mathbf{R}_l$, is shown in Fig. 1 (left). As described by Kumar and Larson,[9] a solution for t_k and t_l can found by assuming each bond is a line, then minimizing the length of $\mathbf{d}_{kl}$ between the two lines:

$$t_k = \frac{(\mathbf{P}_k - \mathbf{P}_l)\cdot\left(R_l^2\mathbf{R}_k - R_{kl}^2\mathbf{R}_l\right)}{R_{kl}^2 - R_k^2R_l^2}, \tag{8}$$

$$t_l = \frac{(\mathbf{P}_l - \mathbf{P}_k)\cdot\left(R_k^2\mathbf{R}_l - R_{kl}^2\mathbf{R}_k\right)}{R_{lk}^2 - R_k^2R_l^2}, \tag{9}$$

where $R_{kl}^2 = \mathbf{R}_k\cdot\mathbf{R}_l$ and $R_k^2 = \mathbf{R}_k\cdot\mathbf{R}_k$. A bond position of $t = 0$ corresponds to the center of the bond, where the bond spans from $t = -0.5$ to $t = 0.5$. If either of the t positions falls outside the bond (i.e., $t > 0.5$ or $t < -0.5$), then t is reset to the nearest bond end (i.e., either $t = -0.5$ or $t = 0.5$). Using this approach, the calculated distance only corresponds to the minimum distance when the head and tail of $\mathbf{d}_{kl}$ occur along the interior of the two bonds (i.e., $|t_k| < 0.5$ and $|t_l| < 0.5$). Otherwise, the calculated distance is too large.

Alternatively, the midpoint-to-midpoint distance vector between the bonds can simply be computed as $\mathbf{d}_{kl} = \mathbf{P}_k$–$\mathbf{P}_l$, as shown in Fig. 1 (right). Computing the midpoint-to-midpoint distance implicitly takes t_k and t_l as zero, and yields an unambiguous distance.

The force acting on a bond given by Eq. (7) is decomposed into bead forces according to the lever rule. For beads i and j in bond k,

$$\mathbf{F}_i = \mathbf{F}^{SRP}_{kl}\cdot L, \tag{10}$$

$$\mathbf{F}_j = \mathbf{F}^{SRP}_{kl}\cdot(1 - L), \tag{11}$$

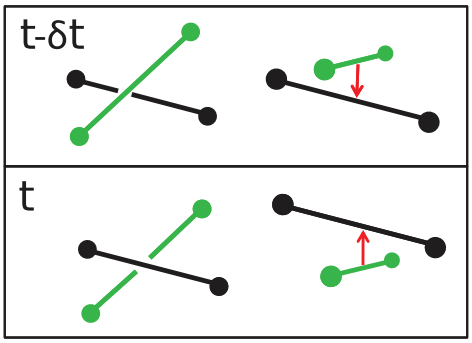

FIG. 2. Example of a topology violation (bond crossing). In this example, the minimum distance vector changes orientation between $t - \delta t$ and t by 180°.

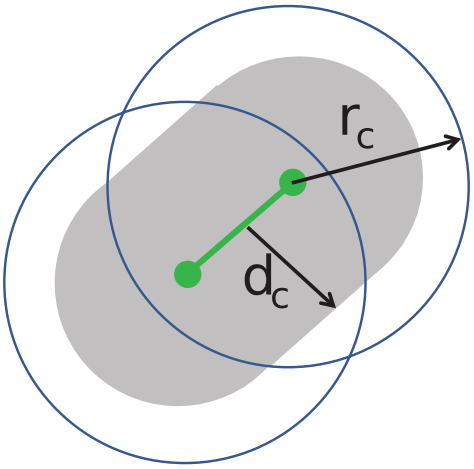

FIG. 3. Non-bonded cutoffs for a chain segment. A single bead has a cutoff of r_c. Two bonded beads are encompassed by the SRP potential with cutoff d_c (shaded).

where L determines the weighting of the force on each bead and is taken as $L = t_k + 0.5$. In the special case that the minimum distance occurs between the ends of the bonds ($|t_l| = 0.5$, $|t_k| = 0.5$), forces are applied only to the two closest atoms. If the midpoint-to-midpoint distance is used, the force is taken as equally divided between beads since $t = 0$ and $L = 0.5$. Adjacent bonds are excluded from all segmental repulsion interactions.

The addition of segmental repulsion with reasonable parameter values greatly reduces topology violations (*TV*), nonetheless a small number will always occur. The number of topology violations can be minimized by systematically varying d_c and b and counting their occurrence. Here, we define a topology violation as a change in direction of $\mathbf{d}_{kl}$ by 90° or more over a single timestep.[10] Figure 2 provides an example of a topology violation. The angle ϕ is computed as the dot product of the $\hat{\mathbf{d}}_{kl}$ unit vector on the previous ($t - \delta$t) and current timestep (t),

$$\cos\phi = \hat{\mathbf{d}}_{kl,t-\delta t} \cdot \hat{\mathbf{d}}_{kl,t}. \tag{12}$$

SRP has been used in the study of fundamental polymer physics and for applications such as entangled polymer brushes.[10] Goujon *et al.*[10] have developed parameters for the functional form given in Eq. (7) that are reasonably effective in preventing topology violations. For this discussion, we define "standard DPD" as the DPD method with Goujon *et al.* parameters for a, r_c, and γ but without segmental repulsion. If standard DPD is supplemented by segmental repulsion given by Eq. (7) where d_{kl} is the minimum bond-bond distance, the term "SRP" is used. Finally, if standard DPD is supplemented by Eq. (7) where d_{kl} is the midpoint-to-midpoint distance, the term "mSRP" is used.

A. Impact of using SRP

The SRP forms a cylindrical volume around the length of the bond and hemispherical "caps" as illustrated in Fig. 3. The large volume within the potential's cutoff distance causes it to participate in more interactions than a standard potential with a radial cutoff, and consequently the thermodynamics of the system are changed compared to standard DPD. For a given temperature, the use of segmental repulsion typically requires an increase of the DPD thermostat parameter σ and a corresponding increase in the dissipative parameter γ according to the fluctuation-dissipation relation (Eq. (6)). In the work presented here with SRP, $\sigma = 10.0$ ($\gamma = 50.0$) is required to maintain the system's temperature,[19] while standard DPD and mSRP use $\sigma = 3.0$ ($\gamma = 4.5$). The need for an elevated σ value in SRP cannot be eliminated by simply adjusting the non-bonded parameters in Eq. (7), since reducing b or d_c will increase topology violations.[10]

Moreover, SRP influences the DPD simulation in other aspects. The interaction of DPD beads effectively becomes more repulsive, and therefore introduces excluded volume.[17] For each repulsive force between beads i and j contributed by the conservative DPD potential (Eq. (2)), there is likely to be another repulsive force contributed from the conservative bond repulsion (Eq. (7)) that also involves beads i and j. Less repulsive or "soft" beads that easily overlap are needed for aggressive coarse-graining. It is also necessary to greatly increase the bond force constant K_B relative to standard DPD.[20] SRP has the effect of compressing the bond length, possibly due to the SRP force being weighted heavily to one bead of the bond by Eq. (10). DPD polymers with SRP require a large K_B and a predetermined equilibrium distance in lieu of balancing the repulsive and harmonic forces.[4]

However, large values of K_B restrict intra-chain distances on small length scales, and may ultimately contribute to chain stiffness. In contrast to the SRP model, softer bead-bead interactions are introduced in the manner proposed here for the mSRP model. mSRP effectively reduces bond crossings, contributes less potential energy than the current SRP definitions, and maintains the non-bonded structure of standard DPD. With the premise that interactions occurring along the interior of the bond (and not the end-

TABLE I. Details of the systems used in diffusion (Diff.), stress-strain (S.S.), parameterization (Para.). Each system is a cubic box with a cell length of L containing M chains and N beads per chain.

N	M	Total	L	Model	Purpose	Time
8	192	1536	8.0	SRP/mSRP	Diff.	10 000 τ
10	300	3000	10.0	SRP/mSRP	Diff.	10 000 τ
20	1200	24 000	20.0	SRP/mSRP	Diff.	10 000 τ
30	2700	81 000	30.0	SRP/mSRP	Diff.	100 000 τ
40	4800	192 000	40.0	SRP/mSRP	Diff.	100 000 τ
60	3200	192 000	40.0	SRP/mSRP	Diff.	150 000 τ
70	2743	192 010	40.0	mSRP	Diff.	300 000 τ
80	2400	192 000	40.0	mSRP	Diff.	300 000 τ
90	2134	192 060	40.0	mSRP	Diff.	300 000 τ
100	1920	192 000	40.0	DPD/SRP/mSRP	Diff.	300 000 τ
40	4800	192 000	40.0	DPD/SRP/mSRP	S.S.	Varies
5	38 400	192 000	40.0	DPD/SRP/mSRP	S.S.	Varies
30	78	2340	9.2[a]	DPD/SRP/mSRP	Para.	20 000 τ

[a]Parameterization with a box of $L = 20$ yielded similar TV values for $d_c = 0.8$, $b = 100$.

points) are most important in preventing bond crossings, we show that mSRP has physical advantages over SRP. In Secs. V–VIII, we determine mSRP parameters by topological, thermodynamic, and structural considerations, then demonstrate the ability of the new mSRP model with these parameters to capture entanglements in a diffusion and stress-strain study.

IV. SIMULATION DETAILS

The SRP and mSRP were implemented into the LAMMPS molecular dynamics software[21] to carry out the simulations described here. For convenience, the DPD reduced units of length, energy, time, and mass are adopted as r_c, k_BT_{set}, $\tau = r_c\sqrt{m/k_BT}$, and m, respectively.

Polymer melts were created with a reduced density of 3.0 by generating M chains with N beads per chain in a cubic box with cell length L, where periodic boundary conditions are applied in all directions. Three sets of systems were considered. (1) For parameterization of the mSRP, a system with $M = 78$ chains and $N = 30$ beads per chain in a simulation box of $L = 9.2$. (2) Diffusion calculations vary N and M, while using the smaller of $L = N$ or $L = 40$. (3) Stress-strain calculations vary N and M with $N \cdot M = 192\,000$ and $L = 40$. See Table I for details.

The DPD non-bonded parameters of $a = 60$ and $r_c = 1.0$ were used for each simulation at a temperature of $k_BT_{set} = 1.0$. For SRP, $K_B = 225.0$, $R_0 = 0.85$, and $\sigma_R = \sigma(\delta t)^{-1/2} = 100$ (corresponding to Goujon *et al.*[10]). Standard DPD and mSRP used these same parameters, except for $\sigma_R = 30$ ($\gamma = 4.5$) for the reasons mentioned previously. All simulations used the velocity-Verlet integrator with a timestep of $\delta t = 0.01\ \tau$.

Each polymer chain less than $N = 60$ was created as a freely joined chain, where beads were generated with a random walk of $N - 1$ steps separated by a distance R_0.[1] In subsequent runs, knowledge of the Flory ratio C_∞ of standard DPD was used to create chains with a predetermined end-to-end distance R according to the relationship $R^2(n) = nl^2C_\infty$, where n and l are the number of segments and average segment length, respectively.[22]

Each system used for the parameterization of the mSRP was equilibrated for $0.5 \times 10^4\ \tau$, prior to a production run of $1.5 \times 10^4\ \tau$. The equilibration time for the diffusion studies depended on the convergence of the monomer and polymer chain center-of-mass (COM) diffusion, and stress-strain simulations used equilibrated systems from the previous diffusion studies.

V. PARAMETERIZATION

A. Topology violations

Pan *et al.*[11] observed reptation behavior with a SRP system for $N = 30$, thus we chose this chain length to determine the non-bonded parameters of the mSRP potential. A series of simulations was performed at $N = 30$ (see Table I) using the mSRP with various cutoff distances and force constants. The cutoff distance d_c and force constant b were varied in increments of 0.1 and 10, respectively. To gauge the effectiveness of each parameter set for mSRP, the number of topology violations TV was measured using Eq. (12) for all three models (DPD, SRP, mSRP). The standard DPD model provides an upper bound for TV. Figure 4 shows TV observed per 100 τ. As evident from Fig. 4, TV can be reduced by either increasing d_c or b. Increasing d_c is very effective up to $d_c = 0.9$, but a further increase does not necessarily prevent topology violations, e.g., the parameters $d_c = 1.0$, $b > 70$ allow more topology violations than $d_c = 0.9$, $b > 70$. As the values of mSRP parameters (Eq. (7): b, d_c) approach the non-bonded DPD parameters (Eq. (2): $a = 60$, $r_c = 1.0$), the segmental repulsion interactions influence the chain dynamics and number of TV differently than for $d_c < r_c$. We did not study this effect since, as explained below, these mSRP parameters lead to poor thermodynamic properties. In general, $d_c > 0.8$ and $b > 80$ allow less than one TV per 100 τ, and are satisfactorily effective at preventing topology violations. As expected,

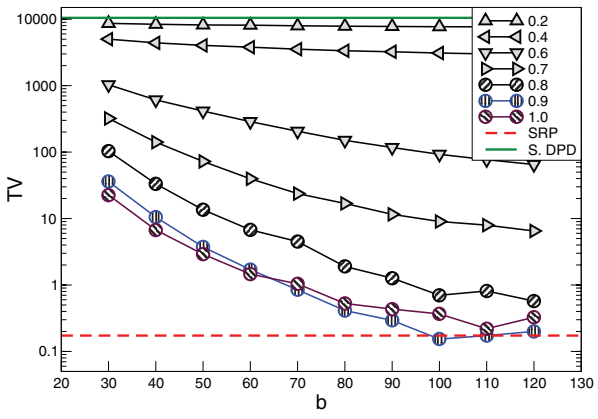

FIG. 4. Topology violations (TV) of mSRP per 100 τ as a function of cutoff distance d_c and force constant b. Lines of constant d_c are shown for 30 $< b <$ 120. SRP and standard DPD (S. DPD) are shown for a single set of parameters (Ref. 10).

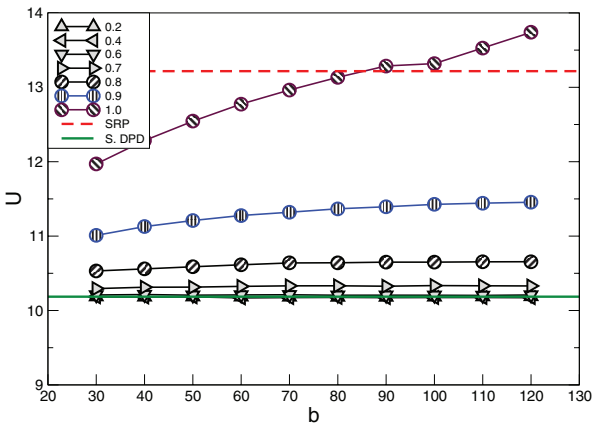

FIG. 5. Potential energy (U) as a function of mSRP force constant b and cutoff distance d_c. Lines of constant d_c are shown. The solid and dash lines correspond to standard DPD (S. DPD) and SRP, respectively.

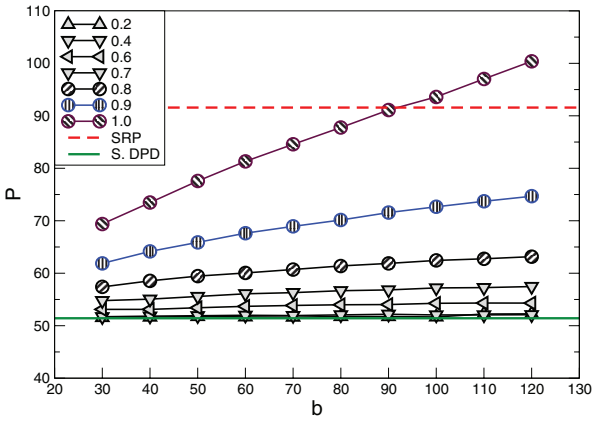

FIG. 6. Pressure (P) as a function of mSRP force constant b and cutoff distance d_c. Lines of constant d_c are shown. The solid and dash lines correspond to standard DPD (S. DPD) and SRP, respectively.

small values of d_c or b converge to the case of standard DPD. Also evident from Fig. 4 is that SRP is very effective, and mSRP parameter sets with $d_c = 0.9$ and $b > 100$ are needed to achieve a similar number of topology violations.

A practical choice of parameters must not only prevent most topology violations, but also lead to reasonable thermodynamic and structural properties. To satisfy the first of these criteria, any parameter set yielding a number of topology violations on the same order of magnitude as SRP is deemed acceptable at this stage of the parameterization, since these values of d_c and b allow very few topology violations. Other upper limits for TV could be defined, but we constrain our parameters to yield low TV values with the goal of capturing entanglements. From Fig. 4, we therefore only consider parameter sets with less than one topology violation per 100 τ.

B. Thermodynamic properties

The effect of each parameter set on the potential energy (U) and pressure (P) was examined, and is shown in Figs. 5 and 6, respectively. Note that we compute the pressure by considering both the kinetic and virial terms of the pressure tensor, but disregard contributions from random and dissipative forces as suggested by Groot and Warren.[4]

The DPD non-bonded potential acting between beads (Eq. (2)) represents the repulsion of nearby monomers, and may be modified in DPD models based on the chemical characteristics of each system. We therefore want the majority of the potential energy to be contributed by the DPD bead-bead potential, and the energetic contribution of mSRP to be minimized. The case of standard DPD provides a lower limit for U and P, while SRP serves as a benchmark from which we strive to improve the thermodynamic properties.

From Fig. 5, the potential energy of SRP is ∼30% higher than standard DPD. For mSRP, U and P increase with increasing d_c and to a lesser extent, b. Parameters $b = 100$ and $d_c = 0.9$ lead to nearly the same number of topology violations as SRP (see Fig. 4), but have U only ∼12% greater than standard DPD. A compromise can be made to further reduce the energetic contribution of mSRP at the expense of slightly increasing the frequency of topology violations. We chose the smallest acceptable cutoff distance that resulted in $TV < 1.0$, i.e., $d_c = 0.8$ and a force constant of $b = 100$, leading to a very reasonable ∼4% increase in potential energy relative to standard DPD. A similar conclusion can be made from the pressure, shown in Fig. 6, where mSRP with $d_c = 0.8$, $b = 100$ leads to a ∼21% increase over standard DPD, compared with a ∼75% increase observed using SRP.

Typical timesteps for DPD simulations of polymers with and without SRP are $\delta t = 0.01$ and $\delta t = 0.04$, respectively.[4,10] We tested five timesteps with mSRP ranging from $\delta t = 0.005$ to $\delta t = 0.04$. The combination of the velocity-Verlet integrator and mSRP produced small differences in energy and temperature for all timesteps, but topology violations increased quickly for $\delta t > 0.01$. Therefore, we use $\delta t = 0.01$ τ throughout this work, except for stress-strain simulations where $\delta t = 0.0075$ τ is used. Figure 7 shows the number of topology violations for $d_c = 0.8$ and $b = 100$ as a function of timestep.

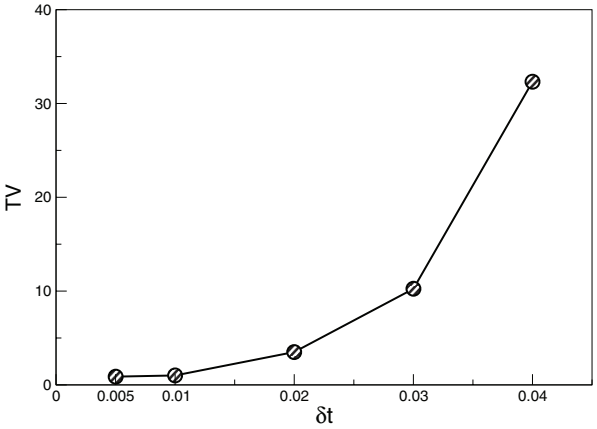

FIG. 7. Topology violations (TV) of mSRP per 100 τ at several timesteps, for $d_c = 0.8$ and $b = 100$.

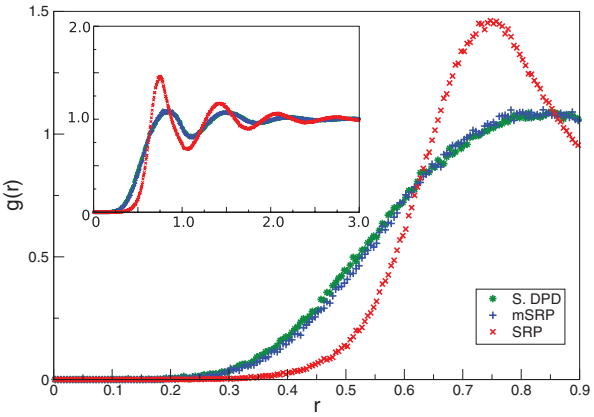

FIG. 8. The radial distribution function for standard DPD (S. DPD), mSRP, and SRP at short distances. Standard DPD and mSRP are overlapping and nearly identical for all distances (inset).

C. Structural properties

The two defining characteristics of the DPD polymer model are soft beads bound into a flexible chain. These characteristics are necessary for high-level coarse-graining[5] and should be preserved as much as possible to achieve simulations of mesoscopic length scales. In particular, the excluded volume near each bead should be as similar as possible to the softly repulsive beads of standard DPD. The radial distribution functions (RDFs) for standard DPD, SRP, and mSRP are shown in Fig. 8.

The overall agreement between mSRP and standard DPD is excellent, which indicates that mSRP has little influence on the inter-chain structure. The RDF for distances near the bead (less than 0.5) reveals that the non-bonded structure using mSRP is very similar to standard DPD, while the more repulsive SRP model creates excluded volume around beads. The peaks of the RDF for SRP are higher and shifted toward a lower r-value with respect to standard DPD and mSRP. The taller and narrower peaks suggest a more ordered inter-chain structure with less thermal motion. The first peak of the RDF for SRP occurs within the cutoff distance of the segmental repulsion potential ($d_c = 0.8$). SRP measures the minimum distance between bonds, meaning that two non-bonded beads separated by less than $d_c = 0.8$ will experience a force from segmental repulsion. The r-value of the first peak of SRP suggests that segmental repulsion will occur often and contribute significant energy. For mSRP, the first peak is broader and at a greater r-value. Further, mSRP measures the midpoint-to-midpoint distance between bonds and does not always contribute energy when two beads approach closer than $d_c = 0.8$. This is consistent with the elevated energies of SRP relative to mSRP.

The characteristic ratio of a polymer, C_n, is an important measure of the conformation and rigidity of individual chains. C_n is determined from

$$C_n(n) = \frac{\langle R(n)^2 \rangle}{n \langle l \rangle^2}. \tag{13}$$

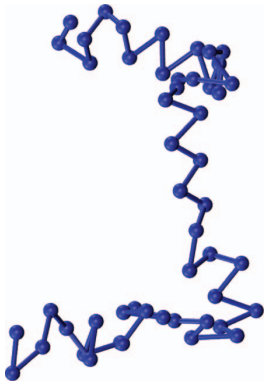

FIG. 9. Example structure of an mSRP chain without an angle potential ($N = 50$, $b = 100$, $d_c = 0.9$).

The characteristic ratio saturates at large n, so that $C_\infty = \lim_{n\to\infty} C_n(n)$.[22]

A visual inspection of the chain conformation for SRP and mSRP suggested that neighboring bonds formed a sharp, acute angle as shown in Fig. 9. This structural defect can be observed as a minimum in $C_n(n)$, shown in Fig. 10 for SRP and mSRP. The value of $C_n(2) < 1.0$ indicates that the first and second neighboring bonds form an unphysical angle of less than 90°, i.e., the first and third beads in any angle of the chain are too close. This defect ultimately causes all of the bead-bead distances to be reduced, and is reflected by the reduced values of C_n for SRP and mSRP relative to standard DPD. The structure could possibly be improved by allowing neighboring bonds to interact with a repulsive potential, however, we have chosen to add an angle potential since this allows the chain structure to be tuned independently from parameters that directly influence topology violations. The angle bending potential is taken as

$$U_{bend} = K_\theta(1 + \cos\theta), \tag{14}$$

where K_θ is a force constant and θ is the angle formed by three consecutive beads in a chain. A small value of K_θ will

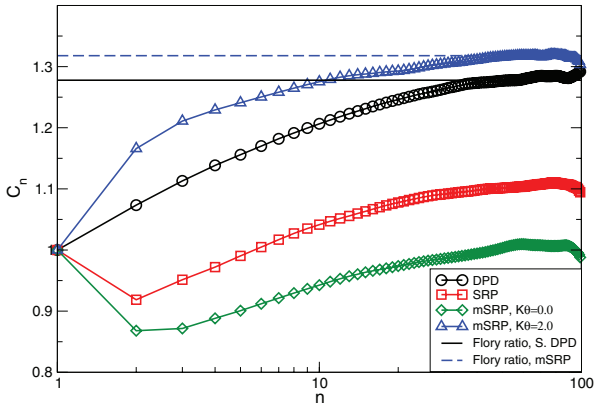

FIG. 10. Characteristic ratio of standard DPD, SRP, and mSRP. Solid and dashed lines represent an asymptotic value determined by fitting $C_\infty = \frac{A}{n} - C_n$.[23]

TABLE II. Structural properties of mSRP polymer systems. The values of mean-squared end-to-end distance $\langle R^2 \rangle$ and mean-squared radius of gyration $\langle R_g^2 \rangle$ are averaged over all chains in a single frame, then over 10 frames.

N	C_n	R^2/R_g^2	R_g^2	R^2
5	1.229	5.405	0.718	3.882
8	1.258	5.577	1.218	6.793
10	1.271	5.593	1.542	8.625
15	1.287	5.725	2.345	13.422
20	1.292	5.728	3.085	17.674
30	1.304	5.765	4.619	26.627
40	1.310	5.836	6.169	36.006
60	1.318	5.908	9.291	54.887
70	1.317	5.906	10.850	64.075
80	1.319	5.920	12.399	73.403
90	1.316	5.953	13.887	82.667
100	1.303	5.941	15.594	92.640

result in the collapse of neighboring bonds, while a high value of K_θ creates a rigid, rod-like chain. In this work, K_θ was varied from $K_\theta = 0$ to $K_\theta = 5.0$ with increments of 0.2. In the limit of large n, $K_\theta = 2.0$ was estimated to yield a Flory ratio of $C_n(\infty) = 1.31$, which was similar to the standard DPD estimate of $C_n(\infty) = 1.27$, and did not demonstrate a minimum in the characteristic ratio at $n = 1$. Figure 10 shows $C_n(n)$ for standard DPD, SRP, mSRP with $K_\theta = 0.0$, and mSRP with $K_\theta = 2.0$. Although the Flory ratio for $K_\theta = 2.0$ is elevated about 0.04 compared with standard DPD, the ratio of the mean-squared end-to-end distance to the mean-squared radius of gyration becomes approximately the same as an ideal chain as n increases, i.e., $R(n)^2/R_g(n)^2 \cong 6$ (see Table II). Another useful measure of chain structure is the mean-squared internal distance (MSID) described by Auhl *et al.*,[22] which represents $\langle R^2 \rangle$ between any two beads within a chain. For short chain lengths, mSRP has greater MSID than standard DPD, but the two models converge for $n > 20$ (see Fig. 11). SRP and $\text{mSRP}_{K_\theta=0}$ experience "folding" of neighboring bonds, which reduces the MSID for all n values. SRP and, to a lesser extent, mSRP have mean-square bond lengths (corresponding to $n = 1$) that are less than standard DPD, suggesting that

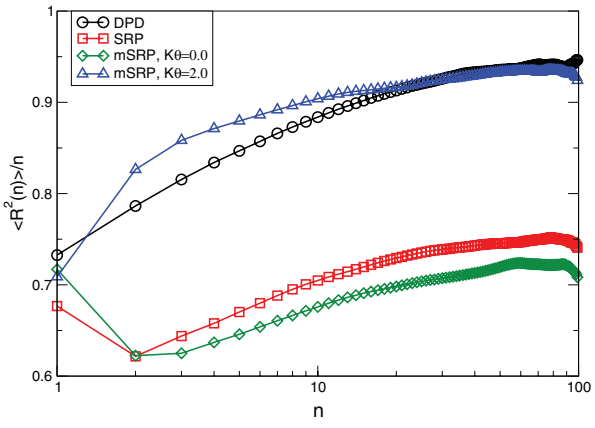

FIG. 11. Mean-squared internal distances for standard DPD, SRP, and mSRP.

bond lengths are reduced due to segmental repulsion, even with a bond force constant of $K_B = 225$.

Finally, we re-evaluated the number of topology violations with the additional angle potential and found an increase from $TV = 0.9$ to $TV = 1.8$ per 100 τ, which is still very infrequent. As a reference, Tzoumanekas *et al.*[18] observed 1.25×10^{-7} topology violations per bead per timestep, which corresponds to $TV = 2.9$ in Fig. 4. The increase in TV may be due to angular restrictions on bond movement that limit the ability of a given bond to move away from an approaching bond. The non-bonded RDF of mSRP remained essentially the same as standard DPD with or without the angle potential (not shown). To summarize, we recommend the following parameters for the mSRP model: $b = 100$, $d_c = 0.8$, and $K_\theta = 2.0$. Our parameterization considered the energy and pressure independently from the angle potential. At the expense of additional computation, the parameterization could be enhanced by reproducing Figs. 4–6 for several values of K_θ, then choosing b and d_c as previously described.

VI. DIFFUSION BEHAVIOR

Diffusion is a useful means of identifying the entanglement length of polymer chains. The mean-squared displacement for the inner monomers (g_1), monomers around the center of mass (g_2), and the center of mass (g_3) were computed by

$$g_1(t) = \langle [\mathbf{r}_i(t_0 + t) - \mathbf{r}_i(t_0)]^2 \rangle, \tag{15}$$

$$g_2(t) = \langle [(\mathbf{r}_i(t_0 + t) - \mathbf{r}_{COM}(t_0 + t)) - (\mathbf{r}_i(t_0) - \mathbf{r}_{COM}(t_0))]^2 \rangle, \tag{16}$$

$$g_3(t) = \langle [\mathbf{r}_{COM}(t_0 + t) - \mathbf{r}_{COM}(t_0)]^2 \rangle, \tag{17}$$

where r_i and r_{COM} are the position of bead i and the COM position of the chain, respectively.

Figure 12 shows the time evolution of g_1, g_2, and g_3 for $N = 40$. To compute the diffusion coefficient D, the system is allowed to equilibrate until the chain COM and monomers diffuse at the same rate, i.e., the values of g_1 and g_3 essentially converge. The convergence of g_1 and g_3 is detected by $\frac{d}{dt}\log(g_3)$ achieving $\cong 90\%$ of $\frac{d}{dt}\log(g_1)$. This test approximately corresponds to the longest relaxation time of the system, and is more rigorous than waiting for the chains to move one radius of gyration (approximately the intersection of g_2 and g_3). Once equilibrated, the COM self-diffusion coefficients are calculated with the Einstein relation, $D = \lim_{t\to\infty} \frac{g_3(t)}{6t}$ on the remaining steps of the simulation (at least 30 000 τ).

Figure 13 shows the diffusion coefficients for chain lengths $N = 8$ to $N = 100$ and the predicted scaling. To better illustrate the Rouse and reptation features, we express diffusion as the product of the diffusion coefficient and number of segments per chain. For mSRP, $Dn \cong const$ for $n < 14$, and $Dn \sim n^{-1.04 \pm 0.06}$ for $n > 69$. Chains lengths of $14 < n < 69$ define a transitional length scale, where entanglements increasingly influence the dynamics. The crossover from

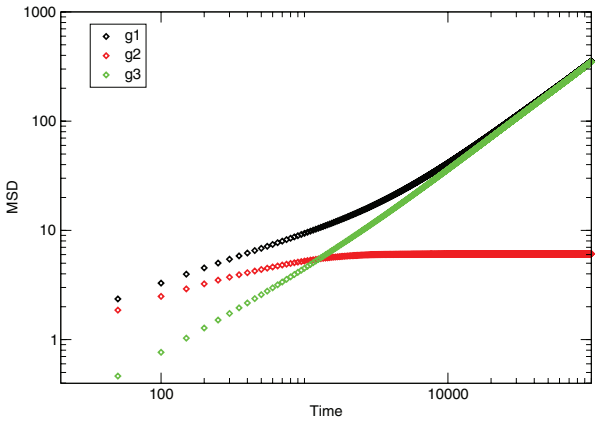

FIG. 12. Relaxation of linear polymer chains with $N = 40$. The MSD of inner monomers (g_1) and chain COM (g_3) asymptotically converge. The g_2–g_3 intersection indicates the time required for a chain to diffuse a distance on the order of its own radius of gyration.

Rouse to reptation dynamics approximately corresponds to twice the entanglement length of the polymer,[3] and can be estimated by finding the intersection of the two lines representing $n^{0.0}$ and $n^{-1.04}$. By this definition, the entanglement length of mSRP is $n = 28/2 = 14$ segments. Diffusion using SRP scales similar to mSRP for short chains, but the first deviations from Rouse dynamics are visible in Fig. 13 at $n = 19$ and diffusion coefficients are generally higher than mSRP for $n > 19$. mSRP requires shorter chains than SRP to capture reptation behavior in the systems we considered, although the difference cannot be directly measured since SRP does not reach reptation scaling for $n = 99$. Any reduction in the entanglement length is computationally useful in decreasing the number of beads in large polymeric systems that require a given number of entanglements in the architecture.

The Rouse regime scaling can be strongly affected by the addition of an angle potential to the chain model. Increasing the angle bending stiffness of the Kremer-Grest model has been shown by Bulacu *et al.*[24] to reduce the slope of $Dn(n)$ for all n, thereby introducing differences from $Dn = const$ in the Rouse regime. For mSRP, a close inspection of Fig. 13 shows our choice of K_θ is sufficiently small to produce only minor deviations from $Dn = const$ in the Rouse regime ($n < 14$), and therefore we consider only structure, not diffusion, in the parameterization of the angle potential.

VII. MECHANICAL PROPERTIES

To demonstrate the utility of mSRP in capturing mechanical behavior, stress-strain curves were generated for standard DPD and mSRP polymer melts. For each model, we consider short, unentangled chains ($N = 5$ beads) and chains sufficiently long to have at least one entanglement ($N = 40$ beads). The simulation box of length L is axially deformed at a constant true strain rate of $\dot{\epsilon} = 10^{-4}$ under constant-volume conditions. The extension along the direction of deformation is performed according to

$$L(t) = L_0 e^{\dot{\epsilon} dt}, \tag{18}$$

where beads undergo an affine deformation in which positions are scaled with L. The stress tensor was computed every 1000 timesteps as

$$\mathbf{P} = \frac{1}{V} \sum_{i}^{N \cdot M} [m_i \mathbf{v}_i \otimes \mathbf{v}_i + \mathbf{r}_i \otimes \mathbf{f}_i], \tag{19}$$

where $\mathbf{f}$, m, and $\mathbf{r}$ are the force, mass, and position of bead i in a system of volume V with $N \cdot M$ beads. The elongation stress σ_e is calculated from the difference in normal stresses as $\sigma_e = -P_{zz} + \frac{1}{2}(P_{xx} + P_{yy})$.

Figure 14 shows the elongation stress as a function of strain for chains with $N = 5$ and $N = 40$, each modeled with mSRP and standard DPD. Chains of length $N = 5$ are too short to support entanglements, while chains of $N = 40$ are greater than the entanglement length suggested by diffusion scaling, and therefore capable of having one or more entanglements per chain. Short chains with mSRP produced small values of

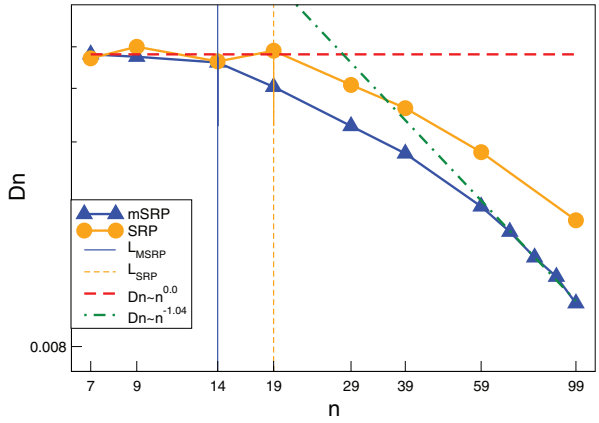

FIG. 13. Diffusion as a function of chain length for mSRP and SRP. Rouse (dash) and reptation (dash-dot) scaling limits intersect at approximately $n = 28$ for mSRP. The initial deviation from Rouse diffusion scaling for mSRP and SRP occurs at $n = 14$ (solid) and $n = 19$ (small dash), respectively.

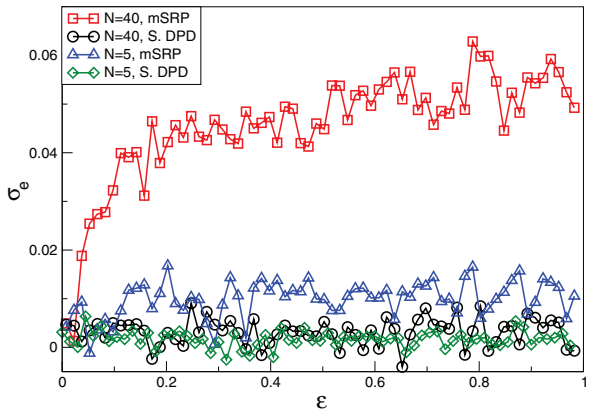

FIG. 14. Stress-strain curves using mSRP and standard DPD for $N = 5$ and $N = 40$ at $\dot{\epsilon} = 10^{-4}$. Each point is a block average of σ_e over $\Delta\epsilon \cong 0.015$ for a single replica of 192 000 beads. The scatter in stress data is likely due to limited sampling.

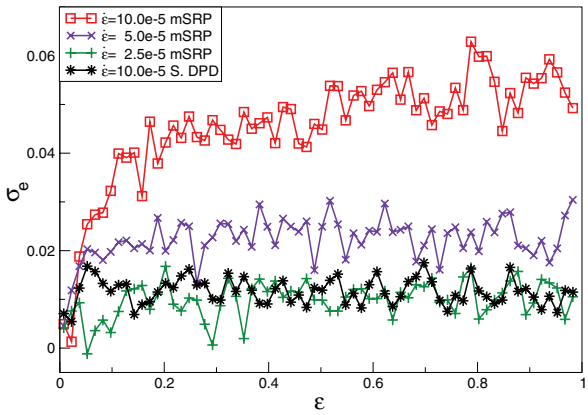

FIG. 15. Stress-strain curves for mSRP and standard DPD for $N = 40$ as a function of strain rate.

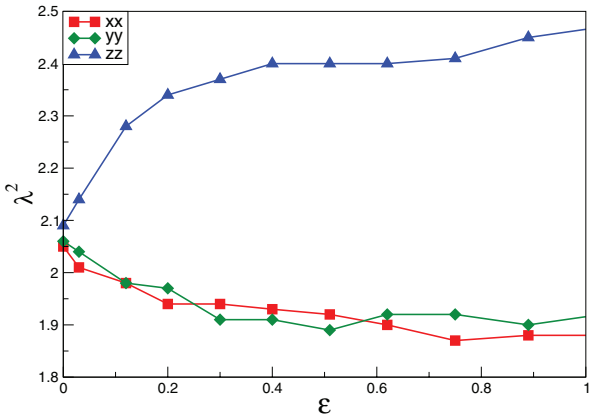

FIG. 16. Components of the gyration tensor (λ^2) during a z-direction strain using mSRP.

σ_e, suggesting a nearly uninhibited flow as strain is applied, while the longer, entangled chains showed the expected features of σ_e–ϵ for an entangled polymer melt. Standard DPD is not capable of capturing entanglements, therefore both the long and short chains of DPD have little stress under the conditions described here. Chains of length $N = 5$ with mSRP have slightly more stress than standard DPD, suggesting that the dynamics of all chains are affected by segmental repulsion, even those much less than the entanglement length. Lahmar *et al.*[17] have also reported differences from DPD when segmental repulsion is applied to short chains.

In general, entanglements greatly increase the time required for chains to relax. To demonstrate the relaxation of stress and the strain-rate dependence of our model, we applied three strain rates to chains of $N = 40$ and monitored the elongation stress. Figure 15 shows stress-strain curves for mSRP at $\dot{\epsilon} = 2.5 \times 10^{-5}$, 5.0×10^{-5}, 10.0×10^{-5} and standard DPD at the highest rate, $\dot{\epsilon} = 10.0 \times 10^{-5}$. For mSRP at the highest rate, a pronounced stress response is observed with a steep initial increase in stress followed by a more gradual increase. These nonlinear stress-strain features are predicted for entangled polymer chains which form transient networks.[25] As the rate is decreased ($\dot{\epsilon} = 5.0 \times 10^{-5}$), features of the mSRP stress-strain curves are reduced until the stress is nearly independent of strain ($\dot{\epsilon} = 2.5 \times 10^{-5}$). Expectedly, standard DPD did not exhibit a strong rate dependence, and produced small stress values even for the highest strain rate. It is encouraging that our model qualitatively reproduces the strain-rate dependence observed in computational and experimental studies[26] at high strain rates and the strain-rate independent behavior expected for low strain rates.

The chains' relaxation under strain can be expressed with the Weissenberg number (*We*), a nondimensional product of the strain rate and longest relaxation time.[27] For $We < 1$, a chain is able to continuously relax into an equilibrium configuration as the strain is applied; for $We > 1$, the chain's configuration deforms along the direction of strain. The mSRP chains considered here have *We* ranging from 7.5 ($N = 5$, $\dot{\epsilon} = 10^{-4}$) to 350 ($N = 40$, $\dot{\epsilon} = 10^{-4}$), thus some degree of deformation is expected to occur, even for unentangled mSRP chains. For $We \gg 1$, the distribution of chain monomers about the COM can be expected to have a measurable dependence on the strain direction. The gyration tensor is useful in interpreting the anisotropic chain conformation.[28] The moments of the gyration tensor are calculated as

$$\lambda^2_{dd} = \frac{1}{N}\sum_{i=0}^{N}(\mathbf{r}_{id} - \mathbf{r}_{COM})(\mathbf{r}_{id} - \mathbf{r}_{COM}). \tag{20}$$

The diagonal principle moments (λ^2_{xx}, λ^2_{yy}, λ^2_{zz}) may be summed to determine the radius-of-gyration or, as seen in Fig. 16, considered individually to understand a chain's configuration around the COM. At equilibrium, monomers have no preference for their orientation about the COM, and each chain approximately occupies a spherical space. When strain is rapidly applied ($\dot{\epsilon} = 10.0 \times 10^{-5}$), the chains extend in the direction of the deformation and cannot relax back to an equilibrium configuration. From Fig. 16, monomers in each chain are initially observed to occupy a spherical space centered on the chain COM ($\lambda^2_{xx} \cong \lambda^2_{yy} \cong \lambda^2_{zz}$) at $\epsilon = 0$, then quickly elongate along the direction of deformation into an ellipsoid at $\epsilon = 0.25$.

The asphericity B is a convenient measurement of the deviation from an equilibrium chain structure[28] and can be determined from

$$B = \lambda^2_{zz} - \frac{1}{2}\left(\lambda^2_{xx} + \lambda^2_{yy}\right), \tag{21}$$

where $\lambda^2_{zz} \geq \lambda^2_{xx} \geq \lambda^2_{yy}$. Figure 17 shows the asphericity for chains with $N = 40$ as a function of strain rate. At the highest strain rate, the deformation is significant with $B \cong 0.5$ for $\epsilon = 0.5$. As the strain rate decreases, the chain's structure approaches an equilibrium state with a spherical configuration (B approaches zero). The form of the asphericity-strain curve is similar to the stress-strain curve shown in Fig. 15, suggesting that chains resist deforming from their initial, spherical configuration. The standard DPD model does not form entanglements, and therefore does not develop significant asphericity even at the highest strain rate.

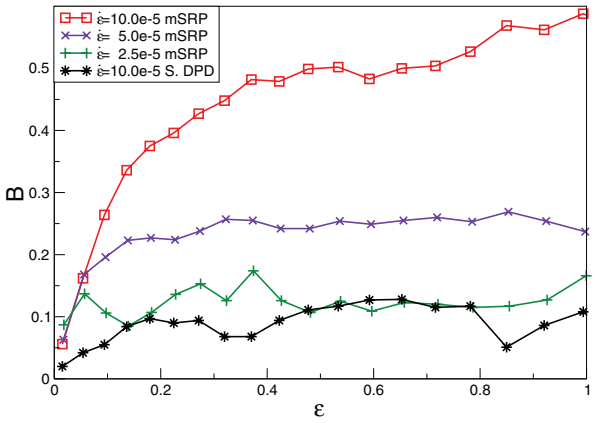

FIG. 17. Asphericity of mSRP and standard DPD for several strain rates.

VIII. CONCLUSION

A long-standing advantage of the standard DPD model of polymer chains has been that microscale systems can reach an equilibrated structure within a reasonable simulation time.[29] However, since chains are able to artificially cross through each other, the dynamic path that such a simulation takes does not necessarily correspond to the true path. As such, the standard DPD model can reproduce equilibrium thermodynamic and structural properties of entangled polymer systems, but not rheological behavior such as stress-strain curves or dynamic response to external stimuli. The mSRP model presented here helps to overcome this deficiency by reproducing the equilibrium properties of the standard DPD model, while also providing a means to reproduce the non-equilibrium behavior of an entangled system. In contrast, other SRP models that capture entanglement do not have a correspondence to a standard DPD model. Therefore, the utility of mSRP lies in that the dynamic behavior of entanglements can be *activated* when simulating non-equilibrium properties based on nearly the same standard DPD model.

As a means of modeling entangled DPD chains, we develop parameters for a modified segmental repulsion potential that redefines the bond-bond separation distance such that "softer" interactions occur between the beads compared with current SRP methods. The soft interactions are accomplished by repelling only the center of bonds, rather than surrounding each bond with a repulsive potential. The mSRP model effectively reduces bond crossings while contributing less potential energy and pressure than would occur if the bond-bond separation is taken as the minimum distance. mSRP only interacts with the center of bonds, makes a small contribution to thermodynamic properties, and allows a smaller value of the dissipative parameter (γ) than the SRP model studied here. When mSRP is combined with an angle potential, the chain structure is similar to standard DPD, but slightly stiffer on short length scales as reflected by the mean-squared internal distances and marginally higher characteristic ratio.

The diffusion of linear melts using mSRP indicate unentangled, Rouse behavior for chains less than 15 beads. As the chain length increases beyond $N = 15$, entanglements become significant and the diffusion approaches the predictions of the reptation model. mSRP appears to be well-suited for large, computationally demanding systems since the entanglement length is comparable with or less than other models, but each evaluation of mSRP requires less numerical operations.

We have shown that mSRP can capture entanglements in the mechanical behavior of polymers, where linear chains modeled with mSRP create length-dependent and strain-rate-dependent stress as the material is deformed. Unentangled mSRP chains relaxed quickly and showed similar stress-strain behavior to standard DPD. Entangled mSRP chains were shown to produce more stress than standard DPD chains at a high rates, but converge to a similar stress for a low strain rate.

Overall, mSRP is an efficient bond-bond potential for entangled polymers that can preserve topological integrity without greatly affecting thermodynamic properties. Different parameter sets for mSRP may be needed if the simulation conditions or forcefield change significantly, but the concept of maintaining soft beads and reducing the impact of the segmental repulsion is independent of the system studied.

A brief comment regarding the computational efficiency of mSRP is worthwhile. If the minimum distance vector between two bonds is computed in a unoptimized fashion, there are 102 multiplications or additions (mult-adds), 2 divisions, and 2 "if" statements required, while 27 mult-adds are required to find the midpoint-to-midpoint vector (including checks for periodicity). To find the minimum distance vector and midpoint-to-midpoint vector, our programming implementation requires about 58 and 18 mult-adds, respectively. Implementing mSRP could result in substantially improved computational performance relative to SRP when bonds are densely packed, such as in a polymer melt. Further, mSRP offers a model that may be competitive with established coarse-graining models for selected systems. For example, phase-separated co-block polymers are often represented by a Lennard-Jones potential having a long, attractive tail which requires many pairwise interactions relative to the purely repulsive DPD potential. A comparison of mSRP with other coarse-grain models is the subject of current work by our group.

ACKNOWLEDGMENTS

This work was funded by the U.S. Army Research Laboratory Enterprise for Multi-Scale Research of Materials. This research was supported in part by an appointment to the Postgraduate Research Participation Program at the U.S. Army Research Laboratory administered by the Oak Ridge Institute for Science and Education through an interagency agreement between the U.S. Department of Energy and USARL. M.L. acknowledges support by the Ministry of Education, Youth and Sports, project LH-KONTAKT II no. LH12020.

[1] *Polymer Phyiscs*, 1st ed., edited by M. Rubinstein and R. Colby (Oxford University Press, Inc., New York, 2003).
[2] H. Tao and T. Lodge, Macromolecules **33**, 1747 (2000).
[3] K. Kremer and G. Grest, J. Chem. Phys. **92**, 5057 (1990).
[4] R. D. Groot and P. B. Warren, J. Chem. Phys. **107**, 0021 (1997).
[5] J. T. Padding and W. J. Briels, J. Phys. Condens. Matter **23**, 233101 (2011).
[6] R. D. Groot and K. L. Rabone, Biophys. J. **81**, 725 (2001).
[7] N. A. Spenley, Europhys. Lett. **49**, 534 (2000).

[8] J. T. Padding and W. J. Briels, J. Chem. Phys. **115**, 2846 (2001).
[9] S. Kumar and R. G. Larson, J. Chem. Phys. **114**, 6937 (2001).
[10] F. Goujon, P. Malfreyt, and D. J. Tildesley, J. Chem. Phys. **129**, 034902 (2008).
[11] G. Pan and C. W. Manke, Int. J. Mod. Phys. B **17**, 231 (2003).
[12] S. P. Holleran and R. G. Larson, Rheol. Acta **47**, 3 (2008).
[13] P. Nikunen, I. Vattulainen, and M. Karttunen, Phys. Rev. E **75**, 036713 (2007).
[14] N. Hoda and R. G. Larson, J. Rheol. **54**, 1061 (2010).
[15] *Dynamics of Polymeric Liquids, Volume 2: Kinetic Theory*, 2nd ed., edited by R. Bird, C. Curtiss, R. Armstrong, and O. Hassager (Wiley, New York, 1987).
[16] P. Nikunen, I. Vattulainen, and M. Karttunen, Europhys. Lett. **30**, 191 (1995).
[17] F. Lahmar, C. Tzoumanekas, D. N. Theodorou, and B. Rousseau, Macromolecules **42**, 7485 (2009).
[18] C. Tzoumanekas, F. Lahmar, B. Rousseau, and D. N. Theodorou, Macromolecules **42**, 7474 (2009).
[19] For the SRP model only, we observed a slight increase in the calculated system temperature ($k_BT = 1.06$), which persisted even when the timestep was reduced to $\delta t = 0.001\,\tau$. We speculate that the marginal performance of the DPD thermostat for SRP occurs due to the choice of chain parameters and the additional energy introduced by the segmental repulsive forces.
[20] P. Malfreyt and D. J. Tildesley, Langmuir **16**, 4732 (2000).
[21] S. J. Plimpton, J. Comput. Phys. **117**, 1 (1995).
[22] R. Auhl, G. Grest, K. Kremer, and S. Plimpton, J. Chem. Phys. **119**, 12718 (2003).
[23] *Conformational Theory of Large Molecules the Rotational Isomeric State Model in Macromolecular Systems*, 1st ed., edited by W. Mattice and U. Suter (John Wiley and Sons, New York, 1994).
[24] M. Bulacu and E. van der Giessen, J. Chem. Phys. **123**, 114901 (2005).
[25] M. Rubinstein and S. Panyukov, Macromolecules **35**, 6670 (2002).
[26] D. L. Goble and E. G. Wolff, Mater. Sci. **28**, 5986 (1993).
[27] *Rheology, An Historical Prospective*, edited by R. Tanner and K. Walters (Elsevier Science, Amsterdam, 1998).
[28] D. N. Theodorou and U. W. Suter, Macromolecules **18**, 1206 (1985).
[29] *Understanding Molecular Simulation*, 2nd ed., edited by D. Frenkel and B. Smit (Academic Press, New York, 2002).

Genetically Engineered Peptides for Inorganics: Study of an Unconstrained Bacterial Display Technology and Bulk Aluminum Alloy

Bryn L. Adams, Amethist S. Finch, Margaret M. Hurley, Deborah A. Sarkes, and Dimitra N. Stratis-Cullum

Advanced Materials, 25 (2013)

Materials Views
www.MaterialsViews.com

ADVANCED MATERIALS
www.advmat.de

Genetically Engineered Peptides for Inorganics: Study of an Unconstrained Bacterial Display Technology and Bulk Aluminum Alloy

*Bryn L. Adams, Amethist S. Finch, Margaret M. Hurley, Deborah A. Sarkes, and Dimitra N. Stratis-Cullum**

Biological systems have evolved the exquisite ability to spatially combine many weak, non-covalent chemical interactions to direct the molecular recognition and self-assembly of incredibly complex materials. The ability to control assembly at the molecular level has led to an interest in harnessing nature's building blocks (e.g., polypeptides, DNA, etc.) to bind inorganic or synthetic compounds for multi-scale fabrication (nano- to macro) of advanced materials. The utility of this approach is evidenced by the large and growing body of research reports highlighting peptides generated through biopanning of surface display peptide libraries.[1–5] Examples include a wide range of peptide binders to pure metals,[6–10] metal oxides,[11–13] metal alloys,[14] metal salts,[15] and semiconductors,[16–18] as well as hydroxyapatite—the inorganic component of teeth and bone.[19] Inorganic binding peptides, no matter the source, are widely recognized for their specificity and design control, and present a remarkable opportunity for advanced materials development.[20] However, the rules governing this type of peptide binding are not fully understood.[18,20,21] A variety of factors have been implicated in playing a role in peptide-inorganic surface interactions, including conformational effects,[22–25] electrostatic effects,[26,27] relative residue placement in the sequence,[28,29] acid-base chemistry,[30] and hydrogen bond formation.[14,21]

Discovery of genetically engineered peptides for inorganics (GEPI) through biopanning surface display peptides is most commonly accomplished using phage display technology.[4] The mainstream use of phage display is due in large part to the commercial availability of M13 bacteriophage display libraries, the diversity of the libraries, and the robustness of the viral host to shear-forces encountered in some biopanning methods. Despite the lack of current commercial availability, bacterial systems, including a number of different *Escherichia coli* (*E. coli*) display technologies (e.g., FliTrx bacterial flagellar display) have been utilized for the discovery of GEPI including inorganic metal-binding peptides.[31] One key advantage of a bacterial system is that the cells and corresponding genetic material of *E. coli* are relatively easy to manipulate, allowing customized libraries to be generated and transformed at very high efficiencies. *E. coli* also has a very rapid growth rate and is easy to culture, which makes biodiscovery of novel peptides a relatively simple process. In contrast to phage-display, the peptide sequences are directly encoded in the bacterial DNA, resulting in a self-sustaining and replicating population that can easily be propagated without requiring elution from the target, thereby minimizing loss of the peptides possessing the greatest interaction.

Recently, an *E. coli* peptide display library has been developed that offers the greatest estimated diversity (3×10^{10} discreet random peptides) to date and is comparable to phage display peptide diversity estimates.[32,33] A unique feature of this library is the display of unconstrained peptides (15mers) on an engineered outer membrane protein scaffold, eCPX. The unconstrained nature of the peptide is of particular importance because the utility of other bacterial peptide libraries has been limited due to poor accessibility to the cell surface, low sequence diversity, and host cell toxicity effects.[34] The eCPX peptide library has shown great potential recently in biopanning for affinity peptide binders for protein targets in a rapid (less than one week), semi-automated biopanning method.[35,36]

In this report, we demonstrate for the first time the development of a methodology for *E. coli* peptide discovery to bulk, inorganic targets using an unconstrained bacterial display peptide library. Using this method, a new series of peptides were identified and their binding interactions characterized. We chose to investigate a readily available aluminum alloy as the initial target and demonstrate the versatility of this display scaffold by incorporating programmed peptides, including aluminum binding peptides produced by phage display.[14] Computational simulation and analysis of peptide conformational fluctuations were used to increase our understanding of sequence-dependent, structure-function relationships. Furthermore, we are the first to show that these relationships contribute to high affinity peptide interactions with this aluminum system.

In order to develop bulk aluminum binding peptides from an *E. coli* eCPX peptide display library, a new biopanning methodology was first developed (**Figure 1**A). Biopanning is an affinity-based selection technique in which high affinity peptide binders are enriched from a peptide library containing millions to billions of individual, genetically encoded cells each

Dr. B. L. Adams, Dr. A. S. Finch,
Dr. D. N. Stratis-Cullum
U.S. Army Research Laboratory
RDRL-SEE-B, 2800 Powder Mill Road
Adelphi, MD 20783, USA
E-mail: dimitra.stratiscullum1@us.army.mil
Ms. D. A. Sarkes
Goldbelt Raven, LLC, 10 N Jefferson St, Frederick, MD 21701, USA
Dr. M. M. Hurley
US Army Research Laboratory, RDRL-WML-B,
4600 Deer Creek Loop, Aberdeen Proving Ground, MD 21005, USA

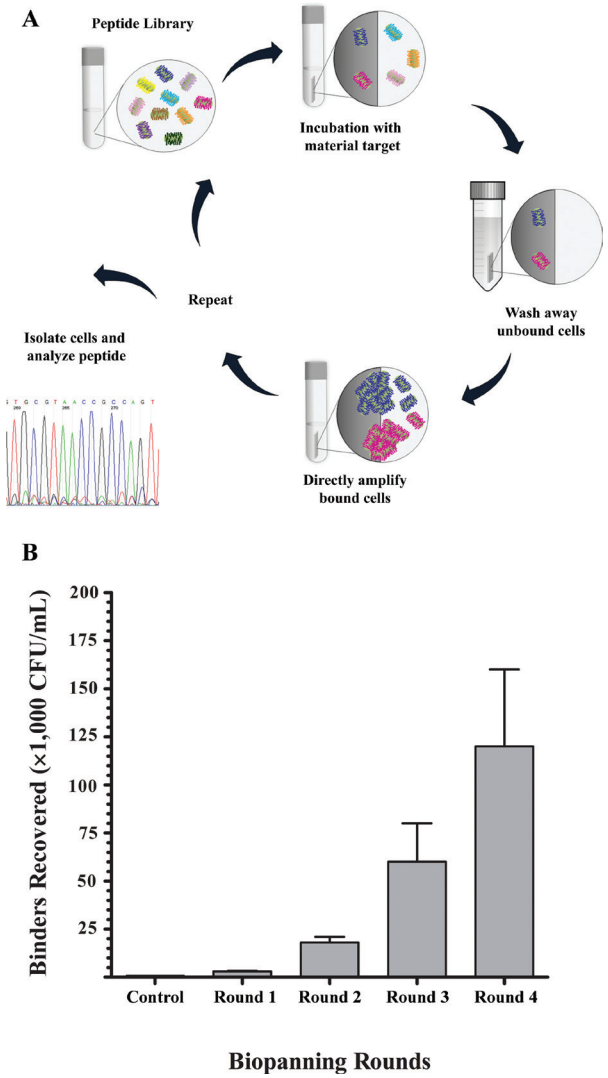

Figure 1. A) Schematic diagram of the biopanning process developed for discovery of metal binding peptides to bulk aluminum using an unconstrained bacterial peptide display library. B) Experimental results showing enrichment of aluminum isolates through progressive rounds of biopanning.

displaying a unique peptide sequence. Isolation and amplification of the peptide isolates with the highest affinity is accomplished through several steps: (1) binding (to immobilize the peptide materials with the greatest affinity to the target material), (2) washing with a series of stringency pressures put on the system (to remove unbound or weekly bound peptides), and (3) enrichment though regrowth of the remaining library members (to build up the population of peptides with the desired properties). The process is repeated several times (typically 3-5 rounds), to enrich the target population with the desired binding properties, and the stringency conditions employed are critical to a successful enrichment process. Negative selections can also be used against materials with similar properties to improve target specificity. Due to the fact that the combinatorial display library is genetically encoded, identification of the final population is easily accomplished through standard DNA sequencing techniques.

In order to monitor the enrichment, an indirect binding assay was developed to recover the population from the aluminum surface after each round, and these results are shown in Figure 1B. Although the indirect assay is not quantitative, a substantial increase in the relative number of bound cells from each successive round was observed, with an overall 40-fold increase from the fourth (and final) round relative to the first. The negative control was identical to any other cell in the library except for the lack of the unique 15mer peptide. It is important to note that few to no cells were recovered from the negative control samples, indicating that the appropriate stringency was employed during the biopanning process. Also, negligible binding by the negative control demonstrates that binding was most likely facilitated by the displayed peptides, and that neither general bacterial cell adhesion elements nor the display scaffold itself had a significant contribution to aluminum surface binding.

Analysis through DNA sequencing of isolated round 4 colonies revealed 17 unique sequences (**Table 1**). All but one sequence exhibited the full length (15mer) peptide, with the exception of DBAD10 (12mer). This truncation was not due to a stop codon or frameshift, and similarly, truncated peptides have been previously isolated from the parent library in other studies with protein target systems.[35] It is important to note that while the peptide is truncated in DBAD10, a full length eCPX scaffold was verified via sequence analysis and expression levels were monitored during FACS analysis. The peptide isolate designated DBAD5 was present once in the population sampled and exhibited the greatest number of hydroxyl and sulfoxyl containing residues. However, the isolated peptide sequence designated DBAD1 was the only sequence present more than once (identified 49 times), and possessed seven hydroxyl and sulfoxyl containing residues. To investigate this further, the 17 isolated colonies (i.e., isolated peptide binders) were assessed individually for their relative affinity to the aluminum alloy (**Figure 2**A) using the indirect binding assay. Overall, the relative affinity to the aluminum target varied significantly, spanning a 2-log variation. All isolates exhibited a greater interaction with the aluminum target, compared to the negative control, and the peptide isolate DBAD1 had a marked increase in interaction, relative to all other peptides. Specifically, DBAD1 exhibited a 360-fold higher target binding relative to the lowest isolated binder (DBAD14), and significantly higher than the next best isolate (DBAD24). It is important to note that the number and composition of isolates were not influenced by a competitive growth advantage. A comparison of planktonic growth (doubling time) of DBAD1 expressing cells to other isolates under the growth and induction conditions utilized during biopanning discovery is provided in Supplemental Figure 1.

To further verify binding interaction from the peptide isolates, scanning electron microscopy (SEM) was used to directly visualize DBAD1 binding to bulk aluminum (a representative figure shown in the Figure 2B inset). Supplemental Figure 2 provides a side-by-side comparison of DBAD1 to the negative control after 24 h of incubation followed by stringent removal

Table 1. Aluminum peptide sequences isolated from round 4 biopanning population with notation of frequency of occurrence and number of hydroxyl or sulfoxyl groups in each peptide. Hydroxyl and sulfoxyl residues are underlined.

Name	Peptide Sequence	Number Hydroxyl or Sulfoxyl Groups
DBAD1	STEARATTLTACDAY	7
DBAD5	LFHRSCPSYDTYSCL	8
DBAD4	HIGPSRYSSAFHCLS	6
DBAD10	SSCCSIHHRDCF	6
DBAD7	GSMFILTGFTGTVSH	5
DBAD19	DHCFRIPNLPTYRSC	5
DBAD8	QVHPRGSYHRAPSIC	4
DBAD11	ASRTALRCVQHRVRT	4
DBAD14	NGATICKAHPSALVT	4
DBAD16	KYRPCYPRLKPFIHT	4
DBAD6	SNIAPIPRNHFIHTS	3
DBAD12	PQALNSYSAIFAAIN	3
DBAD15	VNVSYAWFVHGSRRM	3
DBAD18	STVQAFGPGCVAQHL	3
DBAD20	SGHHCDKEIGARLLH	2
DBAD21	VSPPGPHLRGALPIG	1
DBAD24	LPRIPGNLFTILQPM	1

of unbound cells. Overall, from these data it can be concluded that (1) the biopanning method was successful against a bulk aluminum material, (2) the displayed peptide strongly facilitates the interaction of the isolates with the aluminum target, and (3) the DBAD1 isolate exhibited significantly better binding performance, warranting further investigation.

Although peptide-metal and peptide-metal oxide interactions (e.g., Cu_2O, ZnO, GaAs crystals, TiO_2, etc.) are not fully understood, the consensus of research in this area indicates that the peptide isolates are categorized by a predominance of polar, hydroxyl-containing residues with little to no positional consensus across the isolated population.[7,14,16,26,37] The exact mechanism of the interaction of hydroxyl-containing residues with the aluminum oxide (alumina) surface remains open to debate.[14] However, it is feasible that some measure of hydrogen bonding similar to that found in solvent/oxide surface interactions[38–40] and peptide/oxide interactions[27] may exist. When considering the peptide isolates reported herein (Table 1), it is noteworthy that the hydroxyl containing residues are distributed throughout the length of the majority of these peptides—a fact we will investigate in detail. However, it should also be noted that two of the sequences contain only a single hydroxyl-containing residue, implying that multiple mechanisms for surface binding must exist. A more thorough analysis of the exact mechanism of these interactions is left to future work.

The combined residues from the 17 isolates in Table 1 (weighted by frequency) were examined further for trends (enrichment or depletion) in amino acid character using a similar analysis to that employed by Thai et al.[26] Figure 2B summarizes these calculated results into general categories of

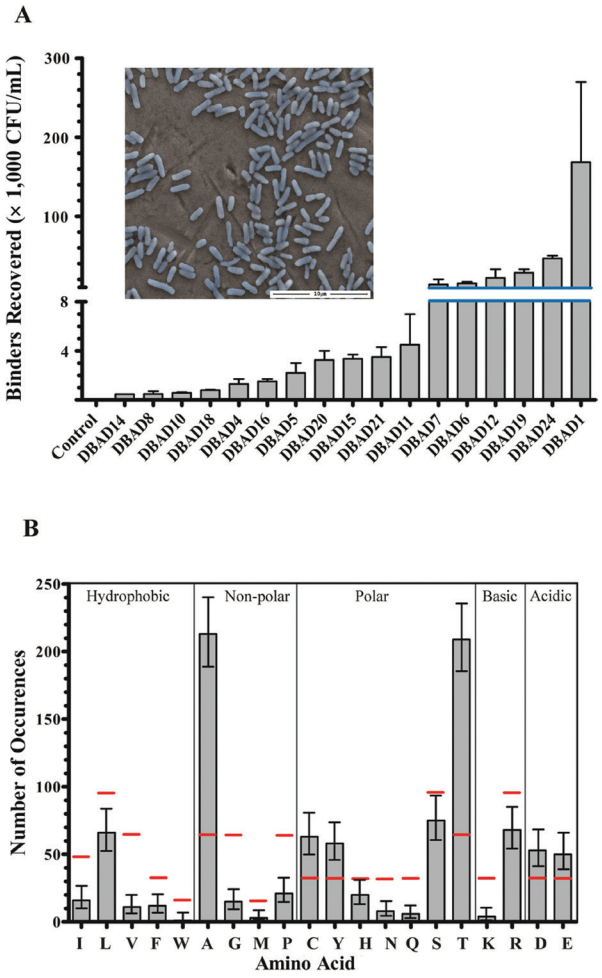

Figure 2. Analysis of aluminum binding peptides. A) Comparison all 17 peptide isolates using an indirect binding assay with aluminum. Inset shows a representative scanning electron microscopy (SEM) image of the DBAD1 isolate bound to the bulk aluminum alloy. B) Statistical analysis allowing comparison of observed and expected frequency of amino acid residues across all 17 peptide isolates. Gray bars indicate the observed residue occurrences in each peptide and corresponding 95% confidence interval. Red lines indicate the theoretical expected residue occurrences, assuming the library was fully randomized.

hydrophobic, non-polar, polar, basic, and acidic. The experimental frequency of each residue is displayed in the bar graph, along with the corresponding 95% confidence interval. The theoretical residue frequency in a given sequence can be estimated from the 20 possible naturally occurring amino acids. However, the DNA codons used to encode the amino acids displayed causes some residues to be present at a higher frequency (i.e., degeneracy) than others. Accordingly, the red lines in Figure 2B represent the theoretical expected residue occurrences, assuming the library was fully randomized. As expected, polar residues, the prime candidate for surface interactions, were enriched. While basic residues were under-represented, the charged acidic residues (glutamic and aspartic acid) were

elevated in a moderate but statistically relevant fashion. Previous analysis of poly-L-glutamic acid on an aluminum oxide surface has demonstrated the dependence of the interaction on pH and salt concentration, positing the direct role of the carboxylate group in binding.[41] Through computational modeling, Dringen et al. demonstrated the adsorption of glutathione disulfide (GSSG, g-GluCysGly disulfide) on alumina nanoparticles and also indicated direct involvement of the carboxylate groups.[30] The statistically large increase in alanine, however, is unexpected. As the side chain of alanine is a simple methyl group, it is unlikely that this enrichment is due to a direct chemical interaction. It is more likely that structural considerations govern these interactions, since alanine is noteworthy as a helix-forming residue.

Similar to our studies, Zuo et al.[14] developed peptides with affinity to aluminum and steel alloys. Their work also suggested that aluminum binding peptides have an expected bias toward hydroxyl-containing amino acids. The DBAD1 peptide isolate has seven hydroxyl containing residues distributed over a peptide length of 15 residues. In comparison Al-S1, the highest affinity peptide in the work by Zuo, has five hydroxyl containing residues distributed over a peptide length of 12 residues. It is difficult to directly compare binding affinities of peptides of varying length, developed and displayed on different scaffolds.[1] However, to further demonstrate the versatility of the eCPX cell surface display scaffold, and directly compare the relative performance with an aluminum binding peptide developed by phage, we genetically engineered the system to allow programmed display of peptide sequences, including Al-S1. Due to the unconstrained peptide display scaffold of eCPX, peptides of dissimilar length from different scaffold origins can be readily incorporated. Comparison of Al-S1 to DBAD1 using the indirect binding assay performed in Figure 2A indicated successful binding by Al-S1 displayed on the eCPX scaffold to the bulk aluminum alloy with significantly greater recovery of DBAD1 (Supplemental Figure 3). Although the indirect assay and analysis is not quantitative, the versatility of the eCPX scaffold with the ability to compare and translate peptides derived from different sources to a biofilm producing system is demonstrated.

The prominence of helix-forming alanine residues in DBAD1 and helix-breaking proline residues in Al-S1 led us to perform molecular dynamics simulations to study structural characteristics that may facilitate surface binding. **Figures 3**A and 3C shows an overlay of each peptide backbone structure during the course of a 40 ns simulation trajectory for peptides DBAD1 and Al-S1, respectively. Al-S1 rapidly lost the initial helical structure and maintained mostly turn and random coil secondary structure (helicity 0.4%). By contrast, DBAD1 maintained the

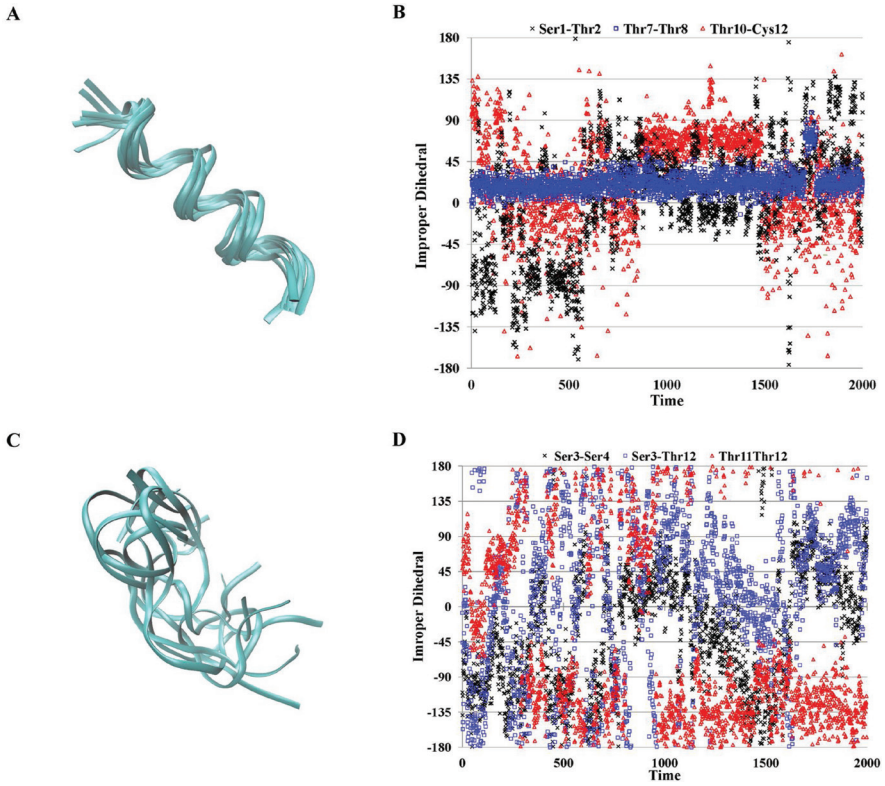

Figure 3. Molecular dynamics study of DBAD1 and A1-S1. (A) and (C) show an overlay of peptide backbone during simulation trajectory for the DBAD1 and Al-S1 peptides, respectively. (B) and (D) show the behavior of improper dihedrals marking relative orientation of hydroxyl groups during the course of simulation for the DBAD1 and Al-S1 peptides, respectively.

initial helical core structure very well (helicity 83%). This agrees with previous studies, which have noted the stability of helices in short (16 residue) alanine-based peptides.[42] Therefore, while both DBAD1 and Al-S1 had a relatively high number of hydroxyl and sulfoxyl groups to present to the aluminum surface, the manner in which these groups were presented to the surface differed.

This can be demonstrated through an analysis of the relative orientation of successive hydroxyl- (or sulfoxyl-) containing side chains along the length of each peptide. To quantify this relative orientation, we measured an improper dihedral angle (Φ_{ij}), defined by the hydroxyl oxygens (or sulfoxyl sulfur) and backbone carbons of two (not necessarily adjacent) residues, i and j. A visual representation of this moiety is shown in Supplemental Figure 4. A Φ_{ij} value in the range of ± 90° implies rough alignment along the same face of the peptide, and denotes the possibility for multiple, simultaneous binding sites as the peptide approaches the surface. A measure of this is shown in Figures 3B and 3D, where the improper dihedral angle (Φ_{ij}) has been tabulated for various pairs of hydroxyl-containing residues along the peptide length during the course of the simulation for DBAD1 and Al-S1, respectively. A marked contrast in the behavior for these two peptides is very evident. DBAD1 maintained a helical character and presented multiple aligned binding groups all along the peptide length. This alignment is shown for residue pairs Ser 1-Thr2, Thr8-Thr10, and Thr10-Cys12, representing a range of locations and lengths scales within the peptide. While some scatter outside the range of ± 90° is seen, the residue alignment overwhelmingly fluctuates quite tightly about 0. In contrast, Al-S1 lacked an overarching structure and any potential binding groups were scattered over the perimeter of the peptide (shown for residue pairs Ser3-Ser4, Ser3-Thr12, and Thr11-Thr12). It is obvious from this analysis that pairs of hydroxyl groups in the Al-S1 peptide had little to no alignment with each other. This means that in the absence of an overriding helical structure, the availability of an individual residue for binding as the peptide approaches the surface is largely a matter of chance. Both peptides will bind, but we suggest that this structural behavior strongly contributes to the improved binding affinity of DBAD1 relative to Al-S1. Further analysis is currently underway on additional peptides, specifically looking for alternative conformational and binding group alignment modes to enable us to draw more general conclusions on features that contribute to successful binding interactions.

To conclude, we demonstrated for the first time a novel and general approach to GEPI discovery using an unconstrained *E. coli* peptide library. Using this approach, we have discovered a unique DBAD1 peptide isolate that we believe to have superior binding performance with the aluminum (alumina) alloy, and attribute the increased interaction to a propensity to sustain an overarching helical structure with preferential presentation of hydroxyl- and sulfoxyl- containing residues to the metal surface. Compared to conventional techniques, our methodology enables direct propagation of the isolated material throughout the GEPI discovery process. This allows for the selection of the best affinity isolates, which are often lost in competing methodologies requiring elution at extreme pH conditions from the bulk material during the biopanning process. The computationally-driven methods employed, allow for a greater understanding of potential structure-function relationships and offer a new standard for GEPI analysis extending to other discovery systems (e.g., phage, yeast, etc.). We believe due to the demonstrated simplicity and versatility, our general methods will broadly extend current capabilities of GEPI discovery towards bulk, inorganic and more complex materials. Furthermore, our work is likely to have significant impact to the design and development of beneficial biofilms, including living paint for common metals (including aluminum) subject to corrosion. Future studies will continue to explore the use of this biological tool for advanced material development and improved understanding of hybrid material interactions.

Experimental Section

Bacterial Strains, Culture Conditions, and Materials: In all biopanning experiments, a previously developed *E. coli* unconstrained peptide display library constructed from an eCPX display scaffold was utilized.[32,33,43] These materials were obtained from the laboratory of Dr. Patrick Daugherty (University of California Santa Barbara) and cells were cultivated and maintained as previously described.[35] Phage derived aluminum binding peptide[14] Al-S1 (VPSSGPQDTRTT) was synthesized (BioBasics) for cloning into a eCPX vector using standard molecular biology methods. Primers used to amplify the peptide insert for cloning were as follows: Forward 5′-TTCCGTAGCTTGTACATGTGGCCAG-3′ and Reverse ′-CACCGCTGCCACCGCT-3′. The 83 bp insert was ligated into the empty display vector, pBad33-nl3, which was constructed with BsrGI and XhoI digestion sites for peptide sequence cloning. The resulting plasmid, named pBad33-AB1, was then transformed into chemically competent MC1061 cells and insertion of the programmed peptide sequence verified by sequencing (Genewiz).

Samples of aluminum sheet (product 5052-H32 Aluminum Sheet, onlinemetals.com) were received as 0.16 cm thick, and 5 cm × 10 cm in size. Prior to use, the aluminum was cut into a size (1 cm × 5 cm) compatible with standard culture tubes and samples were autoclaved using standard sterilization cycle. All molecular and microbiology support materials (e.g., primers, buffers, enzymes, media, Tween20, antibiotics, etc.) were obtained from standard, commercial suppliers (Fisher Scientific, Sigma Aldrich, Invitrogen, NEB, etc.) and used according to standard techniques.

Biopanning Method: Prior to biopanning against the target, the eCPX bacterial display library was prepared as previously described, with arabinose (0.04%) induction occurring at an OD_{600} 0.50–0.55 for 35–45 min.[35] After induction, the cells were chilled on ice for 15–30 min. Sterilized aluminum samples were added to the induced library and placed on a shaker at 4 °C for 15 min. The aluminum samples were briefly rinsed in sterile phosphate buffered saline (PBS) and transferred to PBS supplemented with Tween20 (1%) (PBST). The samples were washed for 5 min and stringency of isolation wash adjusted through additional wash steps with each successive round of biopanning to remove loosely bound cells. After washing, bound cells were recovered by removing the aluminum samples to LB+Cm/Glu and growing at 37 °C with shaking overnight. This overnight culture was then used in the subsequent round, for a total of 4 rounds. Ninety-six randomly selected colonies from round 4 were sequenced using the pBAD Forward universal primer (Genewiz) and the peptides identified from the generated sequences using the InsertMultiSeek analysis tool (www.sequencetools.com).

Indirect Binding Assay: The aluminum binding propensity of each sorting round, a population consisting of a single isolate or the empty display vector (negative control) were compared by quantifying the number of cells recovered from the aluminum surface. This assay was carried out by initially diluting overnight cultures 1:100 into fresh LB+Cm (5 mL), followed by eCPX expression induction with arabinose

as described previously. The induced cells were then chilled on ice for 15-30 min before addition of sterile aluminum samples for 15 min at 37 °C with shaking. The aluminum samples were briefly rinsed in sterile PBS and transferred to PBST (30 mL) and shaken at 150 rpm at room temperature for 30 min, a simpler washing regime that was found to yield the same results as the most stringent regime used during biopanning (data not shown). The aluminum samples were removed to LB+Cm/Glu (6 mL) and incubated at 37 °C with shaking for 1 hour. This incubation step allowed bound cells to be replicated off the aluminum surface. Furthermore, the addition of glucose prevented the expression of the eCPX display scaffold and thus, the cells remained planktonic and could then be enumerated. This was performed by serial dilutions on LB+Cm agar plates and the number of cells mL^{-1} recovered from the aluminum surface tabulated. All samples were prepared as duplicate independent samples, the results averaged, and the standard error of the means calculated.

Planktonic Growth Study: The isometric growth of the isolates were measured by constructing growth curves of the negative control (i.e., empty display vector) and cells displaying peptides Al-S1, DABD1, DBAD24, DBAD8, and DBAD14 in either LB+Cm, LB+Cm with an arabinose induction described previously, or in LB+Cm/Glu. Additionally, a growth curve was also constructed in the LB+Cm/Glu recovery condition for these strains following a typical arabinose induction and 45 min incubation as described previously using a 1:100 dilution. All samples were prepared as duplicate independent samples and the doubling time and 95% confidence intervals were calculated using the nonlinear fit exponential growth equation (Prism 5, GraphPad Software).

Scanning Electron Microscopy: Cell binding to an aluminum alloy surface was directly visualized microscopically. An overnight culture of MC1061 cells harboring either the pBad33-DBAD1 or pBad33-nl3 plasmids were diluted 1:100 in fresh LB+Cm (50 mL) and induced with arabinose, as described previously. After induction, aluminum SEM stubs were added directly to the culture and incubated at 37 °C for 24 hours before transfer to dI H_2O (30 mL) and shaken at 150 rpm at room temperature for 15 min. Samples were then removed and allowed to air dry prior to imaging using a FEI Quanta 200FEG ESEM (FEI) scanning electron microscope. A comparison of cell binding to the aluminum SEM stubs and the bulk aluminum alloy used in binder development were found to be similar (data not shown) and use of the stubs did not require additional sample preparation, as the use of the bulk aluminum did, and yielded better quality, uncoated images.

Statistical Analysis of Critical Amino Acids: Statistical analysis was used to compare the observed number of occurrences of each amino acid found to expected number of occurrences of each amino acid based on codon degeneracy. Although there was a 17 unique peptide sequences found, a total of 65 individual sequences were analyzed because sequence DBAD1 was identified 49 times. Statistical significance of differences between the observed and expected values were determined by calculating the 95% confidence intervals for each residue, as described by Thai et al.,[26] using the MAPLE software.[44] Briefly, the probability of any residue's occurrence is governed by binomial distribution. By using the cumulative binomial probability function (described in detail in reference[26]), which accounts for the number of sequences isolated and the peptide length, the upper and lower 95% confidence limit can be calculated. The values are displayed as error bars in Figure 2B and are asymmetric due to the use of a binomial distribution.

Molecular Dynamics and Helicity Simulations: Individual molecular dynamics simulations were performed for each peptide of interest. Peptide structures were built within VMD[45] from sequence information, solvated with water, and sufficient ions added to neutralize the system. The system was then minimized for 5000 steps, heated to 300 K, and NPT dynamics performed for approximately 40 ns. The simulations were performed using the CHARMm forcefield with a timestep of 2 fs and pressure of 1 atm with the NAMD software of Schulten et al.[46] The propensity for alpha helix formation of peptides were calculated utilizing the scale of Pace and Schultz.[47] STRIDE analysis[48] of the DBAD1 and Al-S1 secondary structure show an average percent helicity of 83% and 0.4%, respectively over a 40 ns simulation.

Supporting Information

Supporting Information is available from Wiley Online Library or from the author.

Acknowledgements

This project is supported in part by appointments to the *U.S. Army Research Laboratory Postdoctoral Fellowship Program* administered by the *Oak Ridge Associated Universities* through a contract with the *U.S. Army Research Laboratory*. Graphical artwork featured in the table of contents image and cover art feature were created by Mr. Eric Proctor at the *U.S. Army Research Laboratory*. The peptide sequence analysis webtool, InsertMultiSeek (www.sequencetools.com), used for batch sequence analysis was custom developed for this project by Mr. Richard Jones at *Integration Dynamics, Inc*. The authors also wish to thank Dr. Patrick Daugherty (UCSB) for providing the initial eCPX bacterial display library materials used in these studies and Dr. Jennifer Getz (Daugherty Lab) for useful discssions on the modifcation of the eCPX system. Additional laboratory technical support was provided by Ms. Mia Hunt at *U.S. Army Research Laboratory*.

Received: April 12, 2013
Revised: May 20, 2013
Published online: July 19, 2013

[1] P. S. Daugherty, *Curr. Opin. Struct. Biol.* **2007**, *17*, 474.
[2] A. C. Jahns, B. H. Rehm, *Microbial Biotech.* **2012**, *5*, 188.
[3] S. W. Lee, S. K. Lee, A. M. Belcher, *Adv. Mater.* **2003**, *15*, 689.
[4] C. Tamerler, D. Khatayevich, M. Gungormus, T. Kacar, E. E. Oren, M. Hnilova, M. Sarikaya, *Pept. Sci.* **2010**, *94*, 78.
[5] C. Y. Chiang, C. M. Mello, J. Gu, E. C. Silva, K. J. Van Vliet, A. M. Belcher, *Adv. Mater.* **2007**, *19*, 826.
[6] Y. Huang, C.-Y. Chiang, S. K. Lee, Y. Gao, E. L. Hu, J. D. Yoreo, A. M. Belcher, *Nano Lett.* **2005**, *5*, 1429.
[7] R. R. Naik, S. J. Stringer, G. Agarwal, S. E. Jones, M. O. Stone, *Nat. Mater.* **2002**, *1*, 169.
[8] E. E. Oren, C. Tamerler, M. Sarikaya, *Nano Lett.* **2005**, *5*, 415.
[9] S. Cetinel, S. Dincer, A. Cebeci, E. E. Oren, J. D. Whitaker, D. T. Schwartz, N. G. Karaguler, M. Sarikaya, C. Tamerler, *Bioinspir. Biomim. Nanobiomater.* **2012**, *1*, 143.
[10] A. K. Sinensky, A. M. Belcher, *Adv. Mater.* **2006**, *18*, 991.
[11] H. Chen, X. Su, K. G. Neoh, W. S. Choe, *Anal. Chem.* **2006**, *78*, 4872.
[12] D. Rothenstein, B. Claasen, B. Omiecienski, P. Lammel, J. Bill, *J. Am. Chem. Soc.* **2012**, *134*, 12547.
[13] N. Nuraje, X. Dang, J. Qi, M. A. Allen, Y. Lei, A. M. Belcher, *Adv. Mater.* **2012**, *24*, 2885.
[14] R. Zuo, D. Örnek, T. K. Wood, *Appl. Microbiol. Biotechnol.* **2005**, *68*, 505.
[15] Y. J. Lee, H. Yi, W.-J. Kim, K. Kang, D. S. Yun, M. S. Strano, G. Ceder, A. M. Belcher, *Science* **2009**, *324*, 1051.
[16] S. R. Whaley, D. English, E. L. Hu, P. F. Barbara, A. M. Belcher, *Nature* **2000**, *405*, 665.
[17] E. Estephan, D. Bajoni, M.-b. Saab, T. Cloitre, R. Aulombard, C. Larroque, L. C. Andreani, M. Liscidini, A. M. Malvezzi, C. Gergely, *Langmuir* **2010**, *26*, 10373.
[18] B. R. Peelle, E. M. Krauland, K. D. Wittrup, A. M. Belcher, *Langmuir* **2005**, *21*, 6929.
[19] M. D. Roy, S. K. Stanley, E. J. Amis, M. L. Becker, *Adv. Mater.* **2008**, *20*, 1830.
[20] B. D. Briggs, M. R. Knecht, *J. Phys. Chem. Lett.* **2013**, *3*, 405.
[21] A. Vallee, V. Humblot, C.-M. Pradier, *Acc. Chem. Res.* **2010**, *43*, 1297.

[22] W.-S. Choe, M. S. R. Sastry, C. K. Thai, H. Dai, D. T. Schwartz, F. Baneyx, *Langmuir* **2007**, *23*, 11347.
[23] N. Kantarci, C. Tamerler, M. Sarikaya, T. Haliloglu, P. Doruker, *Polymer* **2005**, *46*, 4307.
[24] R. Notman, E. E. Oren, C. Tamerler, M. Sarikaya, R. Samudrala, T. R. Walsh, *Biomacromolecules* **2010**, *11*.
[25] S. V. Patwardhan, G. Patwardhan, C. C. Perry, *J. Mater. Chem.* **2007**, *17*, 2875.
[26] C. K. Thai, H. Dai, M. Sastry, M. Sarikaya, D. T. Schwartz, F. Baneyx, *Biotechnol. Bioeng.* **2004**, *87*, 129.
[27] S. V. Patwardhan, F. S. Emami, R. J. Berry, S. E. Jones, R. R. Naik, O. Deschaume, H. Heinz, C. C. Perry, *J. Am. Chem. Soc.* **2012**, *134*, 6244.
[28] E. Oren, Emre, C. Tamerler, D. Sahin, M. Hnilova, U. O. S. Seker, M. Sarikaya, R. Samudrala, *Bioinformatics* **2007**, *23*, 2816.
[29] H. Chen, X. Su, K.-G. Neoh, W.-S. Choe, *Langmuir* **2008**, *24*, 6852.
[30] R. Dringen, Y. Koehler, L. Derr, G. Tomba, M. M. Schmidt, L. Treccani, L. C. Ciacchi, K. Rezwan, *Langmuir* **2011**, *27*, 9449.
[31] F. Baneyx, D. T. Schwartz, *Curr. Opin. Biotechnol.* **2007**, *18*, 312.
[32] J. J. Rice, P. S. Daugherty, *Protein Eng. Des. Sel.* **2008**, *21*, 435.
[33] J. J. Rice, A. Schohn, P. H. Bessette, K. T. Boulware, P. S. Daugherty, *Protein Sci.* **2006**, *15*, 825.
[34] A. Christmann, K. Walter, A. Wentzel, R. Krätzner, H. Kolmar, *Protein Eng.* **1999**, *12*, 797.
[35] J. M. Kogot, Y. Zhang, S. J. Moore, P. Pagano, D. N. Stratis-Cullum, D. Chang-Yen, M. Turewicz, P. M. Pellegrino, A. de Fusco, H. T. Soh, N. E. Stagliano, *PLoS ONE* **2011**, *6*, e26925.
[36] D. Stratis-Cullum, J. Kogot, D. Sarkes, I. Val-Addo, P. Pellegrino, in *On Biomimetics*, (Ed: D. L. Pramatarova), InTech, Online, **2011**.
[37] S. Brown, *Nat. Biotechnol.* **1997**, *15*, 269.
[38] K. C. Hass, W. F. Schneider, A. Curioni, W. Andreoni, *Science* **1998**, *282*, 265.
[39] M.-P. Gaigeot, M. Sprik, M. Sulpizi, *J. Phys.: Cond. Matter* **2012**, *24*.
[40] G. V. Franks, Y. Gan, *J. Am. Ceram. Soc.* **2007**, *90*, 3373.
[41] C. M. Pradier, V. Humblot, L. Stievano, C. Methivier, J. F. Lambert, *Langmuir* **2007**, *23*, 2463.
[42] S. Marqusee, V. H. Robbins, R. L. Baldwin, *Proc. Natl. Acad. Sci.* **1989**, *86*, 5286.
[43] S. A. Kenrick, P. S. Daugherty, *Protein Eng. Des. Sel.* **2010**, *23*, 9.
[44] Waterloo Maple Inc, **2012**.
[45] W. Humphrey, A. Dalke, K. Schulten, *J. Mol. Graph.* **1996**, *14*, 33.
[46] J. C. Phillips, R. Braun, W. Wang, J. Gumbart, E. Tajkhorshid, E. Villa, C. Chipot, R. D. Skeel, L. Kale, K. Schulten, *J. Comput. Chem.* **2005**, *26*, 1781.
[47] C. Nick Pace, J. Martin Scholtz, *Biophys. J.* **1998**, *75*, 422.
[48] D. Frishman, P. Argos, *Proteins: Struct. Funct. Bioinform.* **1995**, *23*, 566.

The Effects of Stoichiometry on the Mechanical Properties of Icosahedral Boron Carbide Under Loading

DeCarlos E. Taylor, James W. McCauley, and Thomas W. Wright

Journal of Physics: Condensed Matter, 24 (2012)

IOP PUBLISHING JOURNAL OF PHYSICS: CONDENSED MATTER

J. Phys.: Condens. Matter **24** (2012) 505402 (11pp) doi:10.1088/0953-8984/24/50/505402

The effects of stoichiometry on the mechanical properties of icosahedral boron carbide under loading

DeCarlos E Taylor[1,3], James W McCauley[1] and T W Wright[2]

[1] US Army Research Laboratory, Aberdeen Proving Ground, MD 21005, USA
[2] Department of Mechanical Engineering, Johns Hopkins University, Baltimore, MD 21218, USA

E-mail: decarlos.e.taylor.civ@mail.mil and james.w.mccauley.civ@mail.mil

Received 13 July 2012, in final form 15 October 2012
Published 19 November 2012
Online at stacks.iop.org/JPhysCM/24/505402

Abstract
The effects of stoichiometry on the atomic structure and the related mechanical properties of boron carbide (B_4C) have been studied using density functional theory and quantum molecular dynamics simulations. Computational cells of boron carbide containing up to 960 atoms and spanning compositions ranging from 6.7% to 26.7% carbon were used to determine the effects of stoichiometry on the atomic structure, elastic properties, and stress–strain response as a function of hydrostatic, uniaxial, and shear loading paths. It was found that different stoichiometries, as well as variable atomic arrangements within a fixed stoichiometry, can have a significant impact on the yield stress of boron carbide when compressed uniaxially (by as much as 70% in some cases); the significantly reduced strength of boron carbide under shear loading is also demonstrated.

(Some figures may appear in colour only in the online journal)

1. Introduction

Boron carbide (BC), due to its extreme hardness, low density, and demonstrated performance, has been used as an armor ceramic for many years [1]. With nominal stoichiometry B_4C, the crystal structure consists of 12-atom icosahedra cross-linked by 3-atom chains as shown in figure 1. Within the structure, there is a high degree of compositional variation with configurations consisting of B_{12} or $B_{11}C$ icosahedra (among others) linked by a variety of 3-atom chains such as C–C–C and C–B–C. BC is generally regarded to have $R\bar{3}m$ symmetry [2], however this can only be true for a *subset* of the available atomic arrangements since placement of even a single carbon atom within an icosahedron causes a monoclinic distortion of the rhombohedral lattice thereby reducing the crystalline symmetry [3]. Configurations of different stoichiometry from ideal B_4C (e.g. $B_{2.75}C$ or $B_{5.6}C$) are referred to as 'polytypoids' and atomic configurations with ideal B_4C stoichiometry, but different arrangement of atoms within the icosahedra (or chains), are termed 'polytypes'. Within each icosahedron, there exist two crystallographically unique sites termed 'polar' and 'equatorial' as shown in figure 2 and hereafter, any atom that specifically occupies a polar or equatorial site within an icosahedron will be labeled with a subscript 'p' or 'e' respectively.

Experimentally, BC can be produced by several methods such as reaction of boric oxide and carbon in an electric arc furnace [4] or carbothermal reduction of a boric acid–citric acid gel [5]. The powders can consist of a range of boron to carbon ratios resulting in a complex phase diagram [6], an example of which is shown in figure 3. Other phase diagrams have also been constructed [7–9]. A new phase equilibrium diagram has just recently been submitted for publication [10] which suggests that stoichiometric B_4C is a line compound with a monoclinic structure that is stable to 600 K. In addition, it is also suggested that a rhombohedral $B_{13}C_2$ solid solution phase is the stable phase above 600 K from about 10 to 20 atomic %C. The issue of a $B_{13}C_2$ phase has been debated for some time after first being identified by Samsonov *et al* in 1956 [11]. In a recent review article [8]

[3] Author to whom any correspondence should be addressed.

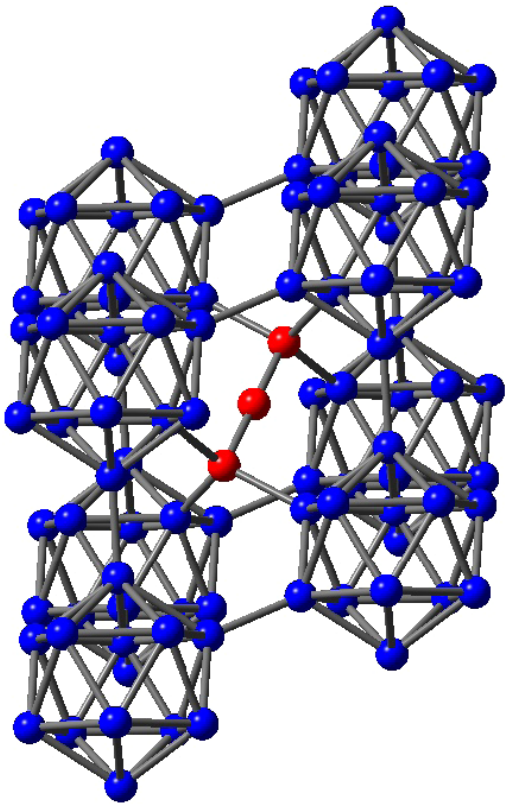

Figure 1. Icosahedral structure of boron (blue) carbide linked by a 3-atom carbon (red) chain. For clarity of representation, only a single chain is included in the image.

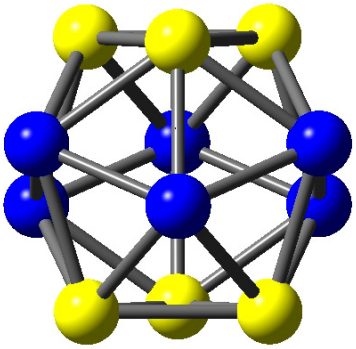

Figure 2. Icosahedron with polar (yellow) and equatorial (blue) positions.

it has been suggested that x-ray diffraction analysis of a series of boron-rich materials indicates a distinct change in the *c* lattice parameters at about 13 atomic %C, the $B_{13}C_2$ composition. Further, in that work, a single crystal of BC was chemically analyzed by Raman spectroscopy and it is clear that even 'single crystals' of BC can have significant stoichiometric variation. McCuistion *et al* [12] compiled chemical compositions of a variety of BC powders also indicating B/C ratios from 3.58 to 4.0. The exact chemical composition of BC grains in two commercial bulk materials was determined by Chen *et al* [13] using Electron Energy Loss Spectroscopy (EELS) with the following results: B/C ratios of

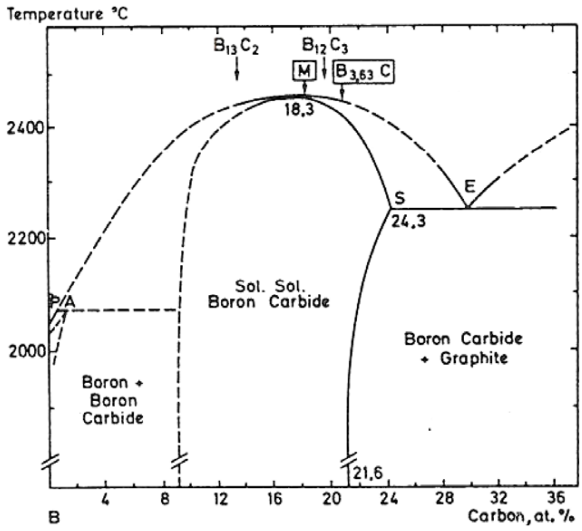

Figure 3. Boron carbide phase diagram. Reproduced with permission from [6]. Copyright 1983 Elsevier.

Table 1. Experimental bulk and shear moduli (GPa) of boron carbide as a function of composition.

Stoichiometry	% Carbon	Bulk modulus	Shear modulus
B_4C	20.0	235	197
$B_{4.5}C$	18.2	237	197
$B_{5.6}C$	15.2	236	197
$B_{6.5}C$	13.3	231	189
$B_{7.7}C$	11.5	178	150

3.81 ± 0.15 and 3.90 ± 0.07. These variations in composition have an effect on the observed mechanical properties, as shown in table 1, where the experimentally measured bulk and shear moduli for samples ranging from B_4C (20% carbon) to $B_{7.7}C$ (11.5% carbon) are presented [8]. The general trend evidenced by the experimental data is a reduction in stiffness as the boron concentration increases. There has been much work on determination of the structure and properties of BC samples of varying composition. Conde *et al* [14] determined the hexagonal lattice parameters of B_4C samples ranging from 10% to 20% C using glancing incidence x-ray diffraction and similar experimental studies of structure as a function of stoichiometry were conducted by Konovalikhin and Ponomarev [15] and Kwei and Morosin [16]. The application of solid state density functional theory (DFT) [17] by Saal *et al* [18] and Vast *et al* [19] provided theoretically determined structures and energies for a range of stoichiometries.

Although the structure and formation enthalpy of BC as a function of stoichiometry has been well documented [18], knowledge of the origins of the deformation and damage mechanisms, and their relation to the macro-mechanical properties, is critical. The discovery of shock-induced localized nanoscale amorphization [20] in hot pressed bulk BC and its relationship to performance is unclear. In addition, the origin of the dramatic loss in shear strength [21, 22] of B_4C in plate impact experiments has not been elucidated. The elastic moduli of 3 BC polytypes, all with 20%

carbon composition, were predicted using DFT by Taylor *et al* [23] and Aryal *et al* [24] under hydrostatic and uniaxial load. Taylor *et al* showed that among the B_{12}(C–C–C), $B_{11}C_p$(C–B–C), and $B_{11}C_e$(C–B–C) polytypes, there was a reduction in the bulk modulus from 234 to 222 GPa when going from a C–B–C to a C–C–C chain at fixed 20% C composition and polytypism was shown to affect the pressure evolution of the elastic moduli as well. Aryal *et al* [24] presented similar results for the elastic moduli under uniaxial load and also presented stress–strain curves for two BC polytypes, both containing 20% carbon and showed that there was a slight difference in the stress–strain response between the two polytypes studied in that work.

Since BC powders are most likely a mixture of BC stoichiometries [8], and given the experimentally observed effect of such compositional variation on the mechanical response of BC, it is important that the mechanical properties of a diversity of compositions be well characterized. This information can play a role in identification of 'soft' configurations that may initiate failure in the BC structure when impacted with high velocity projectiles. In this paper, we present a comprehensive survey, using DFT, of the mechanical properties of 15 BC structures with stoichiometries ranging from $B_{2.75}C$ to $B_{14}C$ as shown in table 2. The $B_{2.75}C$ stoichiometry (26% C) represents a carbon-rich example and, as indicated by the phase diagram in figure 3, would precipitate carbon in the form of graphite at high processing temperatures. However, it was included in the current analysis purely as an example of an extremely carbon rich limit in order to further elucidate the effects of stoichiometry on the mechanical properties of the icosahedral structures under consideration. For each stable configuration, the structure, elastic moduli, and stress–strain response under several loading paths using quantum molecular dynamics (MD) simulations have been determined. We include an analysis of the stress–strain response of each structure under shear, in addition to hydrostatic and uniaxial loading, since shear has been postulated to be a contributing factor to the pressure-induced amorphization [25] phenomenon that has been observed experimentally in BC. The computational approach adopted in this work is described in section 2, followed by presentation of the results and discussion in sections 3 and 4 respectively.

2. Computational approach

2.1. Crystal structure optimization algorithm

A crystal structure optimization program was written, based on the L-BFGS [26] optimization algorithm, where any stress state (hydrostatic, uniaxial, shear) can be imposed. Several software packages (such as CP2K [27]) already offer such implementations, however, many of those programs rotate the input coordinates to a different computational orientation making interpretation of the stress along a specific crystallographic direction, a key component of this work, more difficult to monitor and interpret. To circumvent this difficulty, a program that does not perform a rotation of the input orientation was written and used in this study. At each optimization step, the energy, forces, and stress tensor were evaluated using the Perdew–Burke–Ernzerhof [28] (PBE) functional in a double zeta valence plus polarization basis set with a plane wave cutoff of 800 Ryd provided by the CP2K [27] program. It should be noted that no symmetry restrictions were imposed, i.e., no constraints were applied to enforce linearity of the 3-atom chain. For each system, a $2 \times 2 \times 2$ computational supercell containing 120 atoms was used in order to minimize size effects introduced when using smaller computational cells. At each optimization step, the stress tensor returned by CP2K was converted to cell vector derivatives, required by the L-BFGS algorithm to update the lattice vectors, using the transformation from stress to cell vector gradients given by Doll [29]. Optimization was considered converged when the gradient norm of the cell vector derivatives was below 0.0001 atomic units.

Table 2. Boron carbide stoichiometries used in this study. The subscript e and p labels denote equatorial and polar carbons, respectively.

Structure	Stoichiometry	% C
$B_{11}C_e$(CCC)	$B_{2.75}C$	26.66
$B_{11}C_p$(CCC)	$B_{2.75}C$	26.66
B_{12}(CCC)	B_4C	20.00
$B_{11}C_e$(CCB)	B_4C	20.00
$B_{11}C_p$(CCB)	B_4C	20.00
$B_{11}C_e$(CBC)	B_4C	20.00
$B_{11}C_p$(CBC)	B_4C	20.00
B_{12}(CCB)	$B_{6.5}C$	13.33
B_{12}(CBC)	$B_{6.5}C$	13.33
$B_{11}C_e$(BCB)	$B_{6.5}C$	13.33
$B_{11}C_p$(BCB)	$B_{6.5}C$	13.33
$B_{11}C_e$(BBC)	$B_{6.5}C$	13.33
$B_{11}C_p$(BBC)	$B_{6.5}C$	13.33
B_{12}(BBC)	$B_{14}C$	6.66
B_{12}(BCB)	$B_{14}C$	6.66

2.2. Elastic constants

Elastic constants are related to the second derivative of the total energy with respect to strain, ε_i, via

$$C_{ij} = \frac{1}{V}\frac{\partial^2 E}{\partial \varepsilon_i \partial \varepsilon_j}\bigg|_0 \tag{1}$$

where V is the unit cell volume and $i, j = 1 \cdots 6$ using the compact Voigt notation ($1 = xx, 2 = yy, 3 = zz, 4 = yz, 5 = xz, 6 = xy$). For this work, a program was written that evaluates the second derivatives in equation (1) via a finite difference of analytic first derivatives of the energy with respect to strain (stress tensor) provided by the CP2K code. We have monitored the change in the elastic constants as a function of hydrostatic and uniaxial load and the required stress corrections for elastic constants, C_{ijkl}, under non-zero load were included using:

$$B_{ijkl} = C_{ijkl} + \tfrac{1}{2}(\delta_{ik}\sigma_{jl} + \delta_{jk}\sigma_{il} + \delta_{il}\sigma_{jk} + \delta_{jl}\sigma_{ik} - 2\delta_{kl}\sigma_{ij}) \tag{2}$$

with σ_{ij} being an element of the stress tensor and B_{ijkl} representing the stress corrected effective elastic constant (or 'Birch coefficient') [30, 31].

Table 3. Computed unit cell parameters using 0 K geometry optimization and MD simulation (values in parentheses) at 298 K. The shaded gray area indicates that no stable configuration containing a *linear* 3-atom chain was found. (Lengths in Angstroms, angles in degrees, volume in cubic Angstroms).

Structure	Formula	% C	a	b	c	α	β	γ	Volume
Experiment[37]	$B_{5.6}C$	15.2	**5.19**	**5.19**	**5.19**	**65.18**	**65.18**	**65.18**	**110.02**
$B_{11}C_e$(CCC)	$B_{2.75}C$	26.66	**5.14(5.15)**	**5.21(5.22)**	**5.21(5.22)**	**64.31(64.28)**	**65.19(65.22)**	**65.19(65.22)**	**109.28(109.93)**
$B_{11}C_p$(CCC)	$B_{2.75}C$	26.66	**5.05(5.06)**	**5.21(5.22)**	**5.21(5.22)**	**64.86(64.82)**	**66.05(66.07)**	**66.05(66.07)**	**108.93(109.66)**
B_{12}(CCC)	B_4C	20.00	**5.19(5.21)**	**5.19(5.21)**	**5.19(5.21)**	**66.01(66.01)**	**66.01(66.01)**	**66.01(66.01)**	**112.09(112.81)**
$B_{11}C_e$(CCB)	B_4C	20.00	**5.16(5.17)**	**5.22(5.23)**	**5.22(5.23)**	**66.18(66.18)**	**66.16(66.16)**	**66.16(66.16)**	**112.72(113.38)**
$B_{11}C_p$(CCB)	B_4C	20.00	**5.05(5.06)**	**5.23(5.24)**	**5.23(5.24)**	**66.17(66.14)**	**67.33(67.35)**	**67.33(67.35)**	**112.27(112.90)**
$B_{11}C_e$(CBC)	B_4C	20.00	**5.18(5.18)**	**5.22(5.22)**	**5.22(5.22)**	**64.86(64.84)**	**64.97(64.97)**	**64.97(64.97)**	**110.16(110.77)**
$B_{11}C_p$(CBC)	B_4C	20.00	**5.07(5.08)**	**5.22(5.22)**	**5.22(5.22)**	**65.24(65.22)**	**66.07(66.08)**	**66.07(66.08)**	**109.75(110.43)**
B_{12}(CCB)	$B_{6.5}C$	13.33	**5.16(5.17)**	**5.22(5.22)**	**5.22(5.22)**	**66.79(66.81)**	**67.89(67.83)**	**67.89(67.83)**	**115.29(115.95)**
B_{12}(CBC)	$B_{6.5}C$	13.33	**5.20(5.21)**	**5.20(5.21)**	**5.20(5.21)**	**65.83(65.83)**	**65.83(65.83)**	**65.83(65.83)**	**112.10(112.76)**
$B_{11}C_e$(BCB)	$B_{6.5}C$	13.33							
$B_{11}C_p$(BCB)	$B_{6.5}C$	13.33							
$B_{11}C_e$(BBC)	$B_{6.5}C$	13.33							
$B_{11}C_p$(BBC)	$B_{6.5}C$	13.33							
B_{12}(BBC)	$B_{14}C$	6.66							
B_{12}(BCB)	$B_{14}C$	6.66							

2.3. Quantum molecular dynamics simulations

Quantum molecular dynamics simulations of several of the structures were conducted under hydrostatic, uniaxial, and shear loading paths. For the MD simulations, the computational cell size was increased to a $4 \times 4 \times 4$ supercell (960 atoms) in order to minimize size effects. This is particularly important since large simulation cells are required to properly accommodate large stresses and strains. For each simulation, the atomic coordinates were integrated using the leap-frog algorithm [32] with temperature and pressure controlled using algorithms due to Berendsen [33]. For each MD trajectory, atomic forces and stresses were computed by CP2K using the PBE functional and basis set as described above. Each simulation was run for 5000 time steps (1 time step = 1 fs), resulting in a total simulation time of 5 ps for each system. In order to determine the stress–strain curves for uniaxial and shear loading, small strains were applied in the desired direction at time step $t = 0$, and all strains orthogonal to the initially applied strain were allowed to relax during the remainder of the simulation. The time averaged value of the constrained stress tensor element was used to generate the stress–strain curves.

3. Results

3.1. Structures at zero stress

The lattice parameters for each structure resulting from optimization at 0 K and MD simulation at 298 K are presented in table 3. In terms of the structure at zero load, thermal effects are minimal, with slight expansion in the vector lengths and minor variations in the vector angles, resulting from inclusion of temperature effects. The distortion of the structure from purely rhombohedral symmetry is clearly evident in many of the systems and within each carbon concentration, the a lattice vector shows a larger contraction when the carbon atom resides in the polar site. It is noteworthy that many of the low carbon content stoichiometries produced structures that were either unstable elastically (negative eigenvalue in the elastic constant tensor) or converged to a minimum energy structure with a non-linear 3-atom chain. This seems to contradict some of the findings reported in earlier papers [18], however it is not clear from those publications if symmetry was enforced in their calculations in order to maintain linearity of the 3-atom chain. The bending of the 3-atom chain for these configurations was verified using a plane wave basis as implemented in the solid state DFT software package VASP [34] in place of the mixed Gaussian/plane wave basis approach in CP2K. Further, the bending of the 3-atom chain occurred in both the $2 \times 2 \times 2$ and $4 \times 4 \times 4$ supercells (indicating that the bending is not an artifact of the size of the computational cell used in this work) and was also found to occur when using the local density approximation in place of the PBE functional. It is known experimentally that at an approximately 8% carbon content, boron begins to precipitate from the lattice yielding mixtures of boron carbide and pure boron [35]. The instability of the linear 3-atom chain structure for the many of the boron-rich compositions found in this work supports this finding.

In the double zeta basis set used in this work, the polar icosahedral position is energetically favored over the equatorial site with the polar configurations being 33.9, 53.0, and 35.7 meV/atom lower in energy than their equatorial counterparts for the $B_{11}C$(CCC), $B_{11}C$(CCB), and $B_{11}C$(CBC) structures respectively when using the 0 K optimized configurations. For the $B_{13}C_2$ polytypoids, both containing 13.33% carbon, the CBC arrangement is clearly favorable over the CCB arrangement, which is 163 meV/atom higher in energy.

3.2. Elastic constants

The zero stress elastic constants (with respect to rhombohedral axes), bulk modulus, shear modulus, and Young's

Table 4. Computed zero pressure elastic moduli. All values in GPa. The three values for Young's modulus correspond to the values along the *x*, *y*, and *z* stress axes where the *z*-axis is coincident with the rhombohedrally oriented [111] direction.

Structure	Formula	% C	C_{11}	C_{12}	C_{13}	C_{14}	C_{33}	C_{44}	Bulk[a]	Shear	Young's
Experiment[37]	$B_{5.6}C$	**15.2**	**542.8**	**130.6**	**63.5**	—	**534.5**	**164.8**	**236.8**	**195.6**	**460.1**
$B_{11}C_e$(CCC)	$B_{2.75}C$	26.66	501.7	120.0	65.8	26.7	547.7	190.7	235.4	195.4	467/513/528
$B_{11}C_p$(CCC)	$B_{2.75}C$	26.66	517.9	133.1	58.7	49.1	544.4	173.4	237.4	189.9	464/498/531
B_{12}(CCC)	B_4C	20.00	486.9	188.8	64.9	14.7	518.1	133.6	221.1	173.2	451/451/504
$B_{11}C_e$(CCB)	B_4C	20.00	457.8	119.8	61.5	36.3	536.1	111.6	221.8	162.4	409/438/520
$B_{11}C_p$(CCB)	B_4C	20.00	470.3	124.6	53.6	44.6	505.7	132.5	217.8	170.9	417/441/492
$B_{11}C_e$(CBC)	B_4C	20.00	518.3	116.8	65.9	30.6	522.5	159.6	234.1	196.5	481/522/507
$B_{11}C_p$(CBC)	B_4C	20.00	534.2	120.2	58.1	38.0	525.7	168.4	233.6	199.7	494/519/514
B_{12}(CCB)	$B_{6.5}C$	13.33	395.7	139.4	82.8	61.7	393.7	96.6	202.3	135.6	291/381/373
B_{12}(CBC)	$B_{6.5}C$	13.33	531.3	105.3	54.2	−7.95	528.5	167.1	224.4	201.4	506/506/519

[a] Computed using Voigt–Reuss–Hill average.

modulus for each structure are presented in table 4. In determining the elastic constants, the minimum energy structures found using 0 K optimization (see table 3) were used and temperature effects were not included. This was done to ensure that optimized structures with maximal symmetry were used in computation of the elastic constant tensor in order to allow application of the Born stability criterion [36] for the $\bar{3}m$ point group (discussed below) to identify structural instability under load. Inclusion of temperature, in the context of MD, introduces asymmetry via the random velocities used to initiate the MD trajectories. It should be noted that only the B_{12}(CCC) and B_{12}(CBC) structures strictly adhere to $R\bar{3}m$ symmetry and the small distortions present in the other structures introduce additional non-zero, albeit small, elements in the elastic constant tensor. As a result, for ease of comparison across the range of structures, only the six non-zero C_{ij}'s that are present for $R\bar{3}m$ symmetry are presented. The elastic constants are similar in magnitude for all structures, however B_{12}(CCB) shows a considerable reduction in stiffness compared to the other systems. The experimental values in table 4 were measured by McClellan *et al* using a sample with stoichiometry $B_{5.6}C$ (15.2% C) [37]. However, in their work, the value of the C_{14} modulus was indeterminate due to the hexagonal symmetry assumed in determination of the elastic moduli. The theoretical C_{14} moduli are comparatively small and that for the B_{12}(CBC) structure is negative compared to the positive values obtained for the rest of the structures. The negative C_{14} value for B_{12}(CBC) is consistent with the result reported by Shirai [38]. The relationship of the values reported here to the so-called global minimum Young's modulus reported by McClellan *et al* [37] is not clear. In addition, past research on the boron-rich compositions has been inconclusive on the nature of $B_{13}C_2$. Early work by Samsonov [11] suggested that it was a separate phase however this is still an open question in our opinion.

The evolution of the elastic constants under hydrostatic and uniaxial load for a $B_{11}C_4$ polytypoid, two B_4C polytypes, and a $B_{13}C_2$ polytypoid are shown in figures 4–11. For the uniaxial study, compression was applied along an axis coincident with the 3-atom chain ([111] direction), which is the stiffest elastic direction in the structure. All of the elastic constants, which include the stress corrections given in equation (2), become gradually stiffer with pressure; however, the C_{44} modulus *decreases* with load in all cases except that for uniaxial compression of the extremely carbon rich $B_{11}C_p$(CCC) (figure 8) where it remains essentially constant. This softening of C_{44} has been observed experimentally [39] and theoretically [40] in alpha quartz, which is known to undergo pressure-induced amorphization similar to that observed in BC. This softening of the C_{44} shear modulus with load may play a role in the sudden drop in shear strength of shock loaded boron carbide [21, 22].

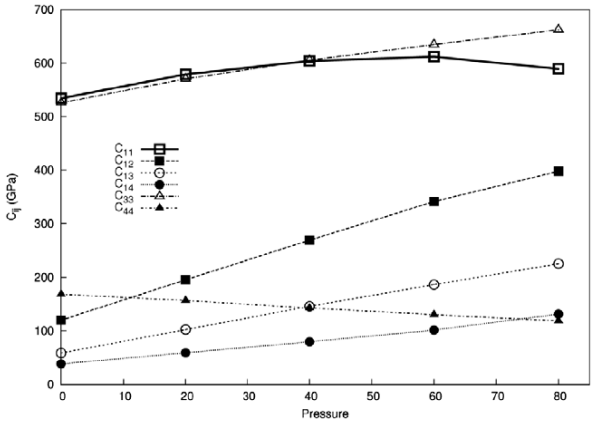

Figure 4. Stress dependent elastic constants for $B_{11}C_p$(CCC) (26% C) under hydrostatic load.

3.3. Born stability analysis

We have applied the Born stability criterion to identify stresses at which stoichiometries within the BC structure may show an elastic instability. Born showed that an expansion of the internal energy of a crystal in a power series in the strain, along with the imposition of positivity of the energy, leads to restrictions on the relative magnitudes of the elastic constants of a stable crystal [36, 41]. Each of the elastic constants varies independently with stress, and at some critical load, the system may reach a structural instability. BC is highly anisotropic elastically, belonging to the crystallographic space group $R\bar{3}m$ with 6 independent elastic constants $\{C_{ij}\}$ and imposition of the Born stability criterion leads to the following

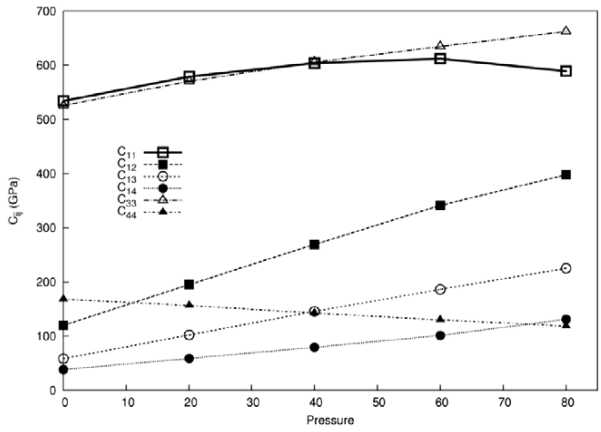

Figure 5. Stress dependent elastic constants for $B_{11}C_p$(CBC) (20% C) under hydrostatic load.

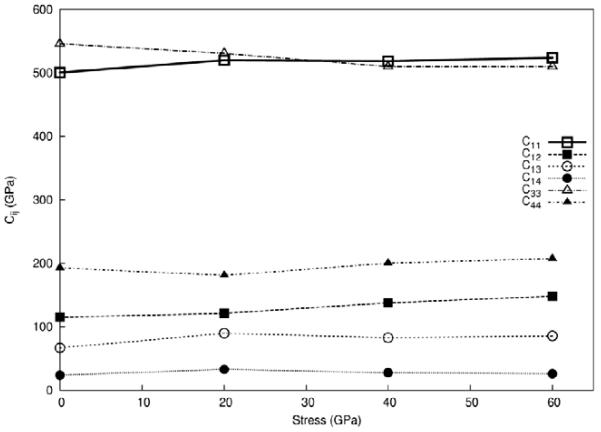

Figure 8. Stress dependent elastic constants for $B_{11}C_p$(CCC) (26% C) under uniaxial load.

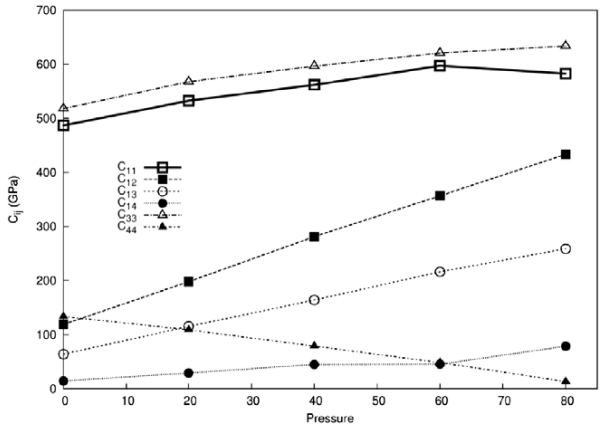

Figure 6. Stress dependent elastic constants for B_{12}(CCC) (20% C) under hydrostatic load.

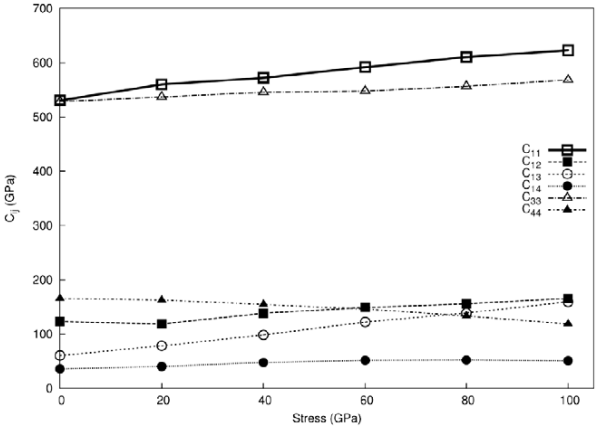

Figure 9. Stress dependent elastic constants for $B_{11}C_p$(CBC) (20% C) under uniaxial load.

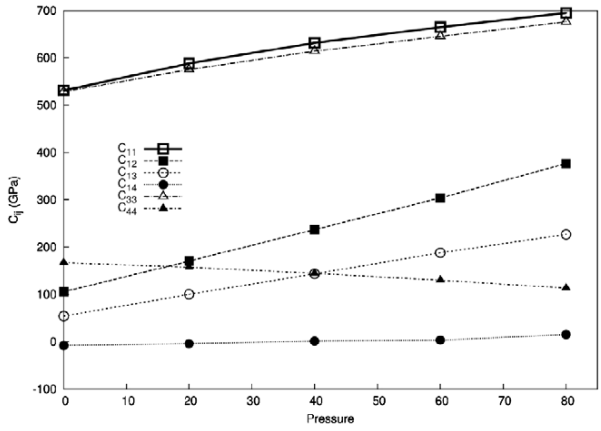

Figure 7. Stress dependent elastic constants for B_{12}(CBC) (13% C) under hydrostatic load.

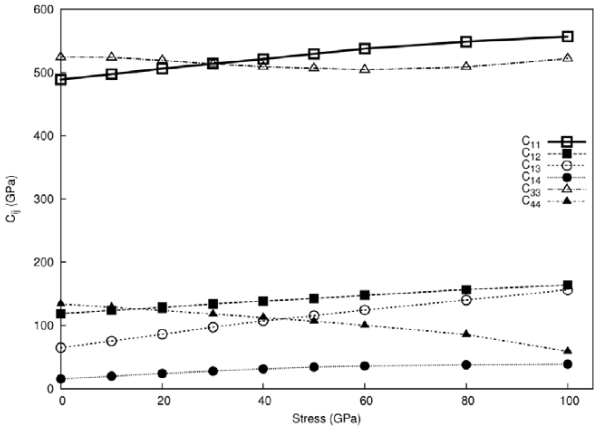

Figure 10. Stress dependent elastic constants for B_{12}(CCC) (20% C) under uniaxial load.

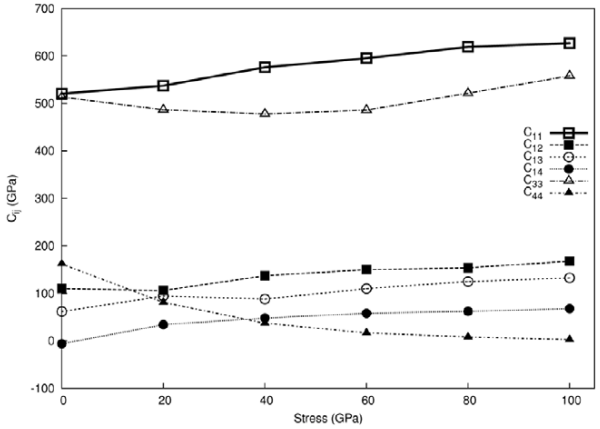

Figure 11. Stress dependent elastic constants for B_{12}(CBC) (13% C) under uniaxial load.

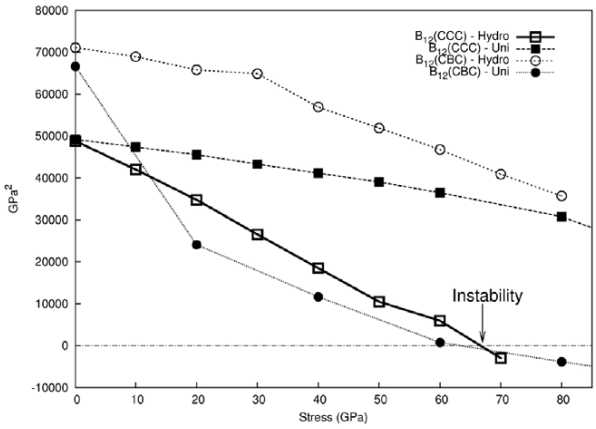

Figure 12. Born stability condition (see equation (5)) for B_{12}(CCC) and B_{12}(CBC).

restrictions on the elastic constants for the BC structure (under hydrostatic load):

$$B_{11} - |B_{12}| > 0 \tag{3}$$

$$(B_{11} + B_{12})B_{33} - 2B_{13} * B_{13} > 0 \tag{4}$$

$$(B_{11} - B_{12})B_{44} - 2B_{14} * B_{14} > 0 \tag{5}$$

where we have used the stress corrected coefficients **B** obtained from equation (2) for elastic moduli at non-zero load, as explained in [31]. The general procedure is to compute the 6 elastic constants as a function of load with evaluation of equations (3)–(5) at each point to determine the onset of the instability. Once the initial instability has been located, evaluation of the 'soft modes' of deformation (atomic displacements corresponding to the instability) can also be determined.

For most of the structures (see table 3) there is a monoclinic distortion at zero load, consistent with conclusions reached by Huhn and Widom [10]. However, for B_{12}(CCC) and B_{12}(CBC), there is no reduction in symmetry and the stability criteria presented above are strictly applicable in these cases. In both cases, the first two relations defined in equations (3) and (4) remained positive over the applied hydrostatic and uniaxial compression ranges, however the condition given in equation (5), as shown in figure 12, reaches a zero value at ≈67 GPa for the B_{12}(CCC) polytype after *hydrostatic* compression and ≈62 GPa for B_{12}(CBC) when compressed *uniaxially* along the 3-atom chain. Equation (5) is violated before the others due to the decreasing magnitude of the C_{44} elastic constant in each structure as the load is increased. Interestingly, B_{12}(CBC), which shows an elastic instability under uniaxial load, does not show a critical point over the applied range under hydrostatic load. However, the hydrostatic curve for this structure, as shown in figure 12, is trending toward zero and extrapolation of the curve suggests an instability will be reached at ≈160 GPa. Similarly, for the B_{12}(CCC) uniaxial curve, extrapolation suggests an elastic instability will occur at ≈141 GPa. The variation in mechanical response to each particular loading pattern is exemplary of the changes that can be induced by variation in the local bonding within the crystal.

Although B_{12}(CCC) and B_{12}(CBC) show an elastic instability as the stress is increased, continual loading along the same path, beyond the instability point, results in no discernible collapse of the structure. Specifically, the structure of the unit cell, for stresses beyond the instability, contains linear 3-atom chains and symmetric icosahedra although the Born criterion indicates that there is a lower energy configuration accessible beyond the critical stress under hydrostatic or uniaxial load. This suggests, at least qualitatively, that other pathways, possibly involving shear, are necessary in order to access these lower energy, lower symmetry, configurations. In the current and previous work [24, 42] the computed stresses accommodated by boron carbide without structural failure have been much higher than those suggested experimentally, however, as suggested previously [24], the conditions of the experiments may be drastically different from the idealized models used computationally. Large shear stresses, which can significantly lower phase transformation pressures [43] may be present experimentally and result in much lower critical stresses than those observed computationally along purely hydrostatic or uniaxial paths. The effect of shear on the mechanical properties of BC will be discussed below.

3.4. Equations of state

The hydrostatic compression data for $B_{11}C_p$(CCC), B_{12}(CCC), $B_{11}C_p$(CBC), and B_{12}(CBC) resulting from quantum MD simulations at 298 K, are shown in figure 13. The pressure response in the absence of shear is essentially equivalent for each structure. The resulting pressure–volume data was fitted to the third order Birch–Murnaghan equation of state [44] and the bulk modulus and pressure derivative for each structure are presented in table 5.

Experimentally, there is a reduction in the bulk modulus as the carbon concentration decreases (see table 1) and this trend is also observed in the computed bulk moduli.

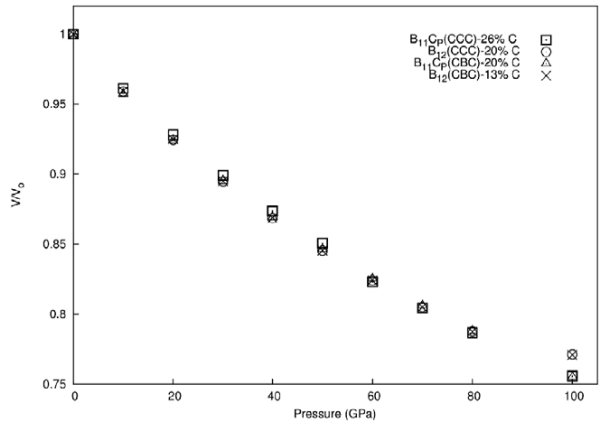

Figure 13. Pressure–volume curves for structures within each stoichiometry.

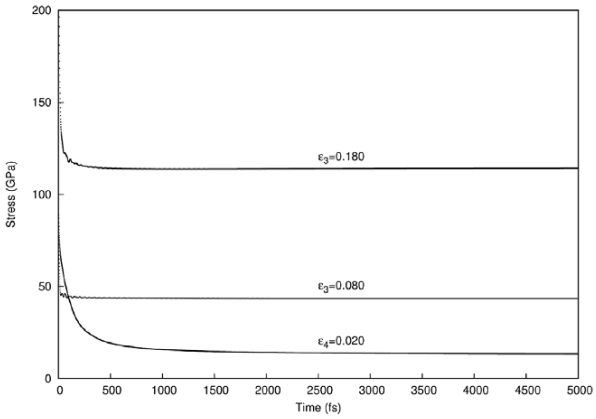

Figure 14. Time trace of the non-zero stress tensor element for simulations of B_{12}(CCC) with uniaxial compressions $\varepsilon_3 = 0.08$, 0.180 and shear strain $\varepsilon_4 = 0.02$.

Table 5. Birch–Murnaghan equation of state for structures within each carbon content.

Structure	Formula	% C	Bulk modulus (GPa)	Pressure derivative
B_{11}C(CCC)	$B_{2.75}$C	26.66	245.5	1.7
B_{12}(CCC)	B_4C	20.0	225.5	3.3
$B_{11}C_p$(CBC)	B_4C	20.0	226.7	3.9
B_{12}(CBC)	$B_{6.5}$C	13.3	223.9	2.7

3.5. Stress–strain curves

Stress–strain curves for each structure were computed using MD simulations at 298 K. A primary concern in analysis of the simulation results is the relatively short simulation time of 5 ps (5000 time steps) used to integrate the trajectories. Representative time traces of the constrained stress tensor element, for uniaxial and shear strain, in B_{12}(CCC) are shown in figure 14. The constrained tensor element (all others are elements are relaxed to zero stress) has reached an equilibrium value in all cases in less than 1000 time steps and remains constant for the remainder of the simulation. Therefore the simulation time of 5 ps is sufficiently long to provide converged stress–strain curves for the systems treated in this work.

Stress–strain curves for uniaxial compression along the 3-atom chain axis for $B_{11}C_e$(CCC), $B_{11}C_p$(CCC), three B_4C polytypes, and B_{12}(CBC) are shown in figure 15. The maximum stress obtained is ≈140 GPa in $B_{11}C_p$(CBC), followed by B_{12}(CBC). The carbon-rich stoichiometries with 26% carbon have curves that closely follow the others in the elastic region, however they reach a failure stress at much lower loads, ≈40 GPa, which is about 3.5 times less than that of some of the other structures. Although such carbon-rich compositions are not relevant according to the phase diagram, this still represents a dramatic demonstration of the effect of atomic structure and stoichiometry on the mechanical properties. For each material, the 3-atom chain remains linear up to the maximum stress and then an abrupt bending of the chain occurs resulting in a loss of strength. Snapshots

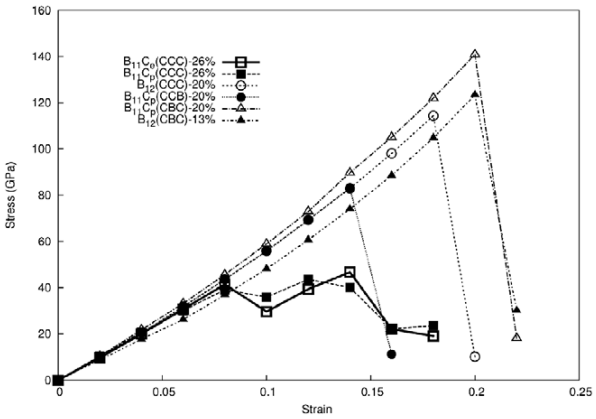

Figure 15. Stress–strain curves for uniaxial compression along axis of 3-atom chain.

of configurations, extracted from the MD trajectory for the $B_{11}C_p$(CCC) structure before and at the critical stress are shown in figure 16. The bending of the 3-atom chain at the failure point is clearly evident in the structure.

In addition to uniaxial compression, we have also simulated the strength of the structures under shear loading. Experimentally, shear loading has been identified as a critical mechanism resulting in amorphization of boron carbide [20] and the shear strength of boron carbide has been shown to be significantly reduced at stresses above the Hugoniot elastic limit [21, 22]. Stress–strain curves under shear, for several structures, are shown in figures 17–19. For each system, an ε_4 shear strain was applied incrementally, until failure, and this was done using initial configurations with uniaxial compression, σ_3, of 0, 10, 20 and 30 GPa along the 3-atom chain axis. In this way, the shear strength of the material can be simulated as a function of the uniaxial load on the system. For each material, the shear strength is substantially less than the uniaxial compressive strength and as the uniaxial load is increased there is a reduction in the shear strength, consistent with experimental observation. The reduction in shear strength is not as marked as what is seen in shock

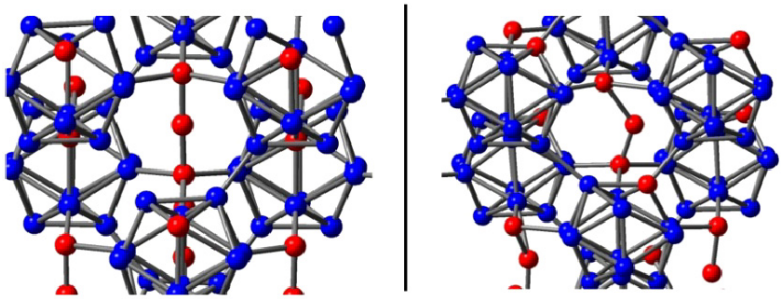

Figure 16. Snapshots of molecular dynamics simulation of $B_{11}C_p$(CCC) under uniaxial compression at 20 GPa (left) and at the failure stress, 40 GPa. Failure is associated with bending of the 3-atom chain (boron = blue, carbon = red).

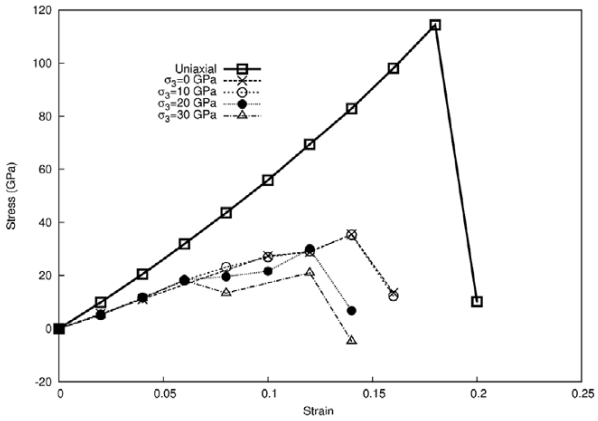

Figure 17. B_{12}(CCC) stress–strain curves resulting from shear strain, ε_4, at several values of uniaxial stress, σ_3, along the 3-atom chain axis. The uniaxial curve (also presented in figure 15), in the absence of shear, is included for reference.

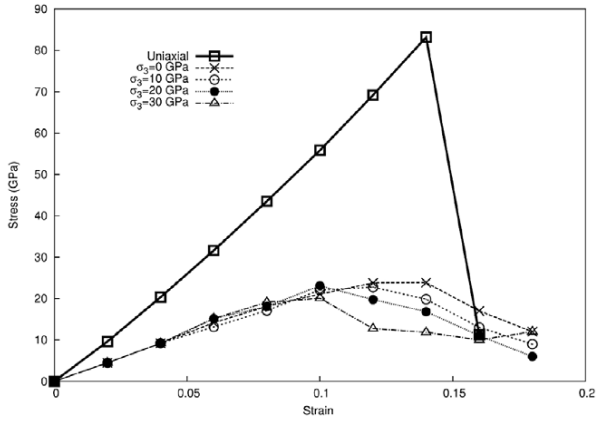

Figure 18. $B_{11}C_p$(CCB) stress–strain curves resulting from shear strain, ε_4, at several values of uniaxial stress, σ_3, along the 3-atom chain axis. The uniaxial curve (also presented in figure 15), in the absence of shear, is included for reference.

experiments. Shock loading is a much more rapid process than the essentially static loading simulations done here, however the reduction in shear strength trend is still evident in the simulated data.

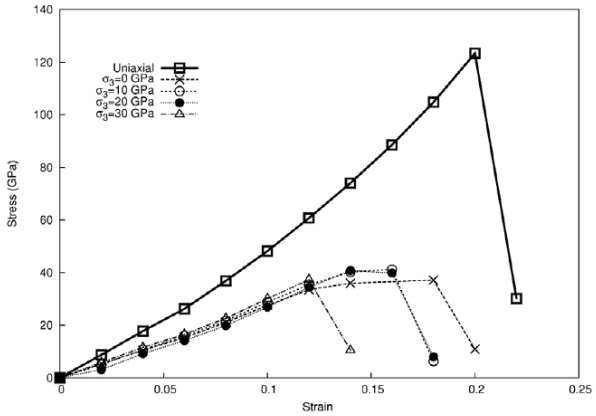

Figure 19. B_{12}(CBC) stress–strain curves resulting from shear strain, ε_4, at several values of uniaxial stress, σ_3, along the 3-atom chain axis. The uniaxial curve (also presented in figure 15), in the absence of shear, is included for reference.

In the work of Yan *et al* [25] the effect of nonhydrostatic stress on the elastic stability of BC at high pressures was examined experimentally. In that work, there was no evidence of amorphization as the pressure was increased. However, as the pressure was gradually decreased, evidence of an amorphous phase was observed, occurring at a pressure ≈20 GPa. As shown in the shear strain curves presented in figures 17 and 18, the yield strength under shear load for each structure is ≈20 GPa. Although a correlation between the experiment and the computed value can be inferred, the implication of this finding is currently not clear and will be the subject of future work.

4. Discussion and conclusion

In conclusion, atomic structure and stoichiometry have a marked effect on the calculated mechanical response of boron carbide. As shown in table 3, placement of even a single carbon atom within an icosahedron results in a monoclinic distortion of the structure which reduces the crystal symmetry via contraction of the *a* cell vector and elongation of the other cell axes. The B_{12}(CCB) structure shows a considerable reduction in stiffness, as evidenced by its C_{11}, C_{33}, and C_{44} elastic moduli, that are considerably

smaller than those of the other structures and the C_{14} modulus of the B_{12}(CBC) structure is *negative* (unlike the remaining structures) with a value of −7.95 GPa. For all structures, regardless of stoichiometry, the C_{44} elastic constant displays a negative slope in response to hydrostatic load and as a result of this C_{44} pressure softening, an elastic instability exists at values of 67 GPa and 62 GPa for the B_{12}(CCC) and B_{12}(CBC) structures respectively. The maximum yield strength under uniaxial compression is ≈140 GPa, obtained for the $B_{11}C_p$(CBC) structure (20% C), followed by the B_{12}(CBC) structure (13% C) that accommodated uniaxial loads up to ≈120 GPa before failure. Within all structures, the collapse of the unit cell is associated with an abrupt bending of the 3-atom chain axis (see figure 16). Also notable is that all of the materials, regardless of stoichiometry, exhibit pressure softening of the C_{44} modulus, in contrast to all the other moduli that increase with pressure. The consistent softening of the C_{44} modulus, regardless of stoichiometry, indicates that this is a feature of the icosahedral/3-atom chain structural framework of the BC atomic structure which is common among all of the materials. The softening of the shear moduli, and the inclusion of shear strain which lowers the yield stress considerably, suggests possible atomic structure mechanisms for the experimentally observed reduction in shear strength during shock loading experiments and the formation of nano-structured amorphous regions observed in ballistic impact experiments at pressures of about 20–25 GPa. In addition, as seen in figures 17–19, the yield strength of B_{12}(CBC) under a shear strain (30–40 GPa) is about twice that of the other structures (10–20 GPa) suggesting that it may be the most stable under shear loading. The softening of the shear moduli is associated with the formation of new bonds between the unsaturated central atom in the 3-atom chain with equatorial atoms in neighboring icosahedra. Uniaxial and hydrostatic loading decreases the spacing between the central chain and equatorial atoms and the formation of these new bonds results in an energetically more favorable configuration. Elastic constants are related to the change in configuration energy as a function of displacement and the reduction in the C_{44} modulus is driven by the formation of these new bonds between the chain and icosahedra.

Computational results have suggested structural stability under much higher loads than what is observed experimentally. It has been suggested [24] that complex strain patterns, principally involving shear, are necessary to access the lower energy, lower symmetry, configurations. Exploration of these complex shear loading paths is possible using quantum mechanical potentials, as done in this work, however the exploration of the six dimensional strain space using different combinations of strain is computationally prohibitive. This calls for the development of a classical potential applicable to icosahedral boron carbide. The Reax [45] forcefield may serve as a good functional form as it can accommodate the charge variation that occurs as a function of geometry and, through the use of bond orders, can properly model carbon atoms which exist in different hybridization states depending on their presence in chains or icosahedra. The large amount of data generated for the structures and elastic properties contained in this work can serve as a parameterization set for the development of such a classical model. Using a classical model, much larger simulations of boron carbide can be performed and studies of the structural response of boron carbide under shock loading can be performed and correlated with the available experimental shock loading data.

Acknowledgments

Financial support of this work was granted as a part of the Director's Research Initiative program at the Army Research Laboratory. All calculations were conducted using computational resources maintained by the Department of Defense High Performance Computing and Modernization Program (Challenge Project No. ARLAPC5L). The authors would also like thank Dr K T Ramesh of the Johns Hopkins University (Baltimore, MD) for many useful discussions.

References

[1] Telle R 1994 *Structure and Properties of Ceramics* ed M V Swain (New York: Wiley)
[2] Clark H K and Hoard J L 1943 *J. Am. Ceram. Soc.* **65** 2115
[3] Lazzari R, Vast N, Besson J M, Baroni S and Dal Corso A 1999 *Phys. Rev. Lett.* **83** 3230
[4] Wilson W S and Guichelaar P J 1997 *Carbide, Nitride, and Boride Materials Synthesis and Processing* ed A W Weimer (London: Chapman and Hall)
[5] Khanra A K 2007 *Bull. Mater. Sci.* **30** 93
[6] Beauvy M 1983 *J. Less-Common Met.* **90** 169
[7] Lipp A 1965 *TR Elektroschmelzwerk Kempten* reprinted from *Technische Rundschau* nos. 14, 28 and 33
Lipp A 1966 *TR Elektroschmelzwerk Kempten* reprinted from *Technische Rundschau* no. 7
[8] Domnich V, Reynaud S, Haber R A and Chhowalla M 2011 *J. Am. Ceram. Soc.* **94** 3605 and references therein
[9] Widom M and Huhn W P 2012 *Solid State Sci.* submitted
[10] Huhn W P and Widom M 2012 *J. Stat. Phys.* submitted
[11] Samsonov G V, Zhuravlev N N and Amnuel I G 1956 *Fiz. Met. Metalloved.* **3** 309
[12] McCuiston R, LaSalvia J, McCauley J and Mayo W 2009 *Proceedings of the 32nd International Conference and Exposition on Advanced Ceramics and Composites* p 153
[13] Chen M W, McCauley J W, LaSalvia J C and Hemker K J 2005 *J. Am. Ceram. Soc.* **88** 1935
[14] Conde O, Silvestre A J and Oliveira J C 2000 *Surf. Coat. Technol.* **125** 1
[15] Konovalikhin S V and Ponomarev V I 2009 *Russ. J. Inorg. Chem.* **54** 197
[16] Kwei G H and Morosin B 1996 *J. Phys. Chem.* **100** 8031
[17] Kohn W and Sham L J 1965 *Phys. Rev.* **140** 1133
[18] Saal J E, Shang S and Liu Z 2007 *Appl. Phys. Lett.* **91** 231915
[19] Vast N, Sjakste J and Betranhandy E 2009 *J. Phys.: Conf. Ser.* **176** 012002
[20] Chen M, McCauley J W and Hemker K J 2003 *Science* **299** 1563
[21] Vogler T J, Reinhart W and Chhabildas L C 2004 *J. Appl. Phys.* **95** 4173
[22] Dandekar D P 2001 *Army Research Laboratory Technical Report* ARL-TR-2456
[23] Taylor D E, Wright T W and McCauley J W 2011 *Army Research Laboratory Memorandum Report* ARL-MR-0770
[24] Aryal S, Rulis R and Ching W Y 2011 *Phys. Rev.* B **84** 184112
[25] Yan X Q, Zhang T L, Guo J J, Jin C Q, Zhang Y, Goto T, McCauley J W and Chen M W 2009 *Phys. Rev. Lett.* **102** 075505
[26] Liu D C and Nocedal J 1989 *Math. Program.* **45** 503
[27] CP2K is freely available from: http://cp2k.berlios.de/

[28] Perdew J P, Burke K and Ernzerhof M 1996 *Phys. Rev. Lett.* **77** 3865
[29] Doll K 2009 *Mol. Phys.* **108** 223
[30] Wang J and Yip S 1993 *Phys. Rev. Lett.* **71** 4182
[31] Kimizuka H, Ogata S, Li J and Shibutani Y 2007 *Phys. Rev.* B **75** 054109
[32] Allen M P and Tildesley D J 1989 *Computer Simulation of Liquid* (Oxford: Clarendon)
[33] Berendsen H J C, Postma J P M, van Gunsteren W F, DiNola A and Haak J R 1984 *J. Chem. Phys.* **81** 3684
[34] Kresse G and Furthmuller J 1996 *Comput. Mater. Sci.* **6** 15
[35] Bouchacourt M and Thevenot F 1981 *J. Less-Common Met.* **82** 219
[36] Born M and Huang K 1954 *Dynamical Theory of Crystal Lattices* (Oxford: Oxford University Press)
[37] McClellan K J, Chu F, Roper J M and Shindo I 2001 *J. Mater. Sci.* **36** 3403
[38] Shirai K 1997 *Phys. Rev.* B **55** 12235
[39] Gregoryanz E, Hemley R J, Mao H and Gillet P 2000 *Phys. Rev. Lett.* **84** 3117
[40] Binggeli N and Chelikowsky J R 1992 *Phys. Rev. Lett.* **69** 2220
[41] Grimvall G, Magyari-Köpe B, Vidvuds O and Persson K 2012 *Rev. Mod. Phys.* **84** 945
[42] Dekura H, Shirai K and Yanase A 2010 *J. Phys.: Conf. Ser.* **215** 012117
[43] Levitas V I and Shvedov L K 2002 *Phys. Rev.* B **65** 104
[44] Birch F 1947 *Phys. Rev.* **71** 809
[45] Chenowith K, van Duin A and Goddard W A 2008 *J. Phys. Chem.* A **112** 1040

Density Functional Theory and Evolution Algorithm Calculations of Elastic Properties of AlON

Iskander G. Batyrev, DeCarlos E. Taylor, George A. Gazonas,
and James W. McCauley

Journal Of Applied Physics 115, (2014)

JOURNAL OF APPLIED PHYSICS **115**, 023505 (2014)

Density functional theory and evolution algorithm calculations of elastic properties of AlON

I. G. Batyrev, D. E. Taylor, G. A. Gazonas, and J. W. McCauley
U.S. Army Research Laboratory, Aberdeen Proving Ground, Maryland 21005, USA

(Received 18 September 2013; accepted 6 December 2013; published online 8 January 2014)

Different models for aluminum oxynitride (AlON) were calculated using density functional theory and optimized using an evolutionary algorithm. Evolutionary algorithm and density functional theory (DFT) calculations starting from several models of AlON with different Al or O vacancy locations and different positions for the N atoms relative to the vacancy were carried out. The results show that the constant anion model [McCauley *et al.*, J. Eur. Ceram. Soc. **29**(2), 223 (2009)] with a random distribution of N atoms not adjacent to the Al vacancy has the lowest energy configuration. The lowest energy structure is in a reasonable agreement with experimental X-ray diffraction spectra. The optimized structure of a 55 atom unit cell was used to construct 220 and 440 atom models for simulation cells using DFT with a Gaussian basis set. Cubic elastic constant predictions were found to approach the experimentally determined AlON single crystal elastic constants as the model size increased from 55 to 440 atoms. The pressure dependence of the elastic constants found from simulated stress-strain relations were in overall agreement with experimental measurements of polycrystalline and single crystal AlON. Calculated IR intensity and Raman spectra are compared with available experimental data.
[http://dx.doi.org/10.1063/1.4859435]

I. INTRODUCTION

Aluminum oxynitride (AlON) is a transparent polycrystalline spinel structure material that has an ideal composition of $Al_{23}O_{27}N_5$, but has a solid solution ranging from about 27 to 40 mol. % AlN in the Al_2O_3-AlN system. It has been termed a non-stoichiometric spinel since an ideal spinel stoichiometry would be $Al_{24}O_{24}N_8$, or 50 mol. % AlN and 50% Al_2O_3.[1] It has a variety of important properties including transparency from the UV to near IR resulting from its band gap at room temperature of 6.5 eV, high hardness and mechanical strength, high temperature stability, and a very low loss dielectric. It has demonstrated many applications including transparent armor and EM domes and windows, among others.

Over the years there have been both experimental and theoretical investigations trying to determine the best crystal and chemical models that accurately describe the atomic structure of Al oxynitride. The models can be divided into two groups with O or Al vacancies in cubic spinel structure. McCauley[2] examined both types of models and concluded that a model with an Al vacancy (constant anion model) was the best model for this material. Few N atoms are randomly distributed over O sites of cubic spinel. There are different ways to describe random crystalline structures. Robust Green's function method is a kind of effective medium theory allowing one to include all details of disordered structure into analytical structure of complex self-energies.[3] Another approach, popular at times when unit cells for band structure calculations were limited to 8–64 atoms, is a generation of special quasirandom structures having radial distribution functions close to a perfectly random structure.[4] Here we apply an evolutionary approach based on density functional theory (DFT) calculations of total energy as a fitness function.[5] Using the ideas of evolutionary search for minimum energy configurations, we developed a suite of shell scripts to control and manipulate the input/output of DFT files using genetic operators. The suite uses the experimentally observed cubic spinel structure and might be considered as a simplified version of a powerful evolutionary algorithm developed in[5,6] for prediction of unknown crystallographic structures.

The model with an Al vacancy in the octahedral sites of a spinel structure suggested in Ref. 2 is found to have the lowest total energy and is therefore the most acceptable model of the system.[7] The energy preference for the model with Al vacancy made in Ref. 7 was based on quantum mechanical calculations of a single configuration for vacancy on Al or O and for Al vacancy at tetrahedral/octahedral sites. The main difference of the present work from previous publications is that DFT calculations were carried using an evolutionary algorithm with permutation, mutation, and heredity operations not for few as in Refs. 7 and 8, but for 100–200 configurations for each case of Al or O vacancy location. The large number of configurations and statistics is found to be important for the search of local minimum corresponding to lowest energy distribution of N atoms over O sites with Al or O vacancies in spinel structure. The importance of size effects on the results have also been examined using two larger computational cells containing 220 and 440 atoms.

II. CALCULATION METHODS

For this work, we used three different density functional implementations: VASP (for optimization of the 55 atom structures), CASTEP (for analysis of atomic charge and vibrational properties), and CP2K (for the larger cells with 220 and 440 atoms). VASP and CASTEP are plane wave implementations where the energy cutoff was 600 eV

(ultrasoft projector augmented waves (PAW) using generalized gradient approximation (GGA)) for VASP and 600 eV norm-conserving pseudopotentials using PBE approximation for the CASTEP calculations. For the Gaussian/plane wave CP2K implementation, the GTH-BLYP functional in a double zeta valence polarization basis for O and N and in a single zeta valence polarization for Al with a kinetic energy cutoff of 800 eV was utilized for plane waves.

Using an evolutionary optimization algorithm, with a population size containing ~200 configurations, low energy structures were identified by random variation of the N and O atoms location in cubic spinel structure relative to the anion or cation vacancy within the 55 atom cell using permutation, mutation, and heredity operations and DFT optimization of each configuration. To do the calculations based on VASP PAWs and cubic spinel structure, we developed a suite of shell scripts to manipulate and control input/output VASP files to run 10–20 generations in one job. Experimentally established cubic spinel structure of AlON was a significant simplification for evolutionary simulations. Initial structures of AlON were chosen to have a random distribution of N atoms in cubic spinel structure with Al or O vacancy and ±5% distribution of lattice vectors relative experimental determined ones. A random rule for selecting parents for the next generation was applied where individuals mainly in the upper and middle parts of the parents (ranked according total energies) were selected with a small fraction (typically 5%) of parents from the bottom part of the list. Parents chosen by this procedure were subject to permutation, mutation, and heredity operators. The operators could be defined differently in various versions of a genetic method. We followed definitions of the operators from Ref. 5. Most common operators in our simulations were (i) permutations (45%) (switching identities of two atoms in a structure) and (ii) mutation (45%) (a random change of the cell vectors and/or atomic positions). Only 10% of the transformations were made by most aggressive operator (iii) heredity (new structures are produced by matching slices (chosen in random directions and with random positions) of the parent structures).

For each optimized structure in the search, the total energy was evaluated using VASP. Lowering of the total energy occurred not with every step, but after certain number of generations, so statistics played important role for the minimum structures search for each of the models with Al or O vacancy. 200 configurations were enough to isolate a local minimum corresponding to the lowest energy structure.

The lowest energy structures identified by the evolutionary search were then subjected to additional analysis including elastic constants calculations and vibrational analysis. Elastic properties were calculated using the usual strain-energy[9] and strain-stress[10,11] relations.

III. STRUCTURAL MODELS

Several spinel-like models of AlON have been suggested in the literature.[1] The model with Al vacancy at octahedral site (constant anion model) is shown in Fig. 1. It corresponds to the formula $Al_{(64+x)/3}\square_{(8+x)}O_{32-x}N_x$, where $x = 5$ and symbol □ is corresponding to Al vacancy. The

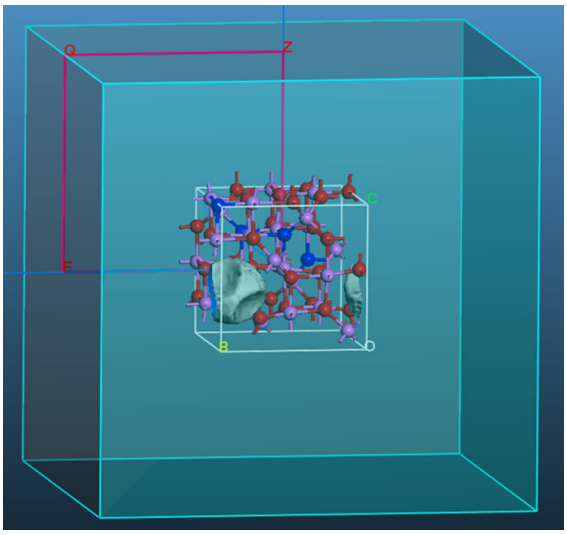

FIG. 1. The 55 atom model with Al vacancy at octahedral site showing the Brillouin zone directions of k-points, and the negative local potential around the Al vacancy. Also illustrated are the oxygen atoms (red), aluminum atoms (pink), and nitrogen atoms (blue).

structure matches up with an AlON composition of 64.3 mol. % Al_2O_3 and 35.7 mol. % of AlN. Another possible structure is related with O vacancy (constant cation model) and may be derived from the formula $Al_{(24)/3}\square_{(72-3x)/2}O_{(72-3x)/2}N_x$. Nitrogen atoms may be randomly distributed along the O sites. The character of the distribution of the N atoms may affect the relative energies of the two models. We performed evolutionary algorithm calculations for several N concentrations implementing ideas of evolution in *ab-initio* calculations for finding lowest energy configurations applying 45% mutation, 45% permutation, and 10% heredity variation operators. For each model from Table I, we calculated ~200 different distributions of N atoms. The calculated total energies of the model with Al vacancy on octahedral site in comparison with that Al vacancy at tetrahedral site (constant cation models) and three different models with O vacancy (constant cation models) were compared with total energies of aluminum nitride $E_{A_iN} = 14.99$ eV/mol and alumina $E_{Al_2O_3} = 37.72$ eV/mol according to the formula,

$$\Delta = E\left(Al_{(2m+n)}O_{3m}N_n\right) - \left[mE_{Al_2O_3} + nE_{AlN}\right]. \quad (1)$$

One may see from the results presented in Table I that the model with Al vacancy at octahedral site (constant anion model) has the lowest energy compared with various molar concentrations of Al_2O_3 and AlN.

Each of the total energies used for calculation of Δ in Table I are the result of calculations of ~200 structures (members of evolution) of the various concentrations of Al_2O_3 and AlN. The Al vacancy at a tetrahedral site has a significantly higher energy (1.57 eV) than at an octahedral site. A random distribution of N atoms has ~0.9–1.2 eV lower energy than that for a cluster distribution which is dependent on the location of N atoms. N atoms migrate away from the Al vacancy neighborhood as a result of DFT evolution of the system driven by lower energy. The total energy as a function of number of members or structures

TABLE I. Comparison of different structures corresponding to the different molar concentrations of Al_2O_3 and AlN.

Models	m = 9, n = 5 Al vacancy (octahedral) 35.7% AlN	m = 9, n = 5 Al vacancy (tetrahedral) 35.7%AlN	m = 10, n = 4 O vacancy 28.6%AlN	m = 8, n = 9 O vacancy 50% AlN	m = 9, n = 6 O vacancy 40% AlN
Δ, eV	1.68	3.25	2.57	3.06	2.94

(8 in each generation) for two models from Table I is shown in Fig. 2. One may see that model with Al vacancy has smoother and faster convergence than the constant cation model. Note also that convergence of the total energy with number of members is not variational and occurs abruptly after a certain number of generations, which might be considered indicative of the importance of accumulated statistics for the minimum energy configuration search. 200 members are found to be enough to get quite close to experimental x-ray diffraction pattern.

The calculated powder X-ray diffraction (XRD) of the lowest energy 55 atom configuration with a random distribution of N atoms not neighboring an Al vacancy at an octahedral site is shown in Fig. 3. Experimental XRD peaks are shown for comparison.[12] The overall excellent agreement between the computed and experimental XRD data indicates the correctness of the model with Al vacancy at octahedral site, conjectured by McCauley,[1] after proper optimization of the N atom locations.

X-ray scattering does not distinguish between N and O atoms and cannot determine the type of distribution of N atoms. Neutron scattering also did not find clear answer about details of N atoms distribution,[13] but clearly indicates that Al vacancies are situated at octahedral sites in agreement with our calculations. The minimum energy model identified above was used for calculation of elastic properties.

IV. ELASTIC CONSTANTS AND THEIR PRESSURE DERIVATIVES

Theoretical elastic constant calculations on AlON were first carried out by Okeke and Lowther[8] in 2008. However, these calculations assumed an ideal spinel composition of Al_3O_3N, which has not been confirmed experimentally. Using the local density approximation (GGA) based technique calculated values were as follows: $c_{11} = 344$ (310), $c_{12} = 179$ (160), and $c_{44} = 184$ (175).[8] In the current work, elastic constant calculations were first performed on a 55-atom unit cell to understand the effect of N atom distribution on the elastic constants. For the calculations, we used the stress-strain method,[10] numerical evaluation of the second order elastic constants[11] and the conventional stress–-energy method.[9] The random versus cluster distribution of N atoms, which substitute O atoms, may be characterized by an average distance R_{av} between N atoms. For the cluster distribution of N atoms used for the calculation of elastic constants in Table II $R_{av} = 2.86$ A, while for the random distribution $R_{av} = 4.61$ A.

It is seen that a cluster distribution of N atoms predicts elastic constants which are of smaller magnitude than for a random N atom distribution using both stress-strain and strain-energy methods of calculation. Our evolutionary algorithm driven DFT calculations show that a cluster distribution is less energetically favorable, becomes unstable, and does not survive evolutionary selection after 5 generations. The minimum R_{av} cluster configuration has ~1 eV higher energy than that of a random distribution of N atoms. Local deviation from an energetically driven distribution of N atoms may occur in AlON, and this may cause different local elastic constants within ALON single crystals as observed for B4C single crystals.[14] Evolution of the system that consists of a cluster distribution of N atoms changes the distribution to a random distribution and N atoms that migrate away

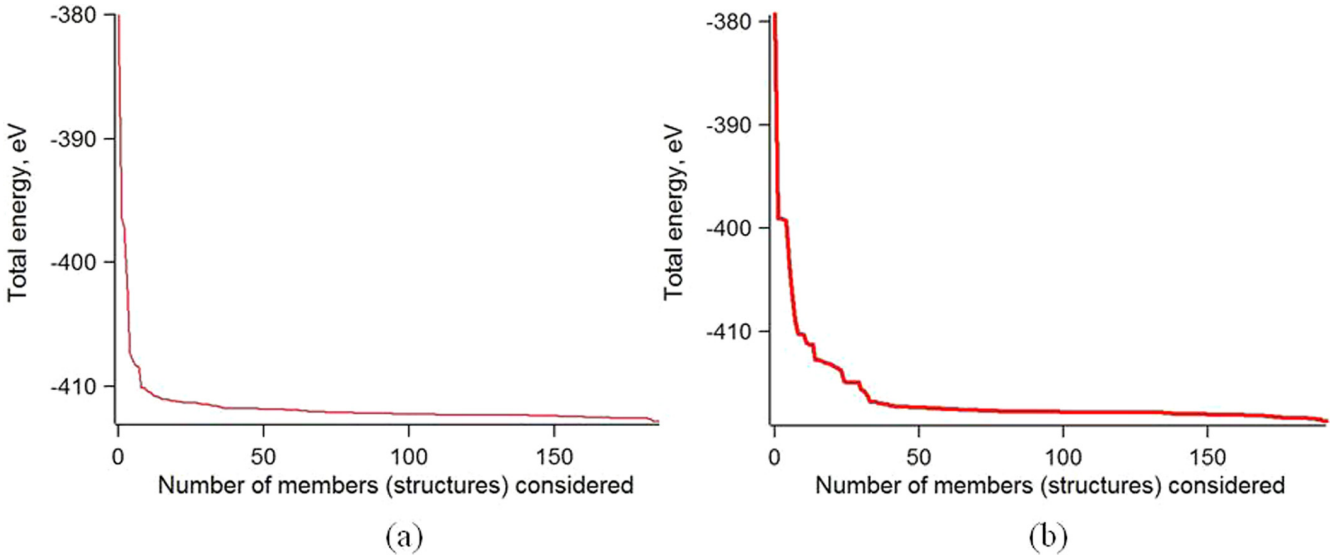

FIG. 2. Total energy convergence of constant anion model with Al vacancy at the octahedral site (35.7% AlN) (thin line, a) and with 28.6 mol. % AlN (thick line, b) corresponding to first and third rows in Table I, respectively.

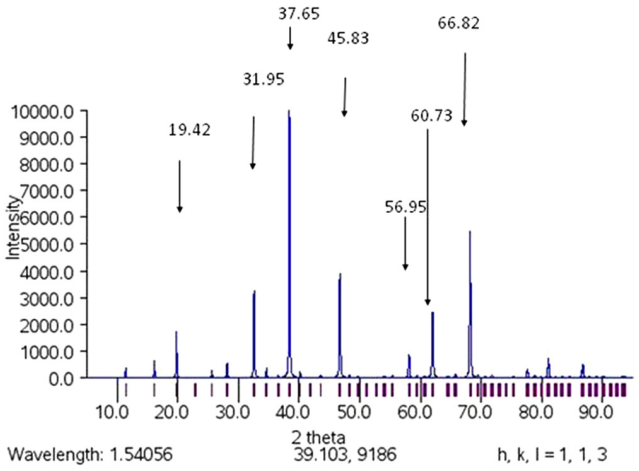

FIG. 3. Theoretically calculated at 1.54 Å wavelength X-ray diffraction powder pattern data based on the lowest energy configuration of the model with Al vacancy at octahedral site in comparison with experimental data (arrows with numbers indicating experimental peak position).

TABLE II. DFT predicted elastic constants determined from stress-strain ($\sigma - \varepsilon$), and strain-energy ($\varepsilon - E$) methods for a random and cluster distribution of N atoms over O sites compared with experimental data based on RUS of polycrystalline and single crystal AlON.

	random		Cluster			
	$(\sigma - \varepsilon)$	$(\varepsilon - E)$	$(\sigma - \varepsilon)$	$(\varepsilon - E)$	Experiment[15]	Experiment[16]
C_{11} (GPa)	296.4	306.16	283.81	283.23	369–393	364.0–386.1
C_{12} (GPa)	150.9	157.75	137.65	148.99	123–132	107.0–120.0
C_{44} (GPa)	164.4	183.33	158.97	157.97	122–128	128.0–132.9
Latt. Const (Å)	8.029	8.029	8.103	8.103	7.956	7.950

from Al vacancy following evolution selection of lower energy configuration.

The pressure dependence of the elastic constants was calculated using the stress-strain method for the minimum energy random N atom distribution structure optimized at pressures from 0 to 40 GPa (Fig. 4). Since the simultaneous relaxation of atomic position and unit cell volume is not possible in VASP 5.2.11, while maintaining a specific Bravais lattice, we performed 5–7 cubic cell optimization simulations relaxing the atoms for the optimized cell.

Our calculation results in estimates for elastic constants derivatives $dC_{11}/dP \sim 4$–6.2 and $dC_{44}/dP \sim 0.8$–1.5. These numbers are in reasonable agreement with experimental measurements of polycrystalline AlON (Ref. 15) $dC_{11}/dP \sim 5.4$–5.7 and $dC_{44}/dP \sim 0.85$–0.95 which are pressure derivatives for elastic constants for polycrystals and portray averaged crystal anisotropy.

The lowest energy structure for the 55 atom cell was replicated to generate $2 \times 2 \times 1$ (220 atoms) and $2 \times 2 \times 2$ (440 atoms) supercell models. The larger unit cell configurations consisting of regular arrangements of aluminum vacancies had the lowest energy among all other Al vacancy arrangements; this is, what one may expect for an ordered system. The larger unit cell systems were used for calculations of the elastic constants by numerical evaluation of the second order elastic constants using a finite difference approximation.[11] This method was implemented for Gaussian basis set of the CP2K code and used for calculation of elastic properties of B4C.[14] Experimental measurements were made using a resonance ultrasound spectroscopy (RUS) system on single crystals of AlON.[16] Results of the calculations and of the measurements are presented in Table III. Improved agreement was obtained between theory and experiment using multiple unit cells in the calculations and experimental measurements on single crystals. Overall agreement of the calculations with biggest unit cell and measurements on large single crystal for three constants is ~15%.

V. VIBRATION SPECTRA

In an insulating crystal, the frequency and the intensity of the Raman peaks are determined by the zone-center phonon frequencies and by the Raman tensor. The phonon frequencies are determined by the dynamical matrix, dielectric constant, and Born effective charges. The Born effective charge tensor of an ion is the partial derivative of the macroscopic polarization with respect to a periodic displacement of all the periodic images of that ion at zero macroscopic electric field. Calculations were carried out with the CASTEP code[17] using norm-conserving pseudo potentials and plane waves with a 600 eV cutoff. For validation of our

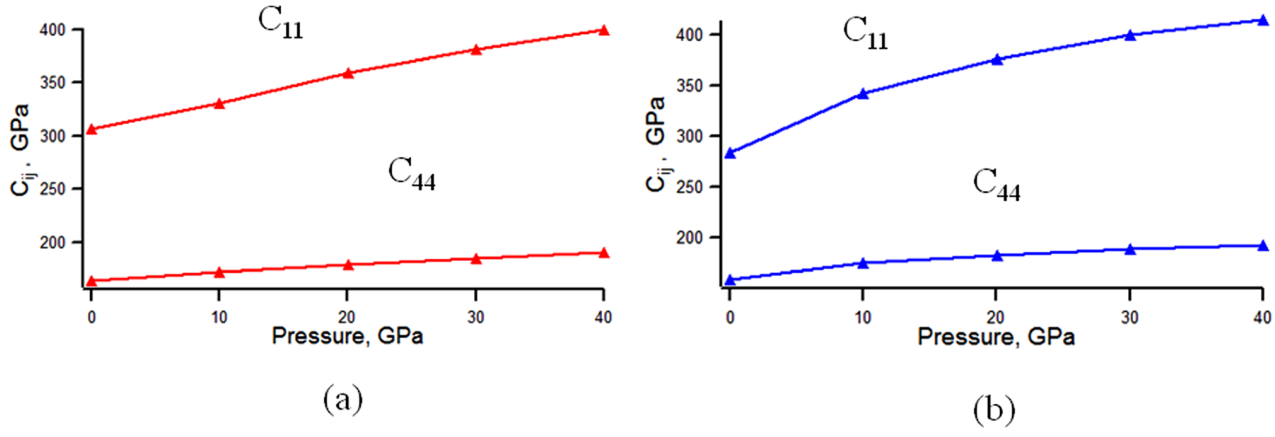

FIG. 4. The pressure dependence of elastic constants for (a) random, and (b) cluster types of N distribution over O sites.

TABLE III. DFT calculated elastic constants of different size unit cell in comparison with experimental results (1) 6.92 mm × 5.82 mm × 2.70 mm; (2)1.00 mm × 1.01 mm × 1.63 mm; (3) 0.87 × 1.49 × 1.74 mm.

	C_{11} (GPa)	C_{12} (GPa)	C_{44} (GPa)
55 atom	303.51	120.25	164.43
220 atom	304.11	123.01	165.58
440 atom	308.45	119.61	163.94
Experiment 1	386.1	120.0	132.9
Experiment 2	364.0	109.0	127.0
Experiment 3	364.0	107.0	128.0

model, we use experimental measurements on aluminum oxynitride amorphous films[18] described by the parameter R = N/(O + N) were used; the cubic spinel AlON structure corresponds to R = 0.18. The closest structure from Figure 5(a) is the upper solid curve (after anneal), which clearly shows formation of 3 IR peaks presumably related to the formation of crystalline phases around 900, 700, and 500 cm^{-1} (Figure 5(a)). IR peaks around 435 cm^{-1} may be attributed to tetrahedral coordination of Al, peaks around 900 cm^{-1} with six fold coordinated Al forming at low N concentration.[19] Calculated IR spectra show peak structures in all these three regions but have more fine peaks because they correspond to single cubic spinel structures. The main peaks according our analysis corresponding to O atoms next to Al vacancy and Al atoms in an octahedral site in the vicinity of the vacancy (green arrows scaled proportionally to IR intensities in Figure 5(c)).

Non-resonant Raman (Figure 6(a)) activities were computed using a hybrid method combining density functional perturbation theory with the finite displacement method. The Raman activity tensor of a mode is given by the derivative of the dielectric polarizability tensor with respect to the mode amplitude. This is evaluated using a numerical central difference approximation between polarizability tensors computed at geometries displaced from equilibrium by small positive and negative amplitudes according to the mode eigenvector.[17] Figure 6(b) depicts the experimental Raman spectra of AlON.[20] The Raman spectrum of cubic AlON is composed of a number of phonon modes at 304, 397, 626, 747, and 915 cm^{-1} related with 3T2g, Eg, and A1g modes of spinel. The modes can be seen in simulations of Raman activities (Figure 6(a)).

VI. SUMMARY

The main conclusion from the genetic algorithm driven DFT simulations that predict the structure and elastic properties AlON are as follows: (1) lowest energy configurations were found for each of several concentrations of Al_2O_3 and AlN compositions in the Al_2O_3-AlN system both for the ~200 structural models with Al or O vacancy each (the simulation results corroborated a constant anion model with the Al vacancy in an octahedral site[2] over all considered concentrations and models); (2) the DFT genetic algorithm simulations showed that N atoms migrate away from the Al vacancies at octahedral sites forming a random N

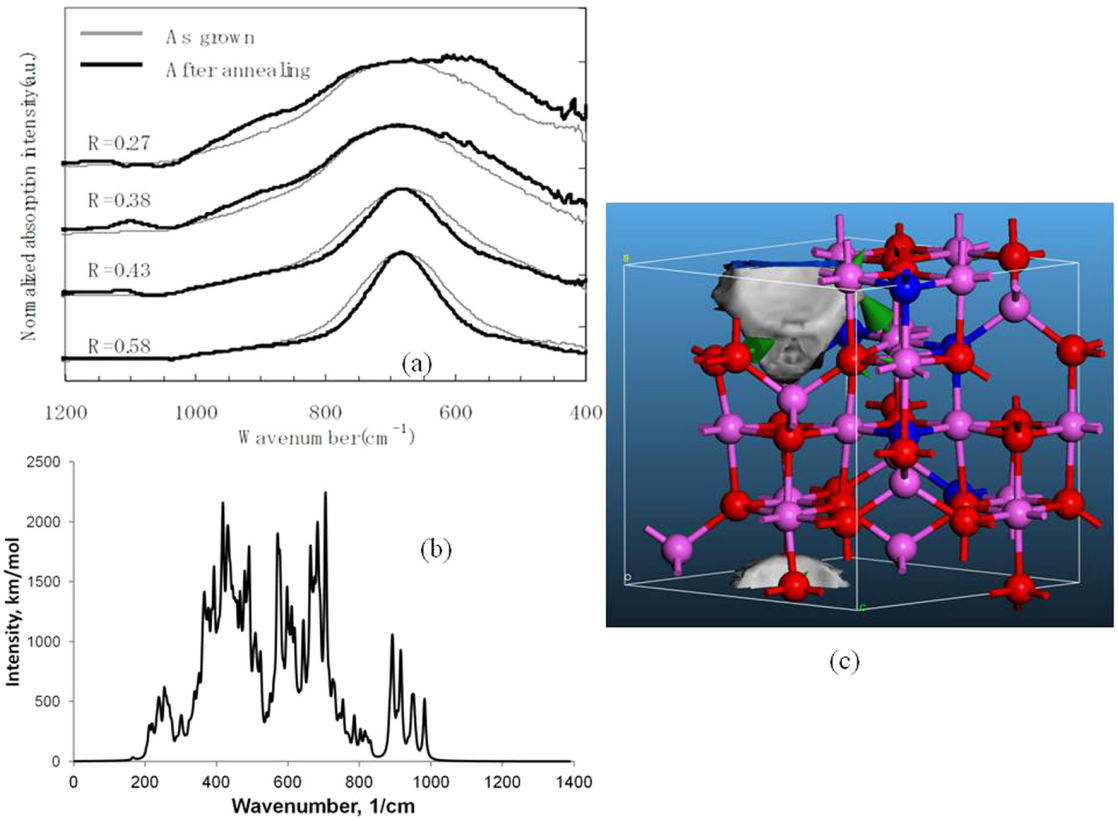

FIG. 5. (a) FTIR spectrum. Reprinted with permission from Yoshida *et al.*, ECS Trans. **16**(21), 1-10 (2009). Copyright 2009 The Electrochemical Society.[18] (b) Calculated IR intensity with 10 cm^{-1} smearing and (c) atomic structure with arrows representing scaled amplitudes of vibrations of oxygen atoms (red), aluminum atoms (pink), and nitrogen atoms (blue). Notations are the same as in Fig. 1.

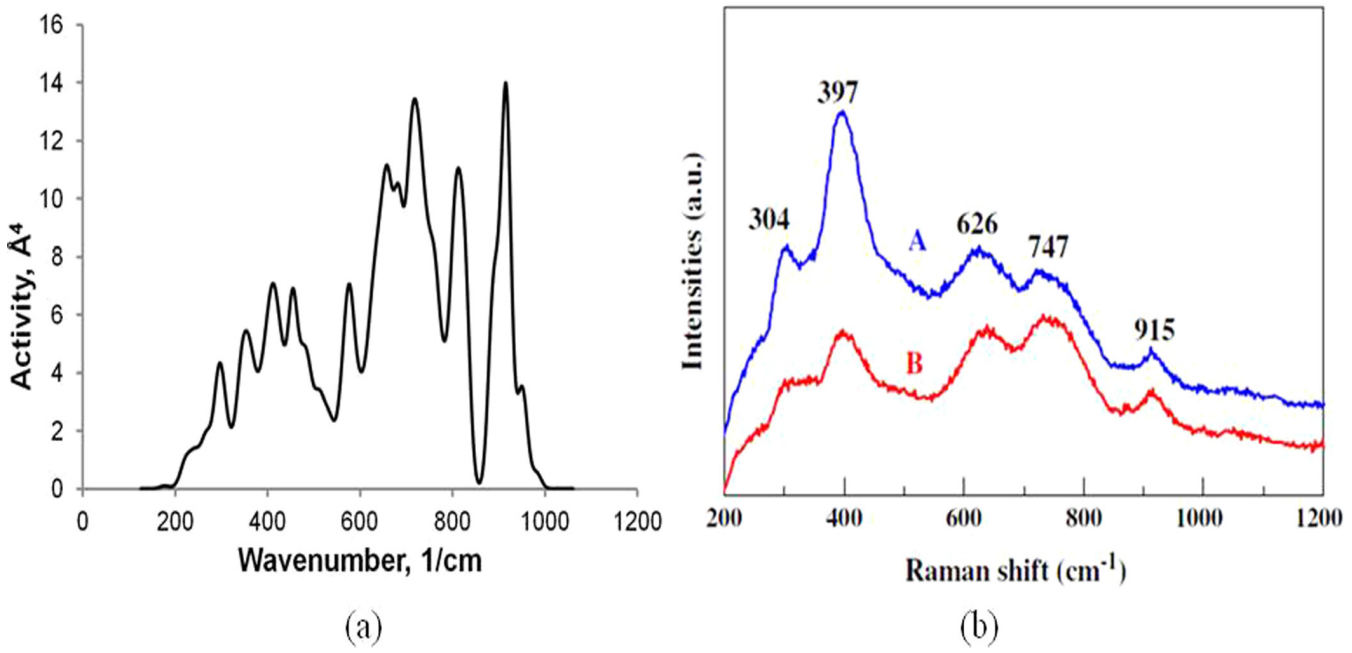

FIG. 6. (a) Raman activity compared with (b) experimental Raman spectra (upper and lower curves correspond to the pristine crystal and indented crystal areas). The indentation does not affect Raman peak position. Reprinted with permission from Guo *et al*., Acta Mater. **59**(4), 1671-1679 (2011). Copyright 2013 Elsevier.[20]

distribution; (3) AlON cubic elastic constants have systematically smaller values for a cluster distribution rather than for a random distribution of N atoms; (4) the calculated values of the pressure dependence of AlON elastic constants are in a reasonable agreement with experimental measurements for polycrystalline AlON; (5) the simulated cubic elastic constants approached experimental measurements of AlON single crystals as the number of models atoms increased from 55 to 440, (6) IR intensity and Raman activity was calculated using density functional perturbation theory and compared with available experimental data. The main peaks of calculated IR intensity corresponded to O atoms next to vacancy and Al atoms in octahedral sites in the vicinity of the vacancy.

ACKNOWLEDGMENTS

The authors thank Betsy Rice and Rosario Sausa for stimulating discussions and James Lorentzos for writing suite of Unix shell scripts with evolution operators.

[1]J. W. McCauley, P. Patel, M. W. Chen, G. Gilde, E. Strassburger, B. Paliwal, K. T. Ramesh, and D. P. Dandekar, J. Eur. Ceram. Soc. **29**(2), 223 (2009).
[2]J. W. McCauley, J. Am. Ceram. Soc. **61**(7–8), 372 (1978).
[3]M. Ogura and H. Akai, J. Phys.: Condens. Matter **24**(45), 455501 (2012).
[4]A. Zunger, S.-H. Wei, L. G. Ferreira, and J. E. Bernard, Phys. Rev. Lett. **65**(3), 353 (1990).
[5]A. O. Lyakhov, A. R. Oganov, H. T. Stokes, and Q. Zhu, Comp. Phys. Commun. **184**(4), 1172 (2013).
[6]Q. Zhu, A. R. Oganov, and A. O. Lyakhov, Phys. Chem. Chem. Phys. **15**(20), 7696 (2013).
[7]C. M. Fang, R. Metselaar, H. T. Hintzen, and G. de With, J. Am. Ceram. Soc. **84**(11), 2633 (2001).
[8]O. U. Okeke and J. E. Lowther, Phys. Rev. B **77**(9), 094129 (2008).
[9]O. Beckstein, J. E. Klepeis, G. L. W. Hart, and O. Pankratov, Phys. Rev. B **63**(13), 134112 (2001).
[10]Y. Le Page and P. Saxe, Phys. Rev. B **65**(10), 104104 (2002).
[11]K. Doll, Mol. Phys. **108**(3–4), 223 (2010).
[12]J. McCauley, ARL-Technical Report **ARL-TR-2740**, 2002.
[13]P. Tabary and C. Servant, J. Appl. Crystallogr. **32**, 241 (1999).
[14]D. E. Taylor, J. W. McCauley, and T. W. Wright, J. Phys.: Condens. Matter **24**(50), 505402 (2012).
[15]E. K. Graham, W. C. Munly, J. W. Mccauley, and N. D. Corbin, J. Am. Ceram. Soc. **71**(10), 807 (1988).
[16]LLC manufactured by General Opto Solutions, during a Phase II SBIR (2012).
[17]S. J. Clark, M. D. Segall, C. J. Pickard, P. J. Hasnip, M. J. Probert, K. Refson, and M. C. Payne, Zeitschrift Fur Kristallographie **220**(5–6), 567 (2005).
[18]S. Yoshida, K. Orita, Y. Hasegawa, A. Mochida, and S. Takigawa, ECS Trans. **16**(21), 1–10 (2009).
[19]F. Ansart and J. Bernard, Phys. Status Solidi A **134**(2), 467 (1992).
[20]J. J. Guo, K. Wang, T. Fujita, J. W. McCauley, J. P. Singh, and M. W. Chen, Acta Mater. **59**(4), 1671–1679 (2011).

Mesoscale Modeling of Nonlinear Elasticity and Fracture in Ceramic Polycrystals under Dynamic Shear and Compression

John D. Clayton, Reuben H. Kraft, and Richard B. Leavy

International Journal of Solids and Structures, 49 (2012)

Contents lists available at SciVerse ScienceDirect

International Journal of Solids and Structures

journal homepage: www.elsevier.com/locate/ijsolstr

Mesoscale modeling of nonlinear elasticity and fracture in ceramic polycrystals under dynamic shear and compression

J.D. Clayton *, R.H. Kraft, R.B. Leavy

RDRL-WMP-B, US Army Research Laboratory, Aberdeen Proving Ground, MD 21005-5066, USA

ARTICLE INFO

Article history:
Received 6 May 2011
Received in revised form 1 March 2012
Available online 9 June 2012

Keywords:
Elasticity
Fracture
Finite elements
Ceramics
Polycrystals

ABSTRACT

Dynamic deformation and failure mechanisms in polycrystalline ceramics are investigated through constitutive modeling and numerical simulation. Two ceramics are studied: silicon carbide (SiC, hexagonal crystal structure) and aluminum oxynitride (AlON, cubic crystal structure). Three dimensional finite element simulations incorporate nonlinear anisotropic elasticity for behavior of single crystals within polycrystalline aggregates, cohesive zone models for intergranular fracture, and contact interactions among fractured interfaces. Boundary conditions considered include uniaxial strain compression, uniaxial stress compression, and shear with varying confinement, all at high loading rates. Results for both materials demonstrate shear-induced dilatation and increasing shear strength with increasing confining pressure. Failure statistics for unconfined loading exhibit a smaller Weibull modulus (corresponding to greater scatter in peak failure strength) in AlON than in SiC, likely a result of lower prescribed cohesive fracture strength and greater elastic anisotropy in the former. In both materials, the predicted Weibull modulus tends to decrease with an increasing number of grains contained in the simulated microstructure.

Published by Elsevier Ltd.

1. Introduction

Ceramic materials typically exhibit high hardness, high elastic stiffness, and low ductility relative to other engineering materials such as metals. Of interest in the present paper is the behavior of polycrystalline ceramics at conditions pertinent to ballistic impact: high loading rates (e.g., strain rates on the order of 10^5/s) and high pressures (e.g., up to several to tens of GPa). The mechanical response of a polycrystalline ceramic under such conditions is dictated by bulk properties of its crystal constituents (e.g., density and elastic coefficients) as well as fracture behavior. Depending on the particular ceramic and loading regime, fracture can be transgranular and/or intergranular. Interactions among fractured and fragmented grains are thought to strongly affect shear strength behavior of damaged ceramics (Shockey et al., 1990; Curran et al., 1993; Gailly and Espinosa, 2002). Under severe loading, complete pulverization may occur; the comminuted ceramic may exhibit behavior approaching that of its powder form (Shih et al., 1998).

A general consensus on correlation between mechanical properties of ceramics and dynamic performance in high rate applications (e.g., resistance to failure, penetration, or perforation) apparently does not exist; relative importance of various properties may depend on the particular application. However, experiments do suggest that certain properties can strongly affect dynamic performance. These properties include hardness, elastic stiffness, fracture toughness, unconfined compressive strength, dynamic shear strength, and failure probabilities (e.g., Weibull parameters) (Sternberg, 1989; Shockey et al., 1990; Curran et al., 1993; Gailly and Espinosa, 2002; Ray et al., 2007; Leavy et al., 2010). Experiments indicate that ceramics exhibit an increase in shear strength with increasing compressive pressure or confinement (Heard and Cline, 1980; Chen and Ravichandran, 2000). After fractures occur, dilatation accompanies sliding of mismatched or misaligned crack faces relative to one another. Increasing pressure resists this dilatation, increasing the amount of shear stress required to enable deviatoric deformation (Curran et al., 1993). This phenomena, which also occurs in rocks and minerals, can be interpreted in the context of Mohr–Coulomb or frictional sliding models (Chen and Ravichandran, 2000; Clayton, 2010a).

Efforts towards computational modeling of macroscopic behavior of polycrystalline ceramics under high strain rates and pressures representative of ballistic events have been underway for over three decades (Wilkins, 1978; Curran et al., 1993). More recently, mesoscale models, in which the behavior of each grain within a polycrystal is addressed explicitly, have provided insight into effects of microstructural properties – e.g., grain sizes and shapes, anisotropic elasticity and/or plasticity, local fracture properties, and distributions of second phases – on deformation and failure behavior of polycrystalline solids (Espinosa and Zavattieri, 2003a,b; Clayton and McDowell, 2004; Clayton, 2005a,b, 2006a,b; Vogler and Clayton, 2008; Foulk and Vogler, 2010; Kraft and

* Corresponding author. Tel.: +1 410 2786146; fax: +1 410 2782460.
E-mail address: john.d.clayton1@us.army.mil (J.D. Clayton).

Molinari, 2008; Kraft et al., 2008; Zhang et al., 2005b,a; Kraft et al., 2010; Gazonas et al., 2010). Much earlier work focused on two-dimensional simulations; however, recent advances in computational hardware (e.g., processor speed and numbers of parallel processors), finite element software (Jung, 2010), and microstructure rendering and meshing technologies (Rollett and Manohar, 2004; Rollett et al., 2007) now enable fully resolved simulations of three-dimensional polycrystalline microstructures incorporating nonlinear material behavior, interfacial fracture, and multi-body contact (Kraft et al., 2010; Gazonas et al., 2010).

Three-dimensional simulations of polycrystalline microstructures are presented in this paper. Specific ceramics under consideration include silicon carbide (6H polytype as most prevalent in SiC-N, hexagonal structure) and AlON (spinel, cubic structure). Detailed descriptions and continuum models of behavior of single crystals of each material with supporting references are given elsewhere (Clayton, 2010c, 2011a). Notably, polycrystalline AlON of adequate quality is transparent, while polycrystalline SiC is opaque. However, SiC typically exhibits a higher elastic stiffness, higher fracture strength, and higher fracture toughness than AlON. Two synthetic microstructures are considered: one consisting of 50 grains, the other consisting of 126 grains. As discussed in more detail later, these microstructures are idealized in the sense that they do not correspond to reconstructions of actual specimens of the ceramics under present consideration; rather, they are synthesized from numerical algorithms incorporating grain growth or Voronoi methods. Synthetic microstuctures of this sort are typically used when digital reconstructions of actual microstructures are not available (Zhang et al., 2005b; Clayton, 2009b; Foulk and Vogler, 2010). Properties of SiC or AlON are assigned to each microstructure in different simulations, and results of various simulations enable comparison between materials holding grain morphology fixed. Nonlinear anisotropic elasticity represents single crystals within each polycrystal. Intergranular fracture is addressed via a multi-body contact algorithm (Jung, 2010), whereby each grain is treated as a distinct solid body. The contact algorithm incorporates a cohesive law enabling tensile and shear fracture and accounting for fracture strength and surface energy of separation. Various initial lattice orientation distributions enable a study of effects of elastic anisotropy, while various loading directions (e.g., shear or compression along different axes) provide insight into effects of grain morphology and enable quantification of anisotropy of failure behavior.

Simulations consider the following boundary conditions: uniaxial strain compression, uniaxial stress compression, and shear with varying magnitudes of superimposed compressive pressure. All simulations are conducted at high loading rates (10^5/s). Uniform strain rates are assigned throughout each microstructure as an initial condition. Results from uniaxial strain and stress simulations are compared with available experimental data. However, the present simulations enable a study of specimens of sizes smaller (in terms of number of grains) than those accessible by standard high-rate experiments (e.g., traditional plate impact and Kolsky bar tests). Shear boundary conditions considered here do not correspond to known dynamic experiments on the materials of present interest and hence provide new insight into dynamic shear strength behavior, with and without pressure. Of particular interest in the present study are the following physical phenomena: dependence of dynamic shear strength on pressure, sensitivity of peak strength to grain morphology and elastic anisotropy, and dependence of statistical variations in peak strength on specimen size (i.e., number of grains) and local material properties. Pressure-dependent strength statistics from mesoscale simulations can be used to provide parameters entering macroscopic constitutive models for ceramic material behavior incorporating statistical failure criteria (Brannon et al., 2007, 2009; Leavy et al., 2010; Graham-Brady, 2010).

This paper is structured as follows. Models for elastic behavior of single crystals, fracture of interfaces, and requisite material properties are described in Section 2. Microstructural representations (e.g., finite element meshes) are described in Section 3. Numerical simulations, important results, and limitations of the modeling approach are described in Section 4. Conclusions follow in Section 5.

Notation of continuum mechanics is used, primarily following index notation for vectors and higher-order tensors which is convenient in the context of anisotropic elasticity. Background on the subject of nonlinear anisotropic elasticity of crystals can be found in several books/monographs (Wallace, 1972; Thurston, 1974; Clayton, 2011b). For simplicity of presentation, all components of vectors and tensors are referred to a fixed set of Cartesian indices in both reference and spatial configurations of the body. Indices corresponding to the reference configuration are written in capitals, while those corresponding to the spatial configuration are written in lower case. Einstein's summation applies for repeated indices, e.g., $a_A b_A = a_1 b_1 + a_2 b_2 + a_3 b_3$.

2. Theory and constitutive models

Governing equations for elastic behavior of single crystals comprising polycrystalline aggregates are provided. Models for intergranular fracture are described. Properties for bulk single crystals and interfaces are tabulated for SiC and AlON ceramics.

2.1. Nonlinear anisotropic elasticity

The behavior of intact single crystals is governed by traditional balance laws of nonlinear continuum mechanics (Thurston, 1974; Clayton, 2011b). Letting t denote time, spatial (x_a) and material (X_A) coordinates are related by the smooth, invertible, and one-to-one (at any given time) functions

$$x_a = x_a(X_A, t), \quad X_A = X_A(x_a, t). \tag{1}$$

The deformation gradient and its inverse are

$$F_{aA} = \partial x_a/\partial X_A = \partial_A x_a, \quad F^{-1}_{Aa} = \partial X_A/\partial x_a = \partial_a X_A, \tag{2}$$

where partial coordinate differentiation (t fixed) obeys

$$\partial_A(\cdot) = \partial(\cdot)/\partial X_A = [\partial(\cdot)/\partial x_a][\partial x_a/\partial X_A] = \partial_a(\cdot)F_{aA}. \tag{3}$$

Volume element dV in the spatial configuration is related to its counterpart dV_0 in the reference configuration by the Jacobian determinant J:

$$J = dV/dV_0 = \det(F_{aA}) = \frac{1}{6}\epsilon_{abc}\epsilon_{ABC}F_{aA}F_{bB}F_{cC} \tag{4}$$

with inverse

$$J^{-1} = 1/J = \det(F^{-1}_{Aa}) = \frac{1}{6}\epsilon_{abc}\epsilon_{ABC}F^{-1}_{Aa}F^{-1}_{Bb}F^{-1}_{Cc}. \tag{5}$$

Permutation symbols are ϵ_{abc} and ϵ_{ABC}. The following identities apply (Clayton, 2011b):

$$\begin{aligned} &\partial J/\partial F_{aA} = JF^{-1}_{Aa}, \quad \partial_A(JF^{-1}_{Aa}) = 0; \\ &\partial J^{-1}/\partial F^{-1}_{Aa} = J^{-1}F_{aA}, \quad \partial_a(J^{-1}F_{aA}) = 0. \end{aligned} \tag{6}$$

Let the following notations denote the material time derivative:

$$d(\cdot)/dt = \dot{(\cdot)} = [\partial(\cdot)/\partial t]|_{X_A} = [\partial(\cdot)/\partial t]|_{x_a} + v_a\partial_a(\cdot). \tag{7}$$

Particle velocity and acceleration, respectively, are

$$v_a = \dot{x}_a, \quad a_a = \dot{v}_a = \ddot{x}_a. \tag{8}$$

The spatial velocity gradient and its trace obey

$$\partial_b v_a = \dot{F}_{aA} F^{-1}_{Ab}, \quad \partial_a v_a = \dot{J} J^{-1}. \tag{9}$$

Cauchy stress σ_{ab}, first Piola–Kirchhoff stress P_{aA}, and second Piola–Kirchhoff stress S_{AB} are related by

$$\sigma_{ab} = J^{-1} P_{aB} F_{bB} = J^{-1} F_{aA} S_{AB} F_{bB}. \tag{10}$$

Conservation laws for mass, linear momentum (with no body forces), and angular momentum are

$$\rho_0 = \rho J, \quad \partial_A P_{aA} = \rho_0 a_a, \quad P_{aB} F_{bB} = P_{bB} F_{aB}, \tag{11}$$

where ρ_0 and ρ are referential and spatial mass densities. Using (6), (9), and (10),

$$\dot{\rho} = -\rho \partial_a v_a, \quad \partial_b \sigma_{ab} = \rho a_a, \quad \sigma_{ab} = \sigma_{ba}. \tag{12}$$

Assuming adiabatic conditions, the balance of energy and entropy inequality are

$$\dot{U} = P_{aA} \dot{F}_{aA}, \quad \dot{\eta} \geqslant 0, \tag{13}$$

where U and η are entropy and internal energy per unit reference volume.

A hyperelastic material response is assumed:

$$U = U(F_{aA}, \eta), \quad \partial U / \partial F_{aA} = P_{aA}, \quad \partial U / \partial \eta = \theta, \tag{14}$$

with θ the temperature. From the chain rule and (14),

$$\dot{U} = P_{aA} \dot{F}_{aA} + \theta \dot{\eta}, \tag{15}$$

which is compatible with adiabatic assumption (13) at finite temperature only when $\dot{\eta} = 0$; i.e., assumptions of adiabatic conditions and hyperelastic response correspond to isentropic conditions. Thus, dependence of internal energy on entropy is dropped henceforward, and thermomechanical quantities are assumed to be measured at fixed entropy (e.g., the usual "adiabatic" elastic coefficients measured ultrasonically).

Define symmetric Lagrangian elastic strain E_{AB} and deformation C_{AB} as

$$E_{AB} = \frac{1}{2}(C_{AB} - \delta_{AB}), \quad C_{AB} = F_{aA} F_{aB}, \quad \det(C_{AB}) = J^2, \tag{16}$$

with δ_{AB} Kronecker's delta. The internal energy at fixed entropy is, to within an arbitrary constant and to third order in strain (Thurston, 1974; Clayton, 2011b),

$$\begin{aligned} U &= \frac{1}{2!} \left. \frac{\partial^2 U}{\partial E_{AB} \partial E_{CD}} \right|_{E_{IJ}=0} E_{AB} E_{CD} + \frac{1}{3!} \left. \frac{\partial^3 U}{\partial E_{AB} \partial E_{CD} \partial E_{EF}} \right|_{E_{IJ}=0} E_{AB} E_{CD} E_{EF} \\ &= \frac{1}{2} C_{ABCD} E_{AB} E_{CD} + \frac{1}{6} C_{ABCDEF} E_{AB} E_{CD} E_{EF}. \end{aligned} \tag{17}$$

Second- and third-order elastic constants at the unstressed reference state are C_{ABCD} and C_{ABCDEF}. In Voigt's notation (Thurston, 1974; Clayton, 2011b), where Greek indices run from 1 to 6, $C_{ABCD} \leftrightarrow C_{\alpha\beta}$ and $C_{ABCDEF} \leftrightarrow C_{\alpha\beta\chi}$. Noting from (10) and the symmetry of E_{AB} and S_{AB} that

$$P_{aA} = \partial U / \partial F_{aA} = (\partial U / \partial E_{BC})(\partial E_{BC} / \partial F_{aA}) = (\partial U / \partial E_{BA}) F_{aB} = F_{aB} S_{BA}, \tag{18}$$

it follows that the second Piola–Kirchhoff stress

$$S_{AB} = C_{ABCD} E_{CD} + \frac{1}{2} C_{ABCDEF} E_{CD} E_{EF}. \tag{19}$$

Properties for SiC and AlON single crystals are listed in Table 1. Third-order elastic constants are tedious to measure and have been reported for relatively few substances. For many single crystals, including those of interest here, full sets of third-order elastic constants have not been reported in the literature. However, third-order elastic constants can be estimated as follows (Clayton, 2010c, 2011a), presuming pressure derivatives of elastic coefficients at the reference state are available. First, note the following identity (Clayton, 2011b):

$$\begin{aligned} \partial J / \partial E_{AB} &= 2 \partial J / \partial C_{AB} = J^{-1} \partial (J^2) / \partial C_{AB} = J^{-1} \partial \det(C_{AB}) / \partial C_{AB} \\ &= J^{-1} \det(C_{AB}) C^{-1}_{BA} = J C^{-1}_{AB}. \end{aligned} \tag{20}$$

Now, assume that the tangent elastic coefficients (denoted with a superposed $\widehat{\ }$) depend only on volume change (via J) and not on deviatoric deformation:

$$\widehat{C}_{ABCD}(J) = \partial^2 U / \partial E_{AB} \partial E_{CD}. \tag{21}$$

Using (20), and letting $\widehat{K} = -V(dp/dV) = -J(dp/dJ)$ denote the tangent bulk modulus with $p = -\sigma_{aa}/3$ the Cauchy pressure,

$$\begin{aligned} \partial \widehat{C}_{ABCD} / \partial E_{EF} &= (d\widehat{C}_{ABCD}/dJ)(\partial J / \partial E_{EF}) \\ &= (d\widehat{C}_{ABCD}/dp)(dp/dJ)(\partial J / \partial E_{EF}) \\ &= -(d\widehat{C}_{ABCD}/dp)(\widehat{K}/J)(J C^{-1}_{EF}) \\ &= -\widehat{K}(d\widehat{C}_{ABCD}/dp) C^{-1}_{EF}. \end{aligned} \tag{22}$$

Table 1
Properties for SiC and AlON single crystals.

Property	Value (SiC)	Reference	Value (AlON)	Reference
Structure	6H polytype		Spinel	
Phase	α		γ	
Crystal system	Hexagonal		Cubic	
Mass density ρ_0	3227 kg/m^3	Leavy et al. (2010)	3714 kg/m^3	Graham et al. (1988)
Elastic constant C_{11}	501 GPa	Kamitani et al. (1997)	301 GPa	Gazonas et al. (2010)
Elastic constant C_{12}	112 GPa		155 GPa	
Elastic constant C_{44}	161 GPa		174 GPa	
Elastic constant C_{13}	52 GPa		$(= C_{12})$	
Elastic constant C_{33}	549 GPa		$(= C_{11})$	
Pressure derivative dC_{11}/dp	3.8	Davydov (2004)	5.1	Batyrev et al. (2011)
Pressure derivative dC_{12}/dp	4.0		2.7	
Pressure derivative dC_{44}/dp	−0.2		1.2	
Pressure derivative dC_{13}/dp	4.0		$(= dC_{12}/dp)$	
Pressure derivative dC_{33}/dp	3.8		$(= dC_{11}/dp)$	
No. independent $C_{\alpha\beta\chi}$	10		6	
Bulk modulus K	222 GPa	Clayton (2010c)	204 GPa	$(C_{11} + 2C_{12})/3$
Shear modulus G	194 GPa		134 GPa	(Voigt average)
Poisson's ratio ν	0.16		0.23	
Shear wave speed $\sqrt{G/\rho_0}$	7.75 km/s		6.01 km/s	
Zener anisotropy $2C_{44}/(C_{11} - C_{12})$	0.83		2.38	
Typical grain size	5 μm	Leavy et al. (2010)	200 μm	McCauley et al. (2009)

Repeating (22) over alternating pairs of indices (AB, CD, EF), evaluating at the reference state where $C_{AB}^{-1} = \delta_{AB}, d\widehat{C}_{ABCD}/dJ = dC_{ABCD}/dJ$, $\widehat{K} = K$ (i.e., dropping the $\widehat{\ }$ notation at the reference state) and averaging the result provides the following estimate of third-order elastic constants with requisite major and minor symmetries:

$$C_{ABCDEF} \approx -(K/3)[(dC_{ABCD}/dp)\delta_{EF} + (dC_{CDEF}/dp)\delta_{AB} + (dC_{EFAB}/dp)\delta_{CD}]. \quad (23)$$

Application of (23) to single crystals of alumina (Al_2O_3), a material for which $\partial C_{\alpha\beta}/\partial p$ and $C_{\alpha\beta\chi}$ are known (Hankey and Schuele, 1970; Clayton, 2009a, 2010b) provides a coarse yet reasonable estimate of 11 of its 14 third-order elastic constants. Application of (23) to single crystals of SiC provides an accurate depiciton of the hydrostat (Clayton, 2010c). As demonstrated in previous modeling efforts for SiC (Clayton, 2010c) and AlON (Clayton, 2011a), third-order elastic constants enable description of the increase in tangent elastic stiffness that accompanies decreasing volume. The exact relationship (Thurston et al., 1966) $\partial C_{ABCD}/\partial p = -S_{EFGG}C_{ABCDEF}$, with S_{ABCD} the compliance, provides an insufficient number of equations for determination of all third-order constants.

2.2. Fracture

A cohesive zone approach is used to model intergranular fracture. Let t_a^n and t_a^t denote traction vector components normal and tangential to a potential fracture site with unit outward normal components n_a:

$$t_a^n = (\sigma_{bc}n_b n_c)n_a, \quad t_a^t = \sigma_{ab}n_b - (\sigma_{bc}n_b n_c)n_a; \quad |t_a^n| = \sqrt{t_a^n t_a^n}, \quad |t_a^t| = \sqrt{t_a^t t_a^t}. \quad (24)$$

Many cohesive laws have been investigated in previous works on heterogeneous polycrystalline solids (Espinosa and Zavattieri, 2003a,b; Clayton and McDowell, 2004; Clayton, 2005a,b; Kraft and Molinari, 2008; Kraft et al., 2008; Vogler and Clayton, 2008; Foulk and Vogler, 2010; Kraft et al., 2010). A simple irreversible cohesive law is prescribed in the present work, with the same functional form and parameters for normal and tangential separations δ^n and δ^t. Specifically, separation is possible after a critical initiation traction of magnitude t^c is attained. The interface then maintains a constant cohesive strength until critical separation distance δ^c is reached. Mathematically,

$$\delta^n = 0 \leftrightarrow |t_a^n| < t^c, \quad 0 < \delta^n/\delta^c < 1 \leftrightarrow |t_a^n| = t^c, \quad \delta^n/\delta^c \geqslant 1 \leftrightarrow |t_a^n| = 0; \quad \delta^t = 0 \leftrightarrow |t_a^t| < t^c, \quad 0 < \delta^t/\delta^c < 1 \leftrightarrow |t_a^t| = t^c, \quad \delta^t/\delta^c \geqslant 1 \leftrightarrow |t_a^t| = 0. \quad (25)$$

Normal separation only occurs for tensile normal stress, i.e., for $t_a^n n_a > 0$; interpenetration of matter is prohibited. After complete separation, interactions between interfaces are addressed via a multi-body contact algorithm (Jung, 2010) enabling sliding between faces but no interpenetration. Atomic bonds are considered irreversibly broken when either δ^n or δ^t exceeds δ^c; i.e., once complete fracture occurs in any direction at a given referential location, cohesive strength is lost in all directions at that location. The advantage of cohesive law (25) is its simplicity: only two parameters, which can be estimated from macroscopic fracture measurements, are needed. Coupling does not exist between normal and tangential contributions to fracture energy in later Eq. (26): surface energy Γ is the same for pure normal or pure tangential fracture, but the total surface energy associated with an interface undergoing mixed mode fracture may exceed Γ. As discussed later in Section 4, (25) produces an adequate representation of macroscopic stress–strain and failure behaviors of ceramic polycrystals under present consideration. More complex cohesive laws incorporating piecewise-linear traction-separation relationships with various slopes were investigated; alternative formulations did not offer any apparent advantages with regards to numerical stability or representation of macroscopic fracture strength but often would require specification of experimentally unknown parameters.

Differently from many previous studies (Espinosa and Zavattieri, 2003a,b; Clayton and McDowell, 2004; Clayton, 2005a,b; Vogler and Clayton, 2008; Foulk and Vogler, 2010), distinct cohesive finite elements are not used in the present numerical framework. In other words, finite element meshes are not seeded a priori with interfacial elements. Rather, the cohesive constitutive law (25) is incorporated directly into the contact algorithm (Jung, 2010), and each individual grain within a polycrystalline aggregate is treated as a distinct solid body from the outset of a given numerical simulation. Prior to attainment of the critical normal or tangential traction, interfaces are rigidly tied, and hence artificial increases in compliance prior to fracture initiation are avoided. Once the critical traction is attained and separation commences, forces resulting from the cohesive traction-separation law are effectively applied to appropriate nodes by the contact algorithm that computes node-face interactions (Jung, 2010, Ch. 7, pp. 377–448).

Properties are listed for SiC and AlON in Table 2, with critical strength and separation distance computed using experimental (macroscopic) values of flexure strength and static fracture toughness. In the context of linear elastic fracture mechanics, fracture toughness κ, surface energy Γ, critical strength t^c, critical separation δ^c, and cohesive zone length l^c are related by (Espinosa and Zavattieri, 2003b; Clayton, 2005b; Kraft et al., 2010)

$$\kappa^2(1-\nu^2)/E = 2\Gamma = t^c\delta^c, \quad l^c \approx \pi E\Gamma/[(t^c)^2(1-\nu^2)]. \quad (26)$$

Young's modulus $E = 9KG/(3K+G)$ and Poisson's ratio $\nu = (3K-2G)/(6K+2G)$. Also shown for purposes of comparison in Table 2 are experimentally measured spall strengths. Spall strengths are comparable to flexure strengths, though the former may vary considerably with impact pressure (Dandekar and Bartowski, 2001; Cazamias et al., 2001) and may also vary from sample to sample tested at similar impact pressures due to brittleness and possible flaws in the material.

The present study incorporates uniform grain boundary strength and frictionless post-fracture sliding between grain boundary facets. It is understood that real ceramic microstructures should exhibit variation among fracture behaviors (e.g., in functional forms of cohesive laws as well as in fracture strengths and energies) at interfaces depending on grain misorientation, grain boundary curvature, impurities, and pre-existing defects. Thus, the assumption of uniform grain boundary behavior is an idealization, albeit one that has been used frequently in other numerical studies of heterogeneous polycrystalline solids (Clayton and McDowell, 2004; Vogler and Clayton, 2008; Foulk and Vogler, 2010; Kraft et al., 2010). Variable grain boundary properties can strongly influence overall behavior of ceramics (Espinosa and Zavattieri, 2003b; Kraft and Molinari, 2008; Kraft et al., 2008); however, assignment of variable properties as an initial condition is problematic since experimental measurements of mesoscopic grain boundary strength distributions are scarce if not nonexistent. A distribution of strengths at the mesoscale could be assigned so that homogenized model results over many simulations would match macroscopic failure statistics (e.g., a Weibull modulus). However, such an approach would reduce model calculations of failure statistics to parameter fits rather than predictive results. On the other hand, assignment of uniform grain boundary properties enables simulation results to provide insight of other sources of variability, such as grain morphology, loading conditions, and elastic anisotropy, on predicted failure statistics.

Table 2
Properties for SiC and AlON interfaces.

Property	Value (SiC)	Reference	Value (AlON)	Reference
Fracture (flexure) strength t^c	0.570 GPa	Leavy et al. (2010), LaSalvia et al. (2010)	0.306 GPa	Corbin (1989)
Fracture toughness κ	5.1 MPa $m^{1/2}$		2.5 MPa $m^{1/2}$	
Surface energy Γ	28.1 J/m^2	Eq. (26)	9.0 J/m^2	Eq. (26)
Critical separation δ^c	0.10 μm		0.06 μm	
Cohesive length l^c	126 μm		105 μm	
Spall strength	0.54–1.3 GPa	Dandekar and Bartowski (2001)	0.14–1.7 GPa	Cazamias et al. (2001)

The assumption of local frictionless contact enables smooth faces to slide freely past one another. However, as will be demonstrated later in Section 4, because grain boundaries are interlocking, grains cannot slide indefinitely without expansion normal to the direction of motion and generation of free volume, i.e., dilatation (Curran et al., 1993; Clayton, 2010a). This phenomenon, due simply to grain geometry, leads to an increase in macroscopic or average shear stress with confinement or compressive pressure, in what may be interpreted as sliding "friction" in the sense of macroscopic Mohr–Coulomb models (Chen and Ravichandran, 2000), even though microscopically contact is treated as frictionless. Locally frictionless contact was also assumed in a previous computational study of shock compression and spall of SiC (Foulk and Vogler, 2010). However, this approach represents a limiting case since local microscopic friction could be non-negligible. Previous two dimensional simulations (Kraft et al., 2008) demonstrated that as the sliding friction coefficient between failed grain boundaries increases, compressive peak strength and its sensitivity to confining stress also increase. As noted later in Section 4.4, omission of friction may contribute to under-prediction of shear strength in the present simulations of the high pressure response under uniaxial strain loading, wherein contributions of frictional forces proportional to normal pressures at interfaces could become important.

As assumed in previous fracture simulations of ceramic polycrystals including Al_2O_3 (Espinosa and Zavattieri, 2003a; Espinosa and Zavattieri, 2003b), SiC (Foulk and Vogler, 2010), and AlON (Gazonas et al., 2010), transgranular (i.e., cleavage) fracture is not addressed. This is a reasonable assumption for certain varieties of SiC (e.g., SiC-N) that contain additives that segregate at grain boundaries, leading to a tendency for grain boundary fracture over cleavage and corresponding to increased toughness (Faber and Evans, 1983; Shih et al., 1998; Lee et al., 2005; Vargas-Gonzalez et al., 2010). On the other hand, this assumption may be less physically reasonable for AlON, in which cleavage fractures have been observed (McCauley et al., 2009).

3. Microstructure modeling

Synthetic microstructures representative of generic polycrystals with equi-axed grains are considered in the present work, in the absence of serial section and/or electron back-scatter diffraction (EBSD) data that could be used to recreate true microstructures from material specimens (Brahme et al., 2006; Rollett et al., 2007). Efforts are presently underway towards reconstruction of microstructures from actual ceramic specimens. In the present approach, volume meshes (tetrahedral elements) are created from stereolithographic (STL) files of surface representations of grains comprising a given microstructure. Surface meshes are generated for three-dimensional microstructures produced using a Monte Carlo grain growth algorithm (Rollett and Manohar, 2004). A conformal triangular surface mesh covers each crystal volume, with an interpolation method used where a triangle separates two materials (Kraft et al., 2010). A three dimensional volume mesh of tetrahedral continuum finite elements is then created to fill the surface mesh of every crystal.

Two microstructures are considered: microstructure I, with 50 grains; and microstructure II, with 126 grains. Each aggregate is a cube of dimensions $L \times L \times L$, where $L = 1$ mm. Absolute dimensions of each aggregate are prescribed to be equal to enable reasonable comparison of dynamic finite element results between microstructures in which traction-free boundary conditions are prescribed on some external surfaces. If, on the other hand, different sized specimens were to be compared, differences in deformation and failure behavior could, in many scenarios, be attributed to differences in dimensions of external boundaries of the aggregate. For example, a planar crack originating at one edge of the aggregate would propagate (at constant speed) in a shorter time across a smaller specimen than a larger specimen, leading to earlier failure in the former case. Times for elastic release waves to traverse different-sized specimens would also differ in dynamic simulations. By using the same absolute size L for each aggregate, any such issues associated with external boundaries are the same in each simulation, so that results obtained from different microstructures can be meaningfully compared. As discussed later in Section 4.3, periodic boundary conditions might be expected to provide more realistic depiction of behavior of grain aggregates embedded inside a much larger sample of material, as considered elsewhere in two-dimensional studies of ceramic microstructures (Espinosa and Zavattieri, 2003a,b).

Microstructures are shown in Fig. 1. Average grain sizes for each microstructure can be estimated as $L/50^{1/3} \approx 270$ μm (microstructure I) and $L/126^{1/3} \approx 200$ μm (microstructure II), which are representative of AlON (McCauley et al., 2009) but are much larger than standard SiC-N (Lee et al., 2005; Leavy et al., 2010). However, other varieties of polcrystalline SiC with large grains can exhibit grain sizes of this order of magnitude (Rice et al., 1994). As mentioned in Section 1, the same microstructures are used to represent both SiC and AlON polycrystals in subsequent dynamic finite element simulations. Use of the same meshes for each material enables quantification of differences in deformation and failure behavior by varying material properties (i.e., mass density, elasticity, cohesive strength, and cohesive energy) while holding the microstructure fixed. Differences resulting from grain morphology are studied by compressing and/or shearing each microstructure in different (e.g., orthogonal and forward/reverse) directions. Finite element meshes contain between 1×10^6 and 2×10^6 tetrahedral elements. Mesh refinement is sufficient to resolve grain boundary surface morphology and cohesive zone lengths (Table 2) and is comparable to that considered in previous polycrystal fracture simulations in two and three dimensions (Clayton, 2005a,b; Kraft and Molinari, 2008; Kraft et al., 2008, 2010; Gazonas et al., 2010). Cumulative grain size distributions for each microstructure are shown in Fig. 2. Let V_g denote the volume V of a particular grain, and define that grain's size as $V_g^{1/3}$. The cumulative number fraction (ordinate of Fig. 2) is defined as the number of grains with $V_g^{1/3} \leqslant V^{1/3}$ divided by the total number of grains in the microstructure. The abscissa of Fig. 2 is $V^{1/3}$ normalized by the average grain size in the microstructure. Grain sizes are somewhat more uniform

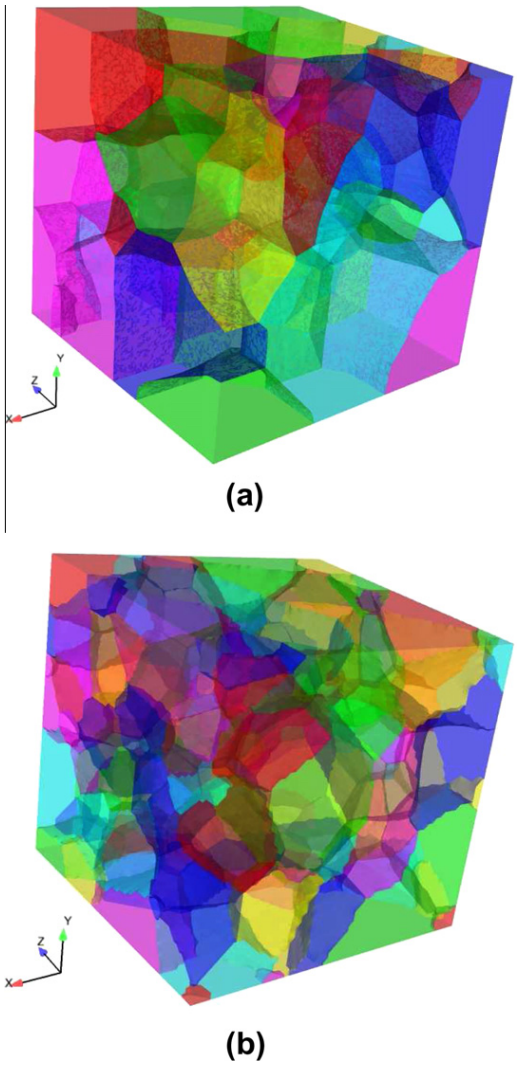

Fig. 1. Finite element representations of polycrystalline aggregates: (a) microstructure I (50 grains) (b) microstructure II (126 grains).

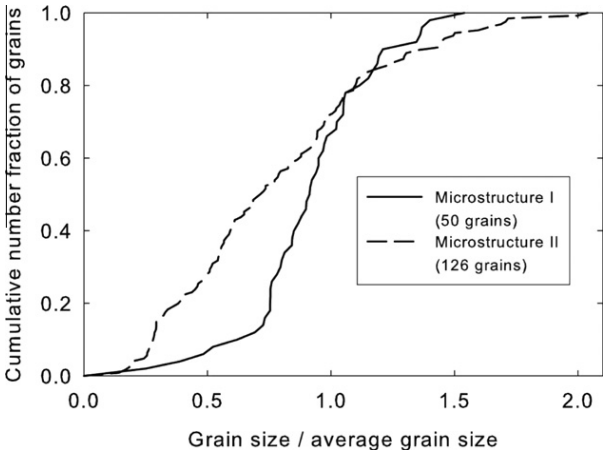

Fig. 2. Normalized cumulative grain size distributions.

in microstructure I, while microstructure II exhibits greater variability (i.e., a wider distribution) of grain sizes. Normalized distributions are qualitatively similar to those observed for Hexoloy SiC and SiC-N (Vargas-Gonzalez et al., 2010).

In all simulations discussed in Section 4, random initial lattice orientations are used for grains comprising each microstructure. Different sets of random initial orientations are investigated in some simulations. Lattice orientation affects model results through the dependence of anisotropic elastic coefficients (C_{ABCD}, C_{ABCDEF}) on crystallographic orientation in the reference configuration.

4. Mesoscale simulations

Dynamic simulations for different boundary and initial conditions are described in what follows: uniaxial strain compression (Section 4.1), uniaxial stress compression (Section 4.2), and shear (Section 4.3) with and without superimposed compressive stress. Results are then summarized in Section 4.4, with limitations of the current approach and areas for further research identified.

Data from numerous mesoscale simulations are collected and analyzed, approximately 180 simulations in total. The SIERRA (Jung, 2010) Lagrangian finite element code with explicit dynamics is used. Each simulation is executed in parallel mode on 32 processors for 24 h wall-clock time, for a total number of cpu-hours consumed of $180 \times 32 \times 24 \approx 1.4 \times 10^5$.

4.1. Uniaxial strain

Results for dynamic uniaxial strain loading are reported first. Let X denote the referential direction of loading, with Y and Z denoting orthogonal directions, and with a corner of the cubic specimen located initially at the origin $(X, Y, Z) = (0, 0, 0)$. Velocity boundary conditions and nonzero initial conditions for uniaxial straining in the X-direction are, respectively,

$$\begin{aligned} &v_x = -\dot{\epsilon}X \quad \text{along } X = L; \\ &v_y = 0 \quad \text{along } Y = 0, L; \\ &v_z = 0 \quad \text{along } Z = 0, L; \\ &v_x = v_y = v_z = 0 \quad \text{along } X = 0; \end{aligned} \tag{27}$$

$$v_x(t = 0) = -\dot{\epsilon}X \leftrightarrow \partial_x v_x(t = 0) = -\dot{\epsilon}. \tag{28}$$

The imposed uniaxial strain rate is $\dot{\epsilon} = 10^5/\text{s}$. Initial conditions (28) impose a uniform initial velocity gradient throughout the domain; a shock wave would arise, on the other hand, if velocity boundary conditions (27) were to be applied to a body initially at rest. Uniaxial strain simulations were also performed via loading in orthogonal Y and Z directions, with analogous boundary and initial conditions. Under these loading conditions, volume V of the aggregate is related to its initial volume V_0 via $V = (1 - \dot{\epsilon}t)V_0$.

Because the material is unstrained at $t = 0$, stress is zero everywhere initially. The strain rate (symmetric part of the velocity gradient $\partial_b v_a$) is initially nonzero and constant throughout the microstructure. If these conditions were to be applied to a homogeneous linear elastic material, stresses would increase linearly with time. In the present simulations, stresses may emerge heterogeneously and nonlinearly with $t > 0$ as a result of elastic anisotropy and elastic nonlinearity, fracture, contact, and stress wave interactions. The authors are unaware of any experimental configuration that exactly replicates these uniform initial and boundary conditions. Similar comments apply for other initial and boundary conditions considered later in Section 4.2 and Section 4.3.

Fig. 3 shows axial stress contours ($\sigma = -\sigma_{xx}$, positive in compression) in SiC (Fig. 3(a)) and AlON (Fig. 3(b)). In each case shown, a 50-grain microstructure is deformed to 5% reduction in volume, i.e., $V/V_0 = 0.95$ via compression along the X-direction. Stresses are significantly higher in SiC than AlON as a result of the larger elastic stiffness and higher fracture strength and toughness in the former (Tables 1 and 2). In each microstructure, cracks associated with axial splitting appear, typical behavior for brittle materials

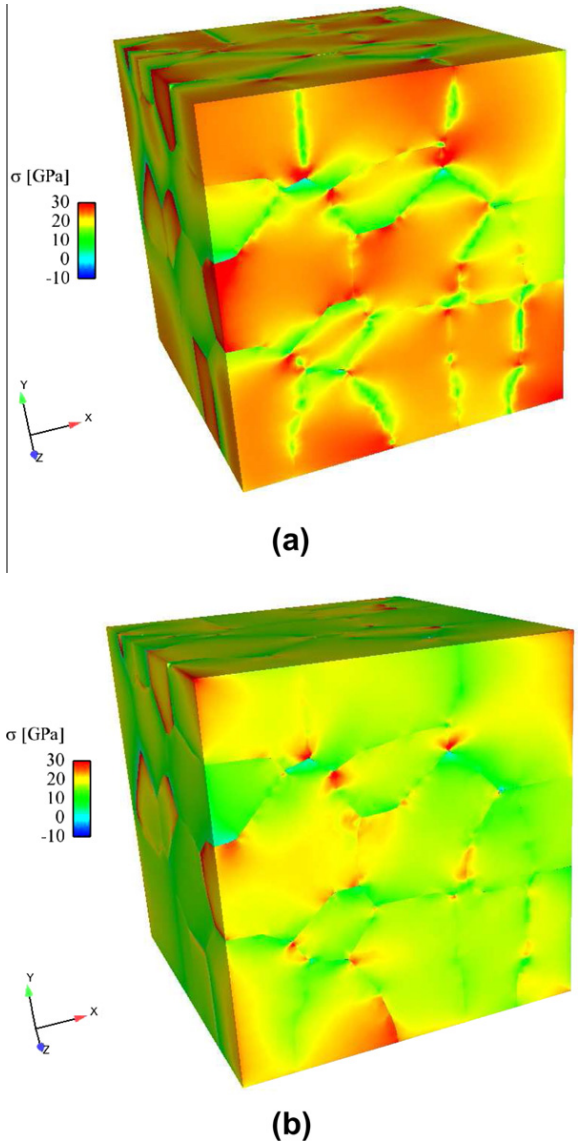

Fig. 3. Axial stress σ (positive in compression) for 50-grain microstructures subjected to uniaxial strain at volume $V/V_0 = 0.95$: (a) SiC (b) AlON.

with low Poisson's ratio (Chen and Ravichandran, 2000). Stress concentrations are visible along certain grain boundaries and triple junctions in both materials.

Average axial stress Σ is defined as the surface integral

$$\Sigma = (1/A)\int_A \hat{t}^n dA, \tag{29}$$

where $\hat{t}^n$ is the magnitude of the component of traction normal to loaded surface A. For example, for uniaxial strain along the X-direction, $\hat{t}^n = |\sigma_{xx} n_x| = |\sigma_{xx}|$ along the surface defined by $X = L$ with area $A = L^2$. Average axial stresses are shown in Fig. 4(a) and (b) for respective microstructures of SiC and AlON loaded along the X-direction. Results are compared for specimens in which fracture is prohibited (i.e., permanently tied contact at grain boundary interfaces), for specimens with different random grain orientation distributions (labeled orientation 1 and orientation 2), and for nonlinear and linear elastic constitutive models. Nonlinear elastic models incorporating both second- and third-order elastic constants are used unless simulation cases are labeled as "linear". For linear models, only anisotropic second-order elastic constants are implemented, and all third-order elastic constants are set to zero. For each material, simulations without fracture exhibit the largest stiffness. Average stresses from simulations incorporating nonlinear elasticity with different lattice orientations are nearly indistinguishable in each of Fig. 4(a) and (b). Also in each material, differences between nonlinear and linear elastic models become apparent at larger compressions (e.g., at $V/V_0 \lesssim 0.97$). For the same material, lattice orientation, and grain geometry, nonlinear elasticity provides for a higher compressive stress than linear elasticity because of the increasing elastic stiffness with increasing compressive pressure reflected by the third-order elastic constants.

Average axial stresses for SiC and AlON microstructures with various lattice orientations strained uniaxially along different directions are compared to experimental shock compression data in Fig. 5(a) and (b). Note that uniaxial strain compression at a rate of $\dot{\epsilon} = 10^5/\text{s}$ is typically deemed representative of plate impact experiments (Grady, 1998; Clayton, 2011a), though the stress state is not uniform in shock compression tests. A uniaxial strain condition with a constant strain rate of $\dot{\epsilon} = 10^5/\text{s}$ was used elsewhere (Holmquist and Johnson, 2002) to calibrate a macroscopic ceramic strength model to plate impact data. Constitutive models used in the present work for nonlinear elasticity, cohesive fracture, and contact include no intrinsic rate dependence. Rate effects arise only from time scales associated with inertia (i.e., elastic wave speeds in anisotropic grains) and crack propagation velocities. Experimental data shown in Fig. 5 correspond to shock compression, wherein the strain rate and stress state exhibit effective jump discontinuities across the shock front. On the other hand, model results are obtained for the more homogeneous uniaxial strain loading path dictated by (27) and (28). Differences between model predictions and experimental data would be expected due to the path dependent nature of the fracture process, e.g., local fractures induced by propagation of a shock front are omitted in the simulations.

Predicted average stresses for SiC shown in Fig. 5(a) are very similar for all orientations and all loading directions. Except for the first experimental data point shown (which corresponds to the elastic regime), predicted stresses are lower than experimental plate impact data (Feng et al., 1998; Yuan et al., 2001). Possible reasons for discrepancies are discussed further in Section 4.4. Predicted average stresses for AlON shown in Fig. 5(b) are also very similar for all orientations and all loading directions. Furthermore, predictions for AlON closely follow the experimental plate impact data (Cazamias et al., 2001; Vaughan et al., 2001; Dandekar et al., 2007).

Tables 3 and 4 report average shear stresses for SiC and AlON, respectively. Simulation cases are tabulated in Table 5. Average shear stress τ and average pressure P follow the usual definitions from shock compression science (Feng et al., 1998; Grady, 1998; Dandekar et al., 2007; Clayton, 2011a,b):

$$\tau = \frac{1}{2}(\Sigma_1 - \Sigma_3), \quad P = -\frac{1}{3}(\Sigma_1 + \Sigma_2 + \Sigma_3), \tag{30}$$

where Σ_1, Σ_2, and Σ_3 are maximum, intermediate, and minimum principal stresses for the polycrystalline aggregate computed analogously to (29). Shear stress increases monotonically with compressive strain in all simulations. In experiments on SiC (Feng et al., 1998), shear strength increases with increasing compressive strain for $V/V_0 \geqslant 0.95$, while in experiments on AlON (Dandekar et al., 2007), shear strength decreases for compressive strain $V/V_0 \leqslant 0.98$. Agreement between model and experiment is closer at larger compressions. Missing entries in Tables 3 and 4 indicate either unreported experimental data or simulations that were terminated due to numerical instabilities prior to attainment of corresponding applied strains. Slight variations in shear strength among simulations of the same material loaded in different directions or with different lattice orientations are evident, generally on the

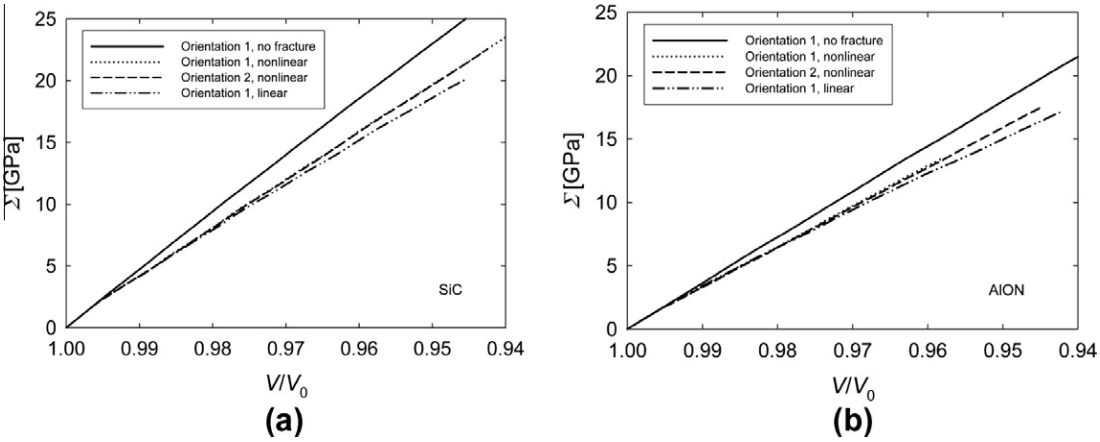

Fig. 4. Average axial stress Σ for the same microstructures subjected to uniaxial strain along X-direction: (a) SiC (b) AlON.

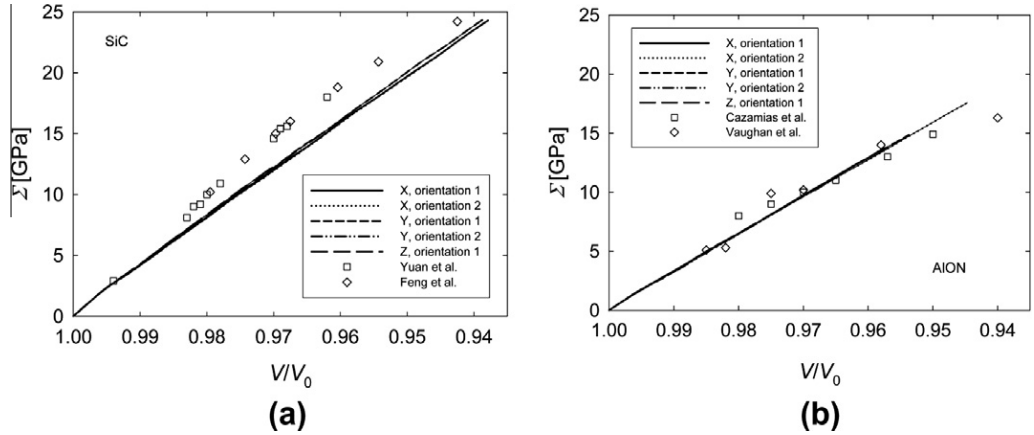

Fig. 5. Average axial stress Σ for the same grain structures subjected to uniaxial strain along different directions, and experimental shock compression data: (a) SiC (b) AlON.

Table 3
Predicted and experimental shear stress for SiC in uniaxial strain compression.

Simulation or experiment	τ [GPa]					
	$\frac{V}{V_0}=0.99$	$\frac{V}{V_0}=0.98$	$\frac{V}{V_0}=0.97$	$\frac{V}{V_0}=0.96$	$\frac{V}{V_0}=0.95$	$\frac{V}{V_0}=0.94$
Simulation 1	1.49	2.70	3.87	4.97	6.00	6.97
Simulation 2	1.46	2.65	3.77	4.86	5.86	–
Simulation 3	1.48	2.68	3.83	4.92	5.94	–
Simulation 4	1.51	2.78	4.04	5.15	6.31	7.29
Simulation 5	1.49	2.74	3.97	5.09	–	–
Simulation 6	1.53	2.84	4.17	–	–	–
Simulation 7	1.54	2.85	–	–	–	–
Experiment Feng et al. (1998)	–	4.18	5.80	6.85	6.95	6.90

Table 4
Predicted and experimental shear stress for AlON in uniaxial strain compression.

Simulation or experiment	τ [GPa]				
	$\frac{V}{V_0}=0.99$	$\frac{V}{V_0}=0.98$	$\frac{V}{V_0}=0.97$	$\frac{V}{V_0}=0.96$	$\frac{V}{V_0}=0.95$
Simulation 1	0.95	1.74	2.52	3.24	–
Simulation 2	0.93	1.73	2.48	3.19	3.85
Simulation 3	1.05	1.82	2.56	3.26	3.84
Simulation 4	0.91	1.70	2.45	3.20	–
Simulation 5	0.89	1.69	2.42	–	–
Simulation 6	0.92	1.77	2.60	3.44	–
Simulation 7	0.98	1.79	2.61	3.35	–
Experiment (Dandekar et al., 2007)	2.0	3.8	–	3.4	3.0

Table 5
Simulations reported in Tables 3 and 4.

Simulation	Load direction	Orientation	Elasticity
1	X	1	Nonlinear
2	X	2	Nonlinear
3	X	1	Linear
4	Y	1	Nonlinear
5	Y	2	Nonlinear
6	Y	1	Linear
7	Z	1	Nonlinear

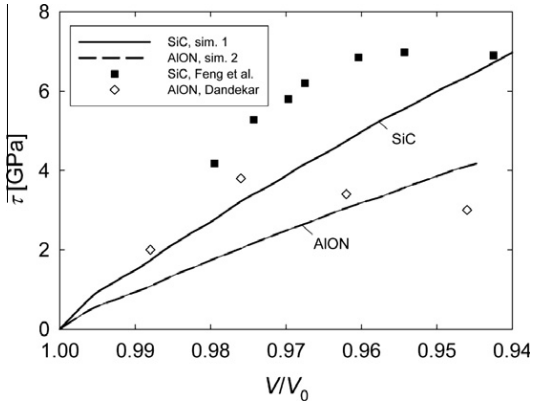

Fig. 6. Shear stress: present simulations (nonlinear elasticity and fracture) and experiments.

order of several percent. Linear elastic models do not always provide an increase in shear stress relative to complementary nonlinear elastic models, in contrast to axial stresses and pressures which are larger when nonlinear theory is used. Shear stresses from representative simulations are compared graphically with experimental data in Fig. 6.

4.2. Unconfined compression

Results for dynamic uniaxial stress loading are reported next. Let X denote the referential direction of loading, with Y and Z denoting orthogonal directions, and with a corner of the cubic specimen located initially at the origin $(X, Y, Z) = (0, 0, 0)$. Boundary conditions and nonzero initial conditions for unconfined compression in the X-direction are, respectively,

$$\begin{aligned} &v_x = -\dot{\epsilon}X \quad \text{along } X = L; \\ &v_x = 0 \quad \text{along } X = 0; \\ &\sigma_{ab}n_b = 0 \quad \text{along } Y, Z = 0, L; \end{aligned} \tag{31}$$

$$v_x(t = 0) = -\dot{\epsilon}X \leftrightarrow \partial_x v_x(t = 0) = -\dot{\epsilon}. \tag{32}$$

The imposed strain rate is $\dot{\epsilon} = 10^5$/s. Initial conditions (32) impose a uniform initial velocity gradient throughout the domain. Uniaxial stress simulations were also performed via loading in orthogonal Y and Z directions, with analogous boundary and initial conditions. Under these loading conditions, the average axial strain of the aggregate is $\Delta L/L_0 = \dot{\epsilon}t$, positive in compression. Fully free, as opposed to periodic, boundary conditions are applied to lateral faces of the microstructure.

Fig. 7 shows representative axial stress contours ($\sigma = -\sigma_{xx}$, positive in compression) in SiC (Fig. 7(a)) and AlON (Fig. 7(b)). In each case shown, a 50-grain microstructure is deformed to 2% strain, i.e., $\Delta L/L_0 = 0.02$ via compression along the X-direction. Stresses are somewhat higher in SiC than AlON as a result of the larger elastic

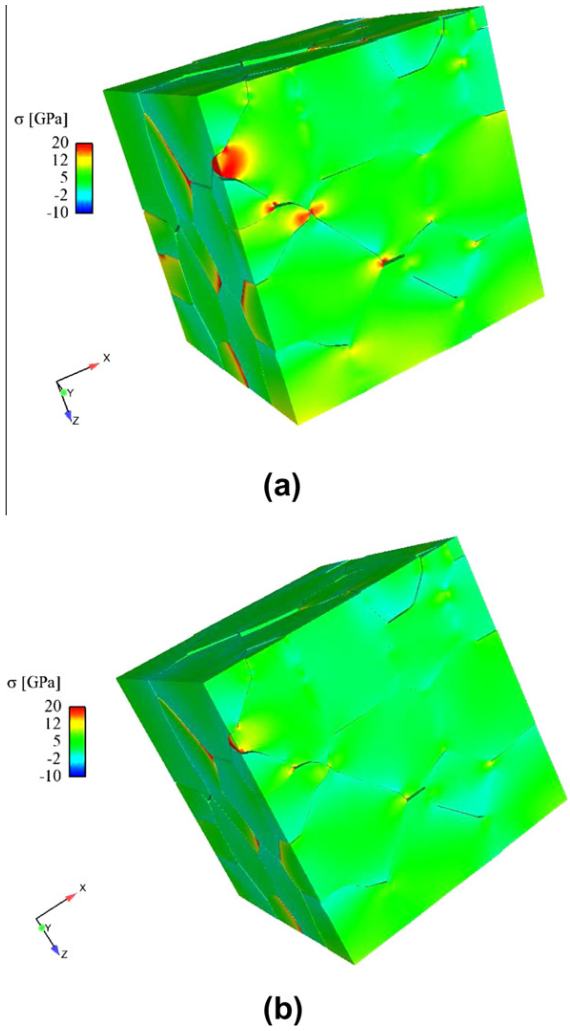

Fig. 7. Axial stress σ (positive in compression) for 50-grain microstructures subjected to unconfined axial strain of $\Delta L/L_0 = 0.02$: (a) SiC (b) AlON.

stiffness and higher fracture strength and toughness in the former (Tables 1 and 2). In each microstructure, cracks associated with axial splitting appear, as do sliding cracks associated with dilatation (i.e., expansion) in directions orthogonal to the loading direction. Fractures are more profuse, and stresses are significantly lower, than those observed in uniaxial strain compression (Section 4.1, Fig. 3).

Tables 6 and 7 show peak axial stress and corresponding failure strain data for SiC and AlON microstructures. Nonlinear elasticity has been used in obtaining all model results shown. Peak axial stress Σ^f is defined as the maximum value of average compressive stress Σ attained over the duration of an experiment/simulation prior to strain softening associated with damage/fracture, and peak strain ϵ^f is the corresponding average compressive strain, i.e., $\partial\Sigma/\partial(\Delta L/L_0) \approx 0$ at $\Delta L/L_0 = \epsilon^f$. Also shown for purposes of comparison are peak stress data from Kolsky bar experiments at strain rates on the order of 10^3/s (Pickup and Barker, 1997; Wang and Ramesh, 2004; Paliwal et al., 2008). Predicted failure stresses for SiC are smaller than experimental values (Pickup and Barker, 1997; Wang and Ramesh, 2004); furthermore, strain rates considered in the simulations are significantly higher (10^5/s), and brittle materials can exhibit an increase in peak compressive strength with increasing strain rate (Grady, 1998; Chen and Ravichandran, 2000). Predicted strengths for AlON are comparable to experimental values

Table 6
Peak axial stress and failure strain for unconfined compression, SiC.

Model/experiment	Load direction	Orientation	ϵ^f [%]	Σ^f [GPa]	Σ^f/t^c
Model	X	1	2.43	4.19	7.35
Model	Y	1	2.79	4.85	8.51
Model	Y	2	2.89	4.82	8.46
Model	Z	2	2.80	4.92	8.63
Experiment (Pickup and Barker, 1997)	–	–	–	6.72–8.17	
Experiment (Wang and Ramesh, 2004)	–	–	–	5.0–7.5	

Table 7
Peak axial stress and failure strain for unconfined compression, AlON.

Model/experiment	Load direction	Orientation	ϵ^f [%]	Σ^f [GPa]	Σ^f/t^c
Model	X	1	3.03	3.24	10.59
Model	X	2	3.00	3.13	10.22
Model	Y	1	2.89	3.59	11.73
Model	Z	1	3.42	3.76	12.28
Experiment (Paliwal et al., 2008)	–	–	–	3.0–4.0	

(Paliwal et al., 2008). Comparing the rightmost columns of Tables 6 and 7, it is clear that predicted unconfined compressive strengths are not directly proportional to prescribed cohesive strength t^c since the ratio Σ^f/t^c is significantly higher in AlON than in SiC for each reported simulation. Variations in predicted peak strength resulting from differences in lattice orientation (i.e., orientations 1 and 2) appear smaller than variations from differences in loading direction (i.e., X, Y, or Z).

4.3. Shear

Lastly, results for dynamic shear loading with and without superimposed compressive stress are reported. Let X denote the referential direction of loading, with Y and Z denoting orthogonal directions, and with a corner of the cubic specimen located initially at the origin $(X, Y, Z) = (0, 0, 0)$. Three kinds of boundary and initial conditions are considered: unconfined shear, confined shear, and shear+compression. Boundary conditions and nonzero initial conditions for unconfined shear in the X direction on the Y plane are, respectively,

$$\begin{aligned} &v_x = \dot\gamma Y \quad \text{along } Y = L, \quad v_x = v_y = v_z = 0 \quad \text{along } Y = 0; \\ &\sigma_{yy} n_y = 0 \quad \text{along } Y = L, \quad \sigma_{ab} n_b = 0 \quad \text{along } X, Z = 0, L; \end{aligned} \tag{33}$$

$$v_x(t=0) = \dot\gamma Y \leftrightarrow \partial_y v_x(t=0) = \dot\gamma. \tag{34}$$

The imposed shear strain rate is $\dot\gamma = 10^5$/s; note that this is equal to twice the imposed deformation rate $\frac{1}{2}(\partial_b v_a + \partial_a v_b)$. Initial conditions (34) impose a uniform initial velocity gradient throughout the domain. Numerous shear simulations were also performed via loading in forward and reverse directions on orthogonal Y and Z planes, providing up to twelve unconfined shear simulations (six off-diagonal components of $\partial_b v_a$ × two directions (positive and negative)) for each set of {microstructure, material, lattice orientation}. Under these loading conditions, the magnitude of average shear strain of the aggregate is $\gamma = \dot\gamma t$.

Boundary conditions and nonzero initial conditions for confined shear in the X direction on the Y plane are, respectively,

$$\begin{aligned} &v_x = \dot\gamma Y \quad \text{along } Y = L, \quad v_x = v_y = v_z = 0 \quad \text{along } Y = 0; \\ &v_y = 0 \quad \text{along } Y = L, \quad \sigma_{ab} n_b = 0 \quad \text{along } X, Z = 0, L; \end{aligned} \tag{35}$$

$$v_x(t=0) = \dot\gamma Y \leftrightarrow \partial_y v_x(t=0) = \dot\gamma. \tag{36}$$

Conditions (35) differ from those for unconfined compression (33) in only one respect: in the former, the plane on which shearing velocities are applied is prohibited from moving in a direction normal to the shearing direction. This results in an increase in compressive stress in the confined case, since the fixed upper boundary resists dilatation accompanying shear-induced fracture within the aggregate. Initial conditions are the same in either case. Again, particular loading planes and directions are varied among many simulations.

Boundary conditions and nonzero initial conditions for shear+compression in the X direction on the Y plane are, respectively,

$$\begin{aligned} &v_x = \dot\gamma Y \quad \text{along } Y = L, \quad v_x = v_y = v_z = 0 \quad \text{along } Y = 0; \\ &v_y = -\dot\gamma Y \quad \text{along } Y = L, \quad \sigma_{ab} n_b = 0 \quad \text{along } X, Z = 0, L; \end{aligned} \tag{37}$$

$$\begin{aligned} &v_x(t=0) = \dot\gamma Y \leftrightarrow \partial_y v_x(t=0) = \dot\gamma; \\ &v_y(t=0) = -\dot\gamma Y \leftrightarrow \partial_y v_y(t=0) = -\dot\gamma. \end{aligned} \tag{38}$$

Conditions (37) specify simultaneous shear and compression deformation, both at an imposed rate of $\dot\gamma = 10^5$/s. Initial conditions (38) provide for a corresponding uniform initial velocity gradient. Again, loading planes and directions are varied among many simulations. In all three cases listed above (unconfined shear, confined shear, and shear+compression), fully free, as opposed to periodic, boundary conditions are applied to lateral faces of the microstructure.

Shown in Fig. 8 are shear stress contours $\sigma = \sigma_{ab}$, where $\partial_b v_a$ is the corresponding component of the applied velocity gradient. The applied shear strain is $\gamma = 0.03$, and material properties are those of AlON. Results in Fig. 8(a) and (b) correspond to unconfined shear (33) and confined shear (35), respectively, of microstructure II. Notice that local stresses are larger in magnitude in the latter case, since the microstructure is unable to expand in the vertical direction to relieve pressure induced by dilatation. The higher pressure leads to an increase in shear stress for the confined condition. Results shown in Fig. 8(c) and (d) correspond to microstructure I (AlON) subjected to shear+compression loading via (37). Results in Fig. 8(d), wherein approximately half of the grains are removed from the image, show stresses in the interior of the microstructure whose exterior is shown in Fig. 8(c). Shear stress magnitudes are significantly greater for simultaneous shear and compression than for shear loading alone.

In all boundary and initial conditions considered in (33)–(38), the microstructure is free to expand or deform in lateral (as opposed to vertical) directions, as is clear from Fig. 8. Effects of restricting motion of the lateral faces are considered in Fig. 9, which shows average shear stress $\bar\tau$ for the same aggregate deformed according to confined shear conditions with and without restricting motion of lateral faces. Precisely, average shear stress $\bar\tau$ for the present loading conditions is computed analogously to (29):

$$\bar\tau = (1/A) \int_A \hat t^t \, dA, \tag{39}$$

where $\hat t^t$ is the component of traction acting in the direction of shear, on sheared surface (plane) with area A. The three curves in Fig. 9 all correspond to the same microstructure, loading plane and direction, and lattice orientation distribution, with nonlinear elastic properties for SiC. Fracture is suppressed (i.e., contact between all grains is rigid) for the stiffest case shown in Fig. 9, which has a slope of 191 GPa, very close to the Voigt-average shear modulus G listed in Table 1. This case corresponds to simple shear of an elastic polycrystalline aggregate. When internal fractures are permitted within the microstructure, but lateral boundaries are moved

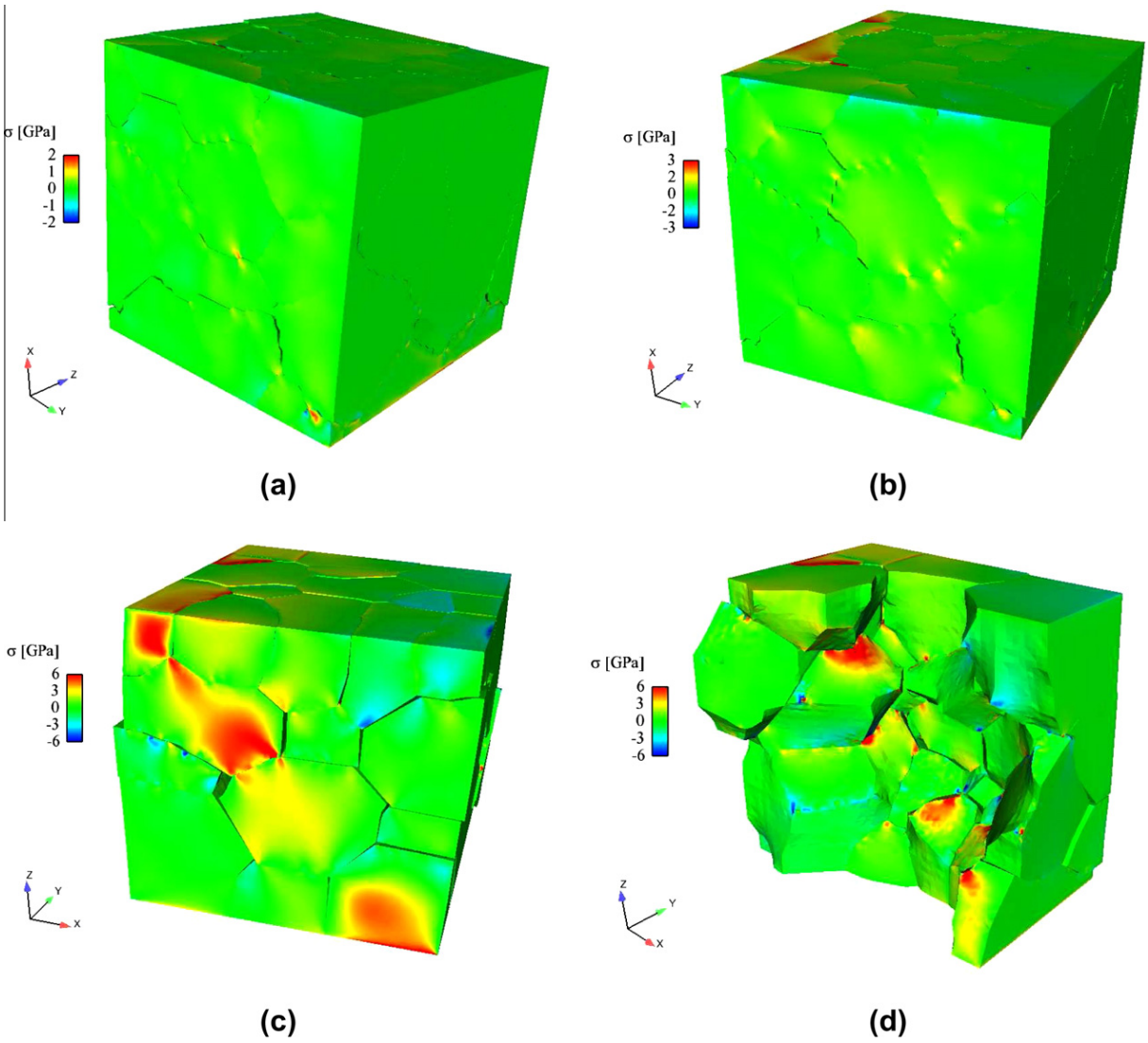

Fig. 8. Shear stress σ for AlON microstructures subjected to shear deformation $\gamma = 0.03$: (a) microstructure II, unconfined shear, nonzero $\partial_x v_y$ (b) microstructure II, confined shear, nonzero $\partial_x v_y$ (c) microstructure I, shear+compression, nonzero $\partial_z v_x + \partial_z v_z$ (d) microstructure I, shear+compression, some grains removed for viewing of specimen interior.

rigidly (i.e., in simple shear) and are prohibited from expanding to accommodate dilatation, the intermediate curve in Fig. 9 results. Note that the average shear stress for this case is lower than that for the case with no fracture at applied shear strain $\gamma \gtrsim 0.5\%$, since fracture and crack opening/sliding within the aggregate tends to reduce the overall stiffness of the aggregate. The lowest average shear stresses are exhibited by the unconfined case (i.e., free lateral faces).

Behavior of a polycrystalline aggregate embedded within a much larger sample of material would be expected to exhibit average shear stress behavior falling in between the two lower curves in Fig. 9, which represent Dirichlet and Neumann boundary conditions, respectively, on lateral faces. Periodic boundary conditions (Espinosa and Zavattieri, 2003a,b) would be expected to produce strength falling between these two curves, leading to a more realistic depiction of shearing behavior of a representative volume element of material embedded within a larger sample. However, uniaxial strain conditions for lateral confinement considered in Section 4.1 are deemed representative of plate impact experiments, as has been assumed in previous studies (Clayton, 2005b; Foulk and Vogler, 2010). And free boundary conditions considered

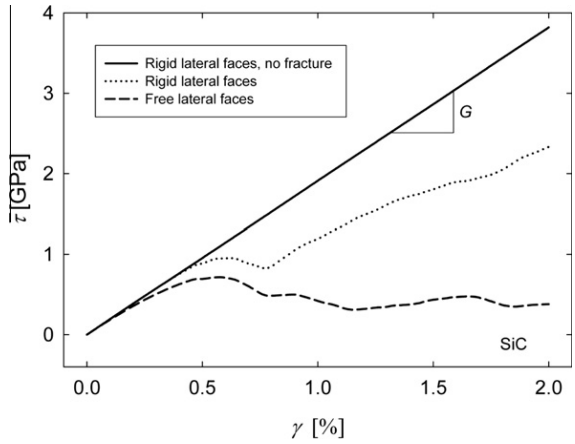

Fig. 9. Average shear stress versus applied shear strain for SiC microstructure I subjected to various lateral boundary conditions.

for unconfined compression in Section 4.2 are deemed more appropriate than periodic boundary conditions for modeling miniature dynamic compression experiments (Paliwal et al., 2008) wherein the actual size of the experimental sample is comparable to that of the simulated polycrystalline aggregate.

Weibull distributions are often used to characterize failure behavior of brittle solids, including polycrystalline ceramics (Warner et al., 2005; Brannon et al., 2007; Foulk and Vogler, 2010; Graham-Brady, 2010; Leavy et al., 2010). Let $\tau \geqslant 0$ denote an independent variable. A two-parameter Weibull distribution (Hayter, 1996) has a probability density function

$$\hat{f}(\tau) = m\sigma_0^{-m}\tau^{m-1}\exp[-(\tau/\sigma_0)^m], \tag{40}$$

and cumulative distribution function

$$f(\tau) = \int_0^\tau \hat{f}(x)dx = 1 - \exp[-(\tau/\sigma_0)^m], \tag{41}$$

where m is the Weibull modulus and σ_0 is a parameter with the same physical dimensions as τ. Analyzed in what follows next are statistics of failure for numerous simulations involving unconfined shear boundary conditions (33). The shear stress at failure (i.e., the shear strength) τ for a given simulation is defined as the peak stress at which $\partial\bar{\tau}/\partial\gamma = 0$. For simulation results analyzed here, the probability f of failure at or below a given shear stress τ is found by ordering the results of many simulations from lowest to highest shear strength and assigning the jth result in a series of n simulations a failure probability $f_j = \frac{1}{n}(j - \frac{1}{2})$ (Warner et al., 2005; Furnish et al., 2007). A plot of $\ln\{\ln[1/(1-f)]\}$ versus $\ln\tau$ exhibits slope m (the Weibull modulus). A "nominal strength" (Warner et al., 2005) for a series of simulations is calculated as $\sigma_0 = \exp(-b/m)$, where b is the vertical intercept of the linear fit to this plot, noting that $f(\sigma_0) = 1 - \exp(-1) \approx 0.632$. Recall that the higher the value of Weibull modulus m, the lower the variability or scatter in variable τ.

Weibull fits to unconfined strength data collected from many simulations of unconfined dynamic shear are shown in Fig. 10(a) for SiC and Fig. 10(b) for AlON. Data from several dozen simulations are considered in each case, incorporating various microstructures, random lattice orientation distributions, and loading directions. Fits to the data are constructed by considering results of each of microstructures I (50 grains) and II (126 grains) individually, as well as data from results of simulations on both microstructures taken together. For each material, microstructure I exhibits a higher Weibull modulus than microstructure II, corresponding to more uniform shear failure statistics. A reduction in Weibull modulus with increasing sample size has been noted elsewhere from static flexure and indentation experiments on SiC (Wereszczak et al., 2010). However, diametral compression data for SiC (Leavy et al., 2010) demonstrate an increasing Weibull modulus and decreasing median strength with increasing sample size. Comparing Fig. 10(a) and (b), predicted Weibull moduli for AlON microstructures are significantly lower that those for SiC.

Table 8 compares Weibull parameters from the present work with those obtained from other modeling (Foulk and Vogler, 2010) and experimental (Klein and Miller, 2001; Warner et al., 2005; Patel et al., 2006; Ray et al., 2007; Furnish et al., 2007; Wereszczak et al., 2010) studies. For the present modeling results, nominal strength σ_0 is substantially greater in SiC (0.52 GPa) than in AlON (0.35 GPa), as would be expected from the prescribed interfacial strengths in Table 2: $t^c_{\mathrm{SiC}}/t^c_{\mathrm{AlON}} \approx 1.9 > 0.52/0.35 \approx 1.5$. Nominal strength σ_0 does not vary appreciably between results for microstructures I and II, in contrast to Weibull modulus m. Weibull moduli computed for SiC in the present work are significantly larger than those observed in experiments (Ray et al., 2007; Furnish et al., 2007; Wereszczak et al., 2010). Note however that loading conditions considered elsewhere (shock loading, static bending, or static indentation) differ from those considered in the present simulations (dynamic unconfined shear). Furthermore, sample sizes considered in the present work are significantly smaller in terms of number of grains than specimens tested experimentally. Weibull moduli computed in the present work for AlON are closer to, but still generally larger than, those measured experimentally (Klein and Miller, 2001; Warner et al., 2005; Patel et al., 2006). It is emphasized that experimental data for Weibull parameters for both materials (SiC and AlON) vary significantly from study to study as a result of differences in material samples (e.g., different processing routes leading to variable defect content), experimental loading techniques, and specimen sizes. However, a general trend of lower nominal strength and lower Weibull modulus in AlON than in SiC is evident in the experimental values listed in Table 8; furthermore, this trend is qualitatively reflected by the present model predictions.

Table 9 shows peak shear strengths for various simulations involving different materials, microstructures, loading directions, and initial lattice orientation distributions. Unconfined boundary conditions correspond to (33); confined boundary conditions correspond to (35). Directions refer to shearing in positive (+) and negative (-) directions on the same plane of loading. The rightmost column of Table 9 lists the percentage difference in peak strength

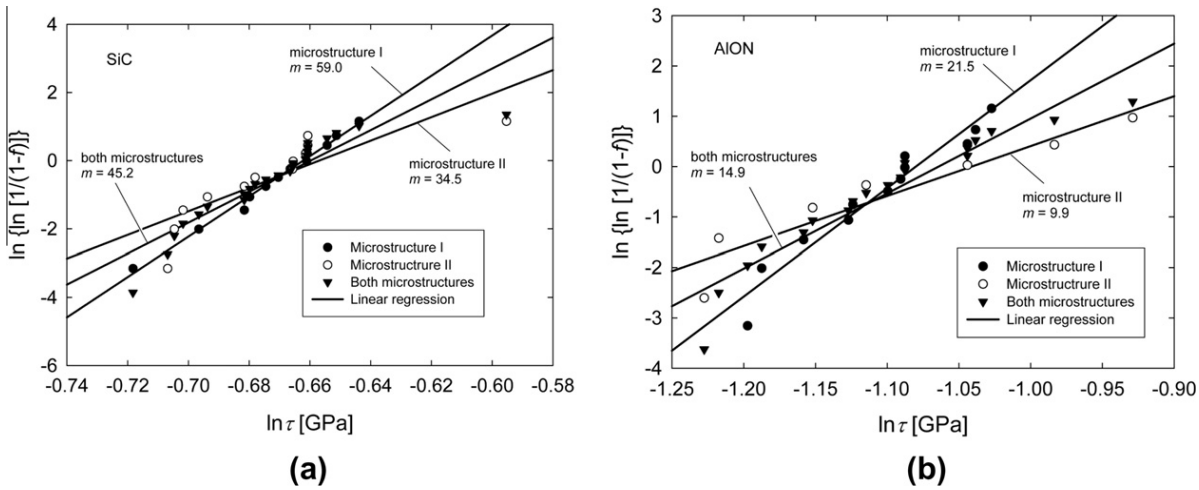

Fig. 10. Weibull fits to all relevant simulation results (multiple microstructures, grain orientations, and loading directions) for peak average unconfined shear strength: (a) SiC (b) AlON.

Table 8
Weibull parameters for SiC and AlON.

Model/experiment	Material	Microstructure	Strength	σ_0 [GPa]	m
Model (present)	SiC	I and II	Unconfined shear	0.517	45.2
Model (present)	SiC	I	Unconfined shear	0.516	59.0
Model (present)	SiC	II	Unconfined shear	0.518	34.5
Model (Foulk and Vogler, 2010)	SiC	–	Spall	11.6–12.3	12–18
Experiment (Ray et al., 2007)	SiC	–	Flexure	0.367–0.617	4.9–26.6
Experiment (Furnish et al., 2007)	SiC	–	HEL	10.23–10.33	14.4–29.7
Experiment (Wereszczak et al., 2010)	SiC	–	Indentation	0.876–2.652	13.9–20.1
Experiment (Wereszczak et al., 2010)	SiC	–	Flexure	0.268–0.776	6.6–12.2
Model (present)	AlON	I and II	Unconfined shear	0.345	14.9
Model (present)	AlON	I	Unconfined shear	0.340	21.5
Model (present)	AlON	II	Unconfined shear	0.353	9.9
Experiment (Klein and Miller, 2001)	AlON	–	Flexure	0.315	4.45
Experiment (Warner et al., 2005)	AlON	–	Flexure	0.288–0.812	2.9–26.3
Experiment (Patel et al., 2006)	AlON	–	Indentation	0.228	8.7

for the two lattice orientation sets considered on a given row, quantifying effects of elastic anisotropy. Specifically, this difference is computed as $2(\tau_1 - \tau_2)/(\tau_1 + \tau_2) \times 100\%$, where subscripts refer to orientation sets 1 and 2. Comparing results for SiC and AlON, it appears that anisotropy has a greater effect on shear strength in AlON than in SiC, especially for unconfined boundary conditions. Recall from Table 2 that the Zener anisotropy factor deviates more from unity for AlON (2.38) than SiC (0.83). However, SiC is hexagonal, and additional anisotropy results from $C_{13} \neq C_{12}$ and $C_{33} \neq C_{11}$. Increased variability due to anisotropy would contribute to a lower predicted Weibull modulus in AlON compared to that of SiC. Differences in peak strength due to differences in loading direction (+ versus -) are also generally larger in AlON than in SiC. Because of its lower prescribed cohesive strength and fracture energy, AlON may be more sensitive than SiC to local variations in microstructure geometry (e.g., grain boundary facets oriented favorably for fracture or stress concentrations at triple points) that would lead to fracture intitiation and subsequent failure. Variablitity due to loading direction (i.e., grain morphology) tends to exceed that due to elastic anisotropy. When the material is loaded in forward and reverse directions, different fracture sites can activate. In all simulations, confinement leads to an increase in shear strength relative to the corresponding unconfined case. Normal stress Σ on the confined surface does contribute to computed average shear strength:

$$\tau = \sqrt{J_2} = [(3\bar{\tau}^2 + \Sigma^2)/3]^{1/2}, \tag{42}$$

where J_2 is the second invariant of the average deviatoric shear stress. For unconfined shear, $\Sigma = 0$ and $\tau = \bar{\tau}$.

4.4. Summary and discussion

Considered collectively, results presented in Sections 4.1, 4.2 and 4.3 demonstrate increasing shear strength with increasing average pressure for both SiC and AlON polycrystals. Relationships between shear strength $\tau = \sqrt{J_2}$ and average pressure P are shown in Fig. 11(a) for SiC and (b) for AlON. Strength corresponds to the peak value of average shear stress defined in (42) for unconfined compression (i.e., $\tau = \Sigma/\sqrt{3}$ for uniaxial stress compression), or for shear loading with or without confinement or superimposed compression. For uniaxial strain loading, following previous models (Lee et al., 2005; Brannon et al., 2007; Leavy et al., 2010), the shear strength from (30), multiplied by $2/\sqrt{3}$ to be consistent with $\sqrt{J_2}$, taken at the compressive strain (i.e., current volume) corresponding to the Hugoniot elastic limit (HEL) is used: $V/V_0 = 0.975$ for SiC (Clayton, 2010c; Feng et al., 1998) and $V/V_0 = 0.970$ for AlON (Clayton, 2011a; Dandekar et al., 2007). Average pressure is always computed via the second of (30) and vanishes for unconfined shear loading. The horizontal intercept at null shear strength (i.e., the hydrostatic tensile strength) follows directly from the prescribed cohesive strength of each material (Table 1) as $-t^c/3$.

Also shown in Fig. 11 are analytical fits (solid lines) to the present model results (SiC and AlON) and fits to experimental data (Lee et al., 2005) (SiC only). Comprehensive shear strength versus pressure data (experimental or numerical) for AlON have not been published elsewhere, to the authors' knowledge. Two functional forms are shown. The first, which has been used elsewhere for SiC (Lee et al., 2005), follows from a cap plasticity model formulated in the context of geomechanics (Sandler and Rubin, 1979):

Table 9
Representative peak shear strengths for SiC and AlON: various microstructures, loading directions, and lattice orientation distributions.

Material	Micro-	Boundary Condition	Loading Direction	τ [GPa] Orientation 1	τ [GPa] Orientation 2	Difference [%]
SiC	I	Unconfined	+	0.521	0.525	0.8
SiC	I	Unconfined	–	0.514	0.516	0.4
SiC	I	Confined	+	0.715	0.713	0.3
SiC	I	Confined	–	0.696	0.704	1.1
SiC	II	Unconfined	+	0.506	0.500	1.2
SiC	II	Unconfined	–	0.496	0.493	0.6
SiC	II	Confined	+	0.643	0.630	2.0
SiC	II	Confined	–	0.636	0.631	0.8
AlON	I	Unconfined	+	0.314	0.333	5.9
AlON	I	Unconfined	–	0.352	0.302	15.3
AlON	I	Confined	+	0.432	0.416	3.8
AlON	I	Confined	–	0.472	0.475	0.6
AlON	II	Unconfined	+	0.325	0.395	19.4
AlON	II	Confined	+	0.402	0.407	1.2

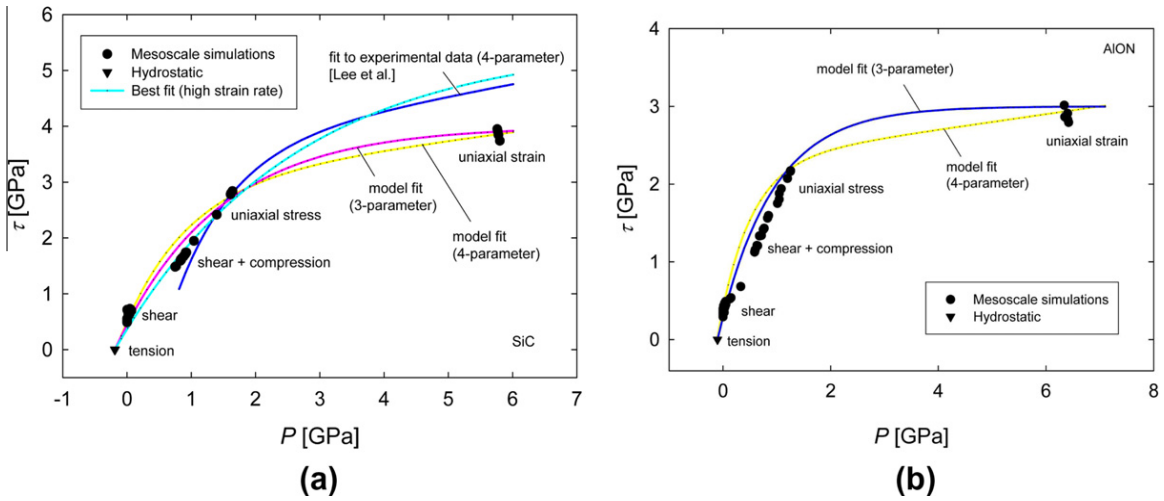

Fig. 11. Average shear strength versus average pressure for all relevant simulation results (multiple microstructures, grain orientation distributions, loading directions, and confinement conditions): (a) SiC (b) AlON.

$$\tau = a_1 - a_2 \exp(-a_3 P) + a_4 P, \tag{43}$$

where a_1, a_2, a_3, and a_4 are constants. Notice that the constants are labeled slightly differently here than in Lee et al. (2005); all constants in (43) are positive in sign and P is positive in compression. The second follows from a continuum damage mechanics model used for ceramics under impact loading (Leavy et al., 2010):

$$\tau = b_1\{1 - \exp[-(b_2/b_1)(b_3 + P)]\}, \tag{44}$$

where b_1, b_2, and b_3 are constants. Parameters for each fit are listed in Table 10.

First consider numerical data from the present simulations. In each material, the increase in shear strength with compressive pressure or confinement is evident. Previous models (Brannon et al., 2007, 2009; Leavy et al., 2010) have assumed that variability in strength decreases with an increase in pressure. This phenomenon is not apparent from the present results. Percentage-wise, differences in strength from simulation to simulation are of the same order of magnitude for unconfined and confined loading, as is evident from Tables 3, 4, and 9. Overall, the shear stiffness of SiC is greater than that of AlON because of the greater prescribed elastic stiffness (e.g., second-order elastic constants), fracture strength, and fracture energy in the former. The analytical fit to experimental results for SiC (Lee et al., 2005) exhibits higher strength than the present model results at high pressures and lower strength than the present results at low pressures; however, the fit to experimental results is valid only for the pressure regime shown and does not extrapolate correctly to lower compressive pressures or the tensile regime. Also shown in Fig. 11(a) is a "best fit" to combined experimental and numerical data deemed most appropriate for dynamic behavior of SiC over the entire pressure regime shown.

Table 10
Parameters for pressure-dependent strength models of SiC and AlON.

Parameter	SiC (simulation)	SiC (Lee et al., 2005)	SiC (best fit)	AlON (simulation)
a_1 [GPa]	3.0	3.5	–	2.3
a_2 [GPa]	2.5	6.3	–	1.9
a_3 [1/GPa]	1.0	1.1	–	1.7
a_4	0.15	0.21	–	0.1
b_1 [GPa]	4.0	–	5.5	3.0
b_2	2.5	–	2.0	3.0
b_3 [GPa]	0.19	–	0.19	0.10

Table 11 summarizes pressure-strength behavior for SiC obtained from various models and experiments. At higher pressures, mesoscale simulation data fit to (44) provides a lower strength than other models and plate impact experiments. The "best fit" to (44) matches strength data reported by (Lee et al., 2005, p. 25) at $P = 10$ GPa but gives a lower shear strength than that reported in Feng et al. (1998). The "JH-1" model (Holmquist and Johnson, 2002) provides stiffer shear strength versus pressure behavior than the present model fits when the ceramic is considered intact, but much lower strength when the ceramic has "failed" due to plastic strain accumulation.

Parameters listed in Tables 8 and 10 can be used directly in macroscopic models of inelasticity and failure of ceramic materials incorporating Weibull statistics and pressure-dependent shear strength (Brannon et al., 2007, 2009; Leavy et al., 2010). The present results may be particularly valuable for AlON, for which experimental data (statistical and pressure-strength) are not as readily available. The present modeling effort considers sample sizes (1 mm^3, ~100 grains) commensurate with finite element sizes used in macroscopic applications (Brannon et al., 2007; Leavy et al., 2010). Furthermore, strain rates considered are applied uniformly to the microstructure through appropriate boundary conditions and initial conditions on the velocity gradient, and are of

Table 11
Strength ($\tau = \sqrt{J_2}$) versus pressure (P or mean stress) for SiC.

Model or experiment	Loading	P [GPa]	τ [GPa]
Mesoscale simulation (Eq. (44))	Uniaxial strain 10^5/s	1.0	2.1
		5.0	3.8
		10.0	4.0
Best fit (Eq. (44))	Various	1.0	2.0
		5.0	4.7
		10.0	5.4
JH-1 intact (Holmquist and Johnson, 2002)	Uniaxial strain 10^5/s	1.0	2.4
		5.0	5.6
		10.0	7.8
JH-1 failed (Holmquist and Johnson, 2002)	Uniaxial strain 10^5/s	$\geqslant 3.3$	0.8
Experiment (Feng et al., 1998)	Plate impact	4.6	4.8
		5.5	5.2
		9.7	7.9
Experiment (Lee et al., 2005)	Plate impact	10.0	5.4

magnitude pertinent to ballistic events (10^5/s). This is in contrast to static data (Lee et al., 2005), extrapolated to the dynamic regime, often used to parameterize such models at lower confining pressures in the absence of very high-rate data (Brannon et al., 2007, 2009; Leavy et al., 2010). Simulation results may also be used to inform macroscopic models explicitly considering crack opening displacements in the context of large deformation kinematics (Clayton and McDowell, 2003, 2004; Clayton, 2005a, 2010a); such an effort may be pursued in future work. The present results suggest two features of current macroscopic ceramic models that warrant further consideration and possible refinement: (i) possible size dependence of the Weibull modulus and (ii) statistical variability in shear strength at various pressures and loading rates. Existing models (Brannon et al., 2007, 2009; Leavy et al., 2010) consider a constant Weibull modulus for hydrostatic tensile strength and assume reduced variability in strength at high pressures (e.g., in the regime of plate impact or uniaxial strain experiments).

Predictions of the present work follow from a number of modeling assumptions. Possible limitations of the present modeling effort are enumerated below:

1. Grain structures considered are synthetic, with random initial lattice orientation distributions used to specify anisotropic elastic constants. Greater physical realism would be attained from finite element meshes of microstructures obtained from sectioned material samples, with intial lattice orientation distributions obtained from EBSD measurements, for example (Brahme et al., 2006; Rollett et al., 2007). In particular, SiC-N can often exhibit relatively elongated grains (Lee et al., 2005; Ray et al., 2007; Vargas-Gonzalez et al., 2010), whereas AlON often exhibits relatively equiaxed grains (Corbin, 1989; McCauley et al., 2009; Guo et al., 2011).
2. Dislocation-mediated plasticity and twinning are not considered. When confining pressures and shear stresses are large, fracture may be suppressed and dislocation motion may occur in ceramics. In hexagonal polytypes of SiC, partial dislocation motion on basal planes and associated stacking fault propagation are thought to be the prominent mode of plastic deformation (Zhang et al., 2005b,a; Clayton, 2010c). In AlON, dislocation slip and twinning on octahedral planes has been observed in experiments (Paliwal et al., 2008; McCauley et al., 2009) and modeled with crystal plasticity theory (Gazonas et al., 2010; Clayton, 2011a).
3. Significant uncertainty exists for some elastic properties. Complete second-order elastic constants have been measured for SiC (Kamitani et al., 1997). The remaining elastic properties listed in Table 1 are theoretical predictions. Pressure dependencies of second-order elastic coefficients of SiC follow from atomic modeling (Davydov, 2004). Anisotropic second-order elastic constants for AlON have been computed using first principles (Gazonas et al., 2010), as have pressure dependencies of second-order elastic coefficients (Batyrev et al., 2011). Recent indentation experiments suggest that AlON may be highly elastically anisotropic (Guo et al., 2011), in qualitative agreement with anisotropic constants used in the present work but contradicting previous work wherein nearly isotropic elastic constants were used (Clayton, 2011a).
4. Uniform cohesive properties (i.e., fracture strength and fracture energy) are assigned to all grain boundaries in a given microstructure. In real ceramic polycrystals, variability in fracture properties may arise from voids, inclusions, and secondary phases, though in some cases secondary phases may be incorporated deliberately to improve fracture toughness (Faber and Evans, 1983; Shih et al., 1998; Vargas-Gonzalez et al., 2010). Grain boundary misorientation may also influence local fracture properties. Highly non-uniform grain boundary properties would be expected to result in greater variability in predicted failure statistics, e.g., lower Weibull moduli. In principle, grain boundary strengths could be seeded to enable simulation results to match experimental failure statistics. However, for statistics obtained from numerical simulations to be labeled as truly predictive, input parameters for mesoscale models should be obtained from independent experiments that measure local property distributions, or from atomic theory (Kohyama, 1999), rather than calibrated to match macroscopic failure data.
5. Contact is assumed frictionless between grain boundary facets. Some sliding friction might be expected between failed surfaces, as has been considered in previous models (Kraft and Molinari, 2008; Kraft et al., 2008). Incorporation of frictional sliding would presumably increase predicted shear strengths of polycrystalline aggregates, especially at higher confining pressures. In particular, omission of contact friction may, at least partially, explain the lower compressive and shear stresses predicted for SiC microstructures in the present simulations relative to corresponding experimental data.
6. Porosity is not considered. Polycrystalline ceramics are not fully dense, with measured porosities in SiC and AlON on the order of one to several percent (Graham et al., 1988; Lee et al., 2005; Dandekar et al., 2007). Pore collapse can influence the high pressure response of ceramics and geologic solids, e.g., resulting in increased compressibility relative to a fully dense material (Clayton, 2008, 2011a).
7. Transgranular failures, i.e., cleavage fractures, are not addressed. Failure in SiC-N is predominantly intergranular (Faber and Evans, 1983; Shih et al., 1998; Lee et al., 2005), although transgranular fractures are observed to a lesser extent (Ray et al., 2007). Transgranular fracture has been observed in AlON deformed at high rates (Paliwal et al., 2008; McCauley et al., 2009) and in static indentation experiments (Guo et al., 2011).
8. Adiabatic conditions are assumed, with isentropic elastic behavior used for single crystals within each microstructure. In real materials, plastic deformation, twinning, pore collapse, and frictional sliding at fractured interfaces could all contribute to dissipation (i.e., entropy production) and temperature rise at high rates of loading. If such effects are significant, consideration of thermal expansion, temperature dependent elastic coefficients, and temperature dependent cohesive properties (Clayton, 2005b) may be warranted.
9. Boundary and initial conditions used in simulations may deviate from those encountered in experiments to which some results have been compared. Specifically, the present uniaxial strain simulations assign homogeneous compression, omitting the shock process that occurs in plate impact tests. The present shear and shear+compression simulations assign free conditions on lateral faces; periodic boundary conditions might be expected to offer a more realistic representation of bulk material behavior and provide somewhat greater strength and stiffness.

In the context of the above limitations, the present results provide a basis for comparison with future work in which more physical details can be incorporated, e.g., reconstructed actual microstructures, dislocations, twins, initial defect distributions, and transgranular fracture.

5. Conclusions

Numerous three-dimensional finite element simulations of dynamic deformation and fracture of polcrystalline ceramic microstructures have been conducted. Uniaxial strain compression, unconfined compression, and shear loading (with and without

confinement) have been considered. Single crystal deformations have been modeled using nonlinear anisotropic hyperelasticity. Intergranular fractures have been modeled using cohesive zone theory with fracture strength and fracture energy obtained from macroscopic flexure data. Properties are representative of SiC and AlON. Various microstructures, lattice orientation distributions, and loading directions have been considered. Failure statistics have been analyzed.

Results obtained provide new insight into dynamic behavior of ceramic polycrystals for small specimen sizes and loading conditions (e.g., uniform velocity gradient boundary and initial conditions at very high strain rates) not accessible through traditional experiments such as plate impact-driven shock compression or Kolsky bar compression. Key findings are summarized as follows:

- Shear strength of polycrystalline aggregates increases with confining pressure in both materials, in qualitative agreement with experimentally observed trends for brittle solids. Confinement inhibits dilatation associated with interfacial sliding among misaligned grains, leading to an increase in shear stress necessary for mode II crack propagation. Analytical fits to pressure-strength data have been developed for use in macroscopic models of inelasticity in SiC and AlON ceramics.
- For uniaxial strain compression, predicted average axial stresses agree favorably with experimental plate impact data on larger specimens of AlON, but are lower than experimental values for SiC by up to 10–20%. Predicted average shear stresses in both materials are in close agreement with experimental values at higher pressures (e.g., at 5% volumetric compression), but are lower than experimental values at lower pressures.
- In both materials, the predicted Weibull modulus for average unconfined shear strength tends to decrease with an increase in number of grains contained in the microstructure, in qualitative agreement with some experimental observations of decreasing Weibull modulus with increasing sample size.
- Predicted Weibull parameters for shear strength are smaller for AlON than SiC, reflecting lower mean strength and greater variability in the former, in qualitative agreement with experiments. It is suspected that the lower prescribed cohesive strength and toughness for AlON contribute to an increased sensitivity to fracture initiation at interfaces or triple junctions most favorably oriented for fracture.
- Shear failure behavior of AlON appears more sensitive to initial lattice orientation than corresponding behavior of SiC microstructures with the same grain morphology, suggesting a greater sensitivity to elastic anisotropy in the former.

The above conclusions follow from analysis of numerical simulations incorporating idealized microstructures and idealized fracture behavior, without consideration of defects such as pre-existing flaws, voids, inclusions, dislocations, or deformation twins. Thus, the present work should be viewed as a reference against which future studies incorporating such defects can be compared.

Acknowledgements

Prof. A.D. Rollett's research group (Carnegie Mellon University), supported in part by the PETTT program, is thanked for supplying several surface meshes (STL files) of polycrystalline microstructures used in this study.

References

Batyrev, I., McCauley, J., Rice, B., Gazonas, G., Oganov, A., 2011. Atomic structure and elastic properties at high pressure of aluminum oxynitride in cubic phase. In: APS March Meeting. Bulletin of the American Physical Society, Dallas TX.

Brahme, A., Alvi, M., Saylor, D., Fridy, J., Rollett, A., 2006. 3D reconstruction of microstructure in a commercial purity aluminum. Scripta Mater. 55, 75–80.

Brannon, R., Wells, J., Strack, O., 2007. Validating theories for brittle damage. Met. Mater. Trans. A 38, 2861–2868.

Brannon, R., Fossum, A., Strack, O., 2009. Kayenta: theory and user's guide, Technical Report SAND2009-2282, Sandia National Laboratories, Albuquerque NM.

Cazamias, J., Fiske, P., Bless, S., 2001. Shock properties of AlON. In: Staudhammer, K., Murr, L., Meyers, M. (Eds.), Fundamental Issues and Applications of Shock-Wave and High-Strain-Rate Phenomena. Elsevier, New York, pp. 181–188.

Chen, W., Ravichandran, G., 2000. Failure mode transition in ceramics under dynamic multiaxial compression. Int. J. Fracture 101, 141–159.

Clayton, J., 2005a. Dynamic plasticity and fracture in high density polycrystals: constitutive modeling and numerical simulation. J. Mech. Phys. Solids 53, 261–301.

Clayton, J., 2005b. Modeling dynamic plasticity and spall fracture in high density polycrystalline alloys. Int. J. Solids Struct. 42, 4613–4640.

Clayton, J., 2006a. Continuum multiscale modeling of finite deformation plasticity and anisotropic damage in polycrystals. Theor. Appl. Fract. Mech. 45, 163–185.

Clayton, J., 2006b. Plasticity and spall in high density polycrystals: modeling and simulation. In: Furnish, M., Elert, M., Russell, T., White, C. (Eds.), Shock Compression of Condensed Matter Conference Proceedings. AIP, pp. 311–314.

Clayton, J., 2008. A model for deformation and fragmentation in crushable brittle solids. Int. J. Impact Eng. 35, 269–289.

Clayton, J., 2009a. A continuum description of nonlinear elasticity, slip, and twinning, with application to sapphire. Proc. R. Soc. Lond. A 465, 307–334.

Clayton, J., 2009b. Modeling effects of crystalline microstructure, energy storage mechanisms, and residual volume changes on penetration resistance of precipitate-hardened aluminum alloys. Compos. B Eng. 40, 443–450.

Clayton, J., 2010a. Deformation, fracture, and fragmentation in brittle geologic solids. Int. J. Fracture 163, 151–172.

Clayton, J., 2010b. Modeling finite deformations in trigonal ceramic crystals with lattice defects. Int. J. Plasticity 26, 1357–1386.

Clayton, J., 2010c. Modeling nonlinear electromechanical behavior of shocked silicon carbide. J. Appl. Phys. 107, 013520.

Clayton, J., 2011a. A nonlinear thermomechanical model of spinel ceramics applied to aluminum oxynitride (AlON). J. Appl. Mech. 78, 011013.

Clayton, J., 2011b. Nonlinear Mechanics of Crystals. Springer, Dordrecht.

Clayton, J., McDowell, D., 2003. Finite polycrystalline elastoplasticity and damage: multiscale kinematics. Int. J. Solids Struct. 40, 5669–5688.

Clayton, J., McDowell, D., 2004. Homogenized finite elastoplasticity and damage: theory and computations. Mech. Mater. 36, 799–824.

Corbin, N., 1989. Aluminum oxynitride spinel: a review. J. Euro. Ceram. Soc. 5, 143–154.

Curran, D., Seaman, L., Cooper, T., Shockey, D., 1993. Micromechanical model for comminution and granular flow of brittle material under high strain rate application to penetration of ceramic targets. Int. J. Impact Eng. 13, 53–83.

Dandekar, D., Bartowski, P., 2001. Spall strengths of silicon carbide under shock loading. In: Staudhammer, K., Murr, L., Meyers, M. (Eds.), Fundamental Issues and Applications of Shock-Wave and High-Strain-Rate Phenomena. Elsevier, New York, pp. 71–77.

Dandekar, D., Vaughan, B., Proud, W., 2007. Shear strength of aluminum oxynitride. In: Elert, M., Furnish, M., Chau, R., Holmes, N., Nguyen, J. (Eds.), Shock Compression of Condensed Matter Conference Proceedings. AIP, pp. 505–508.

Davydov, S., 2004. Effect of pressure on the elastic properties of silicon carbide. Phys. Solid State 46, 1200–1205.

Espinosa, H., Zavattieri, P., 2003a. A grain level model for the study of failure initiation and evolution in polycrystalline brittle materials Part I: Theory and numerical implementation. Mech. Mater. 35, 333–364.

Espinosa, H., Zavattieri, P., 2003b. A grain level model for the study of failure initiation and evolution in polycrystalline brittle materials Part II: Numerical examples. Mech. Mater. 35, 365–394.

Faber, K., Evans, A., 1983. Intergranular crack-deflection toughening in silicon carbide. J. Amer. Ceram. Soc. 66, C94–C96.

Feng, R., Raiser, G., Gupta, Y., 1998. Material strength and inelastic deformation of silicon carbide under shock wave compression. J. Appl. Phys. 83, 79–86.

Foulk, J., Vogler, T., 2010. A grain-scale study of spall in brittle materials. Int. J. Fracture 163, 225–242.

Furnish, M., Vogler, T., Alexander, C., Reinhart, W., Trott, W., Chhabildas, L., 2007. Statistics of the Hugoniot elastic limit from line VISAR. In: Elert, M., Furnish, M., Chau, R., Holmes, N., Nguyen, J. (Eds.), Shock Compression of Condensed Matter Conference Proceedings. AIP, pp. 521–524.

Gailly, B., Espinosa, H., 2002. Modelling of failure mode transition in ballistic penetration with a continuum model describing microcracking and flow of pulverized media. Int. J. Numer. Methods Eng. 54, 365–398.

Gazonas, G., McCauley, J., Kraft, R., Love, B., Clayton, J., Casem, D., Rice, B., Batyrev, I., Weingarten, N., Schuster, B., 2010. Multiscale modeling of armor ceramics: focus on AlON. In: Proceedings 27th Army Science Conference, Orlando FL.

Grady, D., 1998. Shock-wave compression of brittle solids. Mech. Mater. 29, 181–203.

Graham-Brady, L., 2010. Statistical characterization of meso-scale uniaxial compressive strength in brittle materials with randomly occurring flaws. Int. J. Solids Struct. 47, 2398–2413.

Graham, E., Munly, W., McCauley, J., Corbin, N., 1988. Elastic properties of polycrystalline aluminum oxynitride spinel and their dependence on pressure, temperature, and composition. J. Amer. Ceram. Soc. 71, 807–812.

Guo, J., Wang, K., Fujita, T., McCauley, J., Singh, J., Chen, M., 2011. Nanoindentation characterization of deformation and failure of aluminum oxynitride. Acta Mater., 1671–1679.

Hankey, R., Schuele, D., 1970. Third-order elastic constants of Al_2O_3. J. Acoust. Soc. Amer. 48, 190–202.
Hayter, A., 1996. Probability and Statistics for Engineers and Scientists. PWS Publishing Co., Boston.
Heard, H., Cline, C., 1980. Mechanical behaviour of polycrystalline BeO, Al_2O_3 and AlN at high pressure. J. Mater. Sci. 15, 1889–1897.
Holmquist, T., Johnson, G., 2002. Response of silicon carbide to high velocity impact. J. Appl. Phys. 91, 5858–5866.
Jung, J., 2010. Presto 4.16 user's guide. Tech. Rep. SAND2010-3112, Sandia National Laboratories, Albuquerque NM.
Kamitani, K., Grimsditch, M., Nipko, J., Loong, C., Okada, M., Kimura, I., 1997. The elastic constants of silicon carbide: a Brillouin-scattering study of 4H and 6H SiC single crystals. J. Appl. Phys. 82, 3152–3154.
Klein, C., Miller, R., 2001. How to do a Weibull statistical analysis of flexural strength data: application to AlON, diamond, zinc selenide, and zinc sulfide. In: Proceedings of SPIE, vol. 4375, Orlando FL, pp. 241–257.
Kohyama, M., 1999. Tensile strength and fracture of a tilt grain boundary in cubic SiC: a first-principles study. Phil. Mag. Lett. 79, 659–672.
Kraft, R., Molinari, J., 2008. A statistical investigation of the effects of grain boundary properties on transgranular fracture. Acta Mater. 56, 4739–4749.
Kraft, R., Molinari, J., Ramesh, K., Warner, D., 2008. Computational micromechanics of dynamic compressive loading of a brittle polycrystalline material using a distribution of grain boundary properties. J. Mech. Phys. Solids 56, 2618–2641.
Kraft, R., Batyrev, I., Lee, S., Rollett, A., Rice, B., 2010. Multiscale modeling of armor ceramics. In: Swab, J. (Ed.), Ceramic Engineeering Science. Proceedings of Advanced Ceramic Armor VI. Wiley, Hoboken NJ, pp. 143–158.
LaSalvia, J., Campbell, J., Swab, J., McCauley, J., 2010. Beyond hardness: ceramics and ceramic-based composites for protection. JOM 62, 16–23.
Leavy, R., Brannon, R., Strack, O., 2010. The use of sphere indentation experiments to characterize ceramic damage models. Int. J. Appl. Ceram. Tech. 7, 606–615.
Lee, M., Brannon, R., Bronowski, D., 2005. Uniaxial and triaxial compression tests of silicon carbide ceramics under quasi-static loading condition. Tech. Rep. SAND2004-6005, Sandia National Laboratories, Albuquerque NM.
McCauley, J., Patel, P., Chen, M., Gilde, G., Strassburger, E., Paliwal, B., Ramesh, K., Dandekar, D., 2009. AlON: a brief history of its emergence and evolution. J. Euro. Ceram. Soc. 29, 223–236.
Paliwal, B., Ramesh, K., McCauley, J., Chen, M., 2008. Dynamic compressive failure of AlON under controlled planar confinement. J. Amer. Ceram. Soc. 91, 3619–3629.
Patel, P., Swab, J., Staley, M., Quinn, G., 2006. Indentation size effect (ISE) of transparent AlON and $MgAl_2O_4$. Tech. Rep. ARL-TR-3852, US Army Research Laboratory, Aberdeen Proving Ground MD.
Pickup, I., Barker, A., 1997. Damage kinetics in silicon carbide. In: Schmidt, S., Dandekar, D., Forbes, J. (Eds.), Shock Compression of Condensed Matter Conference Proceedings. AIP, pp. 513–516.
Ray, D., Flinders, R., Anderson, A., Cutler, R., Campbell, J., Adams, J., 2007. Effect of microstructure and mechanical properties on the ballistic performance of SiC-based ceramics. In: Franks, L. (Ed.), Ceramic Engineeering Science. Proceedings of Advanced Ceramic Armor II. Wiley, Hoboken NJ, pp. 85–96.
Rice, R., Wu, C., Boichelt, F., 1994. Hardness-grain-size relations in ceramics. J. Amer. Ceram. Soc. 77, 2539–2553.
Rollett, A., Manohar, P., 2004. The Monte Carlo method. In: Raabe, D., Roters, F., Barlat, F., Chen, L.-Q. (Eds.), Continuum Scale Simulation of Engineering Materials. Wiley-VCH, Weinheim Germany, pp. 77–114.
Rollett, A., Lee, S., Campman, R., Rohrer, G., 2007. Three-dimensional characterization of microstructure by electron back-scatter diffraction. Ann. Rev. Mater. Res. 37, 627–658.
Sandler, I., Rubin, D., 1979. An algorithm and a modular subroutine for the cap model. Int. J. Numer. Anal. Methods Geomech. 3, 173–186.
Shih, C., Nesterenko, V., Meyers, M., 1998. High-strain-rate deformation and comminution of silicon carbide. J. Appl. Phys. 83, 4660–4671.
Shockey, D., Marchand, A., Skaggs, S., Cort, G., Burkett, M., Parker, R., 1990. Failure phenomenology of confined ceramic targets and impacting rods. Int. J. Impact Eng. 9, 263–275.
Sternberg, J., 1989. Material properties determining the resistance of ceramics to high velocity penetration. J. Appl. Phys. 65, 3417–3424.
Thurston, R., 1974. Waves in Solids. In: Truesdell, C. (Ed.), Handbuch der Physik VIA/4. Springer-Verlag, Berlin, pp. 109–308.
Thurston, R., McSkimin, H., Andreatch, P., 1966. Third-order elastic coefficients of quartz. J. Appl. Phys. 37, 267–275.
Vargas-Gonzalez, L., Speyer, R., Campbell, J., 2010. Flexural strength, fracture toughness, and hardness of silicon carbide and boron carbide armor ceramics. Int. J. Appl. Ceram. Tech. 7, 643–651.
Vaughan, B., Proud, W., Field, J., 2001. Shock properties of aluminum oxynitride. Tech. Rep. SP-1092, Cavendish Laboratory, Cambridge UK.
Vogler, T., Clayton, J., 2008. Heterogeneous deformation and spall of an extruded tungsten alloy: plate impact experiments and crystal plasticity modeling. J. Mech. Phys. Solids 56, 297–335.
Wallace, D., 1972. Thermodynamics of Crystals. John Wiley & Sons, New York.
Wang, H., Ramesh, K., 2004. Dynamic strength and fragmentation of hot-pressed silicon carbide under uniaxial compression. Acta Mater. 52, 355–367.
Warner, C., Hartnett, T., Fisher, D., Sunne, W., 2005. Characterization of AlON optical ceramic. In: Proceedings of SPIE, vol. 5786, Orlando FL, pp. 95–111.
Wereszczak, A., Kirkland, T., Strong, K., Campbell, J., LaSalvia, J., Miller, H., 2010. Size-scaling of tensile failure stress in a hot-pressed silicon carbide. Int. J. Appl. Ceram. Tech. 7, 635–642.
Wilkins, M., 1978. Mechanics of penetration and perforation. Int. J. Eng. Sci. 16, 793–807.
Yuan, G., Feng, R., Gupta, Y., 2001. Compression and shear wave measurements to characterize the shocked state in silicon carbide. J. Appl. Phys. 89, 5372–5380.
Zhang, D., Wu, M., Feng, R., 2005a. Micromechanical investigation of heterogeneous microplasticity in ceramics deformed under high confining stresses. Mech. Mater. 37, 95–112.
Zhang, K., Wu, M., Feng, R., 2005b. Simulation of microplasticity-induced deformation in uniaxially strained ceramics by 3-D Voronoi polycrystal modeling. Int. J. Plasticity 21, 801–834.

Effect of Electric Field on the Band Structure of Graphene/Boron Nitride and Boron Nitride/ Boron Nitride Bilayers

Radhakrishnan Balu, Xiaoliang Zhong, Ravindra Pandey, and Shashi P. Karna

Applied Physics Letter, 100 (2012)

APPLIED PHYSICS LETTERS **100**, 052104 (2012)

Effect of electric field on the band structure of graphene/boron nitride and boron nitride/boron nitride bilayers

Radhakrishnan Balu,[1,a)] Xiaoliang Zhong,[2] Ravindra Pandey,[2] and Shashi P. Karna[1,a)]
[1]*US Army Research Laboratory, Weapons and Materials Research Directorate, ATTN: RDRL-WM, Aberdeen Proving Ground, Maryland 21005-5069, USA*
[2]*Department of Physics, Michigan Technological University, Houghton, Michigan 49931, USA*

(Received 10 August 2011; accepted 3 January 2012; published online 30 January 2012)

Effect of electric field on the band structures of graphene/boron nitride (BN) and BN/BN bilayers is investigated within the framework of density functional theory. The calculated bandgap of the graphene/BN bilayer increases, although by small amount, with applied electric field. In the case of BN/BN bilayer, the bandgap decreases with the applied field in agreement with earlier studies. The modulation of bandgap in graphene/BN bilayers is dominated by the features of graphene and appears to be related to the modification in molecular orbitals as revealed by the calculated projected density of states. © *2012 American Institute of Physics*. [doi:10.1063/1.3679174]

Periodic systems in two-dimensional arrangements have received a great deal of attention due to their electronic, electrical, and mechanical properties.[1–4] For example, graphene, a planar structure of hexagonal carbon rings shows extraordinary electrical properties in its pristine form and has been the subject of numerous recent studies.[5] Its band structure shows zero gap at the Dirac point, which can be opened by external perturbations such as the application of strain, electric field, and chemical modification.[6,7] The bandgaps of both bilayer (BLG) and trilayer (TLG) configurations of graphene are tunable with an applied electric field[8] and are dependent on the symmetry. For example, in the case of TLG even though inversion symmetry is broken by applied electric field, hexagonal stacking has no bandgap, Bernal stacking has a tiny gap, and only the rhombohedral stacking has sizeable gap. Structurally similar to graphene, hexagonal boron nitride (h-BN), has also received considerable attention as a potential material for nano-scale electronics applications[9] due to its enhanced chemical, thermal, and mechanical stabilities.

In the case of bilayer graphene, recent studies[10,11] have shown that bandgap increases from 0 to 230 meV at 3 V/nm. Such a possibility opens the door for bilayer graphene in switchable electronic devices. Since BN is chemically more stable and already has a sizeable bandgap, it is of interest to investigate the effect of electric field on the graphene/BN and BN/BN bandgaps, both for advancing fundamental understanding of the electronic structures of these important nano-scale materials and also for their potential applications in switchable devices. In this letter, we report the results of our study of the effect of electric field on the band structures of graphene/BN and BN/BN bilayers investigated by first-principles density functional theory (DFT) approach. Our results suggest both graphene/BN and BN/BN layers to exhibit modulation of the band structure by electric field. However, significant qualitative and quantitative differences are noted. The effect on electric field on BN/BN system has been characterized in earlier studies[12] and the band structure modulation described at the DFT level of theory, so our focus will be on graphene/BN bilayer system. Our calculations on BN/BN system agree with earlier results and will be compared against the graphene/BN system to gain further insight into the modulation of band structure with the applied electric field.

Calculations were performed using the full-potential linearized augmented plane wave (FLAPW) method within the framework of local density approximation (LDA)-(DFT). In the FLAPW method, the crystal region is split between non-overlapping muffin-tin spheres around nuclei and interstitial regions. The plane wave basis set is used to describe the interstitial region and radial functions in the muffin-tins to account for the sharply changing potential near the nuclei. The linearized augmented plane wave-based methods are known to give accurate electronic structure description of solids.[13] The LDA-DFT has been previously used to obtain reliable results for graphitic and h-BN band structures.[14–16]

Two dimensional slab geometries were used for the systems studied; the interlayer spacing in the AB (Boron) stacking for graphene/BN and BN/BN equilibrium configurations (Fig. 1) taken from the previous work of Zhong *et al.*[9] are 3.022 Å and 3.071 Å, respectively. The calculated equilibrium configurations associated with the graphene/BN and BN bilayers were fully relaxed, with residual forces smaller than 0.01 eV/Å. The AB stacking for graphene/BN systems was chosen as it is the energetically favored configuration

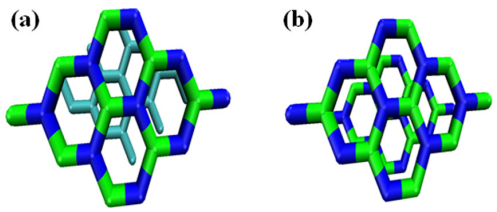

FIG. 1. (Color online) A schematic diagram of graphene/BN (a) and BN/BN (b) bilayers. The cyan, green, and blue represent carbon, boron, and nitrogen atoms, respectively.

[a)]Authors to whom correspondence should be addressed. Electronic addresses: rad.balu@us.army.mil and shashi.karna@us.army.mil.

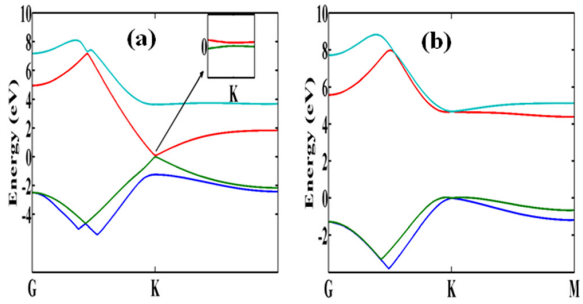

FIG. 2. (Color online) Band structure of (a) graphene/BN and (b) BN/BN bilayers at zero bias. Zero of the energy is set to the valence band maximum. The inset in (2a) shows the bandgap near the K point of graphene/BN bilayer.

over AA stacking at the LDA-DFT (Ref. 9) level of theory. The electric field was applied in the direction perpendicular to the planes of the bilayer by setting up two plates of opposite charges on either side of the bilayer systems as implemented in FLEUR (Ref. 17) electronic structure code.

Fig. 2 shows the band structures of graphene/BN and BN/BN bilayer systems. As expected, the graphene/BN and BN/BN bilayer band structures exhibit sharp distinctions from each other. The zero-field band structure for the graphene/BN bilayer is dominated by the bands associated with the carbon atoms near the Fermi level, with a very small gap of ~104 meV at the Dirac point. The bands near the Fermi level exhibit linear dispersion characteristic of graphene with their slopes less steep than bilayer graphene due to the presence of BN layer. The presence of non-zero gap implies lifting of degeneracy of the bands at the K point. In contrast, the BN/BN bilayer exhibits a nearly two-orders of higher direct gap of ~4.6 eV at the Dirac point. This is in accordance with earlier calculations[9] on BN/BN bilayer system.

The change in the bandgaps of graphene/BN and BN/BN bilayers due to externally applied electric field is depicted in Table I. It is clear from this figure that both bilayer systems exhibit modulation of their bandgaps by the external field. While the graphene/BN bilayer bandgap shows an increase with increasing external field, opposite is the case with the BN/BN bilayer. Further, the relative change in the graphene/BN bandgap appears to be larger than that in the BN/BN bilayer, although the magnitude of the change in the latter is much higher than the former. The decrease in the gap with increase in the electric field in the BN/BN bilayer is consistent with the previously reported results on BN bilayers.[12]

An examination of the band structure reveals that the conduction bands are affected more strongly than the valence bands (Table I) by the external electric field, E, for both the graphene/BN and BN/BN bilayers. For the graphene/BN system, the valence and conductions bands are pushed higher with increasing field with a net increase in the gap. In contrast, the conduction band of BN/BN bilayer is pushed towards the Fermi level with increasing field. While the valence band is pushed higher with increasing field until E = 2.0 V/nm, it decreases at until E = 2.5 V/nm and then again increases monotonically from E = 2.5 V/nm onwards. This results in an overall decrease in the bandgap. The effect of applied field on bands closer to Fermi level can be summarized as follows: (1) For graphene/BN bilayer, both the conduction and valence bands move in the same direction toward higher energies, (2) for the BN/BN bilayer, the valence and the conduction bands move in opposite direction toward the Fermi level. The net result is an increase, although very small in the bandgap of graphene/BN bilayer but a decrease in BN/BN bilayer case.

TABLE I. Energies of bands at Dirac point of the graphene/BN and BN/BN bilayers.

SYSTEM	E (V/nm)	VB (eV)	CB (eV)	Bandgap (eV)
Graphene/BN	0.0	2.157	2.262	0.104
Graphene/BN	1.7	2.219	2.329	0.109
Graphene/BN	2.1	2.227	2.339	0.111
Graphene/BN	2.5	2.235	2.349	0.112
Graphene/BN	3.0	2.241	2.357	0.115
Graphene/BN	3.4	2.245	2.362	0.116
Graphene/BN	4.1	2.251	2.370	0.118
BN/BN	0.0	0.580	5.174	4.594
BN/BN	0.4	0.581	5.172	4.591
BN/BN	0.8	0.585	5.169	4.584
BN/BN	1.2	0.592	5.162	4.570
BN/BN	1.6	0.602	5.159	4.557
BN/BN	2.0	0.805	5.141	4.537
BN/BN	2.5	0.624	5.125	4.501
BN/BN	2.9	0.636	5.102	4.466
BN/BN	3.3	0.648	5.074	4.427
BN/BN	4.0	0.666	5.028	4.362

In order to understand the calculated effect of the applied electric field on band structure in terms of the corresponding effect on the contributing atomic states, the total density of states (DOS) and projected density of states (PDOS) are plotted in Figs. 3 and 4, respectively. The bands closer to Fermi level have dominant contributions from $2p_z$ orbitals of each atom (data not shown) and so we focused on them for the PDOS plots. Fig. 3 represents DOS and PDOS when no electric field is applied to the graphene/BN bilayer. As can be seen the contribution of $2p_z$ orbital from N atom dominates DOS below Fermi level and contributions from B atom dominate unoccupied states, while C and N levels contribute nearly the same in lower valence band region. Without the contributions from the carbon atoms there would be a gap of about 4 eV, reflecting the characteristics of BN

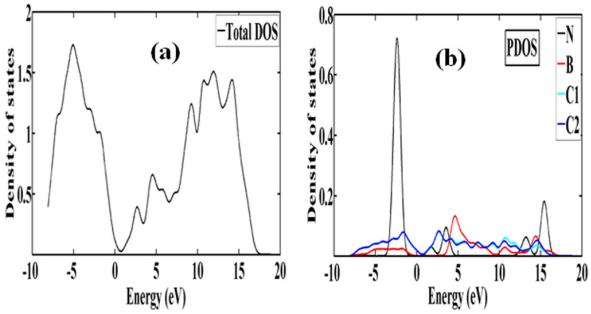

FIG. 3. (Color online) (a) Total DOS and (b) PDOS of $2p_z$ orbitals for graphene/BN bilayer at an applied electric field, E = 0. The energies are subtracted from the Fermi level E_F (−5.525 eV) and a factor of 0.015 used for broadening the DOS.

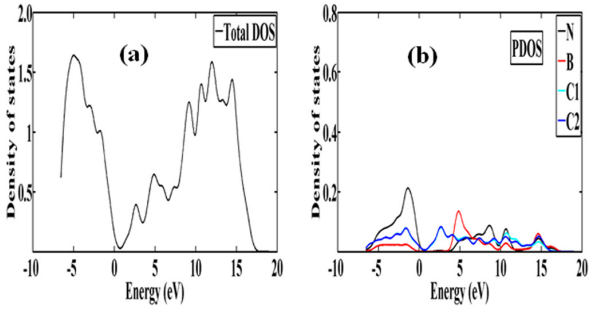

FIG. 4. (Color online) (a) Total DOS and (b) PDOS of $2p_z$ orbitals for graphene/BN bilayer at an applied electric field, $E \neq 0$. The energies are subtracted from the Fermi level E_F (−7.052 eV) and a factor of 0.015 used for broadening the DOS.

system. The presence of graphene layer carbon atoms introduces DOS around the Fermi level, narrowing the gap from 4 eV to around 100 meV. This is not apparent from the figure due to the use of a Gaussian smear (broadening) factor of 0.015 in order to make the plots continuous. The gap is clear in a scattered plot[18] without the broadening factor. It is also interesting to note that in the absence of the field (Fig. 3), the N states are localized in a narrow energy range, both below and above Fermi levels, while the C and B states appear to be more broadened.

Upon application of the electric field, E (Fig. 4), the N states, both below and above the Fermi level, experience a reduction in the density and shift to higher magnitude in the energy, while little change is noticed in C and B states. Also, the N states exhibit considerably broadening (Fig. 4(b)). The overall effect on the modulation of the N levels in the conduction and the valence bands is to introduce a finite, though small, net increase in the bandgap of the graphene/BN bilayer.

We have investigated the effect of the electric field on the graphene/BN and BN/BN bilayer systems. The calculated results show the bandgap in graphene/BN bilayer is dominated by graphene features and is electric field tunable. The inverse relation of bandgap with the applied field in BN/BN bilayer is consistent with earlier results. The calculated electric field tenability of graphene/BN bilayer bandgap suggests new applications for this system in semiconductor devices.

Calculations were performed using the DOD Supercomputing Resource Centers (DSRCs) located at the U.S. Army Engineer Research and Development Center. The work at Michigan Technological University was performed under support by the U.S. Army Research Laboratory through Contract No. W911NF-09-2-0026-133417.

[1]A. K. Geim, Science **324**, 1530 (2009).
[2]L. Liu and Z. Shen, App. Phys. Lett. **95**, 252104 (2009).
[3]A. Lherbier, X. Blase, Y. Niquet, F. Triozon, and S. Roche, Phys. Rev. Lett. **101**, 036808 (2008).
[4]F. Yavari, C. Kritzinger, C. Gaire, L. Song, H. Gullapalli, T. Borca-Tasciuc, P. M. Ajayan, and N. Koratkar, Small **6**, 2535 (2010).
[5]G. Gui, J. Li, and J. Zhong, Phys. Rev. B **78**, 075435 (2008).
[6]F. Schwierz, Nat. Nanotechnol. **5**, 487 (2010).
[7]B.-R. Wu, App. Phys. Lett. **98**, 263107 (2011).
[8]H. Min, B. Sahu, S. K. Banerjee, and A. H. MacDonald, Phys. Rev. B **75**, 155115 (2007).
[9]X. Zhong, Y. K. Yap, R. Pandey, and S. P. Karna, Phys. Rev. B **83**, 193403 (2011).
[10]A. H. C. Net, F. Guinea, N. M. R. Peres, K. S. Novoselov, and A. K. Geim, Rev. Mod. Phys. **87**, 109, (2009).
[11]Y. B. Zhang, T.-T. Tang, C. Girit, Z. Hao, M. C. Martin, A. Zettl, M. F. Crommie, Y. R. Shen, and F. Wang, Nature **459**, 820 (2009).
[12]Z. Yang and J. Ni, J. Appl. Phys. **107**, 104301 (2010).
[13]R. Martin, *Electronic Structure: Basic Theory and Practical Methods* (Cambridge University Press, 2004).
[14]S. B. Trickey, F. Müller-Plathe, G. H. F. Diercksen, and J. C. Boettger, Phys. Rev. B **45**, 4460 (1992).
[15]A. Marini, P. García-González, and A. Rubio, Phys. Rev. Lett. **96**, 136404 (2006).
[16]N. Ooi, A. Rairkar, and J. B. Adams, Carbon **44**, 231 (2006).
[17]D. R. Hamann, Phys. Rev. Lett. **212**, 662, (1979); E. Wimmer, H. Krakauer, M. Weinert, and A. J. Freeman, Phys. Rev. B **24**, 864 (1981).
[18]See supplementary material at http://dx.doi.org/10.1063/1.3679174 for calaculated total density of states (DOS) for graphene/BN bilayer with and without external elctric field, E, and a gaussian broadening (smearing) factor = 0.

Quantifying the Energetics and Length Scales of Carbon Segregation to α-Fe Symmetric Tilt Grain Boundaries using Atomistic Simulations

Nathan R. Rhodes, Mark A. Tschopp and Kiran N. Solanki

Modelling and Simulation in Materials Science and Engineering, 21 (2013)

IOP Publishing Modelling and Simulation in Materials Science and Engineering

Modelling Simul. Mater. Sci. Eng. **21** (2013) 035009 (21pp) doi:10.1088/0965-0393/21/3/035009

Quantifying the energetics and length scales of carbon segregation to α-Fe symmetric tilt grain boundaries using atomistic simulations

N R Rhodes[1], M A Tschopp[1,2] and K N Solanki[3]

[1] Center for Advanced Vehicular Systems, Mississippi State University, Starkville, MS 39762, USA
[2] Oak Ridge Institute for Science and Education Research Fellow, Army Research Laboratory, Weapons and Materials Research Directorate, Aberdeen Proving Ground, MD 21005, USA
[3] School for Engineering of Matter, Transport and Energy, Arizona State University, Tempe, AZ 85287, USA

E-mail: mark.a.tschopp.ctr@mail.mil

Received 11 July 2012, in final form 24 January 2013
Published 8 March 2013
Online at stacks.iop.org/MSMSE/21/035009

Abstract

Segregation of impurities to grain boundaries (GBs) plays an important role in both the stability and macroscopic behavior of polycrystalline materials. The research objective in this work is to better characterize the energetics and length scales involved with the process of solute and impurity segregation to GBs. Molecular statics simulations are used to calculate the segregation energies for carbon within multiple substitutional and interstitial GB sites over a database of 125 symmetric tilt GBs in Fe. The simulation results show that there are two energetically favorable GB segregation processes: (1) an octahedral C atom in the lattice segregating to an interstitial GB site and (2) an octahedral C atom and a vacancy in the lattice segregating to a grain boundary substitutional site. In both cases, lower segregation energies than appear in the bulk lattice were calculated. Moreover, based on segregation energies approaching bulk values, the length scale of interaction is larger for interstitial C than for substitutional C in the GB ($\approx$5 Å compared to $\approx$3 Å from center of the GB). A subsequent data reduction and statistical representation of this dataset provides critical information about the mean segregation energy and the associated energy distributions for carbon atoms as a function of distance from the grain boundary, which quantitatively informs higher scale models with energetics and length scales necessary for capturing the segregation behavior of alloying elements and impurities in Fe. The significance of this research is the development of a methodology capable of ascertaining segregation energies over a wide range of GB character (typical of that observed in polycrystalline materials), which herein has been applied to carbon segregation to substitutional and interstitial sites in a specific class of GBs in α-Fe.

(Some figures may appear in colour only in the online journal)

1. Introduction

The computational design of future alloys will greatly depend on our ability to understand and quantify nanoscale phenomena in metallic material systems. For instance, impurity segregation to grain boundaries (GBs) in alloys can have a profound effect on underlying microstructural processes, which can subsequently be detrimental to mechanical properties in polycrystals, e.g., hardness, toughness and fracture behavior [1–11]. On the other hand, in some cases, atom segregation to GBs can actually be beneficial for macroscale material properties, e.g., by forming intermetallics, strengthening GB cohesion, or preventing grain growth [11–15]. Segregation also plays a role in GB decohesion. For instance, Yamaguchi et al. recently showed that S segregation to Ni GBs leads to a reduction in GB tensile strength by an order of magnitude [16]. Moreover, Solanki et al. found that certain H defects are favored at α-Fe GBs and that these species affect the cohesive GB strength [17]. Since the presence of impurities and atoms at GBs can have such an acute impact on many material properties, understanding their interaction with and segregation to GBs and other lattice defects is crucial to the design of future materials.

One potential application of work in atomic segregation is nuclear materials. Nuclear material design is also dependent upon understanding the segregation of impurities and defects within cladding materials. Radiation damage, through cascade events, ultimately results in numerous vacancies and interstitial atoms within the lattice. Impurities within the material then tend to diffuse with the vacancies or interstitial atoms as they attempt to return to equilibrium positions in the lattice [18–20]. Such non-equilibrium radiation-induced segregation has a profound effect on material properties due to the accelerated segregation kinetics in comparison to the typical kinetics in thermal equilibrium [20–22]. Moreover, since many cladding materials are polycrystalline and GBs are significant sinks for defect and impurity segregation, understanding impurity segregation to GBs is crucial to nuclear material design.

A number of studies have experimentally characterized the presence and effect of impurities on GBs in various materials [4, 12, 13, 23–33]. For instance, Lejček used Auger electron spectroscopy (AES) to show that segregants are equally distributed between fracture surfaces in symmetric tilt grain boundaries (STGBs) and distributed unevenly for asymmetric boundaries in Fe-Si bicrystals [28]. Furthermore, Lejček *et al* comprehensively classified [1 0 0] tilt GBs in α-Fe into special, vicinal and general categories using AES measurements of GB segregation [27]. Such studies have also proven useful in GB engineering. Recently, Kobayashi *et al* used electron backscatter diffraction (EBSD) and orientation imaging microscopy (OIM) to show that intergranular embrittlement caused by sulfur segregation in nickel can be lessened by developing an optimal GB microstructure [29]. Moreover, EBSD experiments of Al–Zr alloys have shown that GB sites in immobile twist GBs have a much higher degree of segregation than at mobile tilt GBs [23]. Researchers have also begun to use high-resolution transmission electron microscopy (TEM) and local electron atom probes (LEAPs) [30–33] to create three-dimensional atom-by-atom representations of solute segregation at GBs and characterize their concentrations. For example, Taheri *et al* utilized a method that combined EBSD and focused ion beam milling specimen preparation with LEAP to measure solute segregation at GBs in an Al alloy [30]. Furthermore, LEAP has been utilized by Isheim and colleagues to illustrate the reduction in impact toughness in low-carbon steels as a result of the combined segregation behavior of C, B, S and P [31]. While critical experiments provide valuable insight into solute segregation to GBs, techniques that aim to probe how atomic structure impacts segregation are often difficult to perform, expensive and very time intensive. Additionally, these sorts of experiments have yet to be used

to study large numbers of boundaries with varying GB character, typical of real polycrystalline materials.

Modeling and simulation of segregation to GBs at the atomic scale can also provide valuable insight into segregation processes in polycrystalline materials [10, 16, 34–53]. Typically, modeling and simulation of GB segregation at the nanoscale use *ab initio* simulations [10, 16, 34–43] or molecular dynamics (MD) [44–53]. *Ab initio* calculations are often used to study the electronic effects of solute presence at GBs and their influence on cohesive strength. For instance, Liu *et al* investigated the preferred site of Mg segregation at Al GBs and determined that Mg forms weaker metallic bonds with Al atoms in the GB region and decreases the cohesive strength of the GB [37]. Wachowicz and Kiejna [40] studied the effect of substitutional and interstitial N, B and O impurities at an Fe GB and found that N in both positions and interstitial B are embrittlers while O in both positions and substitutional B enhance GB cohesion. The segregation energies and cohesive effects of twenty impurities and alloying elements at a Zr twist GB were calculated by Christensen *et al* , who showed that most elements have an adverse effect on GB cohesion, with Cs being the most embrittling [38]. These techniques, however, can be computationally expensive and have typically been used only for a few GBs. On the other hand, MD studies often use empirical or semi-empirical interatomic potentials fit to *ab initio* and experimental properties. These simulations are much less expensive than their *ab initio* counterparts but are limited by the accuracy or availability of interatomic potentials. Nonetheless, MD simulations are increasingly being used to study GB segregation in both fcc and bcc materials. Millett *et al* investigated the impact of dopants at a Cu GB and concluded that, for a particular concentration of each dopant atomic size, the thermodynamic driving force for grain growth could be eliminated [45]. Lezzar *et al* concluded that the driving force for intergranular segregation in Ag(Ni) and Ni(Ag) systems can be primarily attributed to the atomic size effect [50]. While MD has been more commonly used for fcc materials, such simulations have also provided insight into GB segregation in body-centered cubic (bcc) Fe as well [51–53]. For instance, Gao *et al* used MD simulations to show that, at α-Fe GBs, He binding energy increases with excess volume and binds to GBs more strongly in interstitial positions than in substitutional ones [52]. Additionally, Malerba *et al* modeled displacement cascades in an Fe–Cr system with MD to show that a large percentage of Cr atoms are located in interstitial clusters, which may greatly reduce the mobility of interstitial loops when compared to pure Fe [53].

While MD simulations are much less expensive than *ab initio* simulations, very few simulations consider a large number of GBs in their analysis of GB-related properties. GBs have five degrees of freedom associated with them (plus three associated with translation at an atomistic level), and many experimental methods have begun to measure the GB character in terms of these degrees of freedom [54–56] for GB engineering purposes. However, in nanoscale calculations, only a few studies have explored fifty or more GBs in their analysis of nanoscale properties. Tschopp and McDowell have shown that asymmetric tilt GB systems in Cu and Al facet into the structural units of their corresponding symmetric tilt GB counterparts [57–59] and that the GB structure results in very different dislocation nucleation properties and mechanisms [60–63]. Holm *et al* calculated energies of 388 GBs in Al, Au, Cu and Ni, and observed that the GB energy scales with the shear modulus and that boundaries with significant stacking fault character correlate with the stacking fault energy [48]. The classic work of Wolf has shown that, for several Mo and Fe GB systems, GB energy correlates nearly linearly with volume expansion per unit area [49]. The recent work of Tschopp *et al* used $>$150 Fe STGBs to demonstrate that, based on formation energies, self-interstitial atoms display a larger energetic driving force for binding to GBs than vacancies do [64, 65]. Clearly, a similar methodology using molecular statics and dynamics simulations that can analyze how

segregation in α-Fe systems is influenced by GB character would be valuable to understanding GB segregation and, perhaps, to engineering materials by increasing beneficial GBs while decreasing detrimental GBs.

In this work, the research objective is to quantify the energetics and length scales associated with C segregation to Fe GBs. The Fe–C system is chosen as an ideal system because C is known both experimentally [66–68] and computationally [69–73] to segregate to the boundaries, dislocations and surfaces; moreover, a number of experimental studies have shown that C increases the GB cohesive strength in α-Fe [66–68]. The methodology used here provides a means for simulating how GB character impacts the segregation of C to a large number of Fe GBs. In this work, we utilize an interatomic potential [74] specifically formulated to capture the energetics of C interactions with point defects in α-Fe, which is in good agreement with *ab initio* results [75]. This paper is outlined as follows. Section 2 describes the simulation methodology used to simulate and calculate segregation data. Section 3 discusses the results of the simulations and their significance for modeling GB segregation. Section 4 discusses our results, particularly addressing how the present methodology may need to be extended to better model the interaction between GBs and interstitial atom species. Section 5 summarizes this research and provides conclusions based on our results.

2. Simulation methodology

In this work, the segregation energy associated with a single C atom was calculated at sites within or around α-Fe GBs. While it is well known that C occupies octahedral interstitial sites in the perfect single crystal α-Fe lattice, here we examined a few different scenarios for C. As a first-order approximation, we utilize sites formed on the initial GB lattice. This process is meant to mimic the restructuring at the boundary that occurs through an interaction with a vacancy and then a subsequent occupation of an available site in the restructured boundary (at the exact location of the initial vacancy). The hypothesis is that at a GB that has undergone some restructuring due to interactions with point defects, such segregation processes and sites may be energetically favorable. This may be a reasonable assumption given that DFT calculations have shown that another interstitial atom, N, has very similar formation energies in both substitutional and interstitial sites within a $\Sigma5(2\,1\,0)$ GB [40]. Moreover, in an ultra-low C bake-hardening steel sheet, three-dimensional atom-probe measurements have found that C atom concentrations at the GB can be more than 200 times that in the bulk [68]; hence the possibility for C to segregate to both interstitial and substitutional sites is probable. In section 4, this assumption will be further compared with interstitial sites within the GB lattice (as opposed to sites directly on top of the GB lattice) for a few GBs, based on starting coordinates obtained from a Voronoi tesselation of the simulation cell. The first-order process used to calculate the segregation energies of C in α-Fe is as follows:

(i) A GB is selected from a GB database that contains 125 STGBs (50 $\langle 1\,0\,0\rangle$, 50 $\langle 1\,1\,0\rangle$, 25 $\langle 1\,1\,1\rangle$).

(ii) A GB site (within 15 Å) is chosen and a C atom is substituted for the Fe atom at this site.

(iii) A molecular dynamics code (LAMMPS [76]) is used to minimize the energy of the GB with the substitutional C atom.

(iv) The GB, site position and calculated segregation energy of the substitutional C atom are stored.

(v) The process is repeated for all sites within 15 Å of the GB center and for all GBs within the GB database.

The Hepburn and Ackland Fe–C interatomic potential [74] is used to model the Fe GBs and their interaction with the subsitutional C atom. This potential is based on the embedded-atom method (EAM) formalism [77, 78] and is in agreement with density functional theory with respect to the energetics pertaining to interactions between C atoms and Fe self-interstitial atoms, vacancies, and other C atoms. Unlike prior Fe–C potentials, the Hepburn–Ackland Fe–C potential was the first EAM potential to correctly capture covalent bonding of two C atoms within a vacancy. Moreover, previous EAM potentials showed strong binding of C to overcoordinated defects, such as self-interstitial atoms, whereas the Hepburn–Ackland potential correctly captures the strong repulsion between orvercoordinated defects and C, in agreement with *ab initio* results. This repulsion can be important for interactions between C atoms and GBs. Last, this potential has been simulated at temperature yielding dynamics and mechanisms[4] in agreement with *ab initio* results [75]. For instance, Terentyev *et al* [79] recently used this potential to investigate the influence of C atoms on the stability and migration of small clusters of point defects and found that C atoms have an attractive interaction with vacancy clusters containing fewer than four vacancies. This potential provides a reasonably accurate representation of the Fe–C system and is deemed appropriate for studies of single C atoms within the bcc Fe lattice.

The segregation energy is calculated for C as a function of position at each site within 15 Å of the GB. For each GB structure, an Fe atom at a particular site α is replaced with a C atom and the simulation cell is relaxed using the Polak-Ribiére conjugate gradient energy minimization process. The total energy of the simulation cell is calculated and the process is repeated for each atomic site within each GB in the database. The segregation energy calculations follow a similar approach to others, e.g., Liu *et al* [37]. The segregation energy associated with a C atom at site α is calculated with

$$E_{\text{seg}}^{\text{C}^\alpha} = \left(E_{\text{tot}}^{\text{GB,C}_{\text{sub}}^\alpha} - E_{\text{tot}}^{\text{GB}}\right) - \left(E_{\text{bulk}}^{\text{Fe,C}_{\text{sub}}} - E_{\text{bulk}}^{\text{Fe}}\right) \tag{1}$$

where $E_{\text{tot}}^{\text{GB,C}_{\text{sub}}^\alpha}$ and $E_{\text{tot}}^{\text{GB}}$ are the total energies of the GB structure with and without the solute substitution. $E_{\text{bulk}}^{\text{Fe,C}_{\text{sub}}}$ and $E_{\text{bulk}}^{\text{Fe}}$ are the total energies of a single crystal bulk Fe simulation cell with and without the substituted C solute. The bulk energies used a $10a_0$x$10a_0$x$10a_0$ bcc cell with 2000 atoms. Hence, $E_{\text{bulk}}^{\text{Fe}}$ is equal to $2000E_{\text{c}}^{\text{Fe}}$ ($E_{\text{c}}^{\text{Fe}} = 4.013$ eV, i.e. cohesive energy of Fe) and $E_{\text{bulk}}^{\text{Fe,C}_{\text{sub}}} = 2000E_{\text{c}}^{\text{Fe}} + 0.391$ eV. These bulk energies are subtracted in equation (1) to remove the effect of substituting the C atom. Hence, $E_{\text{seg}}^{\text{C}^\alpha} \approx 0$ represents that substituting a C atom into site α in the GB simulation cell results in an equivalent energy difference as substituting the C atom into a perfect bcc Fe lattice. As with prior work, a negative value of $E_{\text{seg}}^{\text{C}^\alpha}$ represents that it is energetically favorable for C to bind to site α compared to the bulk lattice. It should be noted that the segregation energy, $E_{\text{seg}}^{\text{C}^\alpha}$, as defined is equal to (-1) times the binding energy $E_{\text{b}}^{\text{C}\alpha}$. Using the same terms as in equation (1), the binding energy is typically defined as

$$E_{\text{b}}^{\text{C}^\alpha} = \left(E_{\text{tot}}^{\text{GB}} + E_{\text{bulk}}^{\text{Fe,C}_{\text{sub}}}\right) - \left(E_{\text{tot}}^{\text{GB,C}_{\text{sub}}^\alpha} + E_{\text{bulk}}^{\text{Fe}}\right) = -E_{\text{seg}}^{\text{C}^\alpha}. \tag{2}$$

The segregation energy in equation (1) will be used for the subsequent analysis of a C atom in substitutional GB sites. Later, in section 4, the segregation energy equation is discussed in the context of two different scenarios: (1) a C atom in an octahedral site and a vacancy in the bulk lattice combining into C at a GB substitutional site and (2) a C atom at an

[4] The migration energy, $E_{\text{m}} = 0.887$ eV, is in good agreement with the *ab initio* results of Domain *et al* [75], $E_{\text{m}} = 0.902$ eV. Additional dynamic simulations by Hepburn and Ackland [74] at 1400 K with a single C atom in an Fe single crystal lattice show that C exclusively migrates from octahedral to octahedral sites through the tetrahedral sites.

octahedral site occupying GB interstitial sites. That is, the present definition of segregation energy in equation (1) is modified for the Fe–C system to account for the fact that C does not occupy substitutional sites within the bulk lattice. This energy difference is 0.930 eV; hence, $E_{\mathrm{seg}}^{\mathrm{C}^{\alpha}} < -0.930\,\mathrm{eV}$ is necessary for Scenario 1 (octahedral C and vacancy to GB substitutional C) to be energetically favorable. The method outlined in this section was used for each site in all 50 ⟨1 0 0⟩ STGB, as well as 50 ⟨1 1 0⟩ and 25 ⟨1 1 1⟩ STGBs. For each GB, the segregation energies were calculated as a function of atomic location.

3. Simulation results

3.1. GB structure and energy

The GB structure database used in the simulations herein contained 50 ⟨1 0 0⟩, 50 ⟨1 1 0⟩ and 25 ⟨1 1 1⟩ STGBs. Bicrystal simulation cells with three-dimensional periodic boundary conditions were used to create the database [57–59, 80]. To remove any possible interaction between the two boundaries, a minimum distance of 12 nm was used between them during generation. As with past work [57–59], an atom deletion criterion along with multiple initial configurations with various in-plane rigid body translations were utilized to accurately obtain optimal minimum energy GB structure via the nonlinear conjugate gradient energy minimization process.

The structures and energies of STGBs may be important to understand the interaction between C atoms and the boundary. To examine the range of GB structures and energies that might be seen in polycrystalline materials, different GBs from several GB tilt systems were used in the present simulations. The database used in this work is an expanded version of that first utilized in Tschopp *et al* [64]. The ⟨1 0 0⟩, ⟨1 1 0⟩ and ⟨1 1 1⟩ STGB systems chosen have several low-order coincident site lattice (CSL) GBs (e.g., Σ3, Σ5, Σ9, Σ11 and Σ13 boundaries), as well as both general high angle boundaries and low angle GBs ($\theta \leqslant 15^{\circ}$). The GB energy as a function of misorientation angle for the ⟨1 0 0⟩ STGB system is shown in figure 1. This plot is similar to that found previously in Fe–Cr simulations [81] and similar to misorientation-energy relationships found in fcc metals [80, 82–85]. The low-order CSL GBs for the ⟨1 0 0⟩ STGB system (Σ5 and Σ13 boundaries) are also illustrated in this figure. For the ⟨1 0 0⟩ tilt axis, only minor cusps were observed in the energy relationship, most noticeably at the Σ5{3 1 0} boundary (990 mJ m^{-2}). In addition to many general high angle boundaries, several low angle boundaries ($\theta \leqslant 15^{\circ}$) are also plotted. The range of GB energies sampled was 500 mJ m^{-2}.

The GB structure plays an important role on the GB properties [86]. For low angle boundaries, the GB is composed of an array of discrete dislocations and the corresponding energy can be calculated based on the classic Read–Shockley dislocation model. However, at higher misorientation angles, the spacing between dislocations is small enough that dislocation cores overlap and dislocations rearrange to minimize the energy of the boundary. The resulting GB structures are often characterized by structural units [87]. GBs with certain misorientation angles (and typically a low Σ value) correspond to 'favored' structural units, while all other boundaries are characterized by structural units from the two neighboring favored boundaries. An example of structural units in the ⟨1 0 0⟩ STGB system is shown in figure 2, where the two Σ5 boundaries are favored STGBs, and the Σ29(7 3 0) boundary is a combination of structural units from the two Σ5 boundaries. The structural units for the Σ5(2 1 0) and Σ5(3 1 0) STGBs are labeled B and C, respectively, in a convention similar to that used for face-centered cubic metals [80]. Also, notice that the ratio of structural units in the Σ29 GB can be determined by the crystallographic relationship of the two favored boundaries,

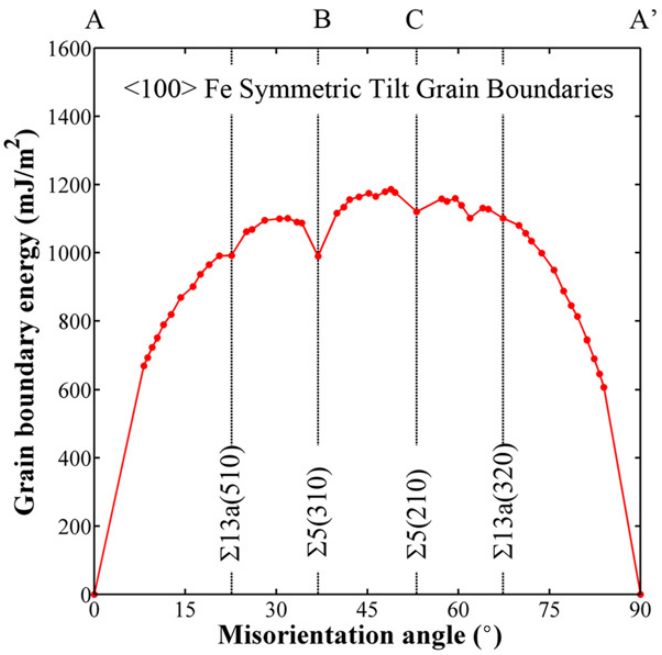

Figure 1. ⟨1 0 0⟩ symmetric tilt grain boundary energy as a function of misorientation angle [65]. The low-Σ grain boundaries (Σ ⩽ 13) in each system are identified.

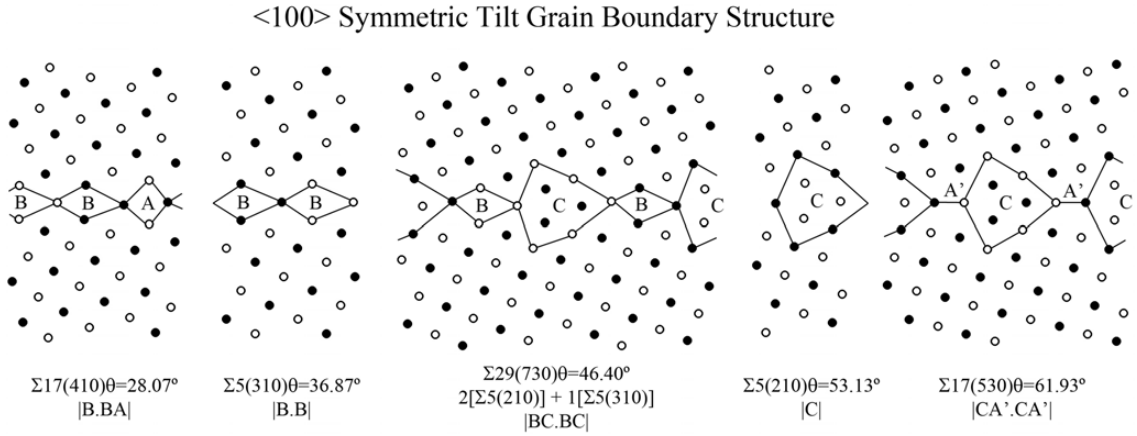

Figure 2. ⟨1 0 0⟩ symmetric tilt grain boundary structures with structural units outlined for the Σ17(4 1 0), Σ5(2 1 0), Σ29(7 3 0), Σ5(3 1 0) and Σ17(5 3 0) boundaries [65]. Black and white denote atoms on different {1 0 0} planes. The different structural units are labeled A, B, C and A'.

i.e. Σ29(7 3 0) = 2[Σ5(2 1 0)] + 1[Σ5(3 1 0)]. In a similar manner, the two Σ17 boundaries are combinations of the favored B and C structural units and 'structural units' of the perfect lattice, A and A'.

3.2. Segregation energy for ⟨1 0 0⟩ boundaries

The segregation energies that correspond to the atomic positions in the middle three GB structures (figure 2) are shown in figure 3. AtomEye is used to visualize the simulation results [88]. In this graph, the color bar is normalized by subtracting the energy of substitutional C in the bulk so that the difference in energy between sites near the GB and in the bulk can be easily compared (i.e. atoms colored white have bulk segregation energies). For all three GBs,

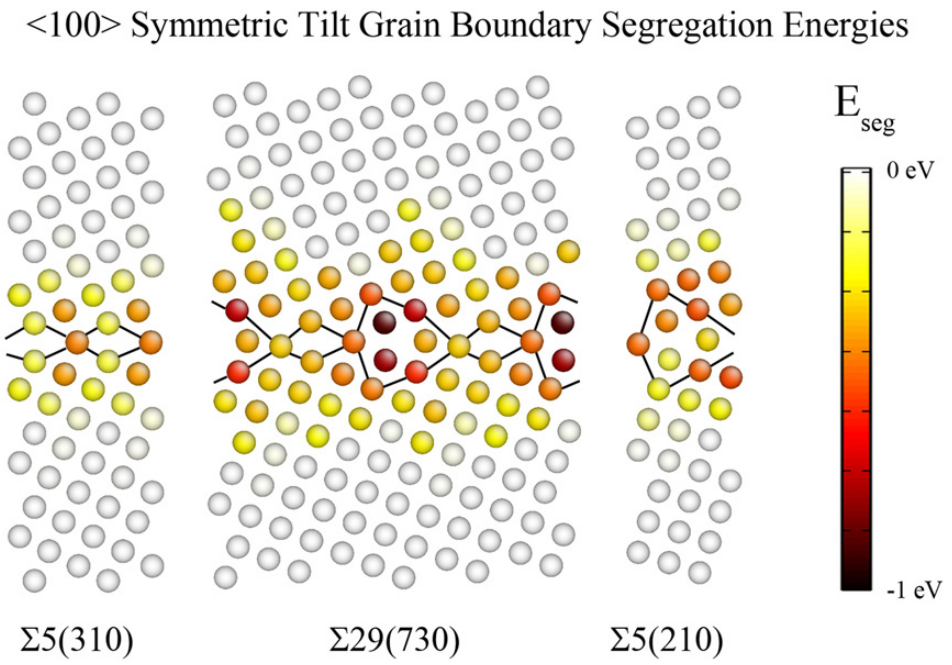

Figure 3. Segregation energy as a function of site location for substitutional C atom in the Σ5(2 1 0), Σ29(7 3 0), and Σ5(3 1 0) boundaries.

the segregation energy becomes lower as the sites are located closer to the GB, meaning that segregation to the GB is favored for substitutional C. However, there is not a simple gradient of the segregation energy from the GB center; the local structure also plays a pivotal role in the segregation energy. For sites located farther from the GB, the segregation energy approaches that of the bulk, as denoted by segregation energies close to 0 eV. Interestingly, although the structural units are the same between these three GBs, there are some segregation energies in the Σ29(7 3 0) that are lower than either of the favored Σ5(2 1 0) and Σ5(3 1 0) STGBs, e.g., inside the C structural unit. That is, the elastic interaction between differing structural units may produce a different distribution of segregation energies than a boundary composed of all the same structural unit. While these trends seem to indicate a driving force for the segregation of C atoms from the bulk to the GB, this segregation energy needs to be further augmented ($E_{\mathrm{seg}}^{\mathrm{C}\alpha} + 0.930$ eV) to account for the fact that C lies in octahedral interstitial sites in the bulk, as will be further discussed in section 4.

Plotting segregation energy against distance from the GB shows information similar to that in figure 3, but provides a convenient method to display the segregation energies of the sites in many different GBs at once. The distribution of segregation energies as a function of distance for the three GB structures seen in figure 3 is shown in figure 4. Near the GB, all three GBs show a trend of negative segregation energies at sites near the boundary, which is the same behavior reflected in figure 3. Moreover, notice the lack of any segregation energies that are near bulk values within 5 Å of the GB center for these three boundaries. Figure 4(*b*) is a plot of the same distribution for all 50 ⟨1 0 0⟩ STGBs, which includes both low angle ($\theta \leqslant 15^{\circ}$) and high angle GBs. As noted in figure 4(*b*), over 10 000 simulation sites (and atomistic simulations) were considered herein. Most of the segregation energies that differ from that of the bulk occur between the GB center and about 7 Å. While the majority of sites within this region have segregation energies less than that of the bulk, there are also a few GB sites that have segregation energies that are higher than in the bulk; most of these sites tend to be located along the centerline of the boundary. There are a cluster of sites around

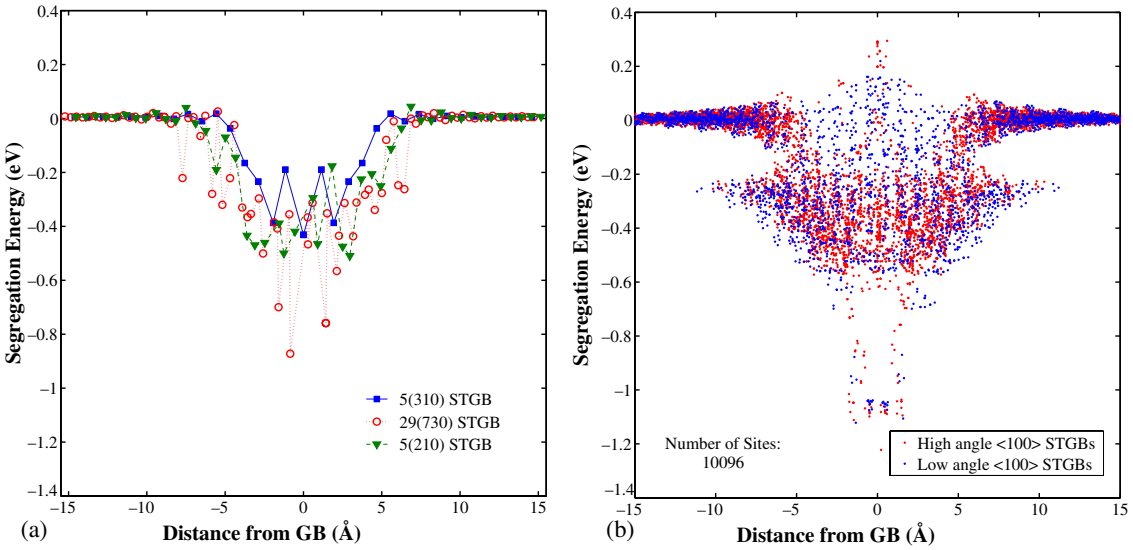

Figure 4. Distribution of segregation energies as a function of distance from the grain boundary for (*a*) the Σ5(2 1 0), Σ29(7 3 0), and Σ5(3 1 0) grain boundaries and (*b*) all 50 ⟨1 0 0⟩ STGBs. $E_{\mathrm{seg}}^{\mathrm{C}\alpha} < 0.0\,\mathrm{eV}$ indicates it is energetically favorable for substitutional C to bind to a substitutional site at the grain boundary. However, since C occupies octahedral sites in the bulk lattice, $E_{\mathrm{seg}}^{\mathrm{C}\alpha} < -0.930\,\mathrm{eV}$ is required for an octahedral C atom and a vacancy to combine and bind to a GB substitutional site.

7–12 Å from the GB that have segregation energies lower than the bulk as well. There is a subtle difference between low and high angle boundaries. Within 5 Å of the GB center, low angle GBs tend to have some segregation energies that are similar to the bulk values. This is as expected, however. Low angle boundaries are composed of dislocations separated by regions of perfect single crystal, which have similar segregation energies to bulk energies.

One way to represent the segregation energies–distance relationship is to bin the energies according to their distance from the GB center and to analyze the statistics associated with each bin (figure 5). Due to the symmetric nature of the GB segregation energies as a function of distance (figure 4), the absolute value of the distance from the GB center was used to provide more data points for the statistical analysis. Furthermore, the energies are split into 1 Å bins to characterize the distributions and compute statistics for sites at a given distance from the GB. An example of the 0 Å bin (−0.5 Å to +0.5 Å) is shown in figure 5(*a*) along with several statistics: number of boundaries, mean, median, standard deviation, and interquartile range[5]. Once the appropriate statistics are calculated, a boxplot (figure 5(*b*)) is used to represent the segregation energy statistics in each bin, i.e. the minimum, 25% percentile, median, 75% percentile, and maximum segregation energies. In the boxplot, the red line in the box is the median while the top and bottom edges of the blue boxes represent the 25% and 75% quartiles. The whiskers extending from the boxes cover the remainder of the range of energies for each bin, and the ends of the whiskers denote the maximum and minimum values of the segregation energies for each bin. The mean value of the segregation energies in each bin is also plotted in green. Boxplots can be very useful for displaying asymmetric distributions.

The mean segregation energy is lowest with sites close to the GB, as shown in figure 5, and it approaches the normalized bulk value of zero as sites are located farther from the boundary. Interestingly, the lowest mean segregation energies actually occur a few Ångstroms

[5] The interquartile range is defined as the difference between the 25% percentile and 75% percentile.

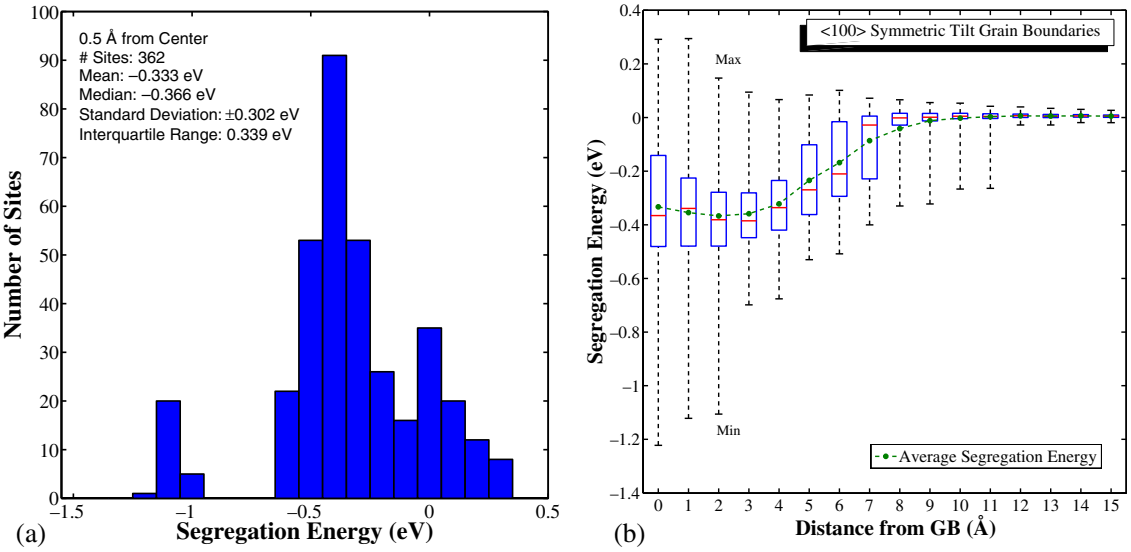

Figure 5. (*a*) The distribution of segregation energies within 0.5 Å of the grain boundary center and the associated statistics. (*b*) Boxplots of segregation energy as a function of distance from the grain boundary for all 50 ⟨1 0 0⟩ STGBs. The data are divided into 1 Å bins, and a boxplot is made for each bin. The red lines are medians, the blue box ends are the first and third quartiles, and the black whisker ends are minimum and maximum values. The mean segregation energy is also plotted in green.

from the center of the boundary. Furthermore, at approximately >8 Å, the boxes are closely centered about the bulk value, which shows that the overwhelming majority of atomic sites display a segregation energy similar to the bulk value. However, it is noticed that there are a number of sites with segregation energies significantly below the bulk value that still persist up to approximately 11 Å. This trend indicates that it may be energetically favorable for substitutional C to segregate to sites within 11 Å of the GB, albeit there is a much larger driving force with decreasing distance from the boundary. Additionally, the majority of bins display energy distributions that are skewed, usually in the direction of negative energy, i.e. the median is closer to the lower edge of the box (mainly for distances less than 7 Å). While the median fluctuates somewhat, the mean segregation energies—which track with the median—follow a much smoother relationship with distance.

3.3. Segregation energy for ⟨1 1 0⟩ *and* ⟨1 1 1⟩ *boundaries*

The same process used for the analysis of ⟨1 0 0⟩ data in figures 3–5 has been repeated for the data of ⟨1 1 0⟩ and ⟨1 1 1⟩ STGB simulations. The distribution of segregation energies as a function of distance from the GB for all 50 ⟨1 1 0⟩ and 25 ⟨1 1 1⟩ STGBs is shown in figure 6. This distribution is similar to that of the ⟨1 0 0⟩ STGBs shown in figure 4(*b*). However, the minimum segregation energies are much lower than that of ⟨1 0 0⟩ STGBs and there are fewer sites with segregation energy higher than that of the bulk.

A statistical representation of the data in figure 6 is shown in figure 7. Similar to figure 5(*b*), the data have binned into 1 Å bins and the median, quartiles, minimum and maximum values of the segregation energies contained within each bin are shown within the boxplots. The mean segregation energy plots trend similarly to that in figure 5, though they display initially lower values close to the GB. The minimum energy whiskers again show favorable C segregation sites in most bins: up to 9 Å for ⟨1 1 0⟩ STGBs and up to 11 Å for ⟨1 1 1⟩ STGBs.

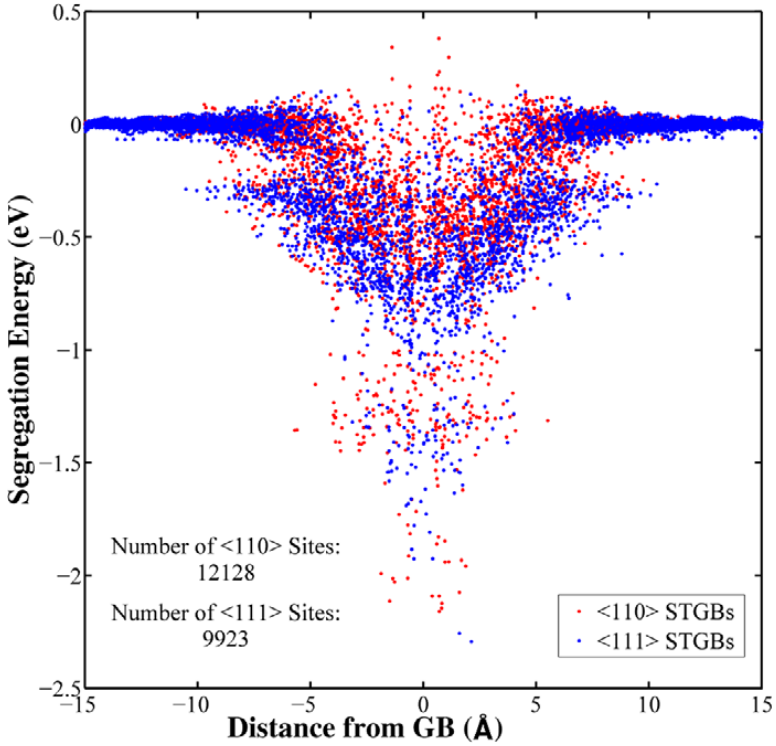

Figure 6. Distribution of segregation energies as a function of distance from the grain boundary for 50 ⟨1 1 0⟩ and 25 ⟨1 1 1⟩ STGBs. Most grain boundary sites within 8 Å have negative segregation energies that decrease with decreasing distance to the grain boundary center.

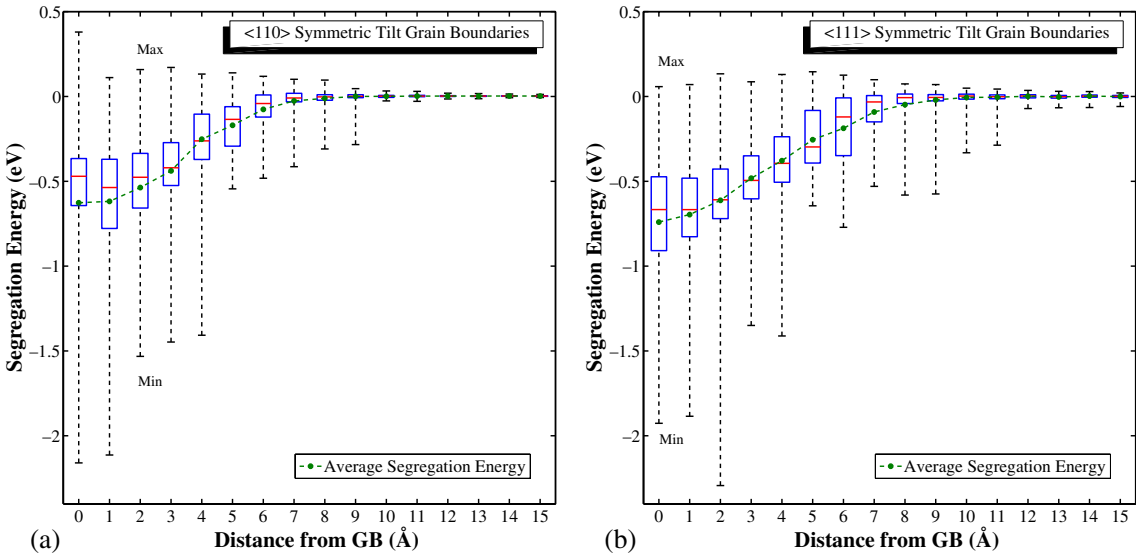

Figure 7. Boxplots of segregation energy as a function of distance from the grain boundary for (*a*) ⟨1 1 0⟩ and (*b*) ⟨1 1 1⟩ STGBs. As in figure 5, the data are divided into 1 Å bins and a boxplot is made for each bin. The red lines are medians, the blue box ends are the first and third quartiles, and the black whisker ends are minimum and maximum values. The mean segregation energy is plotted in green.

3.4. Statistical characterization of segregation energies

Ideally, it would be advantageous to be able to analytically describe the evolution of the segregation energies as a function of distance from the GB. Figure 8 provides further statistical

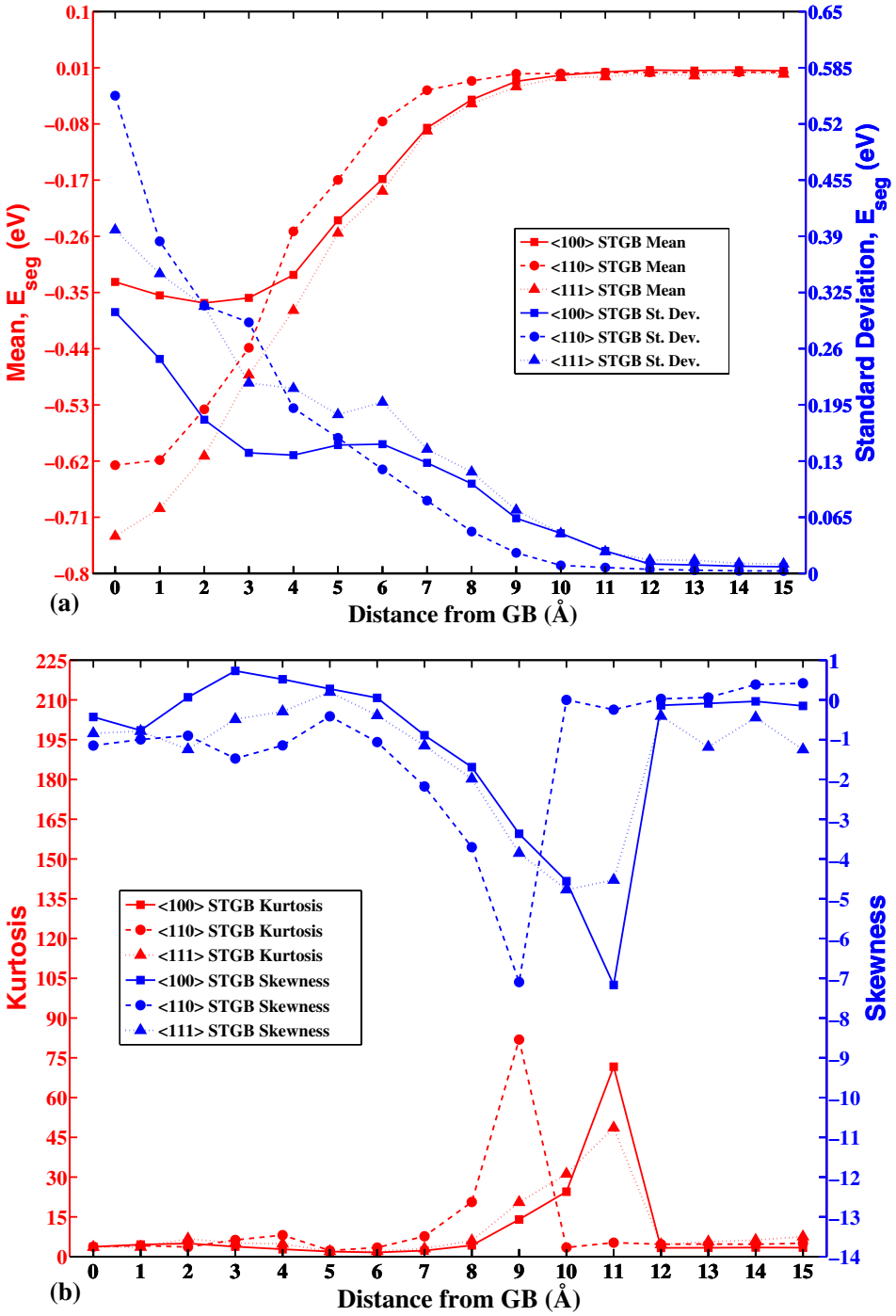

Figure 8. Statistical data for binned segregation energies from figures 5 and 7: (*a*) mean and standard deviation and (*b*) kurtosis and skewness.

data for the binned distributions of segregation energies at given distances from the GB. The mean and standard deviation of the segregation energy distributions are plotted in figure 8(*a*). For each of the GB systems, the mean values trend similarly between 5 and 15 Å, with segregation energy decreasing with increasing distance from the GB. However, within 5 Å, the mean segregation energy for the ⟨1 0 0⟩ STGB system ($E_{\text{seg}} = -0.33$ eV) is significantly higher in magnitude than the ⟨1 1 0⟩ and ⟨1 1 1⟩ STGB systems ($E_{\text{seg}} = -0.63$ eV and

$E_{seg} = -0.74$ eV, respectively). Also plotted in figure 8(*a*) is the standard deviation of the distributions, which steadily decreases toward zero as distance from the GB increases. The decrease is primarily due to the increasing number of sites with bulk energy values at distances far from the boundary. For normal distributions, the mean and standard deviation would be appropriate statistical descriptors to capture the segregation energies. However, the boxplots in figures 5 and 7 clearly show that the distributions are asymmetric to some degree and may have some extreme values or outliers.

To quantify the asymmetric distributions, the kurtosis and skewness of the distributions are plotted in figure 8(*b*). The kurtosis is a measure of how heavily the variance of the distribution is affected by extreme deviations, or outliers. Skewness is a measure of the asymmetry of a distribution and denotes in what direction a distribution possesses a longer tail of values. Figure 8(*b*) shows that the kurtosis is relatively low for most bins but becomes very large for some GB systems at approximately 8–11 Å. This is due to most of the segregation energies approaching bulk values (as viewed by the small box, or interquartile range) except for a few negative extreme values. Interestingly, in this range, increasing kurtosis correlates with decreasing skewness, which is negative for all but a few bins over all three GB systems. The skewness indicates that the majority of segregation energy distributions possess longer tails of negative energies; the kurtosis indicates when these tails are typically the result of extreme deviations. Since the magnitudes of these measures become very large at distances far from the GB, a great majority of these sites have the bulk value of segregation energy. These four statistical parameters (mean, standard deviation, skewness and kurtosis) can be used to better approximate asymmetric segregation energy distributions, e.g., using the Pearson system of distributions.

4. Discussion

Carbon was inserted into prior Fe sites at the GB to examine the influence of a wide range of GB structures on the distribution and magnitude of the segregation energies within the GB region. However, in the perfect single crystal α-Fe lattice, it is known that C occupies octahedral sites. Hence, to accommodate the difference in energy between an octahedral C atom (and vacancy) in the bulk lattice and this same C atom occupying a substitutional site at the GB, the segregation energy associated for substitutional site α can be modified, i.e.

$$E_{seg^*}^{C^\alpha} = (E_{tot}^{GB,C_{sub}^\alpha} - E_{tot}^{GB}) - (E_{bulk}^{Fe,C_{oct}} - E_{bulk}^{Fe}) + (E_{bulk}^{Fe,vac} - E_{bulk}^{Fe}), \tag{3}$$

where the Fe cohesive energy E_c^{Fe} is added to the lefthand term in parentheses to account for using the bulk energy from C in an octahedral site $E_{bulk}^{Fe,C_{oct}}$ in the right-hand term. Since the difference between equations (2) and (3) is constant, this can be calculated. In equation (2), $(E_{bulk}^{Fe,C_{sub}} - E_{bulk}^{Fe}) = 0.391$ eV. In equation (3), $(E_{bulk}^{Fe,C_{oct}} - E_{bulk}^{Fe}) = -6.273$ eV (solvation energy) and $(E_{bulk}^{Fe,vac} - E_{bulk}^{Fe}) = 5.734$ eV. The difference between equations (2) and (3) is 0.930 eV. In other words, this energy (0.930 eV) must be added to the preceding analysis to compare the energetic favorability of C in a substitutional site with that of an octahedral site in the bulk lattice. Interestingly, there are a significant number of GB substitutional sites that represent a lower energy configuration for a vacancy and interstitial C in the bulk lattice ($E_{seg} < 0.930$ eV). Specifically, the interaction length scale where this process is energetically favorable is approximately 3 Å from the GB center (total width of ≈6 Å) with the largest percentage of favorable sites occurring at the GB center: 7.2% (within 0.5 Å), 5.1% (0.5–1.5 Å), 1.1% (1.5–2.5 Å), 0.0% (2.5–3.5 Å). Additionally, the statistical representation of the segregation energy distributions can be used to rapidly quantify the probability of lower energy sites within the GB region as a function of distance from the GB plane.

4.1. Substitutional versus interstitial carbon in grain boundary region

Interstitial sites at the GB can be assessed using a similar methodology. There are an infinite number of potential interstitial starting positions that could be chosen since there is not a set lattice for GB interstitial sites as with substitutional sites. The methodology chosen for selecting interstitial sites was based on the Voronoi tesselation method. The atom positions within each GB simulation cell was used in tandem with a Voronoi tesselation of the cell to generate a list of potential starting positions for interstitial sites. In a three-dimensional space, a Voronoi tesselation divides the space into a set of space-filling polyhedra that have the following properties: (1) any point located within a polyhedron is closest to only one atom, (2) any point on a polyhedron face is equal distance to two atoms, (3) any point on a line connecting two polyhedron faces is equal distance to three atoms and (4) any point located on a polyhedron vertice is equal distance to four atoms. We have chosen to use the vertices of the Voronoi tesselation to populate the set of potential interstitial sites. In the perfect bcc lattice, the polyhedron is a truncated octahedron with 14 faces (8 regular hexagonal and 6 square), 36 edges, and 24 vertices; the Voronoi vertices are located at interstitial tetrahedral sites (i.e. equal distance to four Fe atoms). At the GB, however, the polyhedron takes on different shapes and the Voronoi vertices constitute sites that are equal distance to four atoms, which could potentially be located at the center of GB free volume regions. While a perturbation of this technique could be used to identify interstitial *octahedral* sites in the bulk lattice[6], the present technique is deemed sufficient for identifying potential interstitial sites in the GB.

The following Voronoi-based methodology was applied to 50 ⟨1 0 0⟩ STGBs (>60 000 sites). First, the distance that each C was displaced during minimization was calculated to examine how far each interstitial C moved from its initial site placement. This analysis showed that most C atoms (94.5%) were displaced <0.2 Å during the energy minimization technique, indicating that C initially placed in the tetrahedral sites tends to find a local minimum in energy and does not move to a neighboring octahedral site. Even within the GB region, where most (>99.7%) C atoms displaced greater than 0.2 Å lie, the maximum distance that the C atom was displaced from the initial site was only 0.59 Å (<0.25a_0—the minimum distance from a tetrahedral to an octahedral site). Hence, the initial positions for the C interstitials identifies local minimum energy configurations centered around the tetrahedral interstitial sites in the bulk lattice, and the greatest displacements occur within the GB region, as would be expected. Again, other perturbations of locations based on a Voronoi tesselation of the simulation cell may result in finding interstitial sites with even lower segregation energies at the boundaries, but it is anticipated that the present analysis will capture the relative influence of interstitial sites segregating to the boundary.

The results of inserting C atoms at interstitial sites was then analyzed in a similar manner to C placed at the substitutional sites. In this analysis, equation (1) is modified such that the segregation energy associated with a C atom at site α, $E_{\mathrm{seg}}^{\mathrm{C}_{\mathrm{int}}^{\alpha}}$ is calculated by

$$E_{\mathrm{seg}}^{\mathrm{C}_{\mathrm{int}}^{\alpha}} = \left(E_{\mathrm{tot}}^{\mathrm{GB},\mathrm{C}_{\mathrm{int}}^{\alpha}} - E_{\mathrm{tot}}^{\mathrm{GB}}\right) - \left(E_{\mathrm{bulk}}^{\mathrm{Fe},\mathrm{C}_{\mathrm{oct}}} - E_{\mathrm{bulk}}^{\mathrm{Fe}}\right), \tag{4}$$

where $E_{\mathrm{tot}}^{\mathrm{GB},\mathrm{C}_{\mathrm{int}}^{\alpha}}$ is the total energy of the GB structure with an interstitial C atom. Figure 9(*a*)–(*d*) corresponds to figures 4 and 5, except that the calculated segregation energies are for interstitial C using equation (4). There are several minimum energy states for interstitial C far away from

[6] For instance, some perturbations of the present technique might be to use the midpoints of the polyhedra lines connecting the faces or use the centers of polyhedra faces. In particular, the center of the {1 0 0} faces formed by the four tetrahedral sites would be in exactly the minimum energy octahedral site (0,0.5a_0,0.5a_0). However, this technique would also include the center of the {1 1 1} faces (0.25a_0,0.25a_0,0.25a_0), which turns out to be a high energy interstitial position for this potential.

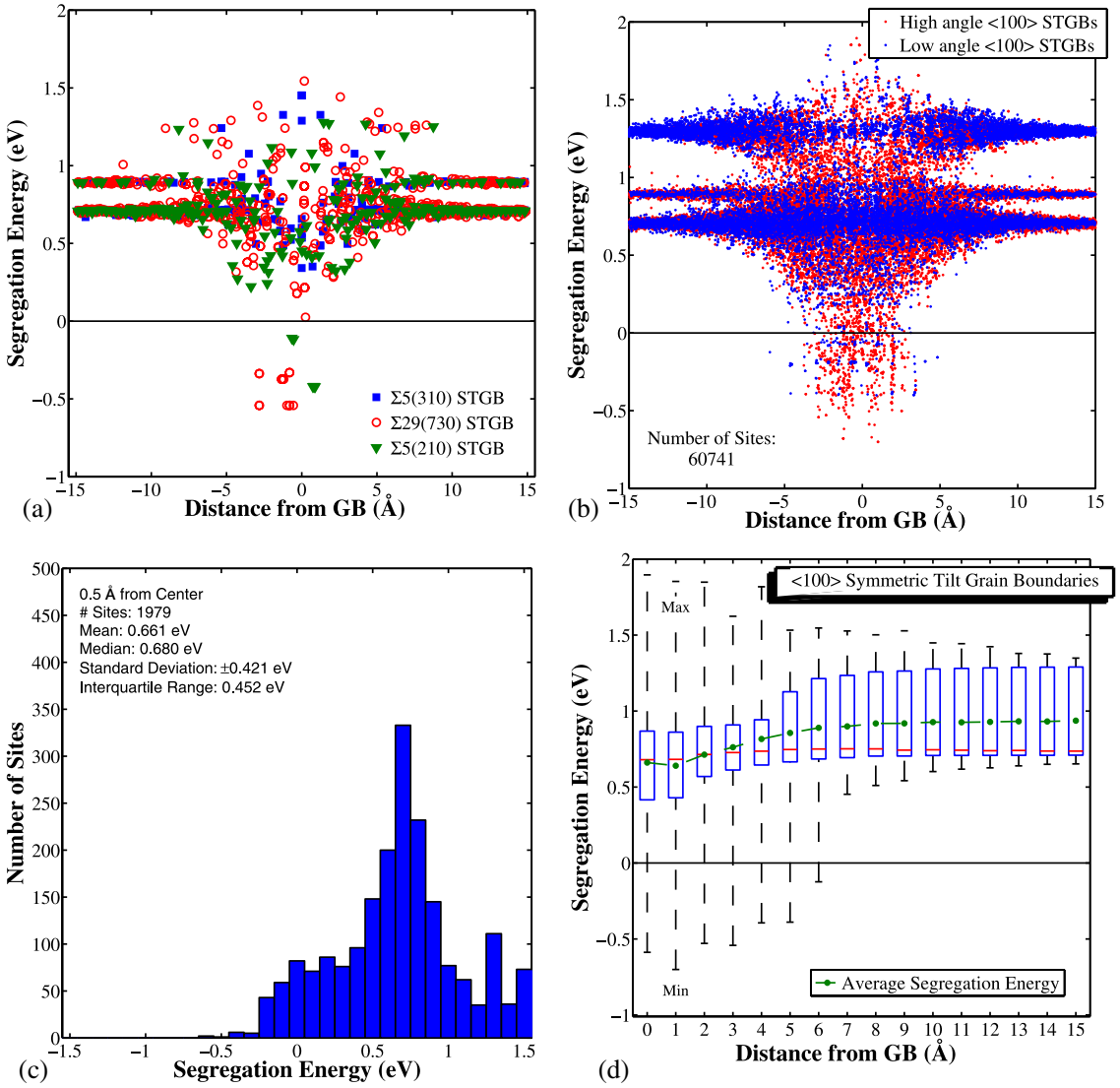

Figure 9. Distribution of segregation energies for interstitial sites as a function of distance from the grain boundary for (*a*) the Σ5(2 1 0), Σ29(7 3 0) and Σ5(3 1 0) grain boundaries and (*b*) all 50 ⟨1 0 0⟩ STGBs, as in figure 4. (*c*) The distribution of segregation energies within 0.5 Å of the grain boundary center and the associated statistics. (*d*) Boxplots of segregation energy as a function of distance from the grain boundary for all 50 ⟨1 0 0⟩ STGBs, divided into 1 Å bins and colored as in figure 5.

the GB (figure 9(*a*)). The energy of ≈0.887 eV corresponds to the tetrahedral site. However, the present Fe–C potential also has minimum energy interstitial sites at other locations, and the Voronoi vertex technique did not locate the octahedral site for the C atom upon energy minimization (i.e. $E_{\mathrm{seg}}^{\mathrm{C}_{\mathrm{int}}^{\alpha}} = 0$ is noticeably absent at large distances). Additional simulations varying the location of interstitial positions in a $10a_0$x$10a_0$x$10a_0$ bcc cell with 2000 atoms show that one of the high energy sites is directly between two Fe atoms along the ⟨1 1 1⟩ direction ($0.25a_0$,$0.25a_0$,$0.25a_0$). In figure 9(*a*), the distribution of segregation energies as a function of distance is shown for the same three GB structures as in figure 4(*a*). The GB region again shows both energetically favorable and unfavorable sites, with several energetically favorable interstitial sites having $E_{\mathrm{seg}}^{\mathrm{C}_{\mathrm{int}}^{\alpha}}$ of up to −0.5 eV (i.e. a binding energy of approximately 0.5 eV). This same trend is also evident for all 50 ⟨1 0 0⟩ STGBs (figure 9(*b*)). In fact, based on this

plot, the interaction length scale ($E_{\mathrm{seg}}^{\mathrm{C}^{\alpha}_{\mathrm{int}}} < 0$) of this GB system is on the order of 10 Å or less. Binning the data from this plot, the distribution of segregation energies within 0.5 Å from the GB center (figure 9(*c*)) show an asymmetric multimodal character with a few peaks centered about the several minimum energy interstitial states observed at large distances from the GBs. Approximately 6.9% of interstitial sites sampled showed a lower energy than C at an octahedral site in the bulk lattice. The boxplots of interstitial C shows a decrease in the mean segregation energy, the interquartile range, and the minimum segregation energy starting at ≈5 Å from the GB center (figure 9(*d*)). Interestingly, there is a larger percentage (11.8%) of energetically-favorable sites in the second bin (0.5–1.5 Å from GB center) than in the first bin (within 0.5 Å) and this percentage decreases with increasing distance from the boundary: 6.9% (0.5 Å), 11.8% (0.5–1.5 Å), 6.2% (1.5–2.5 Å), 3.0% (2.5–3.5 Å), 0.3% (3.5–4.5 Å) and 0.2% (4.5–5.5 Å). There is a high degree of anisotropy in the segregation energies in each bin due to the GB character. Moreover, in contrast to the energetic length scales for point defects in α-Fe using the same interatomic potential, the calculated length scales of interaction between C and the GB are much lower.

4.2. Methodology application and extensions

There are a number of studies that examine the influence of various alloying elements and impurities with grain boundaries. For the case of steels, while the interaction between GB structures and C represents one example of segregation that has been experimentally observed [66–68], many studies also focus on which elements segregate to the GB and how these elements may interact with other alloying elements. For instance, elements that can impact the properties of steels include, for example, phosphorus, sulfur, hydrogen, nitrogen, manganese, silicon, molybdenum, nickel, chromium, antimony and tin (e.g., [89, 90–93]. Also, experiments have shown that there may be competitive processes between elements (e.g., C and phosphorus [66]) at the GB that will also depend on processing conditions, such as equilibration temperature and quench rate. Of course, this is just one example of the complexity of segregation in steels due to the numerous interactions of different elements with GBs and the kinetics of those processes. The present work may be modified to examine how binding behavior between two different atom species (e.g., C-P, C-vacancy) or different atom configurations (e.g., H versus H_2 [17]) are affected by proximity to and within GBs. Understanding these interactions may aid in understanding the complexity of segregation and its subsequent impact on properties in α-Fe and alloy steels.

This methodology makes possible the statistical representation of impurity segregation to GBs while accounting for differences between GB structures. Thus, the results from this method could be used as inputs in other simulations, such as the kinetic Monte Carlo technique, mesoscale models, or analytical models. In this sense, the information being passed is not just scalar values but is distributions of values, which can be used to analyze sensitivity and incorporate variability due to GB structure within multiscale models. Clearly, the present application of calculating these distributions for segregation of C to GBs represents one such example of this concept. Moreover, such studies could be expanded upon to include the the effects of temperature with different solutes and solute concentrations. For example, Rittner and Seidman [94] conducted such a study for 21 ⟨1 1 0⟩ GBs to calculate segregation free energies, entropies and internal energies for a Ni–Pd system. Their work found a linear relation of segregation internal energies and entropies, which suggests the possibility for estimating segregation free energies from internal energies, an easier quantity to calculate. Simulations at temperature may lead to an even better prediction of segregation behavior to GBs in polycrystalline materials.

5. Conclusion

In this work, we have used molecular statics simulations to investigate the segregation energy of a single C atom to thousands of substitutional and interstitial atomic sites in 50 ⟨1 0 0⟩, 50 ⟨1 1 0⟩ and 25 ⟨1 1 1⟩ STGBs. A large number of boundaries, including general low and high angle GBs, were used in order to account for the variability in GB degrees of freedom observed in experimental polycrystalline materials. We can draw the following conclusions based upon our results:

(i) A methodology for calculating and analyzing the segregation energies of thousands of sites within a large number of grain boundaries with molecular statics simulations has been developed. This method samples different boundaries from a grain boundary database and calculates the segregation energy for every grain boundary site to acquire segregation statistics. As a first example, C segregation to α-Fe boundaries was examined. Both substitutional sites were sampled as well as potential interstitial sites, using the polyhedra vertices calculated using a Voronoi tesselation of the three-dimensional α-Fe coordinates. Such a methodology is warranted given that we found a large degree of anisotropy in sites and segregation energies due to varying GB structure.

(ii) The local structure within the grain boundary affects the segregation energy. As an example, the ⟨1 0 0⟩ symmetric tilt system is shown where the two $\Sigma 5$ grain boundaries are both cusps in the energy relationship (figure 1) and contain the favored structural units of this system (figure 2). However, boundaries of intermediate misorientations (e.g., the $\Sigma 29$ boundary)—which contain combinations of the same structural units—do not necessarily have the same segregation energy distributions as the $\Sigma 5$ boundaries (much lower, see figure 3).

(iii) For the substitutional C atom case, we found that it is energetically favorable for interstitial octahedral C and a vacancy in the lattice to combine within the grain boundary at a substitutional site. While this process is highly unfavorable in the lattice, there is a region that extends $\approx$3 Å from the grain boundary center where there are favorable substitutional sites for the grain boundaries sampled. The largest percentage of favorable sites are directly at the grain boundary center.

(iv) For the interstitial C case, we found that it is energetically favorable for a C atom at an octahedral site in the lattice to segregate to the grain boundary with a maximum binding energy of $\approx$0.5 eV. The interaction length scale of the grain boundary with octahedral C is $\approx$5 Å from the grain boundary center with the largest percentage of favorable sites located within the bin just outside of the grain boundary center (0.5–1.5 Å from the grain boundary center).

(v) To quantify the segregation energy distributions as a function of distance from the grain boundary, the energies were separated into 1 Å bins and characterized using several statistical descriptors: quartile values, median, mean and extreme values (see figures 5 and 7). The grain boundary atomic sites have asymmetric distributions of segregation energy with some extreme values that extend over 10 Å from the grain boundary. Furthermore, close to the grain boundary, the majority of these distributions are negatively skewed, indicating longer tails of negative segregation energies. An analytical model informed by these calculations whereby the segregation energy distribution as a function of distance is captured using four statistical parameters (mean, standard deviation, kurtosis, skewness—see figure 8) is hypothesized for upscaling to higher scale models, i.e. parameters necessary for a Pearson system of distributions.

The significance of this research is not just the calculations of the energetics of C segregation in a specific class of grain boundaries in α-Fe, but also the development of a methodology capable of ascertaining segregation energies over a wide range of grain boundary character typical of that observed in polycrystalline materials.

Acknowledgments

MAT would like to acknowledge funding under the U.S. Department of Energy and the National Energy Technology Laboratory under Award Number DE-FC26-02OR22910 and the U.S. Department of Energy's Nuclear Energy Advanced Modeling and Simulation (NEAMS) Program at the Pacific Northwest National Laboratory, which is operated by Battelle under contract No. DE-AC05-76RL01830. KNS would like to acknowledge the support by the Office of Naval Research under contract No. N000141110793. This report was prepared as an account of work sponsored by an agency of the United States government. Neither the United States government nor any agency thereof, nor any of their employees, makes any warranty, express or implied, or assumes any legal liability or responsibility for the accuracy, completeness, or usefulness of any information, apparatus, product, or process disclosed, or represents that its use would not infringe privately owned rights. Reference herein to any specific commercial product, process, or service by trade name, trademark, manufacturer, or otherwise does not necessarily constitute or imply its endorsement, recommendation, or favoring by the United States government or any agency thereof. The views and opinions of authors expressed herein do not necessarily state or reflect those of the United States government or any agency thereof. Such support does not constitute an endorsement by the Department of Energy of the work or the views expressed herein.

Reference

[1] Pugh S F 1991 *An Introduction to Grain Boundary Fracture in Metals* (London: Institute of Metals)
[2] Lejček P and Hofmann S 1995 Thermodynamics and structural aspects of grain boundary segregation *Crit. Rev. Solid State Mater. Sci.* **20** 1–85
[3] Sutton A P and Balluffi R W 1997 *Interfaces in Crystalline Materials* (Oxford: Oxford University Press)
[4] Hondros E D and Seah M P 1977 Segregation to interfaces *Int. Metall. Rev.* **22** 262
[5] Hofmann S and Lejček P 1996 Solute segregation at grain boundaries *Interface Sci.* **3** 241–67
[6] Balluffi R W 1979 *Interfacial Segregation* (Metal Park, OH: American Society for Metals)
[7] Briant C L 1992 *Materials Interfaces: Atomic-Level Structures and Properties* (London: Chapman and Hall)
[8] Foiles S M and Seidman D N 1992 *Materials Interfaces: Atomic-Level Structures and Properties* (London: Chapman and Hall)
[9] Hondros E D, Seah M P, Hofmann S and Lejček P 1996 Interfacial and surface microchemistry *Physical Metallurgy* 4th edn (Oxford: North-Holland) pp 1201–89
[10] Schweinfest R, Paxton A T and Finnis M W 2004 Bismuth embrittlement of copper is an atomic size effect *Nature* **432** 1008–11
[11] McMahon C J 2004 Brittle fracture of grain boundaries *Interface Sci.* **12** 141–6
[12] Chen Q Z, Jones C N and Knowles D M 2004 The grain boundary microstructures of the base and modified RR 2072 bicrystal superalloys and their effects on the creep properties *Mater. Sci. Eng.* A **385** 402–18
[13] Buban J P, Matsunaga K, Chen J, Shibata N, Ching W Y, Yamamoto T and Ikuhara Y 2006 Grain boundary strengthening in alumina by rare earth impurities *Science* **13** 212–15
[14] Geng W T, Freeman A J, Wu R and Olson G B 2000 Effect of Mo and Pd on the grain-boundary cohesion of Fe *Phys. Rev.* B **62** 6208–14
[15] Liu F and Kirchheim R 2004 Nano-scale grain growth inhibited by reducing grain boundary energy through solute segregation *J. Cryst. Growth* **264** 385–91
[16] Yamaguchi M, Shiga M and Kaburaki H 2005 Grain boundary decohesion by impurity segregation in a nickel–sulfur system *Science* **21** 393–7

[17] Solanki K N, Tschopp M A, Bhattia M A and Rhodes N R 2012 Nanoscale investigation of role of grain boundary character on hydrogen segregation and embrittlement in α-Fe *Metall. Mater. Trans.* A **44** 1365–75

[18] Takahashi H and Hashimoto N 1993 Radiation-induced segregation and grain boundary migration in Fe–Cr–Ni model alloy under irradiation *Mater. Trans. JIM (Japan)* **34** 1027–30

[19] Kameda J, Nishiyama Y and Bloomer T E 2001 Non-equilibrium intergranular segregation and embrittlement in neutron-irradiated ferritic alloys *Surf. Interface Anal.* **31** 522–31

[20] Johnson R A and Lam N Q 1976 Solute segregation in metals under irradiation *Phys. Rev.* B **13** 4364–75

[21] Lam N Q, Okamoto P R, Wiedersich H and Taylor A 1978 Radiation-induced solute segregation and precipitation in alloys *Metall. Trans.* A **9** 1707–14

[22] Faulkner R, Song S and Flewitt P 1996 A model describing neutron irradiation-induced segregation to grain boundaries in dilute alloys *Metall. Mater. Trans.* A **27** 3381–90

[23] Taheri M L, Stach E, Radmilovic V, Weiland H and Rollett A D 2005 situ electron microscopy studies of the effect of solute segregation on grain boundary anisotropy and mobility in an Al–Zr alloy *Mater. Res. Soc. Symp. Proc.* **839** 187–94

[24] Molodov D A, Czubayko U, Gottstein G and Shvindlerman L S 1998 On the effect of purity and orientation on grain boundary motion *Acta Mater.* **46** 553–64

[25] Sauvage X and Ivanisenko Y 2007 The role of carbon segregation on nanocrystallisation of pearlitic steels processed by severe plastic deformation. *J. Mater. Sci.* **42** 1615–21

[26] Krakauer B W, Hu J G, Kuo S-M, Mallick R L, Seki A, Seidman D N, Baker J P and Loyd R J 1990 A system for systematically preparing atom-probe field-ion-microscope specimens for the study of internal interfaces *Rev. Sci. Instrum.* **61** 3390–8

[27] Lejček P, Hofmann S and Paidar V 2003 Solute segregation and classification of [1 0 0] tilt grain boundaries in α-iron: consequences for grain boundary engineering *Acta Mater.* **51** 3951–63

[28] Lejček P 1994 Characterization of grain boundary segregation in an Fe–Si alloy *Anal. Chim. Acta* **297** 165–78

[29] Kobayashi S, Tsurekawa S, Watanabe T and Palumbo G 2010 Grain boundary engineering for control of sulfur segregation-induced embrittlement in ultrafine-grained nickel. *Scr. Mater.* **62** 294–7

[30] Taheri M L, Sebastian J T, Reed B W, Seidman D N and Rollett A D 2010 Site-specific atomic scale analysis of solute segregation to a coincidence site lattice grain boundary *Ultramicroscopy* **110** 278–84

[31] Isheim D, Kolli R P, Fine M E and Seidman D N 2006 An atom-probe tomographic study of the temporal evolution of the nanostructure of Fe–Cu based high-strength low-carbon steels *Scr. Mater.* **55** 35–40

[32] Seto K, Larson D J, Warren P J and Smith G D W 1999 Grain boundary segregation in boron added interstitial free steels studied by 3-dimensional atom probe *Scr. Mater.* **40** 1029–34

[33] Krakauer B W and Seidman D N 1998 Subnanometer scale study of segregation at grain boundaries in an Fe(Si) alloy *Acta Mater.* **46** 6145–61

[34] Arias T A and Joannopoulos J D 1992 *Ab initio* prediction of dopant segregation at elemental semiconductor grain boundaries without coordination defects *Phys. Rev. Lett.* **69** 3330–3

[35] Maiti A, Chisholm M F, Pennycook S J and Pantelides S T 1996 Dopant segregation at semiconductor grain boundaries through cooperative chemical rebonding *Phys. Rev. Lett.* **77** 1306–9

[36] Zhang L, Shu X, Jin S, Zhang Y and Lu G H 2010 First-principles study of He effects in a bcc Fe grain boundary: site preference, segregation and theoretical tensile strength *J. Phys.: Condens. Matter* **22** 375401

[37] Liu X, Wang X, Wang J and Zhang H J 2005 First-principles investigation of Mg segregation at $\Sigma = 11(113)$ grain boundaries in Al *J. Phys.: Condens. Matter* **17** 4301–8

[38] Christensen M, Angeliu T M, Ballard J D, Vollmer J, Najafabadi R and Wimmer E 2010 Effect of impurity and alloying elements on Zr grain boundary strength from first-principles computations *J. Nucl. Mater.* **404** 121–7

[39] Yuasa M and Mabuchi M J 2010 Effects of segregated Cu on an Fe grain boundary by first-principles tensile tests *J. Phys.: Condens. Matter* **22** 505705

[40] Wachowicz E and Kiejna A 2008 Effect of impurities on grain boundary cohesion in bcc iron *Comput. Mater. Sci.* **43** 736–43

[41] Chen L, Peng P, Zhuang H L and Zhou D W 2006 First-principle investigation of bismuth segregation at $\Sigma 5$ (0 1 2) grain-boundaries in nickel *Trans. Nonferrous Met. Soc. China* **16** (Suppl 2(0)) s813–19

[42] Wu R, Freeman A J and Olson G B 1996 Effects of carbon on Fe grain boundary cohesion: first-principles determination *Phys. Rev.* B **53** 7504–9

[43] Kart H H and Cagin T 2008 The effects of boron impurity atoms on nickel $\Sigma 5$ (0 1 2) grain boundary by first principles calculations *J. Achievements Mater. Manuf. Eng.* **30** 177–81

[44] Menyhard M, Yan M and Vitek V 1994 Atomistic vs phenomenological approaches to grain boundary segregation: computer modeling of Cu–Ag alloys *Acta Metall. Mater.* **42** 2783–96

[45] Millett P C, Selvam R P, Bansal S and Saxena A 2005 Atomistic simulation of grain boundary energetics: effects of dopants *Acta Mater.* **53** 3671–8

[46] Sutton A P and Vitek V 1982 An atomistic study of tilt grain boundaries with substitutional impurities *Acta Metall.* **30** 2011–33

[47] Olmsted D L 2009 A new class of metrics for the macroscopic crystallographic space of grain boundaries *Acta Mater.* **57** 2793–9

[48] Holm E A, Olmsted D L and Foiles S M 2010 Comparing grain boundary energies in face-centered cubic metals: Al, Au, Cu and Ni *Scr. Mater.* **63** 905–8

[49] Wolf D 1991 Structure and energy of general grain boundaries in bcc metals *J. Appl. Phys.* **69** 185

[50] Lezzar B, Khalfallah O, Larere A, Paidar V and Hardouin Duparc O 2004 Detailed analysis of the segregation driving forces for Ni(Ag) and Ag(Ni) in the $\Sigma = 11$ and $\Sigma = 11$ grain boundaries *Acta Mater.* **52** 2809–18

[51] Kurtz R J and Heinisch H L 2004 The effects of grain boundary structure on binding of He in Fe *J. Nucl. Mater.* **329–333** 1199–203

[52] Gao F, Heinisch H and Kurtz R J 2006 Diffusion of He interstitials in grain boundaries in α-Fe *J. Nucl. Mater.* **351** 133–40

[53] Malerba L, Terentyev D, Olsson P, Chakarova R and Wallenius J 2004 Molecular dynamics simulation of displacement cascades in Fe–Cr alloys *J. Nucl. Mater.* **329–333** 1156–60

[54] Saylor D M, Morawiec A and Rohrer G S 2002 Distribution and energies of grain boundaries in magnesia as a function of five degrees of freedom *J. Am. Ceram. Soc.* **85** 3081–3

[55] Kim C-S, Hu Y, Rohrer G S and Randle V 2005 Five-parameter grain boundary distribution in grain boundary engineered brass *Scr. Mater.* **52** 633–7

[56] Saylor D M, El Dasher B S, Rollett A D and Rohrer G S 2004 Distribution of grain boundaries in aluminum as a function of five macroscopic parameters *Acta Mater.* **52** 3649–55

[57] Tschopp M A and McDowell D L 2007 Structures and energies of $\Sigma 3$ asymmetric tilt grain boundaries in Cu and Al *Phil. Mag.* **87** 3147–73

[58] Tschopp M A and McDowell D L 2007 Asymmetric tilt grain boundary structure and energy in copper and aluminum *Phil. Mag.* **87** 3871–92

[59] Tschopp M A and McDowell D L 2007 Structural unit and faceting description for $\Sigma 3$ asymmetric tilt grain boundaries *J. Mater. Sci.* **42** 7806–11

[60] Spearot D E, Tschopp M A, Jacob K I and McDowell D L 2007 Tensile strength of $\langle 1\,0\,0 \rangle$ and $\langle 1\,1\,0 \rangle$ tilt bicrystal copper interfaces *Acta Mater.* **55** 705–14

[61] Tschopp M A and McDowell D L 2008 Dislocation nucleation in $\Sigma 3$ asymmetric tilt grain boundaries *Int. J. Plasticity* **24** 191–217

[62] Tschopp M A and McDowell D L 2008 Grain boundary dislocation sources in nanocrystalline copper *Scr. Mater.* **58** 299–302

[63] Tschopp M A, Tucker G J and McDowell D L 2008 Atomistic simulations of tension-compression asymmetry in grain boundary dislocation nucleation *Comput. Mater. Sci.* **44** 351–62

[64] Tschopp M A, Horstemeyer M F, Gao F, Sun X and Khaleel M 2011 Energetic driving force for preferential binding of self-interstitial atoms to Fe grain boundaries over vacancies *Scr. Mater.* **64** 908–11

[65] Tschopp M A, Solanki K N, Gao F, Sun X, Khaleel M A and Horstemeyer M F 2012 Probing grain boundary sink strength at the nanoscale: energetics and length scales of vacancy and interstitial absorption by grain boundaries in α-Fe *Phys. Rev.* B **85** 064108

[66] Cowan J R, Evans H E, Jones R B and Bowen P 1998 The grain-boundary segregation of phosphorus and carbon in an Fe–P–C alloy during cooling *Acta Metall.* **46** 6565–74

[67] Papazian J M and Beshers D N 1971 Grain boundary segregation of carbon in iron *Metall. Trans.* **2** 497–503

[68] Takahashi J, Sugiyama M and Maruyama N 2005 Quantitative observation of grain boundary carbon segregation in bake-hardening steels *Nippon Steel Tech. Rep.* **91** 28–33

[69] Hong S Y and Anderson A B 1989 Diffusion and surface segregation of carbon in α-Fe: molecular-orbital theory *Phys. Rev.* B **40** 7508–12

[70] Yan J-A, Wang C-Y, Duan W-H and Wang S-Y 2004 Electronic states and doping effect of carbon in the edge-dislocation core of bcc iron *Phys. Rev.* B **69** 214110

[71] Ruda M, Farkas D and Garcia G 2009 Atomistic simulations in the Fe-C system *Comput. Mater. Sci.* **45** 550–60

[72] Veiga R G A, Perez M, Becquart C S, Domain C and Garruchet S 2010 Effect of the stress field of an edge dislocation on carbon diffusion in α-iron: coupling molecular statics and atomistic kinetic Monte Carlo *Phys. Rev.* B **82** 054103

[73] Hristova E, Janisch R, Drautz R and Hartmaier A 2011 Solubility of carbon in α-iron under volumetric strain and close to the $\Sigma 5(3\,1\,0)[0\,0\,1]$ grain boundary: comparison of DFT and empirical potential methods *Comput. Mater. Sci.* **50** 1088–96

[74] Hepburn D J and Ackland G J 2008 Metallic-covalent interatomic potential for carbon in iron *Phys. Rev.* B **78** 165115

[75] Domain C, Becquart C S and Foct J 2004 *Ab initio* study of foreign interstitial atom (c,n) interactions with intrinsic point defects in α-Fe *Phys. Rev.* B **69** 144112

[76] Plimpton S 1995 Fast parallel algorithms for short-range molecular dynamics *J. Comput. Phys.* **117** 1–19

[77] Daw M S and Baskes M I 1983 Semiempirical, quantum mechanical calculation of hydrogen embrittlement in metals *Phys. Rev. Lett.* **50** 1285–8

[78] Daw M S and Baskes M I 1984 Embedded-atom method: derivation and application to impurities, surfaces, and other defects in metals *Phys. Rev.* B **29** 6443–53

[79] Terentyev D, Anento N, Serra A, Jansson V, Khater H and Bonny G 2011 Interaction of carbon with vacancy and self-interstitial atom clusters in α-iron studied using metallic covalent interatomic potential *J. Nucl. Mater.* **408** 272–84

[80] Rittner J D and Seidman D N 1996 Limitations of the structural unit model *Mater. Sci. Forum* **207–209** 333–6

[81] Shibuta Y, Takamoto S and Suzuki T 2008 A molecular dynamics study of the energy and structure of the symmetric tilt boundary of iron *ISIJ Int.* **48** 1582–91

[82] Wolf D 1989 Structure-energy correlation for grain boundaries in FCC metals: I. Boundaries on the (1 1 1) and (1 0 0) planes *Acta Metall.* **37** 1983–93

[83] Wolf D 1989 Structure-energy correlation for grain boundaries in FCC metals: II. Boundaries on the (1 1 0) and (1 1 3) planes *Acta Metall.* **37** 2823–33

[84] Wolf D 1990 Structure-energy correlation for grain boundaries in FCC metal: III. Symmetrical tilt boundaries *Acta Metall.* **38** 781–90

[85] Wolf D 1990 Structure-energy correlation for grain boundaries in FCC metals: IV. Asymmetrical twist (general) boundaries *Acta Metall.* **38** 791–8

[86] Mishin Y, Asta M and Li J 2010 Atomistic modeling of interfaces and their impact on microstructure and properties *Acta Mater.* **58** 1117–51

[87] Sutton A P and Vitek V 1983 On the structure of tilt grain boundaries in cubic metals: I. Symmetrical tilt boundaries *Phil. Trans. R. Soc. Lond.* A **309** 1–36

[88] Li J 2003 Atomeye: an efficient atomistic configuration viewer *Modelling Simul. Mater. Sci. Eng.* **11** 173

[89] Banerji S K, McMahon C J Jr. and Feng H C 1978 Intergranular fracture in 4340-type steels: effects of impurities and hydrogen *Metall. Trans.* A **9A** 237–47

[90] Briant C L, Feng H C and McMahon C J Jr. 1978 Embrittlement of a 5 pct nickel high strength steel by impurities and their effects on hydrogen-induced cracking *Metall. Trans.* A **9A** 625–33

[91] Yu J and McMahon C J Jr. 1980 The effects of composition and carbide precipitation on temper embrittlement of 2.25 Cr-1 Mo steel: I. Effects of P and Sn *Metall. Trans.* A **11A** 277–89

[92] Yu J and McMahon C J Jr. 1980 The effects of composition and carbide precipitation on temper embrittlement of 2.25 Cr-1 Mo steel: II. Effects of Mn and Si *Metall. Trans.* A **11A** 291–300

[93] Kameda J and McMahon C J Jr. 1981 The effects of Sb, Sn, and P on the strength of grain boundaries in a Ni–Cr steel *Metall. Trans.* A **12A** 31–7

[94] Rittner J D and Seidman D N 1997 Solute-atom segregation to $\langle 1\,1\,0 \rangle$ symmetric tilt grain boundaries. *Acta Mater.* **45** 3191–202

Phase-field Analysis of Fracture-induced Twinning in Single Crystals

John D. Clayton and Jaroslaw Knap

Acta Materialia, 61 (2013)

Available online at www.sciencedirect.com
SciVerse ScienceDirect
Acta Materialia 61 (2013) 5341–5353
Acta MATERIALIA
www.elsevier.com/locate/actamat

Phase-field analysis of fracture-induced twinning in single crystals

J.D. Clayton [a,*], J. Knap [b]

[a] Impact Physics, RDRL-WMP-C, US Army Research Laboratory, Aberdeen Proving Ground, MD 21005-5066, USA
[b] Computational Science and Engineering, RDRL-CIH-C, US Army Research Laboratory, Aberdeen Proving Ground, MD 21005-5066, USA

Received 22 March 2013; received in revised form 17 May 2013; accepted 18 May 2013
Available online 18 June 2013

Abstract

Deformation twinning at the tip of a straight crack or notch is analyzed using a phase-field method that seeks equilibrium twin morphologies via direct minimization of a free energy functional. For isotropic solids, the tendency to twin under mode I or mode II loading is found to depend weakly on Poisson's ratio and elastic nonlinearity and strongly on surface energy and twinning shear (i.e. eigenstrain). Depending on the coherent twin boundary energy, anisotropy of surface energy is important for mode I loading but less so for mode II. Model predictions for several single crystals are in agreement with experimental observations. Calcite demonstrates a preference for mode I cleavage crack extension over crack tip twinning. Magnesium shows a likelihood for tensile twinning from a pre-existing crack on the basal plane. In sapphire, a preference for rhombohedral twins over basal twins is apparent, with the latter thinner in shape than the former.
Published by Elsevier Ltd. on behalf of Acta Materialia Inc.

Keywords: Phase field; Twinning; Fracture; Crystals; Modeling and simulation

1. Introduction

Deformation twinning, i.e. twinning induced by mechanical stress, and cleavage fracture, i.e. transgranular fracture on preferred crystallographic planes, are two fundamental inelastic deformation mechanisms that may occur in crystals. In some cases, twins or twin boundaries may act as nucleation sites for fracture [1]; in others, crack tips may provide the necessary stress concentrations for twin nucleation and growth [2].

In dynamic experiments such as plate impact, both twinning and cleavage fracture may occur, but whether twinning precedes or follows fracture cannot usually be determined from analysis of experimental (e.g. Hugoniot) data and post-mortem material characterization. This is the case for impact experiments on sapphire [3], wherein theoretical strengths for twinning, slip and shear fracture are thought to be of the same order of magnitude [4]. Indentation experiments on ceramics and minerals often show evidence of both fracture and twinning, with surface damage strongly promoting the nucleation and growth of twins in calcite, for example [5,6].

The present work seeks (i) to develop an improved understanding of the general factors affecting twinning induced by fracture; and (ii) to test a predictive model for twinning at a crack/notch tip in several real materials. Phase-field theory and numerical simulation are applied to study twin nucleation and growth from a pre-existing crack or notch. A prior analysis [2] based on the Peierls–Nabarro concept and ideas from Ref. [7] was developed to judge the tendency of a solid to undergo either microtwinning or slip of leading and trailing partial dislocations on the same plane. This treatment demonstrated success for several face-centered cubic metals when compared to results of atomic simulations, but the model requires knowledge of parameters associated with the stacking fault energy surface that seem only to be obtainable from atomic simulation of planar defects. An analytical model

* Corresponding author. Tel.: +1 4102786146.
E-mail addresses: john.d.clayton1.civ@mail.mil (J.D. Clayton), jaroslaw.knap.civ@mail.mil (J. Knap).

predicting the likelihood of twinning or extension of a mode I slit crack is described in Ref. [8]; this model requires knowledge of energetic data associated with total resistance to twinning or fracture that are evidently not available from standard experiments, though twin boundary and cleavage surface energies can be substituted as an approximation. As will be shown later, the current work offers more insight into the total twinning resistance that could be used in such a model.

In the present phase-field approach [9,10], the only constitutive model parameters are the twinning shear (usually known from crystallography), elastic constants (known from experiments), gradient energy coefficient(s), and double-well energy barrier height. The latter two can be related to the twin boundary surface energy (measurable from experiment or atomic simulation) and the thickness of the diffuse interface, which can be assigned physical significance if the normal distance from the phase/twin boundary over which atoms are displaced from their usual positions in a perfect crystal is known, e.g. from atomic simulation. For prescribed boundary conditions and problem geometry, the tendency for a pre-cracked crystal to continue to crack or to twin then necessarily depends on these parameters and the surface energy associated with cleavage fracture. The model does not depend on the numerical method of solution or grid size (i.e. the theory itself is mesh independent), but any discretization should be sufficiently refined to resolve continuum fields where gradients exist, e.g. in interfacial regions.

The present work does not address plastic slip distinct from the motion of twinning partials inherent in deformation twinning. Nanoscale treatments of discrete slip criteria include Refs. [2,7]; mesoscale continuum crystal plasticity models of slip and twinning are described in Ref. [11] and references therein.

Several other relevant modeling approaches are noted. Phase transformation has been studied at tips of moving cracks via analytical solutions to phase-field models [12,13]. Like twinning, phase transformations may be induced by strong local elastic fields at crack tips; transformation strain in the former often includes dilatation, while deformation twinning involves large shear without inelastic volume change. Competition among phase transformation, fracture and plastic deformation was studied using a continuum thermodynamic approach implemented in the finite-element method [14]; twinning was also modeled. Phase-field models of fracture have also been implemented [15–19]. The present paper does not develop a phase-field model for fracture—herein a stationary pre-crack is represented explicitly by a thin notch with free surface boundary conditions—but conceivably both twinning and fracture could be modeled simultaneously using the phase-field approach, with distinct order parameters accounting for transformation to twinned and/or fractured material.

This paper is organized as follows. The phase-field theory developed and implemented in Refs. [9,10] is reviewed in Section 2, including various elasticity models (linear isotropic, linear anisotropic, nonlinear neo-Hookean) considered later. Analysis of possible twinning or crack extension under pure mode I or mode II loading in generic isotropic elastic solids follows in Section 3. In this analysis, a normalized energy functional is derived that depends on several dimensionless material parameters. The effects of these parameters—twinning shear, Poisson's ratio and normalized twin boundary energy—on twinnability are investigated through phase-field simulations. In Section 4, two-dimensional (2-D) simulations of twinning from a mode I crack are reported for calcite ($CaCO_3$), sapphire (α-Al_2O_3) and magnesium (Mg) and compared with experimental observations. In Section 5, three-dimensional (3-D) simulations of basal and rhombohedral twinning in a sapphire single crystal with a pre-existing halfpenny-shaped notch are analyzed. Conclusions follow in Section 6. Regarding notation, vectors and second-order tensors are written in bold italic; scalars and components are written in plain italic, with summation applied over repeated indicial subscripts.

2. Theory

Only essential details of the phase-field theory are reported here; complete descriptions are given elsewhere [9,10]. Let $\boldsymbol{x}$ and $\boldsymbol{X}$ denote sufficiently smooth spatial and material coordinates of a body of reference volume Ω, related by the differentiable mapping $\boldsymbol{x} = \boldsymbol{\chi}(\boldsymbol{X}, t)$ that is one-to-one and invertible at any fixed t. Let $\eta(\boldsymbol{X}, t)$ denote the order parameter that distinguishes between the original (parent) crystal, the twin, and the interfacial boundary regions between parent and twin:

$$\eta = 0 \forall \boldsymbol{X} \in \text{ parent}, \qquad \eta = 1 \forall \boldsymbol{X} \in \text{ twin},$$
$$0 < \eta < 1 \forall \boldsymbol{X} \in \text{ boundary}. \tag{2.1}$$

The deformation gradient is

$$\boldsymbol{F} = \nabla \boldsymbol{\chi} = \boldsymbol{F}^E \boldsymbol{F}^\eta, \tag{2.2}$$

where ∇ denotes the material gradient, $\boldsymbol{F}^E$ accounts for elastic stretch and rotation, and

$$\boldsymbol{F}^\eta = \mathbf{1} + [\varphi(\eta)\gamma_0]\boldsymbol{s} \otimes \boldsymbol{m} \tag{2.3}$$

accounts for twinning shear. Orthogonal unit vectors (in material coordinates) in the twinning direction and normal to twinning plane are $\boldsymbol{s}$ and $\boldsymbol{m}$, the magnitude of maximum twinning shear is γ_0, and $\varphi(\eta)$ is an interpolator satisfying $\varphi(0) = 0,\ \varphi(1) = 1,\ \varphi'(0) = \varphi'(1) = 0,$ where $(\cdot)' = \mathrm{d}(\cdot)/\mathrm{d}\eta$. Defining $\boldsymbol{C}^E = (\boldsymbol{F}^E)^{\mathrm{T}}\boldsymbol{F}^E$, the local ratio of deformed to initial volume is $J = \det\boldsymbol{F} = (\det\boldsymbol{C}^E)^{1/2}$.

The total energy functional for the body is

$$\Psi(\boldsymbol{\chi}, \eta) = \int_\Omega [W(\boldsymbol{F}, \eta) + f(\eta, \nabla\eta)]\mathrm{d}\Omega. \tag{2.4}$$

The strain energy W and interfacial energy f per unit reference volume are of the form

$$W = W[\boldsymbol{C}^E(\boldsymbol{F},\eta),\eta], \qquad f = f_0(\eta) + \boldsymbol{\kappa} : (\nabla\eta \otimes \nabla\eta). \tag{2.5}$$

Let $\partial\Omega$ denote the boundary of Ω. Imposing the variational principle

$$\delta\Psi = \oint_{\partial\Omega} (\boldsymbol{t}\cdot\delta\boldsymbol{\chi} + h\delta\eta)\mathrm{d}S, \tag{2.6}$$

the following local equilibrium equations and boundary conditions are derived [9]:

$$\nabla\cdot\partial W/\partial\boldsymbol{F} = \nabla\cdot\boldsymbol{P} = 0,$$
$$f_0' - 2\nabla\cdot(\boldsymbol{\kappa}\nabla\eta) + \partial W/\partial\eta = 0; \tag{2.7}$$
$$\boldsymbol{t} = \boldsymbol{P}\cdot\boldsymbol{n}, \qquad h = 2\boldsymbol{\kappa} : (\nabla\eta\otimes\boldsymbol{n}). \tag{2.8}$$

Traction per unit reference area is $\boldsymbol{t}$; conjugate force to the order parameter is h; outward normal to $\partial\Omega$ is $\boldsymbol{n}$. Phase equilibrium in (2.7) can be written for homogeneous $\boldsymbol{\kappa}$ as

$$f_0' = 2\boldsymbol{\kappa} : \nabla\nabla\eta + \tau\gamma_0\varphi',$$
$$\tau = \boldsymbol{S} : [\boldsymbol{C}^E(\boldsymbol{s}\otimes\boldsymbol{m})\boldsymbol{F}^{\eta\ -1}], \quad \boldsymbol{S} = 2\partial W/\partial\boldsymbol{C}^E. \tag{2.9}$$

In the present work, attention is restricted to a double-well potential $f_0 = A\eta^2(1-\eta)^2$, with A a constant related to the barrier height. When isotropic surface energy is imposed, for which $\boldsymbol{\kappa} = \kappa\boldsymbol{1}$, with κ a constant, then

$$f = A\eta^2(1-\eta)^2 + \kappa|\nabla\eta|^2, \qquad \kappa = 3\Gamma l/4,$$
$$A = 12\Gamma/l, \tag{2.10}$$

where Γ and l are equilibrium energy per unit area and thickness of an unstressed interface [9]. Anisotropic representations of surface energy are also considered. For example, in a material coordinate frame $\{\boldsymbol{e}_I\}$ with $\boldsymbol{e}_1\|\boldsymbol{s}$ and $\boldsymbol{e}_2\|\boldsymbol{m}$, then $\kappa_{11} > \kappa_{22}$ accounts for the increase in energy at an incoherent twin boundary [20] due to the local (e.g. core) energy of twinning dislocations [21], and $\kappa_{12} = \kappa_{21} = 0$ in this coordinate system.

Several different elastic models are considered [10]. For compressible neo-Hookean behavior

$$W = \frac{1}{2}\lambda[(\ln J)^2 + \mathrm{tr}\boldsymbol{C}^E - 3] - \mu\ln J, \tag{2.11}$$

where λ and μ are usual isotropic elastic constants. The First Piola–Kirchhoff stress is

$$\boldsymbol{P} = \partial W/\partial\boldsymbol{F} = \boldsymbol{F}^E\boldsymbol{S}\boldsymbol{F}^{\eta-\mathrm{T}}$$
$$= \boldsymbol{F}^E[\mu\boldsymbol{1} + (\lambda\ln J - \mu)\boldsymbol{C}^{E-1}]\boldsymbol{F}^{\eta-\mathrm{T}}. \tag{2.12}$$

For linear elastic behavior,

$$W = W[\boldsymbol{\epsilon}^E(\nabla\boldsymbol{u},\eta),\eta] = \frac{1}{2}\mathsf{C}_{IJKL}(\eta)\epsilon^E_{IJ}\epsilon^E_{KL}, \tag{2.13}$$

where the following geometric relationships apply:

$$\boldsymbol{F} = \boldsymbol{1} + \nabla\boldsymbol{u} \simeq \boldsymbol{1} + \boldsymbol{\beta}^E + \boldsymbol{\beta}^\eta; \tag{2.14}$$
$$\boldsymbol{F}^E \simeq \boldsymbol{1} + \boldsymbol{\beta}^E, \quad \boldsymbol{\epsilon}^E = \frac{1}{2}[\boldsymbol{\beta}^E + (\boldsymbol{\beta}^E)^{\mathrm{T}}], \quad \boldsymbol{C}^E \simeq \boldsymbol{1} + 2\boldsymbol{\epsilon}^E; \quad \boldsymbol{F}^\eta = \boldsymbol{1} + \boldsymbol{\beta}^\eta; \tag{2.15}$$
$$\boldsymbol{P} = \partial W/\partial\nabla\boldsymbol{u}, \quad \tau = \boldsymbol{P} : (\boldsymbol{s}\otimes\boldsymbol{m}). \tag{2.16}$$

For anisotropic elasticity, second-order coefficents C_{IJKL} are interpolated between parent and twinned domains using φ [9,10]. For isotropic elasticity, $\mathsf{C}_{IJKL} = \lambda\delta_{IJ}\delta_{KL} + \mu(\delta_{IK}\delta_{JL} + \delta_{IL}\delta_{JK})$, and W and C_{IJKL} do not depend explicitly on η. The elastic driving force for twinning, τ, is the resolved shear stress on the twinning plane in the direction of twinning shear.

Two different interpolation functions are also considered:

$$\varphi = (3-2\eta)\eta^2 \qquad \text{(polynomial)}, \tag{2.17}$$
$$\varphi = 1/[1 + \mathrm{e}^{-2k(\eta-0.5)}] \qquad \text{(exponential)}. \tag{2.18}$$

Polynomial function (2.17) has been used frequently [9,10,22] and yields a gradual change in φ over $0 < \eta < 1$; the Fermi–Dirac function (2.18), here with $k = 15$, provides a steeper increase in φ at $\eta \approx 0.5$, as is clear from Fig. 1.

Solutions to governing equations are obtained numerically using the finite-element method. The solution procedure [9] involves minimization of free energy functional Ψ, subject to possible boundary conditions/constraints, over domain Ω, yielding the equilibrium fields $(\boldsymbol{\chi}, \eta)$. Kinetics and dissipation are not quantified explicitly.

3. Twinning under mode I and II loading in isotropic solids

3.1. Dimensionless parameters

Consider the phase-field theory of Section 2 applied to an isotropic solid. Dividing by the shear modulus, a normalized free energy functional becomes

$$\bar{\Psi} = \Psi/\mu = \int_\Omega (\overline{W} + \bar{f})\mathrm{d}\Omega, \tag{3.1}$$
$$\overline{W} = \frac{\nu}{1-2\nu}(\mathrm{tr}\nabla\boldsymbol{u})^2 + (\nabla\boldsymbol{u} - \gamma_0\varphi\boldsymbol{s}\otimes\boldsymbol{m})_{\mathrm{s}} : (\nabla\boldsymbol{u} - \gamma_0\varphi\boldsymbol{s}\otimes\boldsymbol{m})_{\mathrm{s}}, \tag{3.2}$$
$$\bar{f} = \overline{A}\eta^2(1-\eta)^2 + \bar{\kappa}l^2|\nabla\eta|^2, \tag{3.3}$$
$$\nu = \lambda/(2\lambda+2\mu), \quad \overline{A} = A/\mu = 12\Gamma/(\mu l), \quad \bar{\kappa} = \kappa/(\mu l^2) = 3\Gamma/(4\mu l). \tag{3.4}$$

Notation $(\cdot)_{\mathrm{s}}$ denotes the symmetric part of a second-order tensor. Since $\mu > 0$, a solution $(\boldsymbol{u}, \eta)$ for a given set of boundary conditions on $\partial\Omega$ that minimizes Ψ also minimizes $\bar{\Psi}$; this could be a local (metastable) or global (stable) minimum energy configuration.

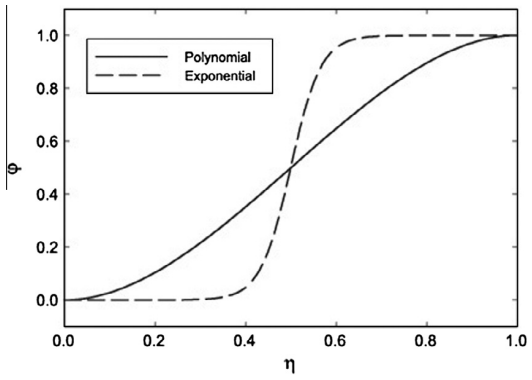

Fig. 1. Phase-field interfacial interopolation functions (2.17) and (2.18).

Let Γ_0 denote a constant reference value of twin boundary surface energy per unit area, and let $\overline{A}_0$ and $\bar{\kappa}_0$ denote the corresponding values of parameters in (3.4) for fixed $\mu = \mu_0$ and fixed l. Then

$$\Gamma/\Gamma_0 = \overline{A}/\overline{A}_0 = \bar{\kappa}/\bar{\kappa}_0. \tag{3.5}$$

In all subsequent analysis l is held fixed. In what follows, representative values of $\Gamma_0 = 100\ \mathrm{mJ\ m^{-2}}$ and $\mu_0 = 25$ GPa, with $l = 1.0$ nm [9,10,22], are used to establish $\overline{A}_0$ and $\bar{\kappa}_0$. During simulations, the effect of surface energy is then studied by varying Γ/Γ_0. In most simulations, isotropic surface energy is assumed, but in some (2-D) simulations, $\kappa_{11} = \alpha\kappa_{22} = \alpha\kappa$ is prescribed, where $\alpha > 1$ accounts for incoherent boundary energy as noted in Section 2. (For a twin system oriented differently from $\boldsymbol{s}\|\boldsymbol{e}_1$ and $\boldsymbol{m}\|\boldsymbol{e}_2$, $\boldsymbol{\kappa}$ is rotated as a second-order tensor.) Accordingly, for a given set of boundary conditions and prescribed initial crystal orientation ($\boldsymbol{s}$, $\boldsymbol{m}$), solutions thus obtained depend on the parameter set (γ_0, ν, Γ/Γ_0, α) and choice of interpolation function φ. The same arguments apply for the isotropic neo-Hookean elastic model of Section 2.

Plane-strain simulations of an initially square domain Ω of size $2a \times 2a$ are reported in Section 4. The domain contains a pre-existing straight edge crack of length a and thickness $2r_0$, with a rounded tip of radius r_0. The crack is assigned a finite radius for two reasons: (i) a perfect slit crack would result in truly singular stress fields at the tip that cannot be fully resolved with conventional finite elements; and (ii) in a real material a finite r_0 on the order of or exceeding a lattice parameter is expected since the separation distance across opposite faces of the crack should exceed a cut-off distance for interatomic cohesive forces that would otherwise result in traction across opposing faces of the crack.

Let the origin of reference coordinate systems ((r, θ) in polar form or (X, Y) in rectangular form) be located at the crack tip. Boundary conditions are imposed as follows. The crack surface Ξ ($\theta = \pm\pi$ rad, $0 < r < a$) is free of traction ($\boldsymbol{t} = \boldsymbol{0}$). Neumann conditions $h = 0$ for conjugate force to the order parameter are assigned along all of $\partial\Omega$. Along external boundary $\partial\Omega\backslash\Xi$ corresponding to X, $Y = \pm a$, displacements $\hat{\boldsymbol{u}}(r, \theta)$ corresponding to the K field for pure mode I or mode II loading [23] are imposed. For mode I:

$$\hat{u}_X = 2\Delta[ar/(2\pi)]^{1/2}\cos(\theta/2)[1 - 2\nu + \sin^2(\theta/2)], \tag{3.6}$$

$$\hat{u}_Y = 2\Delta[ar/(2\pi)]^{1/2}\sin(\theta/2)[2 - 2\nu - \cos^2(\theta/2)], \tag{3.7}$$

$$\Delta = K_\mathrm{I}/(2\mu a^{1/2}). \tag{3.8}$$

For mode II:

$$\hat{u}_X = 2\Delta[ar/(2\pi)]^{1/2}\sin(\theta/2)[2 - 2\nu + \cos^2(\theta/2)], \tag{3.9}$$

$$\hat{u}_Y = -2\Delta[ar/(2\pi)]^{1/2}\cos(\theta/2)[1 - 2\nu - \sin^2(\theta/2)], \tag{3.10}$$

$$\Delta = K_\mathrm{II}/(2\mu a^{1/2}). \tag{3.11}$$

For both modes, the orientation of the twin system ($\boldsymbol{s}$, $\boldsymbol{m}$) is such that the resolved shear stress τ of (2.16) is maximum according to the linear elastic solution [23]. For mode II, $\boldsymbol{s}$ is simply oriented in the sense of positive r along $\theta = 0$. For mode I, $\boldsymbol{s}$ is oriented in the sense of positive r along $\theta = 1.22$ rad.

During phase-field simulations, Δ is increased incrementally. For each increment, the domain is seeded with a small twin nucleus at $r \leqslant r_0$. Displacement boundary conditions are updated according to the mode of loading via (3.6), (3.7), (3.8) or (3.9), (3.10), (3.11), and then the equilibrium solution ($\boldsymbol{u}$, η) in Ω is obtained through energy minimization using the finite-element method. If the driving force for twinning is insufficient, then the initial nucleus will disappear, and the equilibrium solution includes $\eta = 0 \forall \boldsymbol{X} \in \Omega$. Otherwise, at a threshold load parameter $\Delta = \Delta_\mathrm{T}$, a stable twin will appear at the crack tip ($r = 0$). With further increasing $\Delta > \Delta_\mathrm{T}$, the twin will grow in length and/or thickness until it interacts with the external boundary $\partial\Omega\backslash\Xi$.

According to linear elastic fracture mechanics, crack extension (i.e. cleavage) will occur if the applied stress intensity factor or corresponding strain energy release rate exceeds a threshold for a particular material and loading mode:

$$K_\mathrm{I/II} \geqslant K_\mathrm{C} \Longleftrightarrow G_\mathrm{I/II} \geqslant G_\mathrm{C} \Rightarrow \text{fracture}, \tag{3.12}$$

where the fracture surface energies are

$$G_\mathrm{I/II} = K_\mathrm{I/II}^2(1 - \nu)/(2\mu),$$
$$G_\mathrm{C} = K_\mathrm{C}^2(1 - \nu)/(2\mu), \tag{3.13}$$

and here no distinction has been made in notation among threshold fracture energies G_C for different modes. For comparison, dimensionless twinning and fracture parameters associated with the normalized strain energy required for either mechanism can be constructed:

$$\overline{\Gamma}_\mathrm{T} = \Gamma_\mathrm{T}/(\mu l) = a(1 - \nu)\Delta_\mathrm{T}^2/l, \qquad \overline{G}_\mathrm{C} = G_\mathrm{C}/(\mu l). \tag{3.14}$$

The following criteria then emerge that predict either crack extension or twin emission from the crack tip:

$$2\overline{\Gamma}_\mathrm{T}/\overline{G}_\mathrm{C} = 2\Gamma_\mathrm{T}/G_\mathrm{C} \gg 1 \Rightarrow \text{fracture},$$
$$2\overline{\Gamma}_\mathrm{T}/\overline{G}_\mathrm{C} = 2\Gamma_\mathrm{T}/G_\mathrm{C} \ll 1 \Rightarrow \text{twinning}. \tag{3.15}$$

Dimensionless $\overline{\Gamma}_\mathrm{T}$ can be interpreted as an inverse measure of the "twinnability" of a given material subjected to mode I or mode II loading, with smaller values of $\overline{\Gamma}_\mathrm{T}$ denoting an increased tendency for crack tip twinning. The factor of two arises because, in the usual convention of fracture mechanics, the strain energy release rate G_C is twice the fracture surface energy Γ_C. (In this paper, notation "Γ" is associated generically with surface energy, "G" with strain energy release.) When $2\overline{\Gamma}_\mathrm{T} \approx \overline{G}_\mathrm{C}$, strain energy released by twinning and crack extension are comparable, and either mechanism could be expected to occur. Note that because $\Delta \propto a^{-1/2}$, imposed displacements $\hat{\boldsymbol{u}}$ and twinning resistance $\overline{\Gamma}_\mathrm{T}$ do not depend on a, which serves merely as a normalization constant to render these quantities dimensionless.

In phase-field simulations, meshes are used with significant refinement (element size $\ll l$) near the crack tip and along the anticipated path of twin extension, such that solutions are independent of mesh resolution. Twin nucleation depends strongly on local fields near $r = 0$ but not strongly on a; further increasing the domain size above $a/l = 50$ did not significantly affect initial stages of twinning, but as the twin grows and approaches the boundary, the choice of a necessarily affects the solution. Solutions can be modestly dependent on notch radius for small r_0, so two choices of r_0 are explored. Tables 1 and 2 list parameters investigated in simulations reported subsequently in Section 4. The typical (i.e. usual) parameter set referred to as "linear elastic" in subsequent figures is given in Table 1. Normalized twin boundary energy is $\overline{\Gamma}_0 = \Gamma/(\mu l)$. Deviations from these parameters referred to in some later figures are explained in Table 2. In particular, the value of $\alpha = 100$ follows from Refs. [20,21].

3.2. Numerical results

Figs. 2 and 3 show characteristic results for mode I and mode II loading, respectively. The undeformed finite-element (FE) mesh is shown in part (a) of each figure. Twin morphology and a stress component—tensile stress for mode I, shear stress for mode II—are shown in parts (b) and (c), corresponding to a load increment exceeding nucleation, i.e. $\Delta > \Delta_T$. In each case, the twin (i.e. stress-free shear eigenstrain $\gamma_0/2$) relieves much of the stress that would otherwise be large as $r \to 0$ in an elastic medium without a twin. Twin growth to the boundary $\partial\Omega$ is inhibited by the displacement boundary conditions.

Twin morphologies for various simulations of mode I deformation are compared at the same load increment $\Delta = 0.04 > \Delta_T$, i.e. at the same imposed K_I, in Fig. 4. Because differences in twin size and shape are small, it is concluded that model predictions of fully formed twin morphology are not sensitive to choice of linear or nonlinear (i.e. neo-Hookean) elastic model, choice of interpolation function (2.17) or (2.18), twin boundary surface energy anisotropy α, or pre-existing thickness of the crack or notch. However, as discussed later, twin nucleation is affected by these choices in some cases.

Fig. 5 shows the effects of dimensionless material properties on twinning resistance $2\overline{\Gamma}_T$ of (3.14) under mode I loading. Recall from (3.15) that this resistance can be compared with $\overline{G}_C$ to predict whether twinning or cleavage crack extension would be energetically favorable, with smaller $\overline{\Gamma}_T$ suggesting a greater tendency for twinning at the crack tip. Each data point on each piecewise linear curve in Fig. 5 represents the result of a different phase-field simulation in which Δ (i.e. K_I) is increased in increments of 10^{-3} from $\Delta = 0$ to the condition for which a twin or twin nucleus is first observed at $\Delta = \Delta_T$.

Table 1
Basic simulation parameters.

Descriptor	Elasticity model	φ	r_0/l	α	$\overline{\Gamma}_0$
Linear elastic	Linear isotropic	Polynomial	2	1	4×10^{-3}

Table 2
Other simulation parameters.

Descriptor	Difference from basic parameters
Neo-Hookean	Neo-Hookean elastic energy
Exponential interpolant	Exponential φ
Anisotropic $\boldsymbol{\kappa}$	$\alpha = \kappa_{11}/\kappa_{22} = 100$
Thin notch	$r_0/l = 0.5$

Effects of twinning shear γ_0 on crack tip twinnability are shown in Fig. 5a, where discrete values of $\gamma_0 = (0.1, 0.3, 0.5, 0.7, 1.0)$ have been prescribed in simulations incorporating linear elastic or neo-Hookean strain energy density W. Twinning shear significantly affects nucleation. A minimum of twinning resistance $\overline{\Gamma}_T$ is predicted at $\gamma_0 = 0.3$ for each model. For $\gamma_0 < 0.3$, resistance increases since the eigenstrain does not reduce elastic energy so much. Nucleation resistance also increases for $\gamma_0 > 0.3$, presumably because the applied K_I field must be sufficiently strong such that a large eigenstrain relieves the elastic stress field induced by the crack.

The effects of Poisson's ratio ν on twin nucleation resistance are comparatively small, as shown in Fig. 5b for values of $\nu = (0.05, 0.15, 0.25, 0.35, 0.45)$. The low influence of Poisson's ratio on twinning found here agrees with conclusions of a previous linear elastic analysis [24]. Neo-Hookean elasticity is more sensitive than linear elasticity to ν, as expected considering the nonlinear compressibility inherent in (2.11).

As shown in Fig. 5c, twin boundary energy Γ_0 strongly affects twinnability, with resistance $\overline{\Gamma}_T$ increasing with increasing Γ/Γ_0 in all cases. Discrete values $\Gamma/\Gamma_0 = (0.5, 0.75, 1, 1.5, 2)$ have been probed. Twinning resistance increases relative to the linear elastic case when the exponential interpolator of (2.18), anisotropic surface energy ($\alpha = 100$) or a thinner notch/crack is used. Differences increase as the ratio Γ/Γ_0 increases.

Fig. 6 shows effects of dimensionless material properties on twinning resistance $2\overline{\Gamma}_T$ of (3.14) under mode II loading, and is analogous to results for mode I of Fig. 5. Again, each data point represents the result of a different phase-field simulation in which Δ (here proportional to K_{II}) is increased in increments of 1×10^{-3} from $\Delta = 0$ to the condition for which a twin or twin nucleus is first observed at $\Delta = \Delta_T$.

The effects of twinning shear γ_0 on crack tip twinnability are shown in Fig. 6a, where discrete values of $\gamma_0 = (0.1, 0.3, 0.5, 0.7, 1.0)$ have been prescribed in simulations incorporating linear elastic or neo-Hookean strain energy W. Twinning shear significantly affects mode II nucleation, as was the case for mode I. Here, a minimum of twinning resistance $\overline{\Gamma}_T$ is predicted at $\gamma_0 = 0.5$ for each model in mode II loading, which exceeds the minimum associated $\gamma_0 = 0.3$ observed for mode I.

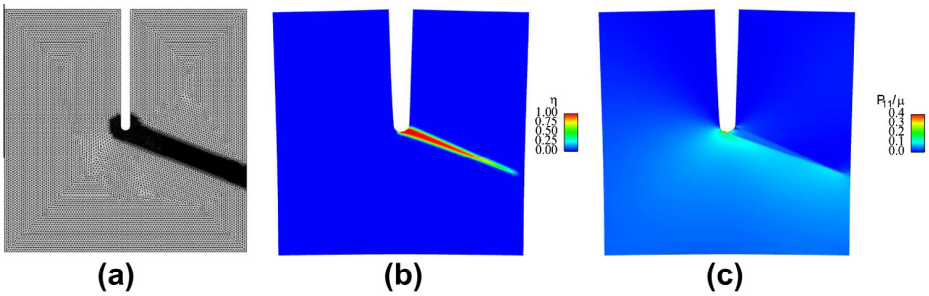

Fig. 2. Mode I loading of isotropic elastic solid $\left[\gamma_0 = \frac{1}{2}, \nu = \frac{1}{4}, \Gamma = \Gamma_0\right]$: (a) finite-element mesh; (b) order parameter at $\Delta = 0.05$; (c) tensile normal stress ($P_{11} = P_{YY}$) at $\Delta = 0.05$. The origin of the (X, Y) coordinate system is at the crack tip, with positive X downward and positive Y to the right. For polar (r, θ) coordinates, θ is measured counterclockwise from the positive X-axis.

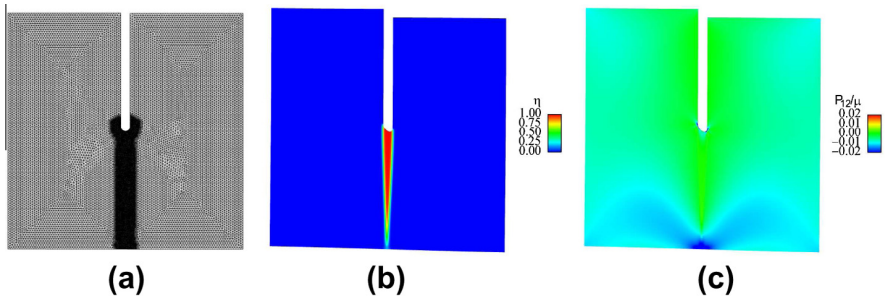

Fig. 3. Mode II loading of isotropic elastic solid $\left[\gamma_0 = \frac{1}{2}, \nu = \frac{1}{4}, \Gamma = \Gamma_0\right]$: (a) finite-element mesh; (b) order parameter at $\Delta = 0.03$; (c) shear stress ($P_{12} = P_{XY} = P_{YX}$) at $\Delta = 0.03$. The origin of the (X, Y) coordinate system is at the crack tip, with positive X downward and positive Y to the right. For polar (r, θ) coordinates, θ is measured counterclockwise from the positive X-axis.

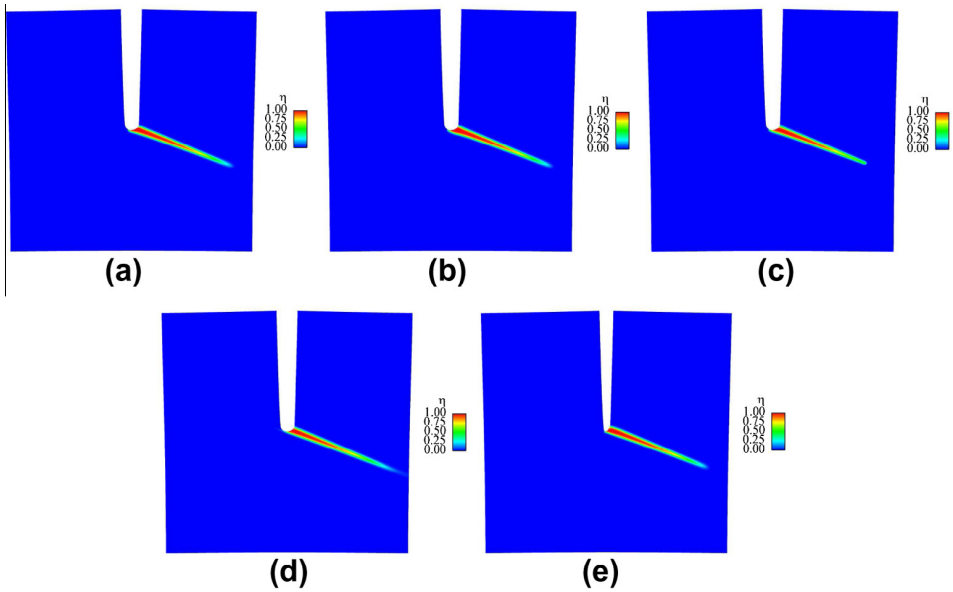

Fig. 4. Order parameter (twin morphology) for mode I loading of isotropic elastic solid at $\Delta = 0.04$ $\left[\gamma_0 = \frac{1}{2}, \nu = \frac{1}{4}, \Gamma = \Gamma_0\right]$: (a) linear elastic; (b) neo-Hookean; (c) exponential interpolant; (d) anisotropic $\boldsymbol{\kappa}$; (e) thin notch.

The effects of Poisson's ratio ν on twin nucleation resistance under mode II loading are comparatively small, as shown in Fig. 6b. Twinning resistance for neo-Hookean elasticity is again more sensitive than linear elasticity to ν.

As shown in Fig. 6c, twin boundary energy Γ_0 strongly affects twinnability, with resistance $\overline{\Gamma}_{\mathrm{T}}$ increasing with increasing Γ/Γ_0 in all cases, as was observed for mode I. Twinning resistance increases relative to the linear elastic

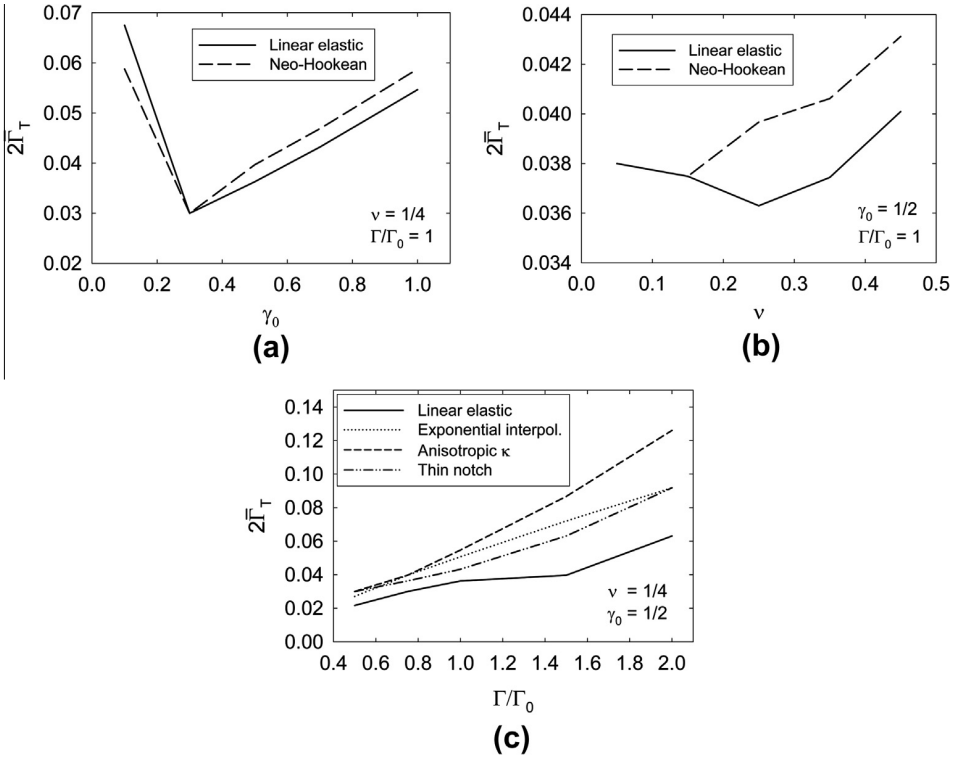

Fig. 5. Normalized twin nucleation energy $\overline{\Gamma}_{\mathrm{T}}$ under mode I loading for (a) variable twinning shear γ_0; (b) variable Poisson's ratio ν; and (c) variable twin boundary surface energy Γ. A low value of $\overline{\Gamma}_{\mathrm{T}}$ correlates with a low value of applied K_{I} needed to initiate a twin at the crack tip.

case when the exponential interpolator of (2.18) or anisotropic surface energy ($\alpha = 100$) is used, though the latter influences the results modestly and only for $\Gamma/\Gamma_0 > 1$. Contrary to results for mode I loading, a thinner notch reduces rather than increases twin resistance under mode II. Differences among cases in Fig. 6c increase as Γ/Γ_0 increases.

Comparing results in Figs. 5 and 6, numerical values of resistance to twinning $\overline{\Gamma}_{\mathrm{T}}$ under mode I loading tend to exceed those under mode II by a factor of the order of 2. For example, for linear elasticity with the parameter set $[\gamma_0 = \frac{1}{2}, \nu = \frac{1}{4}, \Gamma = \Gamma_0]$, phase-field simulations predict $\overline{\Gamma}_{\mathrm{T}} \approx 0.007$ for mode II and $\overline{\Gamma}_{\mathrm{T}} \approx 0.011$ for mode I. This result is not unexpected since a minimum twinning resistance would be associated with the geometry of mode II loading in Fig. 3, i.e. with the twin system aligned perfectly with maximum shear stress at the tip of a mode II crack.

4. Twinning under mode I loading in single crystals

Twinning under mode I loading of a square domain with pre-existing edge crack is investigated next for single crystals with relevant physical properties. Plane-strain simulations on a sample of dimensions identical to that of Section 3 are reported. In this 2-D idealization, only one twin system is permitted to be active in any simulation, and the crack propagation direction in a particular cleavage plane is chosen such that crack opening is in the plane $\theta = \pm\pi$ rad, i.e. the pre-existing crack is along $Y = 0$, $X < 0$. Details regarding properties and results are reported in Table 3; corresponding discussion for each material follows next. As will become clear later, "Model" in Table 3 designates the type of elasticity model and/or twin boundary surface energy representation, with "isotropic" referring to isotropic linear elasticity and isotropic surface energy ($\alpha = 1$), "aniso. W" referring to anisotropic linear elasticity and isotropic surface energy, and "$\alpha = 100$" denoting isotropic linear elasticity with anisotropic surface energy.

4.1. Calcite

Calcite is a soft mineral of trigonal symmetry whose pure crystals are transparent. Calcite twins readily, with little or no plastic slip, under concentrated surface loading. The preferred twin system is e^+, with relatively large shear $\gamma_0 = 0.694$ and geometry $\langle 1\,0\,\bar{1}\rangle\{0\,1\,1\}$ in rhombohedral pseudocell notation [25]. Calcite also cleaves easily on the natural rhombohedral planes (i.e. $\{1\,0\,\bar{1}\}$ planes) of its primitive unit cell, equivalent to $\{1\,0\,\bar{1}\,1\}$ planes in the hexagonal notation of Refs. [26,27]. In the present simulations, a 2-D projection is required, where $\theta = 0.89$ rad is the resulting orientation of the e^+ twin system that receives the maximum stress τ under mode I loading of a cleavage plane. Cleavage surface energy entering $\overline{G}_{\mathrm{C}}$ in Table 3 is obtained from experiments [27]. Properties associated with twinning and elasticity are from Ref. [10] and references

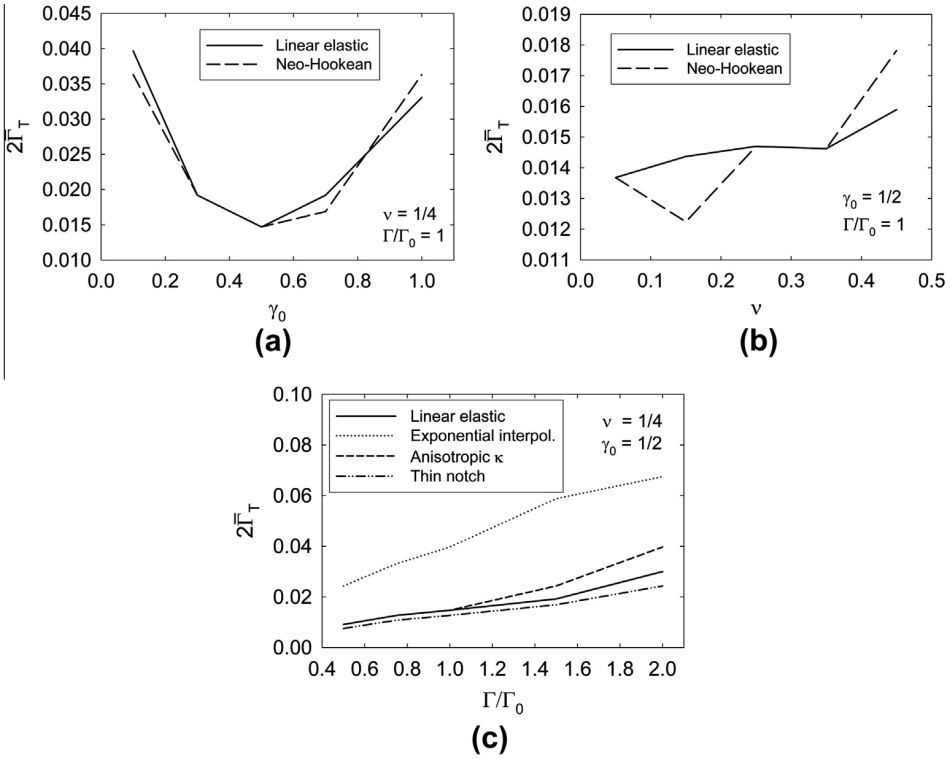

Fig. 6. Normalized twin nucleation energy $\overline{\Gamma}_T$ under mode II loading for (a) variable twinning shear γ_0; (b) variable Poisson's ratio ν; (c) variable twin boundary surface energy Γ. A low value of $\overline{\Gamma}_T$ correlates with a low value of applied K_{II} needed to initiate a twin at the crack tip.

Table 3
Single-crystal properties and results of phase-field simulations.

Material	ν	μ (GPa)	Crack	$\overline{G}_C$	Twin system	γ_0	$2\overline{\Gamma}_0$	Model	$2\overline{\Gamma}_T/\overline{G}_C$	Prediction
Calcite	0.30	40	$(10\bar{1}1)$	0.017	e^+	0.694	0.0091	aniso. W	2.53	Fracture
								Isotropic	2.96	Fracture
Sapphire	0.23	167	(0001)	0.48	Rhomb. (R)	0.202	0.0015	Isotropic	0.02	Twinning
			Max. τ	0.1				$\alpha = 100$	0.11	Twinning
			$(10\bar{1}2)$	0.072	Basal (B)	0.635	0.0089	Isotropic	0.62	Either
			Max. τ	0.1				$\alpha = 100$	0.65	Either
Mg	0.28	19	(0001)	382	$[10\bar{1}1](\bar{1}012)$	0.130	0.0121	Isotropic	2×10^{-4}	Twinning

therein. Both isotropic and anisotropic elastic models are investigated (i.e. forms of W). For the former, the Voigt elastic constants shown in Table 3 apply. For the latter, values ($C_{11} = 165$, $C_{12} = 65$, $C_{13} = 62$, $C_{14} = -23$, $C_{33} = 89$, $C_{44} = 37$ GPa) from Ref. [10] are used. For either elastic model, the displacement field of (3.6) and (3.7) is applied by incrementally increasing Δ or, equivalently, K_I; this is an approximation of the true K_I field when anisotropic elasticity is used.

Results in Fig. 7a and b show the twin at loading soon after nucleation, i.e. at $\Delta = 0.044 \gtrsim \Delta_T$. Nucleation occurs first for the anisotropic model, but the orientation ($\theta \approx 0.9$ rad) and shape of the twin are similar in each case. A secondary twin belonging to the same twin system begins to form at a larger applied K_I field, as shown in Fig. 7c. For anisotropic and isotropic models, $2.5 \lesssim 2\overline{\Gamma}_T/\overline{G}_C \lesssim 3$, meaning that crack extension is preferred over twinning according to criterion (3.15). This result is in qualitative agreement with tensile fracture experiments [26,27] that report no evidence of twinning. Parting fractures induced by twins in calcite have also been noted [28]. These model results do not contradict the possibility of twins induced by defects during other modes of loading, e.g. under spherical indentation, samples with visible surface cracks are known to twin more easily than those without [5].

4.2. Sapphire

Sapphire, also known as corundum or single-crystal alumina, is a hard ceramic/mineral that, like calcite, is of tri-

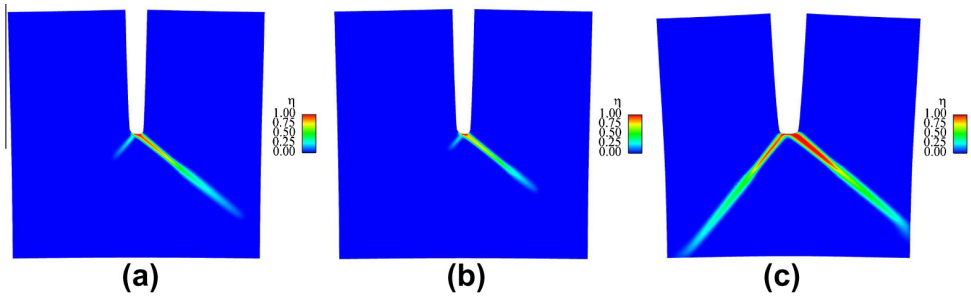

Fig. 7. Order parameter for mode I cleavage of calcite single crystal: (a) anisotropic elasticity, $\Delta = 0.044$; (b) isotropic elasticity, $\Delta = 0.044$; (c) isotropic elasticity, $\Delta = 0.1$.

gonal elastic symmetry and can be transparent. As reviewed in Refs. [4,10], the twin systems are rhombohedral (R) with Miller indices $\langle 1\bar{1}0\bar{1}\rangle\{1\bar{1}02\}$ in the structural unit cell, and basal (B) with Miller indices $\langle 1\bar{1}00\rangle\{0001\}$ in the structural unit cell. Twinning shear for R systems ($\gamma_0 = 0.202$) is less than that for B systems ($\gamma_0 = 0.635$). Surface energies for cleavage on rhombohedral, prismatic and basal planes have been reported, with R planes the most likely to cleave and B planes difficult to fracture [29]. In various phase-field simulations reported next, either a B twin system or a R twin system is active, with a mode I crack located on one of several possible planes. Specifically, the four cases reported in Table 3 correspond to (i) R twinning induced by a basal plane crack ($\boldsymbol{s}$ at $\theta = 1.07$ rad); (ii) R twinning induced by a noncrystallographic plane crack that produces maximum τ ($\boldsymbol{s}$ at $\theta = 1.22$ rad); (iii) B twinning induced by a rhombohedral plane crack ($\boldsymbol{s}$ at $\theta = 1.07$ rad); and (iv) B twinning induced by noncrystallographic plane crack that produces maximum τ ($\boldsymbol{s}$ at $\theta = 1.22$ rad). Cleavage surface energies entering $\overline{G}_C$ in Table 3 are obtained from [29]. For cases (i) and (iii), isotropic surface energy is used. For cases (ii) and (iv), the effects of anisotropic $\boldsymbol{\kappa}$ associated with incoherent twin boundary energy are explored by setting $\alpha = 100$ [21,20]. In all cases, isotropic elasticity is imposed with Voigt elastic constants, noting from previous work [10] that the effects of elastic anisotropy are small in sapphire; elastic anisotropy is also investigated later in 3-D simulations in Section 5, confirming this assertion.

Results for cases (i) and (iii) are shown in Fig. 8a and b at $\Delta > \Delta_T$. The basal twin (Fig. 8a) nucleates at a larger Δ and is thinner than the rhombohedral twin (Fig. 8b). Twinning resistance is compared with fracture energy in Table 3. Since $2\overline{\Gamma}_T \ll \overline{G}_C$ for cases (i) and (ii) involving R twinning, this twinning mode is preferred over mode I crack extension. On the other hand, $2\overline{\Gamma}_T$ is smaller than $\overline{G}_C$, but not significantly so, for cases (iii) and (iv) involving basal twinning. It follows that basal twinning is possible in such cases, but crack extension is also likely, considering possible sources of uncertainty in the phase-field model/parameters and local variations in microstructure (e.g. defects or impurities) inherent in real experimental samples. Predictions are in qualitative agreement with experiments. Specifically, in cleavage experiments [29], basal fracture was found much more difficult to induce than rhombohedral fracture. In recovered specimens fractured by bending [30] on unidentified planes, numerous thicker R twins were found, and fewer thinner B twins were observed. The thicker predicted shape of the R twin relative to the B twin is evident in Fig. 8; it has been noted elsewhere [28] that twin systems with larger γ_0 are prone to yield thinner twins. The presence of both kinds of twins has been reported in shock compression experiments on alumina polycrystals [3].

4.3. Magnesium

Magnesium is a moderately ductile metal with hexagonal crystal structure. A number of slip and twin systems

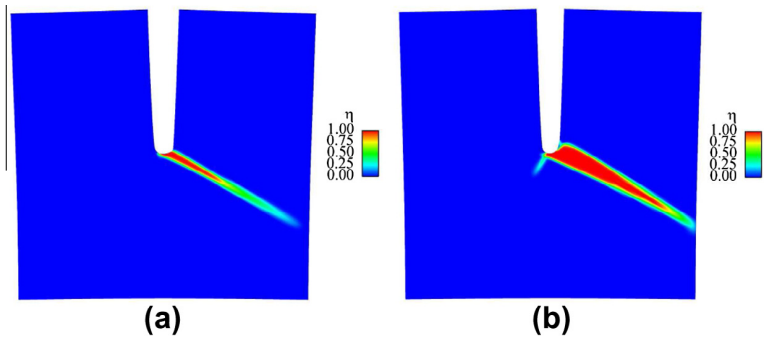

Fig. 8. Order parameter for mode I cleavage of sapphire single crystal: (a) basal twinning and rhombohedral cleavage, $\Delta = 0.057$; (b) rhombohedral twinning and basal cleavage, $\Delta = 0.046$.

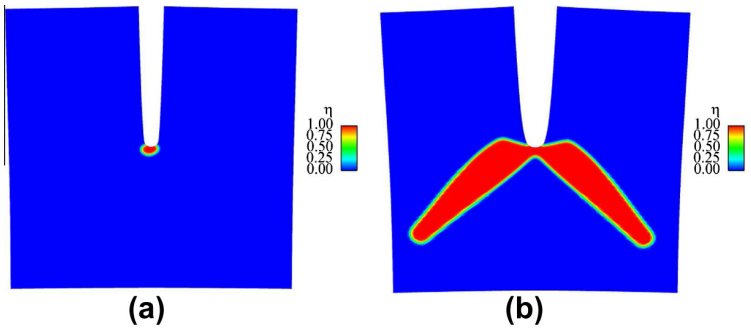

Fig. 9. Order parameter for mode I basal plane cleavage of magnesium crystal: (a) twin nucleation, $\Delta = 0.044$; (b) tensile twinning, $\Delta = 0.1$.

have been identified; the twin system investigated here is the dominant inelastic mechanism observed in single crystals stretched along [0001]: the system $\langle 10\bar{1}1\rangle\{\bar{1}012\}$, with relatively small shear $\gamma_0 = 0.1295$. Elastic anisotropy is very low in Mg; Voigt isotropic elastic constants [9] are used, along with the isotropic twin boundary surface energy listed in Ref. [9]. Although various cleavage modes in single crystals have been reported [31], quantitative values of fracture surface energies are not evident in the existing literature; however, analysis suggests that the fracture energies of prismatic and basal planes should be approximately equal [32]. In the present work, a pre-existing edge crack on the basal plane is modeled, where the value of $\overline{G}_C$ in Table 3 is obtained from the macroscopic fracture toughness of Mg polycrystals [33]. The most favorably oriented twin system is oriented with $\boldsymbol{s}$ at $\theta = 0.75$ rad.

The predicted twin is shown in Fig. 9a at $\Delta \approx \Delta_T$ and in Fig. 9b at $\Delta > \Delta_T$. The rounded shape of the twin nucleus in Fig. 9a is in qualitative agreement with previous theoretical studies [9,34]. The symmetric double-twin morphology in Fig. 9b is similar to atomic simulation results of tensile twinning in a Mg single crystal with a pre-existing center crack on the basal plane [35] (see their Fig. 4). In the present simulations, the blunt shape of the twin(s) correlates with the low value of γ_0 in Mg. Twinning resistance is compared with fracture energy in Table 3. Since $2\overline{\Gamma}_T \ll \overline{G}_C$,

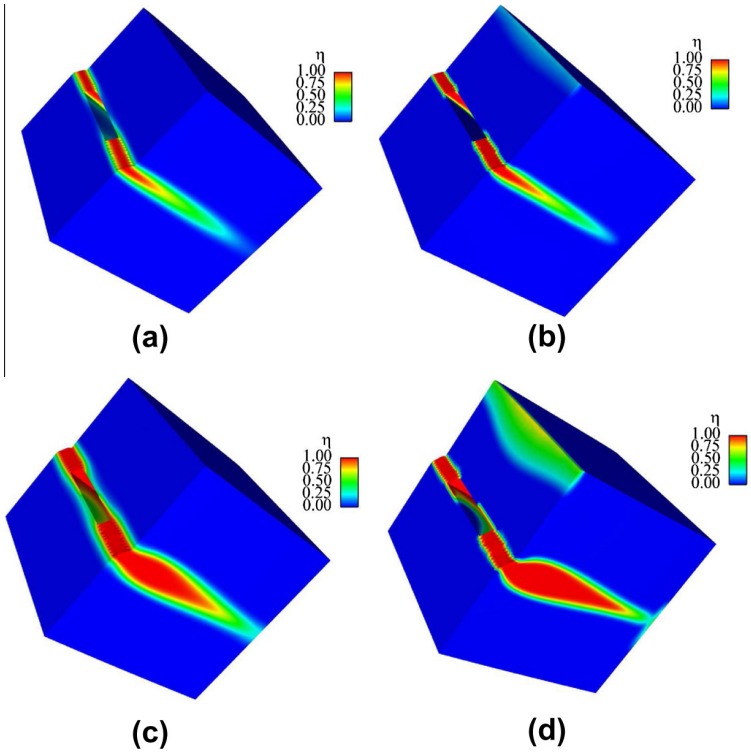

Fig. 10. Order parameter for direct shear loading ($\gamma = 1$) of sapphire single crystal with halfpenny-shaped edge notch: (a) basal twin, anisotropic elasticity and anisotropic surface energy; (b) basal twin, isotropic elasticity and isotropic surface energy; (c) rhombohedral twin, anisotropic elasticity and anisotropic surface energy; (d) rhombohedral twin, isotropic elasticity and isotropic surface energy.

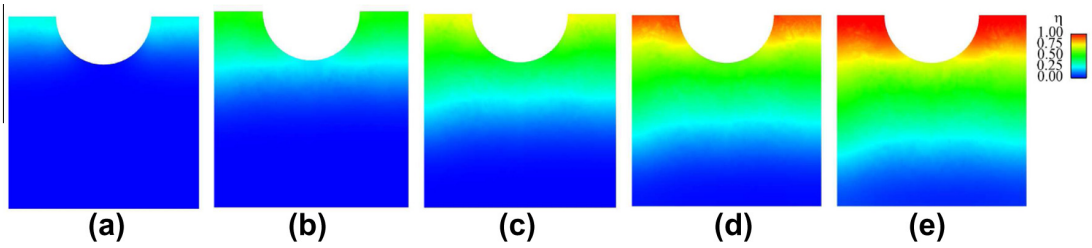

Fig. 11. Twin nucleation and growth along mid-plane $Y = 0$ for direct shear loading of sapphire single crystal, anisotropic model, basal twin: (a) $\gamma = 0.2$; (b) $\gamma = 0.4$; (c) $\gamma = 0.6$; (d) $\gamma = 0.8$; (e) $\gamma = 1.0$.

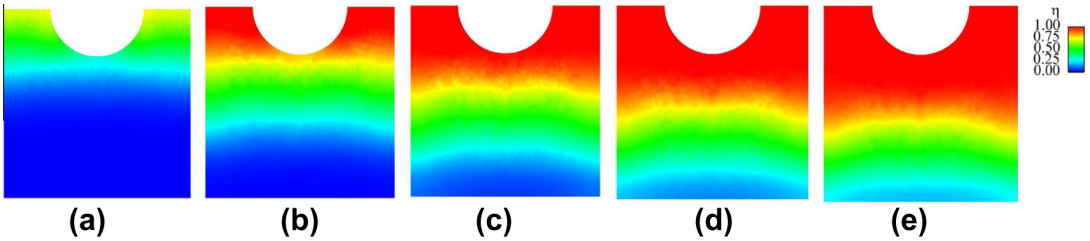

Fig. 12. Twin nucleation and growth along mid-plane $Y = 0$ for direct shear loading of sapphire single crystal, anisotropic model, rhombohedral twin: (a) $\gamma = 0.2$; (b) $\gamma = 0.4$; (c) $\gamma = 0.6$; (d) $\gamma = 0.8$; (e) $\gamma = 1.0$.

twinning is preferred over mode I crack extension for the present boundary conditions.

The analytical model of Ref. [8] suggests the following criterion for twinning vs. crack extension:

$$\chi \cdot (f_T/f_C)^{1/2} > 1 \Rightarrow \text{fracture},$$
$$\chi \cdot (f_T/f_C)^{1/2} < 1 \Rightarrow \text{twinning}, \tag{4.1}$$

where the dimensionless parameter χ depends on load direction, crystal structure (e.g. c/a ratio in hexagonal metals) and anisotropic elastic constants, and f_T and f_C are energies associated with "total inelastic resistance" against twin and crack extension, respectively. For basal plane cleavage and tensile twinning, a value of $\chi = 1.66$ is reported for Mg [8]. Values of f_T and f_C have not been reported; the former can be deduced from the present results if $f_C = \frac{1}{2}G_C$ is assumed. Squaring both sides of (4.1) and comparing with (3.15) yields

$$f_T = \Gamma_T/\chi^2 = \mu l \overline{\Gamma}_T/\chi^2 \approx 0.26 \quad \text{J/m}^2, \tag{4.2}$$

which is significantly larger than the twin boundary surface energy $\Gamma = 0.12\ \text{J/m}^2$. Such a result reinforces the notion that total energetic resistance to twinning depends on other factors besides Γ alone.

5. Twinning in a notched single crystal: 3-D simulations

Three-dimensional simulations demonstrate how the phase-field model can be applied to predict twinning under complex stress states. In the present simulations of single-crystal sapphire, attention is restricted to a single potentially active twin system. Boundary conditions imposing direct, intense shear strain resolved on this system (discussed in detail below) are such that only one system would be expected to be active. Various simulations consider either rhombohedral (R) or basal (B) twinning, with isotropic or anisotropic material models. For the former, isotropic twin boundary surface energy is also used. For the latter, the trigonal elastic constants ($C_{11} = 500$, $C_{12} = 168$, $C_{13} = 121$, $C_{14} = 24$, $C_{33} = 502$, $C_{44} = 151$ GPa) from Ref. [10] are used, and anisotropic twin boundary energy is imposed with $\alpha = 100$. The remaining material properties have already been discussed in Section 4.2 in the context of Table 3.

Consider here is a cube of material with initial dimensions $4a \times 4a \times 4a$, where $a/l = 10$. Six faces are labeled $\pm X$, $\pm Y$, $\pm Z$, where the unit normal of each face is aligned parallel to the corresponding axis in a global Cartesian coordinate system with origin at the center of the cube. A half-cylinder of radius a and height $2l$ is extracted from the $-X$ face of the cube along the mid-plane $Y = 0$. This can be interpreted as a pre-existing, halfpenny-shaped notch or edge crack. Displacement boundary conditions are applied to the $-X$ face and create a region of intense shear deformation of magnitude γ over the region $-l < Y < l$, similar to conditions explored in Ref. [36] for modeling slip, or to what might be observed in the early stages of a dynamic Kalthoff experiment. Specifically, face $-X$ is held fixed for $-2a \leqslant Y \leqslant -l$ and displaced rigidly in the $+X$ direction for $l \leqslant Y \leqslant 2a$. The opposite $+X$ face is held fixed ($\boldsymbol{u} = \boldsymbol{0}$), and lateral faces $\pm Y$, $\pm Z$ are traction free. All surfaces comprising $\partial\Omega$ (six cube faces and the crack surface) are assigned the free ($h = 0$) Neumann condition for the order parameter, enabling possible twin nucleation at any of these surfaces.

Characteristic results are shown in Fig. 10 for an imposed shear of unity ($\gamma = 1$). Specifically, B twinning is depicted in Fig. 10a and b, R twinning in Fig. 10c and d. For each mode of twinning, predictions of linear isotropic and anisotropic elasticity are similar for the order parameter (η) profile in the region of intense shear. Anisotropic surface energy suppresses formation of the partial secondary twins that emerge along the upper edge of the $-X$ face in each of the isotropic simulations (Fig. 10b and d). Simulations with neo-Hookean elasticity were also performed; the results were very similar to those shown for linear isotropic elasticity and are not shown. Consistent with the results of 2-D simulations in Section 4.2 and experimental observations [30], basal twinning is more difficult to enact than rhombohedral twinning under the present direct shear boundary conditions, and B twins tend to be thinner than R twins.

Order parameter contours along mid-plane $Y = 0$ are shown in Figs. 11 and 12, respectively, for B and R twinning for incrementally increasing applied deformation γ. Some asymmetry of the twin boundary front is evident, particularly for the B twin in Fig. 11, a consequence of anisotropy. In these simulations, the semicircular edge crack does not promote or inhibit twinning; however, different boundary conditions explored elsewhere in atomic simulations of shock compression [37] have demonstrated the possibility of R twinning induced at pre-existing planar cracks in sapphire.

6. Conclusions

Twin emission from a crack tip has been studied using phase-field simulations. A parameter associated with resistance to twin nucleation under mode I/II loading has been derived. This parameter can be compared with the fracture energy of the material to suggest whether an existing crack should extend or a deformation twin should emerge and grow. Effects of material properties and phase-field model features on twinning resistance have been studied parametrically, with Poisson's ratio and elastic nonlinearity showing little effect. In contrast, resistance to crack tip twinning depends strongly on twin boundary surface energy and twinning shear. Plane-strain simulations of twinning induced by a pre-existing crack on relevant cleavage planes in calcite, sapphire and magnesium single crystals have been conducted. Results suggest that calcite should cleave, magnesium should twin, and that rhombohedral twinning is preferred to basal twinning in sapphire, all in agreement with experiment. Three-dimensional simulations of shear loading of sapphire demonstrate a preference for rhombohedral over basal twins, with the former thicker in shape, in agreement with experiment.

References

[1] Christian J, Mahajan S. Deformation twinning. Prog Mater Sci 1995;39:1–157.

[2] Tadmor E, Hai S. A Peierls criterion for the onset of deformation twinning at a crack tip. J Mech Phys Solids 2003;51:765–93.

[3] Chen M, McCauley J, Dandekar D, Bourne N. Dynamic plasticity and failure of high-purity alumina under shock loading. Nature Mater 2006;5:614–8.

[4] Clayton J. A continuum description of nonlinear elasticity, slip and twinning, with application to sapphire. Proc Roy Soc Lond A 2009;465:307–34.

[5] Garber R, Stepina E. Rules governing the motion of dislocations during deformation twinning. Soviet Phys Solid State 1965;5:152–8.

[6] Wong T, Bradt R. Microhardness anisotropy of single crystals of calcite, dolomite, and magnesite on their cleavage planes. Mater Chem Phys 1992;30:261–6.

[7] Rice J. Dislocation nucleation from a crack tip: an analysis based on the Peierls concept. J Mech Phys Solids 1992;40:239–71.

[8] Yoo M. Slip, twinning, and fracture in hexagonal close-packed metals. Metall Trans A 1981;12:409–18.

[9] Clayton J, Knap J. A phase field model of deformation twinning: nonlinear theory and numerical simulations. Physica D 2011;240:841–58.

[10] Clayton J, Knap J. Phase field modeling of twinning in indentation of transparent single crystals. Mod Sim Mater Sci Eng 2011;19:085005.

[11] Clayton J. Nonlinear mechanics of crystals. Dordrecht: Springer; 2011.

[12] Boulbitch A, Tolédano P. Phase nucleation of elastic defects in crystals undergoing a phase transition. Phys Rev Lett 1998;81:838–41.

[13] Boulbitch A, Korzhenevskii A. Self-oscillating regime of crack propagation induced by a local phase transition at its tip. Phys Rev Lett 2011;107:085505.

[14] Idesman A, Levitas V, Stein E. Structural changes in elastoplastic material: a unified finite-element approach to phase transformation, twinning and fracture. Int J Plast 2000;16:893–949.

[15] Aranson I, Kalatsky V, Vinokur V. Continuum field description of crack propagation. Phys Rev Lett 2000;85:118–21.

[16] Jin Y, Wang Y, Khachaturyan A. Three-dimensional phase field microelasticity theory and modeling of multiple cracks and voids. Appl Phys Lett 2001;79:3071–3.

[17] Karma A, Kessler D, Levine H. Phase-field model of mode III dynamic fracture. Phys Rev Lett 2001;87:045501.

[18] Spatschek R, Hartmann M, Brener E, Müller-Krumbhaar H. Phase field modeling of fast crack propagation. Phys Rev Lett 2006;96:015502.

[19] Spatschek R, Brener E, Karma A. Phase field modeling of crack propagation. Philos Mag 2011;91:75–95.

[20] Hildebrand F, Miehe C. A phase field model for the formation and evolution of martensitic laminate microstructure at finite strains. Philos Mag 2012;92:4250–90.

[21] Hu S, Henager C, Chen L-Q. Simulations of stress-induced twinning and de-twinning: a phase field model. Acta Mater 2010;58:6554–64.

[22] Levitas V, Levin V, Zingerman K, Freiman E. Displacive phase transitions at large strains: phase-field theory and simulations. Phys Rev Lett 2009;103:025702.

[23] Rice J. Mathematical analysis in the mechanics of fracture. In: Liebowitz H, editor. Fracture: an advanced treatise. New York: Academic Press; 1968. p. 191–311.

[24] Bilby B, Bullough R. The formation of twins by a moving crack. Philos Mag 1954;45:631–46.

[25] Bueble S, Schmahl W. Mechanical twinning in calcite considered with the concept of ferroelasicity. Phys Chem Minerals 1999;26:668–72.

[26] Gilman J. Direct measurements of the surface energy of crystals. J Appl Phys 1960;31:2208–18.

[27] Santhanam A, Gupta Y. Cleavage surface energy of calcite. Int J Rock Mech Mining Sci Geo Abstr 1968;5:253–9.

[28] Cahn R. Plastic deformation of alpha-uranium; twinning and slip. Acta Metall 1953;1:49–70.

[29] Wiederhorn S. Fracture of sapphire. J Am Ceram Soc 1969;52:485–91.

[30] Heuer A. Deformation twinning in corundum. Philos Mag 1966;13:379–93.
[31] Reed-Hill R, Robertson W. The crystallographic characteristics of fracture in magnesium single crystals. Acta Metall 1957;5:728–37.
[32] Yoo M. The elastic energy of slit cracks in hexagonal crystals. Scr Metall 1979;13:131–6.
[33] Somekawa H, Inoue T, Mukai T. Deformation mechanism near crack-tip by finite element analysis and microstructure observation in magnesium alloys. Mater Sci Eng A 2010;527:1761–8.
[34] Wang J, Hoagland R, Hirth J, Capolungo L, Beyerlein I, Tomé C. Nucleation of a (1012) twin in hexagonal close-packed crystals. Scripta Mater 2009;61:903–6.
[35] Tang T, Kim S, Horstemeyer M, Wang P. Atomistic modeling of crack growth in magnesium single crystal. Eng Fract Mech 2011;78:191–201.
[36] Gumbsch P, Gao H. Dislocations faster than the speed of sound. Science 1999;283:965–8.
[37] Kuksin A, Yanilkin A. Formation of twins in sapphire under shock wave loading: atomistic simulations. J Appl Phys 2012;111:033513.

An Algorithm for Massively Parallel Dislocation Dynamics Simulations of Small Scale Plasticity

Kenneth W. Leiter, Joshua C. Crone, and Jaroslaw Knap

Journal of Computational Science, 4 (2013)

Contents lists available at ScienceDirect

Journal of Computational Science

journal homepage: www.elsevier.com/locate/jocs

An algorithm for massively parallel dislocation dynamics simulations of small scale plasticity

Kenneth W. Leiter, Joshua C. Crone, Jaroslaw Knap*

Computational Science and Engineering Branch, RDRL-CIH-C, US Army Research Laboratory, Aberdeen Proving Ground, MD 21005-5066, USA

ARTICLE INFO

Article history:
Received 30 October 2012
Received in revised form 8 February 2013
Accepted 17 February 2013
Available online 15 March 2013

Keywords:
Dislocation dynamics
Finite element method
Parallel computing

ABSTRACT

Accurate modeling of dislocation motion in bounded bodies is essential for the goal of obtaining desired properties, for example electronic or optical, of many microelectronic devices. At present, we lack high fidelity computer codes for such modeling that efficiently utilize modern parallel computer architectures. In contrast, many dislocation simulation codes are available for periodic or infinite bodies. In principle, these codes can be extended to allow for dislocation modeling in finite bodies. However, such extension may involve an additional solver to be employed, coupled with a dislocation simulation code. We present an algorithm for development of parallel dislocation simulation capability for bounded bodies based on such coupling. Subsequently, we analyze the performance of the algorithm for a demanding dislocation dynamics model problem.

Published by Elsevier B.V.

1. Introduction

Behavior of engineering materials is governed by the presence of defects. Among various material defects, dislocations play a pivotal role as primary carriers of inelastic deformation. While cooperative dislocation motion is reasonably well understood and described in macroscopic materials [1,2], its understanding for nano-scale materials is still lacking. A case in point is dislocation motion in microstructurally thin films [3,4]. A microstructurally thin film is a film whose characteristic dimension is comparable to the characteristic microstructural size. Today, most films that comprise integrated circuits, microelectronic devices or magnetic storage media are examples of microstructurally thin films. Understanding how microstructural thin films deform is critical to obtain desired electronic or optical properties of devices [5–7]. Dislocation motion is crucial in this deformation process.

Among countless modeling techniques of material science, dislocation dynamics [8–10] is most likely best suited to accurately describe motion of dislocations in thin films. While there exist several actively developed dislocation dynamics computer codes, including microMegas [11], Tridis [12], Micro3d [13], PARANOID [9,10], and ParaDiS [14], most can only handle simulations of macroscopic materials or simple bounded bodies, such as boxes or cylinders. Moreover, no existing dislocation dynamics code has demonstrated the ability to handle general bounded bodies with high dislocation content on modern parallel computer hardware.

The treatment of small scale plasticity by means of dislocation dynamics commonly requires solution of a boundary value problem of elasticity [15]. Although it is possible to implement routines to solve the boundary value problem directly into an existing dislocation dynamics code [13], efficient parallel implementation may be difficult because of the disparate treatment of the two problems. For example, different domain decompositions can be expected for the two problems in parallel computing environments, which may necessitate a significant amount of communication between them. Furthermore, methods of solving boundary value problems of elasticity are well established and efficient parallel computer codes based on these methods already exist [16,17]. Therefore, a potentially better strategy than direct implementation, and the one we explore in this article, is to couple an existing parallel dislocation dynamics code to an existing parallel boundary value problem solver. This choice has the advantage of introducing minimal modifications to the codes and promotes encapsulation of the distinct problems.

Efficient coupling of disparate computer codes spanning length and time scales is an active area of research in scientific computing [18]. The desire to couple codes is motivated by a need to capture more sophisticated scientific phenomena and take full advantage of large modern computational platforms as they approach the exascale. Over the years, many methodologies have been proposed to address the issue of efficient coupling [19–21]. One of these methodologies, the so-called cooperative parallelism approach, uses remote method invocation to spawn and communicate with numerous child programs. This approach has been successfully employed to couple a coarse parallel finite element application with a fine constitutive material model for multiscale simulation [22].

* Corresponding author. Tel.: +1 410 278 0420.
E-mail address: jaroslaw.knap@us.army.mil (J. Knap).

Cooperative parallelism appears ideal for loosely coupled applications where the number of child programs is unknown and where child programs can fail or be terminated by the parent. In addition, the cooperative parallelism methodology may be well suited for coupling codes with non-deterministic and dynamic communication patterns and where communication is short [23].

Cooperative parallelism, however, may not be well suited as a coupling choice for our application. The communication pattern between the dislocation dynamics and boundary value problem solver is deterministic and persistent. Moreover, a connection-oriented approach may be desirable since the coupled codes may exchange significant amounts of data.

Other coupling methodologies exist, but are not well-suited to modern parallel hardware [24] or are overly application specific for our needs [25,26]. For example, the Intercomm [25] and model coupling toolkit [26] projects provide mechanisms for communication and interpolation of data between two grid-based applications. In contrast, we require a more general coupling approach. To satisfy our requirements for a general coupling approach capable of efficiently handling communication of large amounts of data, we employ distributed shared memory as the coupling mechanism between a dislocation dynamics code and a boundary value problem solver [27]. In this article we describe the coupling algorithm in detail and evaluate parallel performance of the application for handling large dislocation dynamics simulations of small scale plasticity.

2. Dislocation dynamics

In recent years, meso-scale simulations based on dislocation dynamics have been the focus of many researchers [28,11,15,9,10,12,29,13,30,31,8,14,32]. While some minor differences between individual approaches exist, their general features are quite common. Usually, dislocation lines within a linear elastic body are discretized into a set of connected line segments. Subsequently, forces on degrees of freedom associated with these discretized dislocation segments are computed. These forces originate from dislocation line segments interactions via their stress fields and drag on dislocation motion. The drag forces on dislocation line segments are calculated in terms of their respective velocities by recourse to a drag function. The resulting ordinary differential equations are then integrated in time allowing for updated dislocation segment positions to be obtained. It is important to emphasize that during the course of their motion dislocation segments are permitted to intersect with one another. These intersections must be properly accounted for and are ordinarily handled by a set of well-defined topological operations. A concise representation of the main components of a dislocation dynamics simulation is shown in Fig. 1. An in-depth description of dislocation dynamics is beyond the scope of this article. We summarize, however, the main points of the theory below. In our summary we closely follow Bulatov and Cai [8] and Arsenlis et al. [14].

2.1. Representation of dislocation lines

In the classical theory of dislocations (c.f. [33,34]) individual dislocations are treated as lines contained within a linear elastic body $\mathcal{B} \subset \mathbb{R}^3$. These dislocation lines are constrained to terminate at surfaces of the body, $\partial\mathcal{B}$, but are otherwise free to move within $\mathcal{B}$. With each point along a dislocation line we associate the Burgers vector, $\mathbf{b} \in \mathbb{R}^3$, representing the direction of the local distortion of the crystal lattice related to the dislocation. The practicality of dislocation dynamics hinges upon a simplified treatment of these dislocation lines. To this end, each dislocation line is approximated by a set of straight dislocation segments $\mathcal{D} = \{s_1, s_2, s_3, \ldots\}$. In turn, each

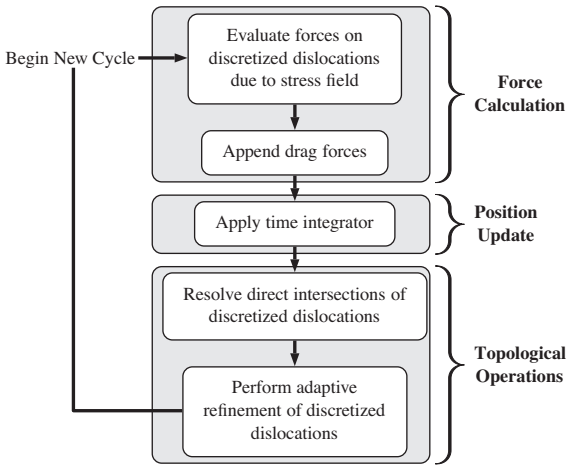

Fig. 1. The main components of a dislocation dynamics simulation.

dislocation segment, s_i, is treated as an ordered pair of vertices, i.e. $s_i = (v_i^1, v_i^2)$, with the corresponding Burgers vector, $\mathbf{b}_i$. We moreover assume that v_i^2 and v_{i+1}^1 are equivalent, i.e. correspond to the same vertex. In addition, while vertices are allowed to belong to multiple dislocation segments, each dislocation segment may only belong to a single discretized dislocation line.

With the above representation at hand, the coordinates of a point $P \in s_i$ along a discretized dislocation line $\mathcal{D}$, $\mathbf{x}(P)$, are readily computed by linear interpolation

$$\mathbf{x}(P) = \mathbf{x}_i^1 (1 - \xi) + \mathbf{x}_i^2 \xi, \tag{1}$$

where $\mathbf{x}_i^1, \mathbf{x}_i^2$ are, respectively, the coordinates of vertices v_i^1, v_i^2, and $\xi \in [0, 1]$ denotes the value of the parametric coordinate along s_i corresponding to P.

We emphasize that a choice of dislocation line representation is not, by any means, limited to the one introduced above. As a matter of fact, other representations have been successfully employed in dislocation dynamics simulations (e.g. [29,9]).

2.2. Computation of forces

The presence of dislocation lines in $\mathcal{B}$, along with applied tractions and displacements on $\partial\mathcal{B}$, induces at every point in $\mathcal{B}$ stress $\sigma \in Sym(\mathbb{R}^3)$ [33–35]. $Sym(\mathbb{R}^3)$ is the space of symmetric second-rank tensors over $\mathbb{R}^3$. This stress field acts on discretized dislocation lines yielding a force density (per unit length) $\mathbf{f}_i^{PK}$ at a point $P \in s_i$ with coordinates $\mathbf{x}(P)$

$$\mathbf{f}_i^{PK}(\mathbf{x}) = [\sigma(\mathbf{x})\mathbf{b}_i] \times \mathbf{t}_i, \tag{2}$$

where $\mathbf{b}_i$ is the segment Burgers vector, $\mathbf{t}_i$ is the tangent direction of s_i, and $\times$ is the vector (cross) product in $\mathbb{R}^3$. $\mathbf{f}_i^{PK}$ can be integrated along s_i and apportioned to each of the two segment vertices according to

$$\mathbf{f}_i^1 = |s_i| \int_0^1 \mathbf{f}_i^{PK}(\xi) \;\; (1 - \xi) \;\; d\xi, \tag{3}$$

$$\mathbf{f}_i^2 = |s_i| \int_0^1 \mathbf{f}_i^{PK}(\xi) \;\; \xi \;\; d\xi. \tag{4}$$

Here, $|s_i|$ denotes the length of s_i and ξ is the parametric coordinate along s_i. Individual segment force contributions (3) and (4) are accumulated at each vertex giving rise to a net vertex force.

It is common to express $\mathbf{f}_i^j, j = 1, 2$ as a composition of three contributions,

$$\mathbf{f}_i^j = \mathbf{f}_i^{j^{ext}} + \mathbf{f}_i^{j^s} + \sum_{k,k\neq i} \mathbf{f}_{ik}^j, \tag{5}$$

where $\mathbf{f}_i^{j^{ext}}$, $\mathbf{f}_i^{j^s}$ and $\mathbf{f}_{ik}^j$ represent contributions due to external loads, s_i's own stress field, and interactions with all other segments within $\mathcal{B}$, respectively. The computation of $\mathbf{f}_i^{j^s}$ and $\mathbf{f}_{ik}^j$ may be carried out by means of efficient methods, both analytical and numerical, that allow to avoid a direct evaluation of (3) and (4) [8,14]. In particular, explicit analytical formulas for the computation of $\mathbf{f}_i^{j^s}$ and $\mathbf{f}_{ik}^j$ exist for infinite elastic bodies [14]. In contrast, $\mathbf{f}_i^{j^{ext}}$ is usually computed directly from (3) and (4) with

$$\mathbf{f}_i^{PK}(\mathbf{x}) = [\sigma^{ext}(\mathbf{x})\mathbf{b}_i] \times \mathbf{t}_i, \tag{6}$$

where σ^{ext} is now the stress field due exclusively to applied tractions and displacements.

2.3. Equations of motion for dislocation segments

The equations of motion for discretized dislocation lines are derived under the assumption that the forces on discretized dislocation lines due to the stress field in $\mathcal{B}$ are balanced by the drag forces to dislocation line motion. More explicitly, for a vertex v_k in a discretization of dislocation lines, the following is assumed

$$\mathbf{F}_k + \mathbf{F}_k^{drag} = \mathbf{0}, \tag{7}$$

where $\mathbf{F}_k$ denotes the vertex force due to dislocation segments and applied tractions and displacements, $\mathbf{F}_k^{drag}$ is the vertex drag force, and $\mathbf{0}$ denotes the null vector in $\mathbb{R}^3$.

The computation of the drag force relies on a drag function $B : \mathbb{R}^3 \mapsto \mathbb{R}^3$, which maps velocity $\mathbf{v}$ to drag force density (per unit length) $\mathbf{f}^{drag}$. The drag function encapsulates the material specific aspects of dislocation motion and usually takes additional arguments, such as pressure and temperature. For clarity, we formally omit these additional arguments.

Following the procedure outlined in Section 2.2, the drag force density can be integrated over segment s_i by means of (3) and (4) with $\mathbf{f}_i^{PK}(\xi)$ replaced by $\mathbf{f}_i^{drag}(\xi) = B[\mathbf{v}_i(\xi)]$. This integration yields drag force contributions to vertices v_i^1 and v_i^2. $\mathbf{v}_i(\xi)$ is the velocity of a point $P \in s_i$ with the parametric coordinate ξ, computed as the time derivative of (1), i.e.

$$\mathbf{v}_i(\xi) = \mathbf{v}_i^1 (1 - \xi) + \mathbf{v}_i^2 \xi, \tag{8}$$

where $\mathbf{v}_i^1, \mathbf{v}_i^2$ are, respectively, the velocities of vertices v_i^1, v_i^2.

Clearly, the drag force $\mathbf{F}_k^{drag}$ is a function of vertex velocities and also, by virtue of additional arguments to the drag function, vertex coordinates. On the other hand, the vertex force $\mathbf{F}_k$ depends on the coordinates of all vertices in a discretization of dislocation lines. As such, Eq. (7) constitutes a non-linear system of ordinary differential equations. Therefore, the problem of finding a solution of (7) amounts to obtaining trajectories of all vertices. It is worth noting that the process of finding a solution of (7) for an arbitrary drag function may be computationally very demanding. For that reason, linear drag functions are frequently employed in practice, allowing to reduce (7) to a system of linear ordinary differential equations.

2.4. Numerical solution of the equations of motion for dislocation segments

The solution procedure for equations of motion (7) is customarily carried out by means of numerical integrators for ordinary differential equations. The role of these integrators is to propagate the solution forward in time given its initial value. A wide body of literature exists pertaining to such integrators (c.f. [36,37] and references therein). Commonly, simple and robust explicit integrators have been employed in dislocation dynamics simulations [14]. While computationally inexpensive, explicit integrators impose a stringent constraint on the size of time change permitted during a single forward integration step. In order to remove this severe limitation, the use of implicit integrators in dislocation dynamics has been advocated by some researchers [14]. It is unclear, however, whether the benefits offered by implicit integrators will be realized since implicit integrators require solutions of a non-linear system of algebraic equations.

2.5. Topological operations on discretized dislocation lines

In the course of a dislocation dynamics simulation, discretized dislocation lines may experience substantial displacements relative to their initial positions. These displacements may result in direct segment–segment intersections or significant changes in segment lengths. Both of these types of events must be properly handled in order for the simulation to remain faithful to the underlying physical phenomena, as well as, to maintain the desired accuracy.

Direct segment–segment intersections may lead to dislocation segment annihilation, junction formation or cross-slip events. All of these events can be efficiently treated by way of insertion or removal of dislocation segment vertices and dislocation segments. It bears emphasis that such operations are not, by any means, arbitrary, but are based solely on the theory of dislocations. An extensive overview of the segment–segment intersections, along with a catalog of operations required to properly handle them, has been provided by Arsenlis et al. [14].

An accurate representation of dislocation lines is essential in order to maintain desired accuracy of the solution. This requirement is usually satisfied by means of adaptive refinement of discretized dislocation lines. The overarching goal of such refinement is to optimize the representation of dislocation lines with respect to accuracy, and is customarily achieved by redistribution of vertices along discretized dislocation lines, as well as, insertion or removal of vertices.

3. Treatment of bounded bodies in dislocation dynamics

The calculation of forces due to dislocation segment's own stress field and interactions with other segments in (5) is, in practice, carried out by recourse to analytical formulas. While, in principle, numerical methods can be employed for this calculation, their computational expense could easily render dislocation dynamics impractical. The analytical formulas are only available, however, under the assumption that the body under consideration fills all of space, i.e. $\mathcal{B} = \mathbb{R}^3$. Additional steps are, therefore, necessary for a bounded body. In our presentation, we follow the classical approach of van der Giessen and Needleman [15].

The theory starts with a linear elastic body containing dislocation lines, $\mathcal{B}$, a bounded subset of $\mathbb{R}^3$. The boundary of $\mathcal{B}$, $\partial\mathcal{B}$, consists of two disjoint parts: the traction free boundary $\partial\mathcal{B}_t$ and the null displacement boundary $\partial\mathcal{B}_u$ (Fig. 2). The fundamental problem of the elasticity theory is concerned with finding a displacement field $\mathbf{u}$ over $\mathcal{B}$ satisfying

$$\begin{cases} \operatorname{div}\sigma = 0 & \text{in } \mathcal{B} \\ \sigma\mathbf{n} = \mathbf{0} & \text{on } \partial\mathcal{B}_t \\ \mathbf{u} = \mathbf{0} & \text{on } \partial\mathcal{B}_u \end{cases} \tag{9}$$

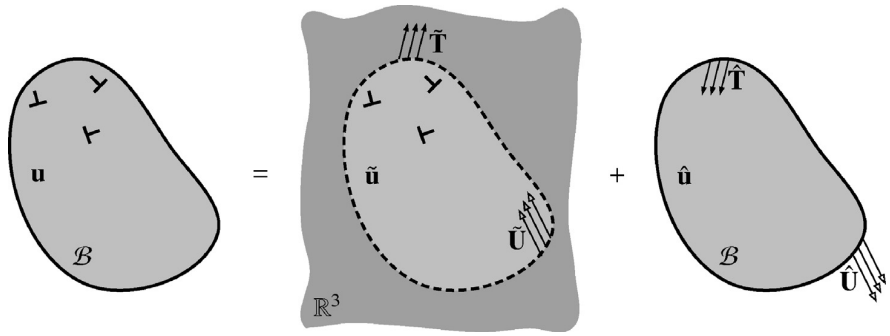

Fig. 2. The decomposition of the problem for a linear elastic bounded body containing dislocations into two problems: (1) dislocations in an infinite body and (2) the body without dislocations.

where $\mathbf{n} \in \mathbb{R}^3$ is the outer unit normal to $\partial\mathcal{B}$, div$(\bullet)$ is the divergence of a tensor field, and $\mathbf{0} \in \mathbb{R}^3$ denotes the null vector. The stress field σ is obtained from $\mathbf{u}$ by

$$\sigma = \mathbb{C} : \nabla\mathbf{u}, \tag{10}$$

where $\mathbb{C}$ is the fourth-order elasticity tensor, $\nabla(\bullet)$ denotes the gradient of a vector field in $\mathbb{R}^3$, and $(\bullet):(\bullet)$ denotes the operation of double contraction of two tensors.

By virtue of its linear structure, the problem (9) can be readily decomposed into two separate problems (Fig. 2). The first problem aims to find a displacement field $\tilde{\mathbf{u}}$ in an infinite linear elastic body containing all dislocation lines. In contrast, the second problem aims to obtain a displacement field $\hat{\mathbf{u}}$ in $\mathcal{B}$ without dislocation lines but with suitably defined applied tractions $\hat{\mathbf{T}}$ and displacements $\hat{\mathbf{U}}$. The solution of (9) can be then obtained simply by pointwise superposition of both displacement fields, i.e. $\mathbf{u} = \tilde{\mathbf{u}} + \hat{\mathbf{u}}$. Subsequently, the stress field σ becomes readily available from (10) and enters into (2) to yield forces on discretized dislocation lines. However, the superposition of displacements carries over to stresses due to the linearity of (10), i.e. $\sigma = \tilde{\sigma} + \hat{\sigma}$. Therefore, contributions to forces on discertized dislocation lines from both $\tilde{\sigma}$ and $\hat{\sigma}$ can be evaluated entirely independently of each another via (2)–(4).

The computation of the displacement field $\tilde{\mathbf{u}}$ can be simplified, again owing to the linear structure of (9), as composed of contributions from individual dislocation lines, i.e. $\tilde{\mathbf{u}} = \sum_i \tilde{\mathbf{u}}^i$. In general, for a dislocation line of arbitrary shape, $\tilde{\mathbf{u}}^i$ may still need to be computed numerically. However, analytical $\tilde{\mathbf{u}}^i$ formulas exist for certain types of dislocation lines [33,34], and in particular, a straight dislocation line segment. Thus, in view of our discussion in Section 2, $\tilde{\mathbf{u}}$ may be assembled simply from contributions of individual dislocation line segments in a discretization of dislocation lines. Once $\tilde{\mathbf{u}}$ is calculated, the associated stress field, $\tilde{\sigma}$, may be found from $\tilde{\sigma} = \mathbb{C} : \nabla\tilde{\mathbf{u}}$. Still, since, in the case of a dislocation line segment, analytical formulas also exist for its stress field, $\tilde{\mathbf{u}}$ may never be explicitly computed. Instead, $\tilde{\sigma}$ may be simply calculated by superposition of stress contributions from individual dislocation line segments. Subsequently, $\tilde{\sigma}$ may be employed in (3) and (4) to yield vertex force contributions on discretized dislocation lines. Oftentimes, however, this route of computing vertex force contributions, as discussed above, is side-stepped entirely, and direct analytical formulas for dislocation line segment–segment forces are employed [14].

Complementary displacement field $\hat{\mathbf{u}}$ is a solution of

$$\begin{cases} \operatorname{div}\hat{\sigma} = 0 & \text{in } \mathcal{B} \\ \hat{\sigma}\mathbf{n} = \hat{\mathbf{T}} & \text{on } \partial\mathcal{B}_t \\ \hat{\mathbf{u}} = \hat{\mathbf{U}} & \text{on } \partial\mathcal{B}_u \end{cases} \tag{11}$$

The tractions on $\partial\mathcal{B}_t$ are $\hat{\mathbf{T}} = -\tilde{\mathbf{T}}$, where $\tilde{\mathbf{T}} = \tilde{\sigma}\mathbf{n}$, and the displacements on $\partial\mathcal{B}_u$ are $\hat{\mathbf{U}} = -\tilde{\mathbf{U}}$, as required to satisfy the traction free and null displacement boundary conditions in the problem (9). Here, $\tilde{\mathbf{U}}$ denotes the restriction of $\tilde{\mathbf{u}}$ on $\partial\mathcal{B}_u$. It is worth noting that $\hat{\mathbf{T}}$ and $\hat{\mathbf{U}}$ are computed on a segment-by-segment basis via analytical formulas [33,34]. As before, the stress field $\hat{\sigma}$ is related to the displacement field $\hat{\mathbf{u}}$ by $\hat{\sigma} = \mathbb{C} : \nabla\hat{\mathbf{u}}$. We emphasize that analytical solutions of (11) exist only for a very narrow class of simple bodies. Thus, in practice, problem (11) is routinely solved by numerical methods [38–40]. Again, with the help of (2)–(4), $\hat{\sigma}$ can be converted directly to force contributions on discretized dislocation lines without the need to explicitly form σ. Such an approach is, of course, preferred when the calculation of $\tilde{\sigma}$ is bypassed altogether in lieu of the direct analytical segment–segment force formulas.

We also note that σ^{ext} in (6) may be obtained from the solution of a problem analogous to (11). Therefore, the computation of σ^{ext} is usually integrated directly into (11) by means of an appropriate modification of the applied tractions $\hat{\mathbf{T}}$ and displacements $\hat{\mathbf{U}}$.

4. An algorithmic framework for coupling of a dislocation dynamics and finite element codes by means of distributed shared memory

The majority of available dislocation dynamics computer codes tend to address only the first problem in the decomposition in Fig. 2, i.e. the motion of dislocations in an infinite or periodic body [8,14]. This choice has been primarily motivated by the use of dislocation dynamics in development of strength models in crystal plasticity [30,31,41,42]. A renewed interest in small scale plasticity in recent years has brought back into focus the use of dislocation dynamics in this context [43–45,32]. The two problem decomposition of the treatment of bounded bodies in dislocation dynamics (Fig. 2) provides a convenient avenue for achieving the goal of dislocation dynamics simulations of small scale plasticity. To this end, an existing dislocation dynamics computer code needs to be simply augmented with a computer code solving problem (11). However, such a coupling between two disparate codes, especially in the context of parallel computing, remains challenging. In this section, we describe, in detail, an algorithmic framework for coupling a parallel dislocation dynamics code and a parallel finite element code.

The solution procedure for problem (11) requires the knowledge of the tractions $\hat{\mathbf{T}}$ and displacements $\hat{\mathbf{U}}$ on suitable parts of the boundary $\partial\mathcal{B}$. The computation of $\hat{\mathbf{T}}$ and $\hat{\mathbf{U}}$, of course, entails the evaluation of analytical formulas for all discretized dislocation lines in $\mathcal{B}$. This task can be best achieved if the discretized dislocation line data is accessible by the finite element code. Thus, there exists a need to establish a link allowing the dislocation dynamics code to provide the discretized dislocation line data to the finite element code. With these data at hand, the finite element

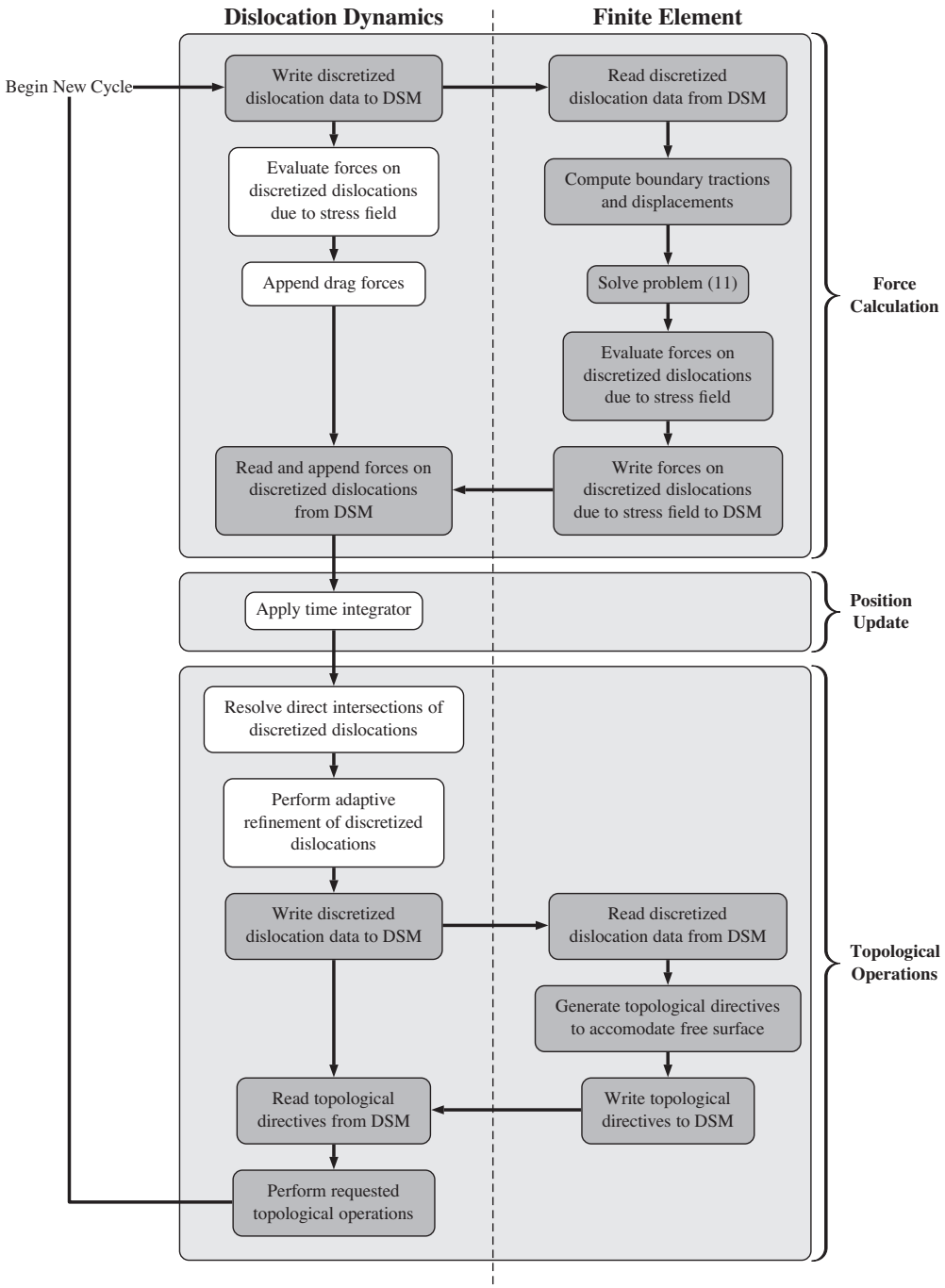

Fig. 3. The algorithm for the coupling of the dislocation dynamics and finite element codes. Unmodified dislocation dynamics routines are colored white. Additional routines introduced to handle bounded bodies are colored dark gray. The dotted line divides the routines into ones implemented in the dislocation dynamics code and those in the finite element code.

code can proceed to evaluate, on a segment-by-segment basis, the analytical formulas yielding $\hat{\mathbf{T}}$ and $\hat{\mathbf{U}}$. Subsequently, the solution of (11), $\hat{\mathbf{u}}$, is employed to yield the stress field $\hat{\sigma}$. Once $\hat{\sigma}$ is available, the finite-element solver can compute force contributions of individual dislocation segments, which are then transmitted to the dislocation dynamics code for addition to locally computed segment–segment force contributions. Further communication between the two codes is also required once the dislocation dynamics code has moved and carried out topological operations on discretized dislocation lines. Since dislocation lines must not terminate within $\mathcal{B}$, additional steps may be necessary as to satisfy this requirement [14]. Therefore, the discretized dislocation data is transmitted again to the finite element code, which enforces the above requirement by accordingly repositioning vertices of discretized dislocation lines. The updated discretized dislocation data is then sent back to the dislocation dynamics code, which updates its representation. The algorithm for the coupled operation of the two codes under consideration is presented in Fig. 3. Obviously, relatively minor modifications are needed for the dislocation dynamics code. However, the crucial aspect of the algorithm is the two-way communication between the two codes. In order to address this aspect of our algorithm we adopt the

concept of distributed shared memory (DSM) [46] as a convenient framework for carrying out the communication. Throughout the remainder of this section we describe details of our DSM algorithm for coupling the dislocation dynamics and finite element codes. For practical purposes, both codes are assumed to employ the message passing interface (MPI) [47,48] for communication.

DSM enables the coupling of parallel applications by providing a shared global memory arena that is available to all processors and which serves as a common storage location for shared data between applications. A global memory arena is formed by DSM as a collection of physically separate local memories. DSM conceals the distributed nature of the shared memory behind an abstraction layer, so that for applications, access to DSM appears identical to interaction with contiguous memory.

For our application we elect to use H5FDdsm, a high level implementation of DSM [27]. In H5FDdsm, the DSM memory is accessed through the Hierarchical Data Format (HDF5) application programming interface (API), commonly employed by scientific applications for storage of data on disk [49,50]. H5FDdsm provides a virtual file driver to HDF5 that seamlessly translates HDF5 file locations to memory addresses in DSM. To client applications, communication with DSM appears equivalent to interaction with an HDF5 file. Parallel communication between applications and DSM is possible through use of HDF5 hyperslabs. Additionally, parallel components of H5FDdsm are built using MPI, meaning that communication between DSM and coupled applications can take advantage of high-speed interconnects like InfiniBand.

In order to correctly couple codes via DSM, strict access rules between client codes and DSM must be enforced to ensure memory coherency. In H5FDdsm, only one code is permitted to access DSM at a time and access must be collective for all application processors to guarantee atomicity. Furthermore, interactions with DSM will block if DSM is already accessed by another code.

For the coupling of codes, DSM must be allocated and accessible to both. In our algorithm, the finite element code is selected to allocate DSM on all of its processors during startup. The desired size of the DSM memory is provided as input. The DSM memory is distributed in equal allocations across all finite element processors. The decision to allocate DSM memory on finite element processors is arbitrary and allocation on dislocation dynamics processors would work equally well. After allocation of DSM memory, the dislocation dynamics code is launched and an MPI intercommunicator is formed between DSM and the dislocation dynamics code to serve as a communication channel. The dislocation dynamics code obtains initial control of DSM and writes parameters to DSM to initialize the coupled application. DSM control is released to the finite element code, which reads and stores the initialization parameters. After initialization, the coupled application enters the main computational loop, consisting of force calculations, position updates, and topological operations at each simulation timestep, as outlined in Fig. 3.

As mentioned above, the first step of the main simulation loop is communication of the discretized dislocation line data from the dislocation dynamics code to the finite element code. In our algorithm, for each dislocation line segment, ten doubles are written to DSM: the start and end segment vertex coordinates $\mathbf{x}_i^1$, $\mathbf{x}_i^2$, the segment Burgers vector $\mathbf{b}_i$, and a flag indicating whether any of the two segment vertices belong to $\partial\mathcal{B}$. The dislocation dynamics code allocates a dataset in DSM of HDF5 data type `H5T_NATIVE_DOUBLE` and size of the total number of dislocation line segments multiplied by ten. Since the dislocation dynamics code is assumed to be parallel, each of its tasks writes data for owned dislocation line segments into the appropriate DSM memory location through HDF5 hyperslabs. The communication of data takes place collectively for all dislocation dynamics tasks, providing parallel communication of data to DSM.

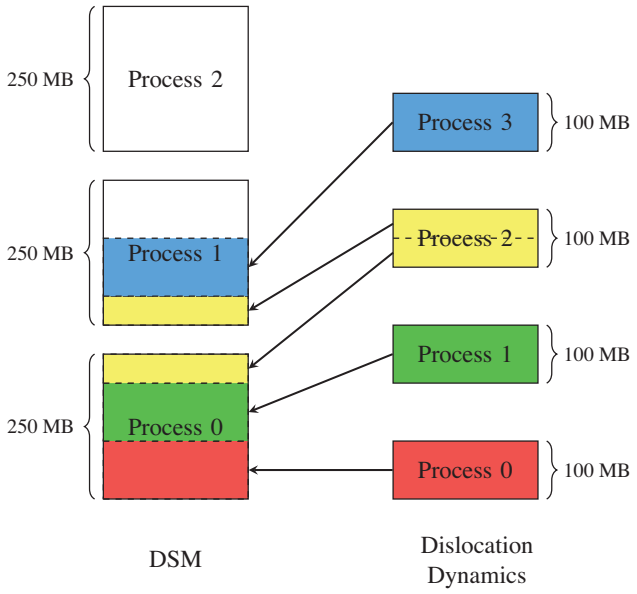

Fig. 4. Communication of data from the dislocation dynamics code to DSM. The dislocation dynamics code consists of four processors each containing a 100 MB dataset. These datasets are written to a 750 MB DSM distributed equally on three processors.

When a parallel code issues a write to DSM, it is up to H5FDdsm to determine how to route data from the code to DSM tasks. An example of how data is routed from the dislocation dynamics code to DSM is presented in Fig. 4. In this example, the dislocation dynamics code is composed of four tasks each containing 100 MB datasets. The datasets are written to a 750 MB DSM distributed equally across three tasks. At present, data written to DSM is distributed in a bottom up fashion, filling the first processor in the DSM before advancing to the next processor. More sophisticated distribution strategies that balance written data throughout the DSM are under development. Data is communicated from the dislocation dynamics code to DSM in parallel using point-to-point MPI communication. Once again, it is necessary to note that routing details between codes and DSM are handled transparently by H5FDdsm and these details are presented here so that a deeper understanding of DSM interaction may be gained.

After the communication of dislocation segment data to DSM has completed, the dislocation dynamics code releases control of DSM to the finite element code and commences its dislocation segment force calculations. At the same time, the finite element code carries out the computation of its contributions to dislocation segment forces. We emphasize that both of these force calculations are completely independent and occur concurrently. This aspect of our algorithm is crucial for performance as the force calculation usually constitutes the most computationally expensive component of dislocation dynamics simulations [51]. The finite element code begins its calculation by reading dislocation segment data from DSM. For simplicity, each finite element task acquires the entire segment dataset into memory as all segments may be needed to compute $\hat{\mathbf{T}}$ and $\hat{\mathbf{U}}$. Upon completion of its calculation, the finite element code writes its dislocation line segment force contributions to DSM as six doubles per segment. Then, the control of DSM is released back to the dislocation dynamics code, which reads the finite element computed dislocation force contributions from DSM in order to append them to form the total dislocation segment forces. We place emphasis here on the fact the dislocation dynamics code may block if the force calculation is still in progress in the finite element code.

Once the force calculation completes, the dislocation dynamics code forms equations of motion (7) with the application of a drag force and, then, employs a numerical integrator to obtain updated coordinates of vertices in the discretization of dislocation lines. In general, since the numerical integrator does not enforce the constraint that the vertices must be contained in $\mathcal{B}$, the updated vertex coordinates are not guaranteed to satisfy it. Owing to the fact that $\partial\mathcal{B}$ is explicitly known only to the finite element code, additional communication with the finite element code must be performed in order to assure that the above constraint is fulfilled. The dislocation dynamics code again writes dislocation segment information to DSM, consisting now of eight doubles per segment: $\mathbf{x}_i^1$, $\mathbf{x}_i^2$ vertex coordinates and a flag for each vertex indicating whether it has been previously marked as a vertex in $\partial\mathcal{B}$. Then, the dislocation dynamics code releases control of DSM and the finite element code reads the dislocation line segment data and begins updating dislocation line segment information to account for bounded $\mathcal{B}$.

The finite element code iterates over received dislocation line segments and generates a list of topological directives for the dislocation dynamics code that are used to modify vertex coordinates. The first step in generating topological directives is determining whether dislocation line vertices are located inside or outside of $\mathcal{B}$. This task may be accomplished by means of an efficient cell-tree element location algorithm, which quickly determines possible encompassing elements for segment vertices through use of a bounding interval hierarchy [52]. If both vertices of a segment are located outside $\mathcal{B}$, a directive is generated to remove the segment entirely from the simulation. In contrast, if one of its vertices is located in $\mathcal{B}$ and the other outside, the dislocation segment must intersect a free surface and a directive is generated to cut the segment at the intersection point. If both segment vertices are inside $\mathcal{B}$, the segment remains unchanged. Additional work may be required in order to handle segment vertices that the dislocation dynamics code has marked as residing in $\partial\mathcal{B}$. These segment vertices are required to remain in $\partial\mathcal{B}$ throughout the simulation to ensure the Burgers vector conservation. Therefore, it may be necessary to update the coordinates of all vertices in $\partial\mathcal{B}$. The finite element code writes thirteen doubles per segment to DSM, which include the updated vertex coordinates $\mathbf{x}_i^1$, $\mathbf{x}_i^2$, the outer normals to $\partial\mathcal{B}$ at $\mathbf{x}_i^1$, $\mathbf{x}_i^2$, and a directive for the topological operation the dislocation dynamics code must carry out. In addition, if a segment pierces $\partial\mathcal{B}$ and is marked for cutting, the new coordinates for the external vertex are taken as the coordinates of the intersection point of the segment and $\partial\mathcal{B}$. After writing data to DSM, control of DSM is transitioned yet again to the dislocation dynamics code, which reads the topological directives and modifies segment data accordingly. Once complete, the end of the computational loop is reached and if required, a new cycle can commence.

After completing all necessary cycles in the computational loop, the dislocation dynamics code instantiates the teardown of the coupled application by issuing a call to disconnect from the DSM. Upon that, the finite element code exits its main computational loop and deallocates the DSM arena. Both codes are now disjoint and exit individually.

We finally note that DSM has been used previously to couple scientific codes. An early version of H5FDdsm, the Network Distributed Global Memory (NDGM) was employed to perform serial one-way coupling of commercial finite element code LS-Dyna to shock physics code CTH for fluid–structure interactions [53]. In addition, H5FDdsm has served to couple simulations to visualization tools for *in situ* visualization [54]. However, the uniqueness of our approach stems from the fact that we use DSM to facilitate parallel two-way coupling of applications, with each application interacting in parallel with DSM.

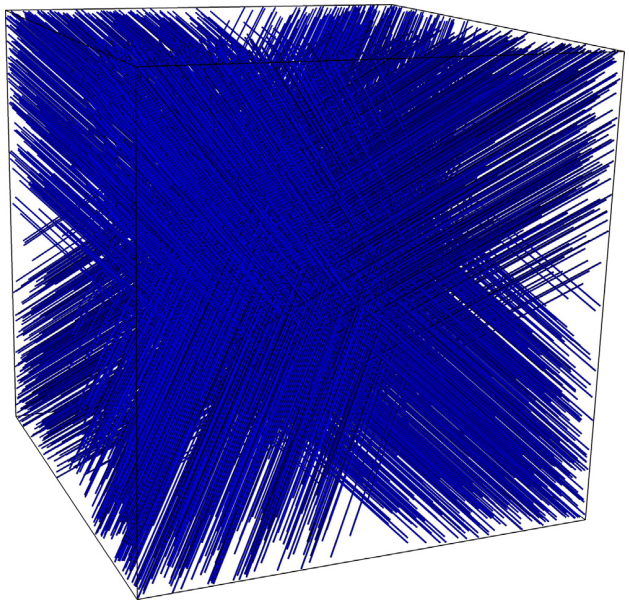

Fig. 5. The cubical body considered for our performance evaluation containing 4096 randomly distributed straight edge dislocations.

5. Results

In this section, we assess the overall performance of our coupling algorithm. To this end, as a dislocation dynamics code we employ Parallel Dislocation Simulator (ParaDiS)-a massively parallel dislocation dynamics simulator under development at Lawrence Livermore National Laboratory [14]. ParaDiS enables three-dimensional dislocation dynamics simulations with the primary focus on strain hardening modeling. Thanks to new mathematical algorithms and their robust implementation, ParaDiS allows for efficient handling of an unprecedented number of dislocations in very large parallel computing environments.

As a solver for problem (11) we utilize a parallel finite element code developed at the U.S. Army Research Laboratory [55]. This solver combines conventional two- and three-dimensional finite element technology [56,57,40] with non-overlapping domain decomposition for parallel processing [58].

Body $\mathcal{B}$ is taken to be a cube of tungsten with dimension 1.3625 μm containing 4096 randomly distributed straight dislocation lines with Burgers vector of 2.725 Å(Fig. 5). Each dislocation line crosses the entire cube, i.e. both of its ends are in the cube surfaces. We discretize the dislocation lines into dislocation line segments no longer than 272.5 Å, yielding the total of 280,261 dislocation segments.

Following Arsenlis et al. [14] we employ a linear drag function which leads to a particularly simple expression for the vertex drag force at vertex v_k, $\mathbf{F}_k^{drag} = \frac{1}{2}\sum_j |s_j|\mathbf{B}_j\mathbf{v}_k$. The summation extends over all dislocation segments connected to v_k. $\mathbf{v}_k$ denotes the velocity of v_k, $|s_j|$ is the length of dislocation segment s_j, and $\mathbf{B}_j$ is the drag tensor for s_j. We take $\mathbf{B}_j \equiv \mathbf{1}$ Pa s, where $\mathbf{1}$ represents the second-rank identity tensor in the space of tensors over $\mathbb{R}^3$. The trapezoidal rule numerical integrator is utilized in ParaDiS in order to propagate the dislocation dynamics solution.

The body is discretized into 1,012,860 quadratic tetrahedral elements for use by the finite element code (Fig. 6). We employ isotropic linear elasticity to describe the mechanical response of tungsten. Specifically, the following form of (10) is used

$$\sigma = \lambda(\mathrm{tr}\nabla\mathbf{u})\mathbf{1} + 2\mu(\nabla\mathbf{u} + \nabla\mathbf{u}^T), \tag{12}$$

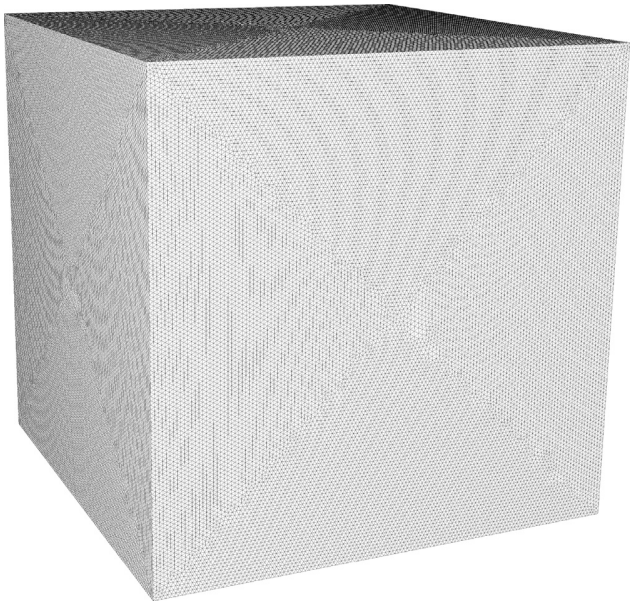

Fig. 6. The discretization of the cubical body considered for our performance evaluation into 1,012,860 quadratic tetrahedral elements.

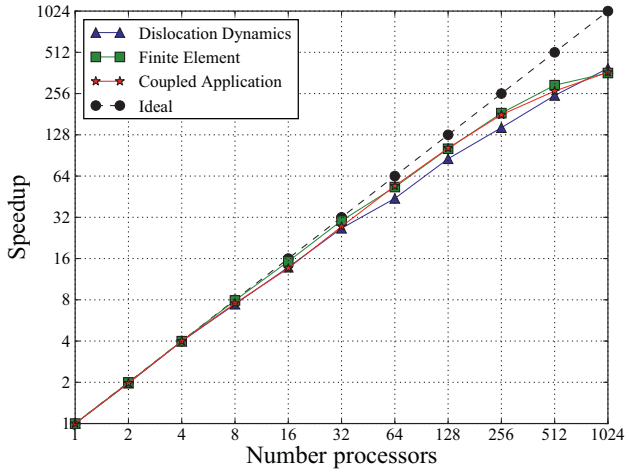

Fig. 7. Scalability of dislocation dynamics, finite element, and coupled applications. The dislocation dynamics code, indicated by blue triangles, has been executed for 10 simulation cycles using a tungsten material containing 4096 dislocations as pictured in Fig. 5. The finite element code, indicated by green squares, has been executed for a single cycle using the mesh in Fig. 6 and the same dislocation system as for the dislocation dynamics code. The coupled application, indicated by red stars, has been executed for a single simulation cycle using the same dislocation system and mesh as in the standalone codes. In the coupled case, number of processors is the number used in each individual application (i.e. a one processor run is the execution of the dislocation dynamics code on one processor and the finite element code on one processor). The ideal scalability is also plotted for reference. (For interpretation of the references to color in this figure legend, the reader is referred to the web version of this article.)

where the Lamé constants are $\lambda = 204$ GPa and $\mu = 161$ GPa. $\mathrm{tr}(\bullet)$ and $(\bullet)^T$ denote, respectively, the trace and the transpose of a second-rank tensor over $\mathbb{R}^3$. We assume null displacements boundary on the bottom of the cube, while the remaining cube surfaces are treated as traction free.

All our performance studies have been carried out on the Pershing supercomputer at the U.S. Army Research Laboratory (ARL), which contains an Intel Xeon Sandy Bridge sixteen-core processor and 32 GB of RAM on compute nodes. The compute nodes are interconnected by FDR-10 InfiniBand. All codes have been compiled with the Intel 12.1.0 MPI compiler.

In Fig. 7, we plot the strong scalability of the dislocation dynamics and finite element codes individually, as well as the coupled application. The strong scalability of the dislocation dynamics code is assessed by executing 10 simulation cycles. Since the initial partition of dislocation line segments among processors may not be necessarily optimal, 200 load balancing steps are executed at the onset of each run. For the finite element code, the discretization of the body is partitioned among processors as to ensure an approximately equal number of elements assigned to each processor. A linear conjugate gradient solver with Jacobi preconditioning is used for solving problem (11) [59]. A single cycle of the finite element code, consisting of computing surface tractions, carrying out the solution, and computing dislocation segment force contributions is executed.

We evaluate parallel performance of the coupled application utilizing identical setups as for assessing individual components. A total DSM size of 100 MB is allocated evenly across all finite element processors. A single cycle of the coupled application is then executed to acquire timings. For the dislocation line configuration under consideration, 21.4 MB of segment data is transmitted from the dislocation dynamics code to the finite element code and 12.8 MB of force data is transmitted back for each dislocation segment force calculation. For each scalability run of the coupled application, we elect to utilize equal numbers of dislocation dynamics and finite element processors, up to 1024 processors each. As evident from Fig. 7, the coupled application exhibits strong scalability that matches well with the scalability of the individual applications.

An additional complexity associated with the coupled application is that the number of processors assigned to each individual application cannot be selected adaptively during the course of execution and instead must be chosen prior to execution. However, a judicious selection of the number of processors assigned to each individual application is crucial for the optimal performance of the coupled application. When examining the algorithm of the coupled application in Fig. 3, it is clear that synchronization points, where the applications exchange data, are important for overall performance. If too many processors are assigned to either of the two applications, one of them may be forced to wait at any of the synchronization points, wasting execution time.

In order to explore the impact of processor assignment on the performance of the coupled application, we denote the total number of processors for the coupled application, N, and partition it into N_{dd}, the number of processors for the dislocation dynamics application, and N_{fem}, the number of processors for the finite element application, i.e. $N = N_{dd} + N_{fem}$. We utilize the tungsten problem setup and execute the coupled application for five simulation cycles. Since the finite element application is most likely more expensive computationally, we employ N_{dd}: N_{fem} ratios of 1:1, 1:3, 1:7, 1:15, 1:31, and 1:63. In Fig. 8, we plot the wall clock execution time as a function of the N_{dd}: N_{fem} ratio. Clearly, the minimal execution time is achieved at N_{dd}: $N_{fem} = 1:15$ for all processor counts studied. Still, differences in execution time between different processor ratios are quite small near the minimum as 1:3, 1:7, and 1:15 execution times are fairly similar to each other.

To further explore the scalability of the coupled application, we take two vertical cuts from Fig. 8, one along the "naïve" 1:1 ratio and one along the optimal 1:15 ratio. We plot these results in Fig. 9. As expected, the execution time is greatly reduced for the optimal ratio. Moreover, the scalability of the coupled application remains strong for both the "naïve" and optimal ratios.

It is important to note that, in general, the ideal partitioning of processors between the dislocation dynamics and finite element

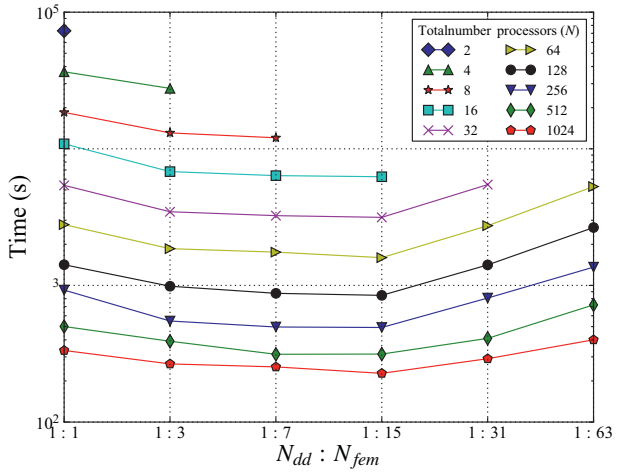

Fig. 8. Wall clock execution time of the coupled application for different ratios of processors assigned to the dislocation dynamics and finite element applications. A total number of processors, N, is split into N_{dd}, the number of processors for the dislocation dynamics application, and N_{fem}, the number of processors for the finite element application, where $N = N_{dd} + N_{fem}$. Wall clock time is acquired for execution of five simulation cycles for a tungsten material containing 4096 dislocations as pictured in Fig. 5 and a finite element mesh in Fig. 6.

applications may be difficult to determine. Many factors may influence this partitioning, chiefly among them, the number of dislocation segments in the system and the finite element mesh discretization. In addition, the ideal partitioning may evolve during the course of a simulation, for example, if new dislocation segments are introduced. However, enabling adaptive processor partitioning remains challenging. Migration of individual processors between the dislocation dynamics and finite element applications would require repartitioning each problem to utilize newly reassigned processors. This task may be difficult to accomplish on the fly without stopping and restarting the applications. It is clear that new ideas and algorithms are needed to enable this type of adaptivity in multiple program multiple data applications.

After exploring the parallel performance and scalability of the coupled application, we wish to examine the performance of individual components of the dislocation force calculation, so that we

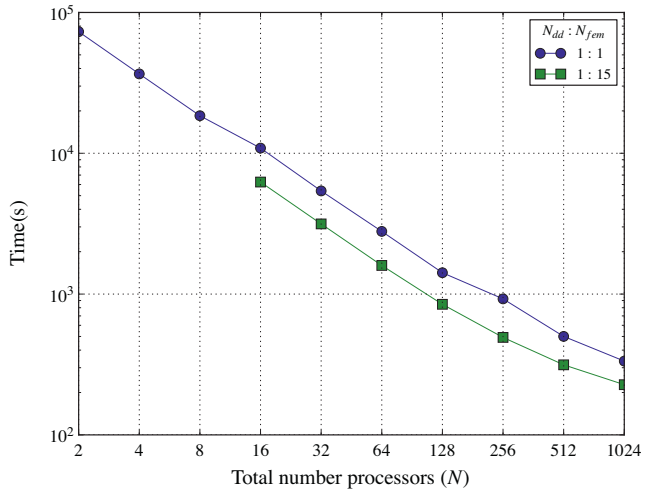

Fig. 9. Wall clock execution time of the coupled application for two different ratios of processors assigned to the dislocation dynamics and finite element applications: the "naïve" case of N_{dd}: N_{fem} of 1:1 and the optimal execution case of 1:15. The plot consists of two vertical slices taken from Fig. 8 in order to clearly demonstrate the scalability of the coupled application.

can target efforts aimed at improving overall performance. We focus on assessing performance of the finite element code and its interactions with DSM, as the finite element calculation is the more expensive part of the coupled application, as revealed by the optimal $N_{dd} : N_{fem}$ ratio of 1:15 for the dislocation configuration studied. More specifically, these components include: (1) dislocation segment data read from DSM, (2) computation of $\hat{\mathbf{T}}$ and $\hat{\mathbf{U}}$ on $\partial\mathcal{B}$, (3) problem (11) solve, (4) computation of dislocation segment force contributions due to $\hat{\sigma}$, and (5) dislocation segment forces write to DSM.

The execution times for the components of the dislocation segment force calculation carried out by the finite element code are plotted in Fig. 10. We acquire timings for two ratios of $N_{dd} : N_{fem}$ processors, 1:1 and the optimal 1:15. As expected, the timings for the two ratios are very similar, as the finite element force calculation executes independently of the number of dislocation dynamics processors employed. The solution time for problem (11) dominates the entire calculation. This fact is scarcely surprising, as this is the most computationally expensive part of the calculation. However, the high cost is offset at large processor counts by excellent scalability.

The computation of surface tractions is the second most computationally expensive component. The traction calculation scales with increasing processor count, but not ideally. This behavior is mostly due to the fact that the partitioning of the discretization of $\partial\mathcal{B}$ derives directly from a partitioning of $\mathcal{B}$, which may lead to a significant imbalance during the course of the traction computation. More specifically, only processors holding elements in the discretization of $\partial\mathcal{B}$ will ultimately be carrying out the calculation, while all others, possibly the majority, will remain idle.

The evaluation of dislocation segment forces displays rather poor parallel performance. This behavior is not unexpected since dislocation segments are not partitioned among finite element processors as the finite element code lacks *a priori* knowledge about the location of the segments within $\mathcal{B}$. Therefore, each processor must iterate over the entire list of dislocation segments when computing dislocation segment forces. Obviously, at present, the relative computational cost of this component remains quite small, but may become more significant at large processor counts. This lack of scalability, however, can be ameliorated by means of fairly simple modifications, as discussed below.

Finally, although accounting for the least execution time among all components for all processor counts studied, time spent communicating data between the finite element code and DSM increases with increasing processor count. Each finite element processor reads the entire dislocation segment dataset from DSM, which means that for larger processor counts, a larger amount of data must be communicated from DSM. Additionally, each finite element processor writes dislocation segment forces for all dislocation segments to DSM, resulting in more communicated data for larger finite element processor counts. Despite the poor scalability of DSM communication, the overall scalability of the coupled application remains good up to 1024 processors as the runtime is dominated by the finite element solve. However, given the execution timing data generated on the test system, it is reasonable to expect that communication costs may, at some point, begin to dominate the runtime at larger processors counts than studied here.

On the basis of our timing data, there appear to be several potential paths that could be explored to increase the overall performance of the coupled application. First, the performance of the finite element solve can be improved via more efficient linear solvers and preconditioning. Second, a partitioning of the surface discretization independent from the partitioning of the volume discretization is bound to yield a better load-balancing of the traction

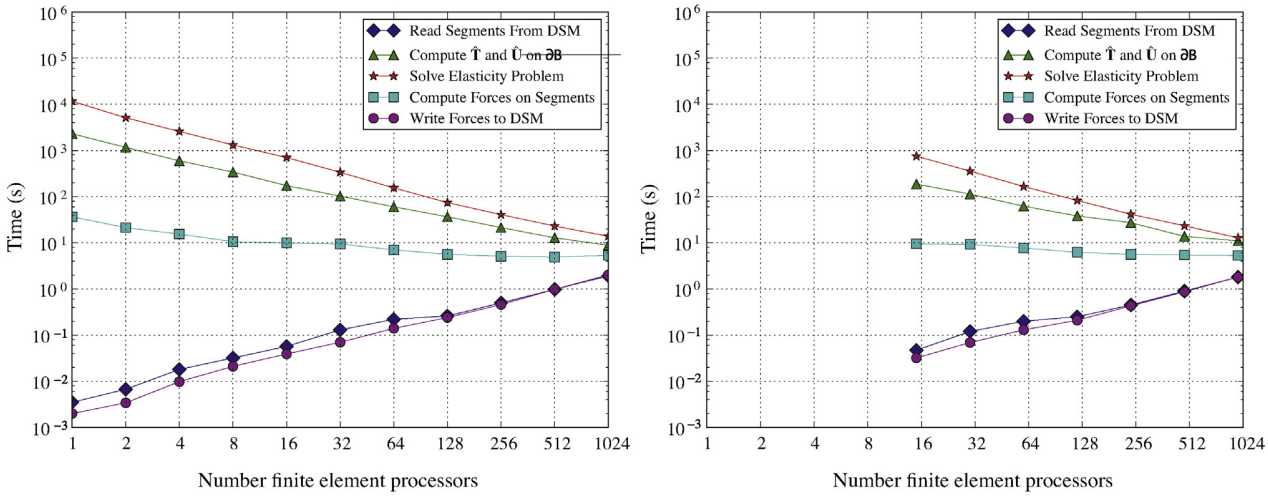

Fig. 10. Timings for individual components of the finite element calculation. Communication between the finite element code and DSM are shown as blue diamonds for the reading of segments and purple circles for writing of computed forces. The other routines include computing $\hat{\mathbf{T}}$ and $\hat{\mathbf{U}}$ on $\partial\mathcal{B}$ (green triangles), solution of the elasticity problem (red stars), and computing forces on segments from the resulting $\hat{\sigma}$ (light blue squares). (For interpretation of the references to color in this figure legend, the reader is referred to the web version of this article.)

computation, allowing, in turn, for increased scalability. Finally, the performance of the dislocation segment force calculation can be readily improved by pruning the dislocation segment list on each processor in order to avoid iterating over all dislocation segments. To this end, the dislocation dynamics code could transmit bounding box data of its partitions to the finite element code in addition to the dislocation segment data. The bounding box data could then be employed to handle only dislocation segment data located in overlapping dislocation dynamics domains. However, avoiding the increasing communication costs between the finite element code and DSM on larger numbers of processors is difficult to achieve, as each finite element processor must read the entire segment list in order to properly compute surface tractions. It may be possible that a more balanced distribution of segment data across DSM processors, rather than the current bottom up allocation, could improve performance by spreading communication costs. But, this approach does not nullify the necessity of communicating larger amounts of data for increasing numbers of processors. A possible approach to reduce the amount of segment data communicated to the finite element code may be to utilize the fast multipole method algorithms that are currently available in dislocation dynamics codes [14]. Utilization of these algorithms may enable communication of a reduced set of data for each multipole cell rather than the entire segment data list. However, it is unclear how the result generated from the finite element force calculation would be communicated to the dislocation dynamics code if only fast multipole cell data is available. Additionally, it is possible that utilization of fast multipole method algorithms may impact the concurrency of the finite element and dislocation dynamics force calculations, possibly reducing performance of the overall application. Given the execution timings and scalability data generated on the example system, it appears possible that efforts to improve DSM scalability should not become the first priority, as solving problem (11) and computing surface tractions clearly dominate execution time of the coupled application.

6. Summary

We have proposed an algorithmic framework, based on a distributed shared memory concept, to couple a parallel dislocation dynamics code and a parallel finite element elasticity solver. The algorithm enables large scale parallel simulations of small scale plasticity by means of dislocation dynamics. The coupled codes communicate data between each other frequently during a computational loop. The communication between the codes and distributed shared memory occurs in parallel. We have carried out a performance analysis of the coupled application and contrasted it with performance of the individual component codes. For our test problem, the coupled application exhibits good performance with strong scalability up to 1024 processors. The distributed shared memory coupling approach employed in this work is generic and likely applicable to a wide range of parallel coupling applications. On the basis of our performance analysis, we have also identified several components of the coupled application that are good candidates for algorithmic modifications in order to increase performance. However, even in its initial state, the coupled code is capable of handling large systems containing tens of millions of dislocation segments and executing on many processors with good performance.

References

[1] J. Lubliner, Plasticity Theory, Macmillan, New York, 1990.
[2] V. Lubarda, Elastoplasticity Theory, CRC, Boca Raton, FL, 2001.
[3] W. Nix, Mechanical properties of thin films, Metallurgical and Materials Transactions A 20 (1989) 2217–2245.
[4] L. Freund, S. Suresh, Thin Film Materials: Stress, Defect Formation and Surface Evolution, Cambridge University Press, Cambridge, England, 2004.
[5] J. Venables, G. Spiller, M. Hanbucken, Nucleation and growth of thin films, Reports on Progress in Physics 47 (1984) 399–459.
[6] D. Schlom, L. Chen, C. Eom, K. Rabe, S. Streiffer, J. Triscone, Strain tuning of ferroelectric thin films, Annual Review of Materials Research 37 (2007) 589–626.
[7] R. Waser, M. Aono, Nanoionics-based resistive switching memories, Nature Materials 6 (2007) 833–840.
[8] V. Bulatov, W. Cai, Computer simulations of dislocations, Oxford University Press, New York, 2006.
[9] K. Schwarz, Simulation of dislocations on the mesoscopic scale. I. Methods and examples, Journal of Applied Physics 85 (1999) 108–119.
[10] K. Schwarz, Simulation of dislocations on the mesoscopic scale. II. Application to strained-layer relaxation, Journal of Applied Physics 85 (1999) 120–129.
[11] B. Devincre, V. Pontikis, Y. Brechet, G. Canova, M. Condat, L. Kubin, Three-dimensional simulations of plastic flow in crystals, in: Microscopic Simulations of Complex Hydrodynamic Phenomena, Plenum Press, pp. 413–423.
[12] M. Verdier, M. Fivel, I. Groma, Mesoscopic scale simulation of dislocation dynamics in fcc metals: principles and applications, Modelling and Simulation in Materials Science and Engineering 6 (1999) 755–770.

[13] H. Yasin, H. Zbib, M. Khaleel, Size and boundary effects in discrete dislocation dynamics: coupling with continuum finite element, Materials Science and Engineering: A 309 (2001) 294–299.
[14] A. Arsenlis, W. Cai, M. Tang, M. Rhee, T. Oppelstrup, G. Hommes, T. Pierce, V. Bulatov, Enabling strain hardening simulations with dislocation dynamics, Modelling and Simulation in Materials Science and Engineering 15 (2007) 553–595.
[15] E. van der Giessen, A. Needleman, Discrete dislocation plasticity: a simple planar model, Modelling and Simulation in Materials Science and Engineering 3 (1995) 689–735.
[16] S. Plimpton, B. Hendrickson, S. Attaway, J. Swegle, C. Vaughan, D. Gardner, Transient dynamics simulations: parallel algorithms for contact detection and smoothed particle hydrodynamics, in: Proceedings of the 1996 ACM/IEEE Conference on Supercomputing (CDROM), IEEE Computer Society, 1996, p. 28.
[17] C. Hoover, A. DeGroot, R. Sherwood, ParaDyn a parallel nonlinear, explicit, three-dimensional finite-element code for solid and structural mechanics user manual, Technical Report UCRL-MA-140943, Lawrence Livermore National Laboratory, 2000.
[18] N.R. Barton, J.V. Bernier, J. Knap, A.J. Sunwoo, E.K. Cerreta, T.J. Turner, A call to arms for task parallelism in multi-scale materials modeling, International Journal for Numerical Methods in Engineering 86 (2011) 744–764.
[19] J. Borgdorff, C. Bona-Casas, M. Mamonski, K. Kurowski, T. Piontek, B. Bosak, K. Rycerz, E. Ciepiela, T. Gubala, D. Harezlak, M. Bubak, E. Lorenz, A.G. Hoekstra, A distributed multiscale computation of a tightly coupled model using the multiscale modeling language, in: Proceedings of the International Conference on Computational Science, ICC, Procedia Computer Science 9 (2012) 596–605.
[20] I. Raicu, Z. Zhang, M. Wilde, I. Foster, P. Beckman, K. Iskra, B. Clifford, Toward loosely coupled programming on petascale systems, in: Proceedings of the 2008 ACM/IEEE Conference on Supercomputing, SC'08, IEEE Press, Piscataway, NJ, USA, 2008, pp. 22:1–22:12.
[21] F. Liu, M. Sosonkina, A multilevel parallelism support for multi-physics coupling, in: Proceedings of the International Conference on Computational Science, ICC, Procedia Computer Science 4 (2011) 261–270.
[22] J. Knap, N.R. Barton, R.D. Hornung, A. Arsenlis, R. Becker, D.R. Jefferson, Adaptive sampling in hierarchical simulation, International Journal for Numerical Methods in Engineering 76 (2008) 572–600.
[23] D. Jefferson, Relationship between Co-op and MPI-2, Technical Report UCRLTR-225783, Lawrence Livermore National Laboratory, 2006.
[24] S. Vinoski, Corba, Integrating diverse applications within distributed heterogeneous environments, IEEE Communications Magazine 35 (1997) 46–55.
[25] A. Sussman, Building complex coupled physical simulations on the grid with intercomm, Engineering with Computers 22 (2006) 311–323.
[26] J. Larson, R. Jacob, I. Foster, J. Guo, The model coupling toolkit, in: V. Alexandrov, J. Dongarra, B. Juliano, R. Renner, C. Tan (Eds.), Computational Science ICCS 2001, Lecture Notes in Computer Science, vol. 2073, Springer, Berlin, Heidelberg, 2001, pp. 185–194.
[27] J. Soumagne, J. Biddiscombe, J. Clarke, An HDF5 MPI virtual file driver for parallel in-situ post-processing, Recent Advances in the Message Passing Interface (2010) 62–71.
[28] L. Kubin, G. Canova, M. Condat, B. Devincre, V. Pontikis, Y. Bréchet, Dislocation microstructures and plastic flow: a 3D simulation, Solid State Phenomena 23 (1992) 455–472.
[29] N. Ghoniem, L. Sun, Fast-sum method for the elastic field of three-dimensional dislocation ensembles, Physical Review B 60 (1999) 128–140.
[30] V. Bulatov, M. Tang, H. Zbib, Crystal plasticity from dislocation dynamics, MRS Bulletin 26 (2001) 191–195.
[31] V. Bulatov, Current developments and trends in dislocation dynamics, Journal of Computer-Aided Materials Design 9 (2002) 133–144.
[32] C. Zhou, S. Biner, R. LeSar, Discrete dislocation dynamics simulations of plasticity at small scales, Acta Materialia 58 (2010) 1565–1577.
[33] J. Weertman, J. Weertman, Elementary Dislocation Theory, Macmillan, New York, 1966.
[34] J. Hirth, J. Lothe, Theory of Dislocations, John Wiley & Sons Inc., New York, 1982.
[35] G. Holzapfel, Nonlinear Solid Mechanics: A Continuum Approach for Engineering, John Wiley & Sons Inc., Chichester, England, 2000.
[36] J. Butcher, Numerical Methods for Ordinary Differential Equations, John Wiley & Sons Inc., Chichester, England, 2008.
[37] E. Hairer, S. Nørsett, G. Wanner, Solving Ordinary Differential Equations I: Nonstiff Problems, Springer Series in Computational Mathematics, Springer, Berlin, 2011.
[38] S. Timoshenko, J. Goodier, Theory of Elasticity, McGraw-Hill, New York, 1970.
[39] G. Beer, I. Smith, C. Duenser, The Boundary Element Method with Programming: For Engineers and Scientists, Springer Verlag, New York, 2008.
[40] O. Zienkiewicz, R. Taylor, The Finite Element Method for Solid and Structural Mechanics, 2, Butterworth-Heinemann, Oxford, England, 2005.
[41] R. Becker, Developments and trends in continuum plasticity, Journal of Computer-Aided Materials Design 9 (2002) 145–163.
[42] N. Barton, J. Bernier, R. Becker, A. Arsenlis, R. Cavallo, J. Marian, M. Rhee, H. Park, B. Remington, R. Olson, A multiscale strength model for extreme loading conditions, Journal of Applied Physics 109 (2011) 073501.
[43] J. Greer, W. Oliver, W. Nix, Size dependence of mechanical properties of gold at the micron scale in the absence of strain gradients, Acta Materialia 53 (2005) 1821–1830.
[44] C. Weinberger, W. Cai, Surface-controlled dislocation multiplication in metal micropillars, Proceedings of the National Academy of Sciences 105 (2008) 14304–14307.
[45] J. Greer, C. Weinberger, W. Cai, Comparing the strength of fcc and bcc sub-micrometer pillars: Compression experiments and dislocation dynamics simulations, Materials Science and Engineering: A 493 (2008) 21–25.
[46] J. Protic, M. Tomasevic, V. Milutinovic, Distributed shared memory: concepts and systems, Parallel & Distributed Technology: Systems & Applications, IEEE 4 (1996) 63–71.
[47] P. Pacheco, Parallel Programming with MPI, Morgan Kaufmann, San Francisco, CA, 1997.
[48] W. Gropp, E. Lusk, A. Skjellum, Using MPI: Portable Parallel Programming with the Message Passing Interface, vol. 1, MIT Press, Cambridge, MA, 1999.
[49] M. Folk, A. Cheng, R. McGrath, HDF5: A New File Format and i/o Library for Scientific Data Management, in: M. David, Mehringer, L. Raymond, Plante, A. Douglas, Roberts (Eds.), Astronomical Data, Analysis software and Systems VIII Proceedings, vol. 172, Astronomical Society of the Pacific, 1999.
[50] A. Cheng, M. Folk, HDF5: High performance science data solution for the new millennium, in: SC2000: High Performance Networking and Computing, pp. 149–149.
[51] G. Hommes, A. Arsenlis, V. Bulatov, W. Cai, R. Cook, M. Hiratani, T. Oppestrup, M. Rhee, M. Tang, ParaDiS on Blue Gene/L: stepping up to the challenge, Technical Report UCRL-CONF-222086, Lawrence Livermore National Laboratory, 2006.
[52] C. Garth, K. Joy, Fast memory-efficient cell location in unstructured grids for visualization, IEEE Transactions on Visualization and Computer Graphics 16 (2010) 1541–1550.
[53] J. Clarke, R. Namburu, A generalized method for one-way coupling of cth and lagrangian finite element codes with complex structures using the interdisciplinary computing environment, in: Proceedings of the 2004 Users Group Conference, IEEE Computer Society, pp. 234-237.
[54] J. Biddiscombe, J. Soumagne, G. Oger, D. Guibert, J. Piccinali, Parallel computational steering and analysis for HPC applications using a ParaView interface and the HDF5 DSM virtual file driver, in: Eurographics Symposium on Parallel Graphics and Visualization, The Eurographics Association, pp. 91–100.
[55] J. Knap, J. Clayton, A Computational Framework for Phase-field Modeling, Technical Report ARL-MR-0760, Army Research Laboratory, 2011.
[56] P. Ciarlet, The Finite Element Method for Elliptic Problems, North Holland, Amsterdam, 1978.
[57] T. Belytschko, W. Liu, B. Moran, Nonlinear Finite Elements for Continua and Structures, John Wiley & Sons Inc., Chichester, England, 2000.
[58] A. Toselli, O. Widlund, Domain Decomposition Methods-algorithms and Theory, Springer, Berlin, 2004.
[59] Y. Saad, Iterative Methods for Sparse Linear Systems, Society for Industrial and Applied Mathematics, Philadelphia, 2003.

Kenneth Leiter is a computer scientist at the Army Research Laboratory. His research interests are on the development of computational algorithms for high performance computers, especially in the context of multiscale materials modeling. He received a B.S. in chemistry and B.A. in computer science from Duke University in 2008.

Josh Crone is a research engineer in the Computational and Information Sciences Directorate of the U.S. Army Research Laboratory. He received his M.Sc. in mechanical engineering from the University of Maryland in 2008. His research interests include small scale plasticity and high performance computing algorithms for physics-based simulations.

Jaroslaw Knap is a staff scientist with the Computational and Information Sciences Directorate of the U.S. Army Research Laboratory. He received his PhD in mechanical engineering from the Arizona State University in 1998. His research interests include computational mechanics, multi-scale materials modeling, and scientific computing.

An Alternative Approach to Integrating Plasticity Relations

Richard Becker

International Journal of Plasticity, 27 (2011)

Contents lists available at ScienceDirect

International Journal of Plasticity

journal homepage: www.elsevier.com/locate/ijplas

An alternative approach to integrating plasticity relations

Richard Becker *

US Army Research Laboratory, High Rate Mechanics and Failure Branch, Aberdeen Proving Ground, MD 21005, United States

ARTICLE INFO

Article history:
Received 24 August 2010
Received in final revised form 14 January 2011
Available online 4 February 2011

Keywords:
Non-quadratic
Plasticity integration
Flow potential

ABSTRACT

A new plasticity integration algorithm is proposed based upon observations from the closed form integration of a generalized quadratic yield function over a single time step. The key to the approach is specification of the normal to the plastic flow potential as a function of the current state and strain increment. This uniquely defines the direction of the stress tensor for a convex, non-faceted flow potential. The stress magnitude and plastic strain increment are computed to satisfy the yield function. A non-quadratic, isotropic, associative flow model is coded to demonstrate accuracy and time step convergence following a step change in loading path. The model is used in additional simulations of strain localization in an expanding ring and a perforated plate.

Published by Elsevier Ltd.

1. Introduction

Traditional plasticity models are defined in terms of rate equations, and the stress and any history dependent state variables must be integrated through time (Hill, 1950). In the context of a displacement based finite element code, a strain increment or an average strain rate over the time increment is provided to the plasticity algorithm, and updated stress and state variables are returned. The stability and accuracy of the material time integration algorithm may limit the time step. Consequently, the computational efficiency of simulations can be affected by the material time integration method.

Time integration algorithms for general plasticity equations typically involve subtracting a plastic strain increment from the total strain increment to arrive back at the yield surface. Extensive literature reviews of strength models and integration procedures in finite element codes are given by Yu (2002) and Kojić (2002), respectively. More recent plasticity integration algorithms have also been described (e.g. Ulz, 2009; Mosler and Bruhns, 2010; Brannon and Leelavanichkul, 2010). Details can vary considerably, but the underlying concept is common: a return mapping to the yield surface from an initial projection. Textbook descriptions (e.g. Dunne and Petrinic, 2005; Hill, 1950) often provide a 2-D depiction of the yield surface, a stress increment projecting some small distance outward from the surface, and a vector in the direction of the plastic strain increment returning to the surface, Fig. 1a. The plastic strain direction is normal to the flow potential surface. This is the same as the yield surface for associative-flow plasticity models.

The manner in which finite element analyses are run can depart significantly from this textbook illustration. Many finite element codes will take strain increments on the order of 10% or more (Abaqus, 2009). If the material yields at a strain of 0.1%, the vector projecting off the yield surface may be 100 times the radius of the surface. The plastic strain direction must project back to the surface. A slight error in the direction could result in missing the surface entirely, Fig. 1b. This projection at large strain increments is a major difficulty for integrating anisotropic material models (Kojić, 2002).

The problem is simplified considerably for J2-Flow theory and an associated flow rule. This yield surface is a hyper-sphere in deviatoric stress space. A vector passing through the center of the yield surface is colinear with the surface normal. Hence, a plastic strain increment directed toward the center of the yield surface intersects the surface at a stress consistent with the

* Fax: +1 410 278 2460.
E-mail address: richard.c.becker@us.army.mil

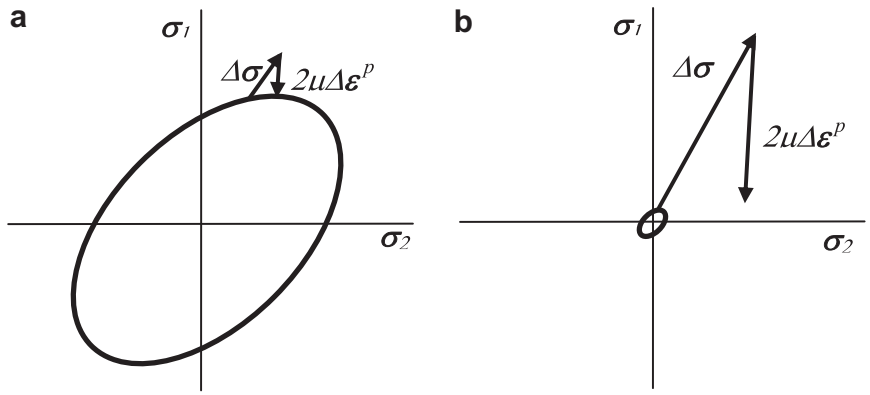

Fig. 1. Stress increment and plastic return mapping using a plastic strain direction estimated from the beginning of the time step for: (a) a small strain increment typically described in text books and (b) many analyses where the strain increment can be more than an order of magnitude larger than the yield strain.

plastic flow direction. The normality condition is satisfied automatically. Implicit integration schemes have to solve for the magnitude of the plastic strain increment, not the direction. This radial return method (Krieg and Krieg, 1977; Wilkins, 1964) is robust, efficient and widely used for J2-Flow theory with an associative flow rule. Radial return can be used for plasticity models where the yield surface is not a hyper-sphere. This results in a non-associative flow rule because the yield surface and plastic flow potential are not the same. The approach remains efficient and robust, but it may give results different than those of an associative flow rule.

J2-Flow theory and other plasticity models for which the rate form can be expressed as $\dot{\boldsymbol{s}} = a\dot{\boldsymbol{e}} + \dot{\lambda}\boldsymbol{s}$ may be integrable analytically or semi-analytically over a time step. Solutions can be obtained for J2-Flow theory (Krieg and Krieg, 1977), kinematic hardening (Krieg and Xu, 1997; Auricchio and Beirão da Veiga, 2003; Arioli et al., 2006), the Drucker–Prager model (Rezaijee-Pajand and Nasirai, 2008; Szabó, 2009), and potentially other plasticity models. These methods have demonstrated accuracy advantages over purely numerical integration algorithms and do not suffer the return mapping direction issues, but the range of models which can be integrated analytically or semi-analytically is limited. Analytical solutions do, however, provide valuable insight into the behavior of plasticity relations. It is this insight that motivates the proposed new plasticity integration scheme presented in Section 3.

The aim of this work is to explore a different approach to plasticity model integration. It is based upon observations from the closed form integration of a generalized quadratic plasticity model over a time step described in Section 2. As an exploration, presentation of the method is the focus. Isotropic elasticity, plastic incompressibility and other assumptions are used to keep the relations simple and more transparent. The implementation is in an explicit finite element code, so formulation of a consistent tangent is not considered. The closed form integration is the starting point for the presentation, followed by: observations leading to the new numerical integration approach; a description of the implementation into a finite element code; simulations verifying the implementation; and results from simple localization calculations.

2. Closed form integration for a generalized quadratic yield function

2.1. Rate formulation

The yield function, ϕ, and flow potential, ψ, for a generalized quadratic plasticity model with an associated flow rule (Karafillis and Boyce, 1993; Maudlin and Schiferl, 1996) can be written as:

$$\phi = \psi = \sqrt{\frac{3}{2}\boldsymbol{\sigma}' : \boldsymbol{K} : \boldsymbol{\sigma}'} - \bar{\sigma} = \sigma_{eq} - \bar{\sigma} = 0, \tag{1}$$

$\boldsymbol{\sigma}'$ is the deviatoric stress; $\bar{\sigma}$ is the material flow strength (a material property); and $\boldsymbol{K}$ is fourth order tensor characterizing the material anisotropy. $\boldsymbol{K}$ is the identity tensor for an isotropic material. $\phi = \psi$ defines an associative flow rule; $\phi \neq \psi$ results in a non-associative plasticity model.

Following the classical plasticity formulation (Hill, 1950), the plastic part of the rate of deformation tensor is normal to the flow potential

$$\boldsymbol{d}^p = \dot{\lambda}\frac{\partial\psi}{\partial\boldsymbol{\sigma}} = \dot{\lambda}\boldsymbol{p} = \dot{\lambda}\frac{3}{2}\frac{\boldsymbol{K} : \boldsymbol{\sigma}'}{\bar{\sigma}}. \tag{2}$$

The plastic multiplier, $\dot{\lambda}$, can be determined from the equivalence of plastic power between the tensor field and material property representations

$$\boldsymbol{\sigma} : \boldsymbol{d}^p = \dot{\lambda}\boldsymbol{\sigma} : \boldsymbol{p} = \dot{\bar{\varepsilon}}\bar{\sigma}, \tag{3}$$

$\dot{\bar{\varepsilon}}$ is the equivalent plastic strain rate for a uniaxial stress test specimen. It is work conjugate to the flow stress, $\bar{\sigma}(\dot{\bar{\varepsilon}}, \bar{\varepsilon}, T, \ldots)$. Eq. (3) leads to an expression for the plastic multiplier

$$\dot{\lambda} = \dot{\bar{\varepsilon}} \frac{\bar{\sigma}}{\boldsymbol{\sigma} : \boldsymbol{p}}, \tag{4}$$

$\dot{\lambda} = \dot{\bar{\varepsilon}}$ if the J2-Flow theory yield criterion and associative flow rule are used.

For a hypo-elastic formulation the deviatoric part of the rate of deformation tensor, $\boldsymbol{d}'$, is decomposed additively into elastic and plastic parts. The Jaumann stress rate is given in terms of the elastic part of the rate of deformation tensor which is expanded by substituting the flow rule from Eq. (2)

$$\hat{\boldsymbol{\sigma}}' = \boldsymbol{L} : \boldsymbol{d}'^{e} = \boldsymbol{L} : (\boldsymbol{d}' - \boldsymbol{d}^{p}), \tag{5a}$$

$$= \boldsymbol{L} : \boldsymbol{d}' - \dot{\bar{\varepsilon}} \frac{\bar{\sigma}}{\boldsymbol{\sigma} : \boldsymbol{p}} \boldsymbol{L} : \boldsymbol{p} = \boldsymbol{L} : \boldsymbol{d}' - \frac{3}{2} \frac{\dot{\bar{\varepsilon}}}{\boldsymbol{\sigma} : \boldsymbol{p}} \boldsymbol{L} : \boldsymbol{K} : \boldsymbol{\sigma}'. \tag{5b}$$

$\boldsymbol{L}$ is the fourth order elasticity tensor.

2.2. Closed form integration over a time step

The objective is to integrate Eq. (5b) in closed form for one time step, Δt, given the average rate of deformation tensor over the time step. The anisotropy creates a rate form that is not amenable to the analytic techniques cited above (e.g., Arioli et al., 2006; Szabó, 2009). The equations are instead integrated by summation over infinitesimal parts of the time step. It is assumed that the flow strength and the plastic multiplier are constants over the time step. It is also assumed that material rotations are applied prior to integrating the stress. The latter is common practice when using the Jaumann rate. Details of the integration are given in Appendix A. The resulting stress at the end of the time step is

$$\boldsymbol{\sigma}'_{t+\Delta t} = exp\left(-\frac{3}{2} \frac{\dot{\bar{\varepsilon}} \Delta t}{\boldsymbol{\sigma} : \boldsymbol{p}} \boldsymbol{L} : \boldsymbol{K} \right) : \boldsymbol{\sigma}'_t + \frac{2}{3} \frac{\boldsymbol{\sigma} : \boldsymbol{p}}{\dot{\bar{\varepsilon}} \Delta t} \left[\boldsymbol{I}' - exp\left(-\frac{3}{2} \frac{\dot{\bar{\varepsilon}} \Delta t}{\boldsymbol{\sigma} : \boldsymbol{p}} \boldsymbol{L} : \boldsymbol{K} \right) \right] : \boldsymbol{K}^{-1} : \boldsymbol{d}' \Delta t. \tag{6}$$

Subscripts t and $t + \Delta t$ refer to the stress at the beginning and end of the time step, respectively. $\boldsymbol{I}'$ is a modified fourth order identity tensor operating only on the deviatoric response, and it is defined by

$$\mathbf{I}' \stackrel{\text{def}}{=} \left(\mathbf{I} - \frac{1}{3} \boldsymbol{\delta} \otimes \boldsymbol{\delta} \right), \tag{7}$$

where $\mathbf{I}$ is the fourth order identity tensor and $\boldsymbol{\delta}$ is the second order identity. Some of the Δt 's could be factored out of Eq. (6) and from subsequent equations, but they are retained as an explicit reminder that the expression are intended to be applied over time increments and are not alternative rate equations. The exponentials are reminiscent of those in analytic solutions for J2-Flow theory (e.g., Arioli et al., 2006) and the Drucker–Pragar model (e.g., Szabó, 2009), but the anisotropy renders these fourth order tensors rather than scalars.

A quick check can be made for small and large strain increments to verify that Eq. (6) behaves appropriately in the limits. In the limit of a small strain increment where only the linear term in the exponential expansion is important, the stress at the end of the step is

$$\boldsymbol{\sigma}'_{t+\Delta t} = \boldsymbol{\sigma}'_t - \frac{3}{2} \frac{\dot{\bar{\varepsilon}} \Delta t}{\boldsymbol{\sigma} : \boldsymbol{p}} \boldsymbol{L} : \boldsymbol{K} : \boldsymbol{\sigma}'_t + \boldsymbol{L} : \boldsymbol{d}' \Delta t. \tag{8}$$

This is the forward integration result. At large strain increments the exponential vanishes, leaving

$$\frac{3}{2} \frac{\dot{\bar{\varepsilon}}}{\boldsymbol{\sigma} : \boldsymbol{p}} \boldsymbol{K} : \boldsymbol{\sigma}'_{t+\Delta t} = \boldsymbol{d}'. \tag{9}$$

Comparing this with the Eq. (2) leads to the condition that the total strain rate and the plastic strain rate are the same in the limit of very large strain increments. This is required for large strain increments to keep the stress bounded in Eq. (5a).

The plastic flow direction (flow potential normal) at the end of the time step follows from Eqs. (2) and (6). To simplify the result, the exponential from Eq. (6) is written as the series expansion. From the expansion it is readily seen that the $\boldsymbol{K}$ premultiplying the stress from Eq. (2) can be placed within the exponential on the left allowing the existing $\boldsymbol{K}$ to be factored out on the right. The resulting expression is:

$$\begin{aligned} \boldsymbol{d}^{p}_{t+\Delta t} &= \frac{3}{2} \frac{\dot{\bar{\varepsilon}}}{\boldsymbol{\sigma} : \boldsymbol{p}} \left\{ exp\left(-\frac{3}{2} \frac{\dot{\bar{\varepsilon}} \Delta t}{\boldsymbol{\sigma} : \boldsymbol{p}} \boldsymbol{K} : \boldsymbol{L} \right) : \boldsymbol{K} : \boldsymbol{\sigma}'_t + \frac{2}{3} \frac{\boldsymbol{\sigma} : \boldsymbol{p}}{\dot{\bar{\varepsilon}}} \left[\boldsymbol{I}' - exp\left(-\frac{3}{2} \frac{\dot{\bar{\varepsilon}} \Delta t}{\boldsymbol{\sigma} : \boldsymbol{p}} \boldsymbol{K} : \boldsymbol{L} \right) \right] : \boldsymbol{d}' \right\} \\ &= exp\left(-\frac{3}{2} \frac{\dot{\bar{\varepsilon}} \Delta t}{\boldsymbol{\sigma} : \boldsymbol{p}} \boldsymbol{K} : \boldsymbol{L} \right) : \boldsymbol{d}^{p}_t + \left[\mathbf{I}' - exp\left(-\frac{3}{2} \frac{\dot{\bar{\varepsilon}} \Delta t}{\boldsymbol{\sigma} : \boldsymbol{p}} \boldsymbol{K} : \boldsymbol{L} \right) \right] : \boldsymbol{d}' \end{aligned} \tag{10}$$

An important, but not surprising observation is that the plastic flow direction at the end of the time step is not necessarily the same as the average plastic flow direction over the time step, which is given by

$$\boldsymbol{d}^p = \boldsymbol{d}' - \boldsymbol{L}^{-1} : (\boldsymbol{\sigma}'_{t+\Delta t} - \boldsymbol{\sigma}'_t)/\Delta t. \tag{11}$$

The direction from Eq. (10) and the average direction are the same in the limit of small strain increments, but there is no requirement for the flow potential normal at the end of the time step to be in the same direction as the average over the time step. Equating the two is a common unstated assumption made in many plasticity algorithms because some additional constraint is needed to close the set of equations. A second observation from Eq. (10) is that the evolution of the plastic flow direction over a time step can take a simple form with well defined limits at small and large time steps.

3. Proposed time integration algorithm

The strategy for the proposed time integration method is to determine the flow potential normal at the end of the time step and use that in conjunction with the flow potential to calculate a stress direction consistent with the normal. The magnitude of the stress will then be adjusted to satisfy the yield condition and flow strength model. The ensuing development is specialized to plastically incompressible materials. Extension to more general models is possible but beyond the scope of this work. It is important to stress that this method is not a direct integration of the constitutive model; it is a general approximate technique motivated by observations from a closed form solution.

3.1. Yield surface normal

The central component of the model is the flow potential normal at the end of the time step. The expression for the normal, $\boldsymbol{n}$, at the end of the time step is motivated by Eq. (10) along with relations from Eqs. (2) and (4) and assuming $\boldsymbol{n} = \boldsymbol{p}\sqrt{2/3}$.

$$\boldsymbol{n}_{t+\Delta t} = \alpha\left\{ exp\left(-\sqrt{\frac{3}{2}}\frac{\bar{\sigma}\dot{\bar{\varepsilon}}\Delta t}{\boldsymbol{\sigma} : \boldsymbol{p}} \left(\frac{\partial \boldsymbol{n}}{\partial \boldsymbol{\sigma}'}\right)_t : \boldsymbol{L} \right) : \boldsymbol{n}_t + \sqrt{\frac{2}{3}}\frac{\boldsymbol{\sigma} : \boldsymbol{p}}{\bar{\sigma}\dot{\bar{\varepsilon}}\Delta t}\left[\boldsymbol{I}' - exp\left(-\sqrt{\frac{3}{2}}\frac{\bar{\sigma}\dot{\bar{\varepsilon}}\Delta t}{\boldsymbol{\sigma} : \boldsymbol{p}} \left(\frac{\partial \boldsymbol{n}}{\partial \boldsymbol{\sigma}'}\right)_t : \boldsymbol{L} \right) \right] : \boldsymbol{d}'\Delta t \right\}. \tag{12}$$

The leading factor, α, allows normalization of $\boldsymbol{n}_{t+\Delta t}$ to a unit tensor at finite time increments where the rate of deformation tensor is not exactly normalized by the plastic strain rate. The normalization by α is only for convenience in the ensuing numerical treatment, the direction is the important feature. An additional extrapolation was made in replacing $\sqrt{3}\boldsymbol{K}/\sqrt{2}\bar{\sigma}$ with the derivative the flow potential normal with respect to stress. The goal in making this generalization is to provide a plausible linearization of the normal in Eq. (12) at small strain increments

$$\boldsymbol{n}_{t+\delta t} = \boldsymbol{n}_t + \left(\frac{\partial \boldsymbol{n}}{\partial \boldsymbol{\sigma}'}\right)_t : \boldsymbol{L} : \left(\boldsymbol{d}' - \sqrt{\frac{3}{2}}\frac{\bar{\sigma}\dot{\bar{\varepsilon}}}{\boldsymbol{\sigma} : \boldsymbol{p}}\boldsymbol{n}_t \right)\Delta t = \boldsymbol{n}_t + \left(\frac{\partial \boldsymbol{n}}{\partial \boldsymbol{\sigma}'}\right)_t : \Delta\boldsymbol{\sigma}'. \tag{13}$$

The middle expression of Eq. (13) is a linearization of Eq. (12), and the $\Delta\boldsymbol{\sigma}'$ in the right hand expression is the stress increment through Eqs. (5a) and (5b). At large strain increments the plastic flow direction must approach the applied strain rate direction in order for the stress to be bounded properly, Eq. (5a). As a result, Eq. (12) should provide an accurate limiting direction for any plastically incompressible flow potential surface.

Eq. (12) could be used as the basis for the integration algorithm, but evaluating the exponential of the fourth order tensors in Eq. (12) would be prohibitively expensive in most explicit finite element applications. Further assumptions are made to obtain a scalar argument for the exponential. A more computationally practicable basis for the proposed time integration scheme is

$$\boldsymbol{n}_{t+\Delta t} = \alpha\left\{ exp\left(-\frac{3\mu\dot{\bar{\varepsilon}}\Delta t}{\boldsymbol{\sigma} : \boldsymbol{p}} \right)\boldsymbol{n}_t + \frac{\boldsymbol{\sigma} : \boldsymbol{p}}{\bar{\sigma}\dot{\bar{\varepsilon}}\Delta t}\sqrt{\frac{2}{3}}\left[1 - exp\left(-\frac{3\mu\dot{\bar{\varepsilon}}\Delta t}{\boldsymbol{\sigma} : \boldsymbol{p}} \right) \right] \boldsymbol{d}'\Delta t \right\}. \tag{14}$$

Eq. (14) is consistent with the exact expression, Eq. (10), specialized to J2-Flow theory. For a more general constitutive model, Eq. (14) gives the proper flow potential normal direction at a zero time step, $\boldsymbol{n}_t$, and at large strain increments, $\boldsymbol{d}'\Delta t$. However, the path along the flow potential connecting these two limits will be in error, particularly at small time steps. This is the trade-off in going from Eqs. (12) to (14). The significance of this path error will be evaluated later through several examples. Eq. (12) would give a better approximation to the path if one could compute it efficiently.

For improved accuracy at small strain increments while using Eq. (14), a traditional backward difference, normal return algorithm is used in place of the new approach. If the strain increment exceeds some value or is beyond the radius of convergence for the traditional normal return algorithm, the new methodology is used. Thus, the traditional forward approach is used where it is accurate and efficient, and the new algorithm provides improved robustness and accuracy at larger strain increments.

3.2. Plastic strain rate estimate

The proposed algorithm using Eqs. (12) or (14) requires an estimate of the plastic strain rate. A reasonable approximation can be obtained through a radial return solution for the time step. In the radial return mapping for an isotropic elastic material, the direction of the plastic flow is assumed to be coaxial with the elastic trial stress, which is defined as;

$$\boldsymbol{\sigma}^T \stackrel{\text{def}}{=} \boldsymbol{\sigma}'_t + 2\mu \mathbf{d}' \Delta t. \tag{15}$$

Consequently, the stress at the end of the time step is in the same direction, Eq. (5a). The strain rate and stress tensor must satisfy the yield function

$$\phi = \mathcal{G}(\boldsymbol{\sigma}) - \bar{\sigma}(\bar{\varepsilon}, \dot{\bar{\varepsilon}}, T, \ldots) = \sigma_{eq} - \bar{\sigma} = 0, \tag{16}$$

as well as the stress increment given by Eq. (5a). If $\phi \leqslant 0$ the material is elastic; the strain rate is zero and the updated stress is equal to the trial stress. If $\phi > 0$ the material will deform plastically, and the strain rate will be determined.

The yield function is homogeneous order one in stress. Using the assumption that the stress is coaxial with the trial stress, the radial return algorithm reduces to finding the plastic strain rate that satisfies

$$\phi = \mathcal{G}(\boldsymbol{\sigma}^T) - 3\mu\dot{\bar{\varepsilon}}\Delta t \left(\frac{\mathcal{G}(\boldsymbol{\sigma}^T)}{\sigma^T_{vm}} \right)^2 - \bar{\sigma}(\bar{\varepsilon}, \dot{\bar{\varepsilon}}, T, \ldots) = 0, \tag{17}$$

σ^T_{vm} is the von Mises stress from the trial stress tensor, Eq. (15). Eq. (17) is solved using a combination Newton–Raphson/Bisection algorithm described in *Numerical Recipes* (Press et al., 1992).

One could stop at this point and determine the stress by

$$\boldsymbol{\sigma}' = \boldsymbol{\sigma}^T \frac{\bar{\sigma}(\bar{\varepsilon}, \dot{\bar{\varepsilon}}, T, \ldots)}{\mathcal{G}(\boldsymbol{\sigma}^T)}. \tag{18}$$

The yield function would be satisfied but the direction of plastic flow does not satisfy the flow potential. For some applications the salient aspects of the constitutive model may be adequately captured by only satisfying the yield function. Otherwise, the Eq. (17) only provides an estimate of the plastic strain rate for use in Eqs. (12) or (14).

3.3. Stress direction calculation

The most significant computational effort in determining the stress tensor is in finding its direction from the flow potential normal.

$$\frac{d\psi}{d\boldsymbol{\sigma}} \left\| \frac{d\psi}{d\boldsymbol{\sigma}} \right\|^{-1} = \mathbf{n}_{t+\Delta t}. \tag{19}$$

In forming the matrix to solve Eq. (19), the shear terms are multiplied by $\sqrt{2}$, where appropriate, to permit standard matrix operations while taking advantage of the symmetry of the stress tensor. The solution of Eq. (19) is a well defined, purely mathematical problem, particularly for smooth, convex flow potentials. The mechanistic approximations and the dependency on time step and material properties have been separated. Alternative methods can be used to solve Eq. (19) to improve efficiency without affecting the algorithm.

Eq. (19) is solved here using Newton–Raphson iteration for the stress tensor. The primary difficulty is that the matrix created from Eq. (19) has a null space of at least order two. The consistent components of the null space are related to the pressure and to the magnitude of the stress tensor. The pressure does not impact the flow potential for materials which are plastically incompressible. The magnitude of the tensor is removed from Eq. (19) by the explicit normalization. The stress tensor itself is normalized after each iteration to maintain a consistent stress magnitude. Other contributions to the null space may come from combinations of stress increments which do not affect the normal direction.

The null space complicates the solution of Eq. (19). A singular value decomposition (SVD) module from the LAPACK library is used in the Newton–Raphson iteration. The LAPACK DGESVD routine returns the input matrix A decomposed into orthogonal matrices U and V and diagonal matrix w

$$[A] \times \{s\} = [U](w)[V]^T \times \{s\} = \{e\}, \tag{20}$$

$\{s\}$ is the correction to the deviatoric stress and $\{e\}$ is the error for the Newton–Raphson equation. The null space is associated with zeros in the diagonal w matrix. Since U and V are orthogonal matrices and w is diagonal, inversion of Eq. (20) is straight forward. When inverting the w matrix, the reciprocals of the zero values are replaced by zeros. This eliminates the contribution of the null space from the solution. The SVD is computationally intensive.

An alternative approach to deal with the null space is to add penalty terms to the matrix. Fourth order tensors are constructed from the outer product of the second order identity with itself and from the outer product of the deviatoric stress with itself. These are multiplied by a penalty parameter and added to matrix. The penalty parameter is 10^6 times the norm of the error, $\{e\}$, with a minimum penalty of 1.0.

3.4. Plastic strain rate determination

The plastic strain rate is determined by first creating a scalar equation from the yield function, the flow rule, and a plastic work equivalence statement. The normalized stress direction determined in Section 3.3 is denoted $\tilde{\boldsymbol{\sigma}}$ and the deviatoric stress at the end of the time step is given by

$$\boldsymbol{\sigma}' = \beta\tilde{\boldsymbol{\sigma}}, \tag{21}$$

where β is an unknown scale factor. The equivalent stress is defined through Eq. (16) as

$$\sigma_{eq} = \mathcal{G}(\boldsymbol{\sigma}) = \mathcal{G}(\boldsymbol{\sigma}') = \mathcal{G}(\beta\tilde{\boldsymbol{\sigma}}) = \beta\mathcal{G}(\tilde{\boldsymbol{\sigma}}) = \beta\tilde{\sigma}_{eq} \tag{22}$$

and similar relations can be constructed for the von Mises stress

$$\sigma_{vm} = \sqrt{\frac{3}{2}\boldsymbol{\sigma}' : \boldsymbol{\sigma}'} = \beta\sqrt{\frac{3}{2}\tilde{\boldsymbol{\sigma}} : \tilde{\boldsymbol{\sigma}}} = \beta\tilde{\sigma}_{vm}. \tag{23}$$

These relations will be use to determine the scale factor β.

The equivalent plastic strain rate is defined such that the plastic work rate from the tensor expression is equal to that defined by the equivalent scalars, Eqs. (1) and (3),

$$\boldsymbol{\sigma} : \mathbf{d}^p = \sigma_{eq}\dot{\bar{\varepsilon}} = \bar{\sigma}\dot{\bar{\varepsilon}}. \tag{24}$$

The plastic part of the rate of deformation tensor is obtained by specializing Eq. (11) to an isotropic elastic material and substituting into Eq. (24). Eq. (24) becomes

$$\sigma_{eq}\dot{\bar{\varepsilon}}\Delta t = \boldsymbol{\sigma} : \left(\boldsymbol{\sigma}'_t + 2\mu\mathbf{d}'\Delta t - \boldsymbol{\sigma}'\right)/2\mu. \tag{25}$$

Making a few substitutions from Eq. (15) and Eqs. (21)–(23), and after some manipulation, Eq. (25) can be written as

$$3\mu\sigma_{eq}\dot{\bar{\varepsilon}}\Delta t = \frac{3}{2}\frac{\sigma_{eq}}{\bar{\sigma}_{eq}}\tilde{\boldsymbol{\sigma}} : \boldsymbol{\sigma}^T - \frac{\sigma_{eq}^2}{\bar{\sigma}_{eq}^2}\tilde{\sigma}_{vm}^2. \tag{26}$$

Using the yield function, Eq. (16), this can be cast into a form similar to Eq. (17) to solve for the plastic strain rate

$$\frac{3}{2}\frac{\tilde{\sigma}_{eq}}{\tilde{\sigma}_{vm}^2}\tilde{\boldsymbol{\sigma}} : \boldsymbol{\sigma}^T - 3\mu\dot{\bar{\varepsilon}}\Delta t\frac{\tilde{\sigma}_{eq}^2}{\bar{\sigma}_{vm}^2} - \bar{\sigma}(\bar{\varepsilon}, \dot{\bar{\varepsilon}}, T, \ldots) = 0. \tag{27}$$

With the plastic strain rate and flow strength known, the deviatoric part of the stress tensor at the end of the time step is determined from Eqs. (21) and (22) as

$$\boldsymbol{\sigma}' = \frac{\bar{\sigma}}{\tilde{\sigma}_{eq}}\tilde{\boldsymbol{\sigma}}. \tag{28}$$

The full stress tensor is recovered by adding the contribution of the hydrostatic stress determined by an equation of state.

3.5. Treatment for reverse loading

If the inner product $\boldsymbol{\sigma}'_t : \mathbf{d}' < 0$, the loading path may project into the yield surface. Development of Eqs. (12) and (14) assumed continuous loading, so these do not apply. Therefore, an alternative solution is needed for reverse loading situations. If the final stress state lies within the yield surface, $\phi < 0$, the increment is elastic and the trial stress becomes the stress at the end of the time step. If the reverse loading increment is sufficiently large, the loading path may cut across the yield surface causing plastic flow in a substantially different direction. The radial return solution of Section 3.2 is adopted for these cases. In such situations the deformation increments are too large to track the path details explicitly over the time step. Consequently, any solution will be approximate, and an efficient and robust method is a practical choice.

4. Examples using isotropic, non-quadratic yield surface

An isotropic, non-quadratic yield surface model with an associated flow rule is used as an example (Hosford, 1972; Karafillis and Boyce, 1993). It is written in terms of principal stresses as:

$$\phi = \psi = \sqrt[q]{\frac{1}{2}\left[(\sigma_1 - \sigma_2)^q + (\sigma_2 - \sigma_3)^q + (\sigma_3 - \sigma_1)^q\right]} - \bar{\sigma} = 0, \tag{29}$$

where q is an even integer exponent. This model reduces to J2-Flow theory for a yield surface exponent of 2, which enables comparisons with the well-known radial return method. It also approximates a Tresca yield surface when high exponents are used. Experimental yield surface measurements on aluminum sheet (Barlat et al, 1997) and polycrystal plasticity simulations (Logan and Hosford, 1980) suggest an exponent of approximately eight for FCC materials. Details of the flow potential

derivatives needed for Eq. (19) are given in Appendix B. The yield function and flow rule were implemented in the Arbitrary Lagrange Eulerian code ALE3D (Nichols, 2009) for evaluation and demonstration.

4.1. Yield function representation

The first verification check is to ensure that the yield function is implemented correctly, independent of the details of the integration algorithm. Time varying velocity gradients were imposed independently on the x, y and z-coordinates of all the nodes of a unit cube.

$$\begin{aligned} x\text{-direction}: &\quad \frac{d\dot{x}}{dx} = \cos(t), \\ y\text{-direction}: &\quad \frac{d\dot{y}}{dy} = \cos\left(t + \frac{\pi}{3}\right), \\ z\text{-direction}: &\quad \frac{d\dot{z}}{dz} = \left(t + \frac{\pi}{3}\right). \end{aligned} \tag{30}$$

The imposed deformation traverses a plane normal to the pressure axis in principle stress space (known as the π-plane). No pressure or shear stress are induced beyond numerical integration error. The yield surface exponent was 20, and the constant yield stress was set to 480 MPa. Deviatoric stresses in the x, y and z-directions were recorded and projected to a 2-dimensional representation of the π-plane according to

$$x = \frac{\sigma'_x - \sigma'_z}{\sqrt{2}} \quad y = \frac{-\sigma'_x + 2\sigma'_y - \sigma'_z}{\sqrt{6}}. \tag{31}$$

The resulting yield surface is shown in Fig. 2 for three different integration schemes: (1) traditional normal return using the rate equations; (2) radial return, which results in a non-associative flow rule; and (3) the new algorithm described in Section 3. All reproduce the same yield surface shape to within a 0.05% at this time step. J2-Flow theory would create a circle with this projection and the Tresca yield criterion would create a hexagon.

4.2. Comparison with radial return for J2-Flow theory

The accuracy of the new integration algorithm is assessed by comparison with the radial return method applied to standard J2-Flow theory. This is achieved in the proposed algorithm by setting $q = 2$ in Eq. (29). A single element is run through an abrupt change in loading path by prescribing the displacements of all of the nodes. The loading rates are defined to maintain an effective plastic strain rate of approximately 0.001 s^{-1} in both loading stages. The initial deformation resembles uniaxial tension with the lateral strain rates prescribed equal to negative one-half of the extension strain rate in the x-direction. The extension rate is 0.001 s^{-1}. At a time of 40 s, the deformation is abruptly changed to pure shear in the xy-plane with a shearing rate of $0.0005\sqrt{3}$ s^{-1}. All of the degrees of freedom of the element are again specified.

The shear modulus is 40 GPa and the constant yield strength is set to 480 MPa. Initial yield occurs at 4 s when the deviatoric stress in the x-direction is 320 MPa. The deformation is isochoric, so the bulk modulus is inconsequential. Since all of the degrees of freedom are prescribed, inertial contributions do not affect the solution.

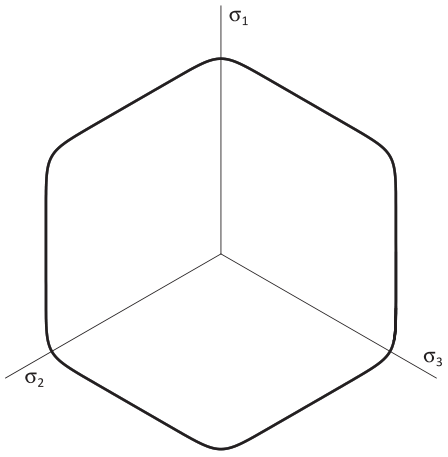

Fig. 2. Yield surface in the π-plane for a yield surface exponent of $q = 20$. Results are plotted for normal return, radial return and the proposed algorithm. They are nearly coincident.

Fig. 3 shows the x-direction stress from the radial return algorithm and the proposed method for runs at several fixed time step sizes. The solid curves are for a time step of 0.002 s. The results for the two methods at this time step are the same to 0.01 MPa, and this is considered to be the converged solution. Time steps of 2 s, 8 s and 40 s are indicated by symbols. These correspond to strain increments of half, twice and ten times the initial yield strain. Fig. 3a displays the radial return results and Fig. 3b shows the results from the new integration scheme. Following the loading path change, the radial return method displays increased error with increasing time step size. The new algorithm matches the baseline solution much more closely with larger time steps. This is expected since method is based on the exact incremental solution for a J2-Flow theory material. Similar plots of shear stress show less time step error for the radial return algorithm and similar time step insensitive results for the new algorithm.

4.3. Evaluation for non-quadratic surfaces

The same loading path change test is run for $q = 8$ in Eq. (29). The baseline result is established using the traditional forward integration method based on the rate equations run at a time step of 0.0002 s. Results are shown in Fig. 4 for the radial return method and the proposed algorithm at two time steps: 0.0002 s and 8.0 s. The latter corresponds to twice the yield strain. The forward time step integration method does not work at this large time step. As indicated in the discussion following Eq. (14), the current algorithm has an integration path error at small strain increments resulting in deviation from the baseline solution. However, this error does not increase with time step, and it is of the same order as the time step errors shown for the J2-Flow theory radial return algorithm in Fig. 3a. The radial return results shown in Fig. 4 appear close to the baseline solutions even though using a radial return for a non-quadratic model creates a non-associative flow rule. One may wonder why not just use the radial return method?

4.4. Evaluation in off-axis loading

The examples reported above involved axial and shear loading which accesses a rather simple path along the yield surface with no rotation. The final unit tests are performed by a path change between two more general loadings. As before, the locations of all of the nodes on the single finite element are prescribed. Path $\mathcal{A}$ is applied for 40 s, and the deformation is abruptly switched to path $\mathcal{B}$. The isochoric velocity gradients associated with these two paths are

$$\mathcal{A} = \begin{bmatrix} 0.5 & 1.0 & 0.4 \\ 0.0 & -0.3 & 0.0 \\ 0.4 & 0.0 & -0.2 \end{bmatrix} \quad \mathcal{B} = \begin{bmatrix} -0.4 & 0.0 & -0.2 \\ 0.5 & 0.7 & 0.4 \\ 0.0 & -0.3 & -0.3 \end{bmatrix}. \tag{32}$$

Similar to Fig. 4, the baseline solution was obtained by using the forward gradient method and a time step of 0.0002 s. Solutions with the radial return method and the new algorithm are run at time steps of 0.0002 s and 8 s.

The results shown in Fig. 5 again show that the proposed integration algorithm tracks the baseline solution and that there is little time step dependence. A behavior not noted in the prior examples is that the radial return method converges to the wrong stress. With these more complex loading states the stress evolution is dependent on the plastic strain rate direction. A radial return is not consistent with the flow potential, so deviations should be expected.

4.5. Strain localization in an expanding ring

One of the goals of using a yield surface with a higher curvature is to allow strain localization more readily than J2-Flow theory. This possibility was investigated using an expanding ring. The plane strain ring has in outer radius of 25.4 mm and a

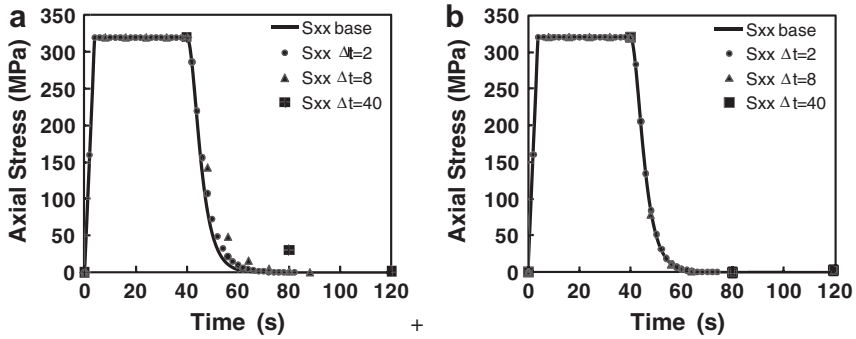

Fig. 3. Axial stress for a J2-Flow theory at various time steps during a loading path change: (a) radial return and (b) proposed algorithm. The solid lines correspond to a baseline time increment of 0.0002 s.

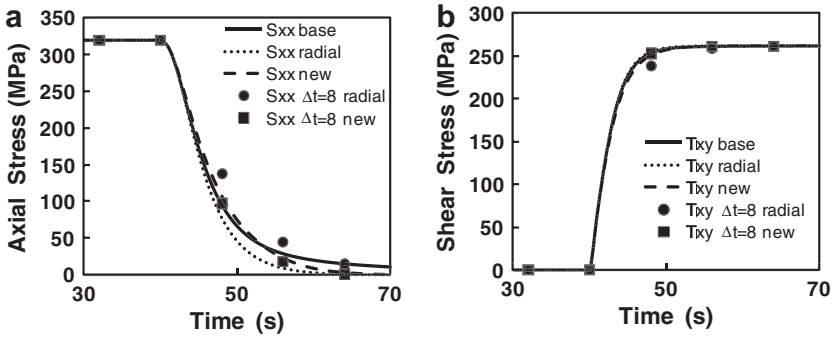

Fig. 4. Results from path change test for isotropic, non-quadratic yield surface, $q = 8$. The baseline solution (base) was with the traditional rate equations, and solutions from a radial return (radial) and the proposed algorithm (new) are shown. (a) Axial stress and (b) shear stress. The lines correspond to a time increment of 0.0002 s.

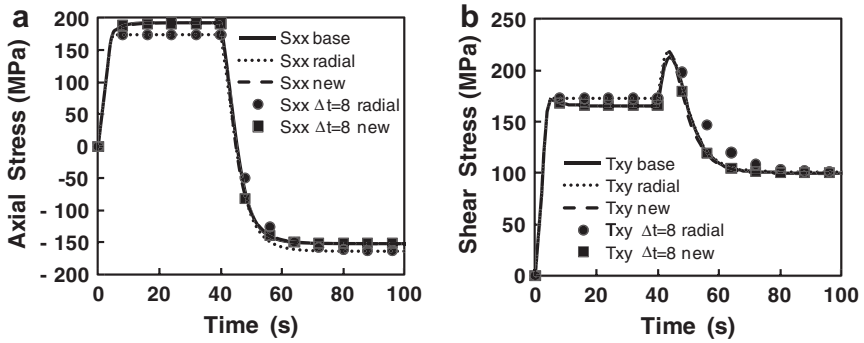

Fig. 5. Stress response during a more general path change: (a) x-direction stress and (b) x–y shear stress. The baseline solution (base) is obtained by forward integration with a time step of 0.0002 s. The radial return (radial) and proposed algorithm (new) are run with $q = 8$ and time steps of 0.0002 s (lines) and 8 s (symbols).

wall thickness of 3 mm. There are 20 constant stress quadrilateral elements across the thickness of the ring and 180 circumferentially in the quarter symmetry model. The density is 7.8 g/cc, the shear modulus 40 GPa and the bulk modulus 66.67 GPa. The yield stress was varied randomly from element to element to provide defects to seed strain localization. The statistics of the strength distribution were Gaussian. The average yield strength was 480 MPa and the standard deviation was 0.96 MPa—representing 0.2% of the initial yield stress. A slight linear strain hardening of 0.005 MPa was used. A constant pressure of 100 MPa was applied to the inner surface from the beginning of the analysis.

Plastic strain rate contours at 60 μs are shown in Fig. 6 for yield surface exponents of 8 and 2. The latter is J2-Flow theory. For $q = 8$, strain localization patterns emerge before 20 μs and are continuously refined as the deformation proceeds, Fig. 6a. These patterns do not appear in the $q = 2$ analysis, even at late times, Fig. 6b. A calculation was also run with $q = 8$ and the radial return algorithm. This provides a $q = 8$ yield surface and a $q = 2$ plastic flow potential. The results are very similar to Fig. 6a, indicating that the yield surface shape is facilitating the localization rather than the direction of plastic flow.

4.6. Plugging during plate perforation

A configuration where the plastic flow direction is likely to be more important is in "plugging" of a plate penetrated by a projectile. In recovered samples, shear bands are observed ahead of the projectile, and the material ahead of the penetrator appears to be pushed as a plug through the remaining plate (Murr et al., 2009). Thermal softening and damage within the shear bands can accentuate the bands in a positive feedback mechanism.

For these simulations, the configuration and material properties are idealized to isolate the role of the plastic flow direction. Temperature dependence, strain hardening and fracture are not included in the calculations so that these factors do not have a role in the current strain localization predictions. A 5.0 mm diameter, 10.0 mm long, right circular steel cylinder is impacted against a 5.0 mm thick, 200 mm diameter aluminum plate at 225 m/s. The steel cylinder has a shear modulus of 71.8 GPa and a bulk modulus of 419 GPa. It remains elastic. The aluminum plate has a shear modulus of 28 GPa, a bulk modulus of 80 GPa and a constant flow strength of 150 MPa. The axisymmetric finite element mesh is uniform in the vicinity of the penetration with an element size of 0.05208 mm in both the r and z directions. This provides 48 elements across the penetrator radius and 96 in the plate thickness. The penetration is simulated in Eulerian mode in ALE3D to preclude mesh motion biases that would complicate comparisons among ALE runs with solution dependent mesh motion. Simulations were

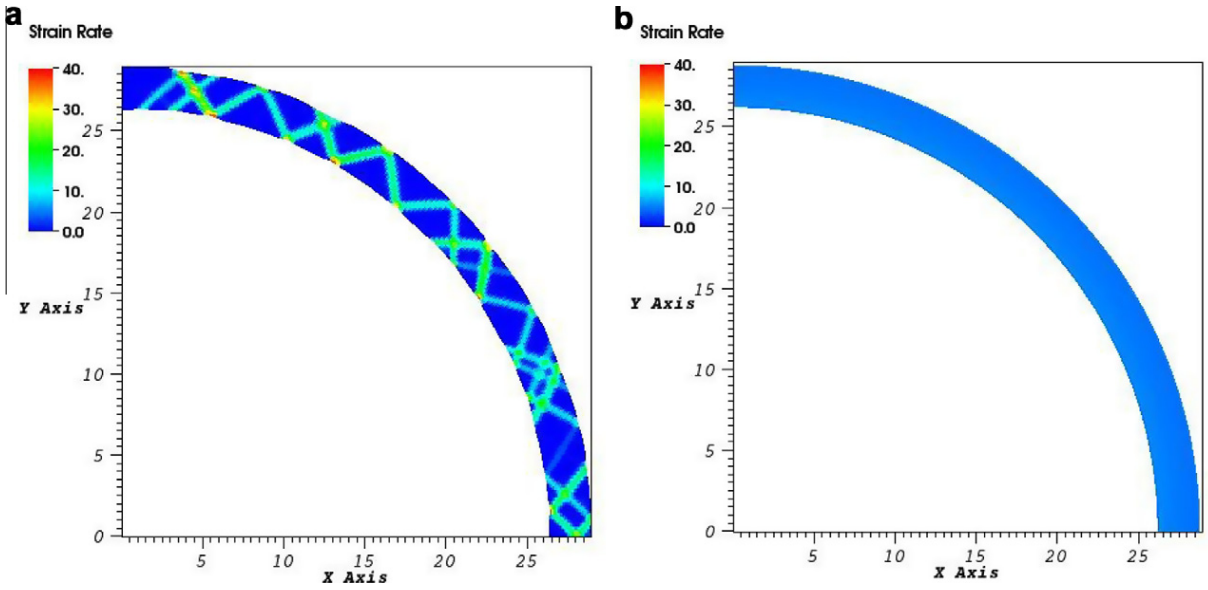

Fig. 6. Strain rate contours at 60 μs for an expanding ring. (a) Non-quadratic yield surface, $q = 8$; and (b) quadratic yield surface. Strain rate legend units are μs^{-1}.

run with: J2-Flow theory; the proposed integration scheme with $q = 8$ and an associative flow rule; and with $q = 8$ for the yield surface and radial return ($q = 2$ flow potential, non-associative flow rule).

Fig. 7 shows strain rate contours (μs^{-1} units) for the three runs at 15 μs. The scale is logarithmic to highlight the strain rate fan ahead of the projectile corner. The plots are similar, but the fan ahead of the corner for the new algorithm is somewhat narrower, Fig. 7b. This indicates greater strain localization than for the other two runs. The fan feature is not steady state and the gap in the fan near the free surface is due to wave reflections.

Significant differences among the runs are not evident until the projectile exits at approximately 50 μs. The projectile exit is earlier for the new model than for the other two runs. The projectile velocity at exit for the J2-Flow theory run is 52 m/s. The exit velocity is 70.5 m/s for $q = 8$ and the new algorithm using an associate flow rule and 58 m/s for a $q = 8$ yield surface and radial return. These latter differences indicate that the alignment of the plastic flow direction changes the ease of shear and the dissipated energy.

The simulations were run in parallel on eight processors on a dedicated compute node. The time increment was set by the Courant limit and advection accuracy criteria, so the number of time steps is very near the same in each run. The wall clock time for the new algorithm with the penalty approach to solve Eq. (19) was 18% higher than for J2-Flow theory with radial return. The time was 50% longer when using singular valued decomposition to solve the matrix. The timing reflects modest impact to the computational analyst for using a more complex material model. It is not a statement of numerical efficiency of the integration algorithm since J2-Flow theory is a much simpler model than the non-quadratic. An implementation of a conventional integration approach for a non-quadratic model would be necessary for a meaningful timing comparison. The CPU time for the non-quadratic model will be much greater than the J2-Flow solution, but the expense of advection and other physics reduces the overall impact on turn-around time. Some fraction of this can be recovered by weighting the domain decomposition so more processors are allocated to work on the aluminum plate rather than the steel and surrounding

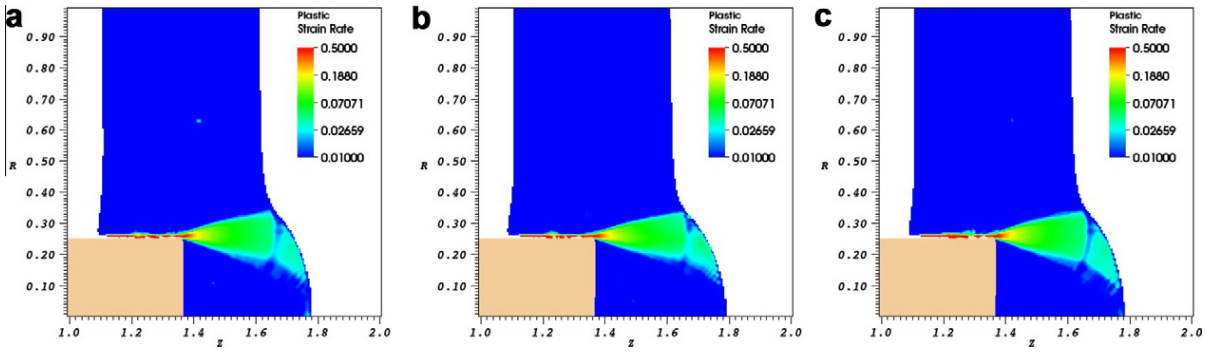

Fig. 7. Plastic strain rate contours (μs^{-1} units) for plugging simulation using: (a) J2-Flow theory; (b) new algorithm with $q = 8$ and associative flow rule; and (c) $q = 8$ yield surface and radial return ($q = 2$ flow potential, non-associative flow).

air. Gains for the proposed approach would also come from a more efficient algorithm to calculate the stress given the flow potential normal.

5. Summary and conclusions

A new approach for integrating continuum plasticity relations has been introduced based on observations from closed form integration of a generalized quadratic yield function over a time step. The normal to the flow potential is computed from a relatively simple expression, and the new stress is calculated to be consistent with the flow potential normal. This introduces a different set of approximations than traditional approaches, and further evaluation will be necessary using a variety of yield surfaces and flow potentials. A consistent tangent was not derived in this work. It should be straight forward, albeit tedious.

The preliminary results presented here are promising. The method may be somewhat less accurate than traditional approaches at small strain increments, but it can be significantly more accurate at large strain increments. The method is also very robust numerically.

The new approach has additional attractive features from a numerical implementation perspective. The physics approximations in the time integration scheme are decoupled from the expensive computations. Thus, the approximations are well defined, and work to improve numerical efficiency can proceed without concerns of impacting the solution quality. Gains may be realized over the current implementation by using a different approach to find the stress tensor given the flow potential normal. No attempts have yet been made to improve the numerical efficiency of the new algorithm. However, a hybrid approach using a forward integration algorithm at small strain increments improves the overall computational efficiency while also providing a more accurate solution for small strain increments.

Although not the focus of this work, it was observed that simulations using the associative and non-associative flow rules give similar results in some circumstances but not others. Depending on the application, one may be able to use a radial return method and get a satisfactory solution at appreciable computational savings. Further investigation along these lines could be fruitful.

Appendix A. Integration of generalized quadratic yield function

Eq. (5b) is integrated over a time step assuming that that corrections for spin have already been incorporated and that $\dot{\lambda}$ and $\bar{\sigma}$ are constant over the time step.

$$\dot{\boldsymbol{\sigma}}' = \boldsymbol{L} : \boldsymbol{d}' - \frac{3}{2}\frac{\dot{\lambda}}{\bar{\sigma}}\boldsymbol{L} : \boldsymbol{K} : \boldsymbol{\sigma}' \tag{A1}$$

The time increment is divided into N steps giving the recursion relation at the M'th sub-step

$$\left[\boldsymbol{\sigma}'_{t+\frac{M}{N}\Delta t}\right] = \left\{\boldsymbol{I}' - \frac{3}{2}\frac{\dot{\lambda}}{\bar{\sigma}}\frac{\Delta t}{N}\boldsymbol{L} : \boldsymbol{K}\right\} : \left[\boldsymbol{\sigma}'_{t+\frac{M-1}{N}\Delta t}\right] + \boldsymbol{L} : \boldsymbol{d}'\frac{\Delta t}{N}. \tag{A2}$$

$\boldsymbol{I}'$ is defined in Eq. (7). Applying this formula to successive sub-steps and noting the trend:

$$\boldsymbol{\sigma}'_{t+\frac{1}{N}\Delta t} = \left\{\boldsymbol{I}' - \frac{3}{2}\frac{\dot{\lambda}}{\bar{\sigma}}\frac{\Delta t}{N}\boldsymbol{L} : \boldsymbol{K}\right\} : \boldsymbol{\sigma}'_t + \boldsymbol{L} : \boldsymbol{d}'\frac{\Delta t}{N}, \tag{A3}$$

$$\boldsymbol{\sigma}'_{t+\frac{2}{N}\Delta t} = \left\{\boldsymbol{I}' - \frac{3}{2}\frac{\dot{\lambda}}{\bar{\sigma}}\frac{\Delta t}{N}\boldsymbol{L} : \boldsymbol{K}\right\}^2 : \boldsymbol{\sigma}'_t + \left\{\boldsymbol{I}' - \frac{3}{2}\frac{\dot{\lambda}}{\bar{\sigma}}\frac{\Delta t}{N}\boldsymbol{L} : \boldsymbol{K}\right\} : \boldsymbol{L} : \boldsymbol{d}'\frac{\Delta t}{N} + \boldsymbol{L} : \boldsymbol{d}'\frac{\Delta t}{N}, \tag{A4}$$

$$\begin{aligned}\boldsymbol{\sigma}'_{t+\frac{3}{N}\Delta t} = \left\{\boldsymbol{I}' - \frac{3}{2}\frac{\dot{\lambda}}{\bar{\sigma}}\frac{\Delta t}{N}\boldsymbol{L} : \boldsymbol{K}\right\}^3 : \boldsymbol{\sigma}'_t &+ \left\{\boldsymbol{I}' - \frac{3}{2}\frac{\dot{\lambda}}{\bar{\sigma}}\frac{\Delta t}{N}\boldsymbol{L} : \boldsymbol{K}\right\}^2 : \boldsymbol{L} : \boldsymbol{d}'\frac{\Delta t}{N} \\ &+ \left\{\boldsymbol{I}' - \frac{3}{2}\frac{\dot{\lambda}}{\bar{\sigma}}\frac{\Delta t}{N}\boldsymbol{L} : \boldsymbol{K}\right\} : \boldsymbol{L} : \boldsymbol{d}'\frac{\Delta t}{N} + \boldsymbol{L} : \boldsymbol{d}'\frac{\Delta t}{N},\end{aligned} \tag{A5}$$

$$\cdots$$

$$\cdots$$

$$\boldsymbol{\sigma}'_{t+\Delta t} = \left\{\boldsymbol{I}' - \frac{3}{2}\frac{\dot{\lambda}}{\bar{\sigma}}\frac{\Delta t}{N}\boldsymbol{L} : \boldsymbol{K}\right\}^N : \boldsymbol{\sigma}'_t + \left[\sum_{M=0}^{N-1}\left\{\boldsymbol{I}' - \frac{3}{2}\frac{\dot{\lambda}}{\bar{\sigma}}\frac{\Delta t}{N}\boldsymbol{L} : \boldsymbol{K}\right\}^M\right] : \boldsymbol{L} : \boldsymbol{d}'\frac{\Delta t}{N}. \tag{A6}$$

Taking the limit as $N \to \infty$ allows simplification. Writing the quantity in braces as

$$\left\{\boldsymbol{I} - \frac{3}{2}\frac{\dot{\lambda}}{\bar{\sigma}}\frac{\Delta t}{N}\boldsymbol{L} : \boldsymbol{K}\right\} = \boldsymbol{A} = \boldsymbol{I}' - \frac{1}{N}\boldsymbol{B} \tag{A7}$$

to shorten the notation, and expanding the binomial gives

$$\boldsymbol{A}^N = \boldsymbol{I}' - \frac{N}{N}\boldsymbol{B} + \frac{N(N-1)}{N^2 2!}\boldsymbol{B}^2 - \frac{N(N-1)(N-2)}{N^3 3!}\boldsymbol{B}^3 \ldots. \tag{A8}$$

Letting N approach infinity results in

$$\lim_{N\to\infty}\left\{\boldsymbol{I}' - \frac{3}{2}\frac{\dot{\lambda}}{\bar{\sigma}}\frac{\Delta t}{N}\boldsymbol{L}:\boldsymbol{K}\right\}^N = \exp\left(-\frac{3}{2}\frac{\dot{\lambda}}{\bar{\sigma}}\Delta t\boldsymbol{L}:\boldsymbol{K}\right). \tag{A9}$$

The simplified form for the summation follows the form for a truncated geometric series

$$\frac{1}{N}\sum_{M=0}^{N-1}\boldsymbol{A}^M = \frac{1}{N}(\boldsymbol{I}' - \boldsymbol{A}^N) : (\boldsymbol{I}' - \boldsymbol{A})^{-1} = (\boldsymbol{I}' - \boldsymbol{A}^N) : \boldsymbol{B}^{-1}. \tag{A10}$$

This can be verified by multiplying Eq. (A10) by $(\boldsymbol{I}' - \boldsymbol{A})$; all but the first and last terms of the resulting summation drop out.

Upon substituting the series results, Eq. (A6) becomes

$$\boldsymbol{\sigma}'_{t+\Delta t} = \exp\left(-\frac{3}{2}\frac{\dot{\lambda}}{\bar{\sigma}}\Delta t\boldsymbol{L}:\boldsymbol{K}\right) : \boldsymbol{\sigma}'_{t+\Delta t} + \frac{2}{3}\frac{\bar{\sigma}}{\dot{\lambda}\Delta t}\left[\boldsymbol{I}' - \exp\left(-\frac{3}{2}\frac{\dot{\lambda}}{\bar{\sigma}}\Delta t\boldsymbol{L}:\boldsymbol{K}\right)\right] : \boldsymbol{K}^{-1} : \boldsymbol{d}'\Delta t. \tag{A11}$$

This becomes Eq. (6) in Section 2.2.

Appendix B. Yield function details

Computation of the yield function

$$\phi = \sqrt[q]{\frac{1}{2}\left[(\sigma_I - \sigma_{II})^q + (\sigma_{II} - \sigma_{III})^q + (\sigma_{III} - \sigma_I)^q\right]} - \bar{\sigma} = 0 \tag{B1}$$

is through the invariants of the deviatoric stress tensor

$$J'_1 = \sigma'_{11} + \sigma'_{22} + \sigma'_{33} = 0, \tag{B2}$$

$$J'_2 = -\sigma'_{22}\sigma'_{33} - \sigma'_{33}\sigma'_{11} - \sigma'_{11}\sigma'_{22} + \sigma'_{23}\sigma'_{32} + \sigma'_{31}\sigma'_{13} + \sigma'_{12}\sigma'_{21} \tag{B3}$$

$$= 0.5\left(\sigma'^2_{11} + \sigma'^2_{22} + \sigma'^2_{33} + 2\sigma'_{23}\sigma'_{32} + 2\sigma'_{31}\sigma'_{13} + 2\sigma'_{12}\sigma'_{21}\right) = \frac{1}{3}\sigma^2_{vm}, \tag{B4}$$

$$J'_3 = \sigma'_{11}\sigma'_{22}\sigma'_{33} + \sigma'_{12}\sigma'_{23}\sigma'_{31} + \sigma'_{13}\sigma'_{32}\sigma'_{21} - \sigma'_{11}\sigma'_{23}\sigma'_{32} - \sigma'_{22}\sigma'_{31}\sigma'_{13} - \sigma'_{33}\sigma'_{12}\sigma'_{21} \tag{B5}$$

and the Lode angle

$$\alpha = \frac{1}{3}\cos^{-1}\left(\frac{3\sqrt{3}}{2}J'_3/J'^{\frac{3}{2}}_2\right) = \frac{1}{3}\cos^{-1}(\lambda) \quad 0 \le \alpha \le \frac{1}{3}\pi \tag{B6}$$

The distinction between the *ij* and *ji* shear stress components is maintained in Eqs. (B2)–(B5) to facilitate taking derivatives later in this section. The principal stresses are given by

$$\sigma'_I = \frac{2}{\sqrt{3}}J'^{\frac{1}{2}}_2\cos\left(\alpha - \frac{1}{3}\pi\right) \quad \sigma'_{II} = \frac{2}{\sqrt{3}}J'^{\frac{1}{2}}_2\cos(\alpha) \quad \sigma'_{III} = \frac{2}{\sqrt{3}}J'^{\frac{1}{2}}_2\cos\left(\alpha + \frac{1}{3}\pi\right). \tag{B7}$$

After a bit of manipulation, the yield function can be expressed in terms of only α and the von Mises stress.

$$\phi = \frac{2}{\sqrt{3}}\sigma_{vm}\sqrt[q]{\frac{1}{2}\left[\sin^q\left(\alpha - \frac{1}{3}\pi\right) + \sin^q(\alpha) + \sin^q\left(\alpha + \frac{1}{3}\pi\right)\right]} - \dot{\sigma} = \sigma_{eq} - \dot{\sigma} = 0. \tag{B8}$$

σ_{vm} is defined as the vonMises stress by the standard definition, Eq. (B4), and σ_{eq} is defined in Eq. (B8) as the equivalent stress. These are equal if $q = 2$, as in the von Mises yield criterion, but they are not equal in general. The von Mises stress is used in the relations to facilitate ties to J2-Flow theory.

Both first and second derivatives of the yield function are needed. It is convenient to define the quantity under the radical of Eq. (B8) as $\mathcal{F}$, resulting in the first derivative being

$$\frac{d\phi}{d\boldsymbol{\sigma}} = \frac{d\sigma_{eq}}{d\boldsymbol{\sigma}} = \frac{\sigma_{eq}}{\sigma_{vm}}\frac{d\sigma_{vm}}{d\boldsymbol{\sigma}} + \frac{1}{q}\frac{\sigma_{eq}}{\mathcal{F}}\frac{d\mathcal{F}}{d\boldsymbol{\sigma}}. \tag{B9}$$

The second derivative is manipulated by using Eq. (B9) to replace all of the first derivatives of $\mathcal{F}$. This produces a form where the required symmetry is evident

$$\frac{d^2\phi}{d\boldsymbol{\sigma}^2}=\frac{1-q}{\sigma_{eq}}\frac{d\sigma_{eq}}{d\boldsymbol{\sigma}}\frac{d\sigma_{eq}}{d\boldsymbol{\sigma}}-\frac{1+q}{\sigma_{vm}}\frac{\sigma_{eq}}{\sigma_{vm}}\frac{d\sigma_{vm}}{d\boldsymbol{\sigma}}\frac{d\boldsymbol{\sigma}_{vm}}{d\boldsymbol{\sigma}}+\frac{q}{\sigma_{vm}}\left(\frac{d\sigma_{eq}}{d\boldsymbol{\sigma}}\frac{d\sigma_{vm}}{d\boldsymbol{\sigma}}+\frac{d\sigma_{vm}}{d\boldsymbol{\sigma}}\frac{d\sigma_{eq}}{d\boldsymbol{\sigma}}\right)+\frac{\sigma_{eq}}{\sigma_{vm}}\frac{d^2\sigma_{vm}}{d\boldsymbol{\sigma}^2}+\frac{1}{q}\frac{\sigma_{eq}}{\mathcal{F}}\frac{d^2\mathcal{F}}{d\boldsymbol{\sigma}^2}. \tag{B10}$$

The first and second derivatives of the von Mises stress needed in Eq. (B10) are

$$\frac{d\sigma_{vm}}{d\boldsymbol{\sigma}}=\frac{d\sigma_{vm}}{d\boldsymbol{\sigma}'}=\frac{3}{2}\frac{\boldsymbol{\sigma}'}{\sigma_{vm}}\quad\text{and}\quad\frac{d^2\sigma_{vm}}{d\boldsymbol{\sigma}^2}=\frac{3}{2}\frac{1}{\sigma_{vm}}\left(\mathbf{I}'-\frac{3}{2}\frac{\boldsymbol{\sigma}'}{\sigma_{vm}}\frac{\boldsymbol{\sigma}'}{\sigma_{vm}}\right), \tag{B11}$$

where $\mathbf{I}'$ is defined in Eq. (7). The derivatives of $\mathcal{F}$ are written with the chain rule in terms of both α and λ to aid in addressing the singular points.

$$\frac{1}{q}\frac{d\mathcal{F}}{d\boldsymbol{\sigma}}=\frac{1}{q}\frac{d\mathcal{F}}{d\alpha}\frac{d\alpha}{d\lambda}\frac{d\lambda}{d\boldsymbol{\sigma}}, \tag{B12}$$

$$\frac{1}{q}\frac{d^2\mathcal{F}}{d\boldsymbol{\sigma}^2}=\frac{1}{q}\frac{d^2\mathcal{F}}{d\alpha^2}\frac{d\alpha}{d\lambda}\frac{d\alpha}{d\lambda}\frac{d\lambda}{d\boldsymbol{\sigma}}\frac{d\lambda}{d\boldsymbol{\sigma}}+\frac{1}{q}\frac{d\mathcal{F}}{d\alpha}\frac{d^2\alpha}{d\lambda^2}\frac{d\lambda}{d\boldsymbol{\sigma}}\frac{d\lambda}{d\boldsymbol{\sigma}}+\frac{1}{q}\frac{d\mathcal{F}}{d\alpha}\frac{d\alpha}{d\lambda}\frac{d^2\lambda}{d\boldsymbol{\sigma}^2}, \tag{B13}$$

λ is defined in Eq. (B6).

The scalar derivatives in Eqs. (B12) and (B13) are

$$\begin{aligned}\frac{1}{q}\frac{d\mathcal{F}}{d\alpha}=\frac{1}{2}\Bigg[&\sin^{q-1}\left(\alpha-\frac{1}{3}\pi\right)\cos\left(\alpha-\frac{1}{3}\pi\right)+\sin^{q-1}(\alpha)\cos(\alpha)\\&+\sin^{q-1}\left(\alpha-\frac{1}{3}\pi\right)\cos\left(\alpha-\frac{1}{3}\pi\right)\Bigg],\end{aligned} \tag{B14}$$

$$\frac{1}{q}\frac{d^2\mathcal{F}}{d\alpha^2}=\frac{1}{2}\left[\sin^{q-2}\left(\alpha-\frac{1}{3}\pi\right)+\sin^{q-2}(\alpha)+\sin^{q-2}\left(\alpha+\frac{1}{3}\pi\right)\right]-q\mathcal{F}, \tag{B15}$$

$$\frac{d\alpha}{d\lambda}=-\frac{1}{3}\frac{1}{\sqrt{1-\lambda^2}}=\frac{-1}{3\sin(3\alpha)}, \tag{B16}$$

$$\frac{d^2\alpha}{d\lambda^2}=-\frac{1}{3}\lambda(1-\lambda^2)^{-\frac{3}{2}}=9\lambda\frac{-1}{3\sin(3\alpha)}\frac{-1}{3\sin(3\alpha)}\frac{-1}{3\sin(3\alpha)}. \tag{B17}$$

The reason for writing Eq. (B17) in this manner will evident shortly. At $\alpha=0$ and $\alpha=\pi/3$ the sine function in Eqs. (B16) and (B17) is zero, and the values are singular. However, the product

$$\frac{d\alpha}{d\lambda}\frac{d\lambda}{d\boldsymbol{\sigma}}=\frac{d\alpha}{d\boldsymbol{\sigma}} \tag{B18}$$

is bounded. The value of the product at the singular points is determined by an abusive application of l'Hôpital's rule.

$$\mathcal{L}_{ij}=\frac{d\alpha}{d\sigma_{ij}}=\frac{\frac{d\lambda}{d\sigma_{ij}}}{-3\sin(3\alpha)}\overset{l'Hospital's\ rule}{\Rightarrow}\frac{\frac{d}{\sigma_{kl}}\left(\frac{d\lambda}{d\sigma_{ij}}\right)}{-9\cos(3\alpha)\frac{d\alpha}{\sigma_{kl}}}=\frac{\frac{d^2\lambda}{d\sigma_{lk}d\sigma_{ij}}}{-9\cos(3\alpha)\mathcal{L}_{kl}}. \tag{B19}$$

The derivative at the singular angles is determine by solving Eq. (B19) for $\mathcal{L}_{ij}$.

$$\mathcal{L}_{ij}=\frac{d\alpha}{d\sigma_{ij}}=\frac{-1}{3\sin(3\alpha)}\frac{d\lambda}{d\sigma_{ij}}=\frac{1}{3}\sqrt{\frac{-1}{\cos(3\alpha)}\frac{d^2\lambda}{d\sigma_{ij}d\sigma_{ij}}}\Bigg|_{\alpha\to0\|\pi/3}. \tag{B20}$$

Note that Eq. (20) takes the diagonal of the second derivative matrix. It will be shown later that the radical is non-singular, so Eq. (B20) addresses the singular values in Eq. (B12) and the first term of Eq. (B13). Further, by the expansion given in Eq. (B17), the result in Eq. (B20) also eliminates two of the three orders of singularity in the second term of Eq. (B13).

The remaining singularities in the second term and in the last term of Eq. (B13) are eliminated because Eq. (B14) is zero at these singular points. Specifically, by series expansion of Eq. (B14)

$$\frac{-1}{3\sin(3\alpha)}\frac{1}{q}\frac{d\mathcal{F}}{d\alpha}\simeq\left\{\frac{-\text{sign}(\cos(3\alpha))}{9\alpha(1+O\alpha^2)}\right\}\left\{\alpha\frac{1}{3}\left(\frac{\sqrt{3}}{2}\right)^q[(q-4)+O\alpha^2+O\alpha^{q-2}]\right\}\simeq-\text{sign}(\cos(3\alpha))\frac{(q-4)}{27}\left(\frac{\sqrt{3}}{2}\right)^q\Bigg|_{\alpha\to0\|\pi/3}. \tag{B21}$$

The limits near $\alpha=0$ and $\alpha=\pi/3$ differ by an algebraic sign. The next highest term is quadratic in α so the limit is accurate numerically in 64 bit calculations to approximately $\alpha<10^{-7}$ of the singularity. A similar expansion could be used to remove the singularities from Eq. (B12). This would be expedient if the second derivatives were not computed for Eq. (B20).

Table B1
Second derivative of the third invariant.

$\frac{d^2J'_3}{d\sigma_{ij}d\sigma_{kl}}$	11	22	33	23	31	12
11	$\frac{2}{3}\sigma'_{11}$	$\frac{2}{3}\sigma'_{33}$	$\frac{2}{3}\sigma'_{22}$	$-\frac{2}{3}\sigma'_{23}$	$\frac{1}{3}\sigma'_{31}$	$\frac{1}{3}\sigma'_{12}$
22	$\frac{2}{3}\sigma'_{33}$	$\frac{2}{3}\sigma'_{22}$	$\frac{2}{3}\sigma'_{11}$	$\frac{1}{3}\sigma'_{23}$	$-\frac{2}{3}\sigma'_{31}$	$\frac{1}{3}\sigma'_{12}$
33	$\frac{2}{3}\sigma'_{22}$	$\frac{2}{3}\sigma'_{11}$	$\frac{2}{3}\sigma'_{33}$	$\frac{1}{3}\sigma'_{23}$	$\frac{1}{3}\sigma'_{31}$	$-\frac{2}{3}\sigma'_{12}$
23	$-\frac{2}{3}\sigma'_{23}$	$\frac{1}{3}\sigma'_{23}$	$\frac{1}{3}\sigma'_{23}$	$-\frac{1}{2}\sigma'_{11}$	$\frac{1}{2}\sigma'_{12}$	$\frac{1}{2}\sigma'_{31}$
31	$\frac{1}{3}\sigma'_{31}$	$-\frac{2}{3}\sigma'_{31}$	$\frac{1}{3}\sigma'_{31}$	$\frac{1}{2}\sigma'_{12}$	$-\frac{1}{2}\sigma'_{22}$	$\frac{1}{2}\sigma'_{23}$
12	$\frac{1}{3}\sigma'_{12}$	$\frac{1}{3}\sigma'_{12}$	$-\frac{2}{3}\sigma'_{12}$	$\frac{1}{2}\sigma'_{31}$	$\frac{1}{2}\sigma'_{23}$	$-\frac{1}{2}\sigma'_{33}$

Considering Eqs. (B16) and (B17), Eq. (B13) can be rewritten as

$$\frac{1}{q}\frac{d^2\mathcal{F}}{d\boldsymbol{\sigma}^2}=\left[\frac{1}{q}\frac{d^2\mathcal{F}}{d\alpha^2}+9cos(3\alpha)\left(\frac{1}{q}\frac{d\mathcal{F}}{d\alpha}\frac{-1}{3\sin(3\alpha)}\right)\right]\frac{d\alpha}{d\boldsymbol{\sigma}}\frac{d\alpha}{d\boldsymbol{\sigma}}+\left(\frac{1}{q}\frac{d\mathcal{F}}{d\alpha}\frac{-1}{3\sin(3\alpha)}\right)\frac{d^2\lambda}{d\boldsymbol{\sigma}^2}. \tag{B22}$$

It is not difficult to demonstrate that the argument of the square brackets is zero at $\alpha=0$ and $\alpha=\pi/3$.

What remains is to specify the tensor derivatives in Eqs. (B12) and (B13). Using

$$\frac{dJ'_2}{d\boldsymbol{\sigma}}=\boldsymbol{\sigma}' \quad \text{and} \quad \frac{d^2J'_2}{d\boldsymbol{\sigma}^2}=\mathbf{I}', \tag{B23}$$

these become

$$\frac{d\lambda}{d\boldsymbol{\sigma}}=\frac{27}{2}\frac{1}{\sigma_{vm}^3}\left[\frac{dJ'_3}{d\boldsymbol{\sigma}}-\frac{9}{2}\frac{J'_3}{\sigma_{vm}^2}\boldsymbol{\sigma}'\right], \tag{B24}$$

$$\frac{d^2\lambda}{d\boldsymbol{\sigma}^2}=\frac{27}{2}\frac{1}{\sigma_{vm}^3}\left[-\frac{9}{2}\frac{1}{\sigma_{vm}^2}\left(J'_3\mathbf{I}'+\frac{dJ'_3}{d\boldsymbol{\sigma}}\boldsymbol{\sigma}'+\boldsymbol{\sigma}'\frac{dJ'_3}{d\boldsymbol{\sigma}}\right)+\frac{135}{4}\frac{J'_3}{\sigma_{vm}^4}\boldsymbol{\sigma}'\boldsymbol{\sigma}'+\frac{d^2J'_3}{d\boldsymbol{\sigma}^2}\right]. \tag{B25}$$

Calculating the derivatives of the third invariant is accomplished by utilizing the derivatives with respect to the deviatoric stress

$$\frac{dJ'_3}{d\boldsymbol{\sigma}}=\frac{dJ'_3}{d\sigma'}+\frac{1}{9}\sigma_{vm}^2\boldsymbol{\delta}. \tag{B26}$$

In component form, the first term on the right hand side of Eq. (B26) is

$$\begin{aligned}
&\frac{dJ'_3}{d\sigma'_{11}}=\sigma'_{22}\sigma'_{33}-\sigma'_{23}\sigma'_{32} \quad \frac{dJ'_3}{d\sigma'_{22}}=\sigma'_{11}\sigma'_{33}-\sigma'_{31}\sigma'_{13} \quad \frac{dJ'_3}{d\sigma'_{33}}=\sigma'_{11}\sigma'_{22}-\sigma'_{12}\sigma'_{21}\\
&\frac{dJ'_3}{d\sigma'_{23}}=\sigma'_{12}\sigma'_{31}-\sigma'_{11}\sigma'_{32} \quad \frac{dJ'_3}{d\sigma'_{31}}=\sigma'_{12}\sigma'_{23}-\sigma'_{22}\sigma'_{13} \quad \frac{dJ'_3}{d\sigma'_{12}}=\sigma'_{23}\sigma'_{31}-\sigma'_{33}\sigma'_{21}.
\end{aligned} \tag{B27}$$

Note that not distinguishing between the *ij* and *ji* shears in taking the derivatives would have increased the corresponding derivates by a factor of 2. The second derivative of J'_3 is given in Table B1.

References

Abaqus, 2009. Abaqus User's Manual. Dassault Systèmes/SIMULIA, Providence, RI, USA.

Arioli, E., Auricchio, F., Beirão da Veiga, L., 2006. A novel 'optimal' exponential-based integration algorithm for von-Mises plasticity with linear hardening: theoretical analysis on yield consistency, accuracy, convergence and numerical examples. Int. J. Numer. Methods Eng. 67, 449–498.

Auricchio, F., Beirão da Veiga, L., 2003. On a new integration scheme for von-Mises plasticity with linear hardening. Int. J. Numer. Methods Eng. 56, 1375–1396.

Barlat, F., Maeda, Y., Chung, K., Yanagawa, M., Brem, J.C., Hayashida, Y., Lege, D.J., Matsui, K., Murtha, S.J., Hattori, S., Becker, R.C., Makosey, S., 1997. Yield function development for aluminum alloy sheets. J. Mech. Phys. Solids. 45, 1727–1763.

Brannon, R.M., Leelavanichkul, S., 2010. A multi-stage return algorithm for solving the classical damage component of constitutive models for rocks, ceramics and other rock-like media. Int. J. Fract. 163, 133–149.

Dunne, F., Petrinic, N., 2005. Introduction to Computational Plasticity. Oxford University Press, Oxford, UK.

Hill, R.J., 1950. The Mathematical Theory of Plasticity. Oxford University Press, Oxford, UK.

Hosford, W.F., 1972. Generalized isotropic yield criterion. J. Appl. Mech. 39, 607–609.

Karafillis, A.P., Boyce, M.C., 1993. A general anisotropic yield criterion using bounds and a transformation weighting tensor. J. Mech. Phys. Solids 41, 1859–1886.

Kojić, M., 2002. Stress integration procedures for inelastic material models within the finite element method. Appl. Mech. Rev. 55, 389–414.

Krieg, R.D., Krieg, D.B., 1977. Accuracies of numerical solution methods for the elastic-perfectly plastic model. J. Pressure Vessel Technol. 99, 510–515.

Krieg, R.D., Xu, S., 1997. Plane stress linear hardening plasticity theory. Finite Elem. Anal. Des. 27, 41–67.

Logan, R.W., Hosford, W.F., 1980. Upper bound anisotropic yield locus calculations assuming <1 1 1> pencil glide. Int. J. Mech. Sci. 22, 419–430.

Maudlin, P.J., Schiferl, S.K., 1996. Computational anisotropic plasticity for high-rate forming applications. Comput. Methods Appl. Mech. Eng. 131, 1–30.

Mosler, J., Bruhns, O.T., 2010. On the implementation of rate-independent standard dissipative solids at finite strain – variational constitutive updates. Comput. Methods Appl. Mech. Eng. 199, 417–429.
Murr, L.E., Ramirez, A.C., Gaytan, S.M., Lopez, M.I., Martinez, E.Y., Hernandez, D.H., Martinez, E., 2009. Microstructure evolution associated with adiabatic shear bands and shear band failure in ballistic plug formation in Ti-6Al-4V targets. Mater. Sci. Eng. A 516, 205–216.
Nichols, A.L., 2009. Users Manual for ALE3D: An Arbitrary Lagrange/Eulerian 2D and 3D Code System. Lawrence Livermore National Laboratory.
Press, W.H., Teukolsky, S.A., Vetterling, W.T., Flannery, B.P., 1992. Numerical Recipes in FORTRAN: The Art of Scientific Computing, second ed. Cambridge University Press, New York, NY.
Rezaijee-Pajand, M., Nasirai, C., 2008. On the integration schemes for Durcker–Prager's elastoplastic models based on exponential maps. Int. J. Numer. Methods Eng. 74, 799–826.
Szabó, L., 2009. A semi-analytical integration method for J2 flow theory of plasticity with linear isotropic hardening. Comput. Methods Appl. Mech. Eng. 198, 2151–2166.
Ulz, M.H., 2009. A Green–Naghdi approach to finite anisotropic rate-independent and rate-dependent thermo-plasticity in logarithmic Lagrangian strain-entropy space. Comput. Methods Appl. Mech. Eng. 198, 3262–3277.
Wilkins, M.L., 1964. Calculation of elastic–plastic flow. In: Alder, B. (Ed.), Methods in Computational Physics, vol. 3. Academic Press, New York, pp. 211–263.
Yu, M.-H., 2002. Advances in strength theories for materials under complex stress state in 20th century. Appl. Mech. Rev. 55, 169–218.

Effect of Particulate/Matrix Debonding on the Formation of Adiabatic Shear Bands

Bryan M. Love and Romesh C. Batra

International Journal of Mechanical Sciences, 52 (2010)

Contents lists available at ScienceDirect

International Journal of Mechanical Sciences

journal homepage: www.elsevier.com/locate/ijmecsci

Effect of particulate/matrix debonding on the formation of adiabatic shear bands

B.M. Love [a], R.C. Batra [b,*]

[a] U.S. Army Research Laboratory, Impact Physics Branch, Aberdeen Proving Grounds, MD 21005-5069, USA
[b] Virginia Polytechnic Institute and State University, Department of Engineering Science and Mechanics, Blacksburg, VA 24061, USA

ARTICLE INFO

Article history:
Received 28 July 2009
Received in revised form
19 October 2009
Accepted 27 October 2009
Available online 3 November 2009

Keywords:
Debonding
Adiabatic shear bands
Cohesive zone failure criterion
Finite element method

ABSTRACT

We use the cohesive zone failure model to simulate debonding and failure in high strain-rate plane strain deformations of a heat conducting particulate composite comprised of initially circular metallic particulates immersed in a metallic matrix, with the goal of delineating the effect of these failures on the initiation and propagation of adiabatic shear bands (ASBs). Failure is assumed to ensue at an interface between two elements when a predefined combination of the normal and the tangential tractions on that interface reaches a critical value. We postulate that the critical value of the traction in the cohesive zone failure model decreases affinely with an increase in the temperature. Both particulate and matrix materials are assumed to be isotropic, heat conducting, and to obey the von Mises yield criterion with the flow stress depending upon the effective strain, the effective strain rate, and the temperature according to the Johnson–Cook relation. The coupled transient thermomechanical problem is analyzed by the finite element method by using 3-node triangular elements and the finite calculus technique to prevent volumetric locking. It is found that the critical strength of the bond between the particulate and the matrix significantly influences the loss of strength of the entire specimen. The time of initiation of an ASB is influenced by the time when debonding ensues which depends upon the values of the critical traction and the mode-mixity parameter in the cohesive zone failure criterion.

1. Introduction

As modeling and simulation is increasingly used to predict the behavior of structures and systems under catastrophic loading, simulation techniques and physical models for dynamic failure have become very important. Dynamic failure of ductile materials is quite often preceded by the initiation and development of adiabatic shear bands (ASBs) which are narrow regions, a few micrometers wide, of intense plastic deformation. ASBs are known to play a significant role in penetration problems, and machining and metal-forming processes. For example, Magness and Farrand [1] have postulated that if in a penetration problem ASBs continuously form and lead to failure near the nose of the projectile, resulting in a projectile with a sharp, rather than a mushroomed, nose, then the penetration depth will be more than that for the case of no ASB formation. Similarly, ASBs facilitate the punching of a hole in a metal cutting process since the kinetic energy required for punching a centimeter thick plate by plugging equals nearly that needed to indent the same plate by less than 1 mm.

Tresca [2] observed ASBs (he called them hot lines) over a century ago during the hot forging of a platinum bar. Subsequently they were reported by Massey [3]. However, Zener and Hollomon's [4] observing them during the punching of a hole in a low carbon steel plate, and proposing that they form when softening of the material due to its being heated up has overcome its hardening due to strain- and strain-rate effects generated considerable interest in the field. Clifton [5] used the criterion that an ASB initiates when the shear stress in quasi-static simple shearing deformations of a homogeneous body attains its maximum value to find the shear strain at the initiation of an ASB in a thermoviscoplastic material obeying a power-law type relation among the shear stress, the shear strain and the temperature rise. Bai [6] postulated that an ASB initiates when infinitesimal perturbations superimposed on finite homogeneous deformations of a body begin to grow. Wright and Walter [7] built upon the numerical solution of Wright and Batra [8] to show that the shear stress collapses at the initiation of an ASB. These results were confirmed experimentally by Marchand and Duffy [9] during torsional deformations of thin-walled tubes. They also reported the shear strain within an ASB being as large as 20. Even though heat conduction plays a significant role in determining the ASB

* Corresponding author.
E-mail addresses: bryan.m.love@arl.army.mil (B.M. Love). rbatra@vt.edu (R.C. Batra).

width, the band is called adiabatic since there is not enough time for the heat to be conducted away from it. Numerical solutions of the coupled nonlinear equations governing simple shearing and plane strain thermomechanical deformations of a thermoelasto-viscoplastic body reveal that an ASB forms much later than when the effective stress attains its maximum value (e.g. see Batra [10]), and the delay between these two instants depends upon the number, the size and the type of defects present in the body. Much of the earlier work on ASBs is summarized in Bai and Dodd's [11] book, the book edited by Perzyna [12], and the review paper by Tomita [13]. Mathematical aspects of the ASB phenomenon are described in Wright's [14] book.

Works enumerated above and numerous others have studied the shear banding phenomenon in homogenous materials. However, many materials are inhomogeneous because of impurities and/or second-phase particles, which are frequently introduced in order to strengthen the material (or give some other desirable property). One such class of materials is metal-particulate/metal-matrix composites, which are frequently produced to tailor bulk properties (density, failure strength, ductility) by varying the volume fraction of two dissimilar constituents.

ASBs in particulate composites have been studied both experimentally (e.g. see Zhou et al. [15]) and numerically (e.g. see Zhou [16], Batra and Wilson [17], Batra and Love [18]). The latter approach has considered both homogenized materials (e.g. see Batra and Love [19]) and analyzing deformations of each constituent (Zhou [16], Batra and Love [18]). During their analyses of a particulate composite by the finite element method (FEM) Batra and Love [18] found that the ASB initiation criterion for a homogeneous material does not apply to particulate composites, and proposed the following alternative criterion: an ASB initiates at a point when the energy dissipation rate there suddenly increases by nearly an order of magnitude. This ASB initiation criterion has subsequently been adopted by Charalambakis and Baxevanis [20] and Batra and Love [19]. Zhu and Batra [21] analyzed the initiation and propagation of ASBs in plane strain deformations of laminated composites, and found that an ASB initiating from a point on an interface between two adjoining layers propagated easily into the softer material. Batra and Kwon [22] studied ASB initiation in simple shearing deformations of a bimetallic body with a defect placed at the interface between the two materials and found that the ratio of the shear moduli of the two materials significantly influenced which material shear banded.

It has been conjectured that during high strain rate deformations of particulate composites, particulates debond from the matrix resulting in the loss of load transfer between the two constituents, preventing or significantly delaying the initiation and development of ASBs. Depending upon the strength of the particulate and the matrix materials and the bond between them, failure may initiate in either constituent or along particulate/matrix interfaces. This differs from earlier studies on ASBs in delineating how crack formation and particulate/matrix debonding affect the formation and evolution of ASBs. This additional knowledge in failure mechanics would allow particulate composites to be constructed such that the ASB formation could be deliberately reduced or enhanced.

In order to make the problem tractable with reasonable computational resources, we adopt a cohesive-zone technique to simulate failure at a point. That is, the formation of a crack is determined by a small dissipative region called a cohesive zone, where the combination of tractions and opening displacements determine the level of failure of a material or of an interface between two distinct materials. The cohesive zone method allows numerical simulation of failure at multiple locations in the body simultaneously and allows these failures to interact.

Dugdale [23] and Barenblatt [24] proposed the use of cohesive zones to model material failure and generate traction-free crack surfaces. Xu and Needleman [25]and Camacho and Ortiz [26] introduced this theory in the FE methodologies to simulate fracture along inter-element boundaries. The technique has been used by numerous researchers to study material failure and delamination of composites. Computed results depend upon values assigned to material parameters in the cohesive zone relation, and to some extent on the FE mesh. In this work cohesive zones are inserted adaptively when surface tractions at an interface between two adjoining FEs reach a critical value. A limitation of this approach is that failure is only allowed to ensue along element boundaries and, therefore, computed results are mesh dependent. Using randomly oriented FEs and conducting the same analysis with multiple meshes is required to increase confidence in results.

The rest of the paper is organized as follows. The problem studied is formulated in Section 2 that also describes the cohesive zone relation and the ASB initiation criterion. The computational algorithm is briefly discussed in Section 3. Results including the effect of the particulate/matrix interfacial strength on the development of ASBs are discussed in Section 4. In Section 5 we remark on similarities and differences between the cohesive zone and the nodal release techniques. Conclusions of this work are summarized in Section 6.

2. Formulation of the problem

2.1. Governing equations

A schematic sketch of the problem studied is shown in Fig. 1. Because of the assumption of plane strain deformations the dimension of the prismatic body perpendicular to the cross section shown in Fig. 1 is very large. A $2\,\text{mm} \times 2\,\text{mm}$ square particulate composite body is compressed by applying in the vertical direction an axial velocity $V(t) = 20\,\text{m/s} = 0.02\,\text{mm/}\mu\text{s}$ on the top surface while the bottom surface rests on a rigid and frictionless surface. The prescribed velocity increases linearly from zero to its steady state value in 1 μs, giving the steady state nominal axial strain-rate of 10,000/s. Circular cylindrical

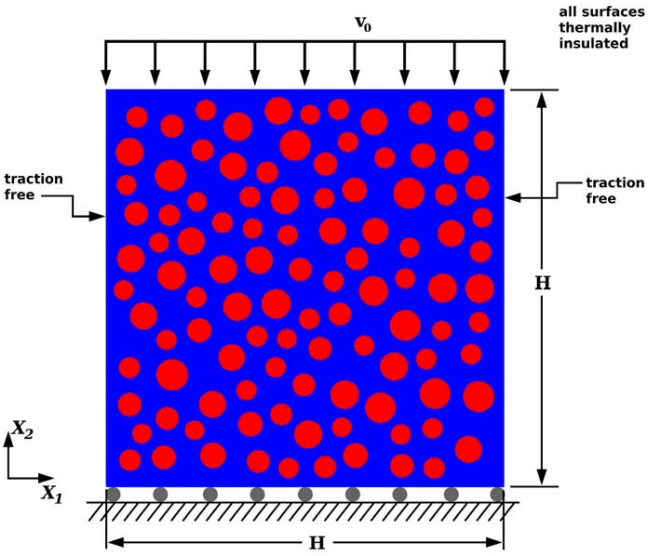

Fig. 1. Schematic sketch of the problem studied.

particulates of diameters ranging from 50 to 80 μm are randomly placed in a metallic matrix.

We use the referential description of motion and rectangular Cartesian coordinates to describe the dynamic thermo-mechanical deformations of the particulate composite. Both the particulate and the matrix materials are modeled as heat-conducting, isotropic, homogeneous thermo-elasto-viscoplastic and exhibit strain and strain-rate hardening and thermal softening. These are characterized by the Johnson–Cook [27] empirical viscoplastic relation:

$$\sigma_y = (A + B(\varepsilon_e^p)^n)\left(1 + C\ln\left(\frac{\dot{\varepsilon}_e^p}{\dot{\varepsilon}_0}\right)\right)(1 - T^m) \tag{1}$$

in which the flow stress σ_y increases with an increase in the effective plastic strain ε_e^p and the effective plastic strain rate $\dot{\varepsilon}_e^p$, but decreases with an increase in the non-dimensional temperature T. In Eq. (1), parameters B and n characterize the strain hardening of the material, C and $\dot{\varepsilon}_0$ its strain-rate hardening, and m its thermal softening. The non-dimensional temperature T is defined as $T = (\theta - \theta_{ref})/(\theta_m - \theta_{ref})$, where θ is the current temperature at the material point and θ_m and θ_{ref} are the presumed melting and the reference temperatures, respectively. Note that θ_m is obtained by fitting the relation (1) to the test data, and need not equal the actual melting temperature of the material. Furthermore, the hardening parameters C and n are considered to be constants, despite a known transition in strain-rate hardening in many metals between quasi-static and dynamic rates. However, this assumption's impact on the results presented here is lessened due to the exclusive consideration of high rates of deformation ($\dot{\varepsilon}_e^p > 10^3/\text{s}$), which are above the transition strain rates seen in the materials of interest; e.g. see Section 4.1. The materials of the particulates and the matrix are assumed to obey the von Mises yield criterion and the associated flow rule.

Deformations of the body are governed by the balance of mass, linear momentum, moment of momentum, and internal energy, which can be found in many continuum mechanics books (e.g. see Truesdell and Noll [28], Batra [29]). Effects of heat conduction are considered with all of the plastic working converted into heating; thus the Taylor–Quinney coefficient is taken to equal 1.

We assume that the body is initially stress-free, at rest, and at a uniform temperature. It is subjected to the following boundary conditions:

$$v_2 = \begin{cases} -v_0\hat{t}/\hat{t}_{ramp}, & 0 \le \hat{t} \le \hat{t}_{ramp} \\ -v_0, & \hat{t} > \hat{t}_{ramp} \end{cases} \quad \text{on } X_2 = H, \tag{2}$$

$$v_2 = 0 \text{ on } X_2 = 0,$$

$$T_{11} = T_{21} = Q_1 = 0 \text{ on } X_1 = 0 \text{ and } X_1 = H,$$

$$T_{12} = Q_2 = 0 \text{ on } X_2 = 0 \text{ and } X_2 = H.$$

Here, $\hat{t}$ represents the analysis time. All bounding surfaces are taken to be thermally insulated, the top and the bottom surfaces to be smooth, and the left and the right vertical surfaces to be traction free. **Q** equals the heat flux measured per unit area in the reference configuration, **T** the first Piola–Kirchhoff stress tensor, and (X_1, X_2) coordinates of a point in the reference configuration with respect to rectangular Cartesian coordinate axes (e.g. see Fig. 1).

Prior to debonding, particulate/matrix interfaces are assumed to have continuous tractions, displacements, temperatures and normal components of the heat flux. Subsequent to debonding, the newly created surfaces are taken to be thermally insulated and tractions on them are computed from the cohesive relation given in Section 2.2. Since the failure occurs in less than 40 μs traction-free crack surfaces being thermally insulated is a reasonable assumption; for longer analyses, a convective boundary condition would be necessary.

2.2. Cohesive zone relations

Fig. 2 demonstrates the traction-separation law used in the computational model. Each interface between two adjoining FEs is considered for failure, where the state variables of the two elements connected to the segment are used to compute the failure state of the segment. Fig. 2a shows one such segment, which is connected to elements 1 and 2. The outward normals to the segment surfaces are denoted by n^1 and n^2, where the superscripts denote the connected elements. The normal tractions (σ^1, σ^2) and tangential tractions (τ^1, τ^2) on the interface are computed using each element's stress tensor σ_{ij} as shown in Eq. (3) (computations are performed for each element; superscripts are deleted for clarity); (e.g., see Truesdell and Noll [28], Batra [29]).

$$\sigma = \sigma_{ij} n_i n_j,$$

$$\tau_i = \sigma_{ij} n_j - \sigma n_i, \tag{3}$$

where a repeated index implies summation over the range $(i = 1, 2)$ of the index, and $\boldsymbol{\sigma}$ is the Cauchy stress tensor. We denote by τ the magnitude of the tangential traction. For the segment, the normal and the tangential tractions $\hat{\sigma}$ and $\hat{\tau}$ are

$$\hat{\sigma} = (\sigma^1 + \sigma^2)/2,$$

$$\hat{\tau} = (\tau^1 + \tau^2)/2. \tag{4}$$

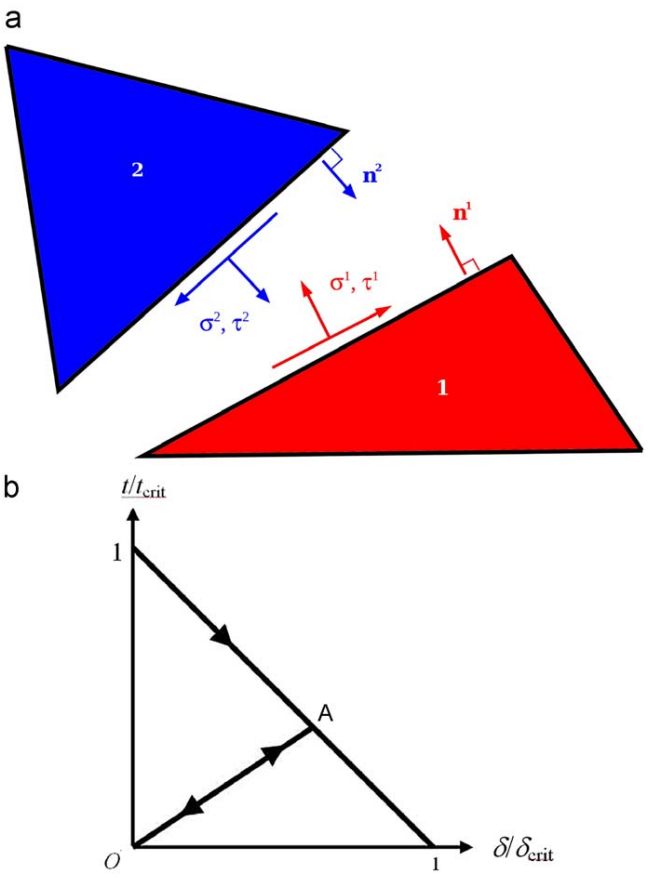

Fig. 2. Cohesive law: (a) tractions at the interface between two adjoining elements and (b) traction/opening displacement relation.

That is, $\hat{\sigma}$ and $\hat{\tau}$ equal the average of magnitudes of the normal and the tangential tractions on the two sides of the common interface; this helps reduce numerical errors introduced by the FE analysis since the magnitudes of the normal and the tangential tractions on either side of the interface are identical in a perfect continuum.

We follow Ortiz and Pandolfi [30] and define an effective traction t as:

$$t = \sqrt{\beta^{-2}|\hat{\tau}|^2 + \max(\hat{\sigma}, 0)^2}, \tag{5}$$

where $\hat{\sigma}$ and $\hat{\tau}$ are the tractions defined in Eq. (4). The parameter β determines the relative importance of the shear traction and therefore represents a form of "mode-mixity" of the crack and the material. This effective traction t is computed at every element interface at every timestep. When t reaches a critical value (defined as t_{crit}), the segment is considered failed, appropriate nodes are duplicated, a new segment is generated, and a cohesive element is introduced. The introduction of the cohesive element and the alteration of the mesh is carried out dynamically in the analysis and does not require the introduction of cohesive elements at the beginning of the analysis. The mesh alteration is also considered irreversible; that is, the material cannot "heal" and re-join two crack faces into undamaged material. The crack faces may meet and stay in contact, but they are still considered two separate segments and are dealt with by the appropriate contact algorithm to avoid inter-penetration of the material across the contact surface.

Upon failure initiation at an interface between two adjoining elements, we define an effective crack opening displacement δ (again, following Ortiz and Pandolfi [30]):

$$\delta = \sqrt{\beta^2 \delta_s^2 + \delta_n^2}, \tag{6}$$

where δ_s and δ_n are the tangential and the normal relative displacements of the two crack faces.

The cohesive zone concept indicates that the material undergoing cracking does not reach two fully traction-free surfaces until a certain amount of work has been performed (which is usually correlated to the familiar Griffith fracture energy). To accomplish this, we adopt the cohesive relation (Eq. (7)) proposed by Camacho and Ortiz [26].

$$t/t_{crit} = 1 - \delta/\delta_{crit}, \ \dot{\delta} \geq 0;$$

$$t = \frac{t_{\max}}{\delta_{\max}}\delta, \ \text{either } \dot{\delta} < 0, \ \text{or } \dot{\delta} > 0 \text{ and } \delta \leq \delta_{\max}$$

on the debonded interface,

$$t = 0, \ \delta \geq \delta_{crit}. \tag{7}$$

As evident from Fig. 2b, Eq. (7) implies that the applied tractions vanish when either (a) one reaches the critical opening displacement δ_{crit} or (b) the AO segments unload as the crack closes (as indicated by the line to the origin in Fig. 2b). For $\delta \geq \delta_{crit}$ the segments are truly independent and one has a pair of traction-free thermally insulated surfaces forming the crack faces. For $\delta \leq \delta_{crit}$, a failed segment is checked for $\dot{\delta} > 0$ or $\dot{\delta} \leq 0$. In the former case, tractions are given by Eq. $(7)_1$ if δ is a monotonically increasing function of time for the segment; otherwise the traction is given by Eq. $(7)_2$ which is also used if $\dot{\delta} \leq 0$. While using Eq. $(7)_2$ the percentage change in both $\hat{\sigma}$ and $\hat{\tau}$ is kept the same. In Eq. $(7)_2$ $t_{\max}$ and $\delta_{\max}$ are values of t and δ, respectively, just prior to reversing of the opening of the segment; $t_{\max}$ and $\delta_{\max}$ satisfy Eq. $(7)_1$. It should be noted that , for monotonic increase of δ to δ_{crit}, the area, $t_{crit}\delta_{crit}/2$, under the $t-\delta$ curve is the energy per unit surface area that is dissipated during fracture and equals the Griffith fracture energy. Molinari et al. [31], among others, have used the cohesive failure model to simulate fragmentation in a bar made of a linear elastic brittle material. They have shown that introducing a slight degree of randomness improves upto two orders of magnitude the convergence of the energy.

Determination of the appropriate critical traction t_{crit} and critical displacement δ_{crit} from experimental results obtained during dynamic loading is difficult. It has been experimentally shown (see Rosakis et al. [32]) that dynamic fracture toughness depends on crack speed. In all likelihood, the fracture toughness depends on the material, the strain-rate and temperature in the vicinity of the crack, and the initial flaw distribution.

Here, we account for temperature effects by assuming that the critical traction decreases affinely with temperature increase according to the following relation:

$$t_{crit} = t_{crit,0}\left(1 - \frac{\theta - \theta_{ref}}{\min(\theta_{melt}) - \theta_{ref}}\right), \tag{8}$$

where $t_{crit,0}$ is the critical traction at the reference temperature θ_{ref} and $\min(\theta_{melt})$ is the lower of the presumed melting temperatures of the particulate and the matrix. This assumption mimics the thermal softening in the Johnson–Cook constitutive relation (Eq. (1)); we have assumed that the critical traction decreases as the yield stress of the material decreases. The functional form (8) of the thermal softening is a postulate; experimental investigation of the dependence of fracture toughness on temperature would benefit the analysis greatly. We have tacitly assumed no strain-rate or other state-variable dependence of the critical traction $t_{crit,0}$.

The mode-mixity parameter β determines the relative strength of the material in mode-I (tensile) and mode-II (shear). Estimates for the mode mixity have been found experimentally by Chen and Ravichandran [33,34] for brittle ceramics; but little experimental work has been done for ductile metals, especially under extreme plastic deformations. Here, we have assumed that β equals 0.866, mainly for lack of information. This value of β represents a moderate mode-mixity ratio seen in a variety of ductile metals (a range between 0.7 and 0.9 has been reported for steels [32] and similar ranges have been used in simulations for brittle ceramics [26]). The effect of the value of β is assessed in Section 4.3. For mode II failure β is close to zero, t given by Eq. (5) approaches infinity and δ equals δ_n. Thus the present approach is not suitable for simulating shear dominated failure.

The critical opening displacement δ_{crit} cannot be readily determined from theoretical knowledge or experimental evidence. The pair t_{crit} and δ_{crit} define the fracture energy per unit surface area. The value of δ_{crit} affects stability of the numerical algorithm, and must be chosen such that the computations (a) are stable (which places a floor on δ_{crit}) and (b) give reasonable results for small crack openings (which places a ceiling on δ_{crit}). Here, the value of δ_{crit} has been taken to be one-tenth the mean element altitude in the specimen (which for the FE-meshes employed herein equals 0.015 mm); this value allows for stable numerical results while allowing for a fairly small crack opening displacement. With an assumed value of δ_{crit}, one can compute the value of $t_{crit,0}$ from published values of the Griffith fracture energy per unit surface area.

2.3. ASB initiation criterion

We assume that an ASB initiates at a point when the energy dissipation rate there suddenly increases by nearly an order of magnitude, the material point is deforming plastically, and deformations in its neighborhood are inhomogeneous. This differs from the ASB initiation criterion proposed by Batra and Kim [35]: an ASB initiates at a point when the shear stress there has

dropped to 80% of its peak value at that point, the material point is deforming plastically, and the deformations of the material surrounding it are highly inhomogeneous. For a simple shearing problem, Batra and Kim's criterion quantifies Marchand and Duffy's [9] experimental observation that the torque required to deform the specimen drops very rapidly when an ASB initiates. As made clear by results presented in Fig. 1 of Batra and Lear's [36] paper, the requirement of the material point deforming plastically rules out false "initiation" of an ASB due to elastic unloading. During high strain rate deformations of particulate composites, Batra and Love [18] found that this criterion can be satisfied at a material point at time $\hat{t}_1$ but is not necessarily satisfied at a subsequent time $\hat{t}_2$ due to the load exchange between particulates and the surrounding matrix.

Experimentalists generally decipher the formation of an ASB through post-mortem examination of failed specimens, calling a narrow region of intense plastic deformation a shear band. Some experimentalists have attempted to capture an ASB in situ through surface observations. As ASB formation is highly sensitive to initial defects, one must take great care when comparing either post-mortem or in situ experimental results to computational results to ensure that one is comparing the same quantity at the same material point. Furthermore, analysis of 3-dimensional deformations have shown that an ASB initiates first at a point in the interior of the body [37,38]. Thus measurements on a surface may not be true indicators of the time of initiation of an ASB.

We note that concepts of fracture toughness and/or the J-integral cannot be used to characterize the initiation and/or the propagation of an ASB; e.g. see Batra and Love [18,39]. However, these are implicitly imbedded in the cohesive zone model and are thus being tacitly used for the initiation of debonding.

Here we hypothesize that an ASB has initiated when the axial load rapidly drops.

3. Numerical solution of the problem

3.1. Brief description of the technique

We analyze the problem by the FEM, using 3-node triangular elements. The FE mesh using triangular elements provides a much larger number of potential crack paths and the mesh generation is easier than a mesh using quadrilateral elements. The problem of volumetric locking is remedied by utilizing a node-centered pressure and the finite calculus technique of Onate et al. [40].

Coupled nonlinear ordinary differential equations obtained from the weak formulation of the problem are integrated by using the conditionally stable explicit central difference method. The time step is controlled by the well documented Courant [41] condition. We employ a lumped mass matrix produced by the row-sum technique and lumped heat capacitance matrix to allow efficient solutions using the explicit central difference method. The constitutive update uses a backward Euler method similar to the radial return algorithm. Deformations during a time step are first assumed to be elastic; if they are not, the stresses, plastic strains, and temperature are updated such that the resulting state is on the yield surface. It is assumed that all plastic work results in an increase in temperature (the Taylor–Quinney coefficient is tacitly assumed to be unity). The heat conduction equation is solved and the resulting nodal temperatures are calculated by taking a forward Euler step after the mechanical step is taken; the very short time steps in this analysis allow this stepping technique to produce reasonable results.

Following the debonding/fracture process detailed in Section 2.2, the interpenetration of the material across an interface is avoided by using a contact algorithm. The algorithm checks for interpenetration after the position/velocity update in the central difference scheme, and then interpenetrations are corrected using a symmetric sliding interface algorithm, similar to that given by Johnson and Stryk [42]. This algorithm has no "defined" master and slave surfaces, and thus is independent of the order of processing. Here, we have assumed no friction between the contacting/sliding surfaces; in reality, the friction between these surfaces is complex and difficult to model at the scale of this problem.

3.2. Verification of the computer code

The computer code has been verified by using the method of fictitious body forces, e.g. see comments following Eq. (20) of Batra and Liang [43]. In this method, a closed form expression for the solution variables is assumed, and these are substituted in the balance laws to find body forces and sources of energy needed to satisfy them. Also, initial and boundary conditions corresponding to the assumed solution are found. The initial-boundary-value problem corresponding to these initial and boundary conditions, body force and the source of internal energy is solved numerically with the code. If the computed solution agrees with the presumed analytical solution of the problem, then the code's accuracy has been verified. The results for a plane-strain shear banding problem were further compared to results from our previous code [18], and ASB initiation times were predicted to within 1% difference in heterogeneous bodies with no debonding.

4. Computation and discussion of results

We assigned the following values to material parameters for the particulates and the matrix:

Particulates (metal 1): $\rho_0 = 19,300\,\text{kg/m}^3$, $E = 400\,\text{GPa}$, $\nu = 0.29$, $\kappa = 160\,\text{W/mK}$, $c_p = 138\,\text{J/kg K}$, $\alpha = 5.3 \times 10^{-6}/\text{K}$.

$A = 730\,\text{MPa}$, $B = 562\,\text{MPa}$, $C = 0.029$, $m = 1.0$, $n = 0.0751$, $\theta_m = 1700\,\text{K}$, $\dot{\varepsilon}_0 = 1 \times 10^{-6}/\text{s}$.

Matrix (metal 2): $\rho_0 = 9200\,\text{kg/m}^3$, $E = 255\,\text{GPa}$, $\nu = 0.29$, $\kappa = 100\,\text{W/mK}$, $c_p = 382\,\text{J/kg K}$, $\alpha = 15.0 \times 10^{-6}/\text{K}$.

$A = 150\,\text{MPa}$, $B = 546\,\text{MPa}$, $C = 0.0838$, $m = 1.0$, $n = 0.208$, $\theta_m = 1225\,\text{K}$, $\dot{\varepsilon}_0 = 1 \times 10^{-6}/\text{s}$.

Here ρ_0 is the initial mass density, E the Young's modulus, ν the Poisson's ratio, c_p the specific heat, κ the thermal conductivity, and α the coefficient of thermal expansion. The reference temperature θ_{ref} was taken to be 293 K.

The parameters for the cohesive law were taken to be:

Metal 1–metal 1: $t_{crit,0} = 1.8\,\text{GPa}$, $\delta_{crit} = 1.5 \times 10^{-2}\,\text{mm}$, $\beta = 0.866$.

Metal 2–metal 2: $t_{crit,0} = 1.5\,\text{GPa}$, $\delta_{crit} = 1.5 \times 10^{-2}\,\text{mm}$, $\beta = 0.866$.

Metal 1–metal 2: $t_{crit,0} = 0.8, 1.0, 1.2, 1.5\,\text{GPa}$, $\delta_{crit} = 1.5 \times 10^{-2}\,\text{mm}$, $\beta = 0.866$.

These values are computed from fracture energies for the respective materials, realizing that the area under the curve in Fig. 2b equals the fracture energy per unit surface area. For $t_{crit,0} = 1.8\,\text{GPa}$, $\delta_{crit} = 0.015\,\text{mm}$, energy dissipated per unit surface area during monotonic debonding equals $13,500\,\text{J/m}^2$. Effects of varying strength $t_{crit,0}$ of the particulate/matrix interface and β on the ASB formation have been studied.

Square specimens of various sizes (1, 2 and 4 mm side) were given random distributions of particulates with radius ranging from 50 to 80 μm, holding the volume fraction of particulates to $31 \pm 0.2\%$. The specimens were meshed with triangular elements with an approximate side length of 0.02 mm. The particulates were arranged such that there was a minimum of three triangular elements (0.06 mm) between any two particulates. Subsequent to

the initial rise in the applied axial velocity, each specimen was subjected to plane strain compression at a nominal axial strain rate of 10,000/s.

4.1. Results without debonding

As a reference, each specimen was deformed without allowing debonding and fracture to occur. ASBs formed in a way consistent with that given in Batra and Love [18]; i.e. large plastic strains and a nearly discontinuous velocity field at about 45° to the loading axis. Figs. 3a and b exhibits contours of the effective plastic strain and the vertical velocity component for one of these cases. It is clear that one dominant ASB with effective plastic strain of ~ 1 and inclined at $\sim 45^{\circ}$ to the loading direction formed. Once the ASB had formed the specimen was divided into two regions; the lower virtually stationary pyramid, and the upper one moving downwards with the velocity imposed on the top surface. There is a sharp gradient in the velocity field between these two regions where strain rates and the effective plastic strain are quite large.

Fig. 4 exhibits fringe plots of the velocity field at $\hat{t} = 25\,\mu s$ and time histories of the effective plastic strain rate at four points. Points 1 and 3 are within the ASB, and 2 and 4 are outside of the ASB; points 1 and 2 are in the matrix, and points 3 and 4 in the particulates. It is clear that the effective plastic strain at these four points are more than $10^4/s$ except at late times when the ASB has developed. The strain rates at points 1 and 3 increase by a factor of 10 as the ASB develops. It is clear from these results that the error, if any, in not considering the dependence of C in Eq. (1) upon the strain rate is negligible.

We note that the random distribution of the particulates does not significantly impact the ASB initiation time. Fig. 5 shows the axial load versus the nominal axial compressive strain for six microstructures with approximately 31% volume fraction of particulates. The axial load is computed from tractions at nodes on the top surface where axial velocity is prescribed, and taking the specimen dimension in the X_3-direction equal to 1 mm. Note that the sudden drop in the applied load (indicative of shear band formation) occurs at the axial strain between 30% and 34% for each of the specimens. Thus the difference between the minimum and the maximum ASB time is 12%.

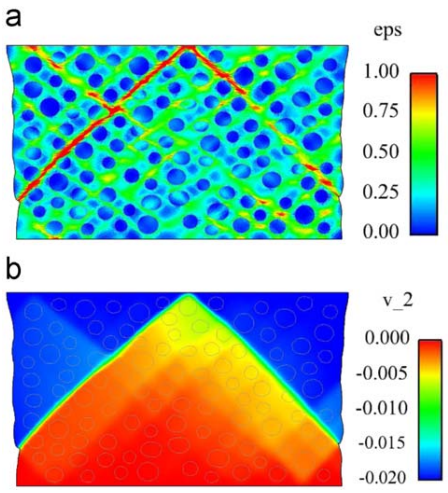

Fig. 3. Contours of (a) effective plastic strain and (b) vertical velocity at time $t = 23.8\,\mu s$ for a particulate composite subjected to plane strain compression at a nominal axial strain rate of 10,000/s.

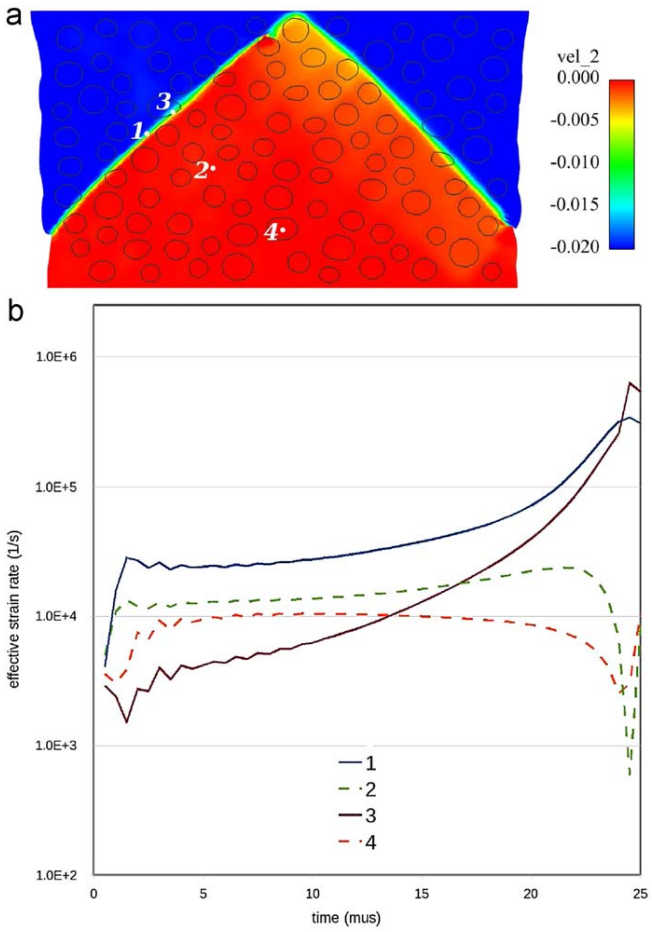

Fig. 4. Strain rate histories for four points; position of points at $t = 25\,\mu s$ shown in (a).

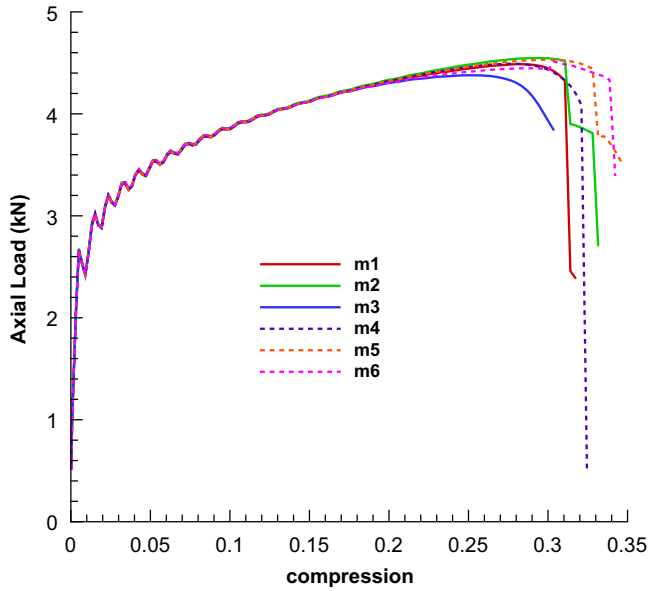

Fig. 5. Axial load versus axial compressive strain curves for six random microstructures of 31% volume fraction particulate.

4.2. Results with material failure

4.2.1. Effect of specimen size

When simulating microstructures, the question of an appropriate size for the specimen always arises. To examine this effect, we subjected 1 mm × 1 mm, 2 mm × 2 mm, and 3 mm × 3 mm specimens to plane strain compression. The particulates were randomly generated with diameters ranging from 100 to 160 μm, and their volume fractions equaled 31% ± 0.2%. The finite element size was held constant throughout all of the simulations. The critical traction $t_{crit,0}$ on the particulate/matrix interface was taken to be 1.0 GPa, and material properties were assumed not to depend on the particulate diameter.

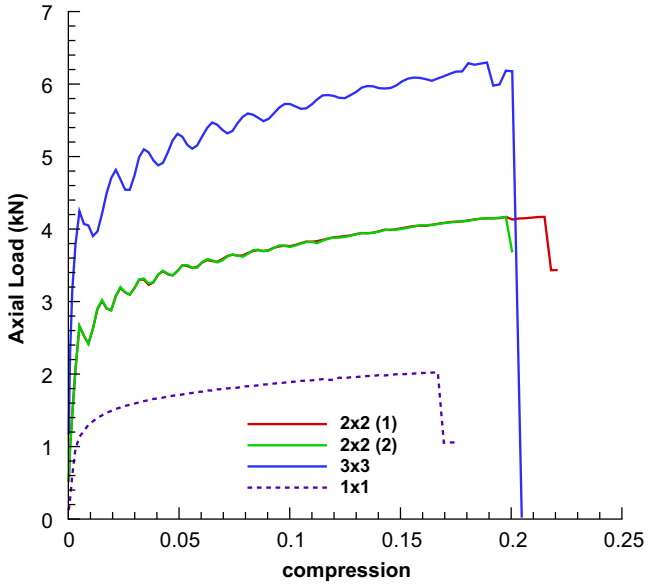

Fig. 6. Axial load versus axial compressive strain curves for three different specimen sizes (mm × mm).

Fig. 6 shows the load versus compression curves for all three specimen sizes. Note there are two 2 mm × 2 mm specimens; these two curves show the typical variation caused by slightly different particulate arrangements but the same volume fraction; this is similar to the effect of microstructures studied in Section 4.1. Note that the ASB initiation time for the 3 mm × 3 mm case coincides with that of one of the 2 mm × 2 mm specimens, but the 1 mm × 1 mm specimen shows a substantially earlier load drop. This difference can possibly be attributed to the number of particulates in the specimen; in the 1 mm × 1 mm specimen, the small number of particulates allows an ASB to form entirely in the matrix at a substantially earlier time. With a sufficient number of particulates, the formation of the ASB is impeded by the harder particulates; this effect was also seen in Batra and Love [18]. Note that the oscillations seen in the load/compression curves are due to the stress-wave reflections in the specimen. The period of these reflections is related to the size of the specimen and thus, a 3 mm × 3 mm specimen is the largest plausible at this loading rate without the stress wave effects becoming significant. The difference in the acoustic impedences of the particulate and the matrix materials affects reflections, refractions and the transmission of waves at interfaces; the acoustic impedance of metal 1 equals 1.81 times that of metal 2. The time integration scheme should be checked for not producing excessive oscillations in the solution due to the acoustic impedance mismatch between the particulate and the matrix.

Until the axial compressive strain of 0.15, the axial compressive load essentially scales with the specimen width, i.e., the axial force for the 3 × 3 specimen is three times that for the 1 × 1 specimen.

For further analyses, we use the 2 mm × 2 mm specimen, as it gives reasonable results with substantially less computational effort than the 3 mm × 3 mm specimen.

4.2.2. Crack-tip pinning

One potential problem that arose early in the analyses is that of crack-tip "pinning" (see Fig. 7) which led to a collapse of an element and the termination of the analysis. This phenomenon

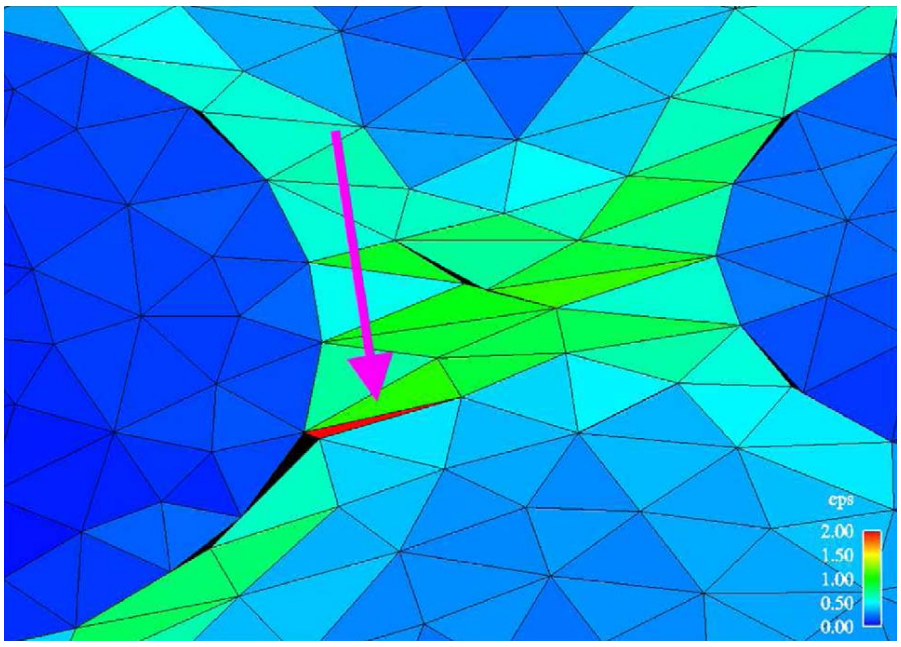

Fig. 7. Crack "pinning" phenomenon that can result in termination of the analysis.

occurs due to compressive stress fields in the domain, which are typical of this loading scenario. A crack nucleates due to shear stress at 45° to the loading direction on the particulate/matrix interface and propagates until it is arrested due to this compressive field. Subsequently, the compressive deformations tend to crush the element near the crack tip in the softer matrix. To allow the analysis to proceed, we resorted to element deletion when the minimum altitude of an element became 1/10,000th of its original value. The element was simply removed from computation (thus removing a small amount of mass from the problem and creating a small void) and contact surfaces were updated and the analysis continued. For the problems studied herein at most ten out of several thousand elements were deleted; thus the error caused due to the deletion of these elements is negligible.

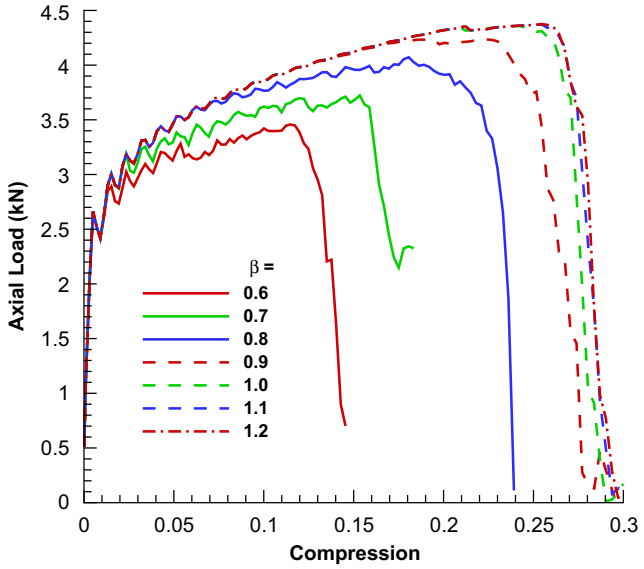

Fig. 8. Axial load versus axial compressive strain curves for various values of the mode-mixity parameter β.

4.3. *Effect of mode mixity*

The parameter β in the cohesive law (see Eqs. (5) and (6)) determines the critical traction under mixed-mode (normal and shear) loading conditions. One determines $t_{crit,0}$ from the pure mode I fracture toughness, and then computes β using the pure mode II fracture toughness. The cohesive law then determines the critical traction under combined loading. Unfortunately, experimental determination of mode II fracture toughness is difficult, particularly under dynamic loading. While there are reasonable estimates for β for monolithic materials (see Chen and Ravichandran [33,34]; Pandolfi et al. [32]), the strength of the interface due to shear is much less well characterized.

Fig. 8 shows the load versus compression for a single microstructure with a range of values of β for the interface. The critical traction was taken to be $t_{crit} = 1.2$ GPa. We consider values of β ranging from 0.6 to 1.2, which should contain the physically meaningful solutions to the problem (note that functions in Eqs. (5) and (6) become singular as β tends to zero or infinity). The load versus compression curves are quite different over this range of β, although the load versus compression curves seem to "converge" for $\beta \geq 1.0$. Further evidence of this is seen in Fig. 9; note the similarity of the results for $\beta = 1.0$ and 1.2.

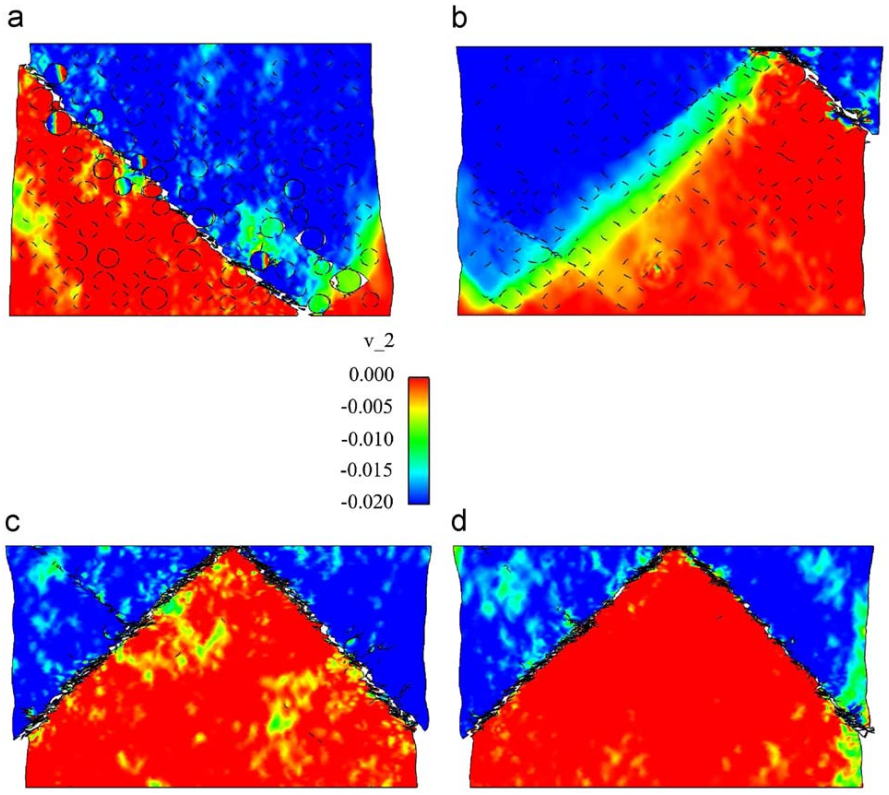

Fig. 9. Contours of vertical velocity for a single specimen for mode-mixity parameter and times of (a) $\beta = 0.6$ and $\hat{t} = 13.2\,\mu s$, (b) $\beta = 0.8$ and $\hat{t} = 19.4\,\mu s$, (c) $\beta = 1.0$ and $\hat{t} = 22.8\,\mu s$, and (d) $\beta = 1.2$ and $\hat{t} = 22.8\,\mu s$. Dark lines denote cracks/new interfaces.

The dark circles in Fig. 9 imply that the matrix has debonded from the particulate. Also white regions imply voids or cracks. The deformed shapes and locations of ASBs for $\beta = 0.6$ and 0.8 are quite different from those for $\beta = 1.0$ and 1.2. Thus the mode-mixity or the cohesive failure criterion plays dominant roles in not only the time of formation of an ASB but also in their spatial locations. A smaller value of β makes the interface more susceptible to shear fracture; for $\beta = 0.6$, many of the particulate matrix interfaces are fractured prior to the development of the ASB. As one would expect this debonding of particulates and matrix materials leads to distinctly different local stress states and velocity fields which in turn change the ASB evolution as evinced by differences in results shown in Figs. 9a and 9b. The ASB initiation time for $\beta = 0.6$ is nearly one-half of that for $\beta = 1.1$. Without experimental data for mixed-mode loading for particulate/matrix interfaces, we continue to use $\beta = 0.866$ for the interface as well as for the monolithic materials.

4.4. *Effect of interfacial strength*

We note that experimental data on the particulate/matrix interfacial strength is not readily available in the open literature. Accordingly, we conduct a parametric study and consider three values of this strength, namely $t_{crit,0} = 1.0$, 1.2, and 1.5 GPa; results for the no debonding case are also presented.

The results for a single microstructure for all three values of the critical traction $t_{crit,0}$ and for the no debonding case are shown in Fig. 10, and the plot of axial load versus axial compressive strain for these four cases is exhibited in Fig. 11. Note that reducing the interface strength generally decreased the ASB initiation time. Furthermore, the lower two values of the interface strength exhibited significant "debonding" of the particulates from the matrix prior to localization, which is evinced from the load versus compression curve deviating from the "no fracture" case. The 1.2 and 1.5 GPa critical stresses

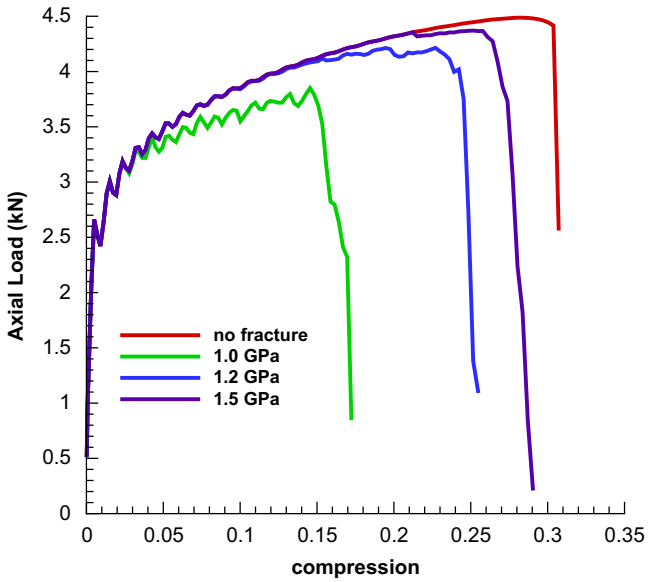

Fig. 11. Axial load versus axial compressive strain for three values of the critical traction and the no fracture case for a single specimen.

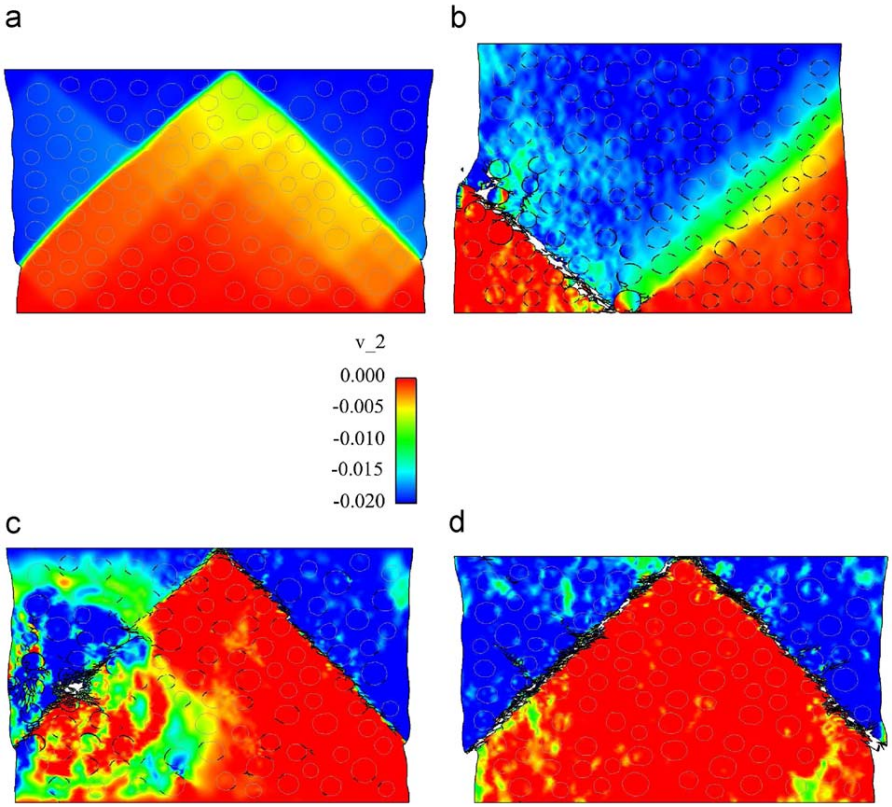

Fig. 10. Contours of vertical velocity for a single specimen for critical tractions and times of (a) no fracture and $\hat{t} = 23.8\,\mu s$, (b) $t_{crit,0} = 1.0$ GPa and $\hat{t} = 15.0\,\mu s$, (c) $t_{crit,0} = 1.2$ GPa and $\hat{t} = 20.4\,\mu s$, and (d) $t_{crit,0} = 1.5$ GPa and $\hat{t} = 23.0\,\mu s$. Dark lines denote cracks/new interfaces while light gray lines denote particulate/matrix interfaces that are still bonded.

showed fracture almost exclusively along the ASB through the bulk material (mainly in the matrix) at fairly late times; note the agreement with the "no fracture" case in the load/compression curve to 20% compression.

Examining the dissipation rate to observe the initiation of an ASB reveals some interesting results. For the case of no fracture, Fig. 12a shows the expected dramatic rise in the dissipation rate for an element in the ASB. For a relatively high value of the critical traction, $t_{crit,0} = 1.5$ GPa in Fig. 12c, the dissipation rates show a similar trend. However, for a relatively low value of the critical traction ($t_{crit,0} = 1.0$ GPa in Fig. 12b), the dissipation rate increases but there is no dramatic change of slope (other than the brief spikes at the time of fracture of segments near the element in question), despite the dramatic drop in load shown in Fig. 11. Examining the details of deformations reveals the difference between these two cases. In the $t_{crit,0} = 1.0$ GPa case, fracture occurs while the axial compressive load is increasing, with little plastic strain near the fractured surfaces (thus indicating "brittle" fracture). The ASB forms along a path through the matrix connecting multiple sites of brittle fractures, and the load drop is due to a combination of the decrease in strength of the material induced by fracture surfaces and the thermal softening of the material in the ASB. For the higher value of the critical traction $t_{crit,0} = 1.5$ GPa, an ASB forms just as in the case of no fracture, and the load drop occurs due to the thermal softening of the material along the ASB. A crack develops in the shear banded material. The crack and the ASB include many particulate/matrix interfaces. The rapid increase in the energy dissipation rate is not a good indicator of ASB formation in the presence of weak particulate/matrix interfaces.

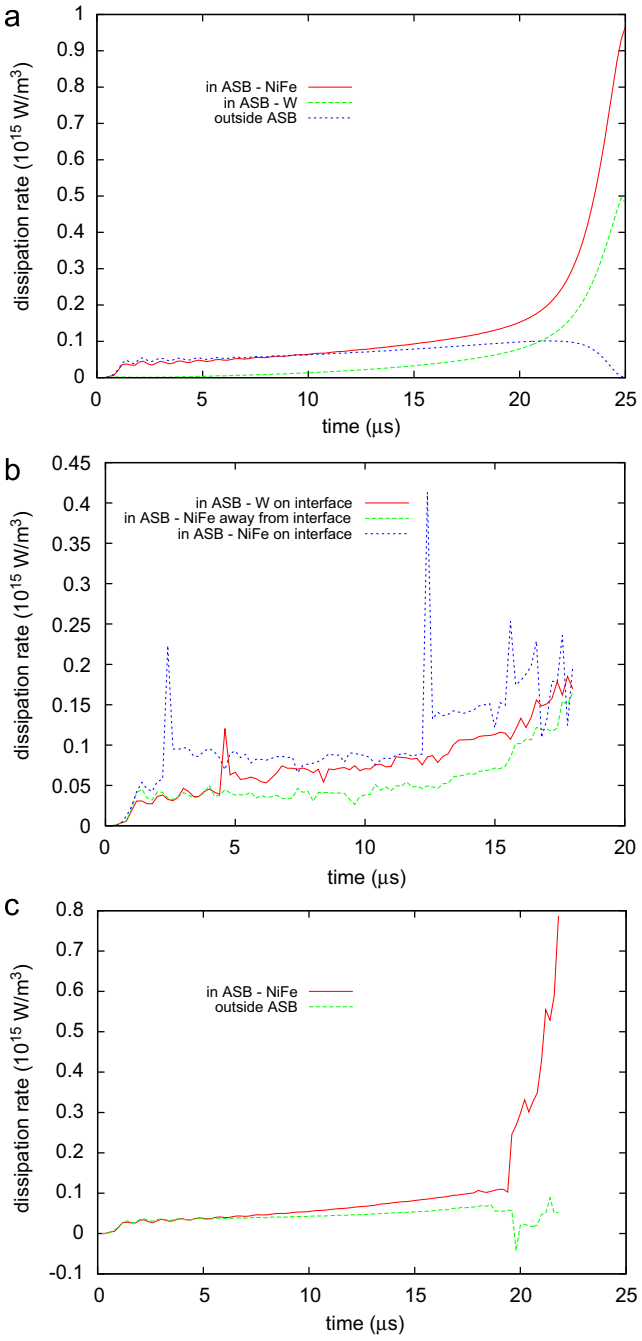

Fig. 12. Energy dissipation rate versus time for points in the body with (a) no fracture, (b) $t_{crit,0} = 1.0$ GPa, and (c) $t_{crit,0} = 1.5$ GPa.

5. Remarks

Batra and Love [39] used the nodal release technique to simulate crack propagation in mode I and mode II deformations of a functionally graded thermoviscoplastic body deformed at high strain rates. When a prespecified local failure criterion was met at a node, it was split into two nodes an infinitesimal distance apart and the nodal connectivity was modified. The brittle failure was assumed to ensue at a point when the maximum principal stress there exceeds three times the quasi-static yield stress, and the ductile failure was initiated when the effective plastic strain equals 1.5. They thus studied crack initiation and propagation in plane strain deformations of an inhomogeneous plate deformed in either tension or shear. Batra and Lear [36] had employed a similar procedure to study crack initiation and propagation in a prenotched steel plate impacted on the notched side, and found computed results to be in reasonable qualitative agreement with those observed experimentally. Hassan and Batra [44] used a similar procedure to study delamination between adjoining layers in a laminated composite plate.

Both the cohesive zone technique and the nodal release method assume that fracture initiates instantaneously once the respective failure criterion has been satisfied at a point. Whereas in the cohesive zone procedure the rate of decrease to zero of surface tractions depends on the rate of increase of the crack opening displacement δ, in the nodal release technique it is decided empirically. In both methods surface tractions are decreased gradually to keep the numerical algorithm stable and mitigate effects of shock waves being released from the crack faces. The mode-mixity of deformations near a crack-tip is approximately accounted for in the cohesive zone failure equations (5) and (6) through the parameter β, it is not considered in the nodal release technique employed in [39,36]. Note that β cannot be assigned either an extremely large or a very small value; otherwise the computational algorithm becomes unstable.

The postulate that the critical traction drops with temperature (see Eq. (8)) was chosen because it allows for fracture in the high temperature regions produced by ASBs. This assumption, however, is not unique-analyses that utilized a critical strain to failure were conducted and the results were qualitatively similar to those given by the temperature dependent traction. In reality, the cohesive zone relation should depend on several state variables, particularly the strain rate and the temperature. This dependence is still an open area of research and published data on it is not available in the open literature.

Here we have employed the Johnson–Cook relation to model the thermo-visco-elasto-plastic response of the particulate and the matrix. It is shown in [45,46] that even when different constitutive relations have been calibrated to give identical shear stress versus shear strain curve at one nominal strain rate, they do not predict the same ASB initiation time and the post-localization response.

6. Conclusions

We have studied the plane strain transient thermomechanical deformations of a particulate composite with the finite element method. Various representative volume elements comprised of approximately 31% metallic particulates dispersed in a metallic matrix were subjected to plane strain compression at an axial nominal strain rate of 10,000/s. Effects of heat conduction, strain and strain-rate hardening, thermal softening, and debonding at interfaces and fracture in each material have been incorporated in the analysis. Computed results for various values of the interface strength parameter have indicated that the interface strength noticeably influences the shear band susceptibility and the load carrying capacity of the composite. Furthermore, debonding between the particulates and the matrix does not deter the formation and the propagation of adiabatic shear bands.

The present work suggests that additional studies are needed to find reasonable values for the critical traction t_{crit} and the mode-mixity parameter β in the cohesive zone relation. Furthermore, the cohesive zone relation should also take into account the strains, strain-rates, and temperatures experienced by the body; here we have used a t_{crit} that is invariant with respect to strain and strain-rate and has a presumed affine softening due to temperature. Experimental investigation into the strength of these interfaces in both mode I and mode II would allow this type of analysis to give results that compare well with experimental findings and then could be used to help predict the onset of adiabatic shear bands in particulate composites, and appropriately design interfaces and composites. The present work suggests that strong interfaces delay the adiabatic shear band initiation.

Acknowledgments

BML's work was supported by the Weapons and Materials Research Directorate, US Army Research Laboratory, and RCB's work was partially supported by the Office of Naval Research grant N00014-06-1-0576 to Virginia Polytechnic Institute and State University with Dr. Y.D.S. Rajapakse as the program manager, RCB's work was also sponsored by the Army Research Laboratory and was accomplished under Cooperative Agreement Number W911NF-06-2-0014. The views and conclusions contained in this document are those of the authors and should not be interpreted as representing the official policies, either expressed or implied, of the Army Research Laboratory or the US Government. The US Government is authorized to reproduce and distribute reprints for Government purposes notwithstanding any copyright notation hereon. Computational resources were provided by the Army High Performance Computing Center.

References

[1] Magness L, Farrand T. Deformation behavior and its relationship to the penetration performance of high-density KE penetrator materials. In: Proceedings of the 1990 army science conference, West Point, NY, 1990.
[2] Tresca H. On further application to the flow of solids. Proc Inst Mech Eng 1878;30:301–45.
[3] Massey H. The flow of metal during forging. Proc Manchester Assoc Eng 1928:21–6.
[4] Zener C, Holloman J. Effect of strain rate upon plastic flow. J Appl Phys 1944;15:22–32.
[5] Clifton R. Adiabatic shear banding. In: Material response to ultra-high loading rates, Washington, DC, NMAB-365, 1980.
[6] Bai Y. Thermoplastic instability in simple shear. J Mech Phys Solids 1982;30:195–207.
[7] Wright T, Walter J. On stress collapse in adiabatic shear bands. J Mech Phys Solids 1987;85:701–20.
[8] Wright T, Batra R. The initiation and growth of adiabatic shear bands. Int J Plasticity 1985;1:205–12.
[9] Marchand A, Duffy J. An experimental study of the formation process of adiabatic shear bands in a structural steel. J Mech Phys Solids 1988;36:251–83.
[10] Batra R. Effect of material parameters on the initiation and growth of adiabatic shear bands. Int J Solids Struct 1987;23:1435–46.
[11] Bai Y, Dodd B. Adiabatic shear localization: occurrence, theories, and applications. Oxford: Pergamon Press; 1992.
[12] Perzyna P, editor. Localization and fracture phenomenon in inelastic solids. Berlin: Springer; 1998.
[13] Tomita Y. Simulation of plastic instabilities in solid mechanics. Appl Mech Rev 1994;47:171–205.
[14] Wright T. The physics and mathematics of adiabatic shear bands. Cambridge: Cambridge University Press; 2002.
[15] Zhou M, Needleman A, Clifton R. Finite-element simulation of shear localization in plate impact. J Mech Phys Solids 1994;42:423–58.
[16] Zhou M. The growth of shear bands in composite microstructures. Int J Plasticity 1998;14:733–54.
[17] Batra R, Wilson N. Adiabatic shear bands in plane strain deformations of a wha. Int J Plasticity 1998;14:43–60.
[18] Batra R, Love B. Mesoscale analysis of shear bands in high strain rate deformations of tungsten/nickel–iron composites. J Thermal Stresses 2005;28:747–82.
[19] Batra R, Love B. Consideration of microstructural effects in the analysis of adiabatic shear bands in a tungsten heavy alloy. Int J Plasticity 2006;22:1858–78.
[20] Charalambakis N, Baxevanis T. Adiabatic shearing of non-homogenous thermoviscoplastic materials. Int J Plasticity 2004;20:899–914.
[21] Zhu Z, Batra R. Analysis of shear banding in plane strain compression of a bimetallic thermally softening viscoplastic body containing an elliptical void. J Eng Mater Technol 1991;113:382–95.
[22] Batra R, Kwon Y. Adiabatic shear banding in a bimetallic body. Acta Mech 1989;77:281–97.
[23] Dugdale D. Yielding of steel sheets containing slits. J Mech Phys Solids 1960;8:100–4.
[24] Barrenblatt G. The mathematical theory of equilibrium of cracks in brittle fracture. Adv Appl Mech 1962;7:55–129.
[25] Xu X-P, Needleman A. Numerical simulations of fast crack growth in brittle solids. J Mech Phys Solids 1994;42:1397–434.
[26] Camacho G, Ortiz M. Computational modeling of impact damage in brittle materials. Int J Solids Structures 1996;33:2899–938.
[27] Johnson G, Cook W. A constitutive model for metals subjected to large strains, high strain-rates, and high temperatures. In: Proceedings of the seventh international symposium on ballistics, 1983. p. 541–7.
[28] Truesdell C, Noll W. The nonlinear field theories of mechanics. Berlin: Springer; 1965.
[29] Batra R. Elements of continuum mechanics. Reston, VA: American Institute of Aeronautics and Astronomy; 2005.
[30] Ortiz M, Pandolfi A. Finite-deformation irreversible cohesive elements for three-dimensional crack-propagation analysis. Int J Numer Meth Eng 1999;44:1267–82.
[31] Molinari J, Gazonas G, Raghupathy R, Rusinek A, Zhou F. The cohesive element approach to dynamic fragmentation: the question of energy convergence. Int J Numer Meth Eng 2007;69:484–503.
[32] Pandolfi A, Guduru P, Ortiz M, Rosakis A. Three dimensional cohesive-element analysis and experiments of dynamic fracture in c300 steel. Int J Solids Struct 2000;37:3733–60.
[33] Chen W, Ravichandran G. Dynamic compressive behavior of ceramics under lateral confinement. J Phys IV 1994;4:177–82.
[34] Chen W, Ravichandran G. Static and dynamic compressive behavior of aluminum nitride under moderate confinement. J Am Ceramic Soc 1996;79:579–84.
[35] Batra R, Kim C. Analysis of shear banding in twelve materials. Int J Plasticity 1992;8:425–52.
[36] Batra R, Lear M. Adiabatic shear banding in plane strain tensile deformations of eleven thermoelastoviscoplastic materials with finite thermal wave speed. Int J Plasticity 2005;21:1521–45.
[37] Batra R, Ravisankar M. Three-dimensional numerical simulation of the Kalthoff experiment. Int J Fracture 2000;105:161–86.
[38] Batra R, Romano R. Failure of dynamically loaded thermoelastoviscoplastic rectangular plate. AIAA J 2007;45:2015–23.
[39] Batra R, Love B. Crack propagation due to brittle and ductile failures in microporous thermoelastoviscoplastic functionally graded materials. Eng Fracture Mech 2005;72:1954–79.

[40] Onate E, Rojek J, Taylor R, Zienkiewicz O. Non-linear dynamic analysis of solids using linear triangles and tetrahedra. In: Onate E, Owen D, editors. Proceedings of the VII international conference on computational plasticity, Barcelona, 2003.
[41] Courant R, Friedrichs K, Lewy H. Über die partiellen differenzendleichungen der mathematischen physik. Mathematische Annalen 1928;100: 32–74.
[42] Johnson G, Stryk R. Symmetric contact and sliding interface algorithms for intense impulsive loading computations. Comp Meth Appl Mech Eng 2001;190:4531–49.
[43] Batra R, Liang X. Finite deformations of smart structures. Comp Mech 1997;20:427–38.
[44] Hassan N, Batra R. Modeling damage in polymeric composites. Composites B 2008;39:66–82.
[45] Batra R, Kim C. Effect of viscoplastic flow rules on the initiation and growth of shear bands at high strain rates. J Mech Phys Solids 1990;38:859–74.
[46] Batra R, Chen L. Effect of viscoplastic relations on the instability strain, shear band initiation strain, the strain corresponding to the minimum shear band spacing, and the band width in a thermoviscoplastic materials. Int J Plasticity 2001;17:1465–89.

Finite Element Analysis of Projectile Size and Shape Effects on the Probabilistic Penetration Response of High Strength Fabrics

Gaurav Nilakantan, Eric D. Wetzel, Travis A. Bogetti, and John W. Gillespie Jr.

Composite Structures, 94 (2012)

Contents lists available at SciVerse ScienceDirect

Composite Structures

journal homepage: www.elsevier.com/locate/compstruct

Finite element analysis of projectile size and shape effects on the probabilistic penetration response of high strength fabrics

Gaurav Nilakantan [a], Eric D. Wetzel [d], Travis A. Bogetti [d], John W. Gillespie Jr. [a,b,c,*]

[a] Center for Composite Materials, University of Delaware, DE 19716, USA
[b] Department of Materials Science and Engineering, University of Delaware, DE 19716, USA
[c] Department of Civil and Environmental Engineering, University of Delaware, DE 19716, USA
[d] US Army Research Laboratory, Aberdeen Proving Ground, MD 21005, USA

ARTICLE INFO

Article history:
Available online 5 January 2012

Keywords:
Aramid fiber
Fabrics/textiles
Impact behavior
Finite element analysis (FEA)
Probabilistic methods

ABSTRACT

The effects of projectile characteristics on the probabilistic impact response of single-layer fully-clamped flexible woven fabrics is numerically studied using a yarn-level fabric model with a statistical implementation of yarn strengths. Six small and large sized spherical, cylindrical, and conical projectiles of the same mass are considered. Probabilistic velocity response curves which describe the probability of fabric penetration as a function of projectile impact velocity are generated for each projectile type through a series of forty impact simulations at varying impact velocities. The probabilistic fabric impact response is observed to be strongly dependent on the shape of the projectile's impact face and the manner of projectile–yarn interactions at the impact site.

1. Introduction

High strength fabrics woven from continuous-filament aramid yarns are used in flexible protective structures because of their excellent impact performance [1]. The state of the art in finite element (FE) modeling of woven fabric impact is continually improving with recent advances in single-layer filament-level fabric modeling by Wang et al. [2], multi-layer yarn-level fabric modeling by Chocron et al. [3], and single-layer multiscale fabric modeling by Nilakantan et al. [4,5]. Yarn-level models are especially useful to parametrically study how fabric impact performance is affected by factors such as fabric architecture, yarn stiffness and strength, friction, and boundary conditions [6–11]. However, a topic that has been not been systematically addressed with simulations is the effect of the projectile characteristics such as size, shape, mass, velocity, and trajectory on the impact response of flexible woven fabrics. Some experimental studies on projectile effects have been reported [12–14], although the generality and fidelity of the results are limited by a number of factors. For example, the uncertainty introduced by fabric boundary slippage can significantly bias the fabric impact response [15]. The projectile trajectory and exact impact location are also difficult to control with precision. A further limitation of experimental testing is the inability to closely monitor and track individual yarn energy dissipations, interactions with the projectile, and yarn failure at the impact site during the impact event, all of which are important in order to fully understand how different projectiles interact with the woven fabric. These limitations can be overcome with numerical studies, thereby proving them to be a potentially useful complement to experimental investigations.

Talebi et al. [16] numerically studied the effect of the nose angle of conical shaped projectiles on the impact response of fully-clamped single-layer plain-weave Twaron fabrics and concluded that a nose cone angle of 60° provided the most penetration efficiency. Nilakantan et al. [17] studied the effect of projectile characteristics on the impact response of fully-clamped single-layer plain-weave Kevlar fabrics. One large and one small spherical, cylindrical, and conical shaped projectile with the same mass and impact velocity were considered. The conical shaped projectiles were observed to most easily penetrate through the fabric due to the tendency of these projectiles to "window" or push aside the principal yarns. The impact responses in terms of projectile velocity histories and energy transformation histories of the large spherical and small cylindrical projectiles were almost identical to each other.

One limitation of the aforementioned numerical studies is that they simulate all material, geometric, and boundary conditions deterministically, and consequently cannot predict the probabilistic impact response of fabrics. For example the tensile strengths of all yarns in these woven fabric models are assumed to be uniform and identical. However experimental studies indicate that yarn strengths are highly statistical in nature [18]. In a recent study

* Corresponding author at: Center for Composite Materials, University of Delaware, DE 19716, USA. Tel.: +1 302 831 8702; fax: +1 302 831 8525.
E-mail addresses: gauravnilakantan@yahoo.com (G. Nilakantan), gillespi@udel.edu (J.W. Gillespie Jr.).

Nilakantan et al. [19] developed a probabilistic computational framework that allowed the sources of variability (e.g. statistical yarn strengths) to be mapped into the fabric finite element model, which then through a series of impact simulations and a subsequent statistical analysis allowed the prediction of the probabilistic fabric impact response. The experimentally observed zone of mixed results (ZMRs) during fabric impact testing was successfully captured within this probabilistic computational framework. In this paper, the probabilistic computational framework from Ref. [19] is applied to study the effects of projectile size and shape on the impact response of fabrics. A statistical yarn strength model based on previous experimental measurements [18] is implemented to generate a probabilistic penetration response. Results from the present study are compared to the deterministic results reported in Ref. [17] to understand how projectile characteristics affect the probabilistic impact response of fabrics. Probabilistic velocity response (PVR) curves, that describe the probability of fabric penetration for a given projectile velocity, are generated for each projectile type and then compared against each other.

2. Numerical setup and methodology

With the exception of the tensile strengths assigned to the woven yarns, the details of the numerical fabric and projectile models are consistent with Ref. [17] and are therefore only briefly repeated here. Fig. 1 displays the six projectiles chosen for this study. All projectiles have a mass of 0.692 g. The spherical and cylindrical projectiles impact the fabric at the center of a yarn cross-over while the conical projectiles impact the gap in-between the yarns at the center of the fabric. The fabric considered is Kevlar S706, a fabric comprised of 600 denier Kevlar KM2 yarns plain woven at 34 × 34 yarns per inch. Fig. 2a displays the impact test setup. The preprocessor DYNAFAB [20] is used to set up the fabric mesh. The fabric is gripped on all four sides with zero slippage boundaries. The yarns are assigned a linear elastic orthotropic material model. Yarn failure is modeled via element erosion using a maximum principal stress based failure criterion. Fig. 3 displays the cumulative distribution function (CDF) used to describe the statistical yarn tensile strengths of 600 denier Kevlar KM2 spool yarns of gage length 50.8 mm obtained from the experimental work of Nilakantan et al. [18]. A 3-parameter Weibull distribution function was used to generate the CDF, and is given by

$$F = 1 - \exp\left(-\left(\frac{(S-\gamma)}{\theta}\right)^{\beta}\right) \tag{1}$$

where F represents the cumulative probability of yarn failure at a strength of S, and β, θ, and γ respectively represent the shape, scale, and threshold parameters of the 3-parameter Weibull distribution. Table 1 lists the values of these three distribution parameters, the

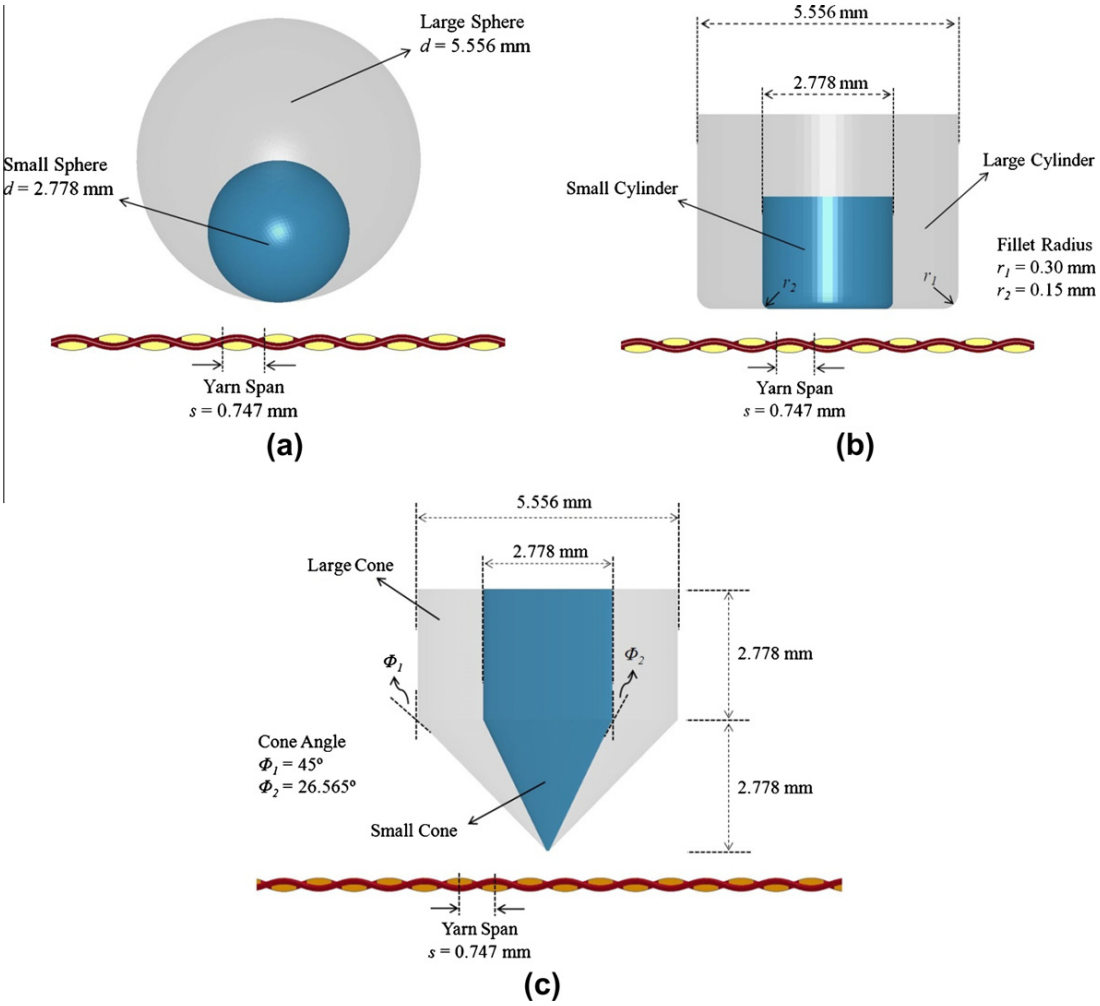

Fig. 1. Shapes and dimensions of the various projectiles used: (a) spherical, (b) cylindrical and (c) conical.

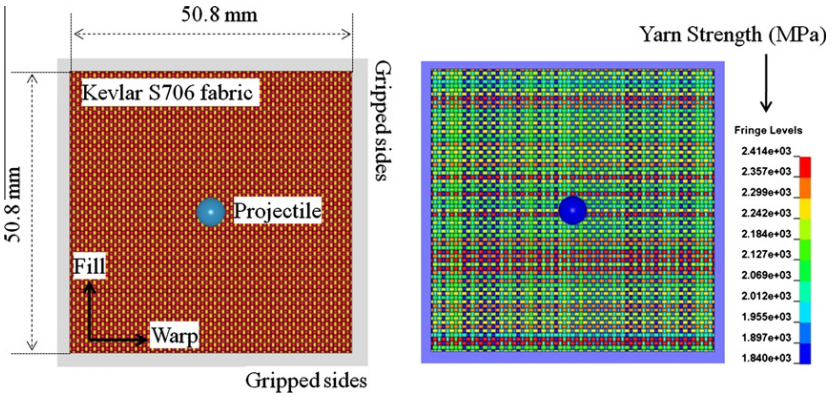

Fig. 2. Numerical model (a) impact test setup, (b) sample yarn strength mappings using the spool based strength distributions adjusted by the filament volume fraction.

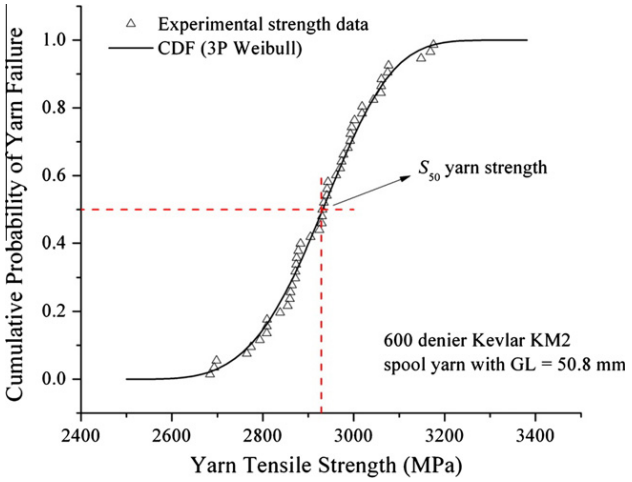

Fig. 3. Yarn strength distribution.

mean (μ) and standard deviation (σ) in the experimental yarn strengths, and the statistical yarn strengths at the 1%, 50%, and 99% probabilities respectively listed as S_1, S_{50}, and S_{99}. The degree of scatter in yarn strengths is given by the coefficient of variation (CV) defined as the percentage ratio of σ to μ.

The statistical yarn strengths are then adjusted by the respective warp and fill yarn filament volume fractions to account for the homogenized nature of the yarn model using the technique described in Ref. [19]. These adjusted strengths are then mapped onto the warp and fill yarns of the fabric model as shown in Fig. 2b where the color map indicates the tensile strength assigned to each yarn. It is assumed that each yarn has a uniform strength that spatially varies from one yarn to another. Forty such unique strength mappings are created. Finally a series of forty impact simulations are run at different impact velocities using the technique described in Refs. [19,21] in order to statistically estimate the Normal distribution parameters (mean η, standard deviation ξ) used to mathematically represent the PVR curve. The dynamic finite element code LS-DYNA [22] is used to run the impact simulations. The CDF of the Normal distribution (i.e. PVR curve) is given by

$$P = \frac{1}{2}\left[1 + \mathrm{erf}\left(\frac{V-\eta}{\xi\sqrt{2}}\right)\right] \tag{2}$$

where P represents the cumulative probability of fabric penetration at an impact velocity V, and erf represents the error function. Because of the symmetry of the Normal distribution, the mean (η) also represents the V_{50} velocity. Using Eq. (2), the expressions for the V_1 and V_{99} velocities are given by

$$\begin{aligned} V_1 &= \eta - 2.3263\xi \\ V_{99} &= \eta + 2.3263\xi \end{aligned} \tag{3}$$

Table 1
Properties of the spool yarn strength distribution [18].

Parameter	Value	Comment
Material	600d Kevlar KM2	Spool yarn with gage length = 50.8 mm
Distribution type	3-Parameter Weibull	3-Parameter Weibull distribution parameters
Shape (β)	4.07	
Scale (θ)	473.36	
Threshold (γ)	2499.34	
S_1 (MPa)	2652	X% of yarns are likely to exhibit a strength less than or equal to S_X
S_{50} (MPa)	2932	
S_{99} (MPa)	3189	
Width = $S_{99} - S_1$ (MPa)	537	
Mean (μ) (MPa)	2929	
Std. Dev. (σ) (MPa)	116	
CV = σ/μ (%)	3.96	

3. Results

Tables 2–4 respectively list the simulation results from the forty impact simulations for the spherical, cylindrical, and conical projectiles. These results include the impact velocity (V_i), residual velocity for penetrating shots (V_r), number of failed warp (N_w) and fill (N_f) yarns, and total number of failed yarns (N_t). The data is arranged in an increasing order of impact velocities. The lowest penetrating shot (V_P) and highest non-penetrating shot (V_{NP}) are listed in bold. Fig. 4 displays the simulation results (symbols) and corresponding PVR curves (smooth lines) for all six projectile cases. The ZMR, defined as the region between V_P and V_{NP} such that $|V_P| < |V_{NP}|$, is successfully captured in all cases. Table 5 lists the maximum likelihood estimates of the mean (η) and standard deviation (ξ) of the Normal distribution functions that are used to represent the PVR curves, the V_1 and V_{99} velocities, and the 95% confidence limits on η and ξ.

The order of impact performance from highest to lowest fabric V_{50} velocities is as follows: large cylinder, small cylinder, large sphere, large cone, small sphere, and small cone. The V_{50} velocities corresponding to the large sphere (45.54 m/s) and small cylinder (45.61 m/s) are almost identical. The V_{50} for the large cylinder (61.21 m/s) is considerably higher than all other projectiles, and the V_{50} for the small cone (20.23 m/s) is considerably lower than all other projectiles.

Table 2
simulation results for the spherical projectiles.

Shot #	Large sphere					Small sphere				
	V_i (m/s)	V_r (m/s)	N_w	N_f	N_{tot}	V_i (m/s)	V_r (m/s)	N_w	N_f	N_{tot}
1	30.00	–	–	–	–	15.00	–	–	–	–
2	35.00	–	–	–	–	25.00	–	–	–	–
3	40.00	–	–	–	–	30.00	–	–	–	–
4	42.50	–	–	–	–	32.00	–	–	–	–
5	43.00	–	–	–	–	32.20	–	–	–	–
6	43.50	–	–	–	–	32.50	–	–	–	–
7	43.80	–	–	–	–	32.80	–	–	–	–
8	44.00	–	–	–	–	33.00	–	–	–	–
9	44.10	–	–	–	–	33.10	–	–	–	–
10	44.20	–	–	–	–	33.20	–	–	–	–
11	44.50	–	–	–	–	33.40	–	–	–	–
12	44.70	–	–	–	–	33.50	–	–	–	–
13	44.80	–	–	–	–	**33.60**	**0.80**	**2**	**2**	**4**
14	45.00	–	–	–	–	33.70	–	–	–	–
15	45.00	–	–	–	–	33.80	–	–	–	–
16	**45.00**	**6.72**	**5**	**4**	**9**	33.80	–	–	–	–
17	45.00	–	–	–	–	33.90	–	–	–	–
18	45.10	2.24	7	4	11	34.00	–	–	–	–
19	45.20	4.34	5	5	10	34.00	3.24	3	1	4
20	45.40	–	–	–	–	34.10	1.01	2	1	3
21	45.50	–	–	–	–	34.20	1.12	2	2	4
22	45.60	6.25	5	5	10	34.30	–	–	–	–
23	45.80	3.56	5	5	10	34.40	2.53	1	3	4
24	45.90	7.85	5	5	10	34.50	–	–	–	–
25	46.00	5.11	6	3	9	34.60	1.44	2	3	5
26	46.20	8.94	5	5	10	34.70	2.63	3	2	5
27	46.40	9.60	5	5	10	**34**.80	–	–	–	–
28	46.50	4.96	5	6	11	34.90	2.00	2	3	5
29	46.60	–	–	–	–	34.90	4.08	3	1	4
30	**46.70**	–	–	–	–	35.00	3.40	2	3	5
31	46.80	0.22	6	5	11	35.00	5.36	2	3	5
32	46.90	9.67	5	5	10	35.10	3.44	2	3	5
33	47.00	6.98	5	5	10	35.20	1.64	2	3	5
34	47.00	14.42	5	6	11	35.30	4.25	3	3	6
35	47.10	5.65	5	5	10	35.40	4.60	2	3	5
36	47.20	11.05	6	5	11	35.50	3.51	2	3	5
37	47.50	3.91	6	4	10	35.80	4.81	1	1	2
38	50.00	14.11	5	5	10	36.00	4.26	1	3	4
39	55.00	15.19	5	6	11	40.00	12.35	3	3	6
40	60.00	30.13	7	5	12	45.00	21.09	2	3	5
	#NP 20	$\boldsymbol{N_\mu}$	5.4	4.9	10.3	**#NP** 20	$\boldsymbol{N_\mu}$	2.1	2.5	4.6
		$\boldsymbol{N_\sigma}$	0.7	0.7	0.7		$\boldsymbol{N_\sigma}$	0.6	0.8	0.9
	#P 20	**Min**	5	3	9	**#P** 20	**Min**	1	1	2
		Max	7	6	12		**Max**	3	3	6

N_μ – mean number of failed yarns.
N_σ – standard deviation in number of failed yarns.
#NP – number of non-penetrations.
#P – number of penetrations.

The degree of variability in fabric impact performance can be assessed by the width of the ZMR or width of the PVR curve, with a wider PVR curve implying greater variability in impact performance. However a more useful measure to compare the impact performance variability between different fabrics and impact scenarios is the CV of the PVR curve ($=\xi/\eta\%$) which provides a normalized measure of the impact performance variability. Fig. 5 displays the widths and CVs of the PVR curves and the V_{50} velocities corresponding to all six projectile cases, arranged left to right from highest to lowest CV values. The plot shows that conical, spherical, and cylindrical projectiles produce the highest, intermediate, and lowest CV values, respectively, demonstrating a clear correspondence between projectile shape and CV performance. The small conical projectile results in the greatest variability in fabric impact performance and the large cylinder results in the least variability. The plot also shows that V_{50} generally trends upwards as CV decreases.

Fig. 6 displays the means and standard deviations in the number of failed warp (N_{warp}) and failed fill (N_{fill}) yarns, as well as total number of failed yarns (N_{total}), for all penetrating impact simulations. The V_{50} values for each projectile are also given in the figure, and the data is arranged in order of increasing N_{total}. The large cylindrical projectile case results in the highest N_{warp}, N_{fill}, and N_{total} values while the small conical projectile case results in the smallest corresponding values. These projectiles were also respectively associated with the lowest and highest CV values (see Fig. 5). However, unlike the CV trends, here the trends for N_{total} are dominated first by projectile size, with the smallest projectiles producing the lowest numbers of failed yarns and the largest projectiles producing the highest numbers of failed yarns. Projectile shape is still significant, with the cone, sphere, and cylinder projectiles providing the smallest, intermediate, and largest numbers of failed yarns within both the small and large projectile groupings. It is also apparent that increasing numbers of failed yarns correlate with increased V_{50} values.

Fig. 7 compares the PVR curves of the large spherical and small cylindrical projectiles, which intersect at the V_{56} velocity. The large spherical projectile PVR curve is wider implying a greater degree of impact performance variability.

Table 3
Simulation results for the cylindrical projectiles.

Shot #	Large cylinder					Small cylinder				
	V_i (m/s)	V_r (m/s)	N_w	N_f	N_{tot}	V_i (m/s)	V_r (m/s)	N_w	N_f	N_{tot}
1	50.00	–	–	–	–	30.00	–	–	–	–
2	55.00	–	–	–	–	40.00	–	–	–	–
3	59.00	–	–	–	–	43.00	–	–	–	–
4	59.50	–	–	–	–	44.00	–	–	–	–
5	60.00	–	–	–	–	44.10	–	–	–	–
6	60.10	–	–	–	–	44.30	–	–	–	–
7	60.30	–	–	–	–	44.50	–	–	–	–
8	60.40	–	–	–	–	44.60	–	–	–	–
9	60.50	–	–	–	–	44.80	–	–	–	–
10	60.60	–	–	–	–	44.90	–	–	–	–
11	**60.70**	**0.13**	**5**	**8**	**13**	45.00	–	–	–	–
12	60.70	2.67	6	7	13	45.10	–	–	–	–
13	60.80	–	–	–	–	45.20	–	–	–	–
14	60.90	–	–	–	–	45.20	–	–	–	–
15	61.00	–	–	–	–	**45.30**	**0.90**	**3**	**3**	**6**
16	61.10	–	–	–	–	45.40	–	–	–	–
17	61.10	–	–	–	–	45.40	–	–	–	–
18	61.20	–	–	–	–	45.50	5.04	3	4	7
19	61.20	–	–	–	–	45.60	3.25	3	3	6
20	61.30	–	–	–	–	45.80	0.18	3	3	6
21	61.30	6.46	6	7	13	45.90	–	–	–	–
22	61.40	2.83	9	6	15	46.00	4.99	3	5	8
23	**61.40**	–	–	–	–	46.00	0.26	3	3	6
24	61.50	2.34	6	7	13	**46.10**	–	–	–	–
25	61.50	5.64	5	7	12	46.10	0.02	3	3	6
26	61.60	2.53	8	8	16	46.20	1.64	3	3	6
27	61.60	6.55	5	7	12	46.20	6.90	3	3	6
28	61.70	1.68	5	7	12	46.30	0.98	3	3	6
29	61.80	6.30	7	7	14	46.30	1.76	4	3	7
30	62.00	6.74	5	7	12	46.40	1.01	3	3	6
31	62.10	7.77	7	7	14	46.50	4.36	3	4	7
32	62.20	3.94	7	7	14	46.80	6.50	3	3	6
33	62.30	6.64	6	7	13	46.90	6.38	3	3	6
34	62.50	8.22	7	7	14	47.00	1.26	3	3	6
35	62.80	10.03	6	7	13	47.20	5.94	4	3	7
36	63.00	6.45	6	8	14	47.30	7.91	3	4	7
37	65.00	11.48	7	8	15	47.50	1.30	3	4	7
38	67.00	14.80	6	8	14	47.70	7.60	4	4	8
39	70.00	21.85	7	10	17	50.00	9.99	3	3	6
40	80.00	34.99	8	9	17	60.00	26.90	3	4	7
	#NP 19	N_μ	6.4	7.4	13.8	**#NP** 18	N_μ	3.1	3.4	6.5
		N_σ	1.1	0.9	1.5		N_σ	0.4	0.6	0.7
	#P 21	**Min**	5	6	12	**#P** 22	**Min**	3	3	6
		Max	9	10	17		**Max**	4	5	8

N_μ – mean number of failed yarns.
N_σ – standard deviation in number of failed yarns.
#NP – number of non-penetrations.
#P – number of penetrations.

4. Discussion

Fig. 5 shows that the PVR curve CV value correlates strongly with the shape of the projectile. Keeping in mind that all simulations are based on fabrics with the same statistical yarn strength distribution (i.e. same mean strength and same degree of scatter in yarn strengths), clearly this difference in CV must arise from the difference in the manner in which the projectiles engage the principal yarns. It was shown in Ref. [17] that the conical projectiles are easily able to push aside the principal yarns (also known as "windowing") by virtue of their sharply pointed impact faces, leading to a highly sequential (time-dispersed) projectile–yarn interaction and failure pattern. Because of the high differences in yarn loadings at each time step, the progression of failure and penetration will be highly sensitive to the individual yarn strengths. In contrast, with their flat-impact face, the cylindrical projectiles induce a more simultaneous loading and catastrophic failure of the principal yarns [17]. By simultaneously engaging a greater number of yarns at the impact site, the yarn strengths are "averaged" to produce a more consistent failure response. Spherical projectiles, with a shape intermediate between cone and cylinder, produce intermediate CV results. One can also then conclude that for a large enough flat-faced projectile that spans the entire range of statistical yarn strengths, one may see little to no variability in impact performance. This hypothesis is supported by the observation that, for the present set of projectiles, the large cylindrical projectile results in the smallest CV values. Furthermore, the strong correlation between CV and projectile shape noted in Fig. 5 reinforces the concept that sequential failure, such as for conical projectiles, leads to wider performance variation while blunter projectiles produce more consistent penetration behavior.

It is important to remember that the conical projectiles impacted the gap between yarns while the spherical and cylindrical projectiles impacted the center of a yarn cross-over at the center of the fabric. Shifting the shot location of the cylindrical projectiles to an interstitial gap would not be expected to have a significant effect on the resulting penetration behavior, due to their blunt face. However, changing the sphere impact location to an interstitial gap would

Table 4
Simulation results for the conical projectiles.

Shot #	Large cone					Small cone				
	V_i (m/s)	V_r (m/s)	N_w	N_f	N_{tot}	V_i (m/s)	V_r (m/s)	N_w	N_f	N_{tot}
1	30.00	–	–	–	–	14.00	–	–	–	–
2	40.00	–	–	–	–	15.00	–	–	–	–
3	41.70	–	–	–	–	17.00	–	–	–	–
4	42.00	–	–	–	–	17.50	–	–	–	–
5	42.20	–	–	–	–	18.00	–	–	–	–
6	**42.30**	**2.12**	**6**	**4**	**10**	18.50	–	–	–	–
7	42.60	–	–	–	–	19.00	–	–	–	–
8	42.70	–	–	–	–	19.10	–	–	–	–
9	42.80	–	–	–	–	19.20	–	–	–	–
10	42.90	–	–	–	–	19.30	–	–	–	–
11	43.00	–	–	–	–	19.40	–	–	–	–
12	43.00	7.56	5	4	9	**19.50**	**3.18**	**1**	**2**	**3**
13	43.10	–	–	–	–	19.60	1.64	1	2	3
14	43.10	–	–	–	–	19.60	–	–	–	–
15	43.20	–	–	–	–	19.70	3.39	1	2	3
16	43.30	5.48	4	4	8	19.80	–	–	–	–
17	43.40	–	–	–	–	19.90	2.98	1	2	3
18	43.50	–	–	–	–	20.00	–	–	–	–
19	43.50	0.18	4	6	10	20.20	1.10	1	2	3
20	43.60	–	–	–	–	20.30	2.77	1	2	3
21	43.70	1.52	5	4	9	20.40	–	–	–	–
22	43.80	–	–	–	–	20.50	3.65	1	2	3
23	43.90	1.90	6	5	11	20.60	–	–	–	–
24	44.00	–	–	–	–	20.70	4.48	1	2	3
25	44.10	3.99	5	4	9	20.80	4.22	2	2	4
26	44.10	–	–	–	–	21.00	4.65	1	2	3
27	44.20	7.93	5	4	9	21.10	–	–	–	–
28	**44.30**	–	–	–	–	21.20	–	–	–	–
29	44.40	5.20	6	5	11	21.30	5.00	2	2	4
30	44.50	2.61	5	5	10	21.40	4.45	2	1	3
31	44.60	2.98	4	4	8	**21**.50	–	–	–	–
32	44.80	6.89	5	4	9	21.60	5.95	1	2	3
33	44.90	10.55	7	4	11	21.70	4.48	2	1	3
34	45.00	9.41	6	4	10	21.80	6.64	2	1	3
35	45.10	1.27	5	5	10	22.10	6.91	1	2	3
36	45.20	6.77	6	4	10	22.20	6.15	1	2	3
37	45.30	5.70	6	4	10	22.50	7.18	2	1	3
38	45.50	11.19	6	4	10	24.00	8.28	1	2	3
39	50.00	16.89	6	5	11	25.00	10.89	2	1	3
40	55.00	24.98	7	4	11	35.00	25.79	2	2	4
	#NP 20	N_μ	5.5	4.4	9.8	**#NP** 19	N_μ	1.4	1.8	3.1
		N_σ	0.9	0.6	1.0		N_σ	0.5	0.4	0.4
	#P 20	**Min**	4	4	8	**#P** 21	**Min**	1	1	3
		Max	7	6	11		**Max**	2	2	4

N_μ – mean number of failed yarns.
N_σ – standard deviation in number of failed yarns.
#NP – number of non-penetrations.
#P – number of penetrations.

likely lead to more windowing, and could lead to a more time-dispersed and sequential failure pattern as compared to the current impact at a yarn cross-over. Therefore, CV values for the spherical projectile might be higher when impacted at an interstitial gap.

It should also be noted that sharp-edged flat-faced cylinders have been experimentally shown [12] to promote a shearing mode of yarn failure at the impact site which can induce failure before tensile elongation based failure limits are reached. Such effects are not captured by the present study, since we only consider a tensile mode of yarn failure due to a lack of available yarn shear strength data. The circumferential edges of our cylindrical projectiles are also given a slight radius to minimize stress concentration effects at the projectile edges.

Fig. 6 shows that the number of failed yarns tracks more with strongly projectile size, rather than projectile shape. This trend is not surprising, since for a fixed yarn architecture a higher number of yarns will be engaged as projectile size increases. Projectile shape still has a significant influence over number of failed yarns, however, since sharper projectiles are more likely to window the fabric and will require fewer yarn failures to accommodate penetration. The strong correlation between V_{50} values and number of failed yarns is also not surprising, as more total projectile energy is required to fail a larger number of yarns.

The probabilistic simulations show nearly identical V_{50} values for the large sphere (45.54 m/s) and small cylinder (45.61 m/s) projectiles. Fig. 7 displays the projectile velocity histories for the large spherical and small cylindrical projectiles with a deterministic implementation [17] of yarn strengths for a non-penetrating and a penetrating shot respectively chosen roughly 10 m/s below (i.e. 35 m/s) and 5 m/s above (i.e. 50 m/s) the V_{50} velocity. These projectile velocity histories almost overlap each other. The similarity between the V_{50} velocities and deterministic simulations can be explained based on the previously observed trend that, for a fixed degree of scatter in yarn strengths and for a given projectile, the V_{50} values for probabilistically modeled fabric impacts trend linearly with the mean yarn strength [21]. Thus the V_{50} velocity can be thought of as a response to the "average" yarn strength. It is therefore logical that if both large spherical and small cylindrical projectiles produce almost identical impact responses when failure is modeled deterministically using the mean yarn strength for all

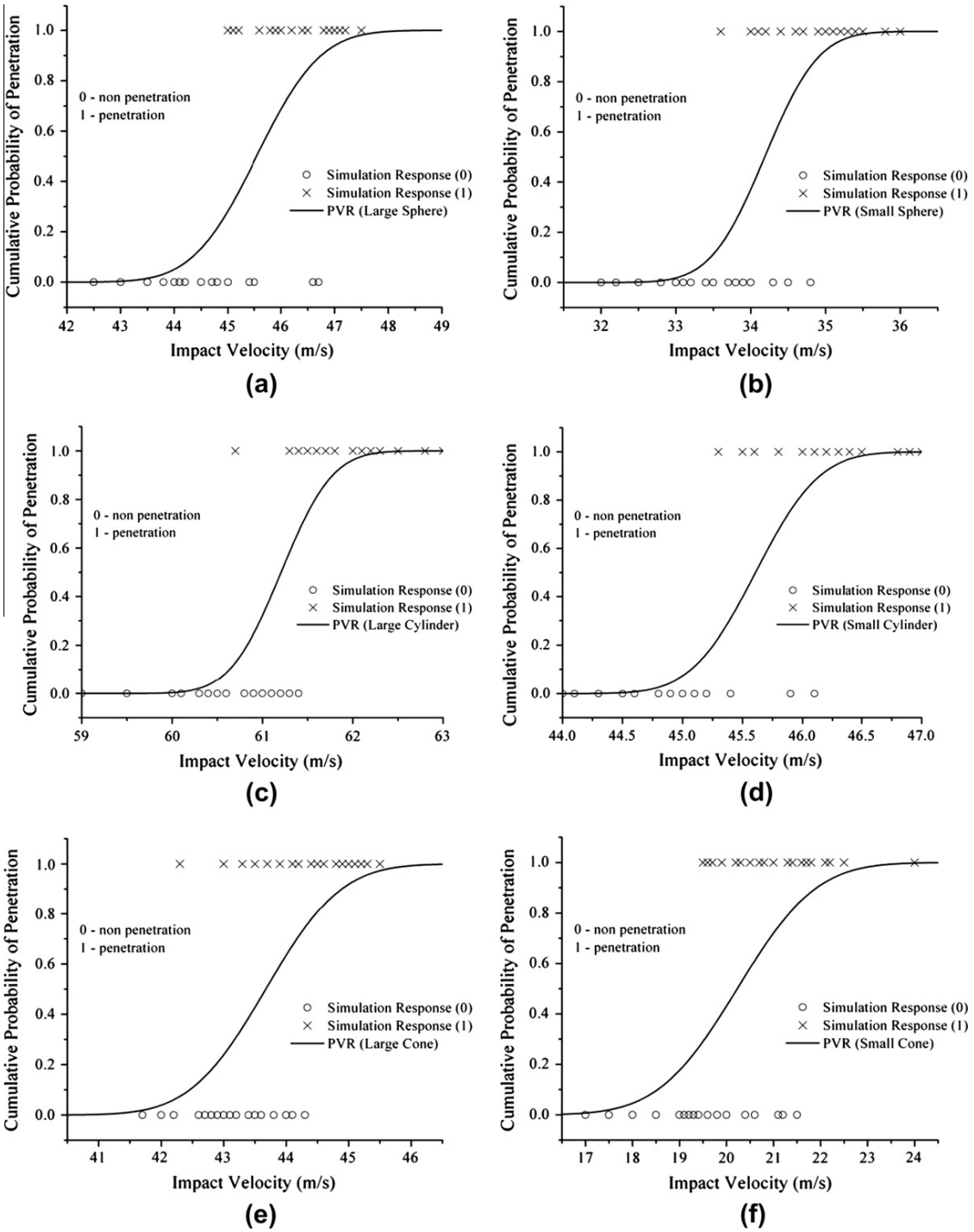

Fig. 4. Simulation results and PVR curves: (a) large sphere, (b) small sphere, (c) large cylinder, (d) small cylinder, (e) large cone and (f) small cone.

yarns, then these same projectiles should also produce similar V_{50} velocities.

In spite of their similar V_{50} values, however, the large spherical and small cylindrical projectiles show different V_1 and V_{99} values, with the large spherical projectile producing a wider fabric PVR curve and a higher CV (Table 5 and Fig. 8). This effect was previously explained based on the manner in which the projectile engages the principal yarns. The more simultaneous loading and catastrophic failure of the principal yarns when engaged by the cylindrical projectile leads a decreased sensitivity to the yarn strength variability and consequently a narrower PVR curve.

5. Conclusions

The probabilistic impact performance of a single-layer fully-clamped plain weave Kevlar fabric impacted by projectiles with the same mass but different sizes and shapes was studied. The yarn-level fabric finite element model was based on a statistical

Table 5
PVR curve parameters.

		Large sphere	Small sphere	Large cylinder	Small cylinder	Large cone	Small cone
# Test shots		40	40	40	40	40	40
MLE estimate of η (m/s)		45.54	34.19	61.21	45.61	43.67	20.23
MLE estimate of ξ (m/s)		0.94	0.57	0.45	0.42	0.95	1.32
CV = ξ/η (%)		2.07	1.66	0.73	0.92	2.18	6.53
V_1 velocity (m/s)		43.35	32.87	60.17	44.64	41.46	17.16
V_{99} velocity (m/s)		47.73	35.50	62.25	46.58	45.88	23.30
Width of PVR = $V_{99} - V_1$ (m/s)		4.38	2.63	2.08	1.94	4.42	6.14
Width of ZMR (m/s)		1.70	1.20	0.70	0.80	2.00	2.00
95% Confidence limits	η_{lower} (m/s)	44.96	33.82	60.92	45.3	43.16	19.43
	η_{upper} (m/s)	46.08	34.53	61.5	45.89	44.21	20.93
	ξ_{lower} (m/s)	0.57	0.33	0.25	0.24	0.57	0.76
	ξ_{upper} (m/s)	1.9	1.12	0.94	0.84	2.2	2.97

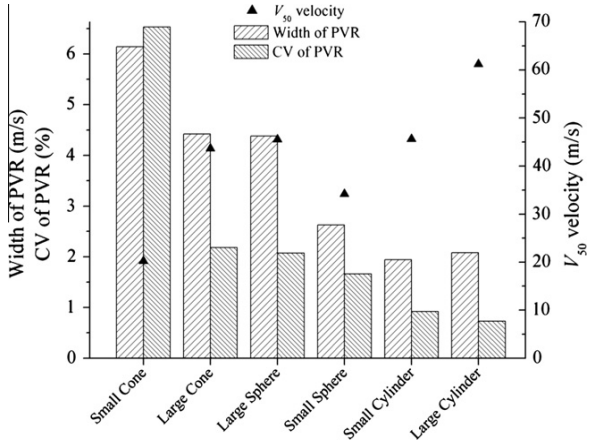

Fig. 5. Comparison of variability in the probabilistic fabric impact performances.

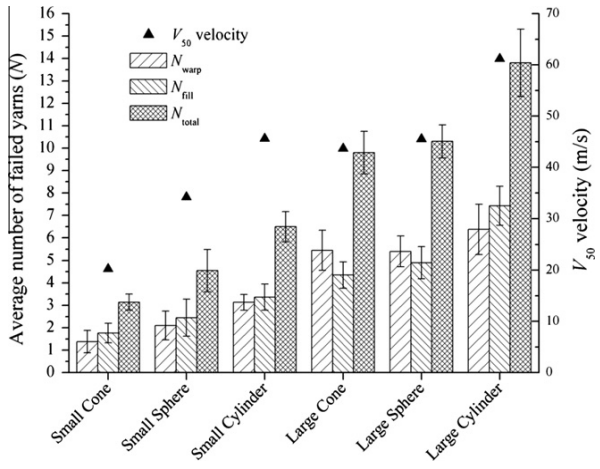

Fig. 6. Yarn failure analysis.

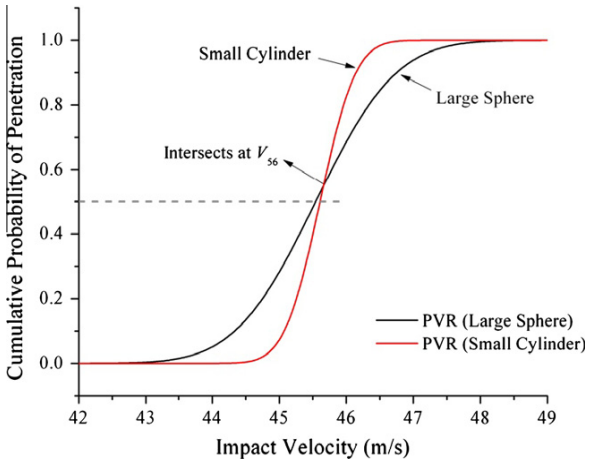

Fig. 7. Comparison of PVR curves for the large sphere and small cylinder cases.

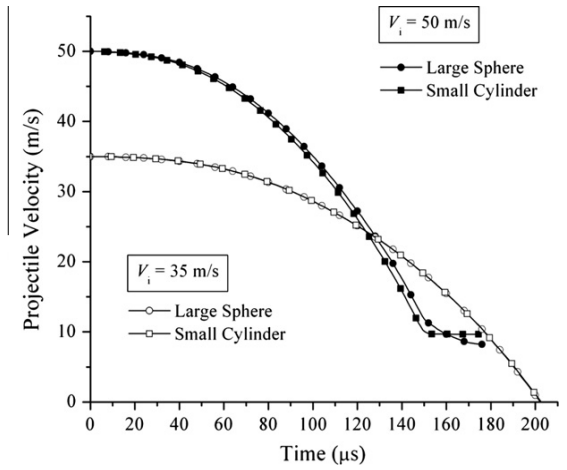

Fig. 8. Comparison of deterministic impact results for the large spherical and small cylindrical projectiles.

implementation of yarn strengths thereby enabling the capture of the zone of mixed results (ZMR). Probabilistic velocity response (PVR) curves were generated for each projectile case through a series of impact simulations and then compared with one another.

The simulations demonstrate that projectile size and shape have an important effect on the probabilistic response of fabrics. Sharper, pointed projectiles such as the conical projectiles result in a sequential manner of projectile–yarn interaction and a sequential (time-dispersed) yarn failure pattern, while flatter and blunter projectiles such as the cylindrical projectiles result in a simultaneous manner of projectile–yarn interaction and a simultaneous or catastrophic yarn failure pattern. The sequential yarn failures lead to more sensitivity to the strengths of individual yarns and a higher variability in response, as evidenced by higher standard deviation and CV values for the PVR curves of conical projectiles as compared to spherical projectiles. The cylindrical projectiles showed the smallest CV values. For a given projectile shape, a larger impact face will result

in a larger total number of failed warp and failed fill yarns at the impact site. However for the same projected impact face area, a pointed projectile will more easily be able to push aside the principal yarns at the impact site resulting in the failure of a fewer number of principal yarns.

These results could have important implications for understanding how practical protective barriers, such as personnel protective clothing, respond to projectiles with different geometries. The concept of reducing penetration response variability, an important constraint on the practical design of protective clothing, by loading more yarns simultaneously may also serve as inspiration for new barrier design concepts.

The probabilistic simulations were able to distinguish between the impact responses of the large spherical and small cylindrical projectiles, which the deterministic simulations were unable to do. An important conclusion drawn was that decisions regarding impact performance cannot be based only on the V_{50} velocity, rather depending on the design criteria of the protective target and projectile, the V_1 and V_{99} velocities respectively become important considerations. Future studies will investigate how the trends reported in this study vary when the fabric boundary conditions are changed from fixed–fixed to fixed–free and free–free, in which case inter-yarn friction will become an important consideration. As suitable material data becomes available, yarn failure modes apart from tensile elongation will be implemented such as yarn transverse shearing and filament crushing modes. Such additional failure modes will become especially important when analyzing multi-layered fabric targets.

Acknowledgements

This research was sponsored by the Army Research Laboratory and was accomplished under Cooperative Agreement No. W911NF-06-2-0011. The views and conclusions contained in this document are those of the authors and should not be interested as representing the official policies, either expressed or implied, of the Army Research Laboratory or the US Government. The US Government is authorized to reproduce and distribute reprints for Government purposes notwithstanding any copyright notation herein.

References

[1] Tabiei A, Nilakantan G. Ballistic impact of dry woven fabric composites: a review. Appl Mech Rev 2008;61(1):010801–13.
[2] Wang Y, Miao Y, Swenson D, Cheeseman BA, Yen C, LaMattina B. Digital element approach for simulating impact and penetration of textiles. Int J Impact Eng 2010;37(5):552–60.
[3] Chocron S, Figueroa E, King N, Kirchdoerfer T, Nicholls AE, Sagebiel E, et al. Modeling and validation of full fabric targets under ballistic impact. Compos Sci Technol 2010;70(13):2012–22.
[4] Nilakantan G, Keefe M, Bogetti TA, Adkinson A, Gillespie Jr JW. On the finite element analysis of woven fabric impact using multiscale modeling techniques. Int J Solid Struct 2010;47(17):2300–15.
[5] Nilakantan G, Keefe M, Bogetti TA, Gillespie Jr JW. Multiscale modeling of the impact of textile fabrics based on hybrid element analysis. Int J Impact Eng 2010;37(10):1056–71.
[6] Nilakantan G, Keefe M, Gillespie Jr JW, Bogetti TA, Adkinson R. A study of material and architectural effects on the impact response of 2D and 3D dry textile composites using LS-DYNA®. 7th European LS-DYNA conference, Salzburg, Austria, May 14–15, 2009.
[7] Nilakantan G, Keefe M, Gillespie Jr JW, Bogetti T, Adkinson R. A numerical investigation into the effects of 3D architecture on the impact response of flexible fabrics. Second world conference on 3D fabrics and their applications, Greenville, South Carolina, USA, April 6–7, 2009.
[8] Rao MP, Duan Y, Keefe M, Powers BM, Bogetti TA. Modeling the effects of yarn material properties and friction on the ballistic impact of a plain-weave fabric. Compos Struct 2009;89(4):556–66.
[9] Duan Y, Keefe M, Bogetti TA, Cheeseman BA, Powers B. A numerical investigation of the influence of friction on the energy absorption by a high-strength fabric subjected to ballistic impact. Int J Impact Eng 2006;32:1299–312.
[10] Gu B, Xu J. Finite element calculation of 4-step 3-dimensional braided composite under ballistic perforation. Composites: Part B 2004;35:291–7.
[11] Gu B. Ballistic penetration of conically cylindrical steel projectile into plain-woven fabric target – a finite element simulation. J Compos Mater 2004;38(22):2049–74.
[12] Tan VBC, Lim CT, Cheong CH. Perforation of high-strength fabric by projectiles of different geometry. Int J Impact Eng 2003;28:207–22.
[13] Lim CT, Tan VBC, Cheong CH. Perforation of high-strength double-ply fabric system by varying shaped projectiles. Int J Impact Eng 2002;27:577–91.
[14] Montgomery TG, Grady PL, Tomasino C. The effects of projectile geometry on the performance of ballistic fabrics. Text Res J 1982;52(7):442–50.
[15] Nilakantan G, Wetzel ED, Merrill R, Bogetti TA, Adkinson R, Keefe M, Gillespie Jr JW. Experimental and numerical testing of the V_{50} impact response of flexible fabrics: addressing the effects of fabric boundary slippage. 11th international LS-DYNA users conference, Dearborn, MI, USA, June 6–8, 2010.
[16] Talebi H, Wong SV, Hamouda AMS. Finite element evaluation of projectile nose angle effects in ballistic perforation of high strength fabric. Compos Struct 2009;87(4):314–20.
[17] Nilakantan G, Wetzel ED, Bogetti TA, Gillespie Jr JW. A deterministic finite element analysis of the effects of projectile characteristics on the impact response of fully clamped flexible woven fabrics. Compos Part B: Eng, submitted for publication.
[18] Nilakantan G, Abu-Obaid A, Keefe M, Gillespie Jr JW. Experimental evaluation and statistical characterization of the strength and strain energy density distribution of Kevlar KM2 yarns: exploring length-scale and weaving effects. J Compos Mater 2011;45(17):1749–69.
[19] Nilakantan G, Keefe M, Wetzel ED, Bogetti TA, Gillespie Jr JW. Computational modeling of the probabilistic impact response of flexible fabrics. Compos Struct 2011;93:3163–74.
[20] Nilakantan G. DYNAFAB User Manual Version 1.0. Nilakantan Composites. ISBN 978-81-910696-0-0, May 2010.
[21] Nilakantan G, Keefe M, Wetzel ED, Bogetti TA, Gillespie Jr JW. Effect of statistical yarn tensile strength on the probabilistic impact response of woven fabrics. Compos Sci and Technol 2012;72(2):320–9.
[22] Livermore Software Technology Corporation. LS-DYNA Keyword User's Manual Version 971, May 2007.

A Ballistic Material Model for Continuous-Fiber Reinforced Composites

Chian-Fong Yen

International Journal of Impact Engineering, 46 (2012)

Contents lists available at SciVerse ScienceDirect

International Journal of Impact Engineering

journal homepage: www.elsevier.com/locate/ijimpeng

A ballistic material model for continuous-fiber reinforced composites

Chian-Fong Yen*

U.S. Army Research Laboratory, Aberdeen Proving Ground, MD 21005, United States

ARTICLE INFO

Article history:
Received 10 November 2010
Received in revised form
27 December 2011
Accepted 28 December 2011
Available online 30 January 2012

Keywords:
Ballistic impact
Composite materials
Damage mechanics
Material model
Rate effect

ABSTRACT

A ply-level material constitutive model for plain-weave composite laminates has been developed to enable computational analyses of progressive damage/failure in the laminates under high velocity ballistic impact conditions. In this model, failure-initiation criteria and damage evolution laws are introduced to account for the major fiber-failure modes (tensile, compressive, punch shear and crush loading). In addition, two matrices related failure modes (in-plane shear and through the thickness delamination) are also accounted for. These types of fiber and matrix failure modes are commonly observed during a ballistic event. The composite-material model has been implemented within LS-DYNA as a user-defined material subroutine and used successfully to predict the damage and ballistic behavior of composite laminates subjected to various ballistic impact conditions. It is hoped that the availability of this material model will help facilitate the development of composite structures with enhanced ballistic survivability.

Published by Elsevier Ltd.

1. Introduction

Composites have long been used in personnel and vehicle protective/structural applications for protection against various ballistic and blast threats. Composite materials are well suited to this role because of their superior stiffness and strength-to-weight properties over many other classes of materials. Utilization of composite materials provides mass efficiency with enhanced survivability for various combat vehicles and protection devices. To rapidly develop novel protective systems, it is essential to employ advanced numerical simulations together with experimental evaluation to assess a range of material and structural solutions. However, in order to accurately capture the protective performance using numerical simulations, the composite material behavior must be modeled correctly. Toward this goal, a robust material model for composites subjected to blast and ballistic impact has been developed and validated by the author in preceding decades [1–4]. This paper reports an extension of the previous work to include a unidirectional model together with the validation of modeling composite ballistic behavior using newly acquired material and ballistic test data.

While composites have been effectively used in personnel and vehicle protection since World War II, modeling the progression of damage and ultimate failure caused by blast and ballistic impact has only been developed since the 1980's. This is due to the enormous complexity of the material loading and failure that occurs when a composite is impacted and perforated. During ballistic impact, composite laminates absorb energy primarily due to the failure of fibers under axial tension/compression, punch shear and crush loading. Failure modeling of composite materials under impact loading has been the subject of numerous studies [5–8]. However, few studies have been reported on modeling progressive damage/failure in composites under high strain rate ballistic loading. The composite failure model originally adopted within LS-DYNA is the Chang–Chang [9] model (MAT 22), which provides various fiber and matrix failure modes solely due to in-plane stresses in unidirectional lamina. In this 2D failure model, the failure mode due to out-of-plane shear and normal stresses are neglected. While this may be sufficient for composite structures under in-plane loading, this model is not expected to adequately represent composite material response under transverse impact loading conditions during which all six stress components are known to contribute to damage/failure development.

A continuum damage mechanics (CDM) model for unidirectional composite layers based on plane-stress state was reported by Matzenmiller et al. [10]. Studies reported by William and Vaziri [11] and Van Hoof et al. [12], have shown that CDM-type post failure-initiation models can significantly improve the prediction of impact progressive damage/failure in composite structures. Note that non-interactive failure criteria (based on maximum strain assumption) due to tension, punch shear and crush loading were originally proposed by Van Hoof et al. [12], to account for the major

* Tel.: +1 410 306 0732; fax: +1 410 306 0759.
E-mail address: chianfong.yen@us.army.mil.

failure modes accompanying ballistic impact of composite materials. This model, however, neglects the rate dependency of the material response. The same deficiency, i.e., a lack of accountability for the strain-rate dependent effects in composite materials, can be assigned to more recent CDM composite material models such as [13–15]. The latter models are highly advanced in capturing various continuously distributed static intra-lamina and inter-lamina damage mechanisms (e.g. fiber breakage within the yarns, fiber/matrix de-bonding, diffuse delamination/inter-lamina separation etc.) as well as in accounting for discrete damage modes (e.g., transverse micro-cracking). Nevertheless, they fail to include the effect of rate dependency in composite materials and, hence, are not considered reliable for modeling the behavior of these materials under high strain rate loading conditions.

High strain rate and high pressure loading conditions generally occur in the impact area when a composite material is subjected to high velocity ballistic impact. Previous studies have shown that certain composite materials subjected to high rate loadings, such as blast and ballistic impact, exhibit significant strain rate sensitivity of both their stiffness and strength. Experimental characterization of the mechanical behavior of composite materials under high strain rate conditions has been reported in literature [16,17]. It has been shown that some protective materials such as woven glass and aramid composites exhibit significant rate sensitivity [18,19].

To enhance the modeling capability of the progressive failure behavior of composite laminates due to transverse impact, a rate-dependent composite lamina model based on the 3D stress field has been developed and reported herein. The model takes into account rate dependency of the composite-material response and can be used to accurately represent the aforementioned experimentally observed strain-rate effects. In this model, damage-initiation criteria have been developed for all major fiber failure (tensile, compressive, punch shear and crush loading) and matrix failure (in-plane shear and through the thickness delamination) modes. These are supplemented with the corresponding continuum damage-mechanics evolution laws/equations which characterize damage progression and the associated decrease in material stiffness.

The model has been implemented into explicit dynamic codes such as LS-DYNA as a user-defined subroutine. This material model can be used to effectively simulate fiber failure, matrix damage, and delamination behavior under different closure/loading conditions of the internal delaminated surfaces/cracks (e.g., crack-face opening, closure and sliding). Furthermore, this progressive failure modeling approach enables the prediction of delamination when locations of delamination sites cannot be anticipated; i.e., locations of potential delamination initiation are calculated without a-priori definition of an interlaminar crack surfaces. This material model has been successfully utilized previously by the author to characterize the impact damage in composite structures for a wide range of impact problems [1–4].

The organization of the paper is as follows: A brief account of the key features/relations of the present material model is provided in Section 2. Determination of the material parameters required by the model is given in Section 3, while the validation of the ballistic modeling capacity is provided in Section 4. The conclusions resulting from the present study are summarized in Section 5.

2. Composite progressive failure model

The ballistic material model for composite laminates reported herein considers the contribution of 3D strain state to damage initiation within plain weave fabric layers and provides an improved treatment of damage evolution (progressive failure). As will be shown later, the model can be used to effectively account for both damage/failure of the fiber reinforcements and the matrix under high strain-rate and high pressure ballistic impact conditions.

Strength-based failure criteria are commonly used with the finite element method to predict failure events in composites structures. A large number of continuum-based criteria have been derived to relate internal stresses and experimentally measured material strengths to the onset of failure. A general tensor polynomial criterion was proposed by Tsai and Wu [20] for failure of brittle unidirectional fiber composites. Hashin [21] pointed out the need of establishing failure criteria based on failure modes due to the fact that a unidirectional fiber composite consists of strong and stiff fibers and comparatively weak and compliant matrix. For these two very dissimilar phases, he proposed four different failure criteria relating to tensile and compressive failure of fibers and matrix for a unidirectional composite layer.

Over the last two decades, several researchers have proposed modifications to Hashin criteria to improve its prediction capabilities. Hashin failure criteria were modified to include the effect of transverse compressive normal stress on the matrix shear strength by Sun, et al. [22]. The application of the Mohr–Coulomb (M–C) criterion to transverse compression under combined transverse normal and axial shear stresses was studied by Chatterjee [23]. Using a simple modification to account for the difference between the transverse and axial shear strengths, he was able to obtain good correlation of matrix failure with experimental data of compression tests of angle ply as well as off-axis unidirectional specimens. The M–C criterion was also used to include the effect of compression on the shear strengths of transverse matrix failure by Puck and Schurmanner [24] and Davila and Camanho [25]. In general, the use of M–C for the transverse matrix failure has improved the accuracy over the Hashin matrix failure criterion. However, the effect of transverse normal stresses on the fiber failure also needs to be considered for accurately predicting the composite ballistic behavior.

The proposed failure model has been established by generalizing Hashin failure criteria [21] to a unidirectional composite lamina to account for 3D stress effects and to include the effects of high strain rate and high pressure on composite failure resulting from a wide range of ballistic/blast loading conditions. The unidirectional model has then been extended to a plain weave lamina. The Mohr–Coulomb (M–C) criterion has also been generalized for modeling the through the thickness fiber/matrix failure of a composite lamina where fracture under compression is very different from the fracture under tension.

2.1. Damage-initiation/progression functions

The unidirectional and fabric layer damage-initiation/progression criteria developed in the present work are expressed in terms of ply-level engineering strains ($\varepsilon_x,\varepsilon_y,\varepsilon_z,\varepsilon_{xy},\varepsilon_{yz},\varepsilon_{zx}$) with x, y and z denoting the in-plane fill, in-plane warp and out-of-plane directions, respectively. Note that for the unidirectional model, x, y and z denote the fiber, in-plane transverse and out-of-plane directions, respectively, while for the fabric model, x, y and z denote the in-plane fill, in-plane warp and out-of-plane directions, respectively. The associated Young's and shear moduli are ($E_x,E_y,E_z,G_{xy},G_{yz},G_{zx}$).

2.1.1. Unidirectional lamina damage functions

Three fiber damage mechanisms are considered: (a) damage under combined uniaxial tension and transverse shear; (b) damage under uniaxial compression; and (c) damage under transverse compressive loading. Matrix mode failures must occur without fiber failure, and hence they will be on planes parallel to fibers. Two

matrix damage mechanisms are considered: (d) damage plane perpendicular to the layer plane under in-plane tensile and shear stresses; and (e) damage plane parallel to the layer plane (delamination) due to through-the-thickness tensile and shear stresses.

Uniaxial tension/Transverse shear

$$f_1 - r_1^2 = \left(\frac{E_x\langle\varepsilon_x\rangle}{S_{xT}}\right)^2 + \frac{G_{xy}^2\varepsilon_{xy}^2 + G_{xz}^2\varepsilon_{xz}^2}{S_{FS}^2} - r_1^2 = 0 \tag{1}$$

Uniaxial Compression

$$f_2 - r_2^2 = \left(\frac{E_x\langle\varepsilon_x'\rangle}{S_{xC}}\right)^2 - r_2^2 = 0,$$
$$\varepsilon_x' = \max\left\{-\varepsilon_x - \langle-\varepsilon_y\rangle\frac{E_y}{E_x}, -\varepsilon_x - \langle-\varepsilon_z\rangle\frac{E_z}{E_x}\right\} \tag{2}$$

Transverse Compression

$$f_3 - r_3^2 = \left(\frac{E_y\langle-\varepsilon_y\rangle}{S_{FC}}\right)^2 + \left(\frac{E_z\langle-\varepsilon_z\rangle}{S_{FC}}\right)^2 - r_3^2 = 0 \tag{3}$$

where $\langle\rangle$ are Macaulay brackets, S_{xT} and S_{xC} are the axial tensile and compressive strengths, respectively, and S_{FS} and S_{FC} are the fiber-shear controlled layer shear strength and crush failure strength, respectively. The damage thresholds, r_i $i = 1,2,3$, which are set to 1 for the initial damage-free material. The individual failure criterion is then used to determine the onset of the associated fiber damage mode when the straining condition provides $f_1 = 1$, $f_2 = 1$ or $f_3 = 1$.

In Eq. (1), the unidirectional fiber tensile/shear damage is given by the quadratic interaction between the associated axial and through the thickness shear strains. This fiber failure is a generalization of the criterion of Hashin for a unidirectional layer. It is, however, important to note that the fiber shear failure, which is commonly observed under ballistic loading conditions, is governed by the layer (punch) shear strength (S_{FS}) and this mode of fiber failure was not covered by the original Hashin's model [21].

In Eq. (2), it is assumed that the in-plane compressive damage in the axial fiber directions is given by the maximum strain criterion, when ε_x is compressive. Note that the effect of transverse compressive strains on the in-plane compressive damage is taken into account.

When a composite material is subjected to transverse impact by a projectile, high compressive stresses will generally occur in the impact area with high shear stresses in the surrounding area between the projectile and the target material. While the fiber shear punch damage due to the high shear stresses can be accounted for by Eq. (1), the crush damage due to the high through the thickness compressive stresses is modeled using the criterion of Eq. (3).

Perpendicular Matrix Damage

$$f_4 - r_4^2 = \left\{\left(\frac{E_y\langle\varepsilon_y\rangle}{S_{yUT}}\right)^2 + \left[\frac{G_{yz}\varepsilon_{yz}}{S_{yz0}+S_{ySR}}\right]^2 + \left[\frac{G_{xy}\varepsilon_{xy}}{S_{xy0}+S_{ySR}}\right]^2\right\} - r_4^2 = 0 \tag{4}$$

Parallel Matric Damage (Delamination)

$$f_5 - r_5^2 = S^2\left\{\left(\frac{E_z\langle\varepsilon_z\rangle}{S_{zUT}}\right)^2 + \left[\frac{G_{yz}\varepsilon_{yz}}{S_{yz0}+S_{zSR}}\right]^2 + \left[\frac{G_{xz}\varepsilon_{xz}}{S_{xz0}+S_{zSR}}\right]^2\right\} - r_5^2 = 0 \tag{5}$$

where r_4 and r_5 are the damage thresholds for modes 4 and 5, respectively; S_{yUT} and S_{zUT} are the transverse tensile strengths in the y and z directions, respectively; and S_{xy0}, S_{yz0} and S_{xz0} are the shear strengths corresponding to the tensile modes in the associated directions, i.e. $\varepsilon_y \geq 0$ or $\varepsilon_z \geq 0$. Under compressive transverse strain, $\varepsilon_y < 0$ or $\varepsilon_z < 0$, the internal surfaces induced by matrix cracking are considered to be in full contact, and the damage strengths are assumed to be dependent on the associated compressive normal strain ε_y or ε_z similar to the Coulomb-Mohr theory, i.e.,

$$S_{ySR} = E_y\tan\ \varphi_U\langle-\varepsilon_y\rangle \tag{6}$$

$$S_{zSR} = E_z\tan\ \varphi_U\langle-\varepsilon_z\rangle \tag{7}$$

where φ_U is the Coulomb's friction angle.

While the damage surface due to Eq. (4) is perpendicular to the composite layer plane and is associated with transverse matrix cracking, the damage surface due to Eq. (5), which is the quadratic interaction between the thickness stresses, is parallel to the composite layer plane and is associated with inter-layer separation/delamination. Note that a scale value S is introduced into Eq. (5) to account for the stress concentration factor at the delamination front. During numerical simulations, S value greater than 1.0 is assigned only to the composite laminate regions adjacent to the delamination front(s). No stress concentration effects are considered in the remainder of the composite laminate and S is set to 1.0.

In order to identify the delamination front elements, an array of elements surrounding the current active element is passed into the material subroutine from the main program of LS-DYNA. If the onset of delamination is computed in the active element during the current loading step, those surrounding elements, which are in the same composite layer plane but are not yet delaminated, are identified as the delamination front elements by flagging a history variable associated with each of those elements for assigning the S value in the later loading steps. When an appropriate value for the scale factor S is selected, this non-local approach was found to provide better correlation of delamination area with experiments. Such optimal value of the scale factor can be determined by fitting the analytical prediction to experimental data for the delamination area.

The damage criteria $f_i - r_i^2 = 0$, $i = 1,\ldots,5$, given in Eqs. (1)–(5) provide the damage initiation/progression surfaces in strain space. For the undamaged state, r_i are set to 1, and, thus, the material remains in the initial undamaged state as long as $f_i - 1 \leq 0$, for each i ($i = 1,\ldots,5$). The damage evolution laws introduced in the next section are used to model the damage progression behavior.

2.1.2. Plain weave fabric lamina damage functions

Similar to the unidirectional model, five fiber damage mechanisms are considered: (a) damage under combined uniaxial tension and transverse shear, fill and warp fibers are treated separately; (b) damage under uniaxial compression, fill and warp fibers are considered separately; and (c) damage under transverse compressive loading, no distinction between fill and warp fibers is made. Two matrix damage mechanisms are also considered: (d) damage under in-plane shear loading; and (e) delamination due to through-the-thickness tensile and shear stresses. The plain weave model was reported in Ref. [1] and is summarized as follows for the sake of completeness.

First, the fiber failure criteria of Hashin for a unidirectional layer are generalized to characterize the fiber damage in terms of strain components for a plain weave layer. The fill and warp fiber tensile/shear damage are given by the quadratic interaction between the associated axial and through the thickness shear strains, i.e.,

$$f_6 - r_6^2 = \left(\frac{E_x\langle\varepsilon_x\rangle}{S_{xT}}\right)^2 + \left(\frac{G_{xz}\varepsilon_{xz}}{S_{xFS}}\right)^2 - r_6^2 = 0$$
$$f_7 - r_7^2 = \left(\frac{E_y\langle\varepsilon_y\rangle}{S_{yT}}\right)^2 + \left(\frac{G_{yz}\varepsilon_{yz}}{S_{yFS}}\right)^2 - r_7^2 = 0 \quad (8)$$

where S_{xT} and S_{yT} are the axial tensile strengths in the fill and warp directions, respectively, and S_{xFS} and S_{yFS} are the layer shear strengths due to fiber shear failure in the fill and warp directions. These failure criteria are applicable when the associated ε_x or ε_y is positive. The damage thresholds r_6 and r_7 are equal to 1 without damage.

When ε_x or ε_y is compressive, it is assumed that the in-plane compressive damage in the fill and warp directions are given by the maximum strain criterion, i.e.,

$$f_8 - r_8^2 = \left(\frac{E_x\langle\varepsilon'_x\rangle}{S_{xC}}\right)^2 - r_8^2 = 0,\ \ \varepsilon'_x = -\varepsilon_x - \langle-\varepsilon_z\rangle\frac{E_z}{E_x}$$
$$f_9 - r_9^2 = \left(\frac{E_y\langle\varepsilon'_y\rangle}{S_{yC}}\right)^2 - r_9^2 = 0,\ \ \varepsilon'_y = -\varepsilon_y - \langle-\varepsilon_z\rangle\frac{E_z}{E_y} \quad (9)$$

where S_{xC} and S_{yC} are the axial compressive strengths in the fill and warp directions, respectively, and r_8 and r_9 are the corresponding damage thresholds.

The crush damage due to the high through the thickness compressive pressure is modeled using the following criterion:

$$f_{10} - r_{10}^2 = \left(\frac{E_z\langle-\varepsilon_z\rangle}{S_{FC}}\right)^2 - r_{10}^2 = 0 \quad (10)$$

where S_{FC} is the fiber crush strengths and r_{10} is the associated damage threshold.

A plain weave layer can be damaged under in-plane shear stressing without occurrence of fiber breakage. This in-plane matrix damage mode is given by

$$f_{11} - r_{11}^2 = \left[\frac{G_{xy}\varepsilon_{xy}}{S_{xy}}\right]^2 - r_{11}^2 = 0 \quad (11)$$

where S_{xy} is the layer shear strength due to matrix shear failure and r_{11} is the damage threshold.

Another failure mode, which is due to the quadratic interaction between the thickness strains, is expected to be mainly a matrix failure. This through the thickness matrix failure criterion is assumed to have the following form:

$$f_{12} - r_{12}^2 = S^2\left\{\left(\frac{E_z\langle\varepsilon_z\rangle}{S_{zT}}\right)^2 + \left[\frac{G_{yz}\varepsilon_{yz}}{S_{yz0}+S_{SR}}\right]^2 + \left[\frac{G_{xz}\varepsilon_{xz}}{S_{xz0}+S_{SR}}\right]^2\right\} - r_{12}^2 = 0 \quad (12)$$

where r_{12} is the damage threshold, S_{zT} is the through the thickness tensile strength, and S_{yz0} and S_{xz0} are the shear strengths for tensile ε_z. The damage surface due to Eq. (12) is parallel to the composite layering plane. Under compressive through the thickness strain, $\varepsilon_c < 0$, the damaged surface (delamination) is considered to be "closed", and the damage strengths are assumed to depend on the compressive normal strain ε_c similar to the Coulomb-Mohr theory, i.e.,

$$S_{SR} = E_z\tan\ \varphi\langle-\varepsilon_z\rangle \quad (13)$$

where φ is the Coulomb's friction angle. Similar to the unidirectional model, a scale factor S is introduced to provide better correlation of delamination area with experiments. The scale factor S can be determined by fitting the analytical prediction to experimental data for the delamination area.

2.2. Damage evolution laws

To quantify the extent of damage-induced stiffness loss, six damage variables ϖ_j with $j = 1,\ldots6$, are introduced, one for each of the six moduli mentioned earlier. The compliance matrix S is related to the damage variables as in Ref. [10]:

$$\left[S^*\right] = \begin{bmatrix} \frac{1}{(1-\varpi_1)E_x} & \frac{-\nu_{yx}}{E_y} & \frac{-\nu_{zx}}{E_z} & 0 & 0 & 0 \\ \frac{-\nu_{xy}}{E_x} & \frac{1}{(1-\varpi_2)E_y} & \frac{-\nu_{zy}}{E_z} & 0 & 0 & 0 \\ \frac{-\nu_{xz}}{E_x} & \frac{-\nu_{yz}}{E_y} & \frac{1}{(1-\varpi_3)E_z} & 0 & 0 & 0 \\ 0 & 0 & 0 & \frac{1}{(1-\varpi_4)G_{xy}} & 0 & 0 \\ 0 & 0 & 0 & 0 & \frac{1}{(1-\varpi_5)G_{yz}} & 0 \\ 0 & 0 & 0 & 0 & 0 & \frac{1}{(1-\varpi_6)G_{zx}} \end{bmatrix} \quad (14)$$

The stiffness matrix C is obtained by inverting the compliance matrix, $[C] = [S^*]^{-1}$.

As suggested in Matzenmiller et al. [10], the growth rate of damage variables $\dot{\varpi}_j$, is defined by the following type of evolution law:

$$\dot{\varpi}_j = \sum_i \dot{\phi}_i q_{ji} \quad (15)$$

where the scalar functions $\dot{\phi}_i$ ($i = 1,\ldots,12$) define the growth rate of damage mode, i, and the binary vector-valued functions q_{ji} ($j = 1,\ldots6$, $i = 1,\ldots,12$) provide the coupling between the individual damage variables, ϖ_j, and one of the previously defined seven damage modes (each characterized by its damage-initiation function f_i).

2.2.1. Derivation of $\dot{\phi}_i$

As described previously, the damage criteria $f_i - r_i^2 = 0$ of Eqs. (1)–(5) or (8)–(12) provide the damage surfaces in strain space. The growth rate of damage type i, $\dot{\phi}_i$, will be non-zero when the strain path crosses the corresponding updated damage surface $f_i - r_i^2 = 0$ and the associated strain-vector increment has a positive component along the outward normal to the damage surface, i.e., when $\sum_k (\partial f_i/\partial \varepsilon_k)\dot{\varepsilon}_k > 0$, where $k(=1,\ldots,6)$ is used to denote six components of the strain vector. Combined with a damage growth function $\gamma_i(\varepsilon_k, \varpi_j)$, $\dot{\phi}_i$ is assumed to have the form

$$\dot{\phi}_i = \sum_k \gamma_i \frac{\partial f_i}{\partial \varepsilon_k}\dot{\varepsilon}_k \tag{16}$$

Choosing

$$\gamma_i = \frac{1}{2}(1-\phi_i) f_i^{\frac{m}{2}-1} \tag{17}$$

and noting that

$$\sum_k \frac{\partial f_i}{\partial \varepsilon_k}\dot{\varepsilon}_k = \dot{f}_i \tag{18}$$

for the quadratic functions of Eqs. (1)–(5) or (8)–(12), leads to

$$\dot{\phi}_i = \frac{1}{2}(1-\phi_i) f_i^{\frac{m}{2}-1}\dot{f}_i (\text{no summation over } i) \tag{19}$$

where ϕ_i is a variable representing the extent of mode-i damage, and m is a material constant that quantifies sensitivity of the material stiffness to the extent of damage. To summarize, Eq. (19) governs the rate of progression of different damage modes and, in turn, the extent of stiffness loss as a function of damage with multiple damage modes. As described in Ref. [10], the γ_i of Eq. (17) is chosen to ensure that a Weibull distribution for damage flaw accumulation is realized for the softening behavior under the unidirectional straining condition.

2.2.2. Derivation of q_{ji}

For the fiber tensile/shear and compressive damage of modes of 6–9 defined in the fabric model, the damage coupling vector q_{6i}, q_{7i}, q_{8i} and q_{9i} are chosen such that the fiber damage in either the fill and warp direction results in stiffness reduction in the loading direction and in the related shear directions. For the fabric fiber crush damage of mode 10, the damage coupling vector q_{10i} is chosen such that all the stiffness values are reduced as an element is failed under the crush mode. For the fabric in-plane matrix shear failure of mode 11, the stiffness reduction due to q_{11i} is limited to in-plane shear modulus, while the through-the-thickness matrix damage (delamination) of mode 12, the coupling vector q_{12i} is chosen for the through thickness tensile modulus and shear moduli. The damage coupling matrix q_{ij} for the unidirectional model can be established accordingly. Consequently, the damage coupling functions q_{ji} for the unidirectional and fabric models, respectively, are then

$$[q] = \left[q_{\text{uni}}, q_{\text{fabric}}\right]$$

$$[q_{\text{uni}}] = \begin{bmatrix} 1 & 1 & 1 & 0 & 0 \\ 0 & 0 & 1 & 1 & 0 \\ 0 & 0 & 1 & 0 & 1 \\ 1 & 1 & 1 & 1 & 0 \\ 0 & 0 & 1 & 1 & 1 \\ 1 & 1 & 1 & 0 & 1 \end{bmatrix}, \left[q_{\text{fabric}}\right] = \begin{bmatrix} 1 & 0 & 1 & 0 & 1 & 0 & 0 \\ 0 & 1 & 0 & 1 & 1 & 0 & 0 \\ 0 & 0 & 0 & 0 & 1 & 0 & 1 \\ 1 & 1 & 1 & 1 & 1 & 1 & 0 \\ 0 & 1 & 0 & 1 & 1 & 0 & 1 \\ 1 & 0 & 1 & 0 & 1 & 0 & 1 \end{bmatrix} \tag{20}$$

Through Eq. (15), the above function q_{ji} relates the individual damage variables ϖ_j to the various damage modes provided by the damage functions of the fabric models.

2.2.3. Derivation of ϖ_j

Utilizing the damage coupling functions of Eq. (20) and the growth function of Eq. (19), a damage variable ϖ_j can be obtained from Eq. (15) for an individual failure mode i as

$$\varpi_j = 1 - e^{\frac{1}{m}(1-r_i^m)}, \quad r_i \geq 1 \tag{21}$$

Note that the damage thresholds r_i given in the damage-initiation criteria of Eqs. (1)–(5) and (8)–(12) are continuously increasing functions with increasing damage. The damage thresholds have an initial value of one, which results in a zero value for the associated damage variable ϖ_j, in accordance with Eq. (21). This condition defines an initial damage-free elastic region bounded by the damage functions in strain space. The nonlinear material response is modeled by enabling the damage surfaces to expand and the damage threshold r_i to increase as a result of increase in damage of type i. This, in turn, causes an increase in the associated damage variable(s) ϖ_j and a decrease in material stiffness. Reduction in material stiffness associated with an increase in damage variables ϖ_j is governed by Eq. (15). In other words, within the strain space bounded by the damage surface material response remains elastic while the material stiffness is governed by the extent of damage. When fiber tensile/shear damage of a fabric layer is predicted in a layer by Eq. (8), the load carrying capacity of that layer in the associated direction is reduced to zero according to damage variable Eq. (21). On the other hand, when fiber compressive damage is predicted in a fabric layer by Eq. (9), the layer is assumed to retain a residual strength in the damaged direction. For the fill and warp fibers, the residual strengths are denoted as S_{xCR} and S_{yCR}, respectively. To account for this residual stiffness/strength effect, the damage variables of Eq. (21) for the compressive failure modes have been modified in the fill and warp directions, as

$$\varpi_j = \left(1 - e^{\frac{1}{m}(1-r_i^m)}\right)(1-\eta_i), \quad i = 3 \text{ or } 4$$
$$\begin{Bmatrix} \eta_3 \\ \eta_4 \end{Bmatrix} = \begin{Bmatrix} \dfrac{S_{\text{xCR}}}{E_{\text{x}}\varepsilon'_{\text{x}}} \\ \dfrac{S_{\text{yCR}}}{E_{\text{y}}\varepsilon'_{\text{y}}} \end{Bmatrix} \tag{22}$$

For through the thickness matrix (delamination) failure in a fabric layer given by Eq. (12), the in-plane load carrying capacity within the element is assumed to be elastic (i.e., no in-plane damage). The load carrying behavior in the through the thickness direction is assumed to depend on the opening or closing of the internal delaminated surfaces. For tensile loading, $\varepsilon_z > 0$, the through-the thickness-stress components are softened and ultimately reduced to zero due to the damage criteria described above. For compressive loading, $\varepsilon_z < 0$, the internal delaminated surfaces are considered to be closed, and thus, σ_z is assumed to be elastic, while τ_{yz} and τ_{zx} are allowed to reduce to a sliding friction stress of Eq. (13). Accordingly, for the through-the-thickness matrix failure of mode 12 under compressive loading, the damage variable Eq. (21) is further modified to account for the residual sliding strength S_{SR} of the form

$$\begin{Bmatrix} \varpi_5 \\ \varpi_6 \end{Bmatrix} = \left(1 - e^{\frac{1}{m}(1-r_7^m)}\right)\left(1 - \frac{S_{\text{SR}}}{\left[(G_{\text{yz}}\varepsilon_{\text{yz}})^2 + (G_{\text{zx}}\varepsilon_{\text{zx}})^2\right]^{1/2}}\right) \tag{23}$$

where the sliding strength is given by Eq. (13). Note that the modifications of ω_j for an unidirectional layer to account for the residual behavior can be carried out similar the procedure described above for a fabric layer.

2.3. Typical stress-strain response and damage surface

Fig. 1 shows typical axial tensile and compressive stress-strain curves obtained using the present progressive-damage composite-material model for a plain weave S2/Epoxy layer with a value of 4.0 assigned to the damage model parameter, *m*. Fig. 1(a) shows that, under monotonic loading, the model provides an initial damage-free elastic response up to the stress values of 586 MPa (85 ksi) for tension and 345 MPa (50 ksi) for compression. This is followed by a post damage-initiation material response characterized by continued softening. Note that the compressive stress reduces ultimately to a residual strength of 103 MPa (15 ksi) and remains constant afterward. Fig. 1(b) shows stress-strain curves due to cyclic loading along the fill-fiber direction (direction *x*). It demonstrates the effect of the accumulated damage on the stress-strain response. Note that during unloading/reloading, the material is more compliant than the initial damage-free material. The associated reduced elastic modulus is equal to $(1-\varpi_1)E_x$, where ϖ_1 is the updated damage parameter for the axial fiber damage mode.

Fig. 2 shows typical axial shear stress-strain curves obtained from the damage model. Shown in Fig. 2a are the shear stress-strain curves for τ_{zx} with tensile through the thickness normal loads (opening delamination). Fig. 2b shows the effect of the compressive through the thickness normal stress (closing delamination), σ_z on the τ_{zx} stress-strain response for a Coulomb's friction angle $\varphi = 20^\circ$.

Fig. 3 shows the typical stress-strain curves of a unidirectional S2/Epoxy layer. It demonstrates the energy absorption capacity in the axial fiber direction is significantly higher than those associated with the fracture due to matrix damage resulted from the transverse tensile and in-plane shear loadings.

2.4. Strain-rate dependent formulation

The effect of strain rate on the mechanical response of composite laminates is modeled by making strength values appearing in Eqs. (1)–(5) and (8)–(12) and the six elastic moduli, strain-rate dependent quantities. Strength values are made strain-rate dependent through the introduction of a scale factor as

$$\{S_{RT}\} = \{S_0\}\left(1 + C_1 \ln \frac{\{\dot{\bar{\varepsilon}}\}}{\dot{\varepsilon}_0}\right)$$

$$\{S_{RT}\} = \begin{Bmatrix} S_{xT} \\ S_{yT} \\ S_{xC} \\ S_{yC} \\ S_{FC} \\ S_{xFC} \\ S_{yFS} \end{Bmatrix}_{RT}, \{S_0\} = \begin{Bmatrix} S_{xT} \\ S_{yT} \\ S_{xC} \\ S_{yC} \\ S_{FC} \\ S_{xFC} \\ S_{yFS} \end{Bmatrix}_0 \quad \text{and} \quad \{\dot{\bar{\varepsilon}}\} = \begin{Bmatrix} |\dot{\varepsilon}_x| \\ |\dot{\varepsilon}_y| \\ |\dot{\varepsilon}_x| \\ |\dot{\varepsilon}_y| \\ |\dot{\varepsilon}_z| \\ |\dot{\varepsilon}_{zx}| \\ |\dot{\varepsilon}_{zy}| \end{Bmatrix} \tag{24}$$

where C_1 is the strain rate constant, and $\{S_0\}$ are the strength values of $\{S_{RT}\}$ at the reference strain rate $\dot{\varepsilon}_0$.

The strain-rate effect on the layer elastic moduli is modeled in an analogous fashion as:

$$\{E_{RT}\} = \{E_0\}\left(1 + C_2 \ln \frac{\{\dot{\bar{\varepsilon}}\}}{\dot{\varepsilon}_0}\right)$$

$$\{E_{RT}\} = \begin{Bmatrix} E_x \\ E_y \\ E_z \\ G_{xy} \\ G_{yz} \\ G_{zx} \end{Bmatrix}_{RT} \quad \text{and} \quad \{E_0\} = \begin{Bmatrix} E_x \\ E_y \\ E_z \\ G_{xy} \\ G_{yz} \\ G_{zx} \end{Bmatrix}_0 \tag{25}$$

where $\{E_0\}$ are the moduli of $\{E_{RT}\}$ at the reference strain rate $\dot{\varepsilon}_0$. The effect of strain rate on the axial stress-strain response is shown in Fig. 4 for $C_1 = 0.02$ and $C_2 = 0$.

3. Material-model parameterization

3.1. In-plane strength and modulus strain-rate dependence parameters

A literature survey has been conducted to identify the effect of strain-rate on the composite strength properties. Reviews of works and development in the area concerning the mechanical behavior of composite materials under high strain rate conditions are reported in Refs. [5,16,17 and 26]. In general, the experimental data indicates that composite failure strength is sensitive to the strain rate for glass/epoxy plain weave composites and much less so for carbon.

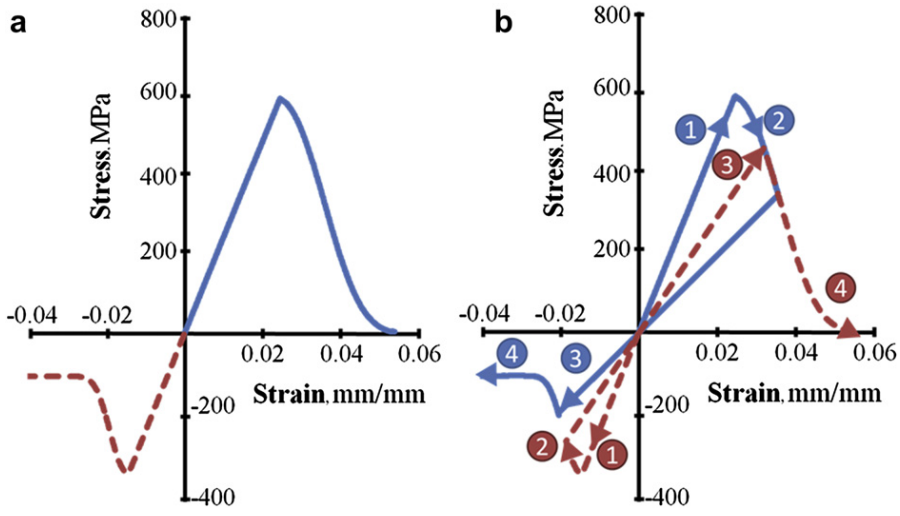

Fig. 1. Axial stress-strain curves for damage model under (a) Monotonic and (b) Cyclic loading conditions.

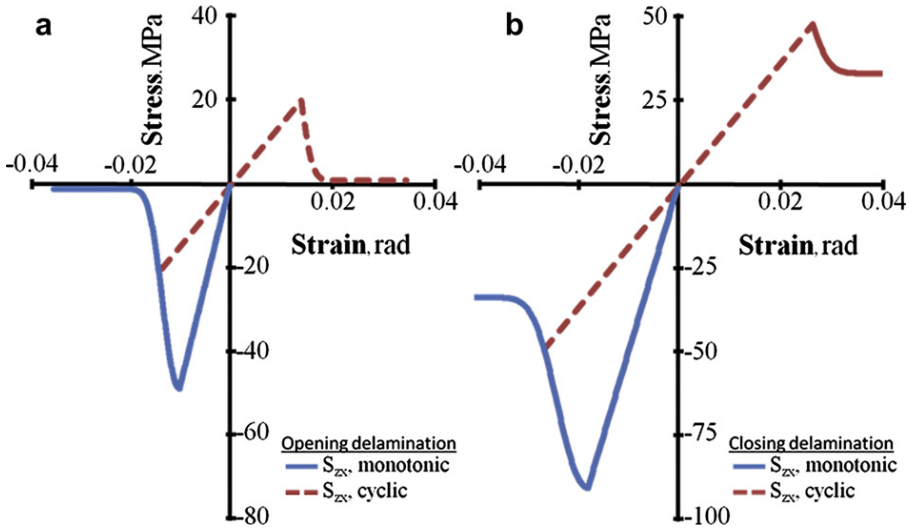

Fig. 2. Shear stress-strain curves for damage model under the effect of through the thickness normal load, (a) Opening delamination and (b) Closing delamination.

Various public-domain experimental data has been utilized to determine strength ($\{S_0\}$ and C_1) and modulus ($\{E_0\}$ and C_2) strain-rate dependency parameters for various composite systems and reported in [2] and [3]. Typical strain-rate dependent tensile and shear punch data for a fine weave glass composite was obtained by Hopkinson Pressure Bar testing (HPBT) and reported in [27] and [18], respectively. It was shown in [2] that these tensile and shear punch stress-strain curves can be accurately represented by the material model using the proper rate-dependent modulus, strength and damage parameters.

Of particular interest in this study is the dynamic behavior of the S2-glass/Epoxy plain weave composite laminates. The dynamic compressive stress-stain data of HPBT was reported by Song et al. [28], and shows in Fig. 5. The plain weave laminate shows a moderate increase in modulus, strength, and strain to failure with increasing strain rate. Fig. 5 also shows the computed stress-strain curves using the proposed material model for strain-rates ranging from 1/sec to 10^4/sec. Note that the modeling results for the GFRP composite were obtained by using the rate-dependent modulus, strength and damage parameters of $C_1 = 0.03$, $C_2 = 0.03$ and $m = 4$. It is seen that the proposed material model can represent the overall rate-dependent nonlinear stress-strain response reasonably well.

It is important to note that in order to accurately account for the experimentally observed strain-rate dependency of the in-plane tensile and punch shear strengths over a wide strain-rate range multiple values of the strain rate constants C_1 and C_2 may be required. However, it should be recognized that under ballistic impact conditions, it is expected that the composite failure will mainly occur under relatively high strain rates, i.e.,$\dot{\varepsilon} \geq 1\ s^{-1}$. Therefore, for the correlation shown in Fig. 5, as well as the ballistic impact analysis reported later, the use of single values of C_1 and C_2 with a cut-off strain rate $\dot{\varepsilon}_c$ is recommended. For the current S2-glass/Epoxy plain weave laminate, it assumes that the strengths remain constant (rate independent) for strain rates below the cut-off threshold at 1.0 s^{-1}.

3.2. Crush compressive and punch-shear fiber strengths

Typical ballistic impact tests as well as ballistic simulation studies have indicated that the fiber shear failure resulting from the

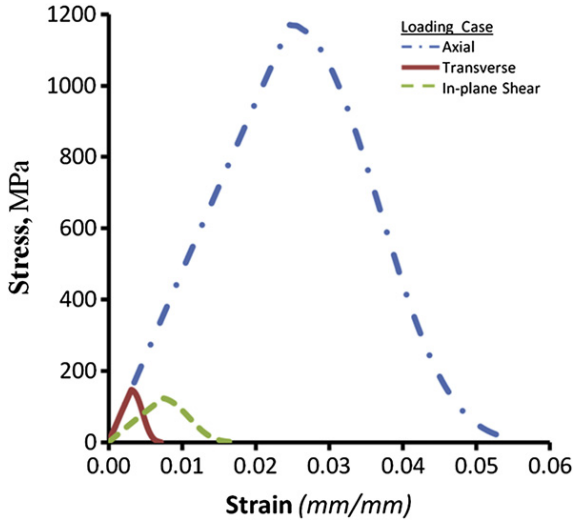

Fig. 3. Stress-strain curves of a unidirectional layer for axial tensile, transverse tensile and in-plane shear loads.

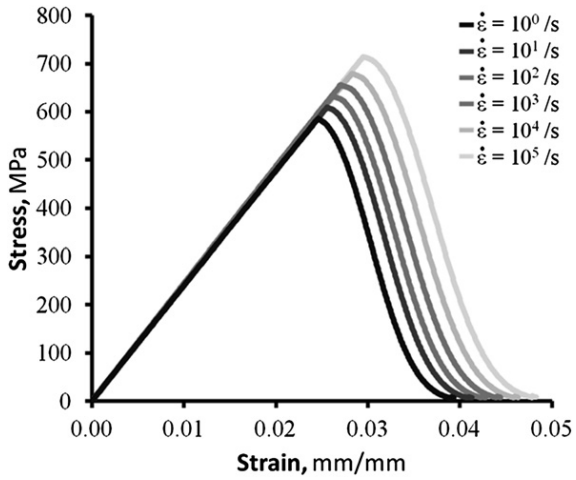

Fig. 4. Axial tensile stress-strain curves for damage model under various constant strain rate loading.

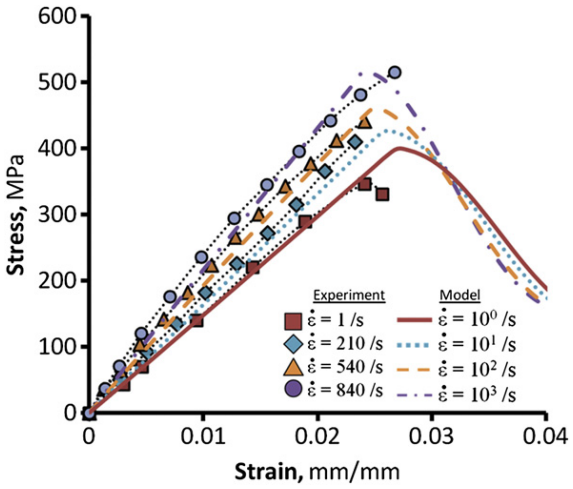

Fig. 5. Comparison of axial stress-strain response between modeling results and test data [28] for various constant strain-rates.

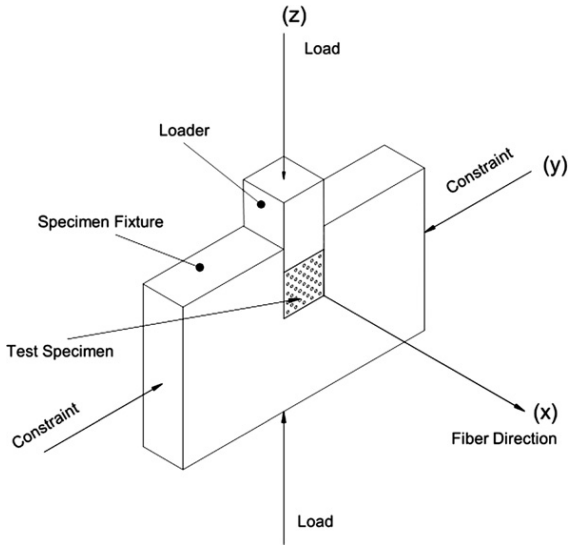

Fig. 6. Laterally constrained transverse compressive test fixture and unidirectional specimen.

through-thickness impact loading has had an important effect on the ballistic capacity of composite laminates [1,2]. It is expected that during high-velocity impact, large normal stresses are created in the direction orthogonal to the layer surfaces and that these stresses may induce shear failure along weak material planes. In unidirectional composites such failure usually occurs without cutting the fibers and this matrix dominated shear strength is typically very low [29,30]. Collin [31] performed compression tests using cube-shaped thick unidirectional-composite specimens by loading in one of the transverse directions, but providing constraint in the axial fiber direction. As the specimen is allowed to expand in the unconstrained transverse direction, matrix dominated failure has been found to occur in the transverse direction. It was mentioned previously that such matrix shear failure under the influence of normal stress can be accurately modeled by taking into consideration the effect of transverse compression under combined transverse normal and axial shear stresses using M–C criterion [23].

The effect of transverse normal stresses on the fiber failure has, however, drawn less attention. It is important to note that fiber failure under transverse compressive loading cannot be accurately predicted by the original Hashin failure model [21] since transverse shear mode of failure was not considered in the original Hashin failure model. In this work, the compressive loading is considered to contribute to both crush failure (Eq. (3) or (10)) and transverse shear failure (Eq. (1) or (8)) of the fibers. The required shear composite failure strengths for the fiber breakage due to the through-thickness compressive loading can be obtained from the laterally constrained compression test (LCCT) procedure.

The laterally constrained compression test procedure originally used by Collin [31] was extended to characterize the shear failure strength of fibers in both unidirectional and plain weave laminates. Fig. 6 shows the transversely constrained compression test fixture introduced by Collin. It is seen that one of the fiber directions of a plain weave composite specimen is arranged in the x direction, the compressive load is applied in the through the thickness direction z (perpendicular to the lamination planes) while the lateral constraint is provided to the other in-plane fiber direction y. Utilizing this LCCT, fiber shear failure is introduced as a result of the transverse compressive load. A failure surface cutting through the fibers with an inclined angle in the compressive loading direction typically results from such a compressive test.

By loading the specimen in the through-thickness direction and constraining laterally in one direction, failure must occur on certain preferred planes cutting the fibers. In particular, for homogeneous materials obeying Tresca or Mohr-Coulomb type strength criterion, failure will occur by sliding on planes perpendicular to the faces which are constrained (the plane making an angle θ to the through-thickness plane as shown in Fig. 7). In plain weave fiber reinforced composites, such failures are possible only after a shear type failure in the fibers occurs. In woven fabric composite with fibers running in two perpendicular directions, one set of fibers (which are more highly stressed) will likely fail in shear before the other. Fig. 6 shows the front view from the constrained side indicating shear failure cutting fibers in the unconstrained direction.

For the case of plain weave specimens with one of the warp (0°) or fill (90°) fiber direction coinciding with the unconstraint direction, the following stresses exist when the compressive stress on the specimen is S_{FC},

$$\begin{aligned} S_{NFS} &= 0.5\, S_{FC} \sin\, 2\theta \\ S_N &= S_{FC} \cos^2\, \theta \end{aligned} \tag{26}$$

where S_{NFS} and S_N are shear and compressive normal stresses, respectively, and θ is the angle of the shear sliding plane shown in Fig. 7. The above equations are obtained using the two principal stresses, i.e., compressive stress S_{FC} and zero. The other (intermediate compressive) principal stress (on planes parallel to the constrained faces) does not contribute to the stresses in Eq. (26).

The crush strength, S_{FC}, for S-2 Glass/Epoxy composite was measured using cubes with sides of 0.5 inch and 0.75 inch. For each specimen size, both of the 0° and 90° plain weave composite

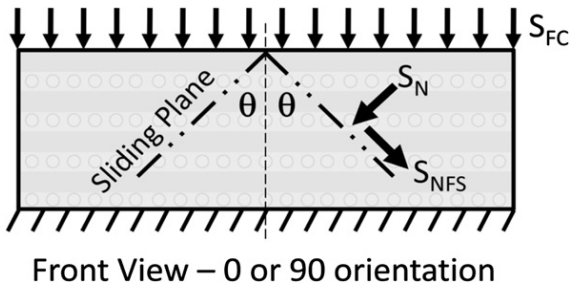

Fig. 7. Shear failure plane cutting fibers under transverse compression.

orientations were tested. The volume fractions of fiber reinforcements in 0° and 90° directions govern the composite fiber shear strength and the crush strength. For the material tested, the amount of reinforcements in the two directions is nearly equal. The crush strengths for the two orientations for 0.75 inch cubes are similar. The average values for 0° and 90° orientations are 758 MPa (110 ksi) and 745 MPa (108 ksi), respectively. For 0.5 inch cubes, the average values for the two orientations differ by 6% with average values of 724 MPa (105 ksi) and 683 MPa (99 ksi). It may be noted that for smaller specimens the amount of fibers may be affected by the location of the machining planes with respect to the fiber yarns. Therefore, test data for 0.7 inch cubes appear to be more reliable and the value of the average of the 0° and 90° crush strengths ($S_{FC} = 751$ MPa (109 ksi)) was used to calculate the punch shear strength S_{FS} using Eq. (26).

Before the value of the fiber punch shear strength S_{FS} can be calculated, one must determine the failure plane angle θ. For plain weave composite-laminate architectures, the failure planes are often corrugated and exhibit a zigzag pattern. A typical fracture surface in plain-weave composite material specimens failed by shear of 0° fibers is shown in Fig. 8. It appears that failure possibly initiates in some fiber yarns in the composite fiber shear failure mode, which is followed by very localized inter-yarn and/or inter-layer de-bonding which offset the shear plane in subsequent layers. The failure planes are measured from the failed specimens and the value of θ lies between 40° and 42°. Therefore, a value of 41° was used to calculate $S_{FS} = 751$ MPa (109 ksi).

The fiber shear failure behavior of a plain weave layer is modeled by Eq. (8) where the required punch-shear strength values of S_{xFS} and S_{yFS} are the S_{FS} values obtained from the laterally constrained transverse compression tests in the x and y directions, respectively. The measured fiber shear strength allows us to construct the failure envelope associated with the through the thickness components (σ_z, τ_{zx}) for the tested S2/Epoxy plain weave layer shown in Fig. 9. The matrix strength failure envelope is governed by Eq. (12) for both the tensile and compressive through the thickness normal stress. The fiber shear strength is given by equation (8), while the crush strength is provided by equation (10). The residual strength of fractured material under shear stress is provided by the Coulomb-Mohr criterion of equation (7) with S_{xz0} set to zero where $\varphi = 8°$ as given in Ref. [1].

4. Material-model additional parameterization and validation

In this section, a series of ballistic impact computational analyses of composite laminates with projectiles is carried out and the results

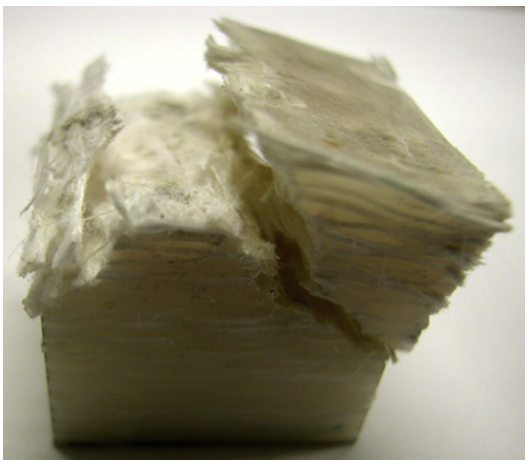

Fig. 8. Typical damage surface of a fractured specimen.

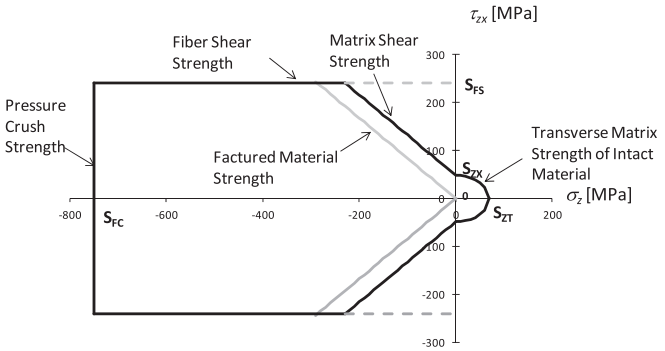

Fig. 9. Failure envelope associates with the through-thickness-stress components (σ_Z,τ_{Zx}) for an S2/Epoxy plain weave layer.

compared with their experimental counterparts. The outcome of this comparison was next used to both identify the still-undetermined material-model parameters and to provide validation for the present material model. The objective of this task is to evaluate the capability of utilizing the proposed progressive failure criteria within 3D brick element of LS-DYNA to model the structural response of composite plates subjected to high velocity ballistic impact conditions. Simulations of the ballistic impact of two S2-Glass/Epoxy composite panels were conducted by accounting for the strain-rate sensitivity properties. Analyses were performed to predict and correlate the measured perforation limit velocity (V50) and damages in the composite plates subjected to fragment simulating projectile (FSP) impact testing. The analyzed ballistic problems were: (1) a 3.41 kg/m^2 composite plate of 30.5 cm × 30.5 cm × 1.8 cm subjected to 0.50 caliber FSP impact [32], and (2) a 1.18 kg/m^2 composite plate of 30.5 cm × 30.5 cm × 0.623 cm subjected to 0.30 caliber FSP impact.

The finite element models for the 1.18 kg/m^2 composite panel and the 0.30 caliber FSP are shown in Fig. 10. Only one quadrant of the composite panel and one quadrant of the FSP with chisel head were modeled due to the geometric and material symmetry. Both the plate and the projectile were modeled with 8-node brick elements with a single integration point. There were 24 layers of elements through the thickness.

The panel was placed over a rigid ring with a rigid body contact surface assumed between the plate and the ring. Initial velocity was provided to the impacter/FSP to start the analysis. The projectile was made out of AISI 4340 steel which was modeled as an elasto-plastic material. An eroding contact algorithm provided within LS-DYNA together with the integrated failure model was used to simulate the contact and penetration between the projectile and the impact area of the plate. Note that the element erosion criterion is associated with the complete fiber failure in both plain weave yarn directions. All failed elements were deleted and the contact surfaces were automatically updated to the newly exposed layers of material.

The material properties for an S2-Glass/Epoxy plain weave composite layer and the AISI 4340 steel FSP, listed in Table 1, were used to perform the simulation. The composite-material quasi-static elastic properties were obtained from the MIL-HDBK-17-3E handbook [33]. The axial tensile and compressive strength values of the plain weave S2-glass/epoxy composite were obtained from the routine tensile and compressive tests, while the punch shear and crush strengths were determined from the LCCT tests described in the previous section. Note that the composite layer strengths related to the fiber failure, which include the in-plane tensile and compressive strengths as well as the out-of-plane punch shear and crush strengths, have strong effects on the composite ballistic behavior.

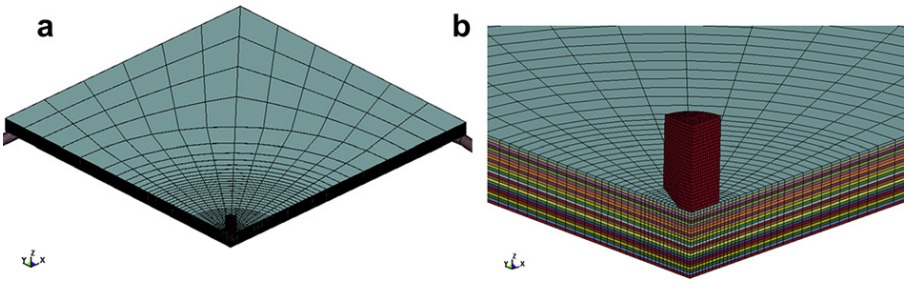

Fig. 10. Finite element model for a composite panel and an FSP impacter, (a) Full view, and (b) Close-up of impact area.

It was described in Section 3.1 that the strain-rate dependent axial stress-strain data provided in Ref. [28] for the current S2-glass/epoxy plain weave laminate can be reasonably represented by the rate effect parameters of $C_1 = 0.03$ and $C_2 = 0.03$, which were used in the current simulations of the test cases (1) and (2). This should provide an improvement over the earlier correlation studies of the test cases of (1) provided in Ref. [1] for which the strain-rate consideration was only limited to the composite strength while the rate effect of elastic modulus was neglected due to the lack of data.

The post failure damage softening parameter, $m = 4$, was chosen due to the fact that it usually provided the best agreement between the computed and the experimentally measured values of the ballistic limit V50 for several cases reported in previous studies [1–3]. Additionally, it is evidently demonstrated that $m = 4$ provided the best agreement between the computed and the experimentally measured value for the ballistic limit V50 for the first case of the 3.41 kg/m^2 plate subjected to 0.50 Caliber FSP impact.

The set of material properties listed in Table 1 were then used to predict the V50 of the 1.18 kg/m^2 composite plate subjected to impact by a 0.30 caliber FSP. Fig. 11 shows the time histories of projectile velocity for three values of initial impact velocity. Note that the initial velocity is negative (downward) and the rebounding velocity is positive, which is not shown in the figure for clarity. It is seen from Fig. 11 that the predicted V50 of the second panel is about 1345 fps (410 m/s), which is about 6% higher than the experimental value of 1270 fps (387 m/s).

For the second series of ballistic tests, the damage zones were visible on each target to compare the relative sizes of damage area. To increase the visibility and contrast, targets were placed against a backlit box, and the images of each impact area were captured. The visible area of each damage zone was quantified using Axio-Vision image processing software (Carl Zeiss, Inc.) [34]. Fig. 12 shows a typical back lit image of a damaged target subjected to an impact velocity of 342 m/sec. The back lit image is compared to the image obtained by using the well-known C-scan with satisfactory result. In Fig. 13, the measured damage areas are plotted with the associated impact velocities.

To determine an optimal value for the stress concentration parameter for delamination propagation, S, a comparison is made between the computed and experimentally measured delamination areas for the first test series. The effect of different S values on the delamination areas as function of the impact velocities is shown in Fig. 13. Based on the results displayed in this figure, the value of $S = 1.1$ clearly provides the best match of predicted damage areas to the experimental data for the impact velocities ranging from partial penetration to complete perforation. Note that the value of $S = 1.1$ was also used in the previous ballistic simulations of the first case and matched the experimental data of delamination areas with reasonable accuracy.

It is important to point out that the main goal of this research is to develop a robust modeling tool which can effectively be used to simulate the ballistic capacity of plain weave laminates of various configurations subjected to impact of different projectiles with a wide range of velocities. The accuracy of the model was validated by providing blind predictions for a series of glass/epoxy laminates of various areal densities subjected to impact by several types of projectiles with measured V50 and residual velocities as reported in Yen and Morris [35] and [4]. Note that a set of material parameters was obtained for the composite by following the procedure described in this paper based on a set of data of a composite system. This was then used for predicting the remaining test cases. The predicted V50s and residual velocities are within 10% of the

Table 1
Material properties used for dynamic analysis.

S2-glass/Epoxy plain weave layer	
$E_x = E_y = 24.1$ GPa (3.5 Msi)	$E_z = 10.4$ GPa (1.51 Msi)
$\nu_{xy} = 0.12$	$\nu_{xz} = \nu_{yz} = 0.40$
$G_{xy} = G_{yz} = G_{zx} = 5.9$ GPa (0.85 Msi)	
$S_{xT} = S_{yT} = 0.59$ GPa (85 ksi)	$S_{xC} = S_{yC} = 0.35$ GPa (50 ksi)
$S_{zT} = 69$ MPa (10 ksi)	$S_{FC} = 0.75$ GPa (108 ksi)
$S_{FS} = 0.37$ GPa (54 ksi)	$S_{xCR} = S_{yCR} = 0.10$ GPa (15 ksi)
$S_{xy} = S_{yz} = S_{zx} = 48.3$ MPa (7 ksi)	
$S = 1.1$	$C_1 = 0.03$, $C_2 = 0.03$, $\dot{\varepsilon}_0 = 1\ s^{-1}$
$\varphi = 8^\circ$	$m = 4$
$\rho = 1783$ kg/m^3 (1.668×10^{-4} lbs-s^2/in^4)	
Steel 4340	
$E = 207$ GPa (30 Msi)	$\nu = 0.33$
σ_y[a] $= 1.03$ GPa (150 Ksi)	E^{tb}[b] $= 6.9$ GPa (1.0 Msi)
ε_f[c] $= 0.35$	$\rho = 7877$ kg/m^3 (7.37×10^{-4} lbs-s^2/in^4)

[a] Yield stress.
[b] Plastic tangent modulus.
[c] Failure strain.

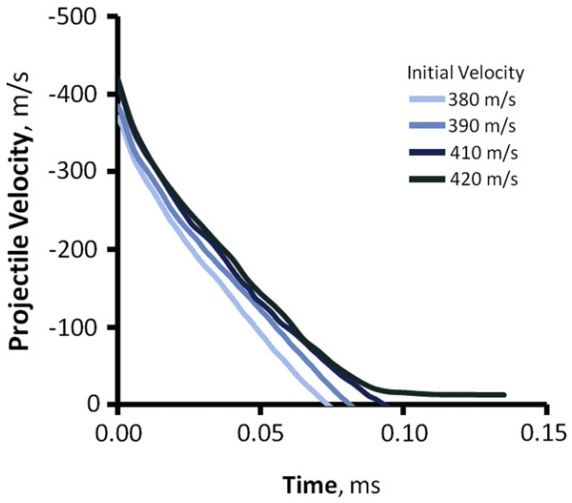

Fig. 11. Computed time histories of projectile velocity for an S2-Glass/Epoxy composite subjected to 0.22 caliber FSP impact.

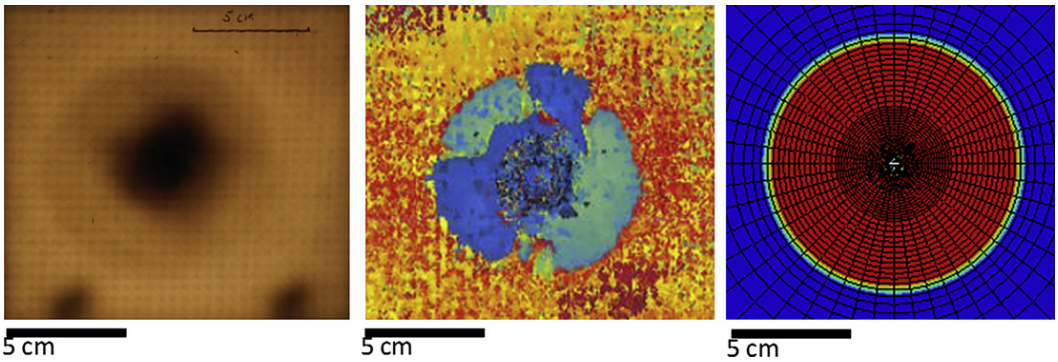

Fig. 12. Predicted maximum delamination area in the impacted composite panel comparing with the damage area of a tested panel using light inspection and C-scan.

associated experimental data. The modeling accuracy has been accomplished by considering strain-rate effects for the fiber failure modes but assuming rate independency for the matrix dominated failure modes with the introduction of a scale factor "S" for modeling the delamination zone, as described in Section 2.

The composite model has also been incorporated in LS-DYNA as the Material 162 (MAT162) since 2003 [36]. The accuracy of the model has been reported by numerous users, e.g. Refs. [37–39]. For examples, the model was used in Deka et al. [36,37] to predict damage progression in a series of composite panels subjected to single- and multi-hit impact. Good agreement between the numerical and experimental results was attained in terms of predicting ballistic limit, delamination and energy absorption of E-glass/PP laminate.

In summary, good correlation between the predicted and experimental results on the ballistic capacities of various composite laminates seems to indicate that the model provides proper prediction of the overall energy dissipation during ballistic events which are dominated by the fiber failure modes. Although the current simplified approach provides satisfactory results on predicting the delamination behavior, the rate effect on matrix dominated modes can be readily included in the model for rate sensitive matrix materials. The model can also incorporate the well-known cohesive element approach for better modeling of the delamination progression. However, this usually requires additional characterization in terms of the interface fracture parameters including the peak strength, critical energy release rate and the associated strain-rate sensitivity properties for the three fracture modes. Furthermore, cohesive elements must be inserted at every inter-layer interface in the finite element model to simulate the laminate delamination. Finally, the use of 3D photogrammetry techniques to acquire the time history of the panel deflection profile during a ballistic event will provide an opportunity for further validation of the models accuracy in future studies.

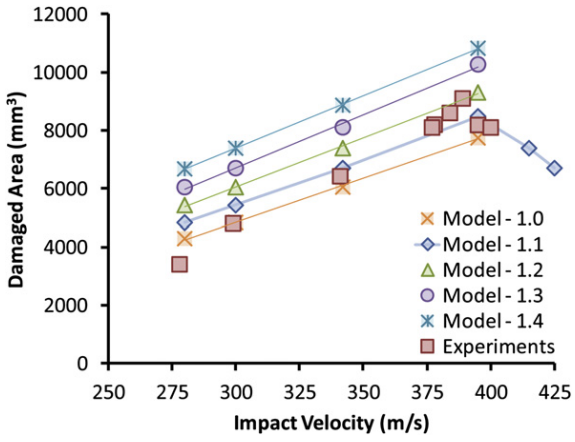

Fig. 13. Comparison of predicted delamination area due to various impact velocities with measured data for various S values.

5. Conclusions

A strain rate dependent lamina model based on continuum damage mechanics has been successfully developed and implemented within LS-DYNA for modeling the progressive failure behavior of plain weave composite layers. It can be used to effectively simulate the fiber failure and delamination behavior under high strain-rate and high-pressure ballistic impact conditions. The integrated code was successfully utilized to predict the ballistic limit velocity of composite laminates subjected to high velocity ballistic impact conditions. Simulations of ballistic impact of composite panels have been conducted by taking into account the strain-rate sensitivity of material response. The strain rate effect will need further investigation by experimentally characterizing the rate dependent behavior of various composite materials. Correlation for impact damage such as delamination area will also need to be conducted when the test data is available in the future.

The present composite material model can provide insight into the damage development and progression that occurs during the ballistic impact of composite panels. By identifying specific damage mechanisms that occur, reinforcement schemes can be determined to suppress them, which may ultimately enhance the survivability of the designed protection systems.

Acknowledgments

Initiation of this work was supported by the U.S. Army Research Laboratory under Contract No. DAAD17-00-C-0059 when the author was working at Materials Sciences Corporation.

References

[1] Yen CF. Ballistic impact modeling of composite materials. In: Proceedings of the 7th International LS-DYNA Users Conference; May 19–21, 2002. Dearborn, MI.
[2] Yen CF. Modeling of composite materials under strain-rate loading conditions. In: Proceedings of the 18th Annual Technique Conference American Society of Composites, MB5-224; October 19–22, 2003. Gainesville, FL.
[3] Yen CF. Ballistic impact modeling of 3D woven composite materials. Presented at 16th Army Symposium on Solid Mechanics, May 4–7, 2003, Charleston, SC.
[4] Yen CF. Modeling of composite material behavior for blast and ballistic impact. In: Proceedings of ESDA 2006, 8th Biennial ASME Conference on Engineering Systems Design and Analysis; July 4–7, 2006. Torino, Italy.
[5] Abrate S. Impact on laminated composites: recent advances. Appl Mech Rev 1994;V47:517–43.
[6] Richarson MOW, Wisheart MJ. Review of low-velocity impact properties of composite materials. Composites 1996;27A:1123–31.

[7] Choi HY, Chang FK. Impact damage threshold of Laminated composites. In: Failure criteria and analysis in dynamic response, AMD, vol. 107. Dallas, TX: ASME Applied Mechanics Division; November 1990. p. 31–5.
[8] Davies GAO, Zhang X. Impact damage prediction in carbon composite structures. Int J Impact Eng 1995;16:149–70.
[9] Chang FK, Chang KY. A progressive damage model for laminated composites containing stress concentration. J Compos Mater 1987;21:834–55.
[10] Matzenmiller A, Lubliner J, Taylor RL. A constitutive model for anisotropic damage in fiber-composites. Mech Mater 1995;20:125–52.
[11] William K, Vaziri R. Finite element analysis of the impact response of CFRP composite plates. In: Scott Murray L, editor; 1995. Proceedings of the ICCM-11, pp. 532–654.
[12] Van Hoof J, Woeswick MJ, Straznicky PV, Bolduc M, Tylko S. Simulation of ballistic impact response of composite helmets. In: Proceedings of the 5th International LS-DYNA Users Conference; 1998.
[13] Ladeveze P. Multiscale computational damage modelling of laminate composites. In: Sadowski T, editor. Multiscale modelling of damage and fracture processes in composite materials. Springer–Verlag; 2005. p. 309.
[14] Ladeveze P, Lubineau G, Violeau D. A computational damage micromodel of laminated composites. Int J Fracture 2006;137:139–50.
[15] Grujicic M, He T, Marvi H, Cheeseman BA, Yen CF. A comparative investigation of the use of laminate-level meso-scale and fracture-mechanics-enriched meso-scale composite-material models in ballistic-resistance analyses. J Mater Sci 2010;45(12):3136–50.
[16] Harding J, Ruiz C. The mechanical behaviour of composite materials under impact loading. In: Key Engineering Materials, vol. 141–143. Switzerland: Trans Tech Publications; 1998. 403–426.
[17] Al-Hassani STS, Kaddour AS. Strain rate effects on GRP, KRP and CFRP composite laminates. In: Key Engineering Materials, vol. 141–143. Switzerland: Trans Tech Publications; 1998. 427–452.
[18] Harding J. The high-Speed punching of woven-Roving glass-reinforced composites. In: Inst Phys Conf Ser No. 47 [Chapter 3]. Bristol and New York: The Institute of Physics; 1979. pp. 318–330.
[19] Welsh LM, Harding J. Effect of strain rate on the tensile failure of woven reinforced polyester resin composite; 1985. Proc. DYMAT 85, Int. Conf. On Mech. And Physical Behaviour of Materials Under Dynamic Loading, Jour de Physique, Colloque C5, pp. 405–414.
[20] Tsai SW, Wu EM. A general theory of strength of anisotropic materials. J Compos Mater 1971;5:58.
[21] Hashin Z. Failure criteria for unidirectional fiber composites. J Appl Mech 1980;47:329–34.
[22] Sun CT, Quinn BJ, Oplinger DW. Comparative evaluation of failure analysis methods for composite laminates. DOT/FAA/AR-95/109. Washington D.C: DOT Technical Report, Office of Aviation Research; 1996.
[23] Chatterjee SN. A Coulomb–Mohr type criterion for matrix mode failure in a lamina. Thirteenth Volume, ASTM STP 1242. In: Hooper SJ, editor. Composite materials: testing and design. American Society for Testing and Materials; 1997. p. 237–56.
[24] Puck A, Schurmann H. Failure analysis of FRP laminates by means of physical based phenomenological models. Compos Sci Technol 1998;58:1001–10.
[25] Davila CG, Camanho PP. Failure criteria for FRP laminates in plane stress, NASA/TM-2003-212663; NASA Technical Report. Hampton, VA: Langley Research Center; November 2003.
[26] Cantwell WJ, Morton J. The impact resistance of composite materials – a review. Composites 1991;V22:347–62.
[27] Harding J, Welsh LM. Tensile testing technique for fibre-reinforced composites at impact rates of strain. J Mater Sci 1983;V18:1810–26.
[28] Song B, Chen W, Weerasooriya T. Quasi-static and dynamic compressive behaviors of a S-2 Glass/SC 15 composite. J Compos Mater 2003;V37: 1723–43.
[29] Yen CF, Cassin T, Patterson J, Triplett M. Progressive failure analysis of thin walled composite tubes under low energy impact. In: 39th AIAA Structures, Structural Dynamics, and Materials Conference; 1998a.
[30] Yen CF, Cassin T, Patterson J, Triplett M. Progressive failure analysis of composite sandwich panels under blast loading. In: Structures under extreme loading conditions, vol. 361. New York: ASME PVP; 1998b. pp. 203–216.
[31] Collin TA. Transverse compressive behavior of unidirectional carbon fiber reinforced plastics. Composites; May 1974:108–16.
[32] Yen CF, Caiazzo AA. Design methodology and validation for multifunctional composite armor. MSC Technical Progress Report. Aberdeen Proving Ground, MD: U.S. Army Research Laboratory; July 2002. Contract No. DAAD17-01-C-0111.
[33] MIL-HDBK-17-3E. In: MIL-HDBK-17-3E. Polymer matrix composites: material properties, vol. 2. West Conshohocken, PA: ASTM International; 2002.
[34] Yu J, Brennan R, Quabili A. Ballistic characterization of composite panels. ARL internal report; (Internal ARL Report) Aberdeen Proving Ground, MD; October, 2011.
[35] Yen CF, Morris A. Blast/ballistic impact damage evaluation of marine composite structures. MSC TFR IH19, NSWCCD, Contract No. 5007-203-45/02. West Bethesda, MD: Naval Surface Warfare Center Carderock Division (NSWCCD); January 2003.
[36] Yen CF. User's manual for LS-DYNA Mat162 unidirectional and plain weave composite progressive failure models. provided to. Livermore, CA: Livermore Software Technology Corporation; 2003.
[37] Deka LJ, Bartus SD, Vaidya UK. Multi-site impact response of S2-glass/epoxy composite laminates. Compos Sci Technol 2009;69:725–35.
[38] Deka LJ, Bartus SD, Vaidya UK. Damage evolution and energy absorption of E-glass/polypropylene laminates subjected to ballistic impact. J Mater Sci 2008; 43:4399–410.
[39] Kevin A, Brown KA, Brooks R, Warrior NA. The static and high strain rate behaviour of a commingled E-glass/polypropylene woven fabric composite. Compos Sci Technol 2010;70:272–83.

Multiobjective Topology Optimization of Energy Absorbing Materials

Raymond A. Wildman and George A. Gazonas

Structural and Multidisciplinary Optimization , DOI 10.1007 (ARL) 19 pp

Struct Multidisc Optim
DOI 10.1007/s00158-014-1117-8

RESEARCH PAPER

Multiobjective topology optimization of energy absorbing materials

Raymond A. Wildman · George A. Gazonas

Received: 4 November 2013 / Revised: 21 April 2014 / Accepted: 13 May 2014

Abstract A method for the multiobjective optimization of local-scale material topology is presented. The topology optimization scheme is based on a constructive solid geometry-like representation, in which convex polygons—defined as the convex hull of arbitrary-length lists of points—are combined using an overlapping function. This data structure is tree-shaped and so genetic programming is used as the optimizer. The forward problem is solved with a multiscale finite element method with automatic cohesive zone insertion to model damage. As a multiscale method, loads and boundary conditions are applied and objective functions measured at a global scale, while the local scale material structure is optimized. The global scale geometry is assumed fixed. Pareto optimal designs are generated, representing optimal tradeoffs between conflicting goals: quasi-static displacement and dynamic strain energy. Results demonstrate the efficacy of the proposed algorithm.

Keywords Topology optimization · Pareto optimization · Genetic programming · Energy absorbing material

1 Introduction

Materials designed to absorb energy have applications in numerous areas: crashworthiness (Mozumder et al. 2012; Guo et al. 2011; Huang et al. 2007; Anghileri et al. 2005), head protection (Rueda et al. 2009), impact resistance (Qiao et al. 2008), and blast resistance (Main and Gazonas 2008; Qi et al. 2013). There are several ways to design an energy absorbing material or system of materials, for example, one could layer several different materials in a one dimensional sense, while optimizing for material placement and thickness. Another approach is to design the geometry or topology of a bi-material system or truss structure in two dimensions or three dimensions. In this work, we take the latter approach, and focus on designing energy absorbing materials at a local scale in a multiscale finite element (FEM) setting.

Our approach to designing materials will be to optimize the topology of a material at a local scale in two dimensions, while applying loads and boundary conditions and computing objectives at the global scale. A heterogeneous representative volume element (RVE) (strictly two materials in our case) will represent the local scale, and the global scale will be assumed to be statistically homogenous with material properties derived from a homogenization of the representative volume element (RVE). At the local scale, boundary conditions will be spatially homogenous using linear displacements, while at the global scale, a material sample will be fixed at one edge, with different loading conditions applied depending on whether we are considering static displacement or dynamic energy absorption. The different loading configurations are used to simulate possible scenarios in which such a material would be used, either as a structural element or an energy absorbing material for blast-like loading. As will be discussed in more detail later, these two loading conditions will be used as two separate goals in a multi-objective optimization problem. There are several options for optimizing such a configuration, the first choice being between a simple geometry or shape optimization method or a topology optimization method. A shape optimization method assumes a specific topology (i.e. each design is homeomorphic in that they must have the same

R. A. Wildman (✉) · G. A. Gazonas
U.S. Army Research Laboratory,
Attn: RDRL-WMM-B, Aberdeen Proving Ground,
MD, 21005, USA
e-mail: raymond.a.wildman.civ@mail.mil

Published online: 24 June 2014

number of shapes and holes), and parameterizes that shape with some type of function expansion, the simplest being a linear interpolation between a given number of vertices. An optimization method, either local, derivative-based or global heuristic, can then be used to solve for the defining parameters of the shape. An example of this approach can be found for the design of energy absorbing tubular structures in Chiandussi and Avalle (2002).

Shape optimization is overly restrictive, however, as one must fix the topology *a priori*. A popular method for topology optimization is known as the solid isotropic material with penalization (SIMP) method, introduced by Bendsøe (Duysinx and Bendsoe 1998; Bendsoe and Sigmund 2003). This method uses a square grid of unknowns (pixels), where each unknown is continuous value representing a graded material. A local optimization method is used to determine the optimal value of graded material at each pixel. Though a structure consisting of graded material is the result, methods exist to regularize the final result to a single material. Level-set methods have also been used to optimize topology (Sethian and Wiegmann 2000), which use contours of a higher dimensional function to represent topology in the plane. Finally, evolutionary methods have also been designed for topology optimization (Xie and Steven 1993, 1997).

To optimize topology, we use a constructive solid geometry (CSG) representation (Requicha and Voelker 1977), which uses Boolean operations to combine shape primitives. While typical implementations of CSG use canonical shapes such as rectangles and circles, we use convex polygons represented as the convex hull of an arbitrary length list of points. This encoding can represent any physically realizable (orientable) topology as a set of line segments. Though line segments are used, their length is not restricted, so arbitrarily small line segments can be used to approximate curves. Genetic programming (GP), a variant of genetic algorithms (GA) that uses a tree-based chromosome, will be used and is a natural fit for this topology representation as CSG can be readily expressed as a tree structure. This approach has been used in several applications including RF microwave inverse scattering (Wildman and Weile 2007, 2010), gravitational anomaly inversion (Wildman and Gazonas 2009), and phononic bandgap material design (Wildman and Gazonas 2011).

The approach presented here can be compared with current methods in two ways: geometry representation and optimization method. Our approach offers an alternative to the SIMP and level set methods in that it ultimately uses a set of line segments to approximate a topology rather than a grid (SIMP) or smooth curves (level-set). As will be described below, multiple materials are also easily represented in this approach. Further, as automatic meshing is used, the discretization of the topology as represented in the optimization method is uncoupled from the discretization used in the forward solver. SIMP and level-set methods typically use a local optimization method that requires gradient information. The genetic programming method used here does not require the computation of gradients and it is well-suited for multi-objective problems as it is a population-based method. The topology representation used here can also be adapted to a local search methodology, as described in Wildman and Gazonas (2009).

Previously, microstructural (or microscale) topology optimization has been performed for different goals: maximum stiffness of a periodic material (Huang et al. 2013), prescribed macroscale constitutive parameters (Sigmund 1995, 1994; Zohdi 2002; Mei and Wang 2004), and extremal microstructural properties (Allaire and Kohn 1993; Sigmund 2000). In this paper, we focus on balancing structural stability with energy absorption in a multiobjective setting. Typical engineering problems involve balancing conflicting goals, using the present example, if we wish to design an energy absorbing material and incorporate it into an overall structure, that material may not be structurally sound and could be unusable in our final design. We could place constraints on the optimization problem, such as a mass constraint, though this approach may leave out important information that could be garnered from the Pareto front, or set of multiobjective designs (Cohon 1978; Cohon and Marks 1975; Steuer 1989). The goal of Pareto optimization is to deliver a set of designs, rather than one single design, that represent the optimal trade-offs between two or more conflicting goals. This set of designs is *Pareto optimal* in that no other design simultaneously outperforms it in all goals. (The Pareto front can be defined as the boundary between the infeasible region of designs, and the dominated region.) Each design in the Pareto optimal set (Pareto front) can only outperform another design in the Pareto optimal set by at most one goal less than the total being optimized (or one goal in a two-goal problem, two in a three-goal problem, etc.).

While an individual design on the Pareto front may be determined using constraints on one or more goals, the shape of the Pareto front can provide information as well. For example, the front's shape may indicate areas of diminishing returns, whereby minuscule improvement in one goal only comes at the severe detriment of another. Here, we will optimize for two goals: a quasi-static loading problem representing a material's structural qualities, and a dynamic loading problem to measure energy absorption. These goals are conflicting because a structural material will be massive and stiff, while an energy absorbing material tends to be soft and compliant.

Three objectives, though only ever two simultaneously, will be considered in a multi-objective setting: Static displacement under uniaxial load, dynamic energy absorption

under hydrostatic, blast-like loading, and total mass. Each goal is defined and measured at the global scale, with no objectives considered at the local scale. The forward solver for the static and dynamic problems is a multiscale FEM code, with a global scale representing a sample of the material and the local scale representing a heterogeneous, repeatable (though not necessarily periodic) RVE, consisting of one or more brittle, elastic materials and void. This method is described in Souza et al. (2008), and commercially available as MultiMech (MultiMech Research & Development 2012). In our approach, the global scale is a fixed, unchanging structure, on which the loads and boundary conditions will be applied. A single design for the local scale will be used (i.e. the global scale will be homogeneous), and it will be assumed to be made of up to two materials or a single material with a void. Damage can also be modeled in the form of automatically inserted cohesive zones. In both the dynamic and quasi-static case, cohesive zones can be inserted at the local scale, representing micro-cracking and damage. In the quasi-static case, these micro-cracks can coalesce into macroscale damage, being inserted at the global scale with an extended finite element method (XFEM) (Chessa et al. 2002). We will consider the different models in turn, showing the difference in results when incorporating damage in the form of cohesive zones.

In summary, we will use a constructive solid geometry-based topology representation in conjunction with genetic programming to optimize the local structure of a material. Loads are applied and objectives measured at the global scale in a multiscale FEM setting. A multiobjective design approach is used, with one goal being a material's static, structural response, and a second being its dynamic, energy absorbing capability. The remainder of this paper is organized as follows: Section 2 details the topology representation and GP optimization method. Section 3 then discusses the multiscale finite element method used as the forward problem to model energy absorbing materials. Section 4 then presents results of the optimization, and Section 5 discusses our conclusions.

2 Optimization method

The optimization of geometry/topology is complicated by the difficulty in representing topology numerically. Here, we use a combinatorial approach based on constructive solid geometry applied to convex polygon primitives. This representation forms a tree data structure, with Boolean operations as function nodes (operators) and convex polygons as terminal nodes (operands), and is most naturally optimized with genetic programming (GP). In this section, we detail the topological data structure (Subsection 2.1) and the optimization method (Subsection 2.2).

2.1 Topology representation

Our approach to topology optimization is based on a CSG representation (Requicha and Voelker 1977), in which complex topologies are generated by combining shape primitives using Boolean operations. Over the past decade, this type of approach has been used for several applications, including optimization of truss joints (Hamza and Saitou 2004), optimization of statically loaded beams (Ahmed et al. 2013), optimization of phononic bandgap structures (Wildman and Gazonas 2011), gravitational inversion (Wildman and Gazonas 2009), and imaging (Wildman and Weile 2007, 2008, 2010; Yamagiwa et al. 2010). Our approach differs in that the shape primitives are based on convex polygons or polyhedra, rather than canonical shapes such as rectangles and ellipses (or cubes, spheres, and cylinders in 3D). Subsection 2.1.1 discusses the use of convex polygons as shape primitives, and subsequently Subsection 2.1.2 discusses generating more complex topologies.

2.1.1 Shape primitives

Typically, CSG methods use a canonical set of shape primitives to generate a desired topology. While, as shown in previous work, this approach can be effective, we use a more flexible representation that can result in smaller tree sizes. Here, shape primitives are convex polygons represented by the convex hull of arbitrary-length lists of points. The convex hull can be defined as the intersection of all half-planes that contain the points, or more colloquially, as the shape that results from stretching an elastic membrane around the points. Figure 1 gives an example of the convex hull (dashed line) of a set of randomly generated points in the plane (black dots). The total number of points allowed in each convex polygon is not restricted, so that curved shapes

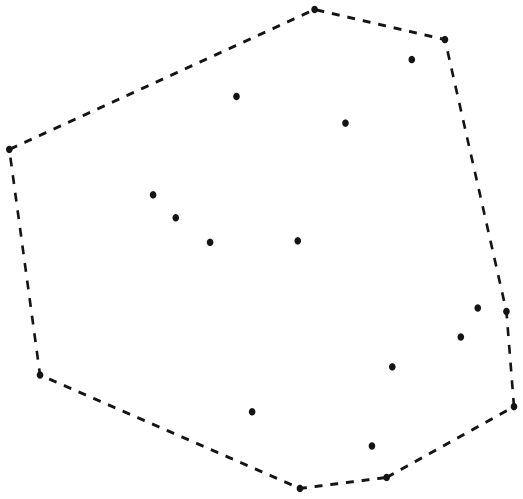

Fig. 1 An example of the convex hull of a set of random points

can be well-approximated by small line segments, while retaining the ability to match sharp corners where necessary.

In CSG methods with canonical shape primitives, each shape may have a few defining parameters such as center location, bounding box size, or rotation. These may or may not be compatible between varying shapes making hybridization or crossover difficult with a GA approach. Here, each shape is described as a list of points, and though its length is arbitrary, we can easily perform crossover as the data has identical meaning across chromosomes. While this convex hull approach is capable of generating a wide variety of shapes, it is incomplete as it is incapable of generating concave shapes and varying topologies; the methodology for deriving concave shapes from convex hulls using Boolean operations is described in Subsection 2.1.2.

2.1.2 Constructive geometry

The convex shape primitives described in the previous subsection can be combined to generate more complex geometries and topologies in a variety of ways. Boolean operations can be used in applications with a single material, such as the microwave imaging of perfect conductors (Wildman and Weile 2007). For problems with more than one material, an overlapping scheme can be used, in which each convex polygon also contains material properties and a priority value designating which operand is placed on top (Wildman and Weile 2010). Here, we will use a scheme similar to the overlapping scheme of (Wildman and Weile 2010), but somewhat simplified by removing priority values from the terminal nodes.

The construction scheme used here is rather simple: Given a binary tree with terminal nodes containing point lists and material properties, at each function node, always place the topology from the left operand on top of the topology from the right operand. This is somewhat equivalent to using only union functions, but assigning each terminal node a sign (essentially the material properties), so that subtraction can be generated with two oppositely signed operands (equivalent to differing material properties). While simple, this approach will generate any physically realizable topology including shapes with holes and multiple disjoint shapes. Consider a few examples, each assuming a two material system embedded in an infinite medium consisting of one of those materials.

First, a concave shape can be generated by overlapping two convex shapes of the same material, essentially resulting in the union of the two shapes. Figure 2 shows a three node binary tree representing the overlap of the convex polygon C_1 on convex polygon C_2. The two (randomly generated) polygons are shown in Fig. 3, with C_1 represented as the solid line resulting from the convex hull of the points marked as circles, and C_2 being the dashed line resulting

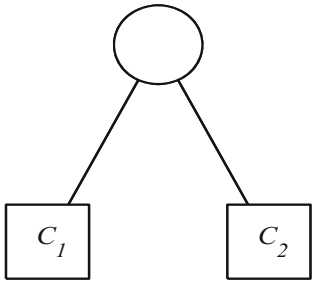

Fig. 2 A three node binary tree

from the points shown as squares. The result of applying the tree of Fig. 2 to the convex polygons of Fig. 3 is shown in Fig. 4. Disjoint topologies can be generated if C_1 and C_2 do not overlap, thus generating two convex polygons in the plane.

Next, a topology with a hole can be generated if a shape contained entirely within another and of a different material is overlapped. Say C_1 is contained within shape C_2 and is made of the same material as the background medium, as shown in Fig. 5. Generating polygons from the convex hulls and overlapping using the tree shown in Fig. 2, the topology in Fig. 6 is generated. These three basic operations described can then be combined with more complex tree structures, generating more complex topologies.

The computational geometric operations used to evaluate a CSG tree are available in the Computational Geometry Algorithms Library (CGAL) (CGAL 2007) as Boolean operations on Nef polyhedra (Bieri 1995). A Nef polyhedron is a polygon or polyhedron that is generated by Boolean operations on half-spaces, which may be open or closed; i.e. they may or may not be inclusive of the defining boundary of the half-space. Nef polyhedra may then have

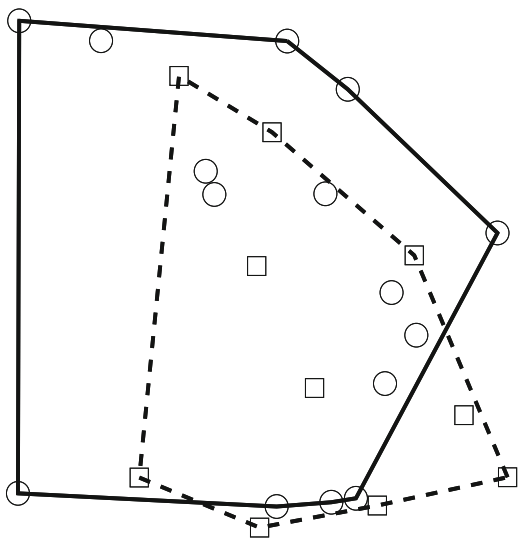

Fig. 3 Two randomly generated sets of points and their convex hulls

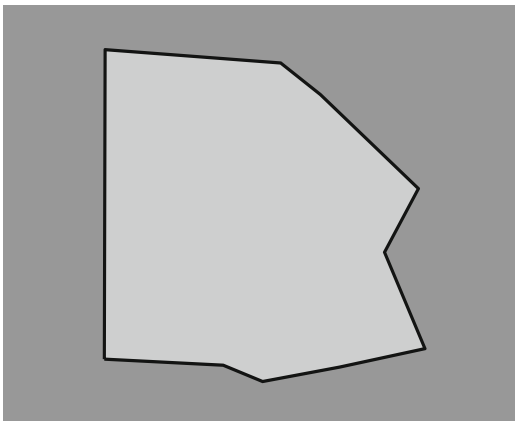

Fig. 4 A concave polygon result generated by applying the tree operation in Fig. 2 to the convex polygons in Fig. 3

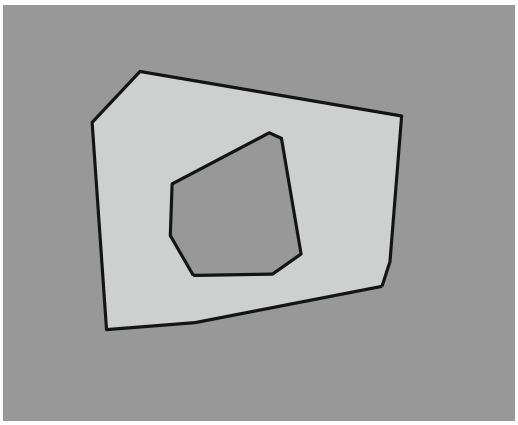

Fig. 6 A hole topology result generated by applying the tree operation in Fig. 2 to the convex polygons in Fig. 5

infinite extents and be open or closed on their boundaries. While there is no specific "overlap" function in CGAL, we can generate one using Boolean operations. Consider a binary overlap function, with Nef polyhedra as operands in general. The first step in computing an overlap function is to compute a boundary inclusive "union mask" of the right operand. This union mask is simply the union of all underlying operands, ignoring material properties and including the defining boundaries of the topology. Next, we subtract the union mask from the left operand with its boundary excluded. Finally, the union of the result of the subtraction operation and the right operand (with boundary excluded) is computed to generate the final topology. Essentially, our binary overlap operator, must include the boundary inclusive union mask as a third parameter, which is updated at each node and passed up the tree during computation.

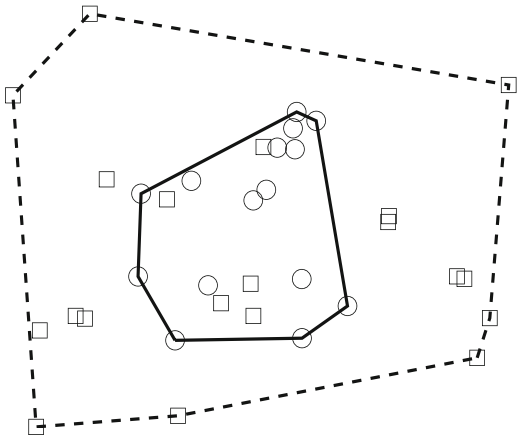

Fig. 5 Two randomly generated sets of points and their convex hulls

2.2 Genetic programming

Genetic programming (Koza 1999) is a variation of a GA, whereby the chromosome structure is tree-shaped, rather than linear with fixed length (Goldberg 1987). It is functionally equivalent to a standard GA because it uses the same three genetic operators—selection, crossover, and mutation—applied iteratively to a population of chromosomes. Because the chromosome is tree shaped, crossover is the same in spirit, though issues such as tree bloat (Banzhaf et al. 1999) preclude a naïve implementation. Due to the flexibility in the chromosome, mutation has several more options than in standard GA. The following subsections discuss the implementation of our topology scheme in GP in more detail.

2.2.1 Chromosome structure

The chromosome in a GA is a data structure that encodes a potential solution to the optimization problem. In a standard GA with a fixed-length, linear chromosome, the position on the chromosome of each "gene" or value in the chromosome has a specific meaning. In other words, if our optimization problem were to find the optimal rectangular solid for a given forward problem, we could parameterize the shape as shown in Table 1, where h is the height of the unrotated rectangle, w is its width, θ is a rotation angle, and x_0 and y_0 are its center location.

Table 1 A chromosome with five genes representing a parameterization of a rectangle

g_1	g_2	g_3	g_4	g_5
h	w	θ	x_0	y_0

Each gene has a specific meaning pertaining to some aspect of the rectangle and of course hybridizing g_1, the height with g_3, the rotation angle, would be meaningless.

In GP, chromosomes are more flexible, and as such, specific data or functions may have to be labeled. For example, if we use a more general binary tree that includes different operations, we would have to label each function node with its function: union, subtraction, etc. As with a standard GA, hybridizing genes with different meanings may not aid in optimization. In order to keep crossover meaningful, we attempt to simplify the data structure as much as possible, so that each function node is identical (i.e. overlap the shape on the left), and each terminal node contains a list of points and material properties. Material properties can either be arbitrary with a given range, or chosen from a database. A complete chromosome is then described by two data structures, a tree giving the constructive geometry, and point lists and material properties for each terminal node of the tree. Table 2 gives an example of the data structure of two terminal nodes that might correspond to the tree shown in Fig. 2.

2.2.2 Selection

GAs have many options for selection. Typical single objective methods include tournament selection, roulette wheel selection, or truncation selection (Goldberg 1987). In this work, we will use selection appropriate for multiobjective problems. GAs are amenable to multiobjective problems because they use a population of potential solutions. Rather than a single solution, we seek a set of solutions corresponding to the optimal tradeoffs between two conflicting objectives. Consequently, to convert a standard GA to a multiobjective GA, the only change necessary is to the selection operator. The most popular multiobjective selection method is known as non-dominated sorting (Srinivas and Deb 1994; Deb et al. 2002), in which the population is ranked based on its performance relative to the current Pareto front.

Non-dominated sorting proceeds as follows: First, the Pareto front is determined by finding all non-dominated chromosomes. The set of dominated chromosomes (for minimization) Y can be defined as

$$Y = \left\{ \mathbf{y} | \exists \mathbf{y}^* \wedge \forall i,\ y_i^* \leq y_i \wedge \exists j,\ y_j^* < y_j \right\}, \tag{1}$$

where $\mathbf{y} = [y_1, y_2, ...]$ is a goal vector or vector of objective function values. The non-dominated set is then just the complement of the dominated set. In other words, the dominated set is simply the set of chromosomes with objective function values that are clearly worse than at least one other chromosome in the population; for each dominated chromosome, there exists another with all objectives less than or equal, and at least one objective strictly less. The chromosomes in the non-dominated set cannot be compared within their set as each will have at least one better performing goal.

With the definition of non-domination in hand, we can now assign a single objective function value to each chromosome, beginning by ranking each in terms of relative distance to the Pareto front. The first non-dominated set of chromosomes is given a rank of one, and temporarily removed from the population. The non-dominated chromosomes of the remaining set are determined and assigned of rank two. After removal, this process is repeated until each chromosome in the population has a rank. An example of this procedure is shown in Fig. 7, with two goals being minimized and four total ranks.

A chromosome's rank gives a measure of a chromosome's relative distance to the Pareto front, however, it can be insufficient as an objective function value for selection as it will not encourage movement along the front. After all, we want a set of designs that well-represents the Pareto front. To encourage a diverse front, we add a sharing value that penalizes chromosomes that are close to each other in goal

Table 2 Example data structure of a chromosome with two terminal nodes

C_1		C_2	
Mat ID		Mat ID	
k		l	
x	y	x	y
x_0	y_0	u_0	v_0
x_1	y_1	u_1	v_1
x_2	y_2	u_2	v_2
x_3	y_3	u_3	v_3
		u_4	v_4
		u_5	v_5

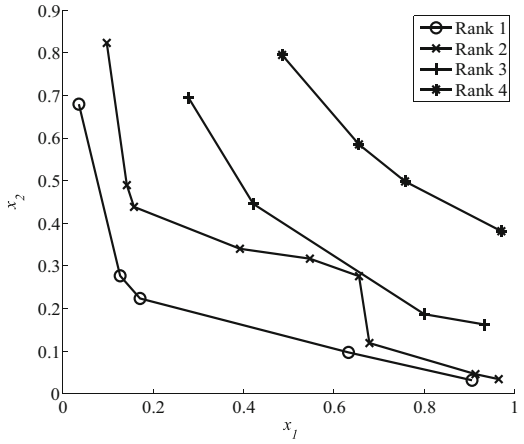

Fig. 7 An example of goal vectors assigned with Pareto ranks

space. Each chromosome i with goal vector $\mathbf{x}_i$ is assigned a sharing value by first finding all other chromosomes within a radius r in goal space. The sharing value for chromosome i is then given by

$$s_i = N_i - \sum_{j=1}^{N_i} \frac{\left\| \mathbf{x}_i - \mathbf{x}_j \right\|}{r}, \tag{2}$$

where $\mathbf{x}_j$ is the goal vector of chromosome j within sharing radius r of chromosome i and N_i is the number of chromosomes within the sharing radius. This approach is described in more detail in Weile et al. (1996).

Finally, a single objective function value that will be maximized can be assigned to each chromosome using its Pareto rank and sharing value. First, all rank one chromosomes are given an objective function value of $f_i^1 = 1/s_i$. Next, the minimum objective function value of the rank one chromosomes is used as the starting value for the rank two chromosomes, i.e. now, for rank two, $f_i^2 = \phi_1/s_i$, where $\phi_1 = \min_i f_i^1$. This process is repeated for rank three and so on. After all chromosomes are assigned an objective function value, standard roulette wheel selection is used.

2.2.3 Crossover

After selection, a new population is generated with an average fitness better than the previous generation. Crossover is then used to combine traits of those surviving chromosomes to hopefully generate even better performing chromosomes. In a standard GA, crossover is typically performed by first randomly choosing two chromosomes from the new population. A gene, say g_3 in Table 1, and hybridized in some way. The genes following (g_4 and g_5) are then swapped between the two chromosomes.

In GP, crossover is performed in a similar way: Two nodes in a tree are chosen at random and hybridized if applicable, and their subtrees are swapped. Given that our function nodes are identical, there is no hybridization to be done, however, if two terminal nodes are chosen, their point lists and material properties can be hybridized. As the point lists are of arbitrary length, they can grow without bound in some situations. This is related to the issue of tree bloat (Banzhaf et al. 1999), in which tree sizes grow without bound as protection against harmful mutations and crossover. Larger trees (or point lists) can contain more redundant information, so that crossovers and mutations with the potential to harm performance are minimized. This can lead to population stagnation, so it is undesirable. For point lists, we then use a two point crossover, ensuring that the number of points exchanged between two terminal nodes is equal so that each point list remains the same length. An example of this process is shown in Table 3: The double-horizontal lines and text in bold in the point lists show the two crossover points, and the coordinates x_i, y_i and u_i, v_i will be swapped between nodes C and D. The crossover points are chosen at random. Additionally, the points at the crossover locations are hybridized, i.e. mixed together by choosing a number t from a uniform random distribution between 0 and 1 as

Table 3 Example of crossover between two terminal nodes

C		D	
Mat ID		Mat ID	
k		l	
x	y	x	y
x_0	y_0	u_0	v_0
$\boldsymbol{u_1}$	$\boldsymbol{v_1}$	$\boldsymbol{x_1}$	$\boldsymbol{y_1}$
$\boldsymbol{u_2}$	$\boldsymbol{v_2}$	$\boldsymbol{x_2}$	$\boldsymbol{y_2}$
$\boldsymbol{u_3}$	$\boldsymbol{v_3}$	$\boldsymbol{x_3}$	$\boldsymbol{y_3}$
x_4	y_4	u_4	v_4
		u_5	v_5

$$\begin{aligned} \mathbf{p}^* &= t\mathbf{p} + (1-t)\,\mathbf{q} \\ \mathbf{q}^* &= t\mathbf{q} + (1-t)\,\mathbf{p}, \end{aligned} \tag{3}$$

where $\mathbf{p}$ and $\mathbf{q}$ are the points at the crossover locations. Finally, because we are using a database of material properties, we do not hybridize materials, although this is not a restriction, as randomly generated constitutive parameters may benefit from hybridization.

To combat tree bloat, we use a crossover probability based on geometric similarity. Typically, the crossover probability is a constant around 80 %, and subtrees are chosen at random between two random chromosomes. Our implementation sets a crossover probability by first selecting a chromosome for crossover. A mate is chosen out of a pool of random chromosomes, the size of which is an input parameter, typically chosen as ten. Each chromosome in the mating pool is assigned a probability by randomly choosing a given number of subtrees (again, usually chosen to be at most ten) in each and comparing their decoded geometries as

$$p_c = \left[\frac{\Delta\left(C_1 \bigcap C_2\right)}{\Delta\left(C_1 \bigcup C_2\right)} \right]^s, \tag{4}$$

where $\Delta\left(C_1\right)$ indicates the area of the topology generated from subtree C_1 and s is a biasing exponent typically chosen as 2.5. Consequently, if C_1 does not overlap C_2, then p_c is zero, and if $C_1 = C_2$ then p_c is one. Now, p_c is computed for a given number of randomly chosen subtrees of a mating pair, and the maximum is saved. After the maximum p_c is found for each mate in the pool, a mate is chosen at random using a weighted roulette wheel with the weights given as the crossover probabilities. In other words, we choose

a random mate from the pool, favoring mates with higher crossover probabilities. Crossover is then performed using the chosen mating pair and subtrees with the maximum p_c.

While this scheme is somewhat convoluted, it is designed to match similar pairs of subtrees, but with some randomness. Matching similar subtrees helps ensure population convergence and randomness aids diversity. Striking a balance between the two is important in the design of a GA, so that it can cover a large search space and resolve fine details simultaneously. These issues are not present with a fixed length chromosome representation as we know *a priori* the function of each gene in a chromosome, thus ensuring that crossover is meaningful.

2.2.4 Mutation

The final genetic operator, mutation, is used to inject new genetic information into a population, preventing premature convergence or stagnation. In our implementation, the flexibility in the chromosome allows for a large number of options for mutation. We can, on one hand, manipulate solely the encoded chromosome (tree structure with point lists at the terminal nodes) and on the other hand, adjust the decoded topology. The mutation rates for the examples in Section 4 are constant throughout, so they are listed here.

First, single points from terminal node point lists are deleted with a given probability. This rate can be set somewhat high (for mutation rates) as terminal nodes tend to grow in length for reasons discussed earlier. Here we use a point deletion rate of 2 % per point. There is a minimum length for terminal nodes of three, as three points are required for a 2D simplex. We also duplicate points in a terminal node with a 0.5 % rate per point. New points are first duplicated then shifted by a random amount according to a Gaussian distribution with standard deviation of 10 % of the largest dimension of the design bounds (20 mm in all examples from Section 4).

Points are also added by splitting existing convex hull segments. First, a terminal node is decoded by taking its convex hull. Next, for each line segment in the hull, we randomly insert a new point at a random location between 10 % and 90 % of its length. This mutation is performed with a rate of 0.5 % per segment.

In a mutation most analogous to a standard GA, points are shifted by a random amount. The shift amount is chosen from a Gaussian distribution with zero mean and standard deviation of 10 % of the region size (as above for point duplication), and the mutation rate is 1 % per point.

One issue with the above point mutation method is that a non-coding point (a point not on a convex hull) can be moved to another non-coding position, meaning that ultimately the mutation had no effect on the decoded topology. A convex hull aware point mutation was designed to remedy this situation. Given a point $\mathbf{p}$ inside a convex hull, the closest segment on the hull is found. Two vectors are formed pointing from the point inside the hull, to the two points $\mathbf{q}_1$ and $\mathbf{q}_2$ defining the closest segment. The point inside the hull is then moved inside the parallelogram formed by the addition of these vectors as

$$\mathbf{p}^* = r_1 (\mathbf{q}_1 - \mathbf{p}) + r_2 (\mathbf{q}_2 - \mathbf{p}) + \mathbf{p}, \tag{5}$$

where r_1 and r_2 are two random values from a uniform distribution between 0 and 1. This mutation then has a 50 % probability of altering the convex hull and is used with an overall rate of 1 % per point.

Points are also deleted by pruning non-coding points that are inside a point set's convex hull. As an extreme example, a point list may contain hundreds of points, but only three actually on the convex hull that defines its decoded shape. These redundant points can be harmful to a population's progress, and so they can be pruned. Points to be pruned are chosen by first computing the convex hull of the point list and scaling it by a random amount between 0.4 and 0.8. All points within this scaled convex polygon are removed from the point list. This mutation is performed at a rate of 5 % per terminal node.

We can also apply affine transformations to the terminal node point lists, effectively altering the overall geometry. Here, we separately apply scaling, rotation, or translation mutations with a rate of 1 % per terminal node. If a node is chosen for affine transformation, scaling, rotation, or translation is chosen at random with equal probability. Each transformation has its defining parameter chosen from a Gaussian distribution: Scaling uses a mean value of 1 and a standard deviation of 0.1, rotation uses a mean of 0 and standard deviation of $\pi/10$, and translation uses a mean of zero and standard deviation of 10 % of the region size for both coordinates.

Material properties can also be mutated. Here we use a database of materials and so, with a given probability of 1 % per terminal node, we simply choose a new material at random from the database.

Finally, we can alter the tree structure of a chromosome. The first type of tree mutation is standard in GP, subtree deletion and regrowth. In this mutation, a subtree is deleted and replaced with a randomly generated subtree with a given probability. This type of mutation can be destructive so it is applied with a low probability of 0.5 % to each node in a tree. Another way of altering the tree structure is to split terminal nodes into a function node with two new terminal nodes. There are a few ways of accomplishing this, first, we can simply split a terminal node's point list at an arbitrary point and separate it into two new nodes. Next, we can separate points internal to a list's convex hull, much like the pruning operation described above. Here, we again scale down the convex hull of a point list, and separate points

Table 4 Summary of mutation rates

Type	Rate	Unit
Point deletion	2 %	Point
Point duplication	0.5 %	Point
Segment splitting	0.5 %	Segment
Point translation	1 %	Point
Convex hull mutation	1 %	Point
Point pruning	5 %	Terminal node
Affine transformation	1 %	Terminal node
Material mutation	1 %	Terminal node
Delete node	0.5 %	Node
Split list	1 %	Terminal node
Split hole	1 %	Terminal node
Split line	1 %	Terminal node
Aggregate lists	6 %	Function node

inside the scaled hull and those outside into two new terminal nodes. Finally, we can split a set of points by placing a line through the polygon and separating all points (geometrically) left of the line into one new list and points right into another. The line is chosen by passing an infinite line through two randomly generated points within the list's convex hull. The intersection points of this line and the convex hull are computed and inserted into each new terminal node to ensure that the decoded subtree is similar to the original. Each of these splitting mutations are performed with a rate of 1 % per terminal node. As these mutations can lead to large tree sizes, subtree point list aggregation is also performed in opposition. In this mutation, a function node is chosen and all point lists in the terminal nodes within the subtree are aggregated into a single terminal node. This is performed at a rate of 6 % per function node.

The types and rates of mutation are summarized in Table 4. The number and complexity of the mutation operators is due to the flexibility in the topology representation, and some work remains in determining the effectiveness and usefulness of each individual operator.

3 Multiscale forward problem

The goal of this work is to optimize a material's local-scale structure. One approach would be to construct a model of a material by repeating a given RVE over a finite region and use a very fine mesh; however, this may lead to overly long execution times due to the fine mesh. Instead, we will use the concurrent multiscale finite element method MultiMech, which uses RVEs to represent a material at a local scale (Souza et al. 2008; Souza and Allen 2010, 2013). We assume that our global scale structure is statistically homogeneous, but has inhomogeneous local structure, which will be optimized. We will consider static loading problems to address structural stability along with dynamic problems for energy dissipation.

3.1 Methodology

Typically, a finite element problem will have the material properties of each element as an input. In a multiscale FEM problem, the global scale only assumes that the material properties over an element are statistically homogeneous, and they are then derived from local scale representative volume elements (RVEs). Each integration node in the global mesh has an associated RVE, each of which is itself a finite element problem, with loads derived from the global mesh. These RVE problems are quasi-static with spatially homogenous (linear displacement in this case) boundary conditions. Material properties are then garnered from the RVE problems and used to solve the global problem. The purpose of this work is to then optimize the topology of the material at the RVE scale, assuming a homogenous set of RVEs, though the model RVE itself is not homogeneous. Figure 8 gives an example of a multiscale problem: A global mesh is shown with points representing integration nodes of a one-point rule. Each integration node then has an RVE attached, the geometry of which is shown in the inset. The global geometry is assumed to have the same RVE geometry at each element, and the RVE itself is a bi-material system, with one material shown in black and one in white in this example; however, this methodology is easily generalized by allowing RVEs to vary from point to point for solution of a globally inhomogeneous optimization problem. The RVE is shown to scale; in this case, it is one tenth the size of the global mesh.

Each RVE is an independent finite element problem and so they can be solved simultaneously. MultiMech can take

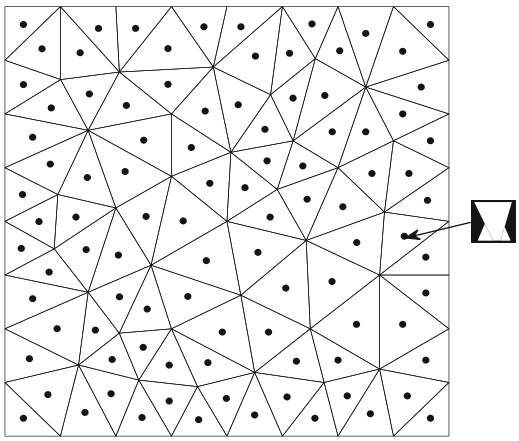

Fig. 8 An example of a global mesh with embedded RVEs

advantage of this and parallelize the computation of the individual RVE FEM problems. We can also parallelize the GA, leading to a parallel problem that requires a large number of compute nodes. Consider a GA running 150 compute nodes in parallel, if we then want to use 16 nodes for each multiscale FEM forward problem, we need 2,400 compute nodes for this problem.

3.1.1 Damage modeling

Damage is modeled in this FEM code using cohesive zones (Xu and Needleman 1994, 1996) at the local scale and XFEM at the gobal scale. At the local scale, cohesive zones are automatically inserted between elements after the traction has exceeded a given value. If a number of cohesive zones coalesce within the RVE, the damage is propagated up to the global scale. In this case, extended finite elements (Chessa et al. 2002) are inserted in the global scale finite element mesh. Currently in MultiMech, XFEM together with multiscale RVEs are only available for static loading, so they are not used in the dynamic problem under consideration. One unfortunate side effect of this approach is that inserting cohesive zones adds elements to the mesh, increasing the number of unknowns. A design that is badly damaged can lead to long run times, so it is important to parallelize both the GA and the forward problem. Finally, triangular elements are used at the global scale throughout, rather than the more standard quadrilateral elements, because the XFEM algorithm in MultiMech is implemented for triangular elements.

3.1.2 Meshing

FEM necessitates the use of a mesh for each design. The global scale can be meshed once and used for each forward evaluation, but each new chromosome must be meshed before it can be used as an RVE. As described in Subsection 2.1.2, the topology is decoded using Boolean operations on Nef polyhedra using CGAL (CGAL 2007), which must be performed with exact arithmetic using rational numbers. We use the meshing algorithm from CGAL, though some care must be taken: CGAL's meshing utilities use inexact arithmetic with floating point numbers, so there can be slight errors on the order of machine precision in converting from exact to inexact numbers. CGAL's meshing algorithm uses a constrained Delaunay triangulation, requiring the input of constraints. After decoding a topology, constraints are simply the edges and vertices of the resulting polygons; however, if a vertex should lie on an edge in a "T"-like junction in the exact representation, but ends up slightly off due to roundoff error during the floating point conversion, the meshing algorithm may crash. Figure 9 gives an example of this issue. The vertex in the center belongs to one polygon and the flat edge on the bottom belongs to a second polygon. The meshing algorithm will attempt to place very small triangles in this area, in an attempt to maintain triangles that are close to equilateral. As the vertex approaches the edge, the number of triangles grows, and at some point the meshing algorithm will crash.

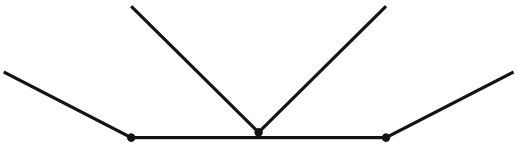

Fig. 9 An example of a difficult meshing case

This situation is most easily handled on the exact side through some pre-processing. We iterate over all vertices and all edges and check if a vertex is "close" to an edge, but is not one of its defining vertices (i.e. a T-junction). "Close" is defined here with an input parameter, which is compared to the length of the vector connecting the vertex and its orthogonal projection onto the edge. If this length is less that the input parameter (used here as 0.01 mm), then the vertex is replaced with its orthogonal projection. In this representation the vertex is now exactly lying on the edge, and so the segment will be replaced with two segments connecting at that vertex during decoding.

As we are using a stochastic optimization method, difficult to mesh designs frequently crop up. There are situations that may lead to meshes with excessively large numbers of triangles, and so these are best discarded as designs that cannot be evaluated to save execution time.

Figure 10 gives a flow chart that summarizes the overall algorithm. The main GA loop is shown in the center, consisting of evaluation, selection, crossover, and mutation. Each stage has an exploded view on the right or left describing those steps in detail.

3.2 Problem setup

We will optimize for two types of loading in a multiobjective setting: Quasi-static and dynamic. The goal of the quasi-static loading problem is to develop a material for structural stability, so we will minimize displacement under a given vertical load. The goal of the dynamic loading problem is to design a material that will absorb energy, so we will maximize strain energy. The two types of problems are described in the subsequent subsections.

3.2.1 Static loading

The quasi-static problem is configured as shown in Fig. 11. We apply a vertical displacement to a 200 mm-by-200 mm block of material that has fixed displacement in both the x

Fig. 10 Algorithm flow chart

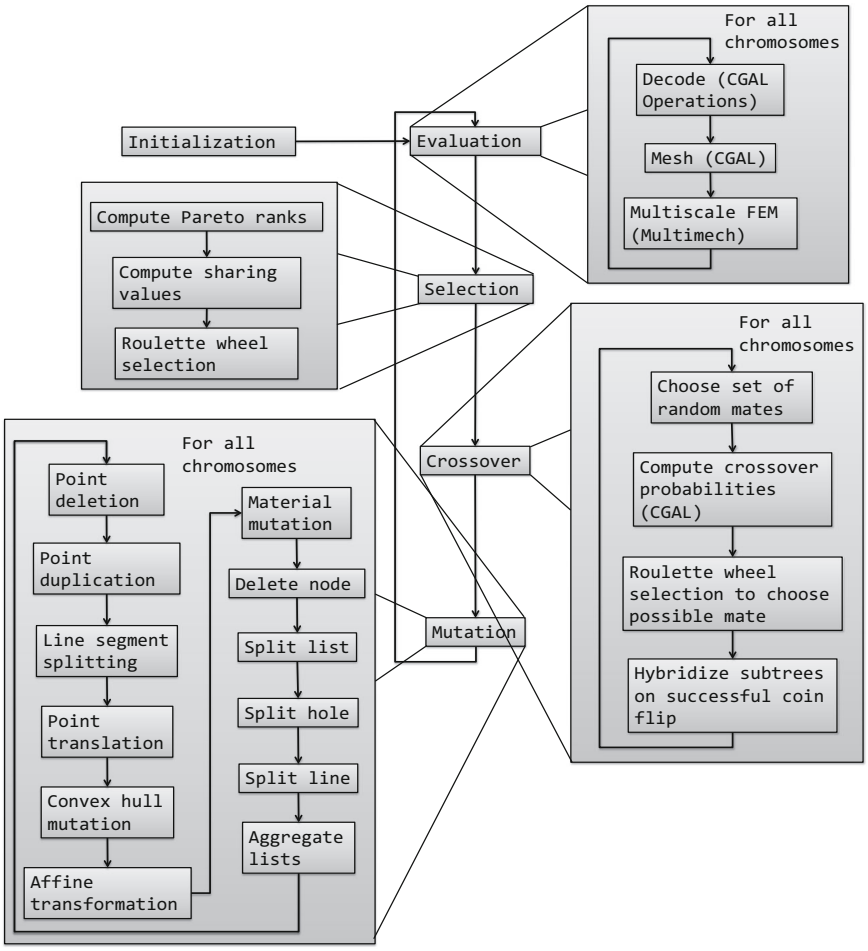

and y directions along the $y = 0$ edge. The size of the RVE is 20 mm-by-20 mm and the problem is plane stress. We apply a load in the $-\hat{\mathbf{y}}$ direction with a value of 2 Pa along the top edge of the structure. The goal of the optimization problem is to minimize the displacement along the loading area, so the objective function is simply the sum of the displacement along the top edge:

$$\mathbf{D} = \int_{\Gamma} \mathbf{u}\left(\mathbf{x}, T\right) d\mathbf{x}, \tag{6}$$

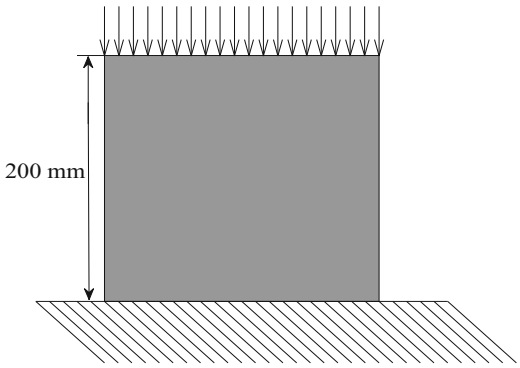

Fig. 11 Static loading problem

where $\mathbf{u}$ is the displacement, T is the time at the final time step, and Γ is the boundary where loading is applied at the global scale. Without the inclusion of damage, the problem is linear so the magnitude of the load is not important because it will be normalized in the objective function. With damage, we use total time of 0.1 s with 200 steps in a quasi-static solver. Another goal used in the static loading case will be total mass of a local scale RVE:

$$m = \int_{\Omega_l} \rho\left(\mathbf{x}\right) dA, \tag{7}$$

where Ω_l represents the local scale region, and ρ is the density.

3.2.2 Dynamic loading

The setup of the dynamic problem (shown in Fig. 12) is similar to that of the static problem, though we apply a horizontal load along the $x = 0$ and $x = 200$mm edges as well and with a pressure-time history shown in Fig. 13. Here, we use a time step size of 1 μs over a total of 300 μs. The

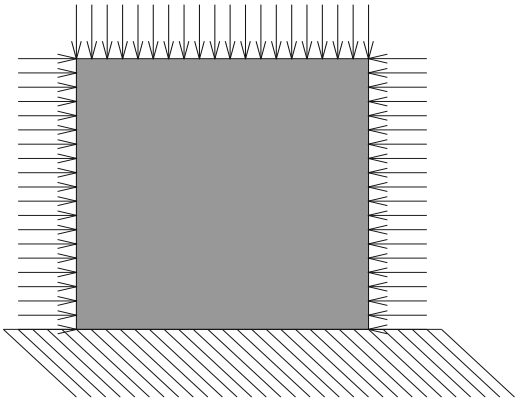

Fig. 12 Dynamic loading problem

objective function is the strain energy at the global scale, summed over the entire run time, as

$$U = \frac{1}{2}\int_0^T \int_{\Omega_g} \sigma_{ij}\left(\mathbf{x}, t\right)\epsilon_{ij}\left(\mathbf{x}, t\right) dA dt, \tag{8}$$

where σ is the stress tensor, ϵ is the strain tensor, Ω_g is the global scale region, and Einstein summation is assumed. This objective will be maximized as we seek a design that absorbs energy. It represents a conflicting goal with the static loading problem, and so we must solve in a Pareto-optimal sense.

4 Results

In this section, results of the optimization are presented. Several design cases are presented, each with the same material system, (a dense, stiff linear elastic material and void), though with varying damage models. To summarize, first, in Subsection 4.1, a baseline linear elastic model at the local scale with no damage modeling is given. Next, in Subsection 4.2, we consider the same linear elastic material,

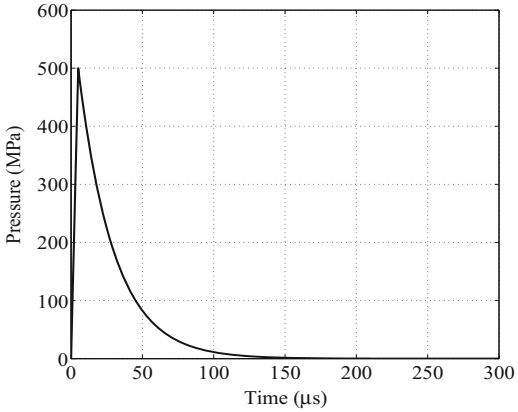

Fig. 13 Pressure load for the dynamic problem

but allow damage in the form of cohesive zone insertion at the local scale only. Finally, in Subsection 4.3, the same local scale model (linear elastic with cohesive zone insertion) is used, but global scale damage is considered using XFEM and a multiscale localization method described below. In each case, we will use two objectives, forming a generic goal vector as:

$$\mathbf{f} = \left[f_1, f_2\right], \tag{9}$$

with f_1 and f_2 being one of the objectives defined above, U, $\mathbf{D}$, or m.

In addition, each example was run twice (with different seeds for the random number generator) and compared to demonstrate stability of the stochastic method. As this is a multiobjective optimization that does not iteratively step through one design goal as a constraint, any comparison between optimization results must consider the curve of the approximate Pareto fronts. To that end, we define the difference in results as the integral of the difference in approximate Pareto fronts, using a linear interpolation between rank-one chromosomes, given by the piece-wise parameterization

$$\mathbf{F}\left(t\right) = \left(n - t + 1\right)\mathbf{f}_n + \left(t - n\right)\mathbf{f}_{n+1},\ n \le t \le n+1 \tag{10}$$

where $n = 1, \ldots, N_1$ and N_1 is the number of rank-one designs. While the results from two runs may have different values of N_1 and different spacings between all f_1, (10) can nonetheless be converted from a parametric form as, by definition of Pareto optimality, it can be defined as a function. Given a suitable mapping to a function $g\left(x\right)$, a relative error measure can then be defined as

$$\text{Error}_{a,b} := \frac{\int_1^{f_{1,\max}} \left|g_a\left(x\right) - g_b\left(x\right)\right| dx}{\sqrt{\int_1^{f_{1,\max}} \left|g_a\left(x\right)\right| dx \int_1^{f_{1,\max}} \left|g_b\left(x\right)\right| dx}}, \tag{11}$$

where $f_{1,\max} = \min\left(\max f_{a,1}, \max f_{b,1}\right)$ is the minimum of the maximum values of goal f_1 of both runs, $f_{a,1}$ is the first goal of one run and corresponds to function g_a, and $f_{b,1}$ and g_b represent a second run. In practice, the two functions are simply discretized on an even, fine grid and the integral is computed numerically.

4.1 Linear elastic

The first results use a linear elastic material in the RVE, with Young's modulus 65 GPa, Poisson's ratio 0.2, and density 2235 kg/m^3. The remaining material was assumed to be void. The global scale geometry is given in Figs. 11 and 12, with loads and boundary conditions as discussed in Subsections 3.2.2 and 3.2.1. Here, the goal vector is given as

$$\mathbf{f} = \left[\left|\mathbf{D}\cdot\hat{\mathbf{y}}\right|, U\right], \tag{12}$$

and we wish to minimize f_1 and maximize f_2.

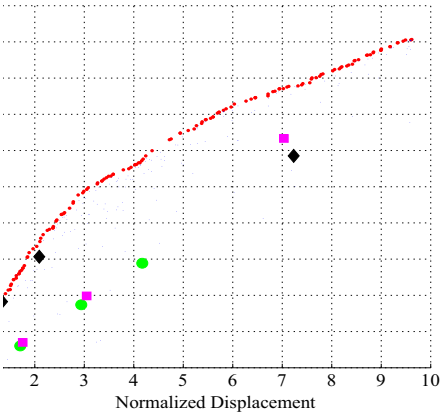

tion for the linear elastic example after 350 generations

thm was run for 350 generations with a pop-
of 500, resulting in the population shown in
ed in goal space. In this figure, the red circles
pproximately Pareto optimal members of the
1 members), while the set of blue × show the
opulation members. The static displacement is
x-axis with the strain energy on the *y*-axis and
rmalized by the value given by a design con-
of the material given above (i.e. no voids). The
Pareto front appears to be devoid of many dis-
nd only contains a small area of large slope

on the left, indicating that any choice on the front would be satisfactory if it fit a problem's constraints. Several designs from the front are shown in Fig. 15, in which the elastic material is shown as black and void is shown as white. The first is the best performing design in terms of strain energy shown in Fig. 15a. The outer frame is deliberately inserted by the algorithm, so that closed cell solutions are generated. The next design is from the center of the front (Fig. 15b), and has a normalized displacement of approximately 5 and a normalized strain energy of approximately 7.5 (in other words, the displacement is 5 times higher and the strain energy is 7.5 times higher than those of a fully dense design). It has an interesting design, with a pillar through the middle of the cell. The final two designs (the first with a normalized displacement 2.3 and a normalized strain energy 4.8 shown in Fig. 15c, and the second with displacement of nearly 1 and strain energy of 1.9 shown in Fig. 15d) show designs with two voids. Designs with normalized values of 1 are fully dense with material, so the final design shows some diminishing returns in terms of displacement, i.e. we have to give up a large amount of strain energy to get only a small amount of displacement. This type of analysis is difficult when simply applying constraints to generate a single design.

To test the significance of the results, a few canonical designs were tested and compared against the designs returned by the optimization algorithm. First, a local scale

ed designs from
e Pareto front

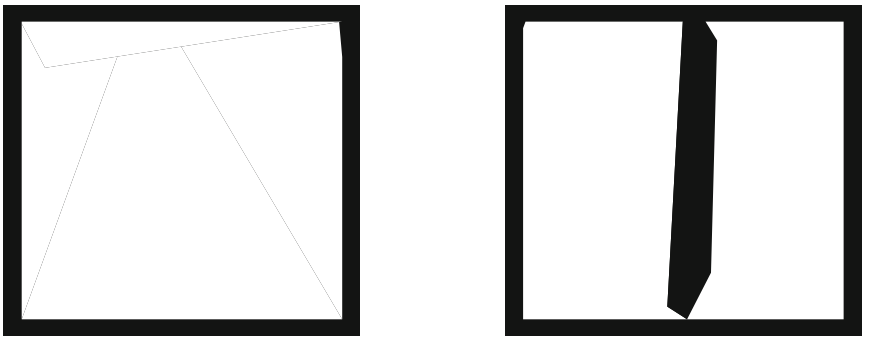

(a) Best strain energy

(b) Tradeoff design

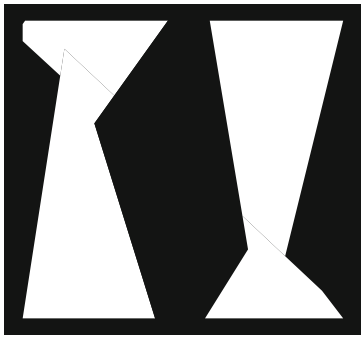

(c) Tradeoff design

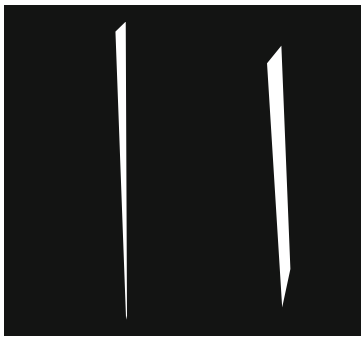

(d) Low displacement

design with a centered, circular inclusion was tested for three different volume fractions, 36 %, 50 %, and 75 %, and are shown in Fig. 14 as the green circles, with the 75 % volume fraction design having the lowest relative displacement. As can be seen from the plot, the designs with circular inclusions do not approach the approximate Pareto front. Next, centered, square inclusions were tested, again with volume fractions of 25 %, 50 %, and 75 % and shown in Fig. 14 as the magenta squares. Again, these designs are not competing with the designs returned by the optimization algorithm, though the optimal design at the minimal displacement and maximal strain energy is a square inclusion due to the constraints placed on the designs. Finally, the SIMP algorithm was run on a 50-by-50 grid constrained at the same volume fractions, with the outer frame forced as solid material and the boundary condition given by the static displacement boundary condition used at the global scale. These designs were then used as the local scale RVEs and their objective function values computed. (Their contours were generated using the built-in Sobel edge detection algorithm from Matlab and the 50 % volume fraction design is shown in Fig. 16 as used in MultiMech before automatic meshing.) The SIMP designs are plotted in Fig. 14 as the black diamonds. The lowest displacement design (75 % volume fraction) lies with the rank-1 GP-generated designs, while the 50 % and 25 % designs are suboptimal in the Pareto sense. That the lower displacement design lies on the approximate Pareto front is not surprising; because low-displacement designs are mostly solid material, small changes in geometry would not produce large changes in strain energy.

To further study the results, local optimization was performed on a design from the approximate Pareto front. As we are interested in two goals, the local optimization will attempt to improve one goal, while holding the second as a constraint using a penalty in the form:

$$f = \left|\mathbf{D}\cdot\hat{\mathbf{y}}\right| + p\left|U_0 - U\right|^2, \tag{13}$$

where p is a weighting factor set to 10 and U_0 is the strain energy of the initial design before local optimization. The CSG description of the solution is converted to a set of linear splines to remove any redundant points, thus reducing the dimensionality of the search space. A gradient-based local search algorithm, BFGS, is used on the components of the points in the linear spline. The initial design is shown in Fig. 17 in red, with the final result shown in blue. After optimization, the normalized displacement of the design was improved to 2.34, over 2.43 of the original. Interestingly, while a small improvement was realizable, the resulting design is no more symmetric than the original, indicating a possible insensitivity to symmetry in the optimization problem.

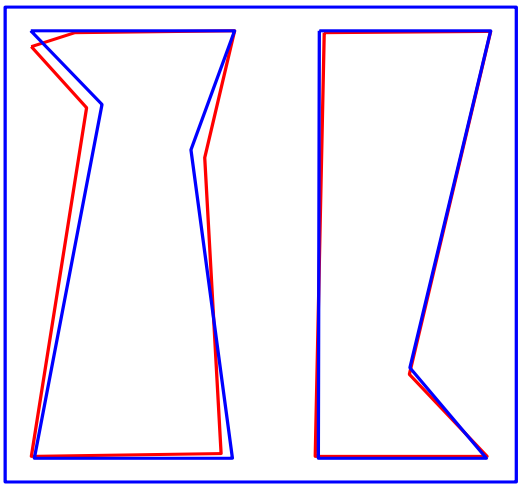

Fig. 17 Result of local optimization

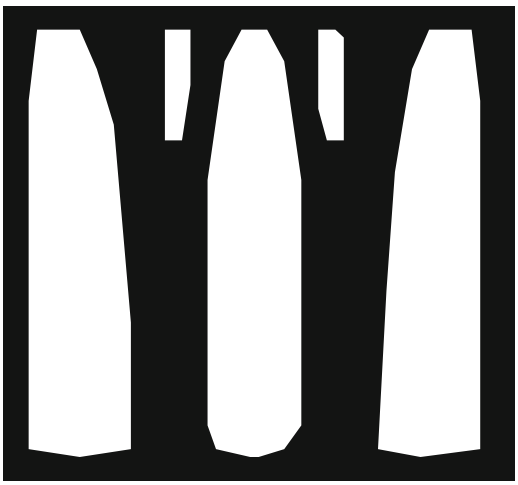

Fig. 16 A SIMP-generated design with 50 % volume fraction

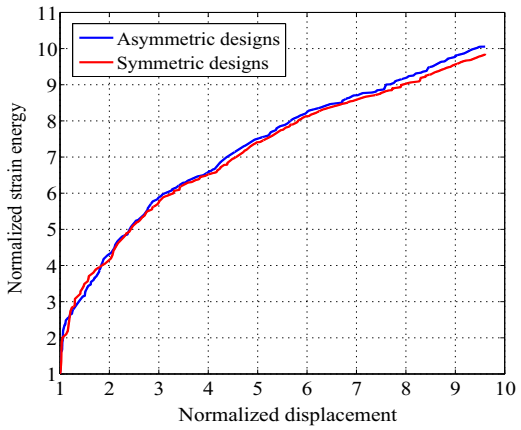

Fig. 18 Approximate Pareto fronts for forced symmetric designs vs. asymmetric designs

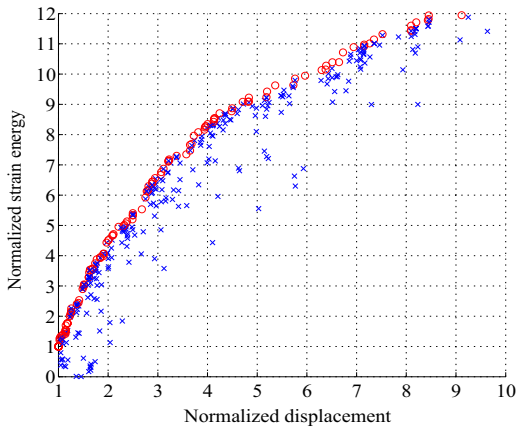

Fig. 19 Population for the example with local scale damage after 250 generations

Finally, as the algorithm tends to generate asymmetrical designs, it was tested with symmetry enforced on the local scale RVE designs. The symmetry plane is $x = 0$ so that the left plane is simply copied and reversed to the right half plane. All dimensions remain the same, though the design domain is now of course restricted to half the original domain. The symmetric designs resulted in an approximate Pareto curve with a difference relative to the asymmetric designs of 1.9×10^{-1}. Overall, the asymmetric designs outperformed the symmetric designs, except for an area below $f_1 < 2$; the two interpolated fronts are plotted in Fig. 18.

4.2 Linear elastic with damage

The problem set up is identical to that of Subsection 4.1, though here we allow insertion of cohesive zone elements at the local scale. Otherwise, all parameters and goals are identical to those in Subsection 4.1, with the cohesive zone model given by the viscoelastic formulation introduced in (Allen and Searcy 2001). The critical opening distances were set to 1 mm, the maximum stresses were set to 10 MPa, and the elastic properties for the model had a Young's modulus of 1 KPa, a Poisson's ratio of 0.2, and a density of 1000 kg/m^3. The approximate Pareto front after 250 generations is shown in Fig. 19, with selected designs shown in Fig. 20. The design in Fig. 20a has a normalized strain energy of 11.9 and a normalized displacement of 9.1, the design in Fig. 20b has a normalized strain energy of 8.3 and a normalized displacement of 4.0, the design in Fig. 20c has a normalized strain energy of 4.5 and a normalized displacement of 2.0, and the design in

Fig. 20 Selected designs from the approximate Pareto front shown in Fig. 19

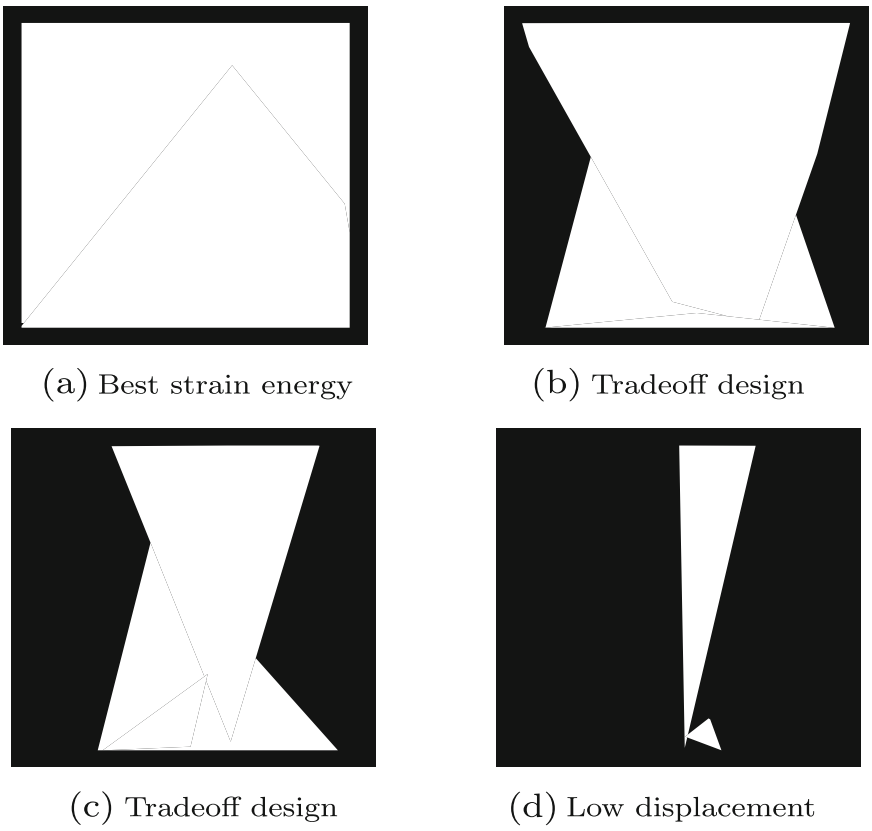

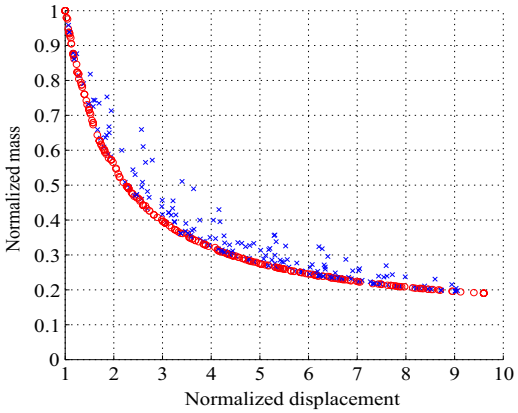

Fig. 21 Population for the example with local scale damage and a mass goal after 500 generations

Fig. 20d has a normalized strain energy of 1.7 and a normalized displacement of 1.14. The addition of damage to the optimization problem seems to have removed designs with a thin, central pillar, rather using an hourglass-like design.

Next, the dynamic loading goal (minimization of strain energy) was changed to minimization of mass, to observe the difference in designs resulting from these two goals. The static displacement goal remains the same, again with the insertion of cohesive zones. The population size was again 500, with the Pareto optimal designs shown in Fig. 21 after 500 generations. The resulting designs are similar to those above in that they do not have any thin segments, though they lack the hour-glass shape seen in designs incorporating strain energy. For example, a design with a similar displacement to that shown in Fig. 20b is shown in Fig. 22, and has a normalized displacement of 1.72 and a normalized mass of 0.63. A second run was performed, and similar results were obtained, with an error as defined by (11) of 4.6×10^{-3}.

Fig. 22 An example of a tradeoff design from Fig. 21

4.3 XFEM results

Finally, an example was run using XFEM at the global scale. The criterion for XFEM element insertion was that a cohesive element is transitioned to the macroscale if the acoustic tensor of the homogenized material tangent degrades to 90 % of its original value, according to

$$\det\left[Q^0_{ij}(t)\right] \leq \chi_c \det\left[Q^0_{ij}(t=0)\right], \tag{14}$$

where Q^0_{ij} is the acoustic tensor at the macroscale at each time step and $\chi_c = 0.9$ is the multiscale localization criterion (Souza and Allen 2011; Nguyen et al. 2011). Here, XFEM element insertion is only available for quasi-static problems, so we use static displacement as one goal and total mass as a second, as

$$\mathbf{f} = \left[\left|\mathbf{D}\cdot\hat{\mathbf{y}}\right|, m\right]. \tag{15}$$

In this example, normal loading (as shown in Fig. 11), a population size of 500, and a total of 280 generations were used. The approximate Pareto front at the final generation is shown in Fig. 23, along with a tradeoff design from the center of the curve (with a value of 1.7 for normalized displacement, and 0.66 for normalized mass) in Fig. 24. This design can be compared with that of Fig. 22, as they have similar objective function values. As expected, for the same displacement, the design using XFEM requires a slightly higher mass, because damage at the global scale weakens the response.

The normal stress (in the y-direction) of a randomly chosen design (with its local scale geometry shown in Fig. 25b) is shown in Fig. 25a along with the inserted XFEM zones (as black lines) at the final time step. A second run resulted in similar results, with an error of 9.8×10^{-3}.

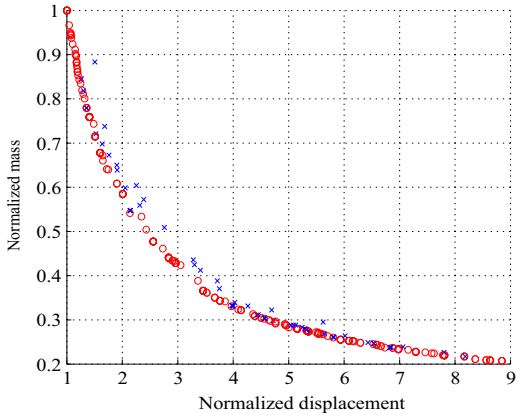

Fig. 23 Population for the example with XFEM 280 generations

Fig. 24 Tradeoff design

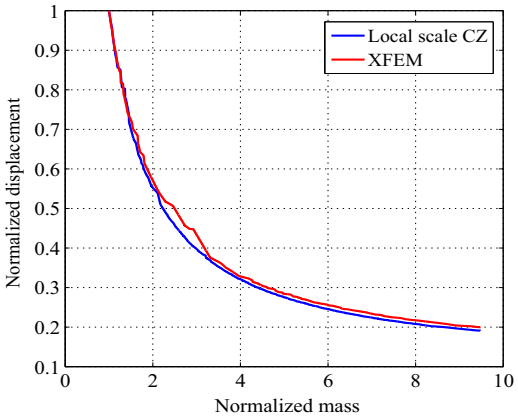

Fig. 26 Comparison between local scale damage model and XFEM

4.4 Discussion

Several design cases are presented above, each producing slightly different results. The design goals always included minimization (at the global scale) of static deflection and either maximization of elastic strain energy or minimization of mass. The use of different damage models (none, local scale CZ, and global scale XFEM) was to establish a baseline design (i.e. no damage model) and compare two damage models, one more accurate but with a higher computational cost (XFEM). The purpose of replacing energy maximization with mass minimization is that they are non-conflicting goals and so it may be possible to replace energy maximization with the more computationally efficient mass minimization.

The results comprise a linear elastic case with no damage, one with damage modeled solely at the local scale in the form of cohesive zone insertion, and XFEM with damage localization at the global scale. The main difference seen between the models that include damage and the baseline is the inclusion of thin supporting members through the center of the RVE. This is sensible as any thin members may incur damage and not contribute to the improvement of static loading, while contributing to the detriment of the strain energy. The main difference seen between the cases including energy maximization or mass minimization as the second goals is the hour-glass like shape of the inclusions. A comparison of Figs. 24 and 20b or 20c reveals that designs accounting for energy maximization tend to form hour-glass structures, while those using total mass result in a more standard structure. Finally, Fig. 26 shows the difference between the Pareto curves generated by the local scale damage model and XFEM. The curves are fairly similar, with a difference of 4×10^{-2}, and, as would be expected, show that the local scale damage model gives results that are consistently better in displacement for the same mass. This figure demonstrates

Fig. 25 An example of the global scale stress and inserted cohesive zones

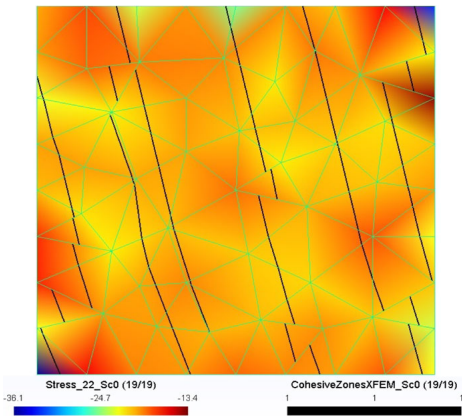

(a) Global scale stress

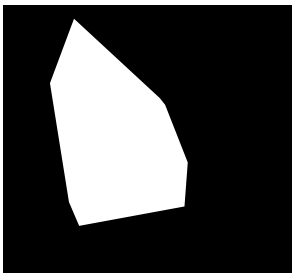

(b) Local scale geometry

that it may be possible to forgo the use of XFEM for this design study.

5 Conclusions

A method for the multiobjective design of energy absorbing materials was presented that uses a GP-based topology optimization method and a multiscale FEM code. Topology was represented using a CSG-like approach, where convex polygons defined by the convex hulls of lists of points were used as primitives and combined with an overlapping function. This approach is flexible in that convex polygons with any number of sides can be combined together generating complicated topologies. Material properties are embedded in the convex polygons as well. A commercially available multiscale FEM code was used that models damage using automatic insertion of cohesive zone elements at the local scale and XFEM at the global scale. Pareto optimal designs were generated for several different cases, including quasi-static and dynamic loadings, with and without local scale cohesive zone insertion, and with and without global scale XFEM insertion.

Future work includes extending the algorithm to 3D designs. The method is easily implemented in 3D as all concepts–convex hulls and CSG–are equally valid in 3D. We also plan to incorporate a hierarchical design scheme, where the global structure is optimized along with the local structure. This can be done again with a homogenous assumption of global scale material properties, or we could enable multiple local scale designs that can be used at the global scale.

Acknowledgments This research was supported by grants of computer time and resources on HPC systems under the Department of Defense High Performance Computing Modernization Program (HPCMP) Challenge Project ARLAP02331C5V.

References

Ahmed F, Bhattacharya B, Deb K (2013) Constructive solid geometry based topology optimization using evolutionary algorithm. In: Bansal JC, et al. (eds) Proceedings of seventh international conference on bio-inspired computing: theories and applications (BIC-TA 2012), Volume 201 of advances in intelligent systems and computing, Berlin, Germany, pp 227–238. Springer-Verlag, Berlin

Allaire G, Kohn R (1993) Optimal-design for minimum weight and compliance in plane-stress using extremal microstructures. Eur J Mech A-Solids 12(6):839–878

Allen D, Searcy C (2001) A micromechanical model for a viscoelastic cohesive zone. Int J Fract 107(2):159–176

Anghileri M, Chirwa E, Lanzi L, Mentuccia F (2005) An inverse approach to identify the constitutive model parameters for crashworthiness modelling of composite structures. Compos Struct 68(1):65–74

Banzhaf W, Nordin P, Keller RE, Francone FD (1999) Genetic programming: an introduction. Morgan Kauffman, Inc., San Francisco

Bendsoe M, Sigmund O (2003) Topology optimization: theory, methods and applications. Engineering Online Library. Springer

Bieri H (1995) Nef polyhedra: A brief introduction. In: Hagen H, Farin G, Noltemeier H (eds) Geometric modelling, Volume 10 of Computing Supplement, pp 43–60. Springer, Vienna

CGAL (2007) Computational Geometry Algorithms Library. http://www.cgal.org

Qi C, Yang S, Yang L-J, Wei Z-Y, Lu Z-H (2013) Blast resistance and multi-objective optimization of aluminum foam-cored sandwich panels. Compos Struct 105:45–57

Chessa J, Smolinski P, Belytschko T (2002) The extended finite element method (XFEM) for solidification problems. Int J Numer Methods Eng 53(8):1959–1977

Chiandussi G, Avalle M (2002) Maximisation of the crushing performance of a tubular device by shape optimisation. Comput Struct 80(27–30):2425–2432

Cohon J (1978) Multiobjective programming and planning. Academic, New York

Cohon JL, Marks DH (1975) A review and evaluation of multiobjective programming techniques. Water Resour Res 11(2):208–219

Deb K, Pratap A, Agarwal S, Meyarivan T (2002) A fast and elitist multiobjective genetic algorithm: NSGA-II. IEEE Trans Evol Comput 6(2):182–197

Duysinx P, Bendsoe M (1998) Topology optimization of continuum structures with local stress constraints. Int J Numer Methods Eng 43(8):1453–1478

Goldberg DE (1987) Genetic algorithms in search, optimization, and machine learning. Addison-Wesley, Reading

Hamza K, Saitou K (2004) Optimization of constructive solid geometry via a tree-based multi-objective genetic algorithm. In: Deb K, et al. (eds) Genetic and Evolutionary Computation Gecco 2004, Pt 2, Proceedings, Volume 3103 of lecture notes in computer science, Berlin, Germany, pp 981–992. Springer-Verlag, Berlin

Huang X, Xie YM, Lu G (2007) Topology optimization of energy-absorbing structures. Int J Crashworthiness 12(6):663–675

Huang X, Zhou SW, Xie YM, Li Q (2013) Topology optimization of microstructures of cellular materials and composites for macrostructures. Comput Mater Sci 67:397–407

Koza JR (1999) Genetic programming III: Darwinian invention and problem solving. Morgan Kauffman, Inc, San Francisco

Guo L, Tovar A, Penninger C, Renaud J (2011) Strain-based topology optimisation for crashworthiness using hybrid cellular automata. Int J Crashworthiness 16:239–252

Main JA, Gazonas GA (2008) Uniaxial crushing of sandwich plates under air blast: influence of mass distribution. Int J Solids Struct 45(7–8):2297–2321

Mei Y, Wang X (2004) A level set method for microstructure design of composite materials. Acta Mechanica Solida Sinica 17(3):239–250

Mozumder C, Renaud JE, Tovar A (2012) Topometry optimisation for crashworthiness design using hybrid cellular automata. Int J Veh Des 60(1–2):100–120

MultiMech Research & Development (2012) MultiMech. http://www.multimechrd.com/

Nguyen VP, Stroeven M, Sluys LJ (2011) Multiscale continuous and discontinuous modeling of heterogeneous materials: a review on recent developments. J Multiscale Model 3(4):1–42

Qiao P, Yang M, Bobaru F (2008) Impact mechanics and high-energy absorbing materials: review. J Aerosp Eng 21(4):235–248

Requicha A, Voelker HB (1977) Constructive solid geometry, TM-25. Technical memorandum. Production Automation Project, University of Rochester

Rueda MAF, Cui L, Gilchrist MD (2009) Optimisation of energy absorbing liner for equestrian helmets. Part I: layered foam liner. Mater Des 30(9):3405–3413

Sethian J, Wiegmann A (2000) Structural boundary design via level set and immersed interface methods. J Comput Phys 163(2):489–528

Sigmund O (1994) Materials with prescribed constitutive parameters - an inverse homogenization problem. Int J Solids Struct 31(17):2313–2329

Sigmund O (1995) Tailoring materials with prescribed elastic properties. Mech Mater 20(4):351–368

Sigmund O (2000) A new class of extremal composites. J Mech Phys Solids 48(2):397–428

Srinivas N, Deb K (1994) Multiobjective optimization using nondominated sorting in genetic algorithms. Evol Comput 2(3):221–248

Souza FV, Allen DH (2010) Modeling failure of heterogeneous viscoelastic solids under dynamic/impact loading due to multiple evolving cracks using a two-way coupled multiscale model. Mech Time-Dependent Mater 14(2):125–151

Souza FV, Allen DH (2011) Modeling the transition of microcracks into macrocracks in heterogeneous viscoelastic media using a two-way coupled multiscale model. Int J Solids Struct 48(22–23):3160–3175

Souza FV, Allen DH (2013) Verification of a two-way coupled multiscale finite element code for dynamic/impact problems. Mech Adv Mater Struct 20(1):74–90

Souza FV, Allen DH, Kim YR (2008) Multiscale model for predicting damage evolution in composites due to impact loading. Compos Sci Technol 68(13, SI):2624–2634

Steuer R (1989) Multiple criteria optimization: theory, computation, application. Krieger, Malabar

Weile D, Michielssen E, Goldberg D (1996) Genetic algorithm design of Pareto optimal broadband microwave absorbers. IEEE Trans Electromagn Compat 38(3):518–525

Wildman RA, Gazonas GA (2009) Gravitational and magnetic anomaly inversion using a tree-based geometry representation. Geophysics 74(3):I23–I35

Wildman RA, Gazonas GA (2011) Genetic Programming-based Phononic Bandgap Structure Design. Technical Report ARL-TR-5733, US Army Research Laboratory

Wildman RA, Weile DS (2007) Geometry reconstruction of conducting cylinders using genetic programming. IEEE Trans Antennas Propag 55(3):629–636

Wildman RA, Weile DS (2008) Greedy search and a hybrid local optimization/genetic algorithm for tree-based inverse scattering. Microw Opt Technol Lett 50(3):822–825

Wildman RA, Weile DS (2010) Inverse scattering of dielectric cylindrical targets using genetic programming. Electromagnetics 30(1–2, Sp. Iss. SI):222–236

Xie Y, Steven G (1993) A simple evolutionary procedure for structural optimization. Comput Struct 49(5):885–896

Xie Y, Steven G (1997) Evolutionary structural optimization. Springer

Xu X, Needleman A (1994) Numerical simulations of fast crack-growth in brittle solids. J Mech Phys Solids 42(9):1397–&

Xu X, Needleman A (1996) Numerical simulations of dynamic crack growth along an interface. Int J Fract 74(4):289–324

Yamagiwa M, Uehara M, Murakami M, Yoneyama M (2010) A reconstruction method for ultrasonic deterioration image by the combination of constructive solid geometry and strongly typed genetic programming. Comput Syst Sci Eng 25(2, SI):161–170

Zohdi T (2002) On the tailoring of microstructures for prescribed effective properties. Int J Fract 118(4):L89–L94

Biographies of ARL Authors

Bryn L. Adams is a molecular microbiologist in the Biotechnology Branch of the Sensors and Electronic Devices Directorate. Her research area focuses on the genetic engineering of bacteria for use in sense-and-respond applications, and is specifically interested in the development of engineered cells for integration into biotech materials and devices. She received her Ph.D. in interdisciplinary biology at the University of North Carolina at Charlotte in 2009. Dr. Adams performed her dissertation work in the civil engineering lab of Dr. Helene Hilger, where she developed a methane-oxidizing bacterial biotarp to mitigate early methane emissions from open landfills. Dr. Adams spent two years as a National Research Council (NRC) postdoctoral fellow, under Dr. James Valdes at Edgewood Chemical Biological Center (ECBC), before continuing as an Oak Ridge Associate Universities (ORAU) postdoctoral fellow at the U.S. Army Research Laboratory (ARL), under Dr. Dimitra Stratis-Cullum. She has authored over 30 articles and presentations on a wide range of biological and engineering topics, and currently holds an invention disclosure for an advanced technical capability she is developing with her fellow team members at ARL.

Jan W. Andzelm serves as the Team Leader of the Multiscale Modeling Team in the Macromolecular Science & Technology Branch at ARL, and is responsible for planning, directing, and performing research to determine properties of materials important for Soldier protection. The team is developing and applying novel computational techniques at quantum mechanical, atomistic, and mesoscale levels aimed at understanding and predicting structural, mechanical, and electronic properties of macromolecules and composite materials. Dr. Andzelm was awarded a Ph.D. in theoretical chemistry from University of Warsaw. He held postdoctoral positions at Edmonton University and later University of Montreal, conducting research in catalysis and developing ab-initio and density functional methods (DFT). From 1987–1991, he was senior computational chemist at Cray Research developing parallel DFT programs capable of optimization of molecular structures. From 1991–2004, he worked at a software company developing computational chemistry programs and conducting research in the field of materials science. In his current position at ARL, Dr. Andzelm is leading several programs in multiscale modeling of mechanical properties of macromolecules and polymer composites under extreme conditions, adsorption and reactions on surfaces of solids, as well as studying electronic structure of nanomaterials. Dr. Andzelm has co-authored over 120 scientific papers and book contributions that attracted 7500 citations total and generated h-index of 36. His research at ARL also led to two patents. Dr. Andzelm has been awarded the 2009 U.S. Army Research and Development Achievement Award, the 2010 ARL Award for Science, the Best Paper Award at the 27th Army Science Conference, and several ARL Director Research Initiative Awards. Dr. Andzelm was selected as a U.S. Army Research Laboratory Fellow in 2010.

Radhakrishnan Balu is a computational scientist with a research focus on application of quantum mechanics to computing, communications, chemistry, physics, and biology. He has been working at ARL since 2007 and uses D-wave system, a quantum annealer, and state-of-the-art quantum mechanics-based software leveraging the high performance computing infrastructure for research. He has over 30 publications, including peer-reviewed journal papers. He has five degrees in science and engineering, with a Ph.D. in computational chemistry from the University of Maryland Baltimore County (UMBC), an M.S in biotechnology from Johns Hopkins University, and a B.S in computer science from the Indian Institute of Science, Bangalore.

Iskander G. Batyrev received his Doctorate degree in solid state physics from Moscow University, Moscow, Russian Federation, in 1995. He worked as postdoctoral researcher at University of Texas, Austin, as research associate at National Renewable Energy Laboratory (NREL), Golden, CO, and as a research professor at Vanderbilt University, Nashville, TN. He started at ARL as an Oak Ridge Associates University (ORAU) senior research fellow in 2008, and was hired in 2010. Dr. Batyrev is a research physical scientist in the Energetic Materials Science Branch, Weapons and Materials Research Directorate of ARL in Aberdeen Proving Ground, MD. He is responsible for initiating, planning, and personally performing research investigations to determine microscopic details of the physical and chemical processes of materials of interest to the U.S. Army, including energetic materials and materials related to armor/armaments. He is a specialist in atomistic simulations of solids, surface/interfaces, and clusters. His research currently focuses on the search for new structures of extended solids, acids, and oxides to predict physical and chemical properties and reactions under extreme conditions.

Richard Becker received a B.S. and M.S. in mechanical engineering from the University of Pittsburgh. His M.S. thesis work on micromechanical modeling of ductile void growth at the U.S. Steel Research Laboratory was continued with modeling and experimental work on ductile fracture at Brown University, where he received his Ph.D. in engineering. Following Brown, he was at the Alcoa Technical Center for 12 years pursuing micro-mechanical modeling of crystallographic texture evolution and anisotropy, thermo-mechanical process modeling, and constitutive model development and implementation. Dr. Becker went to Lawrence Livermore National Laboratory in 1999, where he worked on both the Integrated Codes and the Physics and Engineering Materials aspects of the Advanced Supercomputing Initiative. These efforts involved algorithm and code development, and multi-scale model development and validation for strength and fracture models. Dr. Becker joined ARL in 2009, where he has continued research on material behavior at multiple length scales, and development and implementation of constitutive models in large-scale hydrocodes. Dr. Becker was selected as an ARL Fellow in 2013.

Oleg Borodin works as a scientist at the Electrochemistry Branch of ARL, Adelphi, MD, since 2011. After he obtained a Ph.D. in chemical engineering in 2000, he worked in the area of multiscale modeling of liquid, ionic liquid, and polymer electrolytes for battery and double layer capacitor applications, modeling of energetic composite materials, polymers in solutions, and polymer nanocomposites. He co-authored more than 100 publications and six book chapters. His modeling efforts focus on understanding materials for energy storage applications, the scales from electronic to atomistic, and mesoscale.

John K. Brennan is a research chemical engineer in the Energetic Materials Science Branch, Weapons and Materials Research Directorate of ARL. He is responsible for initiating, planning, and performing computational and theoretical research investigations to determine the physical and chemical processes of materials of interest to the Army at both the atomistic and coarse-grain levels. Dr. Brennan's duties include leading ARL's coarse grain modeling efforts to study the multiscale response of energetic materials. Dr. Brennan received a Ph.D. in chemical engineering from Wayne State University in 1999, with an emphasis in Polymer Engineering. Dr. Brennan then was a research associate at the Institut de Recherché sur la Catalyse (CNRS) in Lyon, France, with Wei Dong, where he carried out modeling studies of the behavior of fluids in nanoporous materials. He went on to another research associate position with Keith E. Gubbins at North Carolina State University, where he performed simulation studies of the behavior of chemical reactions in nanoporous materials. Dr. Brennan has over 50 peer-reviewed publications, a book chapter on coarse-graining, and over 45 presentations at national and international conferences.

Edward F. C. Byrd received his B.S. in chemistry from Duke University in 1996, before continuing his education and receiving his Ph.D. in 2001 from the University of California, Berkeley. He subsequently joined ARL in January 2002 as a National Research Council postdoctoral fellow and was hired to a government position in 2004. Dr. Byrd has received multiple awards for his research, such as an ARL Award for Performance (2009), an Army Research and Development Achievement Award for Technical Excellence (2008), an ARL Award for Publication (2007), and best paper of the Multifunctional Energetic Materials Session of the Materials Research Society Symposium (2006). Dr. Byrd was an invited speaker at the 2012 Energetic Materials Gordon Research Conference and has over 31 open literature publications cited in excess of 2800 times. Dr. Byrd has been active in developing computational screening tools that will allow for prediction of properties associated with performance and sensitivity for notional energetic materials, as well as atomistic modeling of energetic and protection materials. He is responsible for initiating, planning, and personally performing research investigations to determine microscopic details of the physical and chemical processes of energetic materials of interest to the Army.

Tanya L. Chantawansri is currently a staff scientist at the U.S. Army Research Laboratory (ARL) at the Macromolecular Science and Technology Branch (MSTB) of the Materials and Manufacturing Division of the Weapons and Materials Research Directorate (WMRD). She received her Ph.D. in chemical engineering from University of California, Santa Barbara, prior to joining ARL as a postdoctoral research in April 2009. She has extensive experience in polymer modeling using both atomistic and mesoscale techniques, where she focuses on predicting the mechanical properties of glassy, rubbery, and/or phase-separated polymers under extreme conditions of pressure and strain rates. In addition to being the point of contact (POC) for several internal ARL projects, she is also overseeing the integration of the polymer portion of the MEDE program with other internal Mission projects at ARL, polymer software development at ICB, and she also works closely with Army Research Office (ARO) grant recipients at the University of Texas.

Chiung-Chu Chen earned her Ph.D in Environmental Science from New Jersey Institute of Technology in 2000. She continued her research with Prof. Joseph W. Bozzelli at NJIT and became a contractor in ExxonMobil Research and Engineering Company at Annandale, NJ. She came to ARL as a NRC/ORAU research associate in 2006 and was hired as a staff member in 2009. As a member of ARL's Propulsion Science Branch, Dr. Chen is the technical lead for the development of chemical kinetics mechanisms needed to model the combustion chamber dynamics of missile propulsion systems. Employing computationally based methods to characterize potential energy surfaces upon which species involved in the combustion of hypergolic fuel-oxidizer bi-propellants and energetic materials react, and converting those results to reaction rate constants for individual steps of reaction pathways, she develops full, multi-step, chemical kinetics reaction mechanisms for specific advanced propellant formulations. She then validates them by demonstrating their ability to simulate experimental research. Most of the work is devoted to developing chemical kinetics reaction mechanisms for use in a computational fluid dynamics (CFD) model for simulation of a hypergolic propulsion system technology being developed by the U.S. Army Aviation and Missile Research, Development and Engineering Center (AMRDEC). Dr. Chen has over 15 co-authored refereed journal articles and has been nominated for an Army RDA award in 2010.

John D. Clayton has been a technical staff member at ARL since 2003, and is presently team leader of the Multi-Scale Mechanics Team in the Impact Physics Branch of Weapons and Materials Research Directorate (WMRD). He obtained his Ph.D. from the Georgia Institute of Technology in 2002, and conducted graduate research at Sandia National Laboratories. Research areas

include theoretical and computational mechanics of solids, shock physics, and differential-geometric modeling of crystal structures. He has authored or co-authored around 50 journal articles and two books (Springer, 2011; World Scientific, forthcoming 2014). Honors include the ARL Award for Publication (2011), five ARL Director's Research Initiative (DRI) awards, and the National Research Council (NRC) Post-Doctoral Fellowship. He currently serves on the editorial board of two international journals, has guest edited two other journals, and has advised several post-doctoral scholars and Ph.D. students. He is a member of the American Academy of Mechanics, American Physical Society, and American Society of Mechanical Engineers.

Joshua C. Crone received his B.S. and M.S. degrees in mechanical engineering from the University of Maryland, College Park, in 2007 and 2008, respectively. He joined the Simulation Sciences Branch of the Computational and Information Sciences Directorate (CISD) at ARL as summer intern in 2006, and joined the staff full-time in 2008. His research interests are in developing computational algorithms for high performance computing, with an emphasis on multiscale materials modeling. Mr. Crone has been involved in developing physics-based modeling capabilities, ranging from a real-space quantum mechanics to an integrated suite of tools to model under-body blast from initiation to personnel injury assessment. He is currently developing a finite element-based discrete dislocation dynamics (FED3) algorithm, which is designed to model dislocation evolution in finite domains and microstructured materials. He has authored or co-authored 11 publications, and presented at several national and international conferences.

Amethist (Amy) S. Finch is a research chemist in the Biotechnology Branch of ARL. Dr. Finch received her B.A. in Chemistry and Biochemistry in 2000 from Whittier College and her Ph.D. in Chemistry in 2008 from the University of Maryland, College Park. During her tenure at the University of Maryland, Dr. Finch was awarded the Department of Defense (DOD) Science, Math, and Research for Transformation (SMART) Fellowship. Her dissertation focus and research interests include science at the interface of chemistry and biology. The SMART fellowship allowed her to join ARL in 2008 and transition her research interests directly in to the DOD. Dr. Finch has presented her work at numerous national and international conferences and is the lead author or coauthor on over 30 peer-reviewed publications, reviews, and book chapters. She has also authored numerous ARL technical reports.

George A. Gazonas is a research physicist at ARL, where he leads several programs in multiscale modeling of materials, including interdivisional research efforts in transparent aluminum oxynitride (AlON) and non-crystalline ceramics (glass). For over a decade, he has served as a senior research advisor for the National Research Council of the National Academies, a program through which he has stressed communication and outreach to young scientists by mentoring multiple visiting researchers and professors at ARL; he advised/mentored two consecutive Davies Fellows with joint appointments at ARL and the United States Military Academy. With over 35 years experience in the fields of computational mechanics, homogenization methods for fractured media, geophysical inverse methods, and wave propagation in solids, Dr. Gazonas is an internationally recognized expert in the field of computational mechanics with invitations to speak at numerous international conferences. He is a member of the American Geophysical Union, American Society of Mechanical Engineers, and the United States and International Associations for Computational Mechanics, and is an active spokesperson for the organization with over 200 technical presentations at international, inter-laboratory, and inter-agency governmental groups, and author/co-author of over 120 archival journal and book publications, government reports, and peer-reviewed proceedings publications. Gazonas received his Ph.D. in geophysics from Texas A&M University in 1985, and joined the Ballistic Research Laboratory in 1989, after working in the oil and gas industry as chief geophysicist for Hunter Geophysics, Santa Clara, CA; at Hunter, he co-pioneered (with M.D. Wood) the use of a tiltmeter data acquisition/telemetry system, which was coupled to a nonlinear inversion program he developed, that enabled real-time subsurface mapping of hydraulically induced fractures in secondary oil and gas recovery operations throughout the U.S. and Canada.

Alex J. Hsieh received his Ph.D. in materials science and engineering from the Massachusetts Institute of Technology (MIT) and is currently a member of the Macromolecular Science and Technology Branch of the Weapons and Materials Research Directorate (WMRD) at ARL. His research work includes structure-property characterization of transparent glassy amorphous polymers, and his prior findings on dynamic strain hardening characteristics of poly(methyl methacrylate) had transitioned and led to the development of a state-of-the-art ARL Multi-Hit Transparent Armor design and a patent disclosure (ARL Docket #04-40; Parimal Patel, Hsieh and Gary Gilde). Dr. Hsieh had also initiated and completed a very successful FY11/12-DRI program, through a well-coupled multiscale modeling (in collaboration with Dr. Tanya L. Chantawansri) and multiscale characterization approach, where he has instrumentally demonstrated new insight regarding the role of microstructure-mediated segmental dynamics and pathways for the rational design of responsive, hierarchical elastomers with the potential for enhanced ballistic impact protection, shock waves mitigation, and chemical defense for next-generation soldier protective systems. An ARL patent application (ARL Docket #13-03) was completed and filed (S/N 14/022,837) on September 10, 2013. Dr. Hsieh has also served as visiting scientist at the Institute for Soldier Nanotechnologies (ISN) to leverage collaboration with ISN faculty and research staff, as well as new partnerships with the ISN Industry members for technology transition.

Margaret M. Hurley received a B.S. degree with distinction in chemistry from Clarkson University, Potsdam, NY, in 1986, and a Ph.D. degree in chemistry from the Ohio State University, Columbus, OH, in 1992. Dr. Hurley was an Australian research fellow at the University of Sydney, Australia, and a postdoctoral research fellow at the University of Notre Dame before beginning work at ARL, Aberdeen, MD, a Major Shared Resource Center. There she was a contractor in the Director of Computational Chemistry and Materials for the programming environment and training program. She then joined ARL in 2000, and is currently a research physical chemist with the biotechnology branch of the Sensors and Electronic Devices Directorate (SEDD) of ARL. From 2001-2005, Dr. Hurley served as a portfolio manager for the DoD High Performance Computing Modernization Program, common high performance software support initiative portfolio on Materials by Design. Dr. Hurley is a member of the American Chemical Society, American Physical Society, and Gamma Sigma Epsilon National Chemistry Honor Society, and serves on the Scientific Advisory Board for the Aberdeen Science and Math Academy. She is the author of over 30 publications, two reviews, and two book chapters, and has been cited over 800 times. Dr. Hurley has received three department of the Army RDA awards, a 2010 ERDC RDA award, a 2009 L.R. Schaffer RDA award, and three department of the Army Official Commendations.

Sergiy Izvekov is a Physical Scientist who joined the Weapons and Materials Research Directorate at ARL in April 2009. Izvekov holds a Ph.D. in Physics from National University of Kiev (Kiev, Ukraine). Dr. Izvekov has authored 67 articles in peer-reviewed journals (over 2400 citations), four book chapters, and numerous presentations at national and international conferences. Dr. Izvekov received the 27th Army Science Best Paper Award in "Advanced High Performance Computing in Physical Science and Engineering." He was co-recipient of a 2012 Research and Development Award for work titled, "Atomistic and Sub-Grain Modeling of Energetic Materials." Dr. Izvekov is a member of American Chemical Society.

Shashi P. Karna is a senior research scientist for Nanomaterials at ARL, Weapons and Materials Research Directorate (WMRD), where his duties include conducting fundamental research in the area of nanomaterials, serving as the U.S. Army's subject matter expert in Nanotechnology, advising Senior Army and ARL Leadership on research opportunities, policies, and investment strategies; mentoring young scientists, identifying emerging areas of scientific research relevant to Soldier Technologies, and developing research programs involving in-house and collaborative efforts. His current research is focused on theory, modeling, synthesis, and characterization of hybrid nano and bio-nano materials to develop a fundamental understanding of their structure-function-property relationships and application concepts for Army's current and future technologies. Dr. Karna has co-edited three books, including the Defense Applications of Nanomaterials, and has published seven book chapters, three technical magazine articles, and 140 archival journal papers, and over 200 conference proceeding and articles. Dr. Karna is an ARL Fellow and an elected Fellow of the American Physical Society and the Optical Society of America. He is also an active senior member of the Institute of Electrical and Electronics Engineers, a member of the American Chemical Society, the American Association for the Advancement of Science. From 2004–2006, he was the U.S. member of the NATO Exploratory Team on Smart Textiles for the NATO Warfighter, and currently serves as the chair of the NATO Sensors and Electronics Technology (SET) Technical Group on Smart Textiles for the NATO Warfighter. Dr. Karna holds an adjunct professor position at Michigan Technological University (MTU), Houghton, MI, and at Morgan State University, Baltimore, MD, and serves on the External Advisory Board of the Mechanical Engineering-Engineering Mechanics Department of MTU, on the Basic Research Review Board of U.S. Army Natick Soldier Center, and at the U.S. Department of Energy, Office of Basic Energy Sciences, Energy Frontier Research Centers Review Panel.

Jaroslaw Knap is a staff scientist with the Computational and Information Sciences Directorate (CISD) of ARL. He received his Ph.D. in mechanical engineering from the Arizona State University in 1998. His research interests include computational mechanics, multi-scale materials modeling, and scientific computing.

Anthony J. Kotlar received a B.S in chemistry from St. Joseph's College (Philadelphia, PA) in 1971, an M.S. in organic chemistry from the University of Delaware in 1974, where he also completed ROTC and was commissioned a 2nd lieutenant in the Army, and a Ph.D. in physical chemistry from the Massachusetts Institute of Technology in 1978. He then spent two years as a 1st lieutenant at the Ballistic Research Laboratory (BRL) doing research in spectroscopy and combustion diagnostics. He remained at the BRL (now ARL) as a civilian employee until the present. In 2001 he received an M.A. in Theology from St. Mary's Seminary and University (Ecumenical Institute of Theology). His current research at ARL is in thermodynamics, chemical kinetics, energetic material performance and data analysis and experimental modeling.

Richard B. Leavy started working as a researcher at the Ballistic Research Laboratory in 1991, following completion of a B.S. degree in physics from Loyola College. Initial work as a contractor in the Engineering Physics Branch included research in sensors, active protection, and electromagnetic gun programs. Shortly thereafter, he transferred to the Armor Mechanics Branch and began work in armor design. Mr. Leavy was involved in the initial testing of encapsulated ceramics, as well as conventional armor programs for a variety of Army armored vehicles. Leavy took a brief hiatus in 1995 to become an Air Force pilot; he currently holds the rank of Major. Upon completion of the training, Brian was brought back with ARL as a government employee in 1998. In 2001, he completed a M.S. degree in computer science from Towson University, and he is currently pursuing a Ph.D.

in computational solid mechanics at the University of Utah. As a member of the Impact Physics Branch, Mr. Leavy is working on modeling ceramics in a variety of codes, as well as developing new armor technologies and experimental methodologies.

Kenneth W. Leiter has been a computer scientist at ARL since 2011. His research interests focus on the development of computational algorithms for large scale high performance computing, focusing on the formulation of adaptive numerical algorithms for multiscale materials modeling. He received a B.S. in chemistry and B.A. in computer science from Duke University in 2008.

Bryan M. Love received his B.S. and M.S. degrees in mechanical engineering from North Carolina State University in 1999 and 2001, respectively; and his Ph.D. in engineering mechanics from Virginia Polytechnic Institute and State University (VA Tech) in 2004. He joined ARL in 2005, and is currently a team leader in the Materials Response and Design Branch. His research interests are broadly characterized as the dynamic deformation of materials, particularly experimental and computational mechanics to accurately characterize failure of materials during dynamic events.

Up until his retirement on May 31, 2013, **James W. McCauley** was ARL senior research engineer (ST) in ceramics (chief scientist in Materials); he is now in an emeritus/guest researcher position at ARL. He earned his B.S. (cum laude) in geology from St. Joseph's College (Indiana) in 1961, his M.S. in mineralogy in 1965, and Ph.D. in solid state science (crystallography) in 1968, both from the Pennsylvania State University. From 1990–1994, he served as Dean (SUNY Chief Administrative Officer) of the New York State College of Ceramics at Alfred University, and from January 1995–June 1996, he was Professor of Ceramic Engineering. Prior to joining Alfred, he worked at the Army Materials Technology Laboratory for 22 years, serving as founding chief of the Materials Characterization Division and Materials Science Branch, and as liaison scientist, Army Research Office, Far East, Tokyo, Japan, during 1988. He is the author or co-author of 154 open literature publications and reports, has presented 260 oral presentations, was the editor/co-editor of eight books, and holds five patents. He has served on the Army Science Board, the external review committee for the Materials Science and Technology Division of Los Alamos National Laboratory, and on the Visiting Advisory Board of the Department of Materials Science and Engineering of Drexel University. Dr. McCauley is the inventor and name originator of Aluminum Oxynitride Spinel (AlON), a transparent armor and RADOME material. He has been actively involved with the initiation of the Collaborative Research Alliance in "Materials in Extreme Dynamic Environments" and the sponsor of the National Research Council study on "Opportunities in Protection Materials Science and Technology for Future Army Applications". A Fellow and Distinguished Life Member of the American Ceramic Society, he is a past President of the Society and the co-founder of the International Journal of Applied Ceramic Technology. He has been named an Academician of the World Academy of Ceramics, and is a winner of several awards from Penn State and from the National Research Institute in Materials, Japan, and from the Russian Academy of Sciences. He has also won the FY 2007 Senior Scientific-Professional (ST) Employee Presidential Rank Award. He is a past chair of the ARL Fellows and the Army ST Corps.

Michael J. McQuaid is a Research Physical Scientist in the Propulsion Science Branch of the Weapons and Materials Research Directorate. He graduated with distinction from the University of Virginia in 1979, receiving a B.S. in Chemical Engineering. He then worked for four years as a fluid systems design engineer, resolving issues related to operating Nimitz-class aircraft carrier power plants. He subsequently attended Georgia Tech and received his Ph.D. in Physics. He came to what is now ARL as an NRC postdoctoral research associate in 1989, and was hired as a staff member in 1991. Since that time, Dr. McQuaid has been involved in a variety of experimental and theoretical research efforts designed to understand energetic material ignition and combustion. Over the past eight years, his research has focused on using computational quantum chemistry to understand the reaction mechanisms underlying propellant ignition and combustion, and to predict performance-dictating properties of notional energetic materials. He has also developed chemical kinetic mechanism reduction techniques. He has been awarded three Army Research & Development Achievement Awards and two U.S. patents. He has authored or co-authored 24 open literature publications and 38 ARL technical reports.

Lynn B. Munday has been a mechanical engineer in the Simulation Sciences Branch of the Computational Sciences Division within the Computation and Information Sciences Directorate (CISD), since joining ARL in 2011. His research interest is in solid mechanics, especially computational models for inelastic deformation. He is currently working on a coupled finite element—discrete dislocation dynamics simulation tool to model dislocation induced plasticity of heterogeneous materials. His doctoral research was on atomistic models of dislocation motion and nucleation in the energetic molecular crystal RDX. He received a Ph.D. (2011) from the University Of Maryland, an M.S. (2005) from the University of New Mexico, and B.S. (2002) from Montana State University, all in mechanical engineering.

Michael J. Nusca earned his Ph.D. in aerospace engineering from the University of Maryland in 1997. His thesis research focused on the integration of real gas, high temperature, reacting flow physics into high-fidelity computational fluid dynamics (CFD) codes. He is an Associate Fellow of the AIAA, Baltimore Section AIAA Engineer of the Year (2006), Sustained Superior Service Award recipient from JANNAF (2006), Superior Civilian Service Award recipient (2007), Assoc. Ed. of the JANNAF Journal for Propulsion and Energetics, and chairman of the JANNAF Combustion Subcommittee. Dr. Nusca has been with ARL for over 25

years and is the subject-matter expert (SME) for the development and application of multi-dimensional, multiphase, CFD models for combustion in solid propellant gun charges. He is credited with co-development of the Next-Generation interior ballistics code that lead to breakthrough investigations of the U.S. Army's Modular Artillery Charge System for 105/155mm Army cannon. He received an Army Material Command Research and Development Award (RDA) in 2001 for this work, and then in 2003/2009 for coupling the code to structural dynamics codes, predicting projectile response to high-g launch. Dr. Nusca is also the SME for the development and application of multi-dimensional, multiphase, reacting-flow CFD models that numerically model combustion, including instabilities, in small rocket engines fueled with liquid or gelled hypergols and used in tactical as well as strategic missiles. For this work he received RDAs in 2006, 2007, and 2012. Dr. Nusca regularly teams with the U.S. Army Armament (ARDEC) and Aviation & Missile Research Development and Engineering Center (AMRDEC) as well as international research groups (TTCP).

Betsy M. Rice serves as the leader of the Multiscale Reactive Modeling Team in the Energetic Materials Science Branch at ARL, and is responsible for initiating, planning, and personally performing research investigations to determine microscopic details of the physical and chemical processes of materials of interest to the Army, including energetic materials and materials related to armor/armaments. Dr. Rice's expertise lies in the theoretical chemistry areas of classical molecular simulation and quantum mechanical molecular characterization directed toward advanced modeling of materials that are critical components of several DoD weapons and S&T mission areas. Dr. Rice earned a B.S. in chemistry from Cameron University in Oklahoma in 1984, and was awarded a Ph.D. in chemistry from Oklahoma State University in 1987. She held a postdoctoral position in 1988 with Chemical Dynamics Corporation before joining the Army research community in 1989, first as a National Research Council (NRC) Postdoctoral Research Associate, then as a staff member in 1990 with the predecessor organization of ARL, the Ballistic Research Laboratory. Dr. Rice has authored more than 80 open literature publications in chemical physics journals. She has also written 11 invited book chapters on molecular simulations of energetic materials. She was the recipient of the 1999 and 2007 ARL Award for Publication, both of which detail her activities to predict properties of energetic materials related to their performance in weapons systems or their sensitivity to shock impact. She was also awarded the 1997, 2003, and 2008 Army Research and Development Achievement (RDA) Awards for molecular simulations of energetic materials, as well as the 2012 RDA Award for Technical Leadership.

Deborah A. Sarkes received her B.A. in biochemistry and molecular biology, and M.A. in biotechnology (summa cum laude) from Boston University in 2005, in a dual-degree program. She worked with Dr. Lucia Rameh for seven years at Boston Biomedical Research Institute (BBRI) studying phosphoinositides and lipid kinases as they relate to diabetes and cancer, with a first0author publication regarding a novel HPLC method for separating the lipids PI-5-P from PI-4-P. While at BBRI, she also collaborated with the Structural Biology Department of Pfizer RTC, successfully forming protein crystals of PIP4K II isoforms. She joined ARL in 2010 as a contractor for the Sensors and Electron Devices Directorate (SEDD), contributing to several publications. She currently conducts research for the Biomaterials Team of the Biotechnology Branch at ARL, with particular emphasis on protein mutation and purification by FPLC, ELISA assay development, bacterial peptide display, directed evolution and FACS analysis of binders to various biological and material targets.

The objectives of **Yelena R. Sliozberg's** research is to develop multi-scale computational tools to understand critical phenomena that can control properties of macromolecules and enable rational materials design for soft materials. Dr. Sliozberg performed simulations of soft polymers and proteins by means of particle and mean-field methodologies (atomistic, coarse-grained molecular dynamics, dissipative particle dynamics and slip-link model), using commercial and in-house developed computer codes. Results of these studies have been presented at several conferences and published in multiple peer-reviewed journals, proceedings and technical reports. She received her B.S. and M.S. in chemical engineering from D. Mendeleev University of Chemical Technology of Russia in 1994. During her graduate studies at Drexel University Philadelphia (2002-2008), Dr. Sliozberg modeled thermodynamics of the protein folding inside the chaperonin central cavity and studied mechanism of conformational changes of the E. Coli chaperonin GroEL through its reaction cycle.

Timothy W. Sirk is a researcher in the field of computational materials science at ARL. He began his research career at ARL in 2010 as an ORISE postdoctoral fellow working with Jan Andzelm in the Macromolecular Science and Technology Branch. Tim has investigated the mechanics and structure-property relationships of polymers at extreme conditions through the use of a variety of particle-based simulation methods, including atomistic molecular dynamics, Monte Carlo, coarse-graining, and dissipative particle dynamics. His current interests focus on the development of atomistically-informed computational methods that bridge length and timescales to connect with experiments. Prior to joining ARL, Tim earned his Ph.D. in 2009 from the Mechanical Engineering department at Virginia Tech, where he used molecular simulations to relate the chemical structure of tea antioxidants to their anti-bacterial and anti-carcinogenic properties.

Dimitra Stratis-Cullum leads the biomaterials team at ARL. This interdisciplinary research program focuses on developing new tools for understanding the biomolecular peptide recognition and bio(molecular)materials discovery. Dr. Stratis-Cullum received

her Ph.D. in chemistry from the University of South Carolina. She joined the ARL in Adelphi, MD, in 2002 after completing a postdoctoral fellowship at U.S. Department of Energy Oak Ridge National Laboratory. She has 17 years experience as an analytical chemist, including 11 years on enabling technologies for chemical and biological detection with emphasis on novel transduction and synthetic molecular recognition technologies. Her scientific advances are evidenced by 96 open literature publications and several invention disclosures. These publications have been favorably cited more than 730 times. In recognition of her fundamental and applied research in synthetic recognition materials for threat sensing applications, Dr. Stratis-Cullum recently received the 2012 Army Research and Development Achievement Award.

DeCarlos E. Taylor received his Ph.D. in quantum chemistry from the Quantum Theory Project, University of Florida in 2004. His thesis work focused on development of coupled cluster methods, many body perturbation methods, and creation of accurate semiempirical quantum chemistry Hamiltonians, enabling accurate molecular dynamics simulations of condensed phase materials. He currently supports multiple ARL core and customer research programs focused on multiscale modeling of energetic materials, protection materials, and chemical warfare agents. His research responsibilities include the design, execution, and management of innovative computational research programs, enabling a fundamental understanding of the underlying physics and chemistry of materials subjected to high-strain environments for both lethality and protection.

Mark A. Tschopp is currently appointed as a materials engineer at ARL in the Lightweight and Specialty Metals Branch of the Weapons and Materials Research Directorate. He obtained an M.S. in metallurgical engineering from the Missouri University of Science and Technology in 1999, where his research on defect formation mechanisms in lost foam casting won the Best Paper Award at the American Foundry Society conference. He obtained a Ph.D. in materials science and engineering from the Georgia Institute of Technology, where his atomic scale research into grain boundary and dislocation interactions received several awards, including the Sigma Xi Best PhD dissertation award. Before joining ARL in 2012, Dr. Tschopp spent four years in the Advanced Materials Development Center and the Casting Development and Validation Center at General Motors Powertrain, two years in material sustainability and mechanics within the Life Prediction and Behavior group within the Metals branch at the Air Force Research Laboratory, and over four years as faculty at Mississippi State University. Dr. Tschopp has authored or co-authored over 100 journal papers, book chapters, conference papers, and technical reports, with over 60 papers in peer-reviewed materials science and solid mechanics journals. At present, he has been either the author or co-author on over 100 presentations and seminars at national/international conferences and universities, including over 50 invited and keynote talks. His research has been featured on the covers of two journals and in popular press. Dr. Tschopp's current research interests lie in developing, utilizing, and integrating computational and experimental techniques to design materials for lightweight vehicle applications, soldier protection systems, and lethality applications in support of the Warfighter and the mission of the U.S. Army.

Eric D. Wetzel is the Multifunctional Materials team leader at ARL, and is ARL's technical area manager for Materials for Soldier Protection. His research interests span a range of topics, including ballistic textiles, multifunctional composite materials, bio-inspired materials and systems, and power and energy materials. Dr. Wetzel has co-authored over 40 peer-reviewed journal publications and book chapters, 60 conference proceedings articles, and holds 11 patents. Dr. Wetzel has served on review and advisory panels for the Army Research Office (ARO), Air Force Office of Scientific Research, the National Aeronautics and Space Administration (NASA), the Petroleum Research Fund, the National Science Foundation, and the National Institute of Justice. In 2002, Dr. Wetzel's research on shear thickening fluid (STF)-treated protective fabrics was awarded the U.S. Army Paul A. Siple award.

Raymond A. Wildman is a materials research engineer with ARL since 2010. He received the Ph.D., M.E.E, and B.E.E in electrical engineering from the University of Delaware in 2008, 2005, and 2003 respectively. While at the University of Delaware, Dr. Wildman researched and developed improved methods for solving time domain integral equations of electromagnetic scattering in the microwave regime. Also, he developed topology optimization methods for the inverse scattering of conducting objects and inhomogeneous dielectrics. Dr. Wildman joined ARL in 2007 as a post-doctoral researcher, initially working on topology optimization methods for the design of phononic bandgap materials and the inversion of buried structures from their gravitational and magnetic fields. Since then, he has researched peridynamics-based methods for the fracture simulation of brittle elastic solids. Dr. Wildman is a member of the Tau Beta Pi and Eta Kappa Nu engineering honor societies.

Kang Xu has been researching electrolyte materials and interphasial chemistry in electrochemical devices, especially Li-ion batteries, for over 20 years. His research interests cover materials development and interphasial mechanisms for electrochemical energy storage devices, including batteries and capacitors. He has been recognized four times by R&D Achievement Awards from the Department of the Army (1999, 2001, 2002, and 2011), an ARL Publication Award (2005), an ARL Science Award (2011), and the Army Science Conference Best Paper Award (2008). He also received a Citation for Leadership Excellence in DDR&E 2008 Wearable Power Prize Competition (2008), and won "Top 10 Hottest Technologies Contest of DoD" (2011). His work on the "5 V Li-ion battery" was featured as cover story in "Army AL&T" magazine. He has published over 120 papers in peer-reviewed journals, written/edited three chapters/books, and currently holds 18 issued U. S. patents. His publications have

received over 6800 citations in the open literature, with an h-index of 46. He is an active member of the Electrochemical Society and Materials Research Society, and often serves in various academic/governmental/industry panels as an expert in energy storage technology and materials.

Chian-Fong Yen has been with ARL for more than 10 years. He received his Ph.D. and M.E degrees in Engineering Mechanics from the University of Florida and a B.S. degree in civil engineering from the Chung Yuan University, Taiwan. He is a senior program manager and principal investigator in the DoD research and development environment with a proven track record in winning proposals and managing successful programs. Dr. Yen is a multi-disciplined engineer with a wide range of experience in multi-scale material characterization and modeling, dynamic simulation, design and analysis of advanced composite and metallic materials and structures. He also has extensive experience in simulation and design of advanced protection systems against ballistic and blast threats. His current interests include: development and application of design methodologies and innovative concepts for composite materials and vstructures under extreme loading conditions, development and implementation of progressive failure and durability material models for various composite and ceramic systems, design and fabrication of composite and metallic systems for DoD protective applications. He has published over 100 journal articles, reports and conference papers.


U.S. ARMY
RDECOM®